Title
Structure, Mixing, and Dynamics of Controlled Single and Coaxial Jets in Crossflow

Author
Harris, Elijah Weston

Publication Date
2020

Peer reviewed|Thesis/dissertation

UNIVERSITY OF CALIFORNIA

Los Angeles

Structure, Mixing, and Dynamics of Controlled Single and Coaxial Jets in Crossflow

A dissertation submitted in partial satisfaction

of the requirements for the degree

Doctor of Philosophy in Aerospace Engineering

by

Elijah Weston Harris

2020

ABSTRACT OF THE DISSERTATION

Structure, Mixing, and Dynamics of Controlled Single and Coaxial Jets in Crossflow

by

Elijah Weston Harris
Doctor of Philosophy in Aerospace Engineering
University of California, Los Angeles, 2020
Professor Ann R. Karagozian, Chair

This dissertation describes an experimental study of the instability, structural, dynamical, and mixing characteristics of jets in crossflow (JICF). Constituent species of the jet fluid were nitrogen and helium, with additional seeding of tracer particulates for implementation in non-intrusive laser diagnostics of acetone planar laser induced fluorescence (PLIF) imaging, and particle image velocimetry (PIV). Various jet-to-crossflow momentum flux ratios in the range of $61 \leq J \leq 5$ were investigated for three alternative flush mounted circular contracting nozzle injector configurations: a small nozzle ($D = 4.04\ mm$) passively augmented by a small triangular tab placed about the jet exit periphery, a large nozzle ($D = 7.59\ mm$) actively augmented by axisymmetric excitation of the jet flow, and a coaxial nozzle ($D = 3.81\ mm$) with varying degrees of counterflow applied in the outer annulus. Hotwire anemometry was implemented for investigations of the instabilities along the upstream and downstream shear layers of the jet flow, in addition to more in depth analysis of the dynamics of the flow from application of time series analysis techniques to the signal. PLIF imaging served to characterize the JICF by providing qualitative visualizations of the flowfield, and quantitative measurements of the scalar field concentrations and mixing metrics, along both the

centerplane and cross-sectional planes of the developing jet. PIV provided determination of the velocity and vorticity fields, along with further investigation of the flow dynamics from proper orthogonal decomposition (POD) analysis, again from both the centerplane and cross-sectional planes of the developing jet.

Flow conditions corresponding to a naturally absolutely unstable (AU) upstream shear layer (USL) ($J = 7$) and a convectively unstable (CU) condition ($J = 61$) with jet Reynolds numbers of $Re_j = 2300$ were explored for PLIF imaging of the tabbed JICF. Tab location was seen in some cases to significantly alter shear layer instabilities, especially for the case with $J = 7$. Yet acetone planar laser induced fluorescence (PLIF) imaging revealed that more substantive structural changes could be realized with tab placement for the case where $J = 61$. Tab locations with the greatest influence appeared to be consistent with wavemaker regions predicted in numerical simulations of the round transverse jet by Regan and Mahesh (2019), providing evidence for the potential to tailor local shear layer rollup, jet structure, and mixing via simple passive geometrical alterations. For the PIV imaging different J values were explored, ranging from naturally AU USL, for $J = 5$ and 8, to naturally CU conditions, for $J = 20$ and 41, with $Re_j = 1900$. Placement of the tab at or near the upstream region of the jet exit caused a delay in shear layer rollup and, as quantified from the PIV, a reduction in USL vorticity associated with a thickening of the upstream jet momentum thickness. Tab placement was observed to have a symmetrizing influence on nearfield cross-sectional vorticity dynamics at high and low J values, though specific tab locations had differing degrees of influence for different flow conditions. Proper orthogonal decomposition (POD) modes extracted from centerplane velocity field measurements showed significant influence of tab placement on jet upstream as well as wake structures, depending on J. Phase portraits extracted from POD mode coefficient plots produced periodic (circular) shapes for tab placement corresponding to conditions for which the USL was determined to be absolutely unstable.

Flow conditions corresponding to a naturally AU USL ($J = 7$) and a CU condition

($J = 10$) with $Re_j = 1800$ were explored for PLIF imaging of the axisymmetrically excited JICF. Implementation of a novel double-pulse waveform demonstrated significant enhancement of the quantified jet mixing, where the most significant alterations was seen for forcing waveforms which generated nearfield vortical interactions and breakdown. The same forcing waveform yielded differences between the AU and CU jets resulting from changes to the formation number of the vortex rings as suggested by Sau and Mahesh (2010), which resulted in alterations in the celerity, circulation, and nearfield interaction of said vortex rings. Separate investigations treated a jet with a stronger AU USL ($J = 6$) to comparing the novel double-pulse forcing with sinusoidal and square wave excitation of the jet. Synchronization analysis demonstrated dramatic improvement in the ability of the jet to lock-in to the forcing when a square or double-pulse waveform was implemented. Additional Van der Pol oscillator modeling of Fourier approximated square wave forcing suggested greater significance was seen in the proximity of the harmonics to the natural instability of the jet compared to the actual coherence of the waveform, analogoous to findings by Sau and Mahesh (2010). Interestingly, PIV-based POD further suggested the nearfield dynamics and efficacy of mixing were heavily dependent upon the vortex rings which were formed, in some cases quite independent of the state of synchronization to the applied forcing. Application of a quasiperiodic forcing significantly improved the mixing without significantly altering the jet structure.

For the coaxial JICF, a single flow condition corresponding to a CU USL with a naturally highly asymmetric cross-section ($J = 41$), at $Re_j = 1900$, was explored with PLIF and PIV imaging. Suction was applied locally in the upstream and downstream edges of the jet in order to alter the jet shear layer instabilities and vortex dynamics. Indeed, hotwire based spectral characteristics along the USL demonstrated the jet transitioned to an AU flow with strong suction upstream. PIV-based POD also depicted significant enhancement of mode structures along the USL of the jet. Hotwire spectral measurements detected little alteration to the USL with suction applied in the downstream of the jet, where the jet remained CU even

with strong suction. However, PIV-based POD dynamics depicted significant enhancement of structures downstream which resembled upright wake vortices, and appeared coupled with the vortex rollup along the downstream of the jet. Interestingly, the corresponding cross-sectional CVP structure was made quite symmetric with the suction applied both upstream or downstream of the jet, suggestive that the suction applied along the symmetry plane of the jet was able to overcome the jet's natural susceptibility to asymmetric perturbations (Alves et al. (2008)), and further supported the suggested wavemaker region for a CU jet purported by Regan and Mahesh (2019). Mixing metrics determined significant enhancement in mixing due to the applied suction, further establishing agreement in the correlation between the strength of the shear layer dynamics, symmetry of the cross-sectional CVP, and the resulting jet mixing.

The dissertation of Elijah Weston Harris is approved.

Raymond Mitchell Spearrin

Robert T. M'Closkey

Jeffery D. Eldredge

Ann R. Karagozian, Committee Chair

University of California, Los Angeles

2020

"For from Him, and through Him, and to Him are all things. To Him be the glory forever. Amen." - Romans 11:36

TABLE OF CONTENTS

LIST OF FIGURES

LIST OF TABLES

Nomenclature

Roman Symbols

A Area, with the following particular subscripts:

A_{jet} − cross-sectional area of the jet

A_{tot} − total domain of the interrogation area

C Concentration, with the following particular notations:

C_o − concentration of jet fluid inside the potential core region

$\overline{C/C_o}$ − mean concentration of jet fluid over all instantaneous images

C_{rms} − Root-mean-square of concentration values

D Diameter or diffusivity, with the following particular subscripts:

D − (unsubscripted) jet nozzle diameter

$\hat{D}$ − molecular mass diffusivity

f Frequency, with the following particular subscripts or superscripts:

f_c − corner frequency of a low-pass filter

f_f − forcing frequency

$f_{f,cr}$ − critical forcing frequency associated with the start of lock-in

f_h − horseshoe vortex instability frequency

f_n or f_o − natural (fundamental) frequency of jet's upstream shear layer instability

f_n^* − natural frequency modified by forcing

J Momentum flux ratio, with the following particular subscripts:

J − (unsubscripted) jet-to-crossflow momentum flux ratio, $\rho_j {U_j}^2/\rho_\infty {U_\infty}^2$

J_{cr} − critical jet-to-crossflow momentum flux ratio at which bifurcation to a global mode occurs

K Perturbation matrix

K_n Norm perturbation matrix

L/D Non-dimensional stroke ratio related to vortex ring formation, or length to diameter ratio

L_y, L_z dimensions of an interrogation area

M Molecular mass, with the following particular subscripts:
M_j − jet molecular mass
M_∞ − crossflow molecular mass

$\langle M \rangle$ Mixing criterion

m Mode number

$\dot{m}$ Mass flow rate

N_e the number of fluid elements

n Spatial coordinate or number density, with the following particular subscripts:
n − (unsubscripted) normal to the jet fluid concentration centerline trajectory, or the number density of acetone
n_l − parallel to the scalar gradient vector direction

p'_{crit} Critical acoustic pressure perturbation amplitude for lock-in

Q Q-criterion

$\dot{Q}$ Volume flow rate

R Jet-to-crossflow velocity ratio, U_j/U_∞

Re Reynolds number, with the following particular subscripts:
Re_j − jet Reynolds number, based on mean jet velocity U_j and nozzle diameter D, $Re_j = \rho_j U_j D/\mu_j$

Re_∞ – crossflow Reynolds number, based on freestream crossflow velocity U_∞ and nozzle diameter D, $Re_\infty = \rho_\infty U_\infty D/\mu_\infty$

R_{fit} Pearson correlation or correlation coefficient

r_{ring} Ring velocity ratio, $\Delta U_j/U_\infty$

S Jet-to-crossflow density ratio ρ_j/ρ_∞

S_{ij} Symmetric tensor

St Strouhal number based on diameter, fD/U_j

s Spatial coordinate, with the following particular subscripts:

s – (unsubscripted) along the center of the upstream shear layer

s_c – along the jet fluid concentration centerline trajectory in question

$s_{c,unforced}$ – along the unforced jet fluid concentration centerline trajectory

T Period of acoustic forcing, or temperature

t Time

U Unmixedness or mean velocity, with the following particular subscripts:

U_j – mean jet velocity

U_∞ – mean freestream crossflow velocity

U_{yz} – cross-section-based Unmixedness along horizontal coordinate, x/D

$U_{c,sn}$ – centerplane-based Unmixedness along jet centerline trajectory s_c/D or $s_{c,unforced}/D$

$U_{c,xz}$ – centerplane-based Unmixedness along horizontal coordinate, x/D

ΔU_j – peak-to-peak jet velocity amplitude of temporal pulse

$U_{j,wire}$ – mean jet velocity over the hotwire length

$U_{5\%}$ – jet velocity associated with "5 % points" for stroke ratio calculation

$U'_{j,rms}$ Root mean square (RMS) of the jet velocity perturbation

u_j Temporal jet velocity variation

V_{hw} Hotwire voltage

x, y, z Downstream, spanwise, and axial coordinates measured from jet orifice (see Fig. 1.3)

z_p Jet penetration

Greek Symbols

α Duty cycle of square wave forcing or absorption coefficient, with the following particular subscripts:

α – (unsubscripted) an arbitrary duty cycle or absorption coefficient

α_{actual} – actual duty cycle acquired from temporal data, τ_{actual}/T

α_{input} – input or prescribed duty cycle, τ_{input}/T

Δ Δ-criterion

δ Jet spread, boundary layer thickness, or scale length, with the following particular subscripts:

δ_n – jet spread normal to each jet trajectory in question

$\delta_{n,unforced}$ – jet spread normal to the unforced jet trajectory

δ_p – pixel size in PLIF images

δ_s – scale length ($\delta_p \leq \delta_s \leq \delta_{s,max}$)

$\delta_{s,max}$ – maximum scale length

δ_z – vertical jet spread

$\delta_{99\&}$ – boundary layer thickness defined by 0.99 % of free stream velocity

ϵ Strain rate, with the following particular

ϵ_{SDRL} or ϵ_{PLIF} − strain rate extracted from PLIF data via SDRL model

ϵ_{PIV} − strain rate extracted from PIV data

ϵ_{ij} − strain rate tensor

ζ Mixture fraction, with the following particular superscripts:

ζ − (unsuperscripted) mixture fraction in flowfield

ζ^{+} − boundary of the mixture fraction value as $n \to +\infty$

ζ^{-} − boundary of the mixture fraction value as $n \to -\infty$

θ Momentum thickness, with the following particular superscripts:

θ_j − momentum thickness of jet

θ_{infty} − momentum thickness of crossflow

λ_D Scalar diffusion scale

μ Viscosity, with the following particular superscripts:

μ_j − jet viscosity

μ_∞ − crossflow viscosity

ρ Density, with the following particular subscripts:

ρ_j − jet density

ρ_∞ − crossflow density

σ Absorption cross-section

τ Temporal pulse width of square wave forcing,

with the following particular notations:

τ_{actual} − actual temporal pulse width from temporal data

τ_{input} − input or prescribed temporal pulse width

$\Delta\tau$ − temporal interval of two pulses

χ Scalar dissipation rate

ψ	Molecular fraction of acetone vapor within the jet fluid
Ω_{ij}	Antisymmetric tensor
ω_y	Vorticity in the y direction

Acronyms

CVP	Counter-rotating vortex pair
DAQ	Data Acquisition
DEHS	Di-Ethyl-Hexyl-Sebacat
DMD	Dynamical mode decomposition
DML	Downstream mixing layer
DNS	Direct numerical simulation
FFT	Fast Fourier Transformation
FOV	Field of view
FWHM	Full width at half maximum
IRO	Intensified Relay Optics
JICF	Jet in crossflow
K-H	Kelvin-Helmholtz
PCA	Principal Component Analysis
PDF	Probability density function
PIV	Particle image velocimetry
PLIF	Planar laser-induced fluorescence
POD	Proper orthogonal decomposition
PSD	Power spectral density
PVC	Polyvinyl chloride
RMS	Root-mean-square

SDRL	Strained dissipation and reaction layer
SE	Scalar fluctuation energy
SMD	Spatial mixing deficiency
UML	Upstream mixing layer
UV	Ultra violet
VE	Velocity fluctuation energy

ACKNOWLEDGMENTS

For as long as I can remember, I have had the most vivid memory from early childhood, where I was told one day when I was older it would be expected of me to write papers that were a whole five or maybe even ten pages long. The matter seemed completely outrageous and unfathomable to me, and it is from such a perspective that I say the writing this dissertation, along with all of the work which went into the experiments it details, would never have been something I would have begun to pursue, and most assuredly would not have completed, were it not for the incredible support and encouragement of multiple people. Foremost I would like thank my advisor, Professor Ann Karagozian, for the innumerable ways in which she has nurtured and refined my scientific pursuits, and for her heartfelt compassionate care that she demonstrated for my life beyond the workplace. I have been extremely blessed throughout every moment of working under her guidance, and will forever be indebted to her for all the invaluable experiences and opportunities she has provided for me.

Of course I also wish to extend my sincerest thanks to the other members of my committee: to Professor Jeff Eldredge for being one of the best instructors I have ever had the privilege of taking a class from, and for his wisdom about a seemingly endless list of fluid topics, to Professor Spearrin for the opportunity to work with him numerous times with the aircraft propulsion course, and for constantly encouraging me in my career pursuits after UCLA, and to Professor Robert M'Closkey for spending countless hours along side the students in the research lab helping us implement new methods of control to our experiment. Above all I wish to thank each of them for the investment of their time and expertise in serving on my committee and directing the path of my dissertation. I would also like to give a special thanks to Professor Stanley Osher, who graciously served on my committee during my candidacy exam, but due to extenuating circumstances was not able to continue his service during my final defense.

Aside from my committee, I wish to also give a special thanks to Professor Owen Smith for his multitude of ingenious ideas related to experiments, and for the incredibly entertaining stories from his past. An incredibly special thanks is extended to Professor Leo Alves for his extensive assistance in comprehending and furthering our understanding of the instabilities associated with the JICF, and for his personal encouragement to me in my work here at UCLA and beyond. Also, thanks to Professor Luca Cortelezzi for his motivating our pursuits of more novel forcing of the JICF, and for his dedication to working alongside us in the lab.

I would also like to acknowledge all of my colleagues who I have had the privilege of working with in the energy and propulsion research lab (EPRL). A particularly special thanks to Andrea Besnard and Stephen Schein for being amazing research partners, and for their wonderful friendships outside of work. Also to my other labmates for their support and encouragement: Levon Gevorkyan, Ayaboe Edoh, Takeshi Shoji, Richard Abrantes, Miguel Plascencia, Salvador Badillo Rios, Jonathan Tran, Andres Vargas, Daniel Kerr, David Ren, Mathias Ross, John Bennewitz, Hyung Sub Sim, Rosa Padilla, and Davi Bernhard.

An unshakable foundation throughout my life has been my wonderful family. I am incredibly fortunate for their understanding and patience over the years in pursuing my PhD, and for their boundless love and encouragement, especially in the moments when I was unsure of how to continue. Thanks firstly to my parents, for always believing and encouraging my every pursuit in life, and in particular for coming to visit UCLA and motivating me to pursue my PhD when the opportunity presented itself. Also thanks to my grandparents, some of whom are no longer here to see my fulfillment of this pursuit, for so profoundly shaping and influencing me since my youth. Of course, an immeasurable thanks to my wonderful wife, who has been by my side through every high and low moment, up at all hours, and tolerated the most unreasonable circumstances of caring for a newborn baby while I was constantly writing. Beyond this, a thanks to my siblings, other extended family members, and close family friends, for all the little things that boosted my spirits or provided moments of reprieve from the nonstop aspects of work.

This research was supported by the National Science Foundation under grants CBET-1437014, and CBET-1933310, and by the Air Force Office of Scientific Research (AFOSR) under grants FA9550-15-1-0261, and FA9550-19-1-0191.

VITA

2014-2015	Undergraduate Research Assistant, Energy Research Lab, University of California, Davis, CA
2015	B.S. (Mechanical Engineering), University of California, Davis, CA
2015	B.S. (Aerospace Engineering), University of California, Davis, CA
2016	M.S. (Aerospace Engineering), University of California, Los Angeles, CA
2018	Teaching Assistant, MAE 150R/250R - Rocket Propulsion, University of California, Los Angeles, CA
2016-2018	Teaching Assistant, MAE 150P/250P - Aircraft Propulsion, University of California, Los Angeles, CA
2015-present	Graduate Student Researcher, Energy and Propulsion Research Lab, University of California, Los Angeles, CA

PUBLICATIONS AND PRESENTATIONS

E. W. Harris, T. Shoji, A. Besnard, and A. R. Karagozian. Structural and mixing characteristics of passively controlled transverse jets with tabs, presented at the 70^{th} annual meeting of the American Physical Society Division of Fluid Dynamics, Denver, CO, November 2017.

E. W. Harris, A. Besnard, and A. R. Karagozian. Control of local vorticity generation and shear layer instabilities in transverse jets, presented at the 71^{st} annual meeting of the American Physical Society Division of Fluid Dynamics, Atlanta, GA, November 2018.

E. W. Harris, D. W. Ren, S. Schein, R. T. M'Closkey, L. Cortelezzi, and A. R. Karagozian. Dynamics of axisymmetrically excited transverse jets, presented at the 72^{nd} annual meeting of the American Physical Society Division of Fluid Dynamics, Seattle, WA, November 2019.

T. Shoji, A. Besnard, E. W. Harris, R. T. M'Closkey, and A. R. Karagozian. *Effects of axisymmetric square-wave excitation on transverse jet structure and mixing*, AIAA Journal, 57, 1862-1876, 2019.

T. Shoji, E. W. Harris, A. Besnard, and A. R. Karagozian. *Effects of sinusoidal excitation on transverse jet dynamics, structure, and mixing*, AIAA Journal, 58, 3889-3901, 2020.

T. Shoji, E. W. Harris, A. Besnard, S. G. Schein, and A. R. Karagozian. *Transverse jet lock-in and quasiperiodicity*, Physical Review Fluids, 5, 013901, 2020.

T. Shoji, E. W. Harris, A. Besnard, S. G. Schein, and A. R. Karagozian. *On the origins of transverse jet shear layer instability transition*, Journal of Fluid Mechanics, 890, A7, 2020.

E. W. Harris, D. W. Ren, S. Schein, R. T. M'Closkey, L. Cortelezzi, and A. R. Karagozian. Dynamics of an axisymmetrically excited jet in crossflow, presented at the 25^{th} meeting of the International Congress of Theoratical and Applied Mechanics, Milan, Italy, August 2020. [POSTPONED]

E. W. Harris, D. W. Ren, and A. R. Karagozian. Dynamics of coaxial transverse jets, presented at the 73^{rd} annual meeting of the American Physical Society Division of Fluid Dynamics, Chicago, IL, November 2020.

CHAPTER 1

Introduction

1.1 Background, and Motivation

The injection of jet fluid, typically issuing forth from a round orifice, into a uniform crossflow is a cononical flowfield generally referred to as a jet in crossflow (JICF) or transverse jet. This intricate and sophisticated three-dimensional flowfield has been the focus of significant research efforts spanning over the past 75+ years, owing to the multifarious applicability of the JICF to within multiple industrial, environmental, and biological systems (Margason (1993); Karagozian (2014); Mahesh (2013)). The flowfield is distinctly relevant to airbreathing propulsion systems, having been extensively studied over the years with applicability towards thrust vector control (Oh and Schetz (1990); Miller et al. (1999); Barata (2013)), turbine blade film cooling (Karagozian (1986); Bons et al. (2002); Ekkad et al. (2006)), and dilution jets in primary combustion zones of gas turbine combustors and preburner combustion zones in liquid rocket engines (Brzustowski et al. (1977); Nguyen and Karagozian (1992); Holdeman (1993)).Throughout the extensive investigation of the JICF related to these applications, diverse variations of the flow system have been examined, notably consisting of variable flow phases (e.g., liquid-liquid, liquid-gas, and gas-gas injection), variable injection techniques (e.g., flush, or elevated jet injection relative to a wall; square, elliptic, round, or rectangular jets; tabbed jets; triplet or impinging jets), or more complicated flowfields (e.g. compressible flows with shock waves; reactive flows).

For the application of the JICF within gas turbine combustors, introduction of dilution

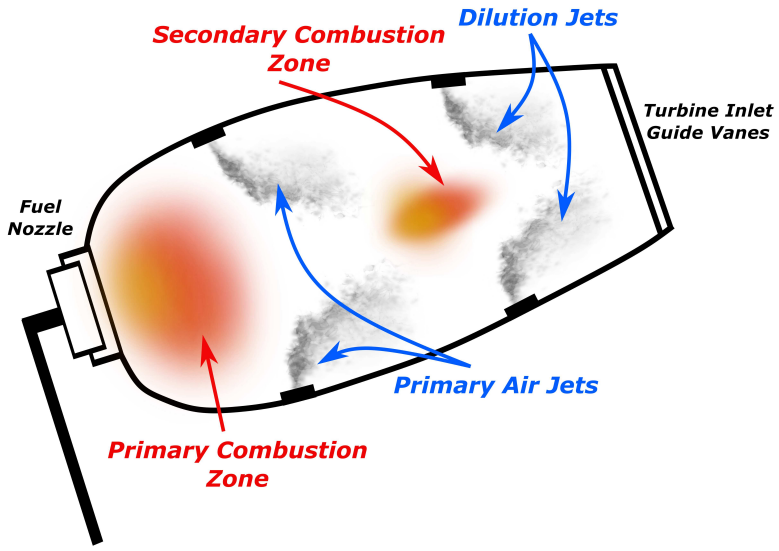

Figure 1.1: Simplified rendering of primary and dilution air jets transversely injected within the combustion zones of a gas turbine engine.

air jets within the primary combustion zone, depicted within figure 1.1, serve as a practical means of appropriate and efficient control over the fuel to oxidizer/diluent equivalence ratio throughout the combustor, and hence the engine emissions. The mixture ratio in low-speed reactive flows is known to be one of the main parameters in dictating the formation of undesirable combustion byproducts such as NO_x and CO (Correa (1993)). Production of NO_x is often minimized within the combustion chamber for operating conditions at which the transition of CO to CO_2 is suppressed, whereby a consequential increase in CO is noted (Bowman (1992)). Selective attenuation of the mixture ratio, via controlled injection of cooling dilution air, can contribute to a reduction in the production of NO_x or CO, depending upon the operating regime of the engine; the tunable nature of a JICF allows for optimization of mixing to reduce NO_x at high power outputs from the engine, while conditioned for off-mixing operation at lower power outputs to reduce CO emissions. Recent practical applications in the reduction of NO_x, stemming from technical advancements in the JICF, are seen in the Pratt and Whitney technology for advanced low NO_x (TALON X) (McKinney et al. (2007)), the GE twin annular premixed swirler (TAPS) (Foust et al.

(2012)), and rich burn, quick-quench, lean burn (RQL) combustors (Samuelsen (2016)).

Meanwhile, perpendicular injection of dilution air jets aft of the primary or secondary combustion regions serve to temper the high temperature combustion products preceding issuance into the turbine sector of the engine (Ramsey and Goldstein (1971); Vermeulen et al. (1982); Karagozian (2010)), as schematically depicted within Figure 1.1. Such implementation of the JICF is borne out of experimental studies regarding the resultant velocity and temperature fields of a singularly injected jet (Keffer and Baines (1963); Kamotani and Greber (1972)), and is furthered through the treatment of injector array configurations (Holdeman (1993); Elattar et al. (2016)). Representative effects of the dilution air on flow entering the turbine are characterized through the alteration of the temperature pattern factor (PF), defined as:

$$PF = \frac{T_{4,peak} - T_3}{T_{4,mean} - T_3} \tag{1.1}$$

where T_3 is the combustion chamber inlet temperature, and $T_{4,peak}$ and $T_{4,mean}$ are the peak and mean temperatures of the flow upon entering the turbine, respectively. The cooler dilution air, in conjunction with mixing and entrainment phenomena associated with the JICF (Fearn and Weston (1974); Broadwell and Breidenthal (1984); Gevorkyan et al. (2016)), can effectively lower the peak temperature of the combustion products, thereby reducing the thermal stresses and allowing for a higher mean temperature threshold, thus improving the overall engine performance via greater power extraction from the turbine (Vermeulen et al. (1992); Hill and Peterson (1991); Kerrebrock (1992)).

Though implementation of dilution air jets aft of the combustor assist in minimizing the PF, lowering the peak temperature entering the turbine, the resulting flow is still at such a high temperature that severe degradation of the turbine blades is noted, thereby necessitating cooling of the blades (Brown (1950); Han et al. (2012); Dixon and Hall (2013)). Utilization of a JICF, applied in multitude across the blade surface (Holdeman (1993)), can serve to passively or actively generate a film cooling layer about the turbine blades (Bons et al. (2002); Eldredge and Bons (2004); Bogard and Thole (2005)). The issuing jet is such

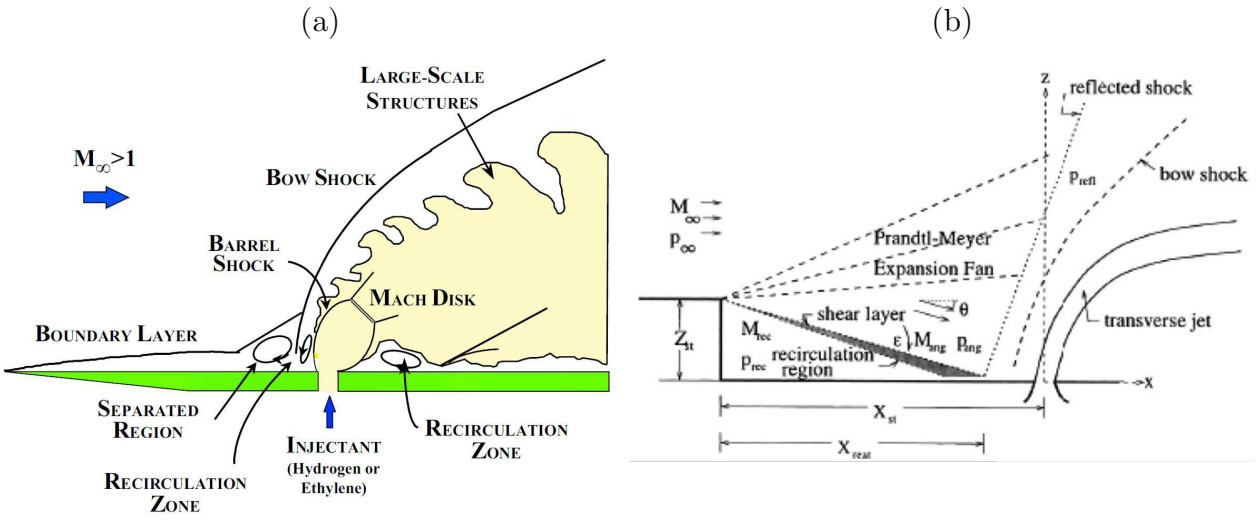

Figure 1.2: Depictions of (a) flow structures for the JICF injected into a supersonic crossflow (adapted from Ben-Yakar (2000)) and (b) the flow regions attributed to a JICF injected downstream of a rearward-facing step with a supersonic crossflow (adapted from Karagozian (2010)).

scenarios, does not endeavor for increased spread, penetration, or mixing, but instead seeks adherence to the blade surface and entrainment of the boundary layer so as to prevent flow separation over the blade chord length. Creating this film layer serves to form a thermal barrier between the blade and the expanding hot combustion gases, mitigating diffusion of heat to the material surface. Actively pulsing jets, in a square-wave manner, may potentially enhance the integration of the JICF within turbine blades, concerned respectively with the effectiveness of film cooling, and increasing cooling rates (Ekkad et al. (2006)).

Aside from low speed reactive flows, transverse jet injection schemes may also be utilized within high-speed airbreathing engines such as ramjets or scramjets. The high air speeds within the combustor (supersonic in the case of a scramjet) present challenges in penetration, mixing, and the resulting initiation and perpetuation of chemical kinetic processes between the fuel and crossflow, given the extremely short residence time of the flow within the combustion zone (Curran (1996)). The JICF can provide rapid molecular mixing, leading to a more stable reaction process, and additionally exhibits some flame-holding characteristics

further stabilizing the combustion process owing to the inherent recirculation zone upstream of the transverse jet, as shown in Figure 1.2(a) (McMillan et al. (1993); Ben-Yakar et al. (1998)). In many supersonic combustors, such integration of transverse jets are realized within or upstream of a cavity, or behind a rearward facing step (as given in Figure 1.2(b)), providing ancillary enhancement of the flame-holding and mixing for greater combustion efficiency (Abbitt et al. (1993); Wang et al. (1995); Karagozian et al. (1996); Gruber et al. (2004)).

Finally, and possibly the greatest focus of application in more recent years, is the integration of the JICF within missles, rockets, and aquatic vehicles for real-time thrust vectoring, as well as similarly noted within V/STOL aircraft for takeoff/landing transition (Humble et al. (1995); Wooler (1969); Cimbala et al. (1988); Barata (2013)). For V/STOL aircraft, such as the Harrier and F-35 Lightning II, added complexity regarding the lift and thrust vectors is noted from loses due to the ground effects, and loses in the thrust when transitioning between takeoff, hover, and wing-borne flight. Injection of fluid via an array of transverse jets about the vehicle nozzle induces a deflection in the main nozzle flow due to the jet impulse, thereby permitting throat-area throttling and alteration of the thrust magnitude and directionality. Enhancements through the fluidic throat skewing technique to the issuing thrust phenomena can result in less mechanically complex nozzles, with a complimentary reduction in overall weight (Miller et al. (1999); Yagle et al. (2001)). The quantifiable losses attributed to implementation of the JICF within the aircraft nozzle may be reduced through active pulsation of the issuing jets (Vermeulen et al. (2004)). Regardless, fluidic thrust vectoring is able to mitigate size, complexity, weight, and drag of the nozzle and aerodynamic control systems, and provides possible extensions to obtainable operating conditions within the vehicle flight envelope.

1.2 Unforced JICF Structure, Stability, and Mixing

1.2.1 Flow Parameters

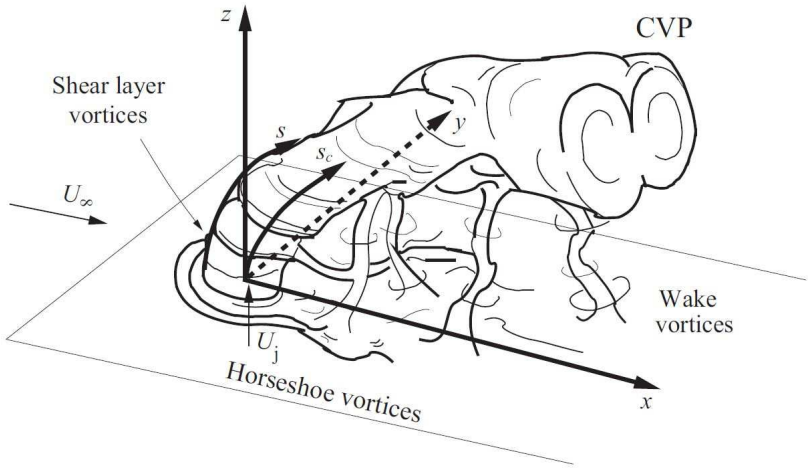

Figure 1.3: Schematic of a flush injected, relative to the injection wall, round jet normal to a transverse flow, with representative depictions of the relevant vortical structures. Appropriate coordinate axes x, y, z, jet shear layer trajectoy s, and jet centerline trajectory s_c are also shown. Adapted from Fric and Roshko (1994).

Figure 1.3 schematically depicts the round jet injected normally into a uniform crossflow, which results in a complex three dimensional flow topology rich in vortical systems and flow structures. The flowfield is composed of a horseshoe vortex which wraps around the jet column, shear layer vortices which periodically form and evolve along the upstream shear layer (USL) of the jet, upright columnar wake vortices bound between the wall boundary layer and the downstream portion of the jet, and a counter rotating vortex pair (CVP) which dominates the jet cross-section (Kamotani and Greber (1972); Kelso et al. (1996); Cortelezzi and Karagozian (2001)). Some of the common nondimensional parameters utilized to characterize this flowfield are the jet-to-crossflow density ratio S, the jet-to-crossflow velocity ratio R, the jet-to-crossflow momentum flux ratio J, the jet Reynolds number Re_j, and occasionally the crossflow Reynolds number Re_∞ (Kamotani and Greber (1972); Fric

and Roshko (1994); Narayanan et al. (2003)), defined as follows:

$$S = \rho_j/\rho_\infty \quad R = U_j/U_\infty \quad J = \rho_j U_j^2/\rho_\infty U_\infty^2 = SR^2 \tag{1.2}$$
$$Re_j = \rho_j U_j D/\mu_j Re_\infty = \rho_\infty U_\infty D/\mu_\infty$$

Additionally, when discussing instability characteristics of the upstream shear layer, the frequency content can be nondimensionalized using a Strouhal numbers, $St = fD/U_j$, based on jet diameter; relevant Strouhal numbers can also be defined in terms of the jet's upstream momentum thickness (Shoji et al. (2020b)). Quantification of the jet momentum thickness may be established on the windward and leeward sides of the jet exit, relative to the oncoming crossflow, owing to the unique three-dimensionality of the flowfield about the issuing jet (Megerian et al. (2007)). Also ocassionally characterized is the Schmidt number,

$$Sc_j = \nu_j/D_{j\to\infty} \tag{1.3}$$

where $D_{j\to\infty}$ is the mass diffusivity of the jet into crossflow. This parameter is of speacial interest in gas-phase JICF studies involving differing mixtures of constituent gas species comprising the jet fluid. As Reynolds numbers are systematically increased into the turbulent regime, the dependency of the flow upon the Schmidt number, as well as the Prandtl number, becomes less pronounced and eventually insignificant due to the increasing dependency of the scalar transport phenomena on the turbulent mixing length scales (Dowling and Dimotakis (1990)). When exploring reactive flows, the chemical reaction time and length scales, and their relative magnitude compared with the other relevant scales attributed to the flowfield, are important to quantify. These relations are typically defined by the Damkökler number Da, which is the ratio between the convective mass transfer rate and the limiting chemical kinetic rate. Within the single phase reactive gaseous JICF the Schmidt number is of the order 1, although this depends on the specific gases constituting the jet and crossflow fluids (Gevorkyan et al. (2018)). The resulting chemical reactions generally proceed much faster than the rate of mass or momentum diffusion ($Da \gg 1$), though in some instances the reaction may exist at similar timescales to that of the diffusion rates ($Da \approx 1$).

With such a wide range of variability over selection of the various flow parameters, extensive exploration of has been directed towards determining scaling laws suited for collapsing the jet trajectories, wherein comparative extrapolations about the different flowfields may be more appropriately made (Kamotani and Greber (1972); Broadwell and Breidenthal (1984); Hasselbrink and Mungal (2001); Muppidi and Mahesh (2005); Forliti et al. (2015)). An oft implemented scaling for incompressible transverse jet velocity centerline trajectories is

$$\frac{z}{RD} = A\left(\frac{x}{RD}\right)^{m} \tag{1.4}$$

where x and z represent the downstream and vertical axes used to parameterize jet trajectory positions, and A and m are constants. Pratte and Baines (1967) give the constants to be $m = 0.28$ and $A = 2.0$ for a flush pipe injected at velocity ratios of $5 \leq R \leq 35$. Smith and Mungal (1998), stipulate that for a flush nozzle injected jet over a similar velocity ratio range, the scaling constants should be $m = 0.27$ and $A = 1.5$. Still others suggest that the nearfield and farfield should be scaled separately (Broadwell and Breidenthal (1984); Hasselbrink and Mungal (2001); Su and Mungal (2004)). More recently numerical investigations by Muppidi and Mahesh (2005) determined that the complete encapsulation of the flow physics were not realized within 1.4, thereby suggesting an improved scaling,

$$\frac{z}{RD} = A_1\left(\frac{x}{RD}\right)^{m_1}\left(\frac{h}{D}\right)^{m_2} \tag{1.5}$$

where h represents the height at which the jet is no longer oriented vertically. Yet even for this scaling equation, New et al. (2006) determined that not all of the trajectory data was able to be collapsed. Inherent to these scaling equations, and others which are discussed in Margason (1993) and Karagozian (2010), is the need to define the trajectory of the developing jet. Many trajectories relating to the JICF may be characterized, such as the local jet velocity maxima, local temperature maxima or minima, or local concentration maxima. Mainly entreated throughout investigations and herein are the upstream shear layer trajectory, parameterized as shown in Figure 1.3 by the coordinate s, and the jet centerline trajectory parameterized by the coordinate s_c in Figure 1.3 (Gevorkyan (2015)), the latter of which is determined

from a power law fit of the locii of maximum jet fluid concentration.

1.2.2 Vortex Systems

The prevalent vortical systems originating from the complex interaction between the jet and crossflow are the main CVP (Kamotani and Greber (1972); Fearn and Weston (1974)), the wake vortices, or upright column vortices, seen on the lee side of the jet (Fric and Roshko (1994)), the horseshoe vortices which are seen to wrap around the potential core of the issuing jet (Krothapalli et al. (1990); Kelso and Smits (1995)), and also ring-like shear layer vortices which periodically form along the upstream shear layer of the jet, and evolve downstream (Andreopoulos (1985); Kelso et al. (1996); Muppidi and Mahesh (2007)). Exploration of these vortical structures, in particular that of the nearfield formation and downstream influence of the dominant CVP, has been of great focus over the years due to correlations with the jet structure and mixing behavior, resulting in the JICF exhibiting enhanced spread, penetration, and molecular mixing as compared to a free jet or buoyant turbulent jet (Brzustowski et al. (1977); Moussa et al. (1977); Broadwell and Breidenthal (1984); Karagozian (1986); Margason (1993)).

Of the flow structures generated in the JICF, perhaps the most significant are the CVP and the shear layer vortices, as it is the development, evolution, and eventual breakdown of the former which has long been understood to be associated with the overall efficacy of mixing between the jet and crossflow, while the latter is attributed with the initiation and growth of the former (LeGrives (1978); Broadwell and Breidenthal (1984); Mahesh (2013); Karagozian (2014); Gevorkyan et al. (2016)). Driving factors in the origination and development of the CVP have been proposed by a variety of distinct theories, such as phenomena "similar to (vortices) in the wake of a cylindrical bluff body" (Beer and Chigier (1972)), the momentum flux from the jet impulse normal to the crossflow (Broadwell and Breidenthal (1984)), or a folding of the jet due to the lateral periphery of the jet being sheared by the crossflow (Margason (1993)). However, the general consensus, owing to experimental

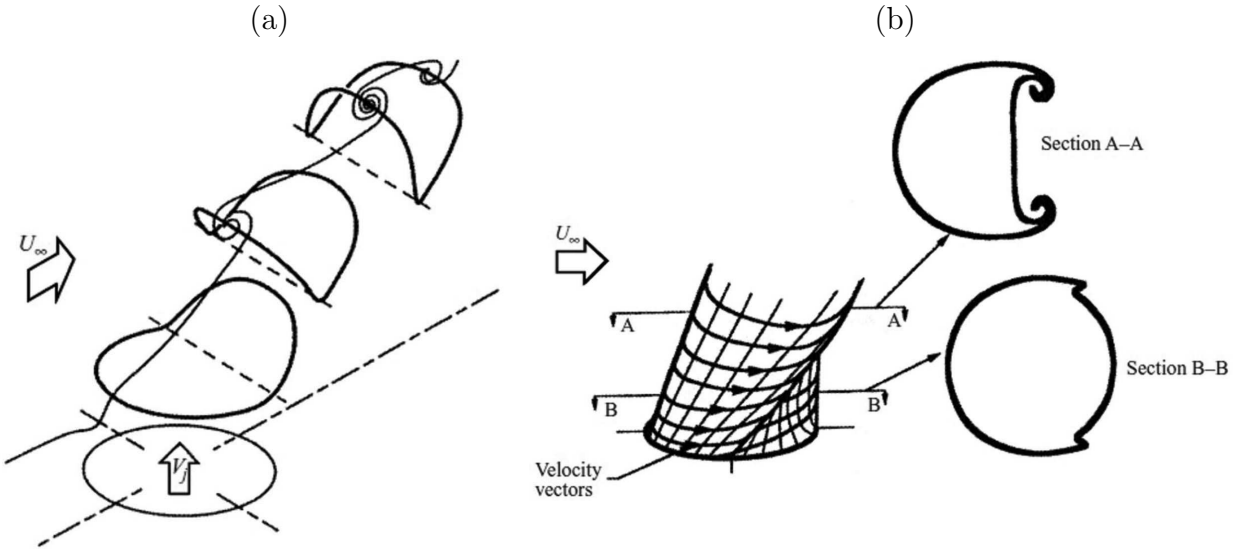

Figure 1.4: Representations of the jet shear layer evolution and re-orientation of shear layer vorticity through (a) tilting of the vortex rings, and (b) folding of the vortex sheet, in leading or contributing to the formation of the counter-rotating vortex pair (CVP). Reproduced from Kelso et al. (1996).

and computational studies within the nearfield of the jet exit, suggest that the CVP is in fact formed by a vortex sheet or thin shear layer emanating from the jet exit, as well as due to pressure differences between the upstream and downstream sides of the jet (Moussa et al. (1977); Fric and Roshko (1994); Kelso et al. (1996); Lim et al. (1998); Smith and Mungal (1998); Cortelezzi and Karagozian (2001); Muppidi and Mahesh (2007); Marzouk and Ghoniem (2007)). In the work by Kelso et al. (1996), experimental studies within both air and water proposed that a tilting and folding of vortex rings, periodically rolling up from the nozzle in a manner similar to that which is noted for free jets, contribute to the overall circulation of the CVP. The combination of tilting and folding of the jet shear layer near the jet exit, schematically depicted in Figure 1.4, produces a re-orientation of the shear layer vorticity leading or contributing to the formation of counter-rotating vortical structures in the downstream. By tracking vortex filaments emanating from the jet exit, Marzouk and Ghoniem (2007) note that there is a distinct difference in the rollup along the windward and leeward sides of the jet, where the leeward side is delayed or stretched downstream due to

an induced upward velocity from the leeside portion of the vortex ring. As the leeside is stretched it leads to upright vortex arms which align with the jet trajectory and are counter-rotating in nature. Earlier vortex element analysis by Cortelezzi and Karagozian (2001) point out that the the degree of interaction or coupling between successive vortex rings, the respective periodicity of the rings, and their resulting impact on the CVP are dependent on initial conditions such as the jet velocity, crossflow velocity, and the upstream boundary layer thickness. Separately, Peterson and Plesniak (2004) indicated the possibility of enhancement or deterioration of the downstream CVP circulation due to vortical structures residing within the jet orifice arising from flow asymmetries upstream of the jet injection plane.

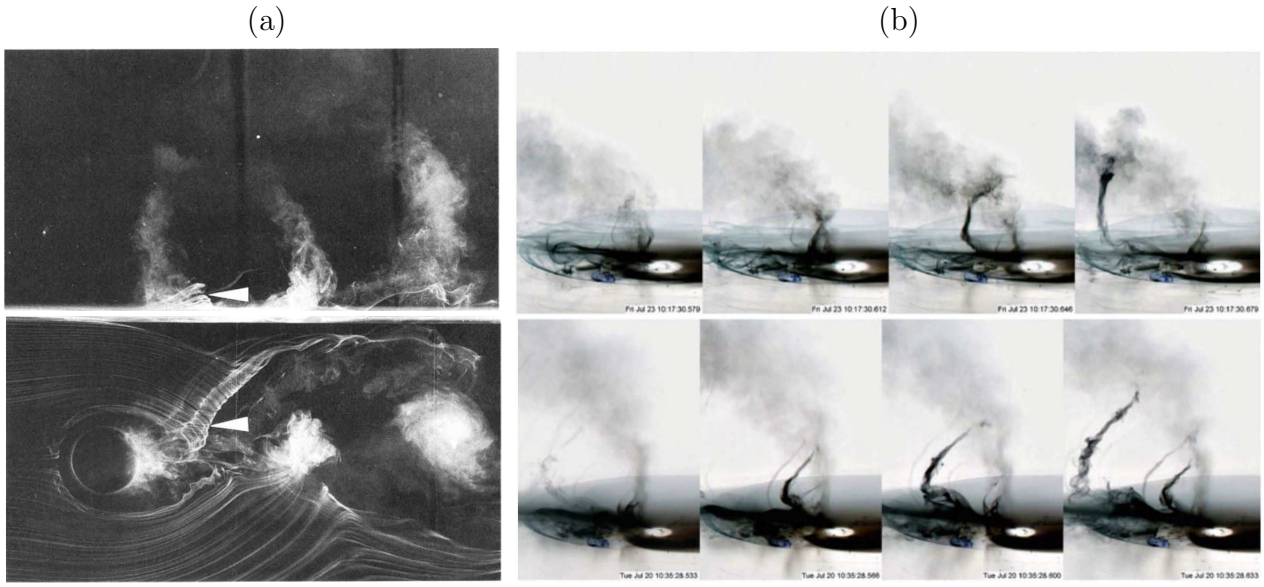

Figure 1.5: (a) Representations of the wake region via smoke visualization from the side and top views (top and bottom images respectively) for a JICF at a $Re_j = 15,200$ and $R = 4$, with crossflow proceeding from the left. Taken from Fric and Roshko (1994). (b) Representations of the temporally evolving wake region for a JICF at $Re_j = 4,154$ and $R = 2$ in the top, and $Re_j = 16,615$ and $R = 8$ in the bottom, with crossflow proceeding from the right. Taken from Milanovic et al. (2012).

The general existence and behavior of the upright wake vortices within the JICF exhibit traits similar to those expressed by a Kármán vortex sheet for flow about a cylinder. However,

the underlying physics governing the formation of such vortex structures are fundamentally different from that of the Kármán vortex sheet, deriving from the adverse pressure gradient on either side of the jet, which leads to separation of the crossflow boundary layer (Fric and Roshko (1994)). Initiations of the wake vortices have been suggested to originate at the intersection of the jet efflux boundary layer and the crossflow wall boundary layer in the lee-side of the jet (Schlegel et al. (2011); Milanovic et al. (2012)), and upon formation are convected downstream remaining attached to the boundary layer and underside of the jet. Such an establishment of upright tornado-like vortex structures, shown in Figure 1.5, are found to entrain fluid from the boundary layer into the main jet, with additional effective deposition within the downstream and wake regions of the jet as well (Fric and Roshko (1994)). Fric and Roshko (1994) suggested there was no periodicity in the overall nature of the wake vortices, while Smith and Mungal (1998) proposed a periodic tendency, possibly owing to a dependence upon the R, Re_∞, and θ_j/D, with Wu et al. (1988) able to see an organization of the wake vortices due to excitation. More recently, it has been expressed that the relative prominence of the wake vortices may be diminished and eventually overtaken by that of the shear layer vortices as the velocity ratio R is decreased (Meyer et al. (2007)).

Generation of the horseshoe vortices for the transverse jet occur near the injection wall, and wrap around the upstream side of the jet. This is thought to result from a behavior comparable to the necklace vortices produced upstream of a blunt object (Baker (1980); Kelso and Smits (1995)), given the interaction between the crossflow and wall boundary layer with the ejecting jet. The horseshoe vortices are seen to exist within three regimes, being that of steady, oscillatory, and coalescing, depending upon the values of Re_∞ and R (Kelso and Smits (1995)). In some cases the periodicity of oscillation has the same frequency as the wake vortices (Kelso and Smits (1995); Rudman (1996)), and is complimented by similar findings for a rectangular jet in crossflow (Krothapalli et al. (1990)). Interaction of the horseshoe vortices with the transverse jet flow is seen to have an effect upon the resulting velocity profile of the jet (Andreopoulos (1985)), which is known to have a subsequent impact upon

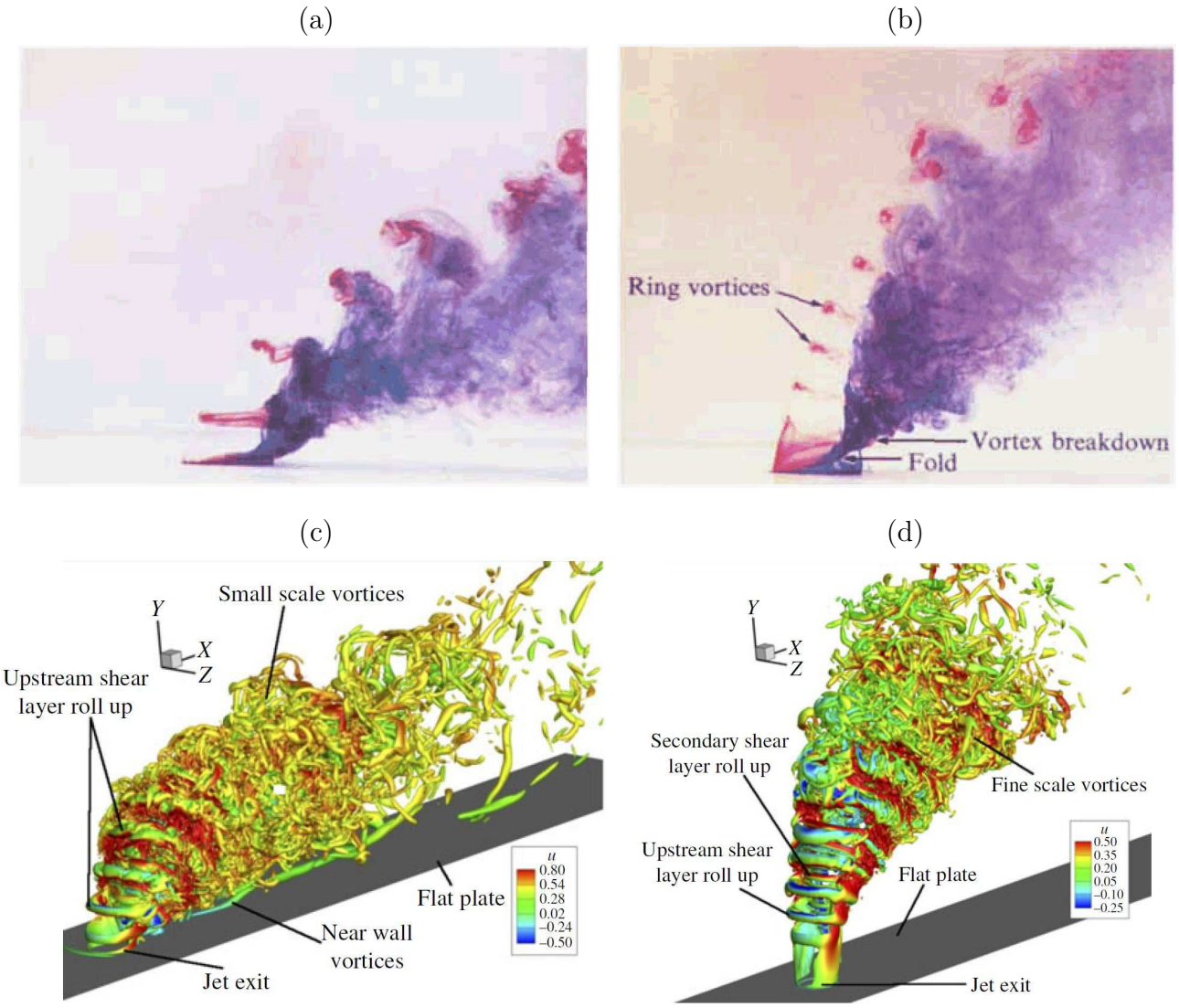

Figure 1.6: Visualizations of the JICF shear layer. Top images depict liquid dye experiments at velocity ratios of (a) $R = 2.2$, and (b) $R = 4.0$ with a crossflow Reynolds number of $Re_\infty = 1600$. The bottom images show direct numerical simulations of gaseous flow at (c) $R = 2.0$ & $Re_\infty = 1000$, and (d) $R = 4.0$ & $Re_\infty = 500$. Taken Kelso et al. (1996), and Iyer and Mahesh (2016) respectively.

the upstream shear layer vortices and their instability characteristics (New et al. (1999); Megerian et al. (2007); Alves et al. (2008); Iyer and Mahesh (2016); Shoji et al. (2020b)).

The shear layer vortices (see Figure 1.6), are attributed to an initiation of a Kelvin-

Helmholtz shear instability in the nearfield of the jet (Kelso et al. (1996); Fric and Roshko (1994); Lim (1997); Yuan and Street (1998)). However it is also suggested that the near-field vortex dynamics are more appropriately given by a global elliptic instability theory for three dimensional vortices given in Landman and Saffman (1987) (Blanchard et al. (1999)), with Camussi et al. (2002) further dissuading from a classical K-H governed instability, instead suggesting a "waving of the jet flow". While the shear layer vortices are known to be of extreme significance to the CVP, recent work suggests the transient nature of the shear layer vortices are not solely necessary for the formation of the CVP structure (Muppidi and Mahesh (2007); Alves et al. (2008); Bagheri et al. (2009)). In addition to the intimate coupling with the development of the CVP, the shear layer instabilities, which are ascribed to the vortex phenomena along the USL, are seen to be quite dominant throughout the other dynamics of the jet flow as well (Megerian et al. (2007); Davitian et al. (2010a); Getsinger et al. (2012); Getsinger et al. (2014)). Given the complexities and interdependencies associated with the system of vortical structures for the JICF, a significant number of recent studies experimentally (Megerian et al. (2007); Davitian et al. (2010a); Getsinger et al. (2012); Shoji et al. (2020b)), numerically (Bagheri et al. (2009); Schlatter et al. (2011); Iyer and Mahesh (2016); Regan and Mahesh (2017)), and theoretically (Alves et al. (2007); Ilak et al. (2012); Souza et al. (2020)) investigate the dynamics of the flowfield, particularly emphasizing the upstream and downstream shear layer instabilities.

1.2.3 Instability Characteristics

Significant interest lies within a comprehension, and harnessing of the shear layer instabilities, given the prominent role the upstream shear layer instabilities and vortical rollup play in the nature of the JICF structure, particulary within the confines of the evolving CVP. Depicted in figure 1.7 are idealized impulse responses for various regimes of flow instabilities denoted from linear stability theory, with classifications of a convectively unstable flow (1.7(a)), a transitional convectively/absolutely unstable flow (1.7(b)), or an absolutely unstable flow

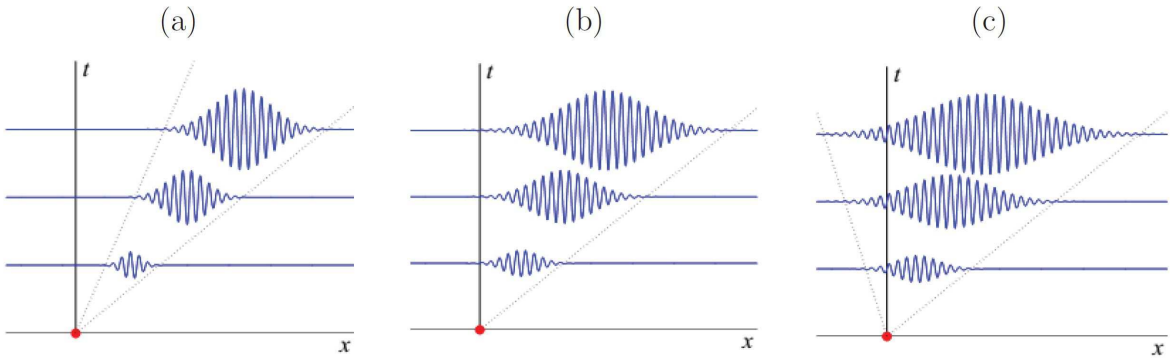

Figure 1.7: Time dependent wavepacket loci of different instability modes: (a) convectively unstable flow, (b) transitional convectively/absolutely unstable flow, and (c) absolutely unstable flow. Taken from Li (2011).

(1.7(c)) respectively (Huerre (2000); Schmid and Henningson (2001)). Within convectively unstable flows, a small perturbation to the undisturbed flow gives rise to a "perturbation wavepacket" which grows and is convected downstream in time. An absolutely unstable flow on the other hand, will generate a wavepacket which grows in magnitude, while expanding both upstream, and downstream in time; a flow undergoing transition from convective to absolute instability is characterized by traits from both types of instability regimes.

Many features about the instability characteristics for a JICF are analogously drawn from or compared with an understanding of the instability phenomena associated with that of free jets (Karagozian (2010)). Free jets are known to generally give rise to a convectively unstable flow regime (Huerre and Monkewitz (1990)), though when the density ratio between the free jet and surrounding quiescent fluid is below a certain critical value, the flowfield is instead seen to be globally unstable (Monkewitz et al. (1990); Kyle and Sreenivasan (1993)). In addition to the transition from convective to absolute instability noted within a free jet below a certain density ratio, similar phenomenological progressions are realized in other shear flows such as counter-current mixing layers above a critical velocity difference (Huerre and Monkewitz (1985); Strykowski and Niccum (1991); Strykowski and Niccum (1992)), and wake flows above a critical Reynolds number (Provansal et al. (1987); Hammond and

Redekopp (1997)). Distinguishing such a fundamental conversion in the nature of the instability characteristics within these shear flows is characteristically marked by changes in the spectral characteristics, in particular: a pronounced alteration of the initial instability Strouhal number, an increase in disturbance amplitude near the shear layer, which is consistent with characteristics of the forced Landau equation (Davitian et al. (2010a); Getsinger et al. (2012)), reductions in strength of subharmonic frequencies, indicating mitigation of vortex pairing along the shear layer, and little transmutation in the spectral content due to an excitation of the flow once it is absolutely unstable (Huerre and Monkewitz (1990); Monkewitz et al. (1990); Sreenivasan et al. (1989); Strykowski and Niccum (1991); Hussain and Zaman (1978)). Investigation of the JICF likewise notes such a transition in the shear layer instabilities from a convectively unstable to an absolute unstable shear layer, the determination of which is denoted from the same alterations of the instability characteristics as seen for a free jet (Megerian et al. (2007); Bagheri et al. (2009); Davitian et al. (2010a); Ilak et al. (2012); Getsinger et al. (2012)).

The nature of the spectral characteristics for the upstream shear layer of a JICF were initially explored by Megerian et al. (2007), where they examine an equidensity flowfield ($S = 1.00$) with jets issuing forth at Reynolds numbers of $Re_j = 2000$ or $Re_j = 3000$, from nozzles with flush and elevated injection planes relative to the wall, over a wide range of jet-to-crossflow velocity ratios ($\infty > R > 1.15$). Hotwire anemometry is utilized, much akin to the methodologies described later in Section 2.2, to capture the nature of the instability characteristics of the jet upstream shear layer as quantified by the fluctuations in the vertical velocity of the flow. The resulting power spectra plots at various downstream locations along the shear layer trajectory, and composite contour plots of finer spatially resolved spectra, are depicted in figures 1.8(a-f) for a few different velocity ratios pertaining to the flush injected jet. The spectra shown in figures 1.8(d-f) represent FFTs of vertical velocity perturbations at different scaled locations s/D along the upstream shear layer of the jet for different velocity ratios, including $R \to \infty$ (figure 1.8(d)). The magnitudes and variation

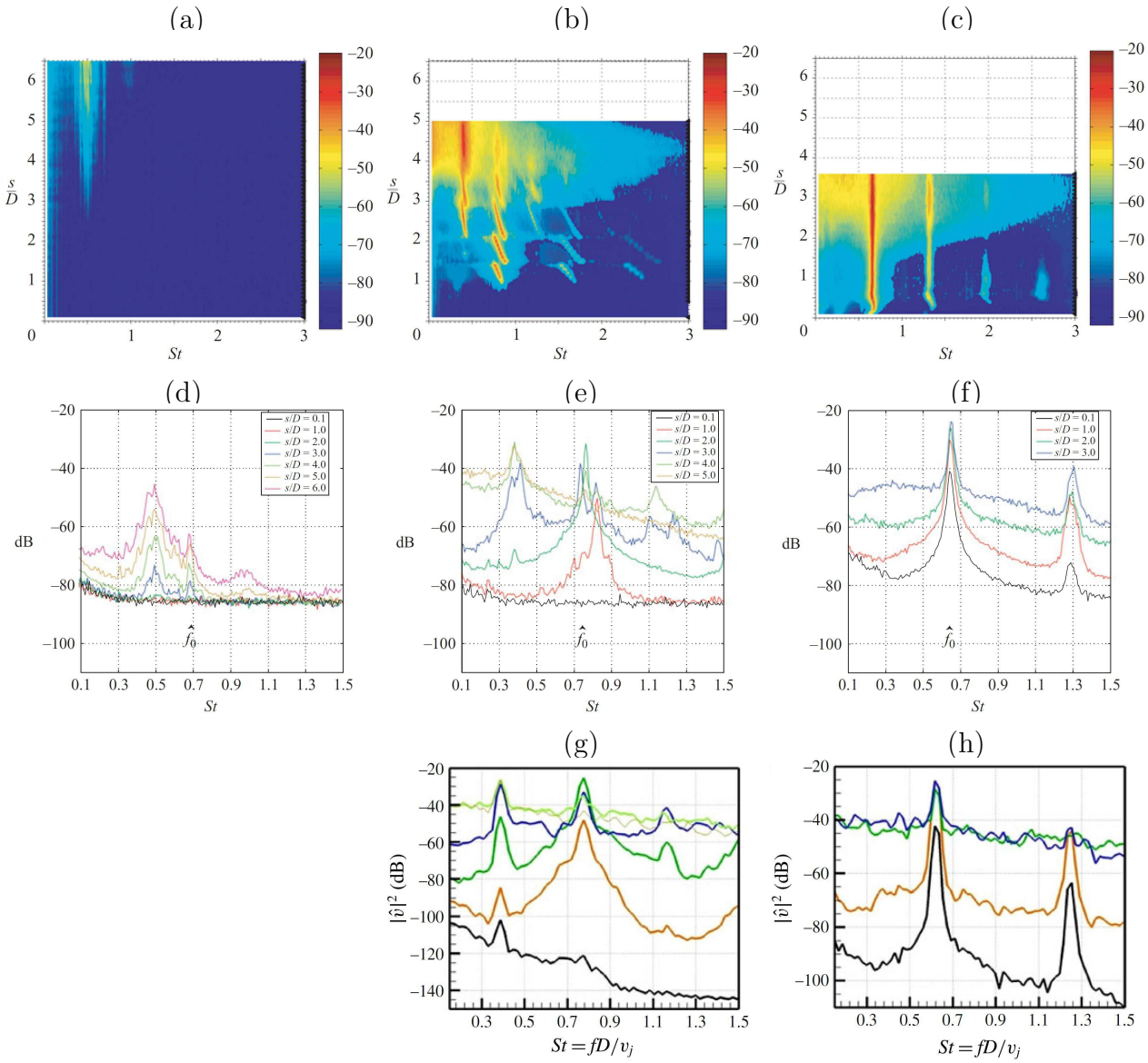

Figure 1.8: Contour plots (a-c) and power spectral plots (d-f) for the experimental JICF at $R = \infty$, $R = 4$, and $R = 2$ from Megerian et al. (2007). Comparatively (g-f) are power spectra plots at $R = 4$ and $R = 2$ for the numerical JICF from Iyer and Mahesh (2016).

in coloring for the more finely resolved spectra represented by the contour plots shown in figure 1.8(a-c) are indicative of the relative strengths of the instabilities and the frequencies, or Strouhal numbers ($St = fD/U_j$), at which they occur. It is typically seen in free jets that the instability modes in initial development along the shear layer undergo an evolution to

a "preferred mode" of the jet which is established farther downstream (Petersen and Samet (1988); Xu and Antonia (2002)), such a trait is indeed observed in figure 1.8(d). Megerian et al. (2007) similarly notes the onset of an initial instability, henceforth referred to as the fundamental frequency f_o of the jet, that is followed by a slight shift in the peak frequency as the hotwire progresses along the shear layer for jets in the relatively high R regime for the JICF as well. Through a systematic decrease in the R value by fixing the jet velocity and increasing the crossflow velocity, pronounced changes in the shear layer instabilities are denoted, including most notably an increase in the strength of the instabilities, onset of their initiation closer to the jet exit, and a progression in the fundamental frequency to lower values. For a moderately high velocity ratio of $R = 4$, the fundamental mode, St_o or f_o, is found to exhibit a frequency-shifting as the hotwire traverses along the shear layer (Figure 1.8(b,e)), indicative of a tonal phenomenon where there is interference between the strengthening shear layer instabilities and the hotwire probe, similar to interference documented for planar and axisymmetric free jets (Hussain and Zaman (1978)). Such convectively unstable flows also demonstrate susceptibility of the flow to external perturbations (Huerre and Monkewitz (1990); Megerian et al. (2007); Davitian et al. (2010a); Getsinger et al. (2012)). Additionally seen for velocity ratios in the moderate regime, as representatively shown in figure 1.8(b) for $R = 4$, are relatively strong spectral peaks at the subharmonics ($St \approx 0.35$) of the fundamental mode ($St \approx 0.7$) evolving downstream along the shear layer trajectory, suggestive of vortex pairing and merger. When Megerian et al. (2007) further reduces the velocity ratio below $R \approx 3.1$, even more dramatic alterations in the shear layer instability characteristics are noted (Figure 1.8(c,f)), similar to those realized in other shear flows undergoing a transition from convective to absolute instability, such as heated or low density free jets (Huerre and Monkewitz (1990); Monkewitz et al. (1990); Sreenivasan et al. (1989); Strykowski and Niccum (1991)). The altered spectral characteristics show the initiation of pure tone, non-shifting, shear layer instabilities quite close to the jet exit (Megerian et al. (2007)), and the decrease in energy transfer from the fundamental mode to a subharmonic.

Hence the evidence in Megerian et al. (2007) and Davitian et al. (2010a) for the equidensity JICF quite strikingly depicts a transition from convective instability to absolute instability for $R \lessapprox 3.1$ for the equidensity JICF with a Reynolds number of $Re_j = 2000$.

Recent direct numerical simulations by Iyer and Mahesh (2016) apply the use of dynamic mode decomposition (DMD) in exploration of a JICF with $R = 4$ and $R = 2$, while matching the flow parameters and jet nozzle injection geometry exactly to those treated within Megerian et al. (2007). Quite appropriately the spectral characteristics, derived from the point-wise temporal vertical velocity measurements, from the DNS study (fig. 1.8(g,h)) are qualitatively and quantitatively well agreed with the experimental work of Megerian et al. (2007), shown in figures 1.8(e-f). Investigation by Iyer and Mahesh (2016) of the flow within the nozzle surprisingly reveals the same dominant frequencies as found externally along the upstream shear layer. Extension of this work by Regan and Mahesh (2019) to linear stability analysis (LSA) and adjoint sensitivity analysis further demonstrate the existence of convectively and absolutely unstable shear layers, and likewise note the originating location of the upstream shear layer instabilities exists in part within the nozzle of the jet. Such significance on the initiating flow is analogously alluded to by Peterson and Plesniak (2004) in examination of a JICF emanating from short orifices, noting the possible symmetry breaking of the JICF due to flow conditions within the jet orifice. Interestingly, from the adjoint sensitivity analyis, Regan and Mahesh (2019) delineates wavemaker regions within the flowfield wherein the jet flow is most susceptible to the introduction of slight perturbations. In the case of the absolutely unstable jet at $R = 2$, the wavemaker was isolated along the upstream edge of the jet exit, but when the shear layer became convectively unstable, the wavemaker region was found to extend around the periphery of the jet exit into the downstream shear layer. They additionally establish that for the $R = 4$ jet, the downstream shear layer actually produces the mode with the largest growth rate, and that the mode is relatively more prominent than in the $R = 2$ case due to the larger shear on the downstream shear layer as $R \to \infty$.

Building upon the equidensity JICF stability studies conducted (Megerian et al. (2007);

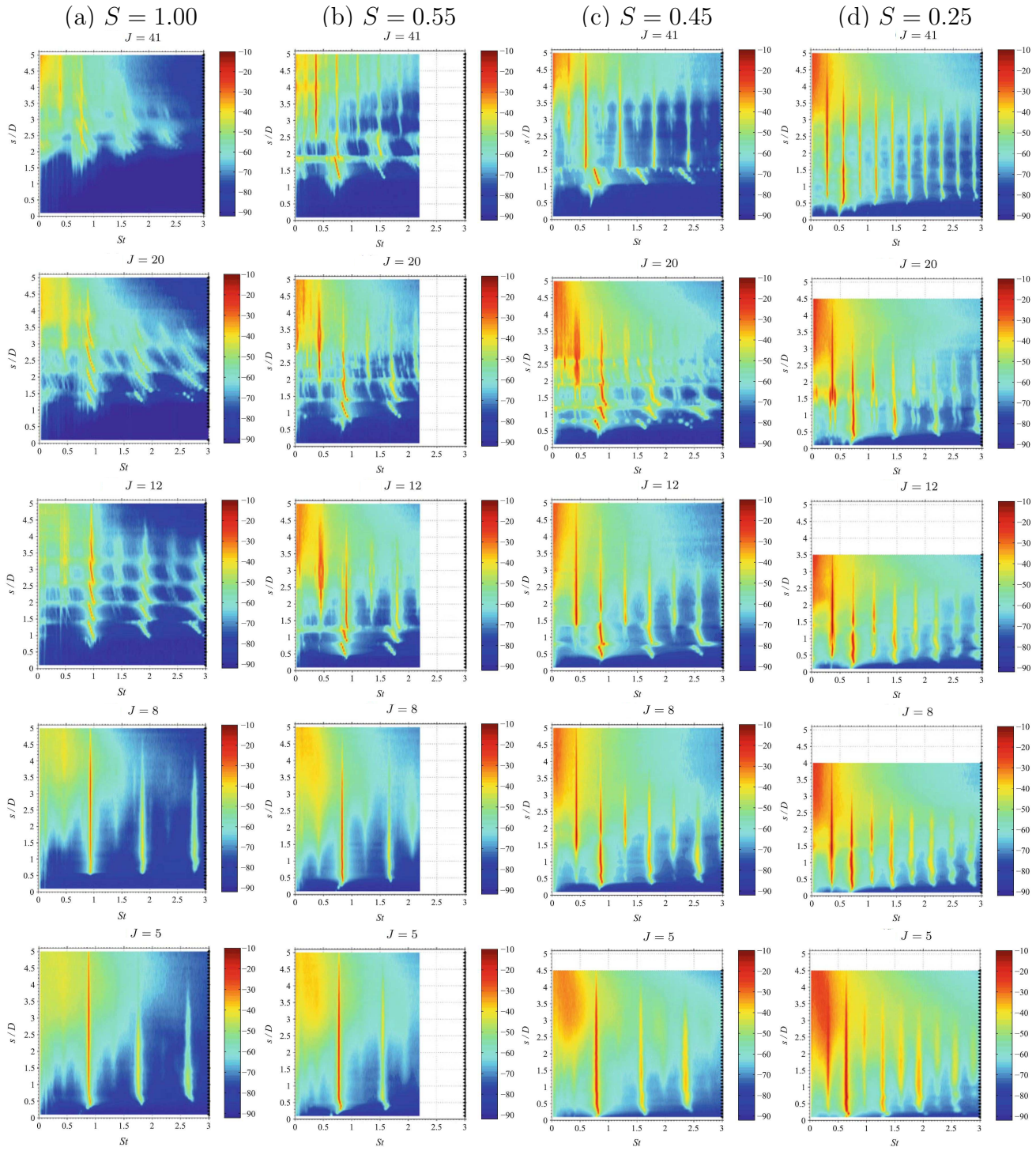

Figure 1.9: Contour plots of the upstream shear layer instabilities along the shear layer trajectory for a flush injected jet at a Reynolds number of $Re_j = 1800$ and various momentum flux ratios, at density ratios of (a) $S = 1.00$, (b) $S = 0.55$, (c) $S = 0.45$, and (d) $S = 0.25$. Adapted from Getsinger et al. (2012).

Alves et al. (2008); Davitian et al. (2010a); Iyer and Mahesh (2016)), Getsinger et al. (2012) explores the nature of shear layer instabilities for a variety of jet to crossflow density ratios S. Shown in figure 1.9 are spectral contour plots of the upstream shear layer instabilities for a range of momentum flux ratios $41 \leq J \leq 5$ at a jet Reynolds number of $Re_j = 1900$ and density ratios of $S = 1.00, 0.55, 0.45,$ & 0.25 for the flush injected jet in crossflow. Getsinger et al. (2012) notes that above a critical density ratio of $S \approx 0.45$, the characteristic indicators of a transition in shear layer instabilities from convective to absolute were observed at a momentum flux ratio of $J \approx 10$; consideration of the equidensity jet (fig. 1.9(a)), recalling that $R = \sqrt{J}$ when $S = 1.00$, reveals commendable agreement in the transitional momentum flux ratio with the findings of Megerian et al. (2007) and Davitian et al. (2010a). Impressively, Getsinger et al. (2012) notes when the density ratio is decreased below $S \approx 0.45$, the shear layer instabilities are determined to be absolutely unstable regardless of the momentum flux ratio, quite amazingly including that of a free jet $J \to \infty$. Such results are found to agree with the findings of Hallberg and Strykowski (2006) regarding low density jet experiments at the Reynolds number explored in the JICF studies.

Getsinger et al. (2014) explores acetone PLIF-based diagnostics to examine JICF structure as well as hotwire quantified shear layer instabilities (the latter without the presence of acetone) in equidensity, and a few cases of low density transverse jets, at a variety of momentum flux ratios J. The study examines jet injection geometrical configurations of a flush nozzle, flush pipe, and an elevated nozzle (see fig. 2.3); the elevated nozzle is comprised of the same inner contraction profile as for the flush nozzle, where the jet fluid is instead introduced 3.75 jet diameters, D, above the flush-wall plane. Details regarding the nozzles may be found in Section 2.1.1. Getsinger et al. (2014) determines that the flush nozzle and flush pipe both exhibit a clear transition from convective to absolute instability at a momentum flux ratio of $J \approx 10$, where strong fundamental modes are initiated close to the jet exit, with corresponding higher harmonics, for the absolutely unstable regime of flows $J \lessapprox 10$. They see quite different behavior within the elevated nozzle however, where the flow

remains convectively unstable for all of the momentum flux ratios considered by Getsinger et al. (2014), thought to be attributable to a component of vertical coflow originating from the crossflow deflecting about the injector (Megerian et al. (2007)), which is known to act as a stabilizer of jet shear layers (Jendoubi and Strykowski (1994)). Once the flow emanating from the elevated nozzle is reduced below $R \approx 1.2$ ($J \approx 1.45$), the spectral characteristics along the shear layer are seen to be quite compatible with those observed in an absolutely unstable flow for the flush injected transverse jet (Megerian et al. (2007)).

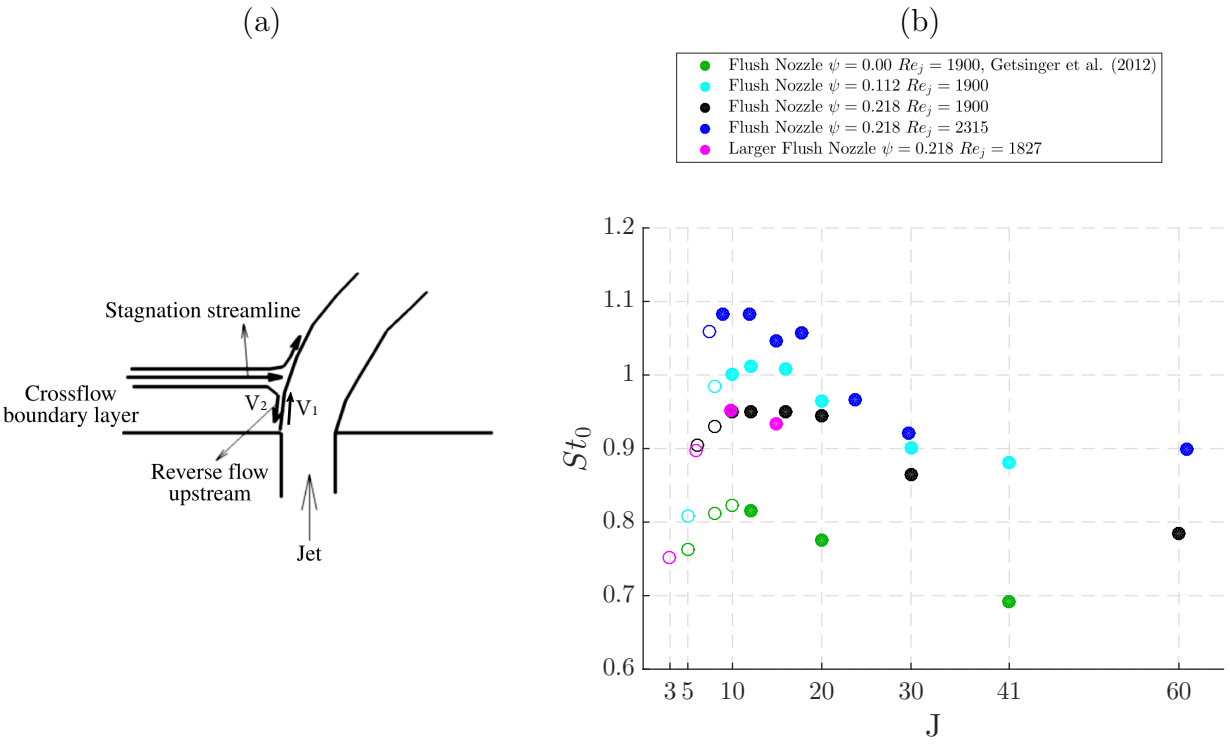

Figure 1.10: (a) Schematic of the effect of jet blockage of crossflow, creating local negative velocity V_2 upstream of the USL adjacent to a positive vertical velocity V_1 within the jet (adapted from Iyer and Mahesh (2016)). (b) Variation in Strouhal number St_o for the fundamental USL mode based on jet diameter and mean jet velocity U_j as a function of J for the equidensity flush nozzle- and larger flush nozzle-injected JICF. Data are shown for Re_j and acetone mole fractions ψ. Filled and open symbols represent the hotwire-determined convectively and globally unstable USL, respectively.

Discernment of a unifying explanation regarding the underlying physical phenomena governing the transition in instability characteristics along the upstream shear layer of the JICF is recently undertaken by Iyer and Mahesh (2016) and Shoji et al. (2020b). Computations by Iyer and Mahesh (2016) investigate the similarity in the JICF USL instability transition to that of a two-dimensional counter-current shear layer (CCSL), where the signs of the velocities of the two streams oppose one another. As indicated schematically in figure 1.10(a), crossflow blockage by the jet can create a stagnation streamline and reverse flow region just outside of the USL near injection, creating a negative velocity $V_2 < 0$ analogous to that in a counter current shear layer, contrasting a positive vertical flow within the jet, $V_1 > 0$. The stagnation streamline generally appears well outside of the crossflow wall boundary layer, even at large velocity ratios Megerian et al. (2007). In general a counter-current shear layer may be characterized by a mixing or shear layer ratio R_1 based on the velocities V_1 and V_2 shown in figure 1.3(a):

$$R_1 = \frac{V_1 - V_2}{V_1 + V_2} \tag{1.6}$$

so that $R_1 > 1.0$ denotes counterflow and $R_1 < 1.0$ denotes coflow. Inviscid spatio-temporal stability analysis of an incompressible, planar counter-current shear layer using a hyperbolic tangent velocity profile Huerre and Monkewitz (1985) indicates that the CCSL becomes absolutely unstable when R_1 exceeds a critical value, $R_{1,cr} = 1.315$. Corresponding experiments for an axisymmetric (round) jet with a finite region of exterior suction Strykowski and Niccum (1991) suggest a critical velocity ratio very close to the theoretical value, $R_{1,cr} \approx 1.32$. Similar inviscid linear stability analysis for the compressible planar counter-current shear layer, with streams of differing densities, has also been performed Pavithran and Redekopp (1989), employing the Crocco-Busemann relation and an equation of state for a perfect gas. Corresponding axisymmetric counter-current jet experiments by Strykowski and Niccum (1992) quantify values of $R_{1,cr}$ for various density ratios S. For the equidensity round transverse jet, Iyer and Mahesh (2016) utilize DNS-generated velocity fields in the USL to compute the effective shear layer ratio R_1 just downstream of jet injection. In the $R = 4$

case, R_1 is estimated in the centerplane ($y = 0$ plane) to be 1.2, while for the $R = 2$ simulation, $R_1 = 1.44$. Even with the simplified parallel flow approximation for the JICF at the low velocity ratio, the findings suggest that these two different JICF flow conditions could straddle the transition between convective and absolute instability when viewed in the context of a local counter-current shear layer occurring at the upstream edge of flush JICF injection. Shoji et al. (2020b) employed the same methodology given by Iyer and Mahesh (2016) in determining the V_1 and V_2 from the experimentally determined velocity profiles at the upstream exit of the transverse jet flows, for a wide range of conditions covering multiple momentum flux ratios J and density ratios S, with and without acetone, which was observed to alter the critical momentum flux ratio at which absolute instability was achieved as visually represented in figure 1.10 (Shoji (2017)). The extensive experimental studies by Shoji et al. (2020b) of this nearfield region of the JICF demonstrate consistency in the CCSL model in understanding transverse jet USL transition to absolute instability. Yet from a quantitative perspective, the critical CCSL velocity ratio for the equidensity transverse jet is lower than that for the planar CCSL, with $R_{1,cr} \approx 1.24$. Details regarding the full extent of this study relating to the influence of nozzle profile, nozzle diameter, momentum thickness, jet momentum flux ratio, density ratio, and jet Reynolds number are detailed in appendix B. Remarkably, recent linear stability analysis by Souza et al. (2020) for the round free jet with external counterflow, accounting for both curvature and viscous effects, predict a critical transition in the CCSL for counterflow corresponding to $R_{1,cr} \approx 1.23$, when the jet diameter-to-momentum thickness ratio D/θ and jet Reynolds number match those of the experiments in Shoji et al. (2020b). Both theory and experiments show, as would be expected, that the momentum thickness of the jet's upstream shear layer plays an important role in this transition as well as in scaling relationships.

1.2.4 Structural Characteristics

In addition to investigation of the shear layer instabilities inherent to the JICF, examination of the developing structural characteristics within the flowfield is pertinent, given their relative bearing in a more comprehensive understanding of the shear layer characteristics, and mixing phenomena (Getsinger et al. (2014); Karagozian (2014); Gevorkyan et al. (2016)). Many studies over the years explore the qualitative and quantitative structural characteristics of the transverse jet from perspectives of the jet centerplane ($x-z$ plane) (Fric and Roshko (1994); Narayanan et al. (2003); Su and Mungal (2004); Muppidi and Mahesh (2005); Shan and Dimotakis (2006)), as well as cross-sectionally ($y-z$ plane) at various downstream ($+x$ direction) locations (Kamotani and Greber (1972); Smith and Mungal (1998); Cortelezzi and Karagozian (2001); Narayanan et al. (2003); Shan and Dimotakis (2006)). Though previous work by our group examine non-forced and forced transverse jet structures through smoke visualization (M'Closkey et al. (2002); Shapiro et al. (2006); Davitian et al. (2010a)), much beyond the jet dynamics, spread, penetration, and structure is unable to be realized, thus our group's more recent work implements the use of non-intrusive laser diagnostic measures for greater detailed quantifications of the flow (Getsinger et al. (2014); Gevorkyan et al. (2016); Shoji (2017); Gevorkyan et al. (2018) Besnard (2019)).

Figure 1.11 display representative acetone planar laser induced fluorescence (PLIF) imaging, discussed in Section 2.3.1, from the work of Getsinger et al. (2014) for perspectives of the equidensity flush nozzle-injected JICF in the instantaneous centerplane, and mean cross-section at $x/D = 10.5$. Through examination of the instantaneous centerplane images, it appears as though decreasing the momentum flux ratio from relatively large values ($J = 61$) to those which are quite small ($J = 3$) correspondingly results in initiation of vortex rollup along the upstream of the jet progressively closer to the jet exit. This noted behavior in the vortex generation along the upstream of the jet is found to be very well agreed with the power spectral measurements of the upstream shear layer instabilities for the flush injected JICF (Getsinger et al. (2012); Getsinger et al. (2014); Gevorkyan et al. (2014)). In addi-

tion to the extremely well correlated behavior of the upstream shear layer instabilities, and the vortex formation and rollup illuminated within the flush nozzle injected JICF, further evidence of good correspondence is seen for the flush pipe and elevated nozzle injected jets, and flush injected jets with non-equidensity density ratios as well (Getsinger et al. (2014)).

In theory, a round jet injected into a uniform crossflow would produce a resulting flow wherein the flowfield is perfectly symmetric about the centerplane axis in the mean. Interestingly however, some studies find that an asymmetric structure is prone to develop in the mean cross-section downstream of the jet injection (Kamotani and Greber (1972); Kuzo (1995); Smith and Mungal (1998); Narayanan et al. (2003); Shan and Dimotakis (2006); Muldoon and Acharya (2010)). This unexpected phenomena is additionally found within the recent work of our group (Getsinger et al. (2014); Gevorkyan (2015); Shoji (2017); Besnard (2019)), and is representatively shown in the cross-sectional PLIF images from Figure 1.11. The asymmetry is not seen to form in all cases, but instead appears to form above a momentum flux ratio of $J \approx 12$ for the flush injected nozzle at the jet Reynolds number of $Re_j = 2300$, which is supported by Kuzo (1995) and Smith and Mungal (1998) who note the asymmetries for relatively large velocity ratios ($R = 10 - 30$) over a range of Reynolds numbers, but especially at lower values. Kuzo (1995) determines the asymmetries are most pronounced below a critical Reynolds number $Re_j \approx 2100 - 7300$, with Shan and Dimotakis (2006) also noting a similar trend in relation to the Reynolds number. Development of such asymmetric structures in the mean cross-section of the jet are predominately examined with respect to a flush nozzle injected jet, though the asymmetric phenomena is also additionally found for a flush pipe injection geometry (Narayanan et al. (2003); Muldoon and Acharya (2010); Getsinger et al. (2014)). Surprisingly, when the JICF is generated from the elevated nozzle in the work of Getsinger et al. (2014), no such formation of an asymmetric jet structure is exposed, which may possibly owe to the stabilizing coflow formed about the issuing jet.

A theoretical explanation regarding the experimentally, and in some cases numerically,

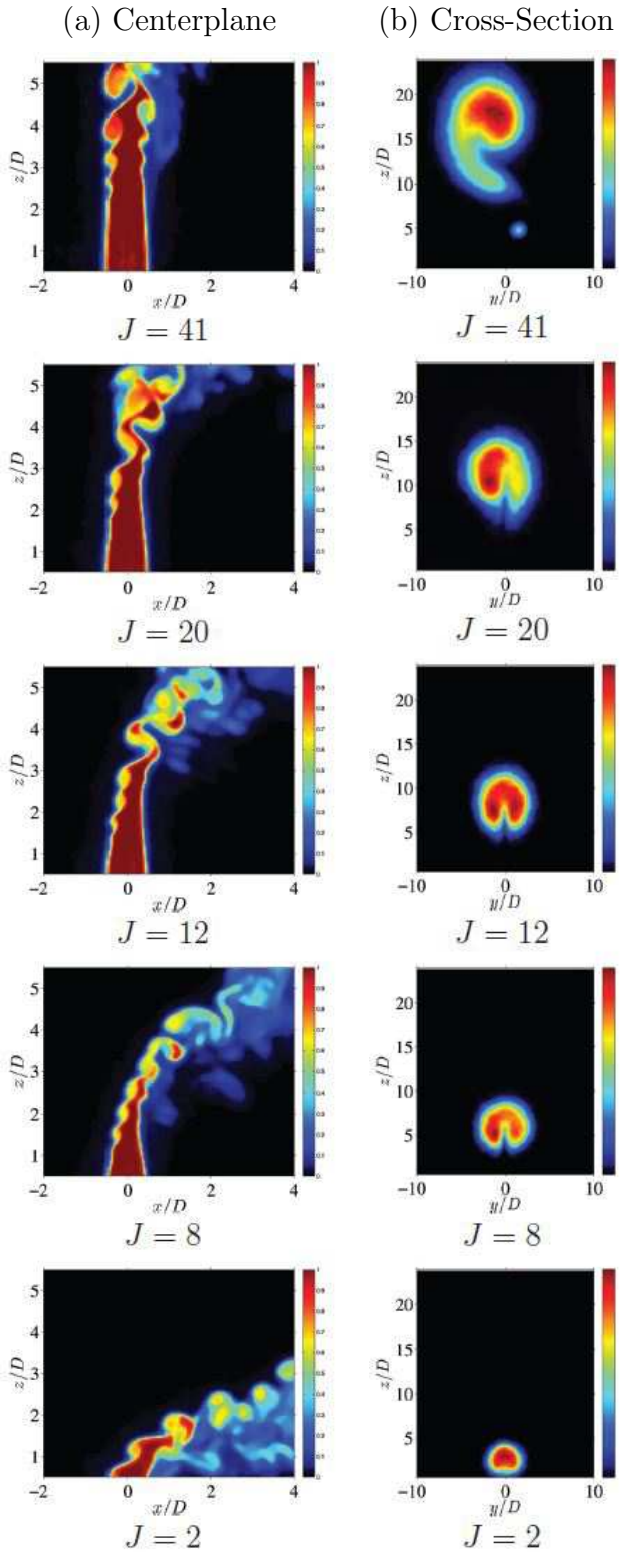

Figure 1.11: (a) Instantaneous centerplane, and (b) Mean cross-sectional PLIF images of the flush nozzle injected equidensity JICF for various momentum flux ratios J. Mean image is averaged over 300 images. Adapted from Getsinger et al. (2012).

discovered cross-sectionally asymmetric jet structure pertaining to the JICF is presented by Alves et al. (2007). The inviscid linear instability theory analysis explores the growth rates of the axisymmetric and helical instability modes. The various azimuthal modes are defined as $m = 0$ for the axisymmetric, and $m = \pm 1$ or $m \pm 2$ for the helical, where the positive/negative notation refers to a clockwise/counterclockwise directionality respectively. It is found that, while at most velocity ratios the axisymmetric mode dominates the shear layer instabilities, at very high values of velocity ratio R, the resulting growth rates of the helical modes are in fact stronger than the axisymmetric mode, with unequal growth rates of the $m = 1$ and $m = -1$ modes, suggesting the potential for asymmetry for a given set of flow conditions (Alves et al. (2007)). A later extension of this inviscid study to transverse jets with a continuous (viscous) base flow revealed the growth rate of the $m = 1$ helical mode is comparable in strength to the axisymmetric mode when at velocity ratios of $R \gtrapprox 10$ (Alves et al. (2008)). Such findings suggest that for lower velocity ratios, the axisymmetric instabilities dominate the JICF, whereas at higher values of R, the helical instabilities may be preserved giving rise to an asymmetric cross-section; this is experimentally supported by Corke et al. (1991) who induces an asymmetry within a free jet via the helical modes. Numerically, Regan and Mahesh (2019) also denotes the presence of unequal growth rates between the helical modes from their DNS investigation of the JICF at $R = 2$ and $R = 4$ with $Re_j = 2000$, and further that the strength of the helical modes, relative to the respective axisymmetric mode, is diminished from the convectively unstable $R = 4$ jet to the absolutely unstable $R = 2$ jet. It is seen within the work of Getsinger et al. (2014) that the directionality of the asymmetries are developed in a consistent and repeatable manner, which is thought to be attributable to the unequal magnitude in the growth rates between the positive and negative helical modes (Alves et al. (2007)).

1.2.5 Mean and Instantaneous Mixing Metrics

Much of the ascribed applicability of the JICF is predicated upon the overall behavior of the jet with respect to its performance in mixing with the crossflow (Margason (1993); Karagozian (2010); Mahesh (2013)). In consideration of this dependency, extensive attention has been directed to the exploration, and quantification of the mixing characteristics of the transverse jet (Kamotani and Greber (1972); Fearn and Weston (1974); Broadwell and Breidenthal (1984); Niederhaus et al. (1997); Smith and Mungal (1998); Johari et al. (1999); Eroglu and Breidenthal (2001); Su and Mungal (2004); Shan and Dimotakis (2006); Denev et al. (2010); Davitian et al. (2010b); Getsinger et al. (2014); Gevorkyan et al. (2016); Shoji (2017)). Mixing has been defined by Danckwerts (1952) as a description of the break-up of fluid clusters from large to smaller scales, altering the molecular diffusion and size of the cluster, thereby overall creating differences in scalar concentration values. Such a depiction regarding the intensities and scales of segregation within a flowfield is further refined by Kukukova et al. (2009), who introduces a concept of "exposure" between scalar concentrations, defining the potential of molecular interdiffusion, analogous to the rates of mass transfer across scalar field interfaces. Characterizing mixing in such a manner is similarly adopted by others (Corrsin (1957); Zwietering (1959); Corrsin (1964); Lee and Brodkey (1964)), while yet additional more diverse approaches cite stirring, folding, swirling, rate of stretching, and striations in a concentration field in relation to mixing (Danckwerts (1952); Mathew et al. (2005); Gubanov and Cortelezzi (2010)). A complete understanding of the physical mixing phenomena is composed from measurements of the mean entrainment, the turbulent stirring, and the molecular mixing, which are all interdependently connected. Properly defining a characteristics definition of mixing within a flowfield is therefore obviously quite complex, due to the range of possible constituent length- and time-scales, which consequentially results in an array of metrics utilized in defining a mixing process.

Historically, some of the earlier examinations of mixing for the JICF are made through determination of centerline jet fluid concentration decay (Smith and Mungal (1998); Su

and Mungal (2004)), centerline velocity decay (Fearn and Weston (1974)), and the classical mixing metrics of jet spread δ, and penetration P (Kamotani and Greber (1972); Su and Mungal (2004); Davitian et al. (2010b); Getsinger et al. (2012)), all of which are evaluated from the perspective of the jet centerplane ($x-z$ plane, $y=0$). Despite these investigations of the JICF from the centerplane, it is known that the developing jet largely exists outside of the centerplane, as is especially evident when the flow becomes asymmetric (discussed in Section 1.2.4). In light of such out of plane components of motions, scalar concentrations, and possible asymmetries about the jet centerplane, it is unlikely that the centerplane mixing metrics determine the true JICF mixing behavior with complete accuracy, which in turn brings to forbearance an inspection of the JICF in the cross-section. Inherent to all of the above approaches for examining the mixing of the JICF, is a necessitated treatment of the flowfield as a mean, thereby inhibiting an understanding of the temporal features of molecular mixing within the flowfield. Treatment of the JICF in accounting for instantaneous scalar concentration variation, for both the centerplane and cross-sectional orientations, has led to the implementation of mixing metrics such as Unmixedness (Dimotakis and Miller (1990)), Probability Density Function (PDF) (Kollman (1990)), Spatial Mixing Deficiency (SMD) (Bockhorn et al. (2010)), and the Mix-Norm and Mix-Variance (Mathew et al. (2003); Mathew et al. (2005); Gubanov and Cortelezzi (2010)), with the relevant formulations shown as follows:

$$f(C) = \frac{1}{A_{tot}} \left| \frac{dA(C)}{dC} \right| \tag{1.7}$$

$$U = \frac{1}{L_y L_z} \int \int \frac{(\frac{C}{C_o} - \frac{\overline{C}}{C_o})^2}{\frac{\overline{C}}{C_o}(1 - \frac{\overline{C}}{C_o})} dydz \tag{1.8}$$

$$SMD = [\frac{1}{L_y L_z} \int \int \{\frac{C - \overline{C}}{\overline{C}}\}^2 dydz]^{1/2} \tag{1.9}$$

Each of the instantaneous metrics investigate the intensity of segregation within the flow, though they approach molecular mixing phenomena with emphasis upon slightly different

flowfield traits: the Probability Density Function (Equation 1.7) describes the distribution of the normalized scalar data; Unmixedness (Equation 1.8), defined as the second moment of the scalar field, essentially is a variance measurement about a spatial mean, scaled by the variance assuming the a completely unmixed flow; Spatial Mixing Deficiency (Equation 1.9) is very similar to Unmixedness, except that the variance is taken about the mean and scaled by the mean; Mix-Norm integrates the square of a mean spatially or temporally averaged function over various length scales within the interrogation space. Within the different equations, $L_y L_z$ or A_{tot} refers to the area or interrogation window, area $A(C)$ is the function representing the area within the domain containing a specific scalar concentration of jet fluid, C/C_o, where C is the local concentration value within the instantaneous image, and $\overline{C}/C_o$ or $\overline{C}$ is the average of the concentration over the spatial domain.

In the work by Fearn and Weston (1974), Smith and Mungal (1998), and Su and Mungal (2004), the decay rates of velocity (for the former) and concentration (for the latter two), along the centerline are found to proceed in an exponential manner once outside the potential core of the jet, where the exact rates are dependent upon the particular flowfield conditions and configurations. For an equidensity gaseous JICF in the velocity ratio range of $10 \leq R \leq 25$, Smith and Mungal (1998) find that the concentration decay rate follows a power law of $s_c^{-1.3}$ in the nearfield, and after a downstream trajectory location of $s = 0.3R^2D$, decays at a rate of $s_c^{-2/3}$; for contrast a free jet is typically seen to decay at a rate of s^{-1}. In the work by Su and Mungal (2004) for a JICF with $R = 5.7$, the concentration is found to decay at the same rate as a free jet, with no marked transition in behavior at any downstream location. Yet another slight difference in concentration decay rates are seen in the results from Gevorkyan et al. (2016), wherein a variety of momentum flux ratios $5 \leq J \leq 41$, and density ratios $0.35 \leq S \leq 1.00$ are treated for a flush injected jet. Some of these discrepancies may be attributable to the differences in jet velocity profile at the exit plane, where Smith and Mungal (1998) and Gevorkyan et al. (2016) implement a top-hat profile, while Su and Mungal (2004) treat a fully developed parabolic profile. Figure 1.12 from Gevorkyan et al.

(2016) depicts jet concentration decays of the flush injected JICF for momentum flux ratios of $7 \leq J \leq 61$, along with the results from Smith and Mungal (1998) and Su and Mungal (2004). The decay rates are plotted as a function of centerline concentration trajectory normalized by the jet diameter (s_c/D), such that the jets are scaled allowing for easier comparisons. It is seen that reductions of the momentum flux ratio produce shorter potential cores for the jet (regions of pure jet concentration), corresponding to an enhancement of mixing (Gevorkyan et al. (2016)). Gevorkyan et al. (2016) additionally find that for a fixed momentum flux ratio J, relating to a convectively unstable jet, decreasing the density ratio S such that the jet transitions to absolute instability results in a shortening of the potential core. Such findings are consistent with the resulting strengths of upstream shear layer instabilities documented by Getsinger et al. (2014), with the exception of when the originating equidensity jet is already absolutely unstable, in which case the lower density jets obtained longer potential core lengths (Gevorkyan et al. (2016)).

Spreading of the JICF is a measurement which may be calculated either normal to the jet centerline concentration trajectory s, or along the vertical axis relative to the bounding wall (z direction), while the penetration is measured solely normal relative to the injection plane. Evaluation of the jet spread δ, and/or penetration P, is predicated upon an determination of a minimum jet fluid scalar concentration value that may still be treated as a constituent of the jet; Su and Mungal (2004) truncat the jet at a concentration of 20%, while Getsinger et al. (2012) and Gevorkyan et al. (2016) select a limit of 5%, and the recent work of Shoji (2017) proposes a threshold of 1%. It has been found, that as the momentum flux ratio is increased for a fixed jet Reynolds number, i.e. greater jet momentum relative to the crossflow, the resulting jet penetrates farther into the flowfield (Davitian et al. (2010b); Gevorkyan et al. (2016)). When examining a jet with fixed momentum flux ratio and jet Reynolds number, while systematically decreasing the density ratio, it is discovered that the jet decreases in penetration and vertical spread, but displays an enhancement in trajectory-normal spread (Gevorkyan et al. (2016)). Such results are in contrast to long held assumptions that the

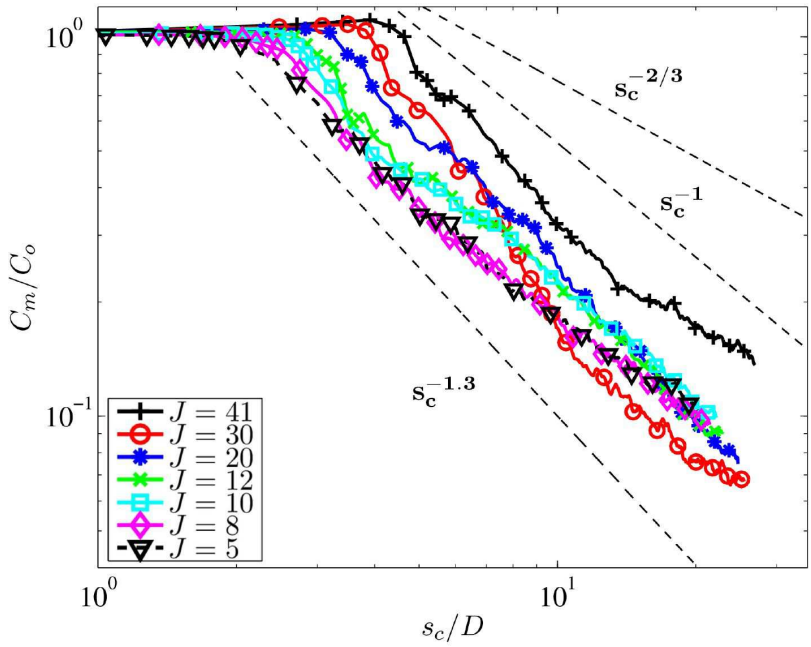

Figure 1.12: Mean concentration (C_m/C_o) decay along the jet centerline trajectory s_c, for the equidensity flush nozzle injected jet at a fixed Reynolds number of $Re_j = 1900$, for a variety of momentum flux ratios J. Adapted from Gevorkyan et al. (2016).

spread and penetration are directly coupled (Kamotani and Greber (1972)), and speaks to the significance of the reference frame in which jet spread is calculated. For the work of Smith and Mungal (1998), the determination of spread is separated between the windward and leeward components of the jet, wherein the leeward is found to spread at a much greater rate than the upstream side of the jet. This is thought to arise due to the fluid entrainment noted from wake vortices, and the differences in pressure gradients about the jet periphery.

Smith and Mungal (1998), and Shan and Dimotakis (2006) leverage the spatial PDF for examinations of the JICF from the centerplane and cross-section respectively. Given a theoretical fluid which is uniformly distributed throughout the total area A_{tot}, a homogeneous mixture, the PDF would yield a Dirac delta function at the mean value, whereas a completely segregated/unmixed flow would produce two Dirac delta functions with concentration values of 0 and 1. Decreasing the degree of segregation, or enhancing the mixing, results in a

development of valleys within the PDF, while simultaneously noting strong peaks at or about the most probable mean concentration. Shan and Dimotakis (2006) sees that the cross-sectional PDFs demonstrates an enhancement in homogeneity of the flowfield for the JICF as the jet Reynolds number Re_j is increased. The work by Gevorkyan et al. (2016) also examine cross-sectional PDFs for the JICF, instead exploring variation in momentum flux and density ratios; the results for the equidensity transverse jet with differing momentum flux ratios are found in Figure 1.13. Gevorkyan et al. (2016) sees that for a stated J value, methodical progression downstream of the jet injection reveals progressively sharper and stronger peaks at the preferred mean concentration value within the PDFs, indicating that the mixing is improved as the jet convects downstream. The PDF calculations from Gevorkyan et al. (2016) additionally determin that for the investigations on adjusting density ratio at a fixed J, the trends seen from the mean mixing metric of concentration decay in the centerplane are validated, where a reduction in S enhances the mixing, until examining low J values such as $J = 5$. Gevorkyan et al. (2016) also observes a general improvement in mixing, as quantified by the PDF, with improved JICF cross-sectional symmetry. Given the improvement in cross-sectional symmetry for a fixed J value with increasing jet Reynolds number, as documented in Getsinger et al. (2014), it appears there is consistency with the Reynolds number variation effects observed by Shan and Dimotakis (2006).

A widely and successfully applied to the JICF is the instantaneous mixing metric of Unmixedness (Smith et al. (1997); Getsinger (2012); Gevorkyan et al. (2016); Shoji et al. (2019); Shoji et al. (2020a)), which is treated in both the centerplane and cross-section. Quite aptly, the Unmixedness provides a quantification of how un-mixed a flow is, within a given domain of integration. In examining the cross-sectional images of the JICF the interrogation domain simply corresponds with the entire image. However, when treating images in the centerplane, careful consideration must be made to select an appropriately defined window of examination, a thorough investigation of which is made by Gevorkyan (2015) and Shoji (2017). In a like manner to the characterization of the jet spread, the centerplane Unmixedness calcula-

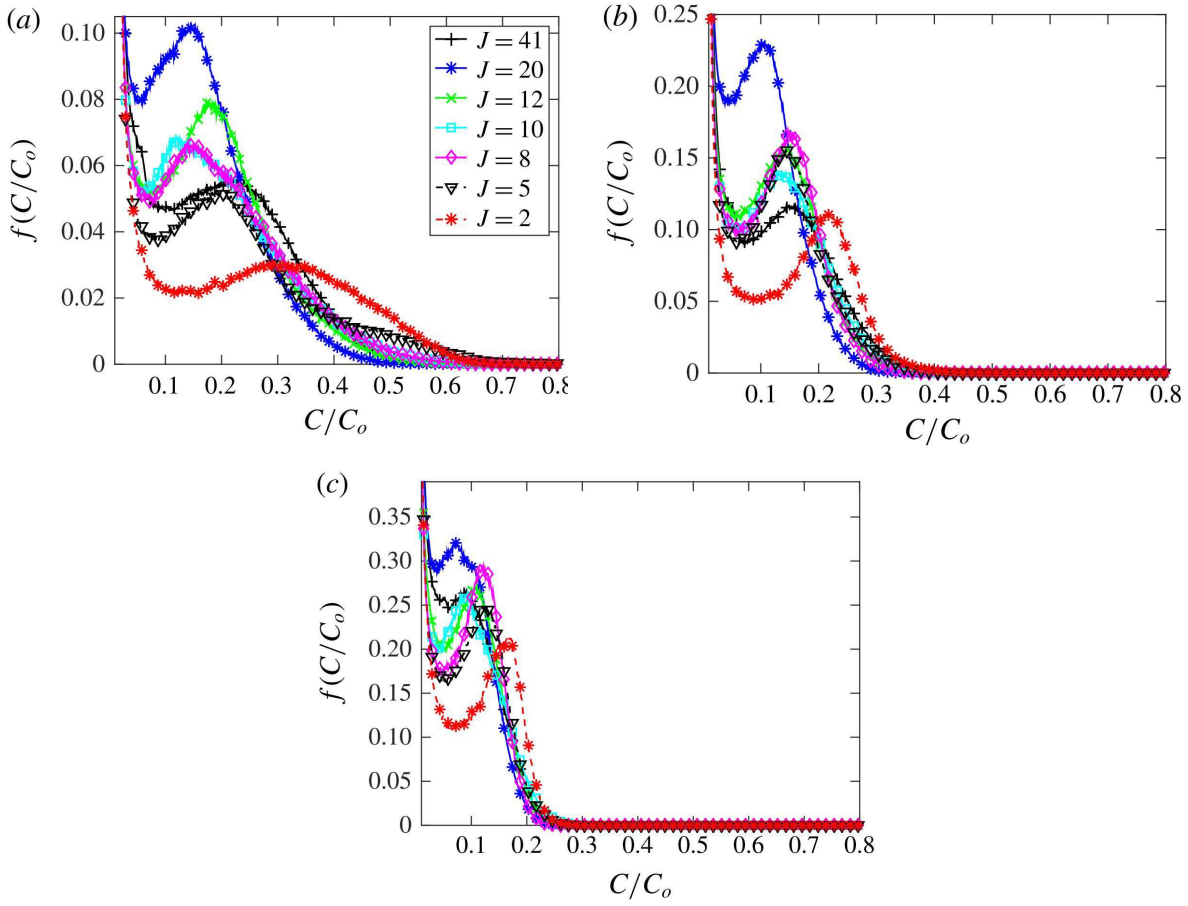

Figure 1.13: Cross-sectional based spatial PDF for the equidensity flush nozzle injected transverse jet, measured at locations of (a) $x/d = 2.5$, (b) $x/D = 5.5$, and (c) $x/D = 10.5$. Reprinted from Gevorkyan et al. (2016).

tions may be performed relative to the vertical or trajectory-normal planes. Representative plots for the centerplane and cross-sectional based Unmixedness data from Gevorkyan et al. (2016) are given in figures 1.14(a-b) and (c), where it is clear that as the momentum flux ratio is decreased the molecular mixing between the jet and crossflow is enhanced. Such a phenomenon may be due to the increasing strength of the upstream shear layer instabilities as J is reduced, and the probable contribution from the shear layer to the generation of a symmetric CVP structure, the formation of which is attributed to enhanced mixing (Kelso et al. (1996); Karagozian (2014); Mahesh (2013)); the higher momentum flux ratios

($J = 41, 30$) may display worse mixing due to the asymmetric cross-sectional jet structures which form downstream (Getsinger et al. (2014); Gevorkyan et al. (2016)). The Unmixedness evaluations of lower density ratio jets, with high and low momentum flux ratios, reveal great agreement with findings from the PDF, and concentration decay calculations accordingly (Gevorkyan et al. (2016)). That is, for a high J, decreasing S below unity enhanced the molecular mixing, whereas for a low J, such as $J = 5$, a decrease in S was marked by a worsening of the molecular mixing (Shoji (2017)). Gevorkyan et al. (2016) demonstrate that this worsened mixing for the low density JICF at $J = 5$ results from differences in the entrainment of jet fluid vs. crossflow fluid into upstream shear layer vortices.

The other mixing metrics of Spatial Mixing Deficiency (SMD) and Mix-Norm, like the Unmixedness calculations, in essence examine the degree of the instantaneous molecular mixing within the flow, though the Mix-Norm additionally accounts for the degree stirring within the flowfield. It is sufficient to say that when the calculations are accordingly normalized by the mean, the instantaneous molecular mixing quantifications from the SMD, Unmixedness, and Mix-Norm metrics are found to agree quite well (Getsinger (2012); Gevorkyan (2015)). Therefore, current experimental studies by our group focus the mixing quantifications on the classical mean parameters, as well as those of the instantaneous PDF and Unmixedness (Shoji (2017); Besnard (2019)). Regardless of the current mixing methodologies selected, there remains shortcomings in completely quantifying the phenomena transpiring within the flowfield, leaving room for discussion as to which metrics and definitions of mixing are truly accurate and comprehensive for the flow dynamics being studied.

1.3 Temporally Forced JICF

In supplementation to the instability characteristics which have been explored experimentally for the unforced, or uncontrolled JICF, an enhancement and further validation of those instability trends and behavior (see Section 1.2.3) are treated through relatively low level

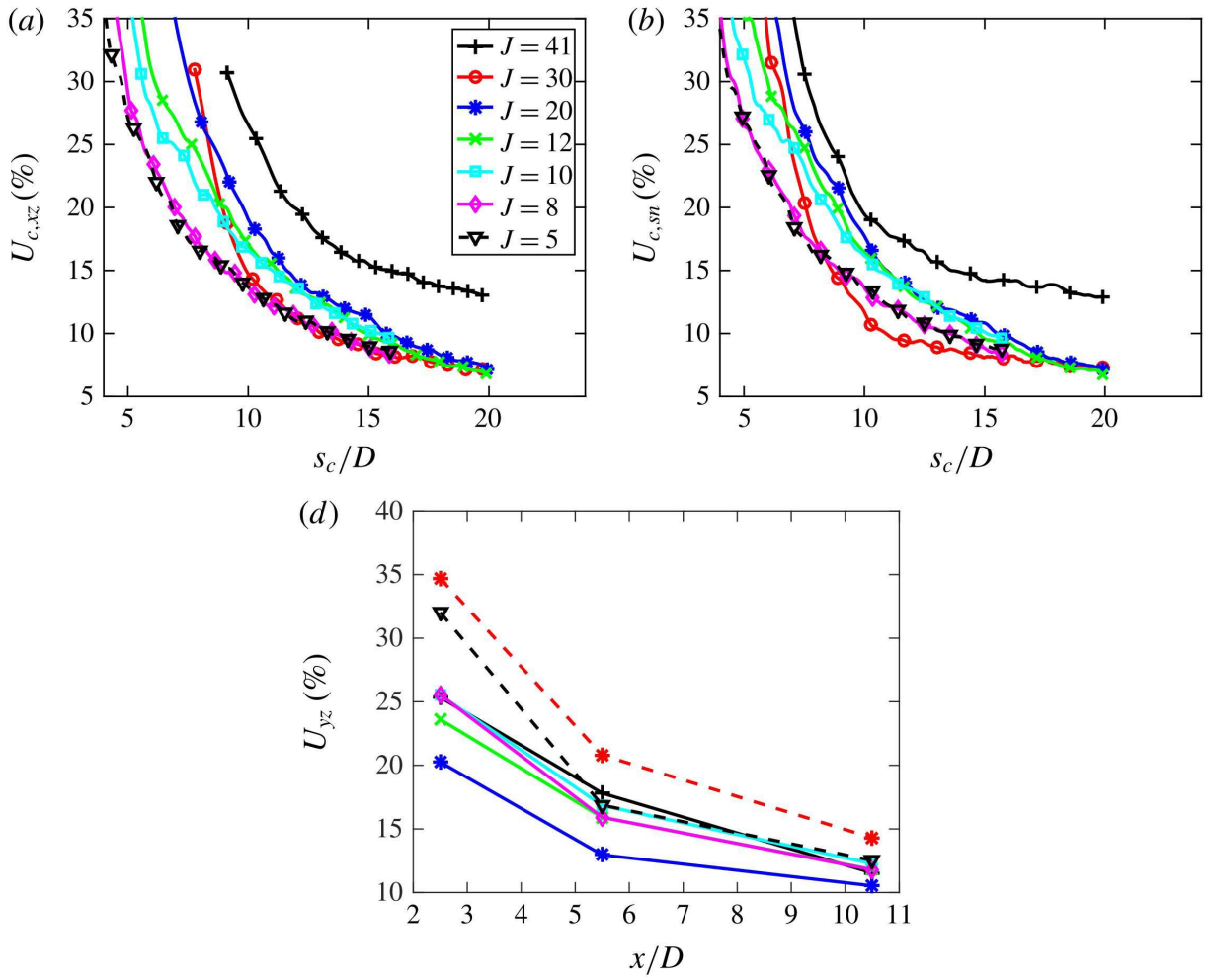

Figure 1.14: Unmixedness calculations for the equidensity flush nozzle injected transverse jet: (a) Centerplane Unmixedness calculated in $x-z$ direction $U_{c,xz}$, (b) Centerplane Unmixedness calculated in $s-n$ direction $U_{c,sn}$, (c) Cross-sectional U_{yz} Unmixedness. Reprinted from Gevorkyan et al. (2016).

temporal sinusoidal jet excitation for the JICF (Megerian et al. (2007); Bagheri et al. (2009); Davitian et al. (2010a); Ilak et al. (2012); Getsinger et al. (2012); Shoji et al. (2020c)). Within the realm of low density free jets, Juniper et al. (2009) and Hallberg and Strykowski (2006) find that strong sinusoidal external excitation of the jet, when the flowfield is globally unstable, can be utilized to overpower the fundamental instability f_o, and force a "lock-in" of flow at the respective frequency of forced sinusoidal excitation f_f, depending on the

frequency and amplitude of excitation. For a non-reacting free jet and a buoyant jet diffusion flame, Juniper et al. (2009) apply the excitation experimentally via a loudspeaker, whereby there is a critical input voltage required to generate the lock-in effects, they find varies depending upon the excitation frequency applied. Shown in figure 1.15(a) is the generated lock-in diagram from Li and Juniper (2013a) for a non-reactive free jet, depicting a V-shape linear dependence between the forcing frequency and the fundamental frequency $|f_f - f_o|$, which is suggestive of a Hopf Bifurcation to the global modes; Hopf Bifurcations are detailed within Huerre and Monkewitz (1990). Li and Juniper (2013a) further delineate multiple types of nonlinear dynamical response of the jet to the applied forcing: (1) cases wherein the flow does not significantly respond to the forcing, and the fundamental/natural frequency, or one which is slightly shifted, dominates during low amplitude forcing, (2) possible cases of "quasiperiodicity" where the dynamical response is characterized by the funadmental and applied forcing frequencies, and their respective linear combinations for moderate amplitude forcing, and (3) cases demonstrating "1:1 lock-in" where the forcing frequency dominates and the fundamental freuency is diminished for high amplitude forcing. Given the aforementioned correspondence of the JICF with free and buoyant turbulent jets, such procedures exploring lock-in are extended to the JICF, where Davitian et al. (2010a) also realize a relatively linear dependence upon lock-in behavior for an equidensity jet at low velocity ratios R, seen in figure 1.15(b). For figure 1.15(c), Getsinger et al. (2012) determines the existence of lock-in behavior for a lower density JICF ($S = 0.55$), and finds that decreasing the momentum flux ratio and/or the density ratio results in a strengthening of the instability modes, producing lock-in diagrams where greater amplitudes of excitation are required to overcome the natural mode (an effective steepening/closing of the V-shape). In a like manner, the numerical simulations of Bagheri et al. (2009) and Ilak et al. (2012) are able to confirm the development of linearly globally unstable flow via eigenvalue analysis, and find that in some cases different globally unstable eigenmodes are generated from bifurcations in the jet, which are dependent upon the velocity ratio of examination. Interestingly Getsinger et al.

(2012), Li and Juniper (2013a), and Shoji et al. (2020c) note asymmetries within the lock-in diagrams about the fundamental frequencies, suggesting an increased resistance to the higher forcing frequencies as compared to frequencies at a similar linear displacement below the fundamental frequency. It may be that this results from the vortex formation along the upstream shear layer being unable to keep up with the high frequencies at which the jet is forced, thereby limiting the response of the jet. Investigation of the JICF via forced sinusoidal excitation while conversely within the realm of convective instability characteristics is found by Davitian et al. (2010a) to produce a lock-in diagram where the V-shape was completely opened and flat, demonstrating the receptivity and response of the jet flow to any frequency of excitation even at relatively low amplitude levels of forcing. More recently and quite remarkably, Shoji et al. (2020c) actually demonstrates lock-in diagrams for the convectively unstable JICF at relatively high momentum flux ratios, denoting that while the shear layer is weakely unstable, for forcing frequencies below the fundamental frequency of the jets significant forcing is required to achieve lock-in. Further, investigation of the a free jet also demonstrated lock-in, instead in the higher frequency forcing range. These findings are shown in figure 1.15(d). They note these observed lock-in traits for convectively unstable shear layers in the transverse jet actually agrees with the theoretically determined growth rates of the axisymmetric modes observed from linear stability theory by Alves et al. (2008).

Aside from illuminating upon the strength, receptivity, and transition of instability characteristics within jets, excitation of jet flows has also long been implemented for the more pertinent usage of altering the structural and mixing phenomena of the flowfield, which at first was accomplished within free jets (Crow and Champagne (1971); Binder and Favre-Marinet (1973); Hill and Greene (1977); Vermeulen et al. (1986); Vermeulen and Yu (1987); Reynolds et al. (2003)). Extension to application within the JICF also yields significant impacts in augmenting the flowfield structures, vortex interactions, and mixing properties (Vermeulen et al. (1992); Johari et al. (1999); Eroglu and Breidenthal (2001); M'Closkey et al. (2002); Narayanan et al. (2003); Shapiro et al. (2006); Davitian et al. (2010b); Shoji

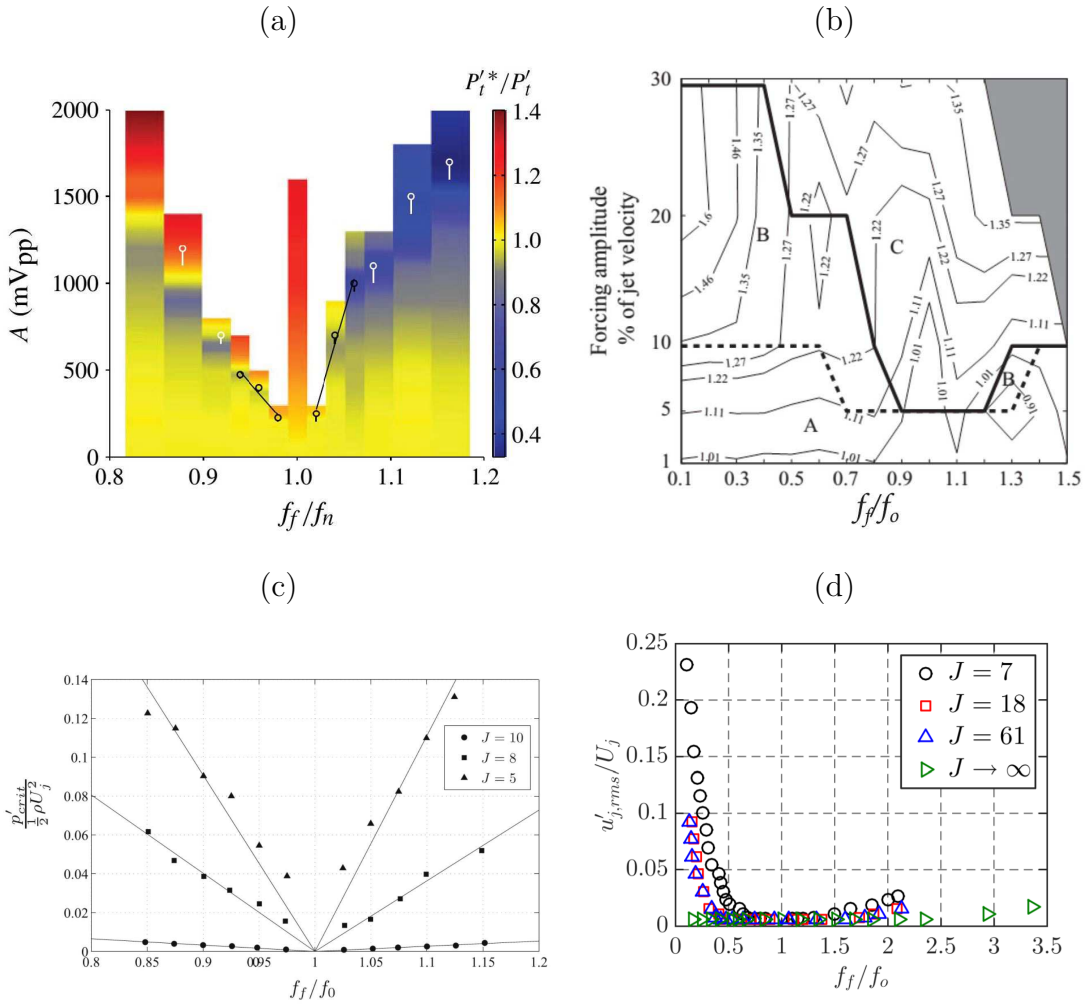

Figure 1.15: Reprinted lock-in diagrams for (a) the non-reactive free jet of Li and Juniper (2013a), (b) the equidensity transverse jet of $R = 1.5$ of Davitian et al. (2010a), (c) the low density transverse jet at $S = 0.55$ of Getsinger et al. (2012), (d) the equidensity transverse jet with absolutely and convectively unstable shear layers of Shoji et al. (2020c).

et al. (2019); Shoji et al. (2020a); Besnard (2019)). Utilization of forcing in controlling the developing JICF behavior has inherently differing approaches dependent upon which instability modes are to be advantageously exploited, thereby resulting in treatment of flow from both axisymmetrically, and helically excited perspectives, given the $m = 0$ and $m = \pm 1, 2$ modes respectively. Expounding from these excitation regimes, is a further delineation in

the nature of the excitement applied to the flowfield, such as axisymmetric application of sine, square, or double-pulsed waveforms, and helical clockwise or counter-clockwise traveling waveforms.

1.3.1 Axisymmetric Excitation of the Jet

Axisymmetric excitation of the JICF is employed through perturbations of the jet flow before issuance into the crossflow, thereby generating an unsteady periodicity to the mass flow rate of jet fluid. For experimental investigations, such behavior is typically produced via an acoustic loudspeaker Vermeulen et al. (1992); M'Closkey et al. (2002); Shapiro et al. (2006); Davitian et al. (2010b); , modal or piston shaker (Hendrickson and M'Closkey (2012)), or by diverting/constricting flow with carefully timed valves and actuators (Johari et al. (1999); Eroglu and Breidenthal (2001); Anderson et al. (2001)). Given such an array of excitation methods, and the unique capabilities each provides, a wide range of forcing types are able to be entreated, including sine waves, single pulsed square waves, double pulsed square waves, or even that of full modulation of the jet flowrate.

Early investigations of sine wave forcing of the JICF are performed experimentally by Vermeulen et al. (1988)(1992), M'Closkey et al. (2002), Narayanan et al. (2003), and Shapiro et al. (2006), while early complimentary numerical simulations are conducted by Blossey et al. (2001). These studies suggested that the jet spread and penetration could be enhanced through the temporal variation of the jet velocity, which is thought to arise due to the temporal control of jet vorticity generation (M'Closkey et al. (2002)). Vermeulen et al. (1992) notes that the optimal jet penetration, for a cold jet in hot crossflow with $J \equiv \rho_j \overline{U}_j^2 / \rho_\infty U_\infty^2 = 3.13$, is produced at a forcing Strouhal number of $St_j = 0.27$, whereby the penetration is enhanced 100%, and the mixing improved as well. The work of Narayanan et al. (2003) additionally note for a flowfield of $R = 6$ and $Re_j = 5000$, there is a susceptibility to, and amplification of, low level excitation of the jet. Conversely, M'Closkey et al. (2002) and Shapiro et al. (2006) note no significant alterations in the jet spread or pene-

tration given the implementation of sinusoidal forcing. Later extensive exploration of the instability characteristics along the upstream shear layer, as detailed in Sections 1.2.3 & 1.3, reveal the necessity for the temporal waveforms utilized in the excitation of the jet to be strategically selected given the differing responses to perturbations if the jet shear layer is convectively or absolutely unstable. This proposed selective dependency or "strategic forcing" is validated within the work of Davitian et al. (2010b). In accordance with the lock-in behavior, convectively unstable jets are quite responsive to low level sinusoidal excitation, whereas absolutely unstable jet yield minimal differences in spread and penetration, unless the forcing frequency f_f was quite close to the fundamental frequency f_o, or the amplitude of excitation is quite large. The recent work of Shoji et al. (2020a) evaluates the JICF under similar conditions as treated by Davitian et al. (2010b), finding that strategic sinusoidal excitation is able to produce jet structures which are more symmetric in the cross-section, and have enhanced mixing as given from the classical mean mixing metrics, as well as from instantaneous Unmixedness, and Probability Density Function (PDF).

Some of the earliest modifications to the JICF are also realized by square-wave pulsations, or even full modulation of the jet flow (Kelso et al. (1996); Johari et al. (1999); Schuller et al. (1999); Eroglu and Breidenthal (2001)). Similar to the findings with sinusoidal excitation, pulsing of the jet flow in a square-wave manner is complimented by enhancement of the spread, and penetration of the jet into the crossflow. Johari et al. (1999) explores full modulation of a turbulent reactive (acid-base) water jet in crossflow, and notes that optimal penetration is achieved for a Strouhal number of $St_j \equiv fD/\overline{U}_j = 0.004$ for a jet with a mean velocity ratio of $R = 5$. The drastic enhancement of the jet's penetration is marked by the formation of distinct vortex rings or puff-like structures, or a more elongated/stretched vortical structure depending upon the pulse-width of excitation, where the puff-like vortices are typically noted for control of the jet at lower duty cyles, such as $\alpha = 20\%$ (M'Closkey et al. (2002)); for square wave excitation, duty cycle is defined during a particular cycle as the temporal pulse-width τ divided by the period T, and is taken as a percentage. The

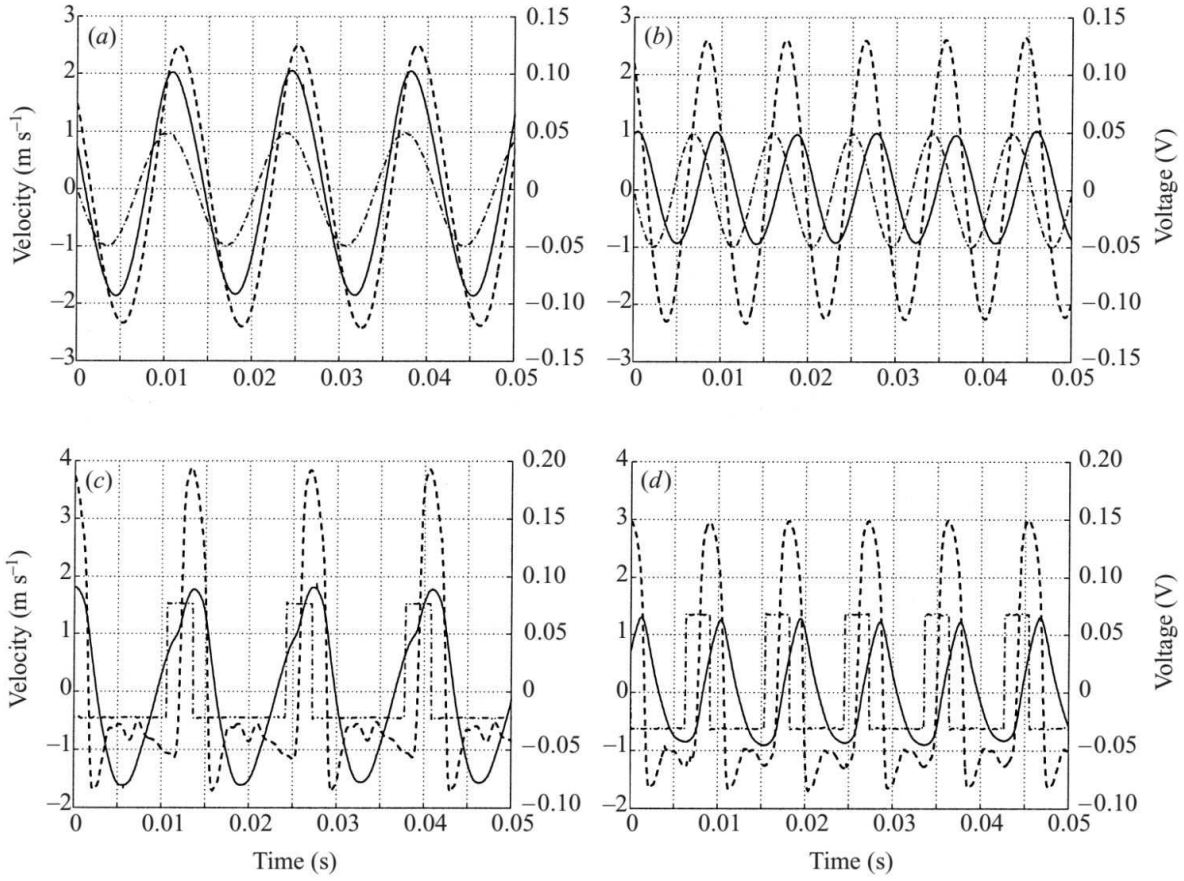

Figure 1.16: Comparison of input waveform to the actuator (dotted-dashed), uncompensated waveform (solid), an compensated waveform (dashed) for: (a) sine wave iput at 73.5 Hz, (b) sine wave input at 110 Hz, (c) square wave input at 73.5 Hz and $\alpha = 22\%$, and (d) square wave input at 110 Hz and $\alpha = 31\%$. Velocity perturbations for the compensated waves were matched in all cases at $U'_{j,rms} = 1.7m/s$. Adapted from M'Closkey et al. (2002).

relatively short temporal pulse-widths produced at the lower duty cycles of square wave forcing introduce sharp distinct impulses of vorticity, which due to the self-induced velocity fields (Chang and Vakili (1995)), are able to penetrate quite deeply into the crossflow. The temporal spacing between pulses provides physical spacing between the puffs, such that the vortices do not interact in a negative manner to inhibit the enhancement of penetration and mixing. Similar findings are made by Eroglu and Breidenthal (2001).

Despite the promising results of the early studies utilizing square-wave pulses and modulation of the jet, it is distinguished by Johari et al. (1999) and Schuller et al. (1999) that the temporal variation of the jet velocity at the exit plane could in fact be quite different from the applied excitation waveforms, a discrepancy which appears to be apparatus dependent. M'Closkey et al. (2002) was then the first to implement an open loop or "compensated" jet control method in order to more precisely dictate the forcing waveforms, where figure 1.16 displays the uncontrolled and controlled square wave experimental waveforms of the jet, and within figure 1.17 are the resulting dramatic responses noted for the jet structure. The jet when excited in a square wave manner, but uncompensated (fig. 1.17(d)), does not show any significant differentiation from that of the unforced jet (fig. 1.17(a)), yet once compensation of the jet is applied, the jet structure is completely transformed, resulting in deeply penetrating puff like vortices (fig. 1.17(e)). M'Closkey et al. (2002), and then later Shapiro et al. (2006) and Davitian et al. (2010b) through the utilization of such compensated waveform forcing, find the jet responds most dramatically to excitation at frequencies which are subharmonics of the natural instability frequency detected along the jet upstream shear layer. These studies in addition to characterizing the nature of waveform type, frequency, and duty cycle, also match among all excitation conditions the resultant root mean square (RMS) of the perturbation to the jet, as given by the equation,

$$u'_{j,rms} = \sqrt{\frac{1}{T}\int_{t_1}^{t_1+T} (u_j - U_j)^2 dt} \tag{1.10}$$

Such a description of the modification to the jet from the applied forcing allows for direct comparison of between excitation methods, and their resulting impact upon the flowfield. Interestingly, it is seen that for an absolutely unstable jet, sine-wave forcing, even at relatively high amplitudes of excitation, is unable to alter the jet penetration significantly, whereas square wave forcing is able quite dramatically alter the jet behavior even at low levels of excitation (M'Closkey et al. (2002); Shapiro et al. (2006); Davitian et al. (2010b); Shoji et al. (2019)). Figure 1.17, from the work of M'Closkey et al. (2002), displays smoke visualizations of the unforced, sine-wave, and square-wave excited forced JICF at $R = 2.58$ and $Re_j = 1500$,

where the forcing perturbation is matched at $U_{j,rms} = 1.7m/s$ in all cases. Quite clearly, compensated or uncompensated sine wave forcing (Figure 1.17(b-c)), and uncompensated square-wave forcing (Figure 1.17(d)), which has a resultant waveform similar to the sine-wave excitation, displays no significant changes to the JICF. The compensated square-wave forced JICF (figs. 1.17(e-i)) does dramatically alter the jet behavior, where the systematic increase in duty cycle is marked by a transition from puff-like deeply penetrating vortices, to that of elongated vortical structures, followed by a jet structure which appears unchanged from the unforced jet, at a duty cycle of $\alpha = 62\%$. The visually established sensitivity of the jet to duty cycle, with a distinguished preferential enhancement of the JICF at lower duty cycles, validates the findings noted in the earlier works of Johari et al. (1999), and Eroglu and Breidenthal (2001).

Illumination regarding the dependency of the JICF to the duty cycle, or temporal pulse-widths, of applied square wave modulation is provided by Shapiro et al. (2006) and Johari (2006). Johari (2006) defines an effective stroke ratio parameter L/D in equation 1.11, based on the square wave temporal jet exit velocity u_j, temporal pulse width τ, jet cross-sectional area A_{jet}, and the jet exit diameter D; a stroke ratio is typically defined for a piston movement as the length of the piston stroke L, nondimensionalized by the diameter of the piston head D.

$$\frac{L}{D} = \frac{1}{A_{jet}D}\int_0^\tau \int_A u_j(dA)(dt) \simeq \frac{\overline{U}_j\tau}{D} \tag{1.11}$$

With the given definition of stroke ratio, Johari (2006) defines a flow regime map, which is shown in figure 1.18(a), where the resulting jet vortical structures produced are characterized by the duty cycle and stroke ratio of the square wave forcing. Shapiro et al. (2006) links the calculated optimal pulse-width phenomena to the work of Gharib et al. (1998), who investigates the implications of a piston stroke ratio on the optimal formation of a single coherent vortex ring. Gharib et al. (1998) discovers there is a critical stroke ratio at which the generated vortex ring is completely saturated with jetting fluid, found to be a value of $L/D \approx 4$, and referenced as the formation number. Above this stroke ratio it is seen that the

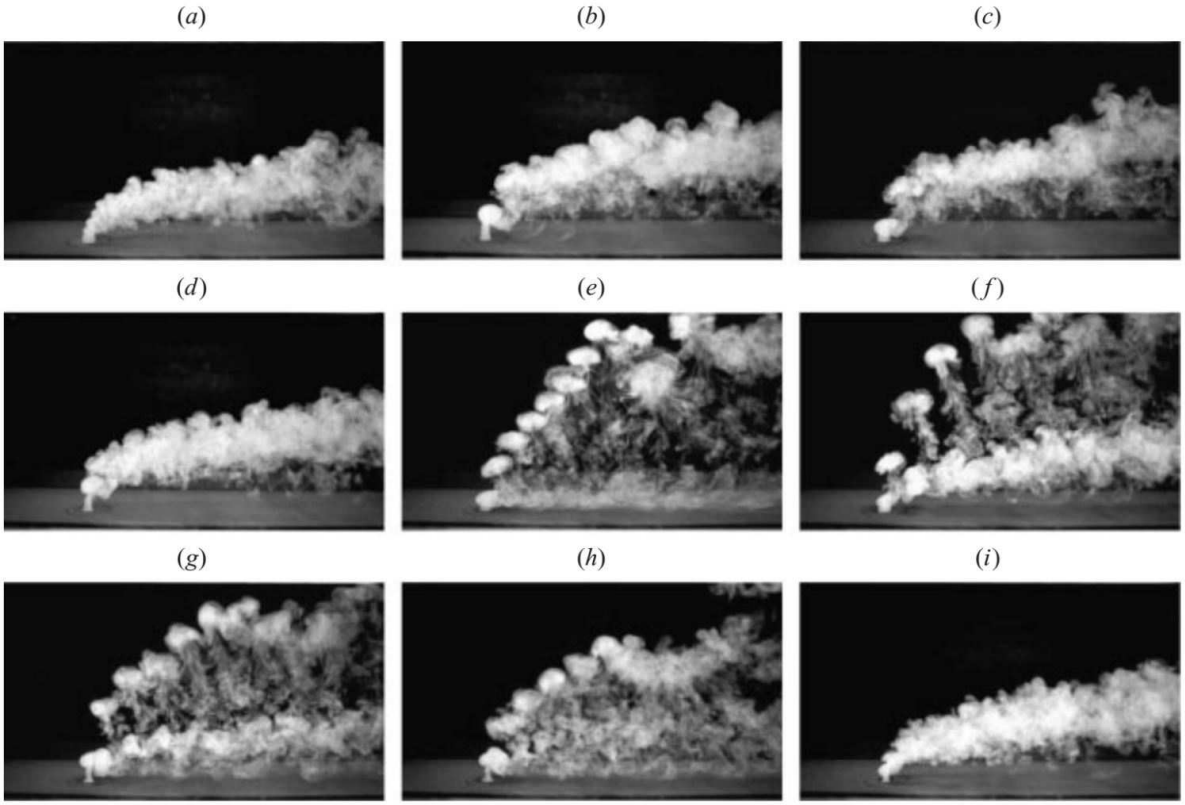

Figure 1.17: Smoke visualizations of the JICF at a mean velocity ratio of $R = 2.58$, with RMS amplitude of excitation matched at $U'_{j,rms} = 1.7m/s$. Results shown for (a) unforced JICF, (b) uncompensated sine wave at 73.5 Hz, (c) compensated sine wave at 73.5 Hz, (d) uncompensated square wave at 110 Hz and $\alpha = 31\%$, (e) compensated square wave at 110 Hz and $\alpha = 31\%$, (f) compensated square wave at 55 Hz and $\alpha = 15\%$, (g) compensated square wave at 73.5 Hz and $\alpha = 22\%$, (h) compensated square wave at 85 Hz and $\alpha = 24\%$, and (i) compensated square wave at 220 Hz and $\alpha = 62\%$. Adapted from M'Closkey et al. (2002).

vortex ring is unable to coherently entrain any more fluid, and thus results in a trailing jet column traveling behind the ring, whereas when the stroke ratio is sub-critical, the vortex ring is not completely filled, and thus not of optimal circulation or strength. These behaviors noted for the single vortex ring in quiescent surroundings, and the distinguished critical stroke ratio of $L/D \approx 4$, are discovered to agree remarkably well for the findings of the vortical structures produced by the square-wave excited JICF (Shapiro et al. (2006); Johari (2006)).

Davitian et al. (2010b), and more extensively Shoji et al. (2019), later determine the optimal stroke ratio for the best spread and penetration actually varies as the momentum flux ratio is changed. Shoji et al. (2019) sees that as the momentum flux ratio, for an equidensity jet, is decreased from $J = 61$ to $J = 7$ the optimal L/D also decreases, irrespective of convective or absolute instability characteristics along the upstream shear layer. Recent work by Shoji et al. (2019) distinguish that for square wave excitation of a weak CU flow, the stroke ratio producing the best molecular mixing is very near the established value of $L/D \approx 4$ suggested by Gharib et al. (1998) for a starting jet. They also note as the crossflow is strengthened and the jet eventually transitions to an AU flow, the optimal stroke ratio for best molecular mixing is reduced, analogous to the trends in optimal vortex ring formation with reducing r_{ring} set forth by Sau and Mahesh (2008). Such findings very importantly demonstrate that the best spread and penetration, long considered as suitable markers of the overall efficacy of mixing between the jet and crossflow, do not always correspond to the best molecularly mixed JICF. Compounding the findings regarding the momentum fux ratio, Shoji et al. (2019) also explores the impact of varying the RMS of the jet excitation, where it is seen that as the RMS is increased, the stroke ratio required to enhance the jet spread and penetration increases as well, which is found to agree well with the noted trends from Sau and Mahesh (2010). These results regarding the optimal stroke ratio for either the best spread and penetration or the best mixing, and their dependence upon momentum flux ratio and forcing RMS are shown in Figure 1.19.

Numerous numerical investigations regarding single pulse square wave excitation of the JICF have also been conducted (Sau and Mahesh (2007)(2008)(2009)(2010); Muldoon and Acharya (2010); Coussement et al. (2012)), yielding findings of enhanced spread, penetration, and mixing for specific forcing conditions, in line with results which are derived experimentally. Sau and Mahesh (2007) investigates the scalar mixing of a vortex ring without the presence of a crossflow, validating the theorized optimal stroke ratio proposed by Gharib et al. (1998). They note that the presence of a trailing column behind the vortex ring actu-

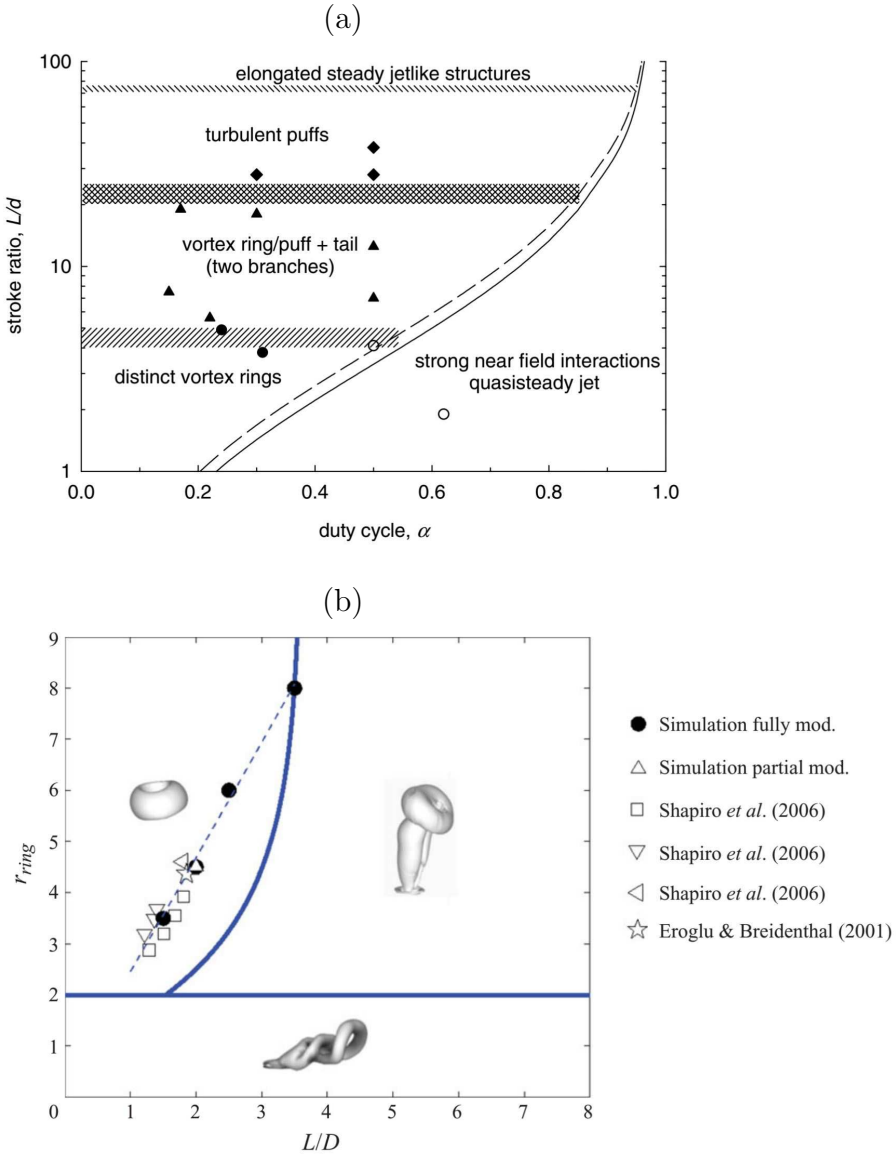

Figure 1.18: (a) Flow regime map for vortical and flow structures. Experimental data was composed of distint vortex rings (solid circles), vortices with trailing flows (solid triangle), turbulent puffs (solid diamond), and strongly interacting quasisteady structures (hollow circle). Reprinted from Johari (2006). (b) Flow map for optimal forcing conditions corresponding to best spread and penetration, from numerical simulations and experimental data. Reprinted from Sau and Mahesh (2010).

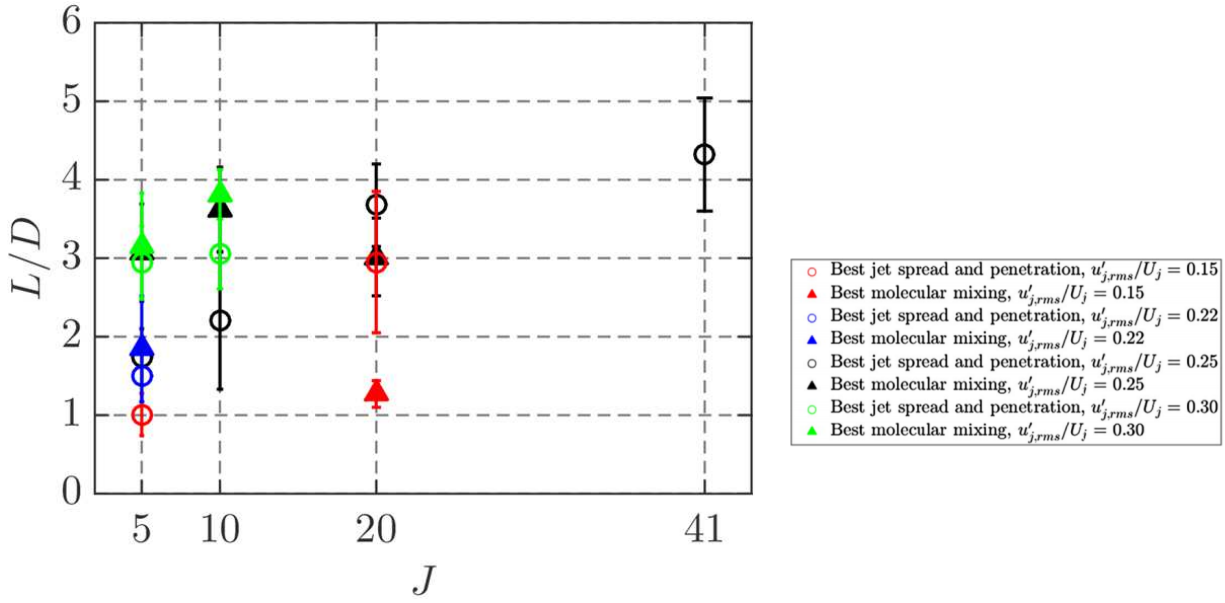

Figure 1.19: Flow map of optimal stroke ratio for best spread and penetration (circles), and best molecular mixing (triangles), explored for a range of momentum flux ratios and RMSs of perturbation (colors). Adapted from Shoji et al. (2019).

ally detracts from the mixing process. Interestingly, Sau and Mahesh (2008) finds that when crossflow is introduced to the flowfield, a small degree of trailing fluid behind a single vortex ring can actually instead enhance the mixing. Interestingly, they additionally show that the presence of a crossflow can also result in a reduction of the optimal stroke ratio for the formation of a fully filled vortex. Sau and Mahesh (2008) introduces a parameter called the ring velocity ratio, defined as the peak-to-peak jet velocity divided by the crossflow velocity,

$$r_{ring} = \frac{\Delta U_j}{U_\infty} \tag{1.12}$$

noting that as the ring velocity ratio is decreased, the optimal stroke ratio decreases to a minimum value of $L/D \approx 1.5$, after which further reducing r_{ring} results in the production of hairpin vortices rather than coherent vortex rings. These findings support the experimentally demonstrated decrease in optimal stroke ratio for best molecular mixing as given by Shoji et al. (2019). The DNS of Sau and Mahesh (2010) numerically treats a JICF under similar conditions as explored by Shapiro et al. (2006), where the resultant behavior is extremely

well correlated with the experimental findings of the development various vortical structures given the nature of the ascribed forcing. Figure 1.18(b) depicts a flow regime map for the optimal square-wave forcing conditions to produce the best spread and penetration, based on the stroke ratio and ring velocity ratio. The plot compares the numerical results of Sau and Mahesh (2010) with the experimental studies of Shapiro et al. (2006) and Eroglu and Breidenthal (2001), in which it is seen that as the vortex ring velocity ratio is decreased, the required stroke ratio for optimal spread and penetration is likewise decreased, as also noted by Shoji et al. (2019). However, the most interesting discovery from the numerical study of Sau and Mahesh (2010) is regarding the degree of compensation necessary for exciting the flow in a square-wave manner. It is found that even under implementation of an imperfect waveform, as long as the perturbations are characterized by a sharp upsweep and downsweep, flow responds accordingly (Sau and Mahesh (2010)). Most recently, the work of Coussement et al. (2012) performs large eddy simulations (LES) of the JICF for the same forcing conditions as employed by M'Closkey et al. (2002). The study distinguishes the formation of puff-like vortical structures and jet bifurcations for some cases, which are generally more readily seen for the lower duty cycles of excitation, in agreement with earlier experimental studies (Johari et al. (1999); M'Closkey et al. (2002); Shapiro et al. (2006)).

The recent work of Shoji et al. (2019) and Shoji et al. (2020a) seek to quantify mixing associated with sine and square wave excitation via acetone PLIF and utilization of molecular mixing metrics such as Unmixedness. Shoji (2017) also preliminarily examines advantageously utilizing the knowledge gained from single pulse square-wave forcing, regarding the formation and propogation of vortex rings, to enhance the jet mixing by inducing vortex interactions/collisions, merger, and subsequent breakdown through double pulse forcing of the JICF. A representation of a produced waveform is given in figure 1.20, where it is theorized that a low amplitude and relatively long temporal pulse width waveform would produce a slow moving vortex ring, while the high amplitude short temporal pulse width would produce a sharp impulse in the jet, resulting in a fast moving vortex ring which would then catch

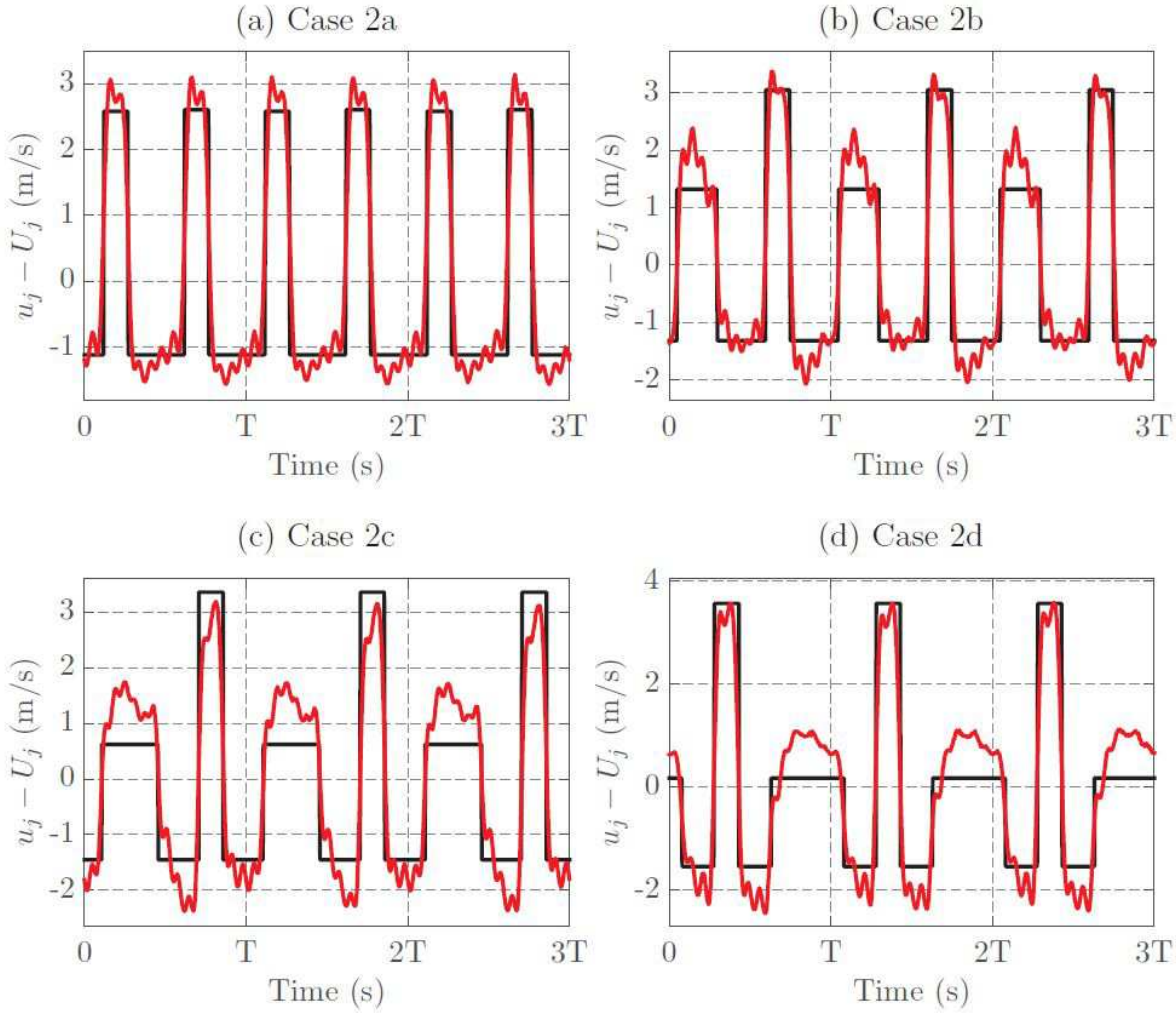

Figure 1.20: Idealized (black), and actual (red) compensated waveforms for double wave forcing of the JICF at $f_f = 55Hz$, and matched RMS of $U'_{j,rms} = 1.7m/s$. Measurements of resulting waveforms recorded with hotwire anemometry. Adapted from Shoji (2017).

up to, and interact with the more slowly traveling initial vortex ring. Realization of such collisions requires the careful selection and control of numerous forcing parameters, such as the temporal pulse-widths, the temporal delay between the pulses, and the respective amplitudes of forcing. Shown in figure 1.21 are a series of succinctly captured instantaneous centerplane PLIF images, which display the formation of the two vortex structures and their subsequent nearfield collision.

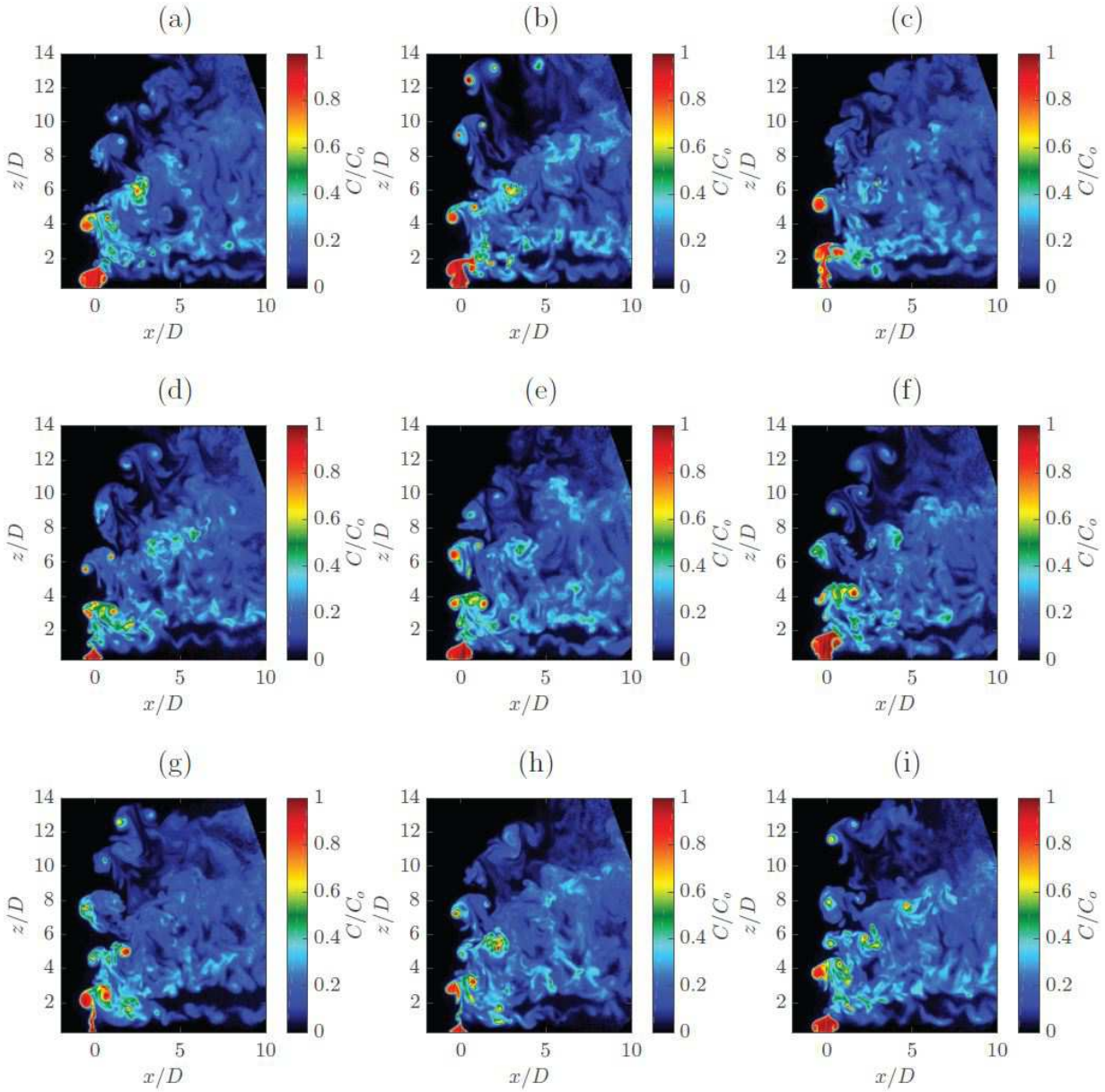

Figure 1.21: Sequential instantaneous centerplane PLIF images for the flush nozzle injected JICF at $J = 6.7$ and $S = 1.00$. Forcing conditions are $f_f = 55Hz$ abd $U'_{j,rms} = 2.0m/s$, corresponding to Case 2b from Shoji (2017). Images recorded at framing rate of 1 Hz. Adapted from Shoji (2017).

1.3.2 Helical Excitation about the Jet

Implementation of axisymmetric forcing throughout the years has displayed a remarkable ability to actively control the development of the JICF, given the advantageous exploitation

of forcing the upstream shear layer instability characteristics as detailed in Section 1.3.1. In light of such findings, it is additionally proposed that a similar control of the JICF may be realized through asymmetric forcing of the jet flow, whereby the helical instability modes $m = \pm 1, 2$ are entreated, instead of the axisymmetric mode $m = 0$. There are a variety of experimental studies regarding swirling jets (Chanaud (1965) Cassidy and Falvey (1970)), vortices confined in a tube (Garg and Leibovich (1979)), and leading edge or tip vortices over wings (Singh and Uberoi (1976); Roos and Kegelman (1990)), which demonstrate that there are coherent periodic oscillations in the wake flow, which are suggested to be correlated with the first helical mode of the time averaged mean flow profiles. Progressing simultaneously in the literature with these experimental studies are theoretical examinations of the helical instability modes within such swirling flows (Lessen et al. (1974); Duck and Foster (1980); Mayer and Powell (1992)). Preliminarily Michalke (1971) notes that at lower velocities, where the instabilities are weaker and more convectively unstable, the asymmetric modes are stronger than the axisymmetric mode within a free jet, a phenomena Leibovich (1983) attributes to an energy transfer from the axial to helical modes. Cohen and Wygnanski (1987a) validates such theories through experimental simultaneous excitation of both the helical and axisymmetric instability modes for a jet, finding the helical mode gains energy from the excitation due to the nonlinear interactions between the modes. Unfortunately these prior experimental, and theoretical investigations are unable to distinguish between the $m = 1$ or $m = -1$ modes respectively. In the case of linear stability theory, this is a result of the required squaring of the azimuthal mode number (Cohen and Wygnanski (1987b)). Gursul (1994) performs an experimental study regarding leading-edge vortices over a delta wing, and finds that it is the $m = 1$ helical mode which is preferentially excited; Cohen and Wygnanski (1987a) finds similar results regarding the $m = 1$ helical mode when performing excitation of a free jet via eight speakers positioned circumferentially about the jet.

Much of the fundamental findings regarding control or excitation of the helical modes are

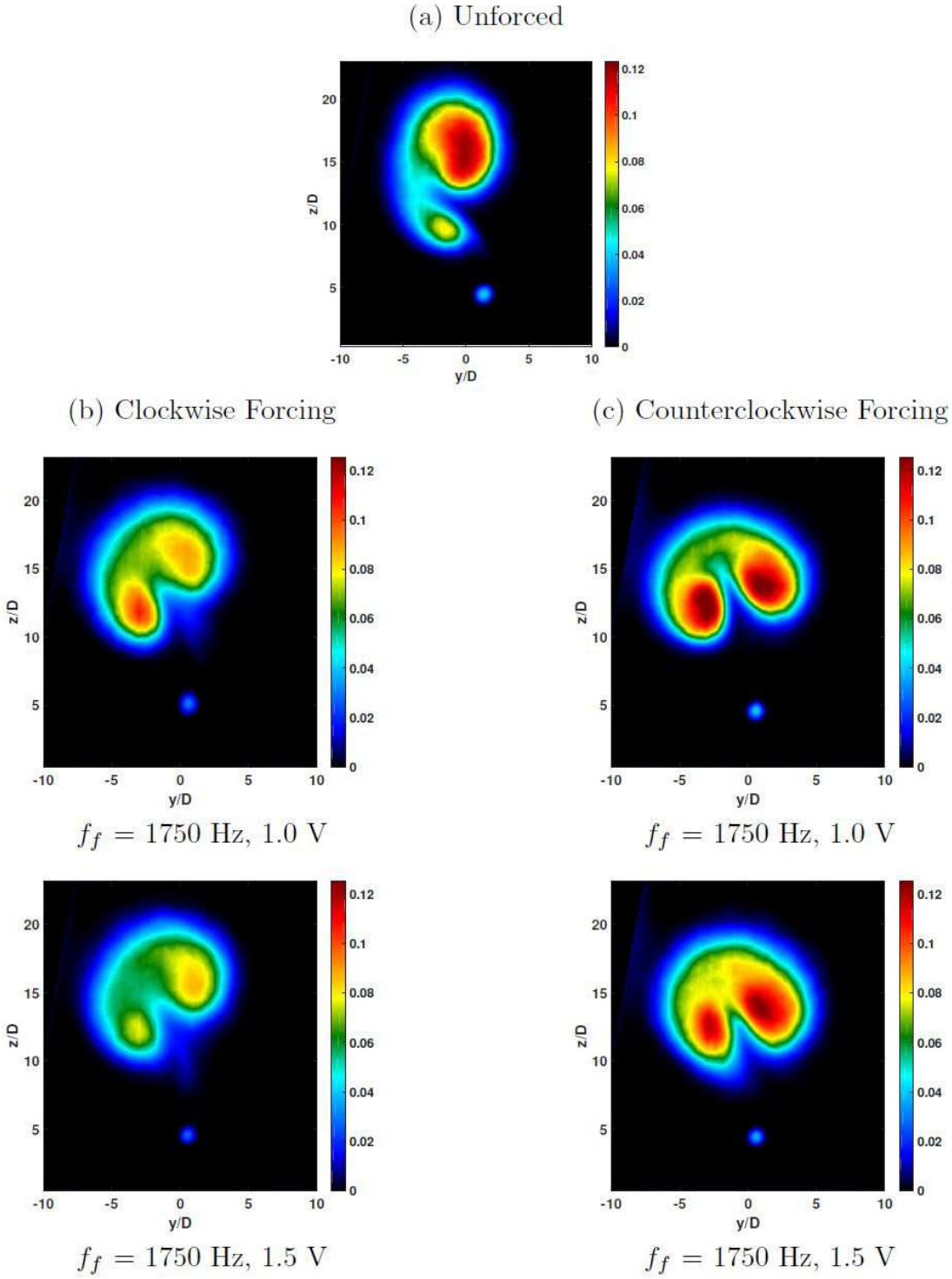

Figure 1.22: Mean cross-sectional PLIF images of the equidensity flush nozzle injected JICF at $J = 41$, and $x/D = 10.5$, with (a) no forcing, (b) clockwise forcing, and (c) counter-clockwise forcing. Mean figures averaged over 500 instantaneous images. Adapted from Besnard (2019).

in relation to free jets (Batchelor and Gill (1962); Mattingly and Chang (1974); Plaschko (1979); Strange and Crighton (1983); Kusek et al. (1990); Hilgers and Boersma (2001); Reynolds et al. (2003) Gallaire and Chomaz (2004)). Syred and Beer (1974) finds that the helical modes are present within the vortex breakdown of the jet, while Panda and McLaughlin (1994) note the growth of Kelvin-Helmholtz instabilities and vortex pairing is suppressed in the wake. Such findings suggest the enhanced spreading, and entrainment in the shear layer of the jets are due in some manner to the helical instability modes and not to a Kelvin-Helmholtz instability (Panda and McLaughlin (1994); Gursul (1996)). The experimentation of Gursul (1996) explores helically perturbing a swirled free jet, and interestingly, finds that fluctuations in the radial velocity arises due to the periodicity of exciting the jet, which in turn excites the $m = 1$ mode, the only helical mode capable of attaining a nonzero radial velocity (Leibovich (1983); Lessen et al. (1974)). An important finding by Kusek et al. (1990) regarding helically exciting jets is the need for the proper control of gain and phase for each individual speaker when acoustically exciting the jet externally by an array of azimuthally placed speakers. Samimy et al. (2007) finds that helically exciting the free jet at the preferred Strouhal number or fundamental frequency enhances the jet spread and concentration decay rate, thereby shortening the potential core length, and providing the optimal enhancement in mixing. Hilgers and Boersma (2001) similarly determines the effective enhancement of mixing parameters within the free jet are dependent upon the forcing frequency.

Besnard (2019) conducts extensive experimental investigations into the implementation of helical excitation for a JICF, given the promising findings related to the free jet experiments. However, Alves et al. (2007) demonstrates from linear stability analysis that the nature of instability characteristics for a JICF are markedly different from those characterized for a free jet, only behaving similarly to a free jet for momentum flux ratios which are very large ($\infty > J \geq 275 - 160$). Later viscous stability analyses conducted by Alves et al. (2008) determines that despite the inherent differences with the free jets, similar traits regarding the feasibility of helical excitation and preferential tendency for the $m = 1$ helical mode are

seen. Besnard (2019) helically excites the $m = \pm 1$ modes of the flush injected equidensity JICF at a momentum flux ratio of $J = 61$, and a jet Reynolds number of $Re_j = 2300$, via the placement of four mini speakers circumferentially about the jet, embedded coplanar with the jet injection plane (see figure 2.2). It is found, as is shown within figure 1.22, that helical excitation at the fundamental frequency of the transverse jet results in an enhancement of the CVP structure, and a symmetrization of the typically asymmetric cross-sectional jet structure, the degree or extent of which is in part governed by the amplitude of excitation applied (Besnard (2019)). Interestingly, it is also seen that forcing counter-clockwise, or with the $m = -1$ mode, shows greater enhancement of the molecular mixing as compared to the clockwise direction, or $m = 1$ mode, when the forcing is applied below the fundamental frequency of the jet (Besnard (2019)). Surprisingly, the reverse is seen for forcing about the fundamental frequency, wherein the clockwise forcing produces the more pronounced enahncements in mixing. Interestingly, the study notes that mode dynamics, as represented from PIV and PLIF based POD analysis, along with the coefficient mapping for the dominant modes (α_1 vs α_2 vs α_3) yield psuedo phase space depictions which may be representative of strange attractors.

1.4 Passive Control Methods

Motivation within Section 1.3 is predicated upon the desire to precisely control characteristics of a JICF such as spread, penetration, and molecular mixing, so as to tailor the issuing jet in a manner such that the resulting flowfield is optimized for a particular application (Karagozian (2010)). For some applications, as detailed in Section 1.1, it would be ideal if the JICF behavior could be adapted, or updated in real time to maintain optimal performance within a variable flowfield. Given the necessity for such finely tuned alterations of the issuing jet, active control methods such as forcing/pulsing of the jet are employed. The results stemming from such investigations demonstrate remarkable influence over the structural,

instability, and mixing characteristics of the JICF (Megerian et al. (2007); Shapiro et al. (2006); Davitian et al. (2010b); Sau and Mahesh (2010); Coussement et al. (2012); Getsinger et al. (2014); Gevorkyan et al. (2016); Shoji (2017), Besnard (2019)). In all of these cases however, especially denoted within the experimental studies, achieving such definite control over the flowfield can be quite complex (e.g. feedforward or feedback controllers (M'Closkey et al. (2002); Hendrickson and M'Closkey (2012); Shoji (2017); Besnard (2019))), difficult to implement (e.g. acoustic speakers (Davitian et al. (2010b); Shoji (2017); Besnard (2019)), pistons (Hendrickson and M'Closkey (2012)), or precisely timed valving systems (Eroglu and Breidenthal (2001); Anderson et al. (2001))), and in general are expensive from the standpoint of an energy input requirement. In light of such an array of challenging hurdles surrounding the implementation of active control methods, the possibility passive control of the JICF is presented as an alternative mechanism in governing the jet behavior.

Control, in the sense of governance of a jet or jet in crossflow, has suggestively been defined "as the capacity to modify the development of the flowfield by directing energy into selected turbulence scales" (Wlezien and Kibens (1986)). In light of such a definition, passive control may be thought of as any simplistic method by which alterations to an evolving jet may be realized without the input of an external energy source, which is most readily realized through variation of nozzle geometry. Historically various studies of passive control methods have included free jet distortion via tabs (Bradbury and Khadem (1975); Zaman et al. (1991)(1992)(1994); Zhang and Schneider (1994); Zaman (1993)(1996); Carletti et al. (1996); Hu et al. (2000);), stepped or sawtooth nozzles (Wlezien and Kibens (1986); Longmire and Duong (1996)), crowned or v-notched nozzles (Longmire et al. (1992); Lim et al. (2004)), inclined exit geometries (Wlezien and Kibens (1986); Webster and Longmire (1997)), lobed injectors (Eckerle and adn J. Awad (1992); Smith et al. (1997); O'Sullivan et al. (1996); Mitchell et al. (2004)), and of course non-circular exit geometries such as triangular, star-shaped, square, rectangular, or elliptic (Husain and Hussain (1983); Ho and Gutmark (1987); Gutmark et al. (1989); Toyoda and Hussain (1989); Quinn (1992)).

It is known that for an axisymmetric jet at moderately high Reynolds number, the formation and subsequent merger phenomena of coherent vortex rings dominate the shear layer growth in the nearfield acting to entrain the surrounding fluid (Crow and Champagne (1971); Liepmann and Gharib (1992)). Approaching the onset of three-dimensionality, self-induction, vortex shedding, and reconnection become the dominant dynamic processes (Hussain (1986)). Investigation of non-circular jet exit geometries find that while the jet develops similarly to the geometry of the nozzle at the exit plane, but with progressive angular rotation of axes, known as the axis switching phenomenon (Zaman (1996b)). With such a non-uniform curvature azimuthally, the vortex rings which are formed developed a self-induced Biot-Savart deformation, which ultimately resulted in an added complexity to the flowfield, whereby energy is realigned between the azimuthal and streamwise vortices, and leads to increases in the small scale content of the jet (Gutmark and Grinstein (1999)). Ho and Gutmark (1987) find that elliptic and rectangular jets attain much greater entrainment of quiescent fluid, compared to the circular jet, owing to the self-induction of vorticity. Zaman (1996a) conducts experimental work for a variety of asymmetric injector geometries, and finds that in the subsonic regime the asymmetric injectors slightly increase the spread over that of a circular geometry, but when the geometries are treated within a supersonic flow regime however, the enhancements are found to be significantly more profound. It is seen that regardless of flow regime, the exit geometry which contains 2 tabs at the jet exit plane produces the best spreading of the jet (Zaman (1996a)). A plot depicting normalized mass flux, or ability of the jet to entrain surrounding fluid, for the respective geometries explored within Zaman (1996a) is shown in figure 1.23, where it is seen that the tabbed geometry enhances the jet performance best.

Much like the non-circular jet injectors with rectangular, elliptical, triangular, etc. geometries, implementation of small tabs or protrusions about the jet exit periphery seeks to violate the azimuthal symmetry of an issuing jet. The initial investigation of tab geometries within jet flowfields is treated by Bradbury and Khadem (1975), whereby it is found that

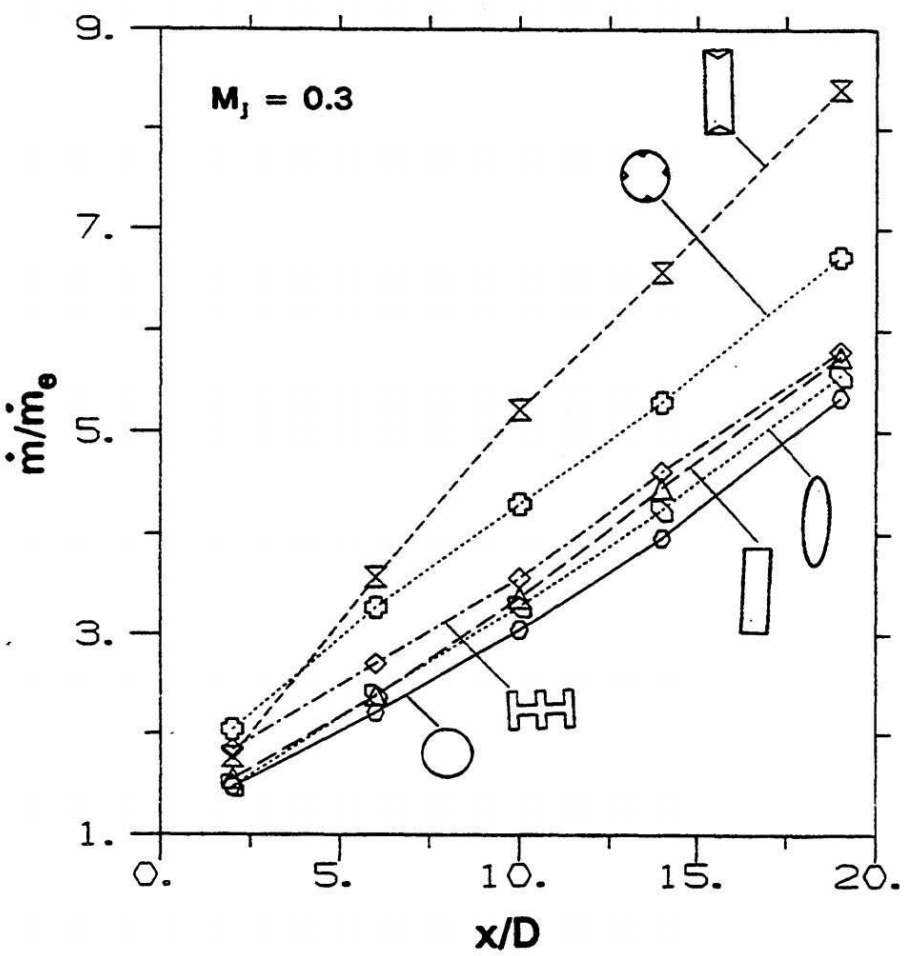

Figure 1.23: Streamwise variation in the normalized mass flux for a variety of non-circular injectors, compared to a circular injector for injection at Mach 0.3. Reprinted from Zaman (1996a).

simple tabs blocking a mere $1-2\%$ of the exit plane can increase the decay rate of the centerline velocity, and shorten the potential core length, and in some cases bifurcate the jet. In line with this initial study Ahuja and Brown (1989) and Zaman et al. (1991) determined the placement of small tabs at the injector exit act to azimuthally excite the flow and enhance streamwise vorticity generation. Early investigations regarding tabbed geometries, or such modified corrugated nozzles, find that the jet vorticity evolves from vortex-ring self-deformation, and interactions between the vortex rings and rib vortices, which are formed in the braid regions between vortex rings (Gutmark and Grinstein (1999)). Zaman et al. (1994) and Bohl and Foss (1995) propose that vorticity is generated from the tabular protrusions

into the jet flow due to two sources, which are depicted in figure 1.24. The two sources of vorticity emanating from the tab are ascribed to a pressure hill upstream of the issuing tab, and from vortex sheets shed from the sides of the tab (Zaman et al. (1994)), which when combined for a single tab are theorized to produce a jet structure as shown in figure 1.25. Further explorations of tabbed jets by Ahuja and Brown (1989) and Zaman et al. (1992) determine that spread and mixing are enhanced at low speeds, as well as in high speed and high temperature flowfields. Zaman (1993) conducts a series of experimental investigations regarding the optimal shape and geometrical integration of tabs to the free jet. The study determines that delta tabs, or triangular tabs bent 45° downstream of the issuing jet produce the greatest effect in the developing structures for a particular flow area blockage (Zaman (1993)). Zaman et al. (1994) further investigates the effect of number of tabs present about the jet periphery, finding that four delta tabs equally spaced circumferentially provides the greatest enhancement in entrainment, followed by two delta tabs. Implementation of two delta tabs results in a bifurcation of the jet, while four delta tabs stretches the jet, producing four respective flow "fingers" (Zaman et al. (1994)). Similarly, investigation of three and five delta tabs about the exit each also produce a cross-sectional jet structure with a corresponding number of fingers, however when implementing six delta tabs, the flow cross-section returns to three fingers owing to interactions between the streamwise vortices, which is theorized in figure 1.25(b) (Zaman et al. (1994)).

In light of such an immense wealth of findings supporting the ability to control a jet via passive means, respective investigations implementing aforementioned techniques of inclined jets, non-circular injector geometries, and tab protrusions have been explored within the JICF (Roberts and Toms (1987); Lee et al. (1992); Liscinsky et al. (1995); Zaman and Foss (1997); New et al. (2003)(2004); Plesniak and Cusano (2005); Sau et al. (2006); Colettie et al. (2013)). Initial investigations regarding the implementation of tabs at the about the periphery of the JICF are conducted by Liscinsky et al. (1994), who suggests that, based on the determinations of Zaman et al. (1994) and Bohl and Foss (1995) regarding the strength

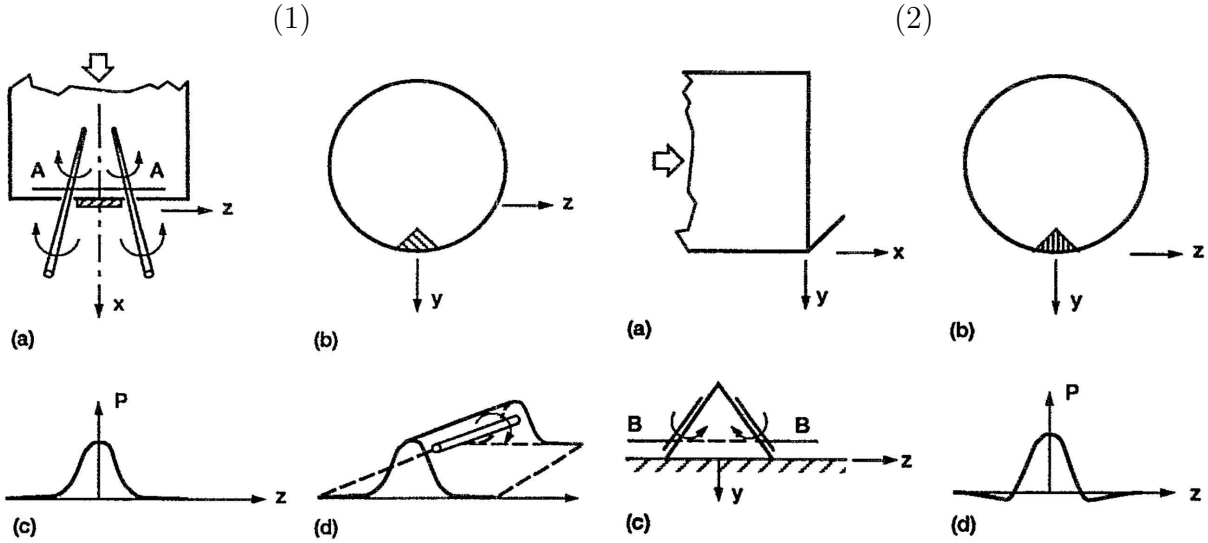

Figure 1.24: Sources of vorticity due to a tab from (1) the pressure hill upstream of the tab, and (2) vortex sheets shed from the tab edges. Reprinted from Zaman et al. (1994).

and orientation of vorticity emanating from a single triangular tab, placement of the tab in the leeside of the jet would result in an enhancement of the CVP structure. Unfortunately, Liscinsky et al. (1994) finds that the integration of a a single tab, or two tabs spaced 180° apart produces no significant enhancement of the jet mixing, especially as compared to the findings noted for free jets.

Later investigations by Zaman and Foss (1997) for a JICF at $J = 21.1$ & $J = 54.4$, over a Reynolds number range of $Re_j \approx 24,000 - 48,000$, validate the ineffective behavior of placing the tab along the leeside of the jet, determining that the lack of expected vorticity generation is possibly pursuant to the pressure gradients in the wake region which negated the formation of a pressure hill source of vorticity. Interestingly, Zaman and Foss (1997) does note that placement of a tab along the windward side of the jet is able to produce significant alterations to the flow structures and mixing. Similarly to the work of Zaman et al. (1994) regarding free jets, Zaman (1998) investigates the effect of tab size, and inclination angle on the development of the JICF for momentum flux ratios in the range of $10 < J < 90$. The tabs are oriented in the upstream edge of the jet, where it is found that all of the tab

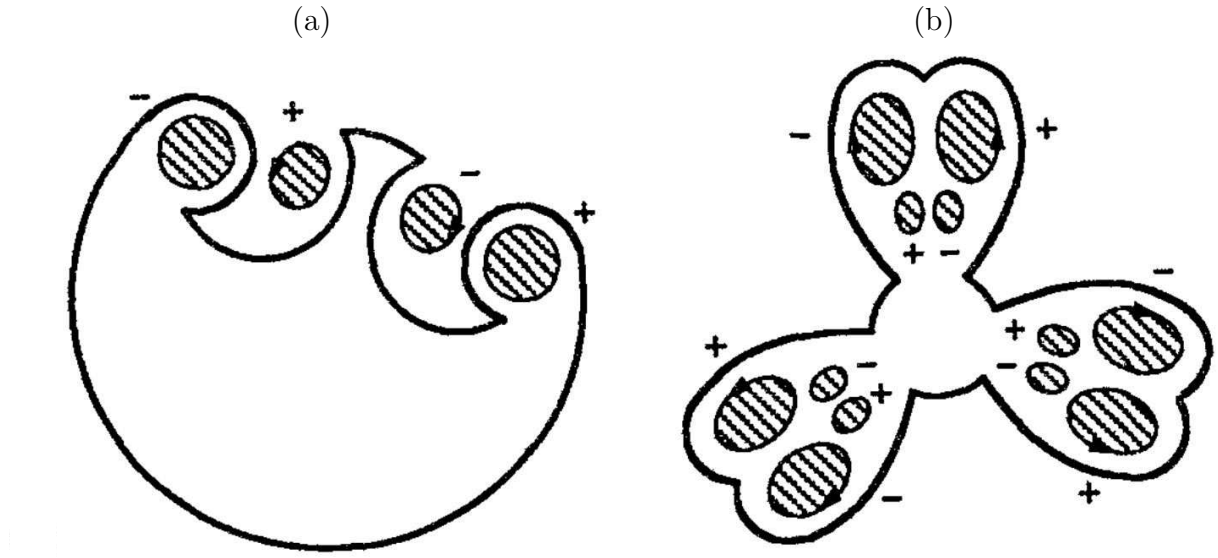

Figure 1.25: Likely vorticity distribution along a jet cross-sectional slice for (a) a single delta tab, and (b) six delta tabs. Reprinted from Zaman et al. (1994).

configurations reduce the penetration of the jet, though the degree of reduced penetration is more pronounced at higher momentum flux ratios, or with larger tabs (Zaman (1998)). It is discovered that for a given effective flow blockage, the resulting tab orientation plays little affect in governing the jet structure and mixing.

The implications of tab placement about the periphery of the JICF are explored in greater detail by Bunyajitradulya and Sathapornnanon (2005), who treat a single tab positioned at eight different azimuthal locations for a JICF with $S = 0.86$, $J = 16$, and $Re_j = 15,000$. It is found that the JICF did not significantly respond to the placement of the tab along the leeside of the jet, and that the marked alterations seen in the windward side of the jet are systematically diminished in rotating about to the leeside Bunyajitradulya and Sathapornnanon (2005). Accompanying the rotation of the tab placement about the periphery is a notable corresponding rotation and transformation of the mean cross-section of the jet from a kidney shape to more of an asymmetric comma or reverse question mark (Bunyajitradulya and Sathapornnanon (2005)). More recently Zaman and Milanovic (2012) employ

tabs placed in the sides of the issuing jet under a periodic oscillatory motion at subharmonics of the fundamental frequency of the upstream shear layer instability to alter the flowfield. It is found that the oscillating tabs incite a periodic rotation of the CVP structure, the effectiveness of which deteriorates with decreasing momentum flux ratio, and all but disappear for $J < 15$ (Zaman and Milanovic (2012)). Zaman and Milanovic (2012) note an enhancement of the spread, in the cross-sectional plane, due to the tabbed oscillatory motion, though it is admitted this effect may simply be due to an averaging effect of the unsteady flow.

1.5 Current Endeavors

From the perspective of passive alterations to the JICF, the recent studies regarding implementation of tabbed geometries about the periphery of the JICF exit plane have been found to yield resulting flowfields which in a certain light are somewhat incoherent as to the true overall effectiveness of tab utilization for improved control of jet mixing phenomena. Early studies found little enhancement of the jet spread and mixing for a small array of tab placements, most notably discovering no alteration of the JICF for the supposed idealized tab placement on the leeside of the jet (Liscinsky et al. (1995); Zaman and Foss (1997)). Yet Zaman and Foss (1997), and Zaman (1998) do see an impact when the tab is placed on the windward side of the jet, and Bunyajitradulya and Sathapornnanon (2005) even provides results which suggest a variability in the tab effectiveness dependent upon tab location relative to the windward side of the jet. To this author's knowledge no investigations regarding impact of the tabular geometry upon the nature of the upstream shear layer instabilities has been conducted, which is seen from section 1.2.3 to be quite profound in dictating the phenomenological development of the JICF. Additionally the findings of these previous studies, with the exception of Liscinsky et al. (1995), explore the tabbed JICF without the utilization of any instantaneous mixing metrics, deriving the enhancement or degredation of mixing phenomena from the spread and penetration, which is noted in some cases to not

have aligned trends with the molecular mixing (Shoji et al. (2019)).

Then in the context of active control applied to the JICF, the recent work by Shoji et al. (2020c) demonstrates the significance of the natural instabilities along the jet shear layer in achieving lock-in of the jet to an applied sinusoidal waveform. Similarly, multiple studies document the distinct differences in effectiveness of sinusoidal and square wave excitation of the jet depending upon the natural instability characteristics of the jet (Davitian et al. (2010b); M'Closkey et al. (2002); Shoji et al. (2019)). Yet interestingly, little is known with regard to the jet lock-in of square wave forcing, and what, if any, role the synchronization characteristics of the flowfield to a given forcing waveform plays in the resulting effectiveness of the prescribed waveform in altering the dynamics and mixing of an absolutely unstable flow. Additionally, preliminary investigations are made into the selective tuning of the production of vortex rings through a novel double-pulse waveform so as to promote vortex interactions, collisions, and breakdown (Shoji (2017)). However, nothing is quantitatively understood about the actual vortex structures formed, and much in the way of selective optimization of the waveform shape is left unexplored. Additionally, understanding of this type of waveform as applied to an absolutely unstable flow, wherein square wave or square wave like forcing is necessitated for effective alterations of the flow (M'Closkey et al. (2002); Shoji et al. (2019)), is unexplored.

Lastly, in relation to the more fundamental perspectives of the unaltered or unperturbed JICF, multiple recent works look at better understanding the origins of the shear layer instabilities within the flowfield, and particularly focus on comprehending the mechanism by which the upstream shear layer transitions from a convective to absolute instability (Iyer and Mahesh (2016); Regan and Mahesh (2019); Shoji et al. (2020b)). The dominant upstream shear layer axisymmetric and helical modes are seen to form at the leading edge of the jet, and as the flow is made more weakly convectively unstable, modes along the downstream shear layer become relatively more prominent (Regan and Mahesh (2019)), and the jet becomes more susceptible to the formation of an asymmetric CVP structure further downstream

(Getsinger et al. (2014)). Additionally, Regan and Mahesh (2019) establish wavemaker regions defining spatial locations for the optimal perturbation of the jet along the upstream edge of the jet and wrapping around to the downstream as the flow becomes weakly convectively unstable, demonstrating good correspondence to the originating locations of the instability modes. Separately, both numerical (Iyer and Mahesh (2016)) and experimental (Shoji et al. (2020b)) studies model the strengthening of the shear layer instabilities, and eventual transition from convective to absolute instability, as a CCSL analogy applied locally in the upstream edge of the jet. The correlations between this CCSL analogy and the spatial locations of the originating instabilties along with the respective wavemaker regions is quite profound. Yet, to this author's knowledge no investigations have been made to attempt to induce a certain type of shear layer instability from the application of a counter-current flow in the leading edge of the jet. Further, no investigations of such a selective tuning of the instabilities through a counter-current augmentation of the flow at/near the wavemaker region on the downstream side of a convectively unstable jet is explored either.

Pursuant to these prior investigations, and the perceived remaining questions assessed with those studies, the current work is threefold in approach. This study seeks to expound and further explore passive control of tabbed geometries about the exit plane of the JICF, active control through the lens of jet synchronization to various applied forcing waveforms, and selective optimization of JICF dynamics and mixing from careful tuning of pulsing parameters for a novel double-pulse forcing waveform, and greater understanding of the shear layer dynamics and instabilities from application of an induced counter-current flow about the exit of the JICF. The studies will examine the described flowfield detailing the upstream shear layer instabilities, centerplane and cross-sectional vorticity generation and dynamics, centerplane and cross-sectional structural characteristics, and evaluations of mixing efficacy.

CHAPTER 2

Experimental Setup and Diagnostic Procedures

2.1 Jet in Crossflow Experimental Apparatus

Experimental investigation of the jet injected transversely into crossflow was conducted within a low speed wind tunnel, a general depiction of which may be found in Figure 2.1. The issuing crossflow of air was generated by a centrifugal blower (Baldor M3546-T) positioned upstream of the main tunnel apparatus, connected by a small section of flexible corrugated metal ducting to minimize the impact of mechanical vibrations instigated by the blower. To power the system a small electric motor was utilized wherein the blower frequency of rotation was tunable to a precision of 0.01 Hz, or 0.016% relative to the overall frequency operating range. Selection of operating frequencies were dictated by the desired crossflow velocity, U_∞, the accuracy of which was established via calibration of the resulting flow with a pitot tube and an accompanying hotwire anemometry, details of which may be found in Section 2.2. In addition to, and immediately downstream of the flexible tubing, the airflow was further conditioned passing through a series of honeycomb structured cells and screens of decreasing grid/mesh sizes, systematically breaking down the turbulent flow into smaller dissipative scales; impact of honeycomb cells and screens in formatting uniformity from turbulent flow may be briefly reviewed in Barlow et al. (1999). Following this, the air passed through a 9:1 area contraction smoothly leading to the main test section platform, where measurements in the freestream suggested the maximum attainable velocity was approximately $U_\infty = 7.00\ m/s$ with a resultant turbulence level of less than 1.5 %.

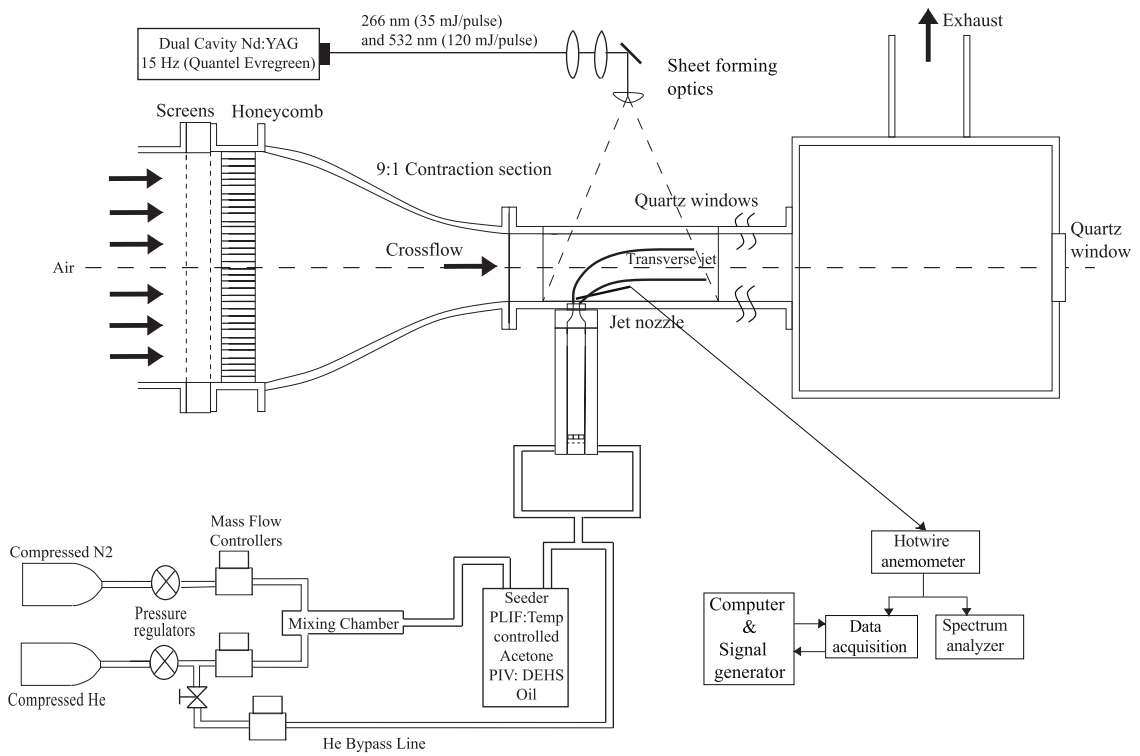

Figure 2.1: Low speed wind tunnel, laser system, hotwire anemometry, and variable density jet injection comprising the experimental JICF Configuration.

The main test section was a 12 *cm* x 12 *cm* 82.5 *cm* aluminum tunnel with cutouts along the entire length of (full-length cutouts along) 3 of the sides, providing optical access for the non-intrusive laser diagnostic and imaging methods employed, discussed in greater detail in Section 2.3. The top cutout was fitted with a fused silica quartz window to accommodate the ultra-violet laser light, whereas the side paneling utilized plexiglass windows, giving the cameras direct viewpoint access into the tunnel. In some experimental scenarios where a free-jet behavior was desired, the top quartz window was removed, and the crossflow turned off. Likewise the plexiglass panels were also able to be removed, which allowed for the substitution of a non-reflective black panel to serve as a background when performing optical measurements with the camera oriented normal to the centerplane (xy-plane). In circumstances necessitating the hotwire anemometry or pitot tube, modified black paneling was installed which contained small access ports for insertion and traversal of the measurement

devices in question. The entirety of the test section was black anodized, and then further coupled with a matte black finish heat-resistant coat of paint to minimize the significance of reflections from laser light off of the surfaces.

Pursuant to the varying range of experimental investigations for the jet in crossflow conducted within the low speed wind tunnel, a section of the main tunnel floor was designed to be removable. The flexibility of a detachable floor allowed for cost-effective, quick, and easy transformative alterations of the flowfield geometry. Various flowfield geometries treated thus far have been the flush mounted jet with passive control via tabs (part 2.3.2 of this study), the flush mounted jet with axisymmetric acoustic excitation (Shoji et al. (2019); Shoji et al. (2020a); Shoji et al. (2020c); part 5.2 of this study), flush mounted jet with asymmetric helical excitation (Besnard (2019)), and the flush mounted jet with coaxial suction about the jet exit periphery (part 8.2 of this study). Representative computer aided design (CAD) drawings of these floors are seen in Figure 2.2. The removable section of flooring accounted for a 9.3 cm by 22.3 cm exposed surface area of the tunnel floor, and was inlaid with the leading edge 3.8 cm downstream from the 9:1 area contraction. Mounting to the main tunnel floor was made via a 0.6 cm lap joint, with supporting stanchions placed beneath to anchor the removable piece in place ensuring a tight seal about the seams. Measurements of the boundary layer and turbulence levels determined no characteristic differences to the crossflow due to the implementation of the removable floor as compared with the original tunnel floor used in extensive earlier studies (Megerian et al. (2007), Davitian et al. (2010b), Getsinger et al. (2012), Gevorkyan et al. (2016)).

Downstream of the test section a wooden box of 30 cm x 30 cm x 63 cm was affixed, providing a chamber in which the flow was able to dissipate, and then be expelled vertically through the exhaust system. The box served to dispel any attenuation of the upstream flowfield due to a pressure drop from the suction of the exhaust. Fitted in a side of the wooden chamber was a 90 mm x 90 mm quartz window establishing optical access downstream (negative x direction) of the issuing jet and crossflow, whereby planar cross-sectional (yz-

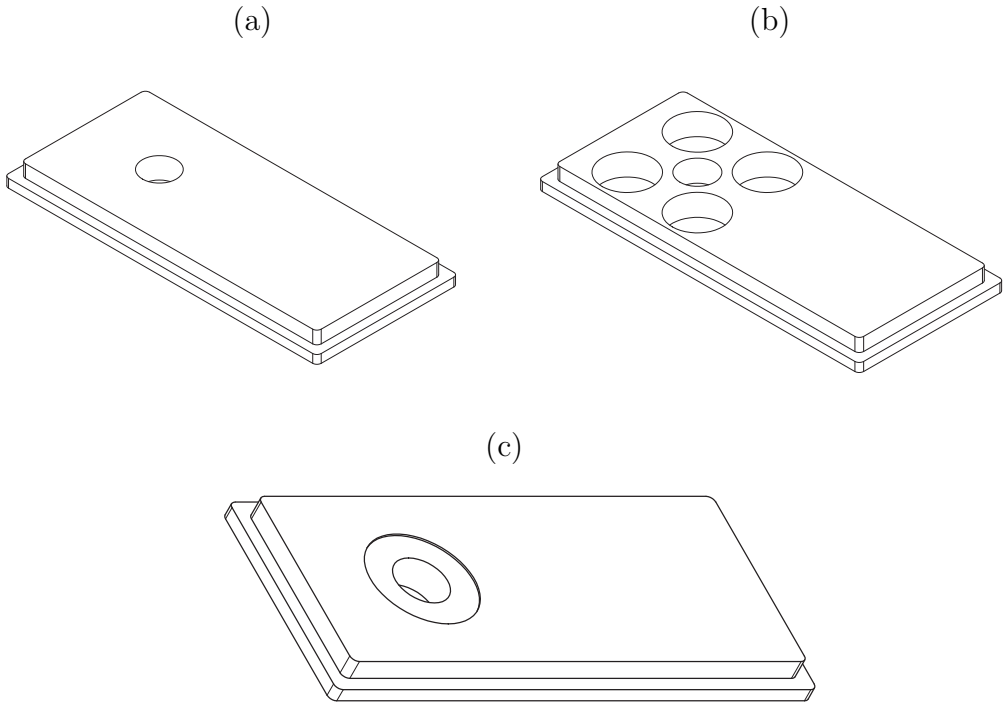

Figure 2.2: CAD drawings for the various removable floors integrated to the main wind tunnel for investigation of different aspects of the JICF: (a) plain flush mounted jet injection floor for unforced and axisymmetrically-excited jet, (b) flush mounted floor with speaker cavities for helically-excited jet, and (c) recess mounted jet floor for passive control of the jet via tabs.

plane) images of the flowfield were recorded. Due to limitations from the focal length of the various lenses implemented on the camera, the quartz window mounting was recessed into the wood box thereby allowing the camera to situate at the proper distance from the field of view, while simultaneously not interfering with proper exhaustion of the flow.

2.1.1 Jet Injection

Jet fluid, consisting of mixtures of nitrogen, helium, and seeding particles for optical diagnostics, was introduced perpendicularly into the test section 9.5 *cm* downstream of the area contraction via a system mounted to the removable floor. Issuance of the jet fluid, and thus the resulting flowfield characteristics, were governed in part by the type of injector

implemented; herein considered was a flush mounted nozzle, though previous studies have treated a variety of jet injectors (see Megerian et al. (2007), Getsinger et al. (2014), and Gevorkyan et al. (2016)). Figure 2.3 depicts the interior surface profiles of the flush nozzle (a), elevated nozzle (b), and the flush pipe (c). Each of the injectors was machined with a desired uniform exiting diameter of 4 mm, the execution of which was not perfectly realized due manufacturing tolerances and machining defects; the flush nozzle had an exit diameter of 4.04 mm, the elevated nozzle 3.94 mm, and the flush pipe 3.77 mm. The interior surface profile for the flush and elevated nozzles were generated as a 5^{th} order polynomial contraction resulting in a top-hat velocity profile and relatively thin momentum thickness at the nozzle exit. Megerian et al. (2007) demonstrated however, that as the jet-to-crossflow velocity ratio, R, was decreased from that of a free jet (i.e. increasing the crossflow velocity), the behavior of the velocity profile and momentum thickness was altered, noting a distinct thickening of the upstream momentum thickness as the velocity ratio decreased below 4. The only notable difference between the 2 nozzles was the plane of jet injection into the crossflow; the flush nozzle exit was coplanar with the test section floor, while the elevated nozzle was offset 3.75 jet diameters above the test floor. By introducing the jet 3.75 diameters above the floor, one was able to study the interaction between jet and crossflow absent the influence of any boundary layer effects. The third injector was the flush pipe, which had a length of 0.6 m, or a $L/D = 159$, such that the resulting jet was fully developed, and of a parabolic profile at the exit plane.

For experimental configurations utilizing the flush and elevated nozzles, a 0.9 m long PVC pipe was attached below the injectors. The long pipe, distinct from the flush pipe injector, was utilized in conjunction with honeycomb flow straighteners (0.3 cm grid sizing and 2.5 cm in length), both of which sought to normalize and enhance the symmetry of the jet velocity profile as it approached the nozzles. The length of the PVC pipe was sufficiently long enough to generate fully developed flow conditions upstream of the entrance to the injector for the jet Reynolds number explored. Beneath these flow conditioners was

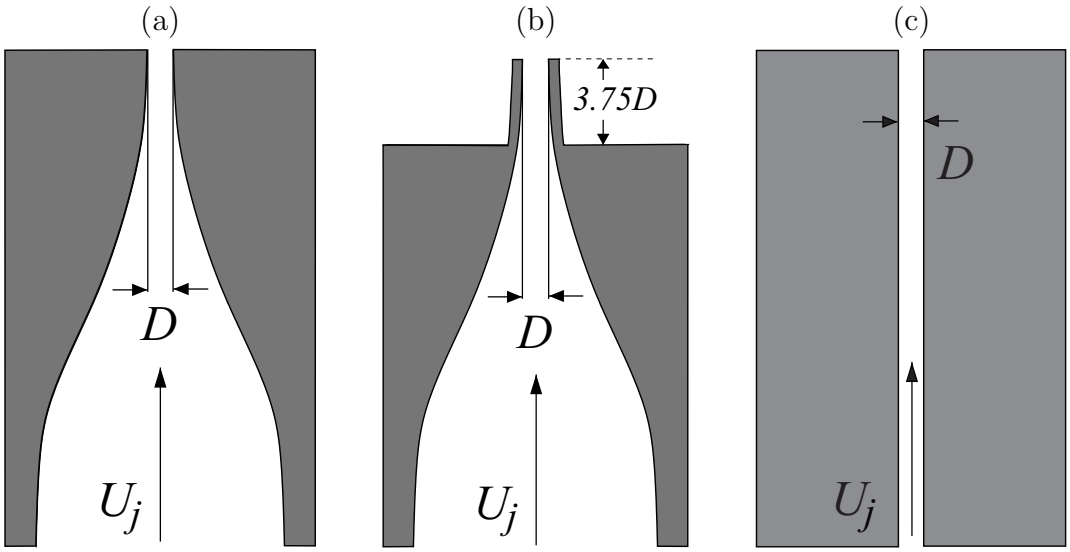

Figure 2.3: Jet injectors considered: (a) Flush nozzle, (b) Elevated nozzle, and (c) Flush Pipe.

a plexiglass plenum which housed a 4" loudspeaker (Radioshack 40-1022B), providing the option of axisymmetric acoustic excitation of the jet flow in a sinusoidal, single-pulse or double-pulse square-wave, or like manner, details of which may be found in M'Closkey et al. (2002), Shapiro et al. (2006), Davitian et al. (2010a), and Shoji (2017). The plenum was removable, and thus able to be integrated with the flush pipe injector as well, or implemented with the nozzles absent the presence of the long pipe. In effort to negate the influence of flow swirl, and inconsistent interaction with the loudspeaker, the jet fluid was introduced via 4 ports equally spaced circumferentially about the plenum.

The jet fluid had constituent species of Helium, Nitrogen, and acetone and/or Di-Ethyl-Hexyl-Sebacat (DEHS) oil, the precise molar fractions of which were dependent upon the laser diagnostic methods employed (see Section 2.3), and the specified jet-to-crossflow density ratio, S. Density ratios in the range of $0.35 \leq \ S \leq \ 1.00$ have been studied in the past, (Getsinger et al. (2014), Gevorkyan et al. (2016), and Shoji (2017)), though so far in this study only equidensity conditions were explored. To generate the proper composition of the jet, the flowrates of Helium and Nitrogen were regulated by Tylan mass flow controllers (model FC-260). The controllers operated in a range of 0 to 5 normal liters per minute

(NLPM) with a calibration accuracy of 1%, and a repeatability of 0.2%. Activation and authority over the controllers was featured on a dSPACE 1104 data acquisition (DAQ) board operated by the user interface from ControlDesk software; voltage inputs were assigned to the Tylan devices, and were validated by a multimeter (Fluke model 77 series II). For the select case of a density ratio of $S = 0.35$ an additional mass flow controller (MKS model GM50A) was utilized to regulate the density ratio and the mole fraction of tracer particles concurrently, bypassing some gas past the seeding section of tubing. The MKS was designated a static IP address whereby it was controlled via a network-based user interface. Operating limits of the MKS gave a flowrate of 0 to 70 NLPM, with an accuracy of 1% and a repeatability of 0.3%. Calibrations of all flow meters were conducted with a 1000 mL manual bubble flow meter.

Helium and Nitrogen were delivered to the injector system by industrial grade supply tanks, which were further filtered upstream of the flow controllers to remove any additional impurities in the gases. Downstream of the flow controllers, the separate lines were united and passed into a long cylindrical mixing chamber filled with a packed bed of 15 mm diameter glass marbles, thereby generating a homogeneous mixture. The uniform flow was then introduced to seeding chambers for the respective tracer particles of interest (acetone or DEHS oil). For the acetone chamber, the temperature and pressure were regulated so as to ensure the proper molar concentration within the jet fluid; like the Tylan flow controllers, the thermocouple and pressure transducer were incorporated into the dSPACE board, details of which are found in Section 2.3.1. Ultimately the seeded flow was directed to the loudspeaker plenum via the 4 access ports described above for injection to the test section.

Variation in flow rates and molar concentrations of the jet fluid constituents provided the ability to vary the jet-to-crossflow density ratio S, the jet Reynolds number Re_j, and the jet-to-crossflow momentum flux ratio J, the latter of which was also governed by changes in crossflow velocity for a fixed jet velocity. Validations of the resultant jet flow gas mixture densities for density ratios down to S=0.55 were previously made by Getsinger (2012)

through implementation of an acoustic wave guide, utilizing methodologies outlined in Canzonieri (2009). The jet fluid at the various density ratios was seen to agree with theoretical estimations to within 1.5%, assuming thermally perfect gases. The jet Reynolds number for the flow was determined by the jet density ρ_j, jet viscosity μ_j, injector exit diameter D, and the bulk jet velocity at the exit plane U_j. Determination of the effective mixture viscosity were made by the Wilke formulation when not seeded with acetone (Bird et al. (1960) and Wilke (1950)) or by the Reichenberg method when containing acetone tracer particles (Poling et al. (2001)). Recent efforts were made to validate the calculated flow rates of the jet for a variety of different constituent species compositions. The experimental determination of the flow rates and the corresponding theoretical approach with the Wilke formulation or Reichenberg method are detailed in appendix A. Variation of the jet Reynolds number and density ratio were controlled through the jet flow rate and constituent species respectively, while the jet momentum flux ratio was adjusted through alterations to the crossflow velocity while keeping the jet properties fixed.

2.2 Hotwire Anemometry

Measurements of the mean jet velocity profile, the crossflow velocity profile directly upstream of the jet injection, and spectral characteristics of the jet upstream shear layer were made implementing a single component, boundary-layer type hotwire probe (Dantec 55P15). Quantification of the jet velocity profiles by Megerian et al. (2007) demonstrate the proper formation of the suggested top-hat velocity profile from the flush and elevated nozzles, and the parabolic profile from the flush pipe respectively. Sample plots of the measured velocity profiles for the flush pipe, and flush nozzle are shown in Figure 2.4. Getsinger (2012) utilizes the hotwire anemometry to define characteristics of the crossflow boundary layer just prior to the jet exit, and furthermore makes examinations of the turbulence intensities in the freestream of the crossflow. Aside from direct evaluations of velocity components for the

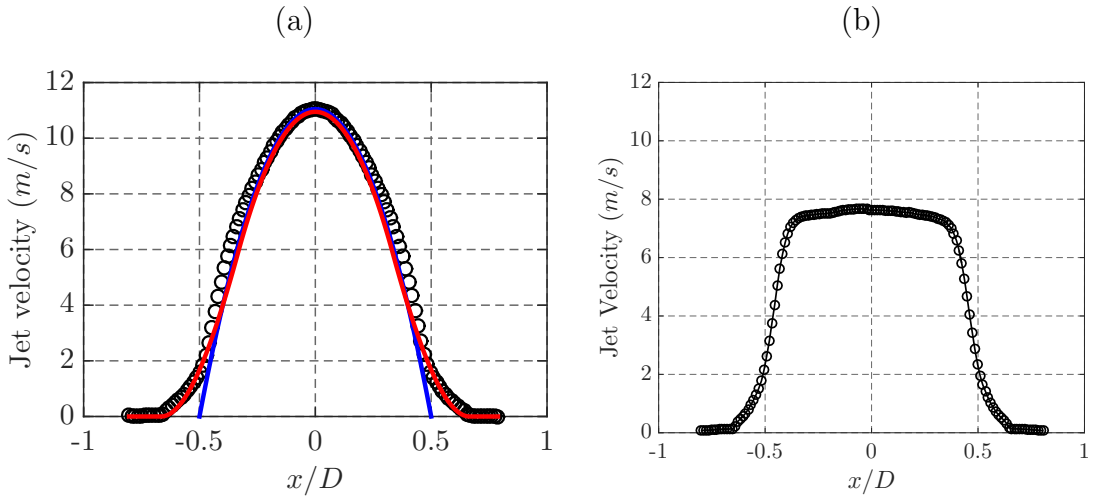

Figure 2.4: Jet velocity distributions for a nitrogen jet injected into quiescent surroundings at a jet Reynolds number $Re_j = 1900$: (a) parabolic profile from the flush pipe in the $y = 0$ plane (adapted from Shoji (2017)), and (b) top-hat velocity profile for the flush nozzle in the $y = 0$ plane. Data points ($\circ$) were captured by hotwire anemometry at $0.1D$ above the jet exit.

free jet or isolated crossflow, the hotwire additionally captured fluctuations of the vertical velocity component along the upstream shear layer of the transverse jet as performed by Megerian et al. (2007), Davitian et al. (2010a), and Getsinger et al. (2012). A fast Fourier transform (FFT) was performed on the latter data, thereby generating spectral plots of the behavior and dominant modes for the upstream shear layer of the JICF.

The hotwire probe was mounted to a triple axis platform comprised of linearly actuating stages with movement presicion in all 3 directions of $1\mu\ m$. The stand was situated adjacent to the test section such that the probe was introduced via the small access ports in the black side paneling from the negative or positive y directions. The particular insertion orientation of the probe, relative to the jet and crossflow, allowed for minimal blockage or interference of the flowfield being measured. Outputs from the hotwire were fed to a 90C10 constant temperature anemometry module which was housed within a Dantec StreamLine 90N10 unit. Subsequently the signal was passed to a conditioning unit produced and detailed by Hendrickson (2012) and Shoji (2017), after which analysis was performed by a dSPACE 1104

digital signal processing DAQ in conjunction with ControlDesk software. When analyzing the recorded data for spectral measurements, the signal was instead passed to dual channel dynamic signal analyzer (HP model 35665A), and averaged over 40 instantaneous signaling samples. For greater details on the nature of the spectral measurements, see Getsinger (2012) and Getsinger et al. (2012).

For calibration purposes, the hotwire anemometry and a pitot tube were both placed within the test chamber such that freestream crossflow of air was able to pass over them (i.e. near the center of the chamber). Utilization of 2 pressure transducers was made with the pitot tube, depending upon the magnitude of the crossflow velocity being measured. When the crossflow velocity was at the lower end of the spectrum a $0 - 0.25$" H_2O transducer (Omega PX653-0.25D5V) was implemented, whereas the larger velocities necessitated a $0 - 3$" H_2O transducer (Omega PX653-03D5V). In addition to calibrating the hotwire probe, this methodology also calibrated the crossflow itself, as alluded to in Section 2.1. With the crossflow simply being composed of air, calibration of the hotwire was not translatable to flowfield conditions with lower density jets, or jets seeded with acetone tracers. For calibration of the hotwire with acetone seeded flows, the flush pipe was employed in a free jet format; knowing the mass flow rate, and bulk velocity of the jet, allowed for the application the laminar pipe-flow method (documented by Lee and Budwig (1991), and detailed by Shoji (2017)) given the jet velocity followed the Hagen-Poiseuille relation in the laminar regime. In experiments of jets seeded with the DEHS oil however, hotwire anemometry studies were not investigated due to the auto-ignition temperature of the oil, and the relative operating temperatures of the hotwire probe, hence the potential for damage to the anemometry system.

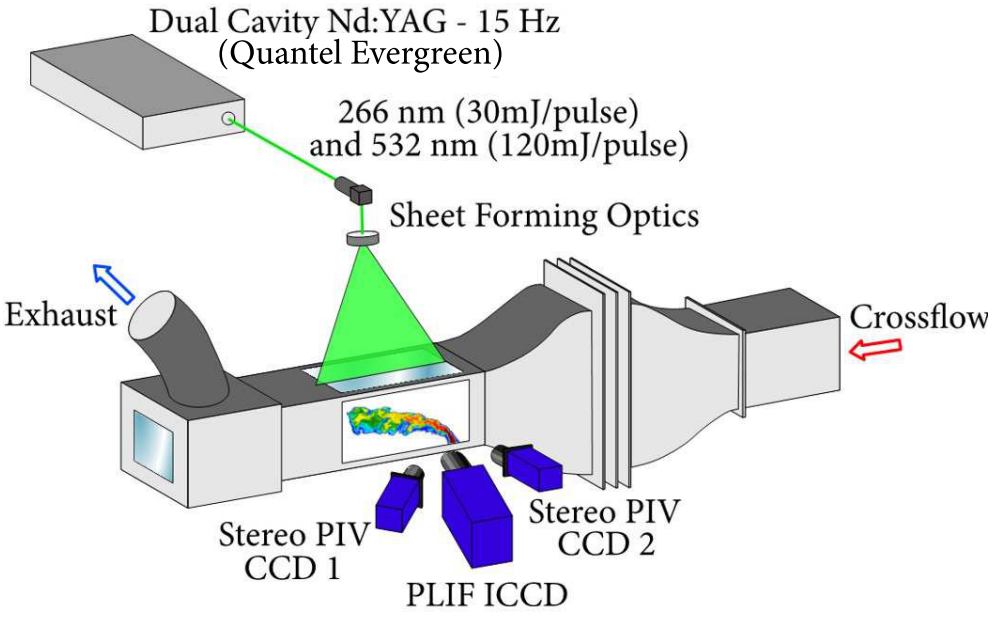

Figure 2.5: Depiction of the standard laser excitation, and optical imaging configuration for stereoscopic PIV, and acetone PLIF

2.3 Optical Diagnostics

Despite the hotwire anemometry capacitating a variety of highly temporally resolved flowfield measurements, there is a desire for diagnostic techniques wherein physical intrusiveness was minimal compared with that which is inherently noted for a hotwire system. Given the minimalistic transmutation of a flowfield due to laser diagnostic techniques, in conjunction with a large spatial domain and refined resolution, their implementation has become quite popular within experimental investigations of fluids flowfields. The planar imaging techniques invoked throughout this study were planar laser induced flourescence (PLIF) of acetone seeded in the jet, providing structure and mixing characterization, and stereo particle image velocimetry (PIV) of DEHS oil in the jet and smoke particles in the crossflow, whereby quantification of the velocity, vorticity, and strain field were resolved.

A simplified depiction of the laser diagnostic system in relation to the complete experi-

mental apparatus was given in Figure 2.1, while a more complete visual understanding of the optical configuration may be seen in Figure 2.5. All laser experimentation was performed with laser energy generated by a dual cavity Q-switched Nd:YAG laser (Quantel Evergreen 30266). Within the system housing, monochromatic light was initially generated at a wavelength of 1064 nm (infrared spectrum) by both cavities. Each source was then subsequently directed through second, and fourth harmonic generators producing refined beams at 532 nm (green spectrum), and 266 nm (ultraviolet spectrum), respectively. The visible green laser light was implemented in PIV measurements, while the ultraviolet light served to excite the acetone tracers for PLIF imaging. The cavities were individually capable of producing laser pulses at 8 ns full width at half maximum (FWHM) with energy levels of approximately 30 mJ and 120 mJ for the 266 and 532 nm wavelengths respectively. The maximum operating frequency at these given conditions was 15 Hz, though actual experimentation was only performed up to a repetition rate of 7.5 Hz. Triggering of the Nd:YAG laser, systematically synchronized in collaboration with the camera system, was performed by a programmable external timing unit controlled with LaVision's DaVis 8.2 software.

The laser unit was mounted on an optical railing system so that traversal of the laser along an axis parallel to the wind tunnel was possible, moreover serving to mitigate manipulation of the open beam laser in directing the light through the quartz window embedded along the upper surface of the chamber. To direct the beam path, the laser was initially focused at a desired location in passing through 2 spherical lenses (LaVision 1108406; wavelengths 220-800 nm). Before coming into focus the laser utilized a 90 degree turning mirror (LaVision 1108407) redirecting the beam into the test section normal to the xy-plane. Optics were configured such that the focal point of the laser was positioned just beneath the plane of the test section floor. Establishing a focal length of the laser just underneath the test section floor was necessitated for calculations regarding the laser light absorption correction, discussed in Section 2.3.1. Just prior to passing through the fused silica quartz window wind tunnel mounting, a $f = -10\ mm$ cylindrical lens (LaVision 1108406; wavelength 220-800

nm, and 20 degree divergence angle) was utilized to form a thin diverging laser sheet from the properlly focused laser beam providing the large spatial domain implemented within the PLIF and PIV techniques. Placement of the cylindrical lens permitted for rotation about the z-axis, and thus afforded turning of the laser sheet for transitioning between centerplane and cross-sectional imaging. To assist investigations of the JICF at various downstream cross-section locations, the entire wind tunnel was mounted to a platform controlled and linearly traversed along the x-axis by a small stepper motor while the laser and optics remained unperturbed.

Proper validation of focal location was made by measuring the energy level of the 266 nm laser light, via a pyroelectric energy detector (Newport 818E-10-50-S) and an optical power/energy meter (Newport 842-PE) situated beneath the test section. A razor blade was affixed to the hotwire traversal apparatus described in Section 2.2, and systematically propagated normally through the laser sheet. Resultant laser energy levels relative to the axial location of the razor blade were representative of a theoretical error function profile, and thus recorded energy vs location data were fitted to the following error function profile equation,

$$E = a\left[erf\left(\frac{X-b}{c}\right)+1\right] \tag{2.1}$$

where E is the radiated energy intensity, and X the razor blade location relative to the laser sheet. Differentiation of the error profile with respect to the relative spatial location resulted in a Gaussian profile representative of the energy profile for the laser sheet. Thickness of the laser sheet was determined based on the spatial distance between the 2 initial points on the Gaussian profile where the $1/e^2$ criterion was satisfied. The implementation of this methodology, known as the scanning knife-edge technique may be seen in Figure 2.6, and further detailed in Clemens (2002) and Wang and Clemens (2004).

For PLIF measurements two 266 nm dichroic mirrors were situated upfield of the spherical lenses described above, such that laser energy produced in the green spectrum was dimin-

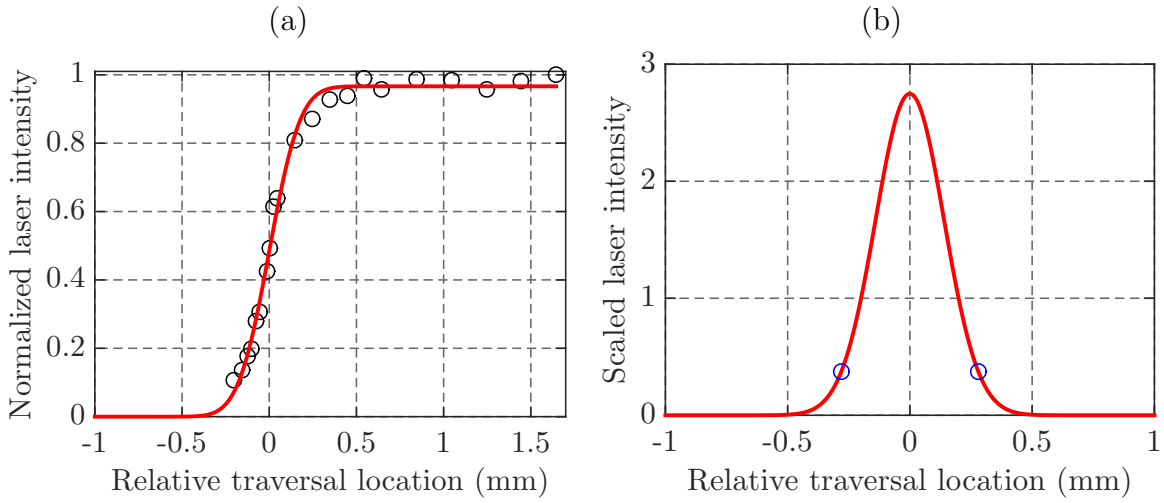

Figure 2.6: (a) Error function fitting (—) based on equation 2.1 for the raw data (∘) recorded via the knife-edge technique with a resultant Pearson correlation coefficient of $R = 0.997$. (b) Laser sheet thickness approximation based on $1/e^2$ criterion points (∘) from Gaussian laser intensity profile (—) generated from derivative of the error fitting. Adapted from Shoji (2017).

ished, while the ultraviolet spectrum light was transmitted; this procedure mainly sought to improve the signal-to-noise ratio within the resulting PLIF images. Additionally a 3 mm uncoated UV grade fused silica lens (Edmund Optics 65865) was placed between the dichroic mirrors and the spherical lenses when performing PLIF calculations. The UV lens served to reflect a portion of the filtered laser energy (approximately 7%) which was then directed to the pyroelectric energy detector and accompanying power meter. Establishing energy levels during PLIF experimentation was brought to bear during image processing, described in Section 2.3.1, as a scaling factor. These additional lenses and referenced energy levels however are not included for PIV techniques. In experimental setups performing simultaneous PLIF and PIV measurements the energy meter was unable to resolve distinct readings between the 2 pulses due to the short temporal separation ($6 - 17.5\ \mu s$), and thus the PLIF images therein were not scaled/corrected with respect to laser energy.

2.3.1 Planar Laser Induced Fluorescence (PLIF) Imaging

Laser induced fluorescence spectroscopy (LIF) is a highly powerful optical measurement technique wherein quantifications of species concentrations, energy-level distributions, and energy transfer processes in molecules may be established. Fluorescence is generated by molecules which are excited to a higher energy state, above their ground state, via absorption of laser radiation, and then subsequently decay back to their ground state; the decay process is conditional upon the extempore emission of a photon. The intensity of emitted photons, fluorescence, is of course dependent upon the energy of incident laser radiation, and the excited-state species number density. Emission from decaying molecules also range in fluorescence spectrum, resulting from sensitivity to the rate and type of energy transfer processes occurring. Considering the noted sensitivity of fluorescence to a variety of parameters, this technique is presented as very becoming for methodically quantifying concentrations of the excitable molecule, under the assumption of an accurate understanding of their collisional and radiative transfer behavior. Due to the limited temporal lifespan (order of ns) of fluorescence after excitation, and the relatively nonintrusive methodology of implementation, LIF has become significantly utilized throughout fluid flowfield research. A subdivision of this highly promoted spectroscopy technique is planar laser induced fluorescence (PLIF), quite simply an application of LIF to that of a planar domain of investigation; greater detail about the development and implementation of PLIF techniques, especially for that of reactive flowfields, may be found in Hanson et al. (1990) and Radziemski et al. (1987).

Implementation of LIF techniques within fluids experiments is greatly dependent upon the attributes of the molecule being excited and fluorescing. Many molecules present themselves as suitable candidates, and in the case of many reacting flows are a naturally occurring byproduct of the chemical reactions taking place, such as OH, NO, or CH. For flowfields wherein the constituent species do not fluoresce in a spectrum which may be capitalized upon, or possibly do not fluoresce at all, introduction of an excitable tracer molecule to the flowfield becomes necessary; careful consideration is given to seeding species such that the

dominant reactions continue while the tracer behaves in a non-participatory manner. For LIF measurements some prevailing seeding molecules are rhodamine or fluorescein dyes, toulene, biacetyl, acetone and its derivatives, and even in certain cases NO. Exploited throughout this experimental research was acetone ($CH_3 - CO - CH_3$), the careful selection of which was predicated upon multiple advantageous properties: low cost of overhead, mild toxicity when handling, high seeding concentrations due to high vapor pressure, favorable separation between fluorescence spectrum (300-500 nm) and the excitation band (225-320 nm), and heritage implementation within low speed flows (Lozano (1992); Lozano et al. (1992); Smith and Mungal (1998); Thurber et al. (1998); Su and Mungal (2004)). Detailed examination of the excited photoluminescence for acetone reveals both a high intensity fluorescence and lower intensity phosphorescence. The phosphorescence arises from the possible compounding effects of energy transfer between molecules and laser energy which was previously alluded to. In such scenarios the excited molecule is also denoted by a change in spin state; obtaining a different spin state results in slower energy emissions due to forbidden quantum mechanic energy state transitions. Emission lifetimes for the fluorescence (4 ns) and the phosphorescence (200 μm), naturally suggest the utilization of a gated imaging technique on the camera to minimize fouling of the fluorescence signal due to the phosphorescence. Further attributed to the purification of the acetone LIF measurements is the degradation of phosphorescence when exposed to oxygen molecules, a trait not denoted for acetone fluorescence. Greater details on the photoluminescence and photophysics of acetone, and subsequent applications as a tracer particle may be found in Lozano (1992), van Cruyningen (1990), and Heicklen (1958).

Considering acetone was introduced to the flowfield as a tracer particle, rather than as a naturally occurring molecule, two seeding chambers were integrated within the jet tubing as depicted in Figure 2.1. Homogeneous mixtures of Helium and Nitrogen were fed to the seeders, oriented in series with one another, via sintered nozzles inserted at the base of the chambers. The initial acetone repository was a 0.25 m tall x 0.13 m diameter steel

cylindrical chamber, which provided the bulk of the seeding. Subsequently the partially seeded flow passed through the second 0.18 m tall x 0.19 m diameter steel cylindrical chamber wherein the precise molar fraction of acetone in the jet was ascribed via explicit control of the liquid acetone temperature and pressure. These properties were monitored by a T-type thermocouple (Omega) with analog thermocouple conditioner (Omega Analog Device 2B50A, $1°C$ max uncertainty), and a pressure transducer (Omega PX409-015G5V, 0-15 PSIG, 0.08% BSL accuracy), the outputs from which were directed to a DSP board (dSPACE 1104) and ControlDesk software. Regulation of the acetone temperature was governed by a refrigerant re-circulatory pump which fed water through copper coils contained inside the secondary acetone seeder, capable of achieving acetone temperatures in the ranger of $5°C \leq T \leq 25°C$; relevant experimental scenarios required temperature regulation in the range of $12 - 18°C$, corresponding to $11 - 22\%$ mole fraction of acetone in the mixture. Establishing proper seeding chamber temperature and pressure was an iterative process wherein temperature was varied, thereby necessitating calculation and revision for all of the various gas flowrates so as to achieve desired density ratios, until a converged seeder pressure was established. The seeder temperature was maintained below the ambient room temperature in all cases so as to prevent condensation of acetone species. In light of the lower temperature flow, tubing downstream of the seeding chamber was not insulated, thereby allowing for equilibration of the flow before entering the wind tunnel.

Image recording processes were conducted with two distinct camera systems. In the case of PLIF measurements only, a 14-bit charge coupled device (CCD) camera (LaVision Imager ProX) with a resolution of 1600x1200 pixels was applied for measuring concentrations of acetone species within the transverse jet. In order to magnify the intensity of recorded fluorescence an external image intensifier (LaVision IRO) was appended to the camera, consequentially reducing the resolution to a maximum window of 1500x1200 pixels due to the 1500 pixel diameter aperture of the intensifier. When performing experimental measurements of PLIF and PIV simultaneously, a 12-bit internally intensified CCD camera (LaVision NanoS-

tar) was instead utilized for the PLIF imaging; the 14-bit CCD Imager ProX camera was used in duplicate for PIV imaging, detailed in Section 2.3.2. The NanoStar camera had a resolution of 1280x1040 pixels, and was distinctly absent the reduced circular aperture since implementation of an external intensifier was not required. Both the internal and external intensifiers operated at a gate time of 200 ns, which corresponds to an exposure time that is 1% of the lifetime for phosphorescence of acetone molecules. During the gated image exposure time both of the Nd:YAG laser cavities would pulse, separated temporally by a 50 ns; the given separation time was able to effectively enhance the energy of incident laser within the FOV by two, while not introducing any temporal smearing of the fluorescence signal due to being several orders smaller than any relevant timescales. Careful consideration of the temporal spacing was required such that nonlinear interaction between the 2 pulses resulting in deconstructive interference and a decrease in energy output was not generated.

Lenses mounted to the cameras were contingent upon the orientation plane and field of view for the measurements being performed. For PLIF imaging of the JICF along the centerplane (xz-plane), a Nikon 50 mm lens at $f/2.0$ was partnered with a Vivitar +2 dioptre close-up lens to provide the relevant field of view (FOV). When a more refined FOV was required in centerplane PLIF, a Nikon 60 mm lens at $f/2.8$ was conveniently affixed. Variation in the desired centerplane FOV was predicated upon a dichotomy between ease of implementation and assured capture of the complete flowfield within the large FOV, with that of arduously established higher spatially resolved data yielding quantification of the local scalar dissipation rate χ and strain rate ϵ in the smaller FOV. While conducting simultaneous centerplane PLIF and PIV measurements the NanoStar camera, which recorded the PLIF data, was fitted with a Sigma 90 mm AF at $f/2.8$ accompanied by a Vivitar +2 dioptre close-up lens. Wherein cross-sectional PLIF data collection was concerned, a Nikon 200 mm lens at $f/4.0$ was attached to the Imager ProX camera. In all PLIF imaging configurations detailed, an optical bandpass filter was implemented to clarify light in the acetone fluorescence spectrum from that of other irradiated background light. Though not

currently explored, the experimental apparatus, optical access ports, and camera systems do allow for investigation of cross-sectional simultaneous PLIF and PIV measurements.

Prior to recording of the experiments being conducted, the camera(s) were calibrated with a two-plane calibration plate (LaVision Type 7). The calibration plate featured white dots uniformly dispersed on the two-plane plate by a distances of 4 mm in each direction, whereby the pixels within the image FOV were transformed to the laboratory coordinate reference frame. For centerplane PLIF imaging with the larger FOV, resulting in-plane spatial resolution was on the order of 80 μm per pixel. Due to lengthy computational times associated with image processing, 2x2 hardware binning was applied when capturing the raw images. The reduced resolution (140 μm to 170 μm per pixel) had the effect of decreasing the required computational time for processing, while additionally improving the signal-to-noise ratio (SNR) of fluorescence within the images. Shoji (2017) demonstrated that despite reduced resolution, the binned images maintained accuracy in calculating concentration and mixing parameters within the flowfield as contrasted with results derived from un-binned images. When quantifying the scalar dissipation and strain rates from PLIF centerplane images (Gevorkyan (2015) and Gevorkyan et al. (2018)), the smaller FOV was implemented whereby the resolution was refined to the order of 35 μm per pixel. While performing simultaneous centerplane PLIF and PIV measurements, the FOV featured a 2x2 binned PLIF image resolution on the order of 65 μm per pixel. In conducting cross-sectional PLIF experimentation the spatial resolution within the images was 60 μm to 90 μm when un-binned, and decreased to 120 μm to 160 μm with 2x2 hardware binning. Representative depictions of the various image resolutions for the instantaneous centerplane PLIF measurements may be seen in Figure 2.7. For proper statistical convergence of evaluated structures, concentrations, and mixing of the JICF, 500 instantaneous PLIF images were taken for each flow condition examined.

In all PLIF images captured, the camera recorded fluorescence data wherein the laser sheet illuminating the FOV was relatively quite thin. Methodology for determination of the

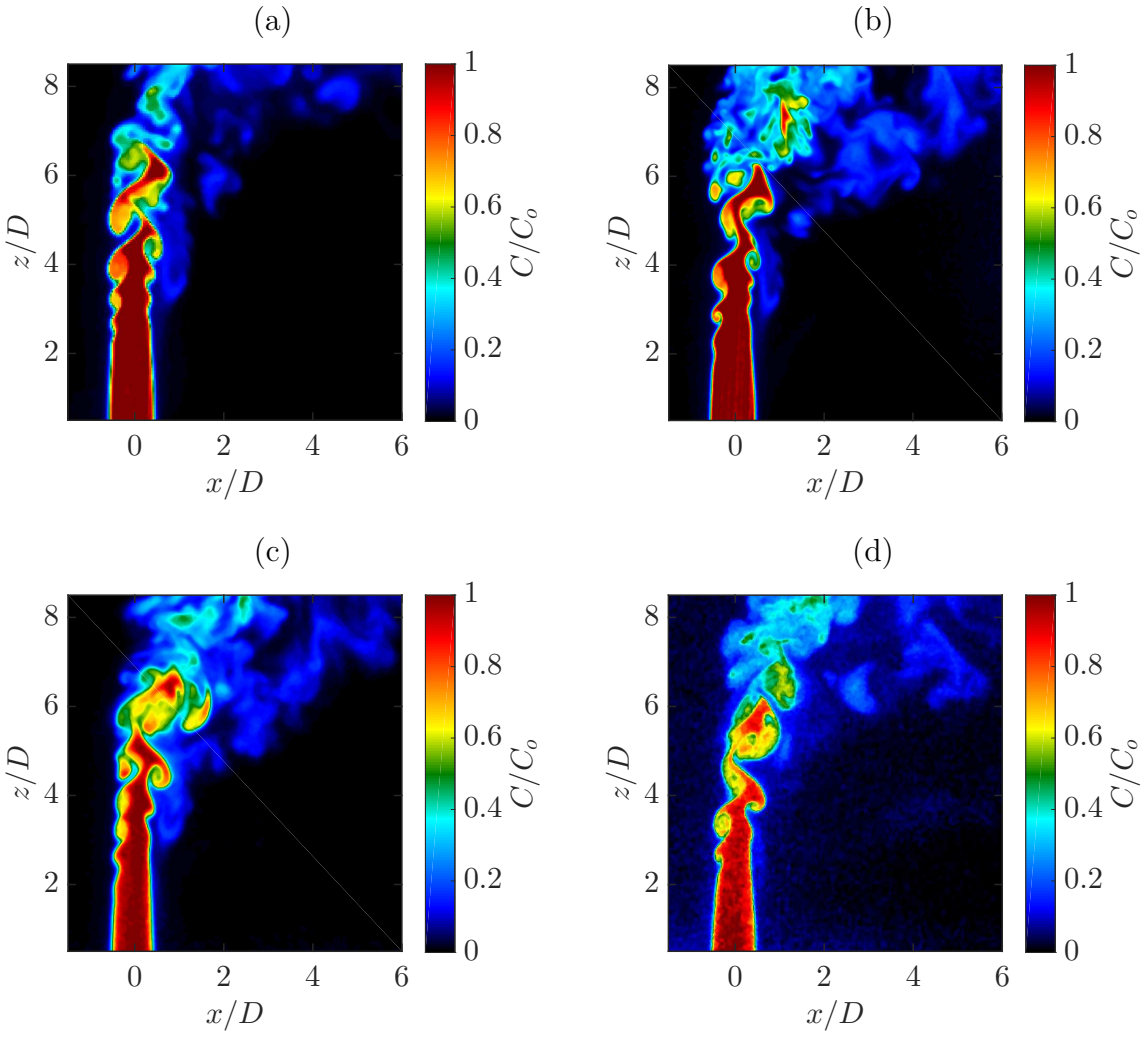

Figure 2.7: Comparison of the equidensity flush-nozzle injected JICF at $J = 41$ with various image recording techniques for instantaneous centerplane PLIF experimentation: (a) Large FOV image with 2x2 hardware binning, (b) Small FOV image without binning, (c) Large FOV image without binning, and (d) image from simultaneous PLIF/PIV measurements with 2x2 hardware binning. Data adapted from Shoji (2017)

laser sheet thickness was detailed in Section 2.3. Thicknesses for the 266 nm laser sheet were in the range of 400-900 μm within the considered optical FOV for centerplane and cross-sectional PLIF. Thinner laser sheet thicknesses were generated when the smaller FOV was utilized in centerplane PLIF, specifically on the order of 360-450 μm. As for simultaneous

PLIF and PIV measurements, the laser sheet was formed to be much thicker (1.4-1.9 mm) for reasonable correlations with the PIV measurements, further explained in Section 2.3.2. The sheet thickness provided for the 3^{rd} dimension (depth) of spatial resolution, in collaboration with the planar spatial resolution per pixel, for the captured images. Given the discrepancies between length scales associated with the spatial resolution, it might be considered that the limiting parameter is the UV sheet thickness. Gevorkyan (2015) dissuades one from such assumptions however, noting that partial derivative concentration magnitudes with respect to directionality are extremely important when determining the limiting resolution, and further expounded by studying the impact of pixel width and sheet thickness on the resolution degradation of mixing and dissipation/strain rate calculations.

Post-processing of the raw recorded PLIF images was a multi-step operation conducted internally within LaVision's DaVis software, conjointly with external codes employed by Matlab. Correction of quantifiable errors inherent to the images and imaging system which were performed within DaVis 8.2 software included subtraction of bias errors composed from dark noise and background light signals, correction of flat-field non-uniformities within the images despite exposure to uniform test sources, and normalization of shot-to-shot fluctuations in the incident laser sheet intensity. Great detail regarding the proper corrections and implementation procedures for image processing are described in Getsinger (2012) and Gevorkyan (2015).

Given the highly excitable nature of acetone molecules at the UV laser sheet wavelength of 266 nm, the incident laser energy was readily absorbed within the flowfield. This desirable phenomena supported the selection of acetone as the tracer particle, but consequentially deteriorated the incident laser energy as the sheet penetrated further into the flowfield. Therefore, the perceived scalar field of excited acetone (i.e. the seeded jet flow) showed a greater concentration nearer to the ceiling of the wind tunnel as compared to the concentration levels at the jet exit plane, despite intuitive knowledge that the greatest concentration should be seen as the jet initially entered the crossflow. Correction of laser intensity and

energy absorption throughout the FOV, in addition to accounting for non-uniformity due to optics forming a laser sheet which was not collimated, was administered within Matlab. The correction further applied a controlled interrogation box about this proposed potential core of the jet wherein the concentration levels were theorized to be at a maximum. The mean concentration value inside the box, the size of which was carefully selected to remain within the jet for each of the 500 instantaneous images, was then utilized as a scaling factor to normalize the pixels within all centerplane images.

Proper modification of images via laser absorption were predicated upon understanding of the generated laser sheet, and in such manner dictated the recording of an isolated sheet image as well as a laser source image. The source image was created simply by placing a small obstruction in the path of the laser sheet whereby a portion of the incident laser light was blocked, allowing for a trace of the angular expansion of the blocked laser back to an imaginary point of origin. Knowledge of the hypothetical source location was utilized to transform the laser sheet into a warped collimated laser sheet within Matlab. The transformation was performed to remove somewhat erroneously weighted laser energy decay estimations, as was previously conducted by Getsinger (2012) and Gevorkyan (2015), where a weighting scheme was applied akin to that which was detailed by Smith (1996). The newly collimated sheet tracked the laser energy decay in the vertical direction along several columnar locations, and fit the data to the Beer-Lambert law described in Modest (2013):

$$E(x) = E_0 e^{-\sigma n x} = E_0 e^{-\alpha x} \tag{2.2}$$

Resulting from the Beer-Lambert law was an estimated absorption coefficient, α, which better accounted for the decrease in incident energy near the tunnel floor. An iterative method was subsequently employed wherein the warped-sheet estimation of absorption coefficient was perturbed over a range of values to determine the coefficient which was best suited to provide uniformity throughout the potential core of the jet images. Shoji (2017) discusses in detail the methodology employed for proper warping of the laser sheet, and absorption coefficient selection.

The final processing procedures applied to the instantaneous PLIF images was filtering to remove some of the remaining noise within the FOV while preserving scalar gradients. The filtering applied consisted of a 5x5 median filter and a 3x3 thresholding/smoothing filter, tools which are discussed thoroughly in Ghandhi (2006). Impact of the various processing procedures on the perceived fluorescence of the jet are demonstrated in Figure 2.8. When filtering for simultaneous PLIF and PIV images, inherently noisier due to the different camera configuration, a 5-pass 3x3 median filter was applied, though no smoothing filter was applied afterwards so as to better preserve the scalar gradients. The resulting signal to noise ratio (SNR) for the various configurations of PLIF imaging was calculated by dividing the average concentration within the potential core of the instantaneous jet images by the standard deviation of the concentration within the respective areas. Gevorkyan (2015) averaged the SNR over the 500 instantaneous images and found respective SNRs of 55, 40, and 25 for the 2x2 binned large FOV centerplane PLIF, un-binned small FOV centerplane PLIF, and 2x2 binned centerplane simultaneous PLIF and PIV.

Given that the existence of a potential core was undetectable within measured cross-section PLIF images, unless measurements were made of the jet exit, calibration of the scalar concentration field necessarily depended on another means of normalization. To accomplish this vertical concentration profiles at a specific downstream locations (x/D) in the mean centerplane image were correlated with the mean cross-sectional image concentrations at the same downstream position. The resulting difference in magnitudes produced the normalization factor by which the cross-sectional data could be corrected. The complete treatment of this procedure, including special considerations, is given by Shoji (2017). Unfortunately for a few cross-sectional cases, agreement between the centerplane and cross-sectional concentrations were not well correlated. This was particularly noted with significant asymmetry of the jet in the xy-plane at moderate to far downstream locations, and as a result normalization of the images could not accurately be administered. However those particular cases, while not providing quantifiable measurements of molecular mixing, still served to illuminate

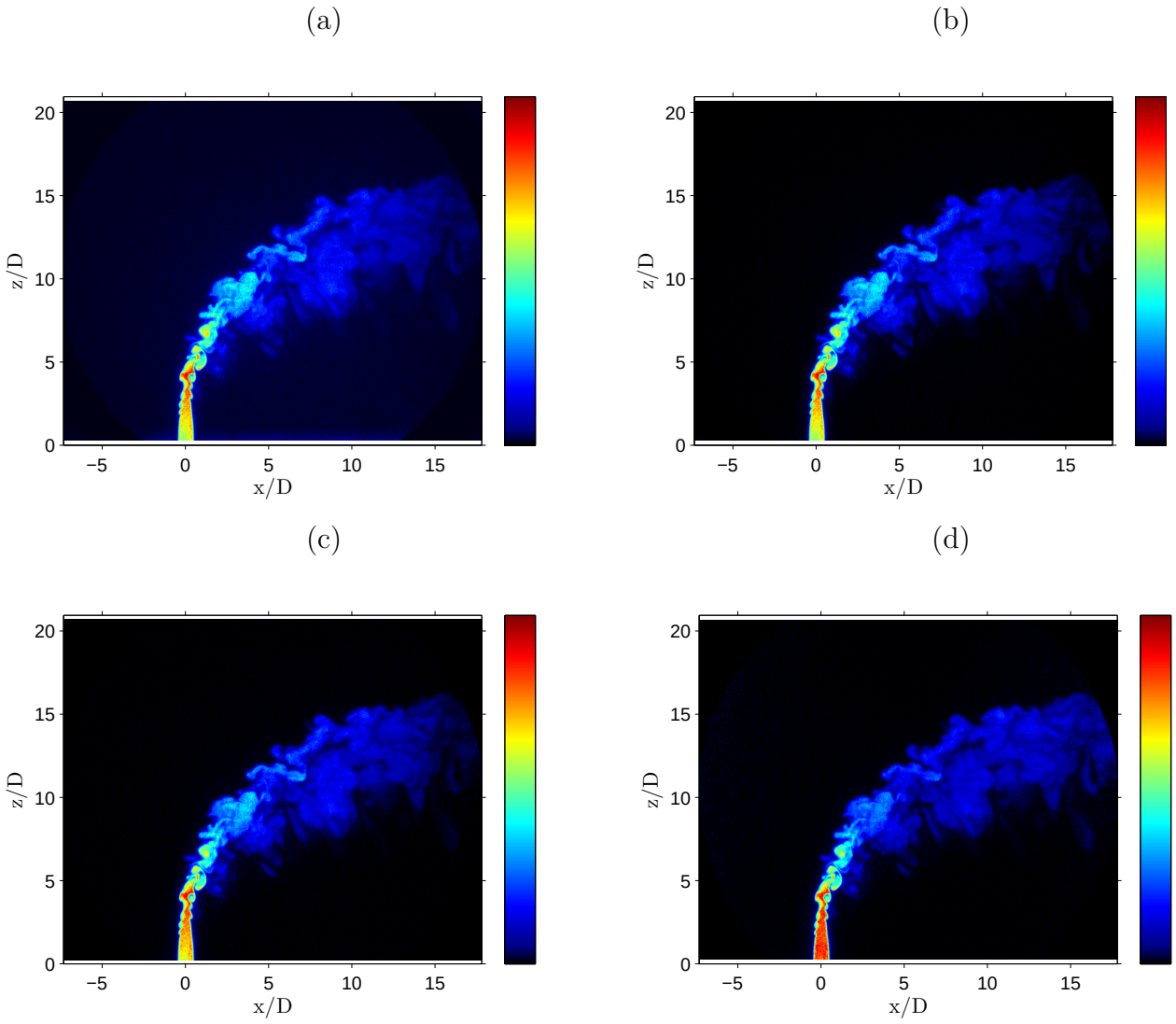

Figure 2.8: Representative depictions of image processing steps for a centerplane PLIF image of the equidensity flush-nozzle injected JICF at $J = 20$: (a) Raw image, (b) After background subtraction, (c) Flat-field corrected and warped, and (d) Laser sheet profile and absorption corrected. Data adapted from Getsinger (2012)

characteristics of the jet structure and behavior.

2.3.2 PIV

Establishing a quantitative understanding of the velocity, vorticity, and other pertinent flow parameters within an experimental flowfield via non-intrusive laser methods has been a greatly developed measurement technique congruent with the advent of powerful laser systems. Particle image velocimetry (PIV), also called pulsed laser velocimetry, particle image displacement velocimetry, digital PIV, or particle tracking velocimetry, is a methodology wherein the inherent definition of velocity is exploited from the displacement of small tracer particles tracked over a given temporal advancement of the flowfield. Laser energy is pulsed twice with a known separation time, in each case illuminating the seeded flowfield, whereby camera systems capture the Mie scattering of the particles. Relative displacements of the particles between the two images then yields estimations of velocity for the particles, given a small time step. Thorough background and recent developments within the field of PIV may be found in Adrian and Westerweel (2011).

Proper selection of the seeding particles was predicated upon a particle which was small enough to follow the flow with negligible influence of Stokes Drag (see Westerweel (1997) regarding more refined requirements for particle-flowfield interaction), yet simultaneously large enough to scatter sufficient amounts of light for purposes of accurate tracking. Utilized within this experimental configuration for the jet flow was DEHS oil ($C_{26}H_{50}O_4$, LaVision 1108951). To inject the oil particles within the jet flow, a portion of the jet was directed through a particle generator (TSI 307600). Fine tuning of the seeding density was controlled via a needle valve which determined the about of jet fluid directed to the particle generator. In order to properly visualize the flow velocities within the entire FOV, the crossflow was also seeded with glycol-based smoke particles (0.2 μm mass-median diameter) by a commercial smoke machine (Pea Soup Rocket) at the centrifugal blower inlet. Seeding density of the crossflow was established by visual evaluation of the uniformity of seeded particles throughout the entire flowfield.

PIV measurements of the JICF employed the same laser excitation system and optical setup which was described in Section 2.3. The Nd:YAG laser was specifically chosen for the dual applicability to PLIF and PIV investigations by means of the harmonically generated wavelengths at 266 nm and 532 nm respectively. Unlike the optical setup for PLIF, the two dichroic mirrors and the beam splitting UV lens were removed such that the 532 nm wavelength light (visible green spectrum) was the dominating source within the test section. The laser sheet thickness was formed at the range of 1.4-1.6 mm, the determination of which was made by the knife-edge technique. The sheet thickness was formatted such that it was sufficiently thin enough to be considered a planar measurement field, while yet still able to capture out-of-plane motion of the particles for stereo PIV assessment. The temporal separation between laser pulses was in the range of 6 μs to 17.5 μs for previous JICF studies (Gevorkyan (2015) and Shoji (2017)), and was governed by the type flow conditions being examined, in addition to the magnitude of in-plane particle displacements normalized by the image spatial resolution. Adrian and Westerweel (2011) provides guiding parameters on estimating a suitable Δt for this resolution criterion on both in-plane and out-of-plane displacements for stereo PIV measurements.

Stereoscopic PIV imaging, depicted in Figure 2.5, was collected by an optical system consisting of two 14-bit cross-correlated CCD cameras (LaVision Imager ProX). Cross-correlation of a camera corresponded to an imaging technique where two distinct images with single exposures were recorded, as opposed to auto-correlation where a single double exposure image would be captured. The two cameras were oriented through the side optical window for centerplane PIV, at angles displaced from perpendicular to the zx-plane. For the work by Gevorkyan (2015), the angles were 60° relative to the jet injection plane. The other camera specifications were those given in Section 2.3.1, though the implementation of the external intensifier was not necessary. Mounted to each camera was a Nikon 60 mm lens at $f/11.0$, coupled with a 532.5 nm narrowband filter. To assist in the fine tuning of the imaging a Scheimpflug lens mount (LaVision 1108196 version 1) was integrated with the

lenses allowing for tilting of the lens plane relative to the CCD array so as to maintain focus over the entire domain. Resultant imaging of the laser illuminated flowfield were able to examine the same particle displacements, but from the perspective of two differing orientation planes. Consequentially, inconsistencies between the differing viewpoints regarding the particle displacements allowed for resolution of the out-of-plane motion of the particles, and assisted in removing bias error of the in-plane motion. This methedology of resolving all 3 components of particle motion, or 3-component PIV, is referred to as the 2D3C technique. This approach to resolving each component of motion within flow was chosen for the relative ease of implementation and cost as opposed to tomographic-PIV, which uses volumetric illumination of the flow and a minimum of 4 cameras.

Calibration of imaging plane for stereo PIV utilized the two-plane calibration plate (LaVision Type 7) similarly applied in PLIF imaging. The calibration process mapped the raw camera coordinates to real-world corrdinates via a 3^{rd} order polynomial model found within LaVision's DaVis 8.2 software. Additionally adapted after capturing the images was a self-calibration method using the crossflow (Wieneke (2005)), whereby discrepancies between the position and orientation of the calibration plate and the laser sheet could be resolved. For completion of image processing after transforming coordinates, the images were also corrected by a global background subtraction, further removal of background effects via local 8-pixel sliding, and filtering of particle intensity for contrast normalization.

Determination of velocity vectors from the particle displacements was performed by processes self-contained within LaVision's DaVis 8.2 software. User defined parameters afforded the selection of vector calculations via a multi-pass stereo cross-correlation with a decreasing window sizing of interrogation for improved accuracy (2 passes at 32x32 pixel interrogation area at a 50% overlap, and 4 passes at 24x24 pixel area at a 75% overlap). Selection of the stated windowing sizes were made for improved vector yield and accuracy of subsequently derived gradient values. Post-processing was applied to further filter and refine the quality of correlated vectors, which culminated in a final PIV pixel resolution on the order of 120 μm in

past work (Shoji (2017)). This resolution however was not indicative of the effective spatial resolution, which was better established by the density of well-correlated vectors within a given image as performed by Westerweel (1997), Su and Mungal (2004), and Kothnur and Clemens (2005). In the work by Shoji (2017), approximately 58100 velocity vectors were recoverable from a 1600x1200 pixel raw image, resulting in a density of 0.03 vectors per pixel. Such a vector density was reasoned to be sufficient to ascribe the nature of the strain rate within the flow, given that the work performed by Kothnur and Clemens (2005), focusing on strain rates in a comparatively finer flowfield, featured a similar vector density of 0.036.

Part I

Tabbed Single Jet in Crossflow

CHAPTER 3

Motivation and Features of the Tabbed JICF

3.1 Motivation

Despite the JICF's classification as an efficient mixer, there have been numerous efforts over the years to further improve the efficacy of mixing through passive and/or active control of the jet. While active control involves temporal variation in flow parameters, with the potential for sensor-based feedback to the actuation system (M'Closkey et al. (2002); Davitian et al. (2010b); Shoji et al. (2019)), passive control typically is simpler to employ, for example with a fixed geometrical change jet shape (Haven and Kurosaka (1997)). Among the passive control measures that have seen relatively limited exploration is that where there is an alteration in the jet exit profile due to the presence of small tabs or vortex generators placed about the jet exit. For the free jet, such tabs can demonstrate remarkable enhancement of entrainment and jet mixing (Bradbury and Khadem (1975); Ahuja and Brown (1989); Zaman et al. (1992); Carletti et al. (1996)). Ahuja and Brown (1989) and Zaman et al. (1991) show that the placement of small flush tabs at the injector exit can act to azimuthally excite the flow and enhance streamwise vorticity generation. Zaman et al. (1994) and Bohl and Foss (1995) further suggest through experimental observations that the vorticity generation from a tabular protrusion into the jet flow originates from two sources: a "pressure hill" upstream of the issuing tab, and shed vortex sheets from the sides of the tab.

For the transverse jet, given the sensitivity of the CVP and the shear layer vortices, to the initial jet flow conditions, the utilization of a tab at the jet exit could well provide alterations

to the flowfield and mixing characteristics. In the earliest studies of a tabbed JICF, a small tab is placed on the downstream/lee side of the jet exit so that the proposed net vorticity production from the tab would align with and enhance the circulation of the CVP, thereby potentially improving the mixing (Liscinsky et al. (1995); Zaman (1998)). However, these investigations ultimately show that for a range of jet Reynolds numbers ($Re_j = 24,000 - 54,000$), and multiple momentum flux ratios (J = 8.5, 21, and 54), the tab is actually ineffective and has negligible influence on the flowfield when placed on the downstream side of the jet. In contrast, Zaman and Foss (1997) find for the same flow conditions that placement of a tab in the upstream edge of the jet periphery is able to alter the jet, where the penetration and strength of the CVP are both significantly reduced. They theorize the differences in effectiveness between tab orientations is attributable to a lower static pressure on the downstream side of the jet, resulting in a reduced tab vorticity generation from the pressure-hill source when positioned downstream. The implications of tab placement about the periphery of the JICF are explored in greater detail by Bunyajitradulya and Sathapornnanon (2005), who examine a single tab positioned at eight different azimuthal orientations for a heated JICF with $S = 0.86$, $J = 16$, and $Re_j = 15,000$. They observe the strength of alterations to the jet to be systematically diminished as the tab orientation transitions from the upstream edge towards the downstream, at which point little to no impact from the tab is seen. Interestingly, tabs that are positioned at locations other than at the upstream or downstream positions are able to produce a skewing of the jet cross-sectional symmetry.

Studies examining a tabbed JICF have not extensively explored the implications of tab orientation on mixing characteristics of the jet, and the only one which has done so explores flows at relatively high momentum flux ratios, $J > 20$ and jet Reynolds numbers, $Re_j > 24,000$ (Liscinsky et al. (1995)). Understanding mixing characteristics over a range of flow regimes is not only of practical importance, but it is of great interest to understand the impact of a tab on the previously mentioned USL instabilities given the significance of the nature

of the instability characteristics to the development of the CVP and associated molecular mixing (Gevorkyan et al. (2016)). The experimental study in chapter 4 seeks to investigate these tab effects in detail via PLIF imaging, on transverse jet USL stability characteristics, the associated jet structure, and resultant molecular mixing characteristics. While structural and mixing characteristics which are documented in chapter 4 reveal important insights for the influence of passive tabs on the JICF and its applications, there are a number of open questions on the mechanisms by which such changes take place. The means by which the tabs themselves alter the vorticity field at the exit, and hence the shear layer rollup, are of interest, given the importance of the eventual CVP to mixing enhancement. Simultaneous stereo particle image velocimetry (PIV) and acetone PLIF imaging in the experiments of chapter 5 can answer such questions. Further, proper orthogonal decomposition (POD) of such imaging can assist with understanding the dynamical character of the flowfield and modifications that can be created even by simple passive structures. Such explorations can also help to explain observations made in others' much earlier studies.

3.2 Supplemental Setup and Experiment Modifications

The general experimental setup and configurations are given in chapter 2, which details the wind tunnel, flow plumbing, optical setup, and diagnostic tools and methods. Here details are given which were specific to the studies conducted in chapters 4 and 5. For this experimental investigation of the JICF, a small tabular protrusion into the jet fluid was placed around the periphery of the exit plane of the issuing jet. In order to retain the flush nature of injection to the wind tunnel, the jet injection system (section 2.1.1) was affixed to the removable floor shown in figure 2.2(c) such that the flush nozzle was recessed from the plane of the main tunnel floor. The recession in the surface of the removable floor allowed for the placement of an insert which accommodated the tabular protrusion. The insert was made of 20 gauge (0.813 mm) 7075 Al sheet metal with an outer diameter of 5 cm, sufficiently large enough to

displace the edge seam at a relatively far distance from the jet exit in effort to mitigate effects of possible flow disturbances; the thickness of the tab insert was dictated the machinability and rigidity of the final tab. Additionally benefited by integrating the tab via an inlay was the ability to rotate the orientation of insertion, such that the tab location relative to the upstream shear layer of the jet could be systematically varied without any alteration in the crossflow and its interaction with the flush jet.

The tab geometry used in the present experiments built on findings in prior free jet experiments (Carletti et al. (1996); Bradbury and Khadem (1975); Zaman et al. (1994))as well as JICF testing (Zaman (1998)). In the present experiments the tab consisted of a simple triangular protrusion oriented coplanar with the tunnel floor, where the base tab length of 1/4 jet diameters resulted in an effective jet flow blockage of approximately 4%. The template in which the tab was machined is shown in figure 3.1(a), with an outer diameter of the disc equal to 5 cm; the circular opening into which the tab was machined had the same diameter as the jet nozzle, 4.04 mm. A magnified view of the tab within the orifice template is shown in figure 3.1(b). The design of the template was such that the tab position could be rotated to any azimuthal position desired, relative to the oncoming crossflow. Labeling for the various tab positions is shown in figure 3.1(c). An additional template, of the same thickness (0.813 mm) as the tabbed template, but with only a round opening of diameter 4.04 mm, was also used in the present experiments. This enabled a more accurate comparison of the influence of the tab on the JICF as compared with the jet without a tab but with an extension of the same thickness. Hotwire anemometry was instrumental in examining the nature of the modified free jet velocity profile; sample plots of the measured velocity profiles demonstrating the influence of the tabbed flush nozzle are shown in figure 3.1, which can be compared with the regular flush nozzle or flush pipe injector velocity profiles in figure 2.4.

Two distinct flow conditions were treated within these studies, corresponding to flow for the high-resolution PLIF imaging and the simultaneous PLIF/PIV imaging respectively. The jet in chapter 4 consisted of an equidensity flow with constituent species mole fractions

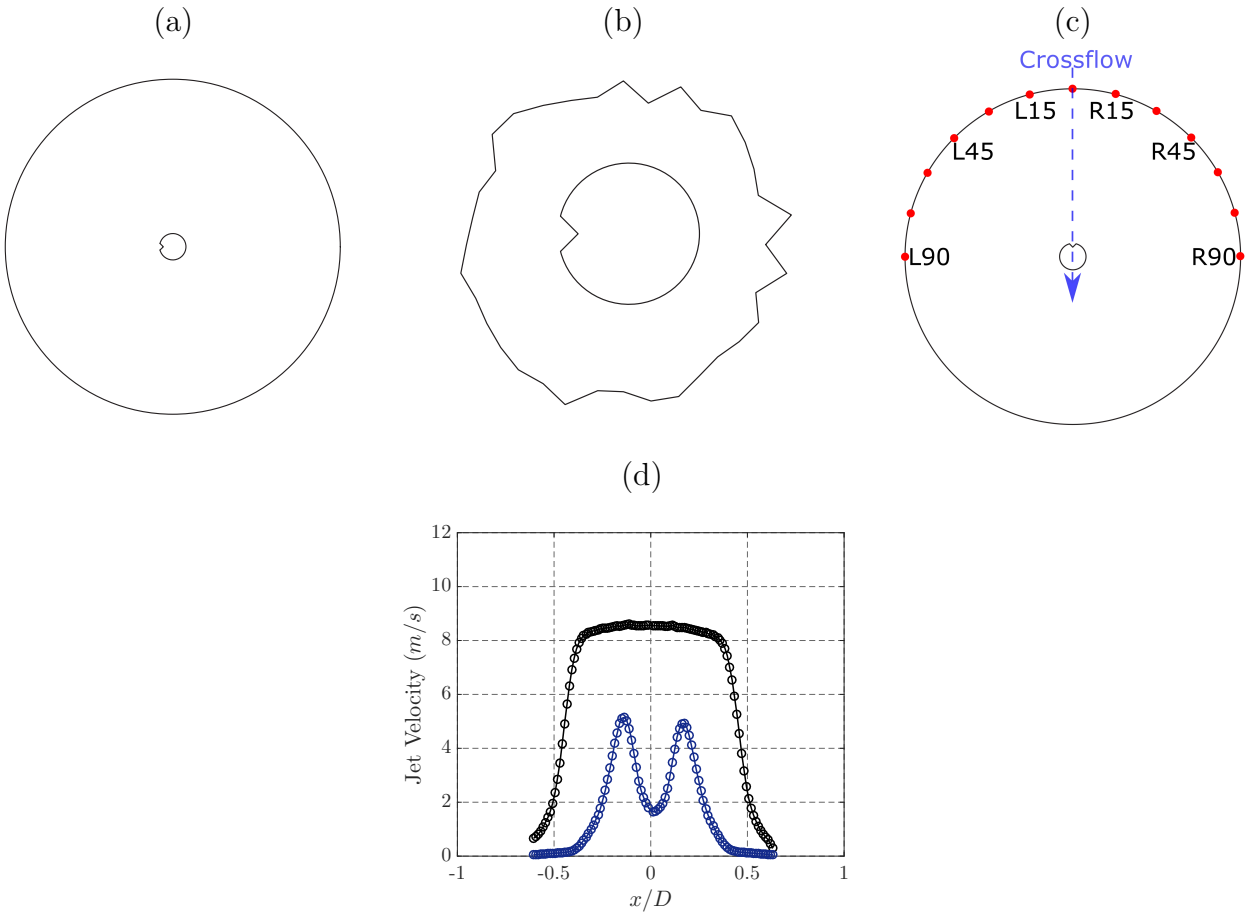

Figure 3.1: (a) CAD drawing of the single triangular tab insert with an approximate flow blockage of 4%. (b) Magnified depiction of the jet orifice with tab protrusion for the single tab insert. (c) Depiction of tab orientation relative to oncoming crossflow. (d) Jet velocity distributions for a nitrogen jet injected into quiescent surroundings at a jet Reynolds number $Re_j = 1900$ with the velocity profiles for tab flush nozzle in the $x = 0$ plane (—) and $x = -0.45D$ plane (—). Data points (∘) were captured by hotwire anemometry at $0.1D$ above the jet exit.

of 0.218, 0.234, and 0.548 for the acetone, He, and N_2 respectively. The jet had a Reynolds number of $Re_j = 2300$, with a resulting bulk jet velocity of $U_j = 7.91m/s$, and specifically looked at momentum flux ratios of $J = 7$ and $J = 61$, which straddle the transition of the USL from absolute to convective instability. In chapter 5, the equidensity jet instead had

constituent species mole fractions of 0.112, 0.100, and 0.788 for the acetone, He, and N_2 respectively. The flow had a Reynolds number of $Re_j = 1900$, with a bulk jet velocity of $U_j = 6.80m/s$ and examined momentum flux ratios ranging from $J = 5$ to 41. The flow conditions treated for this chapter were slightly different from those of chapter 4 owing to the slight changes in the jet constituent species, as well as a correction in the methodology in which the flowrates were calculated, which is detailed in appendix A.

CHAPTER 4

High Resolution PLIF

The results presented in this chapter are taken with slight modification from the article "Effects of tabs on transverse jet instabilities, structure, and mixing", currently submitted for publication.

4.1 Results

4.1.1 Shear Layer Instability Characteristics

As noted, for a flush nozzle-injected jet in crossflow, the instabilities along the upstream shear layer of the jet undergo a transition from convective instability to absolute/global instability as the jet-to-crossflow momentum flux ratio J is lowered below a critical threshold J_{cr} (Megerian et al. (2007); Davitian et al. (2010a); Getsinger et al. (2012)). More recently Shoji et al. (2020b) observe that even very small changes in the jet constituent species, causing a change in the bulk viscosity of the jet mixture for example, due to the presence of acetone, can alter this transition point if other nondimensional parameters such as J, Re_j, and S remain fixed. Such changes in the jet-to-crossflow viscosity ratio result in slight changes to the mean jet velocity, and as a result alter the jet momentum thickness at the nozzle exit, which is noted by Megerian et al. (2007) and Alves et al. (2008) to play a significant role in the developing shear layer instabilities, as is the case in other shear layer instabilities (Michalke (1971)). Experimentally, one of the very clear indicators of this transition point for the jet in crossflow is through observed changes in hotwire-based spectral

contour plots of vertical velocity power spectra along the evolving shear layer trajectory. When the flow is convectively unstable, the contour plots depict relatively weak broadband instability peaks, frequency shifting along the trajectory due to a tonal interference with the hotwire probe (Hussain and Zaman (1978); Getsinger et al. (2012)), and the formation of a subharmonic instability peak. When the flow becomes absolutely unstable, the contour plots show a stronger and more pure-toned instability with higher harmonics which do not vary significantly along the shear layer, in addition to elimination of the subharmonic presence.

For an equidensity flush nozzle-injected jet with a jet Reynolds number of $Re_j = 2300$ and an acetone mole fraction of $\psi = 0.218$, the critical transition from convective to absolute instability takes place at $J_{cr} \approx 8$ (Shoji et al. (2020b)). Representative spectral contour plots for the original 5^{th} order polynomial flush nozzle in the present studies are shown in figure 4.1(a) for the case of an absolutely unstable USL at $J = 7$, and in figure 4.2(a), for the case of a convectively unstable USL for $J = 61$. Along the abscissa, frequency content was non-dimensionalized to show a Strouhal number based on jet diameter, $St \equiv fD/U_j$, while in the ordinate the shear layer trajectory location s was normalized by the jet exit diameter D. Strong pure-tone instability characteristics in figure 4.1(a) and delayed, weaker instabilities with frequency shifting, representing tonal interference, in figure 4.2(a) are consistent with AU and CU USL instabilities, respectively.

To explore the influence of the presence of a tab placed about the jet exit periphery on the upstream shear layer instabilities, the tab insert was oriented at various positions relative to the upstream, including upstream and downstream locations, and resulting upstream shear layer spectral characteristics for these cases are shown in figures 4.1(c)-(f) and 4.2(c)-(f). Because the tab extensions had a finite thickness, increasing the nozzle length by $0.19D$, it was also necessary to explore the effect of the simple round template without a tab, replacing the tab extension template, to examine that influence on USL instabilities, and these results are shown in figures 4.1(b) and 4.2(b).

For the naturally AU cases at $J = 7$, the simple round (tabless) thin extension in figure

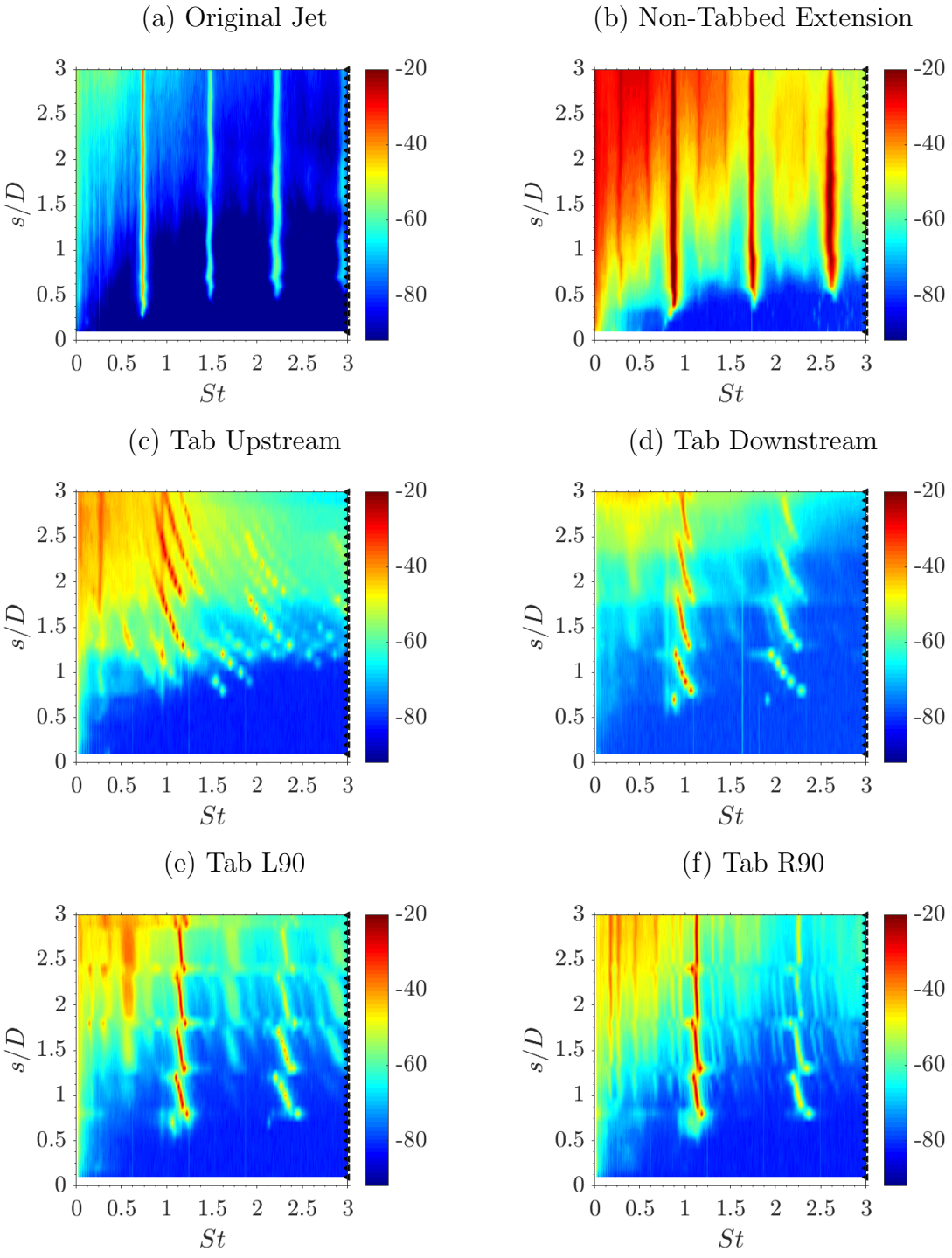

Figure 4.1: Upstream shear layer spectral contour maps of the shear layer instabilities evolving along the shear layer for an acetone seeded, equidensity, $Re_j = 2300$ jet at $J = 7$, with (a) the original nozzle, (b) the nozzle with a thin non-tabbed round extension, and (c)-(f) tab positioning at locations indicated.

4.1(b) shows that the shear layer instabilities were only slightly altered as compared with the original flush nozzle. Here the shear layer instability was still strong and pure-toned, with only a very slight increase in the associated frequency or Strouhal number of the dominant mode. These changes due to the nozzle extension were relatively small, and the resulting jet was certainly considered to be absolutely unstable, but it did appear that the small straight extension at the nozzle end may have altered the upstream momentum thickness of the jet, hence affecting the dominant instabilities (Alves et al. (2008)). These alterations in the velocity field and momentum thickness are explored in separate studies (Harris et al. (2020a)).

The presence of the physical tab in the extension to the nozzle for $J = 7$ had a much more significant influence on shear layer instabilities, in many cases. When the tab was situated in at the upstream location (fig. 4.1(c)), a relatively large change in the spectral characteristics took place, producing clear features of convective instability in the USL, with a more significant delay in initiation of the instabilities and frequency shifting over a large span of frequencies. Unexpectedly a lower frequency peak was formed at $St = 0.32$, which did not correspond to the typical subharmonic of the fundamental range ($St_0 \approx 1.1 - 1.5$), as observed for CU conditions in Megerian et al. (2007). Interestingly, a Strouhal number of 0.32 is in the range of established values of preferred modes for the free jet emanating from a nozzle (Gutmark and Ho (1983); Petersen and Samet (1988)), but at much higher jet Reynolds numbers, of the order 10^5. This difference in dominating subharmonic frequencies would be consistent with alterations of the jet momentum thickness, recalling from linear stability theory that as D/θ changes, so do the growth rate curves of the instabilities, and thus the dominant instability frequency (Alves et al. (2008)). When the tab was placed in the downstream shear layer (fig. 4.1(d)), the resulting instability characteristics were more representative of a convective instability, with a delay in initiation along the USL and persistent frequency shifting typical of tonal interference for a CU USL. When the tab was oriented at the L90 and R90 orientations (figs. 4.1(e) and 4.1(f), respectively), the instability

characteristics were slightly weakened, as compared with the instabilities for the nontabbed case in figure 4.1(b). There was slight frequency shifting for the entire 3 diameters along the shear layer in addition to a delay in the initiation of the instabilities. In the L90 tab orientation, there was also a clear emergence of a subharmonic instability, but this was not the case for R90, which produced spectral characteristics closer to those of the tabless insert in figure 4.1(b). These factors suggested that the presence of the tab at these orientations transitioned the USL from being AU without the tab to CU or nearly so with the tab.

The influence of the non-tabbed and tabbed inserts on USL instability characteristics for the naturally convectively unstable flow at $J = 61$ is shown in figures 4.2(b)-(f). Similar to the naturally AU case in figure 4.1(b), the simple round thin extension to the nozzle produced spectral characteristics which were very similar to the original jet without any extension (fig. 4.2(a)) with a slight increase in the average of the dominant frequency. Note that the tonal interference characteristic of the JICF with a convectively unstable upstream shear layer was clearly evident in both cases, though the instability strengths associated with the color maps in figure 4.2(b) as well as figure 4.1(b) were slightly altered from other cases due to differences in the method for extracting spectra. For the cases with a tab partially blocking the jet flow, when the tab was oriented at the downstream position (fig. 4.2(d)), or at L90 or R90 (4.2(e) or 4.2(f) respectively)), the resulting instability characteristics were also very similar to the original jet configuration. When the tab was oriented at the upstream region of the jet (fig. 4.2(c)), however, a rather significant alteration to the instabilities along the shear layer trajectory took place, where the initiation of the instability was delayed to a distance of $s/D = 3$ along the shear layer, in contrast to the initiation location of $s/D \approx 2$ without the tabless insert in figure 4.2(a). This delay in the onset of the shear layer instabilities not only suggested a weakening of the disturbance, but also indicated spectral characteristics at a high J value that were similar to those for a free jet or transverse jet emanating from a pipe rather than a nozzle, as seen by Getsinger et al. (2014). This observation also were consistent with an increase in the momentum thickness in the upstream region of the jet

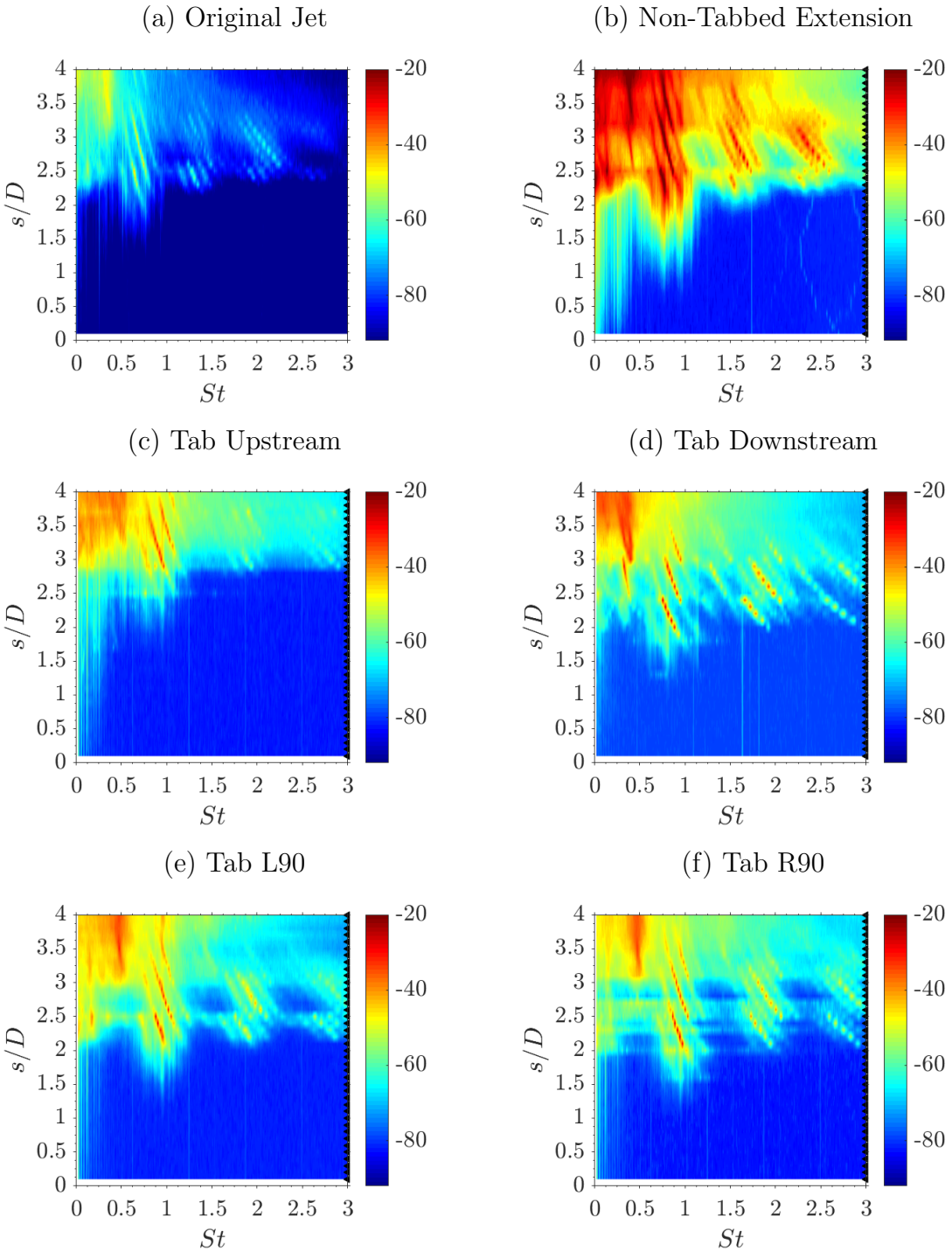

Figure 4.2: Upstream shear layer spectral contour maps of the shear layer instabilities evolving along the shear layer for an acetone seeded, equidensity, $Re_j = 2300$ jet at $J = 61$, with (a) the original nozzle, (b) the nozzle with a thin non-tabbed round extension, and (c)-(f) tab positioning at locations indicated.

due to the presence of a tab. Situating the tab upstream appeared to alter the subharmonic formation and shear layer rollup, producing weaker and more diffuse or broadband energy transfer to the subharmonics from the fundamental instability.

Hence in both the $J = 7$ and $J = 61$ cases, the most significant influence of the tab on the USL was, as would be expected, when it was positioned within the upstream shear layer. Yet it is interesting that the naturally absolutely unstable USL for $J = 7$ was also influenced by tab positioning away from the upstream, even at the downstream location, in contrast to a lack of influence for such tab positions on the naturally CU case of $J = 61$. These behaviors in fact agree with the computationally predicted wavemaker regions of both convectively and absolutely unstable low speed jets-in-crossflow, that is, the regions of greatest sensitivity to perturbations within the flowfield (Regan and Mahesh (2019)). These direct numerical simulations (DNS) indicate that a naturally AU transverse jet has a wavemaker region in the upstream nearfield region of the jet, whereas the wavemaker region for a naturally CU JICF extends along the entire upstream shear layer of the jet and wraps around to the downstream side of the jet. This similarity between experiments and simulations will be discussed in greater detail with regard to the structural changes in the following section.

4.1.2 Structural Characteristics

The structural characteristics of the tabbed jet-in-crossflow were explored through instantaneous centerplane and mean cross-section PLIF images. Representative PLIF images are shown in figure 4.3 for the case of $J = 7$ and in figure 4.4 for the JICF with $J = 61$. The color bars for the images represent the relative concentration of jet fluid scaled from 0 for pure crossflow to 1 for pure jet fluid, as was found in the potential core visible in the centerplane images. Cross-sectional concentration values were calibrated by a comparison of the spatially averaged cross-sectional concentration with that in a thin slice of a mean centerplane image, as described in Gevorkyan et al. (2016). Hence the upper limit of the concentration scales corresponded to the maximum value within each individual image. Cross-sectional images

represent an average of 500 instantaneous snapshots of the flowfield, and in the experiments were taken at x/D locations of 2.5, 5.5, and 10.5 downstream of the jet injection. In figures 4.3 and 4.4, only cross-sectional images corresponding to $x/d = 10.5$ are shown since they depict the more developed and visually obvious implications of tabs on the jet structure. The overall study investigated multiple J values and tab orientations, but herein only a few of the more significant results are discussed. The results deal primarily with the conditions examined in the preceding section, 4.1.1. In addition to the non-tabbed thin insert and upstream, downstream, and L90/R90 tab positioning, results are also shown for a few tab orientations between the upstream and L90/R90 locations.

The instantaneous centerplane and mean cross-sectional images for $J = 7$ in figure 4.3 show that the jets were similar to one another in terms of overall spread and penetration in the centerplane and relative cross-sectional symmetry, though there were some subtle differences in each. In the instantaneous centerplane images in figure 4.2(a), one sees clear USL vortex rollup for the non-tabbed jet with the thin extension, consistent with the pure tone instability observed in fig 4.1(b). But with the tab in the upstream position, the weakening in the USL as indicated in fig. 4.1(c) was manifested in a weakening and smoothed imaging of the upstream shear layer. This weakening was observed in other centerplane images with tabs placed close to the upstream region, e.g., at R30 or L45. For such cases there was also a small but discernible decrease in the penetration of the jet into the crossflow, especially for upstream tab placement. Such observations on penetration have been seen in prior studies of the tabbed jet-in-crossflow when a tab is placed upstream (Liscinsky et al. (1995); Zaman and Foss (1997); Bunyajitradulya and Sathapornnanon (2005)). These studies suggest the decrease in penetration arises due the conflicting signs of vorticity generation from the tab and counter-rotating bound vortex pair. Cross-sectional imaging here can help to explore this conjecture.

The cross-sectional images in figure 4.3 show the classic symmetric CVP structure for the non-tabbed jet with a thin extention (fig. 4.3(a)), but when the tab was placed upstream

(a) Non-tabbed Extension

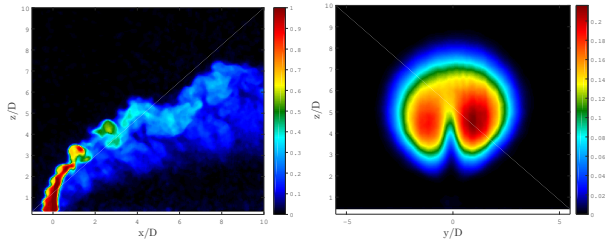

(b) Tab Upstream

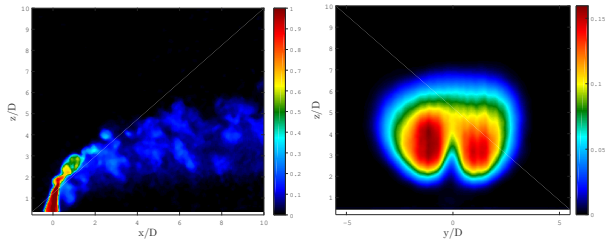

(c) Tab Downstream

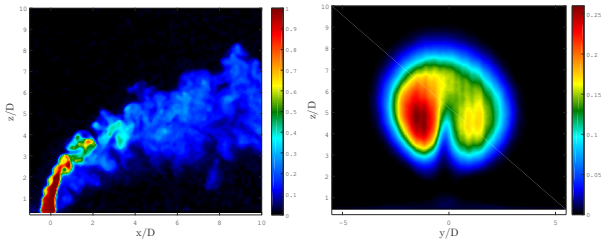

(d) Tab L30

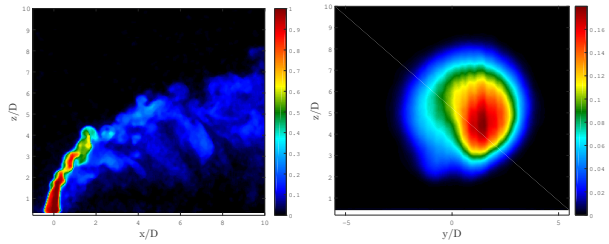

(e) Tab R30

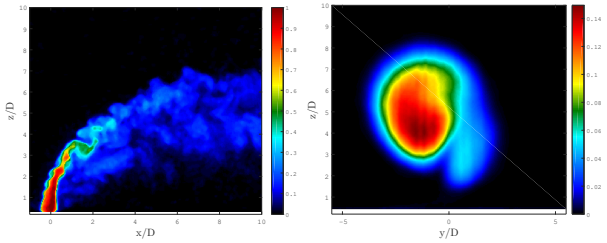

(f) Tab L45

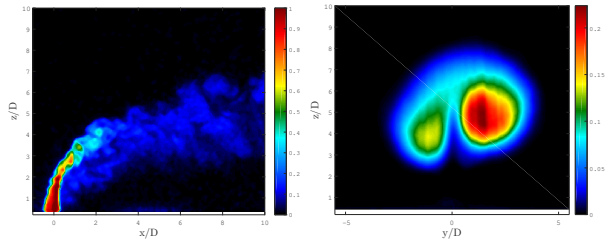

(g) Tab R45

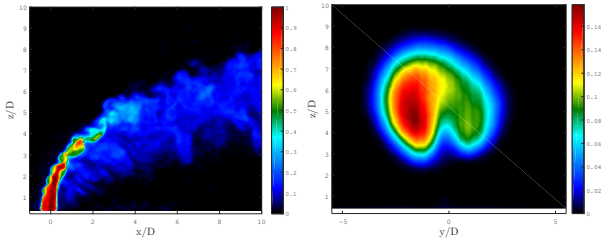

(h) Tab L60

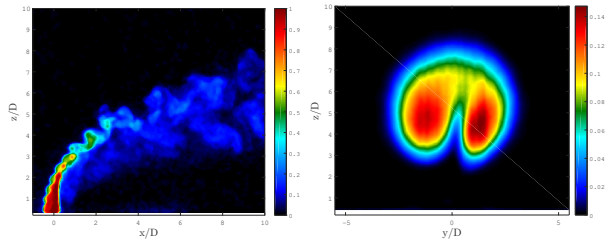

(i) Tab R60

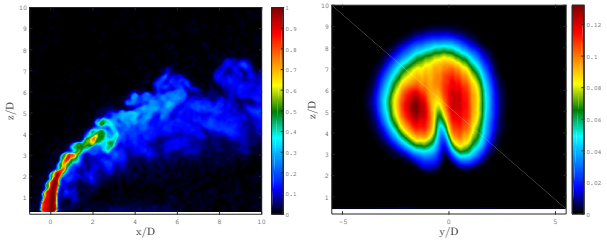

Figure 4.3: continues to following page

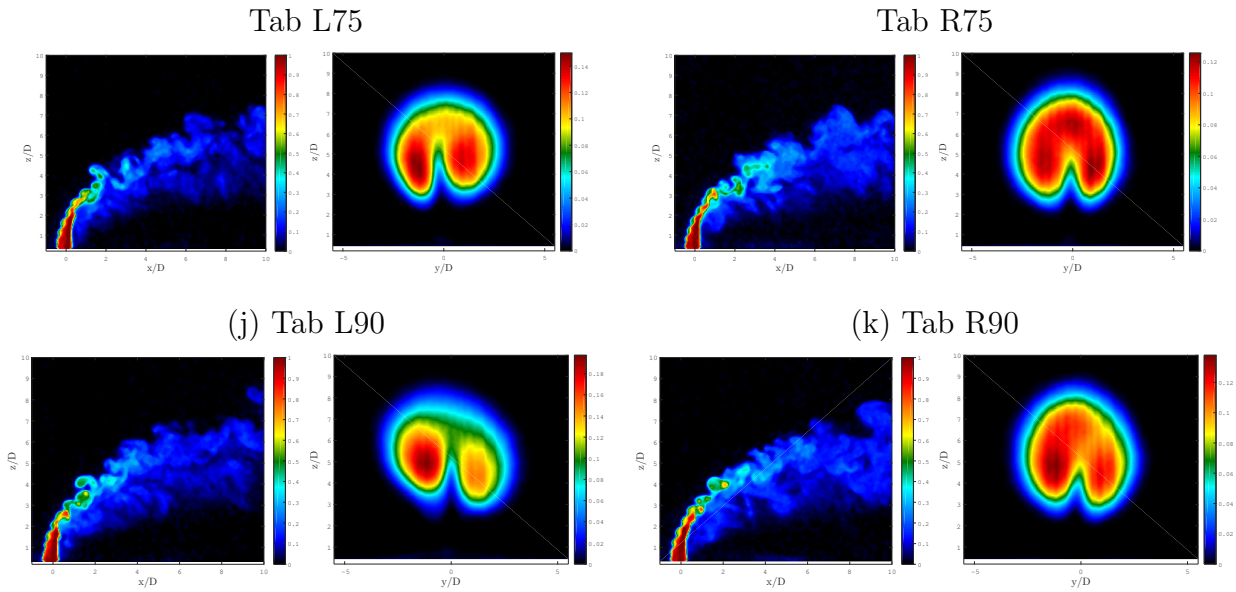

Figure 4.3: Structural Characteristics for momentum flux ratio of $J = 7$ for: (a) the non-tabbed case and (b)-(k) various tab orientations about the jet periphery. Shown for each condition is an instantaneous centerplane image and mean cross-sectional PLIF image at $x/D = 10.5$.

(fig. 4.3(b)), the weakened USL had the effect of flattening the CVP structure, though it retained the same general CVP-like shape. Other tab locations in which there was a smoothing/weakening of the USL vortices produced cross-sectional structures that were asymmetric, and in fact did not appear to create a CVP, such as the cases where tabs were placed at L30, R30, or R45. In other instances the CVP structure became tilted or asymmetric as a result of the tab. Thus USL vortex rollup and CVP symmetry appeared to be linked, consistent with the more significant effect of the tab on USL instabilities in spectral plots for $J = 7$ (figure 4.1) as well as ideas on formation of the CVP from 3D vortex simulations (Cortelezzi and Karagozian (2001)). For the asymmetric jet cross-section, the bulk of the jet fluid was aligned opposite to or deflected away from that of the tab position. The asymmetries generated agreed with the findings of Bunyajitradulya and Sathapornnanon (2005), who note asymmetric structures arising from azimuthal placement of the tab away from the upstream

of the jet. Also in agreement with their work, we observed a decrease in the severity of CVP alteration as the tab was moved further from the upstream region of the jet, where angles past L60/R60 towards the downstream region of the jet showed few perceptible differences in the cross-section and centerplane as compared with the non-tabbed case. These findings on the sensitivity of tab placement with respect to its proximity to the upstream region also were consistent with the proposed wavemaker region of an absolutely unstable JICF from adjoint sensitivity analysis of the DNS by Regan and Mahesh (2019), incorporated the same geometry as in the original nozzle in our experiments.

While the USL spectral alterations for the naturally AU $J = 7$ transverse jet were rather significant (fig. 4.1) and the centerplane-based and cross-section-based PLIF images showed corresponding alterations consistent with these spectral changes (fig. 4.3), when the momentum flux ratio was increased from $J = 7$ to $J = 61$, as shown in figure 4.4, PLIF images showed more dramatic alterations than expected from the relatively minimal spectral changes shown in figure 4.2. For the non-tabbed thin round template (fig. 4.4(a)), the mean cross-section at $x/D = 10.5$ showed a highly asymmetric structure, forming a sort of reverse question mark shape with a small tertiary vortical structure, as observed in earlier studies for the original nozzle-generated JICF at a high momentum flux ratio. Under these conditions the jet has a relatively weak CU USL, and as a result it is susceptible to perturbations or imperfections in the incoming flow (Getsinger et al. (2014)). These earlier studies explore alternative injection arrangements with the same flush nozzle as well as small alterations in the incoming crossflow to attempt to alter this asymmetry, yet the asymmetry persists and remains highly repeatable to within the present experimental capabilities. Such natural asymmetries are consistent with earlier linear stability analyses suggesting that growth rates for natural helical instability modes for the JICF at larger momentum flux ratios J have different positive and negative signs (Alves et al. (2007)), and thus could be associated with asymmetry in the flow.

With the presence of small tabs, as was seen for the jet at $J = 7$, in figure 4.4 for $J = 61$,

(a) Non-tabbed Extension

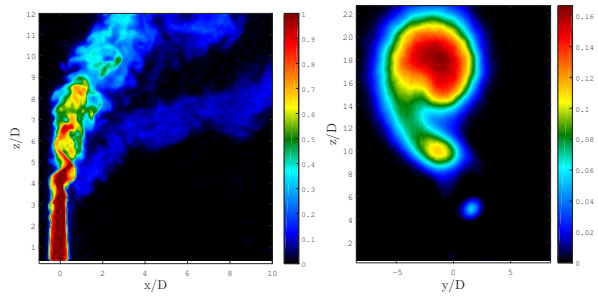

(b) Tab Upstream

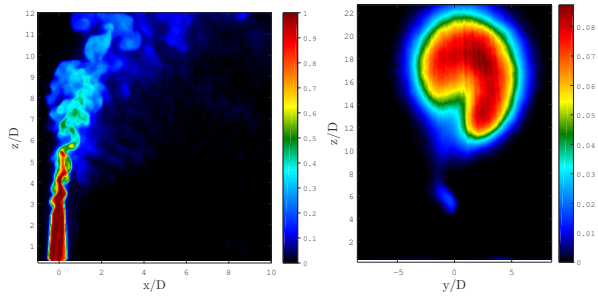

(c) Tab Downstream

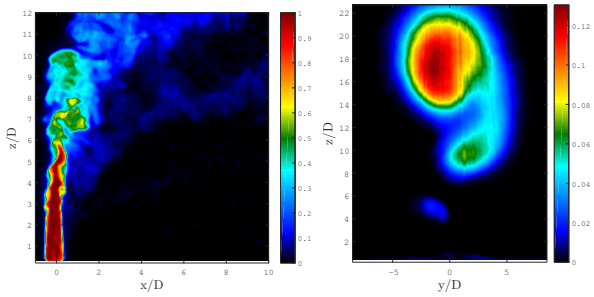

(d) Tab L15

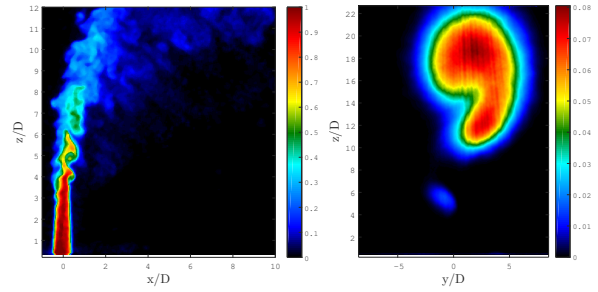

(e) Tab R15

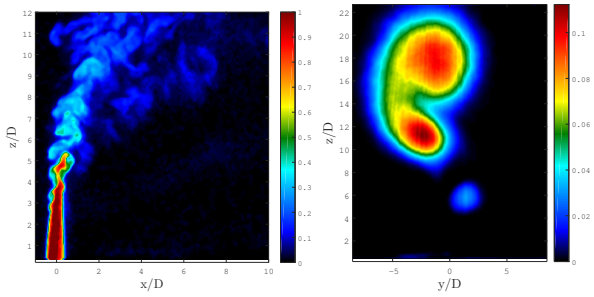

(f) Tab L30

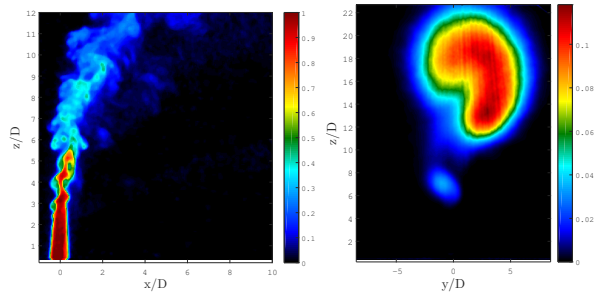

(g) Tab R30

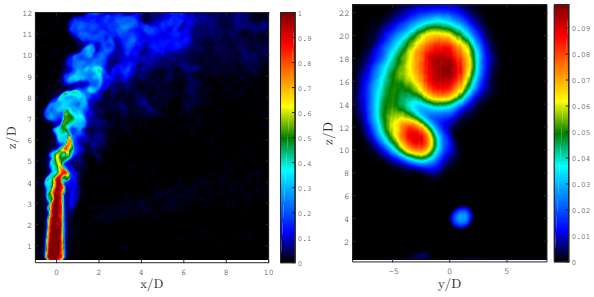

Figure 4.4: continues to following page

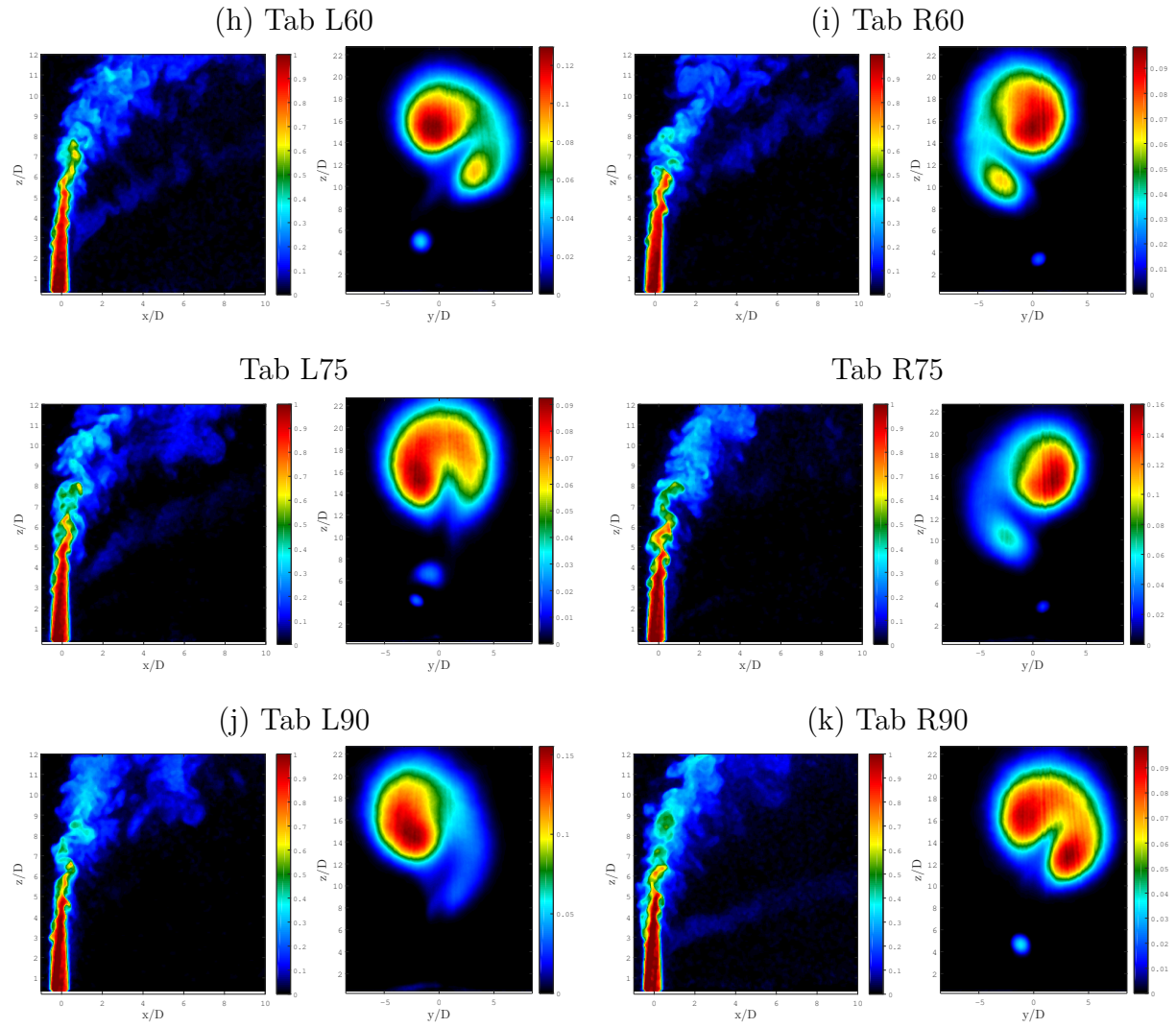

Figure 4.4: Structural Characteristics for $J = 61$ for: (a) the non-tabbed case and (b)-(k) various tab orientations about the jet periphery. Shown for each condition is an instantaneous centerplane image and mean cross-sectional PLIF image at $x/D = 10.5$.

placement of the tab upstream had the most profound impact on the issuing jet, consistent with the rather large alterations to spectral characteristics created by the upstream tab, shown in figure 4.2. In figure 4.4(b), the tertiary flow structure was generally weakened or eliminated, and the cross-section appeared to flip in its asymmetric orientation. Among all of the tab placements for $J = 61$, the upstream positioning caused the cross-section to become more symmetric, closer to the classical CVP structure and potentially affecting the jet's molecular mixing (Gevorkyan et al. (2016)), as will be discussed in the next section. As the tab orientation was rotated away from the upstream location azimuthally towards the downstream, the jet was seen to bulk deflect away from the tab. While this was noted for $J = 7$ to a limited degree, the alteration in cross-section with tabs for this higher J condition was quite dramatic, with complete flipping of the asymmetric structure from one side to the other, depending on tab placement. Tabs placed to the left or the right side of the jet orifice by the same angle appeared to create cross-sections that were reversed (though not mirrored) images of one another between 15 and 60 degrees. This was not observed as extensively for tabs at 90 degrees nor at the downstream position, however. Such observations are remarkable in that the effects of the tabs on the localized upstream shear layer instabilities, indicated in figure 4.2, were rather minimal, except for upstream placement, yet the effect of tabs on the jet cross-sectional shape was quite significant in most cases. Further, unlike the $J = 7$ cases, the influence of the tab at $J = 61$ remained quite impactful well past the R60 or L60 orientations, where the R90, L90, and tab downstream configurations all produced changes in the cross-sectional structure of the jet. While these findings cannot be explained by USL spectral changes alone, they are supported by the proposed wavemaker region of a convectively unstable JICF. Adjoint sensitivity analysis of the DNS by Regan and Mahesh (2019) for a JICF with $J = 16$ indicates that the wavemaker extends along the entire upstream shear layer of the jet, and even wraps around towards the downstream side of the jet as the flow is deflected and reoriented with the crossflow. In light of this, it may be that the wavemaker region continues to grow around the periphery

of the jet nozzle exit as the momentum flux ratio is increased until the downstream side of the jet is enveloped. Irrespective of the origins of the jet behavior at such conditions, the alterations to the structural characteristics with the tab placed beyond the upstream region were quite remarkable, as they depict the first documented alteration of the JICF under such conditions due to such a tab placement. All prior studies of the tabbed JICF theorize that the tab downstream would have the greatest impact upon the flow, but instead they find that placement to have no significant influence (Liscinsky et al. (1995); Zaman (1998); Bunyajitradulya and Sathapornnanon (2005)). Yet it should be noted that these prior studies explore the JICF at much higher jet Reynolds numbers than in the current study, with symmetric cross-sectional flow structures in the absence of the tab. Clearly, further exploration of the influence of the tab for a range of jet Reynolds numbers and potentially for different injector configurations would help to illuminate the reasons for these differences.

4.1.3 Mixing Characteristics

Quantification of the molecular mixing between the jet and crossflow was explored via the unmixedness parameter, which as noted earlier represents the second moment of the scalar concentration field, and can be derived from the PLIF images. The equation defining unmixedness in the jet cross-section is shown in equation (1.8), where the lower the local unmixedness, U, the better the molecular mixing. The unmixedness was calculated from centerplane and cross-sectional views of the jet, where the former provided a continuous downstream evolution of the jet mixing, and the latter provided a more complete picture of the local mixing for a particular downstream location. In either approach, the general mixing trends as the jet evolves are shown to be generally in agreement with one another (Gevorkyan et al. (2016)). The conditions presented in the plots which follow depict every tab orientation tested, consisting of the non-tabbed round thin extension and cases with the tab upstream, tab downstream, and with tab orientations at every 15 degrees azimuthally

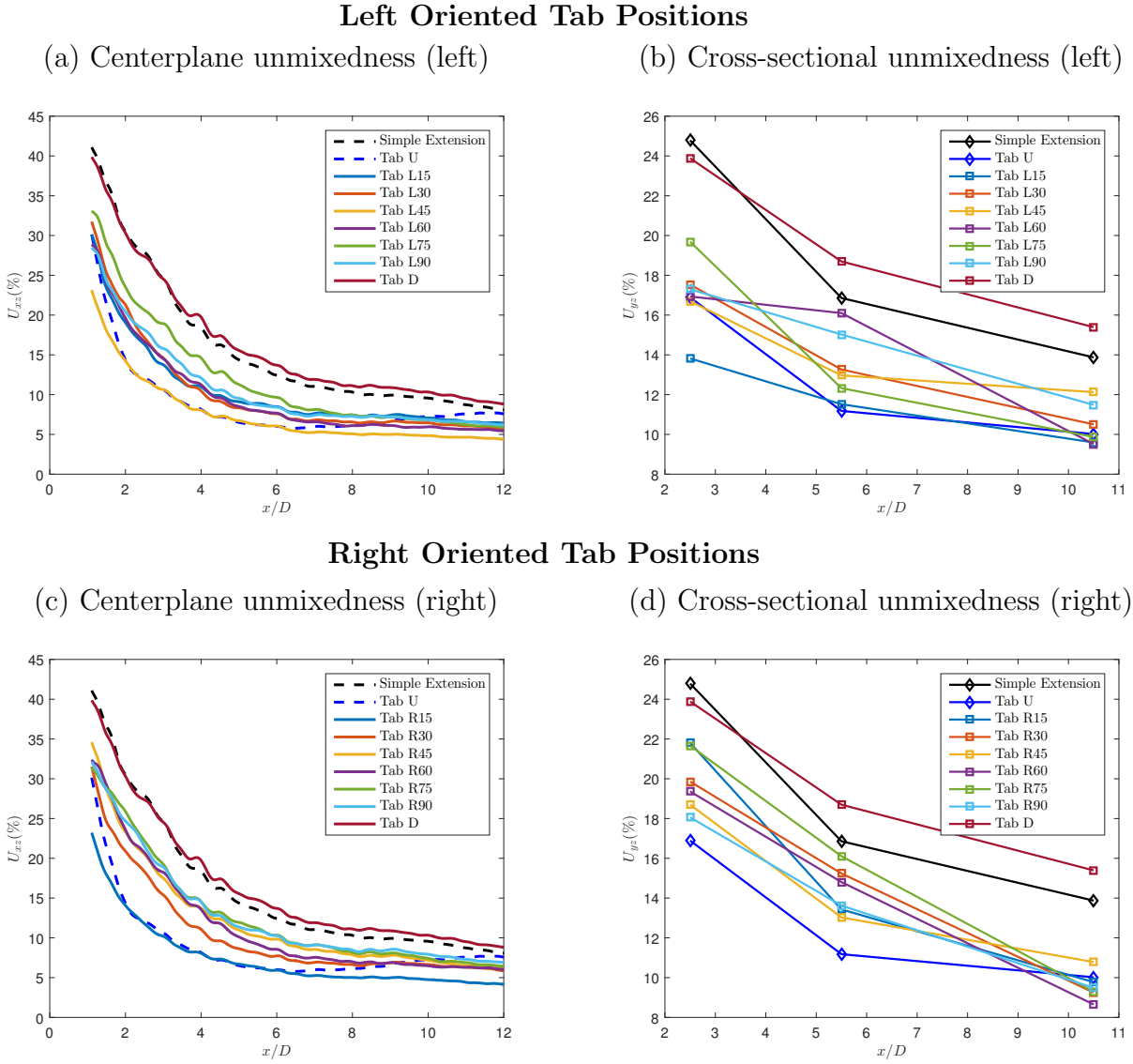

Figure 4.5: Downstream evolution of centerplane unmixedness U_{xz} and cross-section-based unmixedness U_{yz} for $J = 7$, for the non-tabbed case and various tab orientations about the jet periphery.

from the upstream to the L90 and R90 locations.

Figure 4.5 shows plots representing the centerplane and cross-sectional mixing of the $J = 7$ jet, where the results are separated such that all of the left oriented tab locations

appear in one plot, and all of the right oriented locations appear in another, with the non-tabbed, tab upstream, and tab downstream appearing in both for comparative purposes. Unmixedness determined from the cross-sectional imaging is shown at the three locations explored, $x/D = 2.5$, 5.5, and 10.5. Among the least effective mixing configurations (highest U) were the cases with the non-tabbed simple extension and the downstream tab, and these were consistent for both centerline-based and cross-section-based unmixedness. This finding was consistent with the ineffectiveness of the downstream tab in improving JICF mixing documented in experimental studies by Liscinsky et al. (1995). The apparent worsening of the downstream tab's mixing as compared with the non-tabbed case in figure 4.5 may be linked to the transition of the USL instabilities from AU to CU, seen in fig. 4.1(d), with an associated asymmetry in the jet cross-section (fig. 4.3(c)). This correlation among the state of the USL instability, cross-sectional structure, and molecular mixing are known to exist for the unforced, original nozzle-based JICF studied in Gevorkyan et al. (2016).

Yet interestingly, the mixing results in figure 4.5 also suggested that the tab upstream orientation, which introduced an even more significant weakening of the USL from AU to CU, and a flattened (yet still symmetric) cross-sectional CVP structure, appeared to be the best mixer, with a remarkable improvement in molecular mixedness over that of the non-tabbed jet. This behavior was documented in both the centerplane and cross-sectional views. Hence the weakened USL instability here was not as significant to the mixing alteration, likely because the cross-section remained mostly CVP-like, potentially with improved local entrainment of crossflow. It is also noted that the thicker USL at injection created by the upstream tab was reminiscent of a thicker upstream shear layer created by a pipe rather than a nozzle, as explored in prior studies. Getsinger et al. (2014) noted that for the same flow conditions as explored in this study, for $J = 7$, an absolutely unstable jet producing a fully developed pipe flow has a more diffuse, flattened CVP structure and, per the quantification in Gevorkyan et al. (2016), it tends to be a better mixer than the absolutely unstable jet issuing with a top hat velocity profile from a nozzle, especially further downstream. The initial USL

differences here could be the relevant factor in structural and mixing enhancement.

In examining other tab orientations, the L45 and R15 cases also appeared to be excellent mixers per the centerplane mixing quantifications, matching the unmixedness values of the tab upstream case. The fact that different tab angles between the left and right orientations produced more optimal mixing was likely attributable to the centerplane's representing a very thin slice of the jet, and indeed, when looking in the cross-section, the trends were slightly different. For cross-sectional mixing quantification, the L15 and R90 appeared to be the next best mixers following the upstream tab configuration. These findings for $J = 7$ jets with a tab suggested that while there can be improvements to the mixing of the jet due to the presence of a tab, optimal tab orientation may be more difficult to establish, due in part to the asymmetric jet structure for which there can be relatively small differences in mixing statistics. Regardless, it is clear that qualitative trends showed as the tab orientation was shifted from the upstream towards the downstream, the improvement in mixing was systematically reduced.

A similar presentation of mixing characteristics for the naturally convectively unstable $J = 61$ JICF is shown in figure 4.6. Notably, and in contrast to the $J = 7$ results, positioning of the tab downstream actually improved the molecular mixing compared with the non-tabbed jet. Despite its not altering the jet shear layer instabilities (fig. 4.2(d)), the tab downstream was able to impact the structural characteristics (fig. 4.4(c)), and in fact caused the asymmetry in the jet cross-section to completely reverse, though the tertiary vortex structure for the downstream case was weaker than for the original (non-tabbed) jet. For the configuration with the tab upstream, while the USL instability was weakened and delayed compared with the non-tabbed jet (fig. 4.2(c)), structurally a somewhat more symmetric jet was produced, per fig. 4.4(c), and correspondingly figure 4.6 showed the configuration improved mixing to a significant degree. Even other tab orientations for which cross-sectional flow structures remained quite asymmetric still improved the molecular mixing of the jet over that of the tabless jet, e.g., for L90 or R45. The marked improvement in mixing regardless

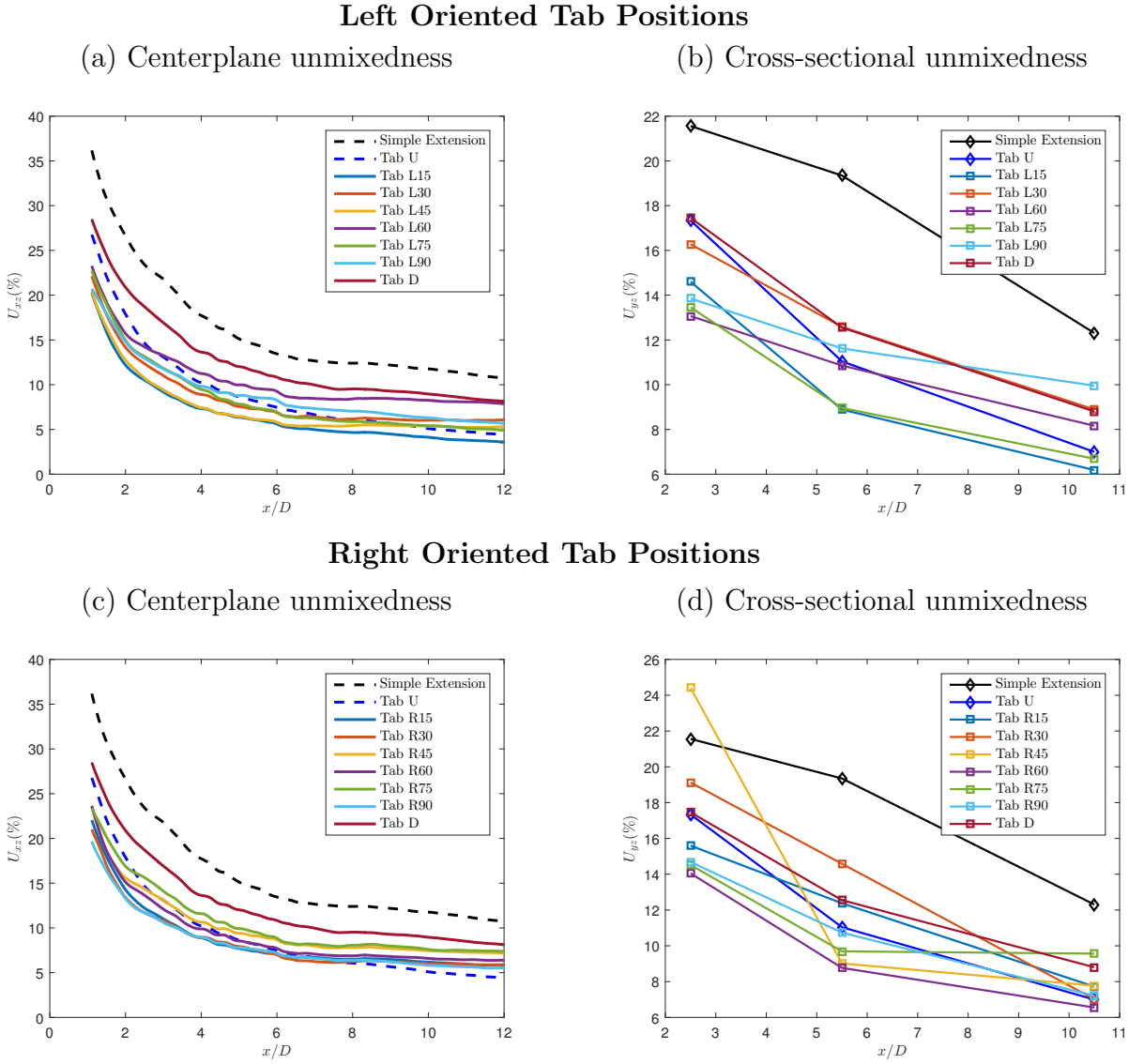

Figure 4.6: Downstream evolution of centerplane unmixedness U_{xz} and cross-section-based unmixedness U_{yz} for $J = 61$, for the non-tabbed case and various tab orientations about the jet periphery.

of tab orientation in figure 4.6 may speak to the relative weakness of the crossflow and the shear layer instabilities surrounding the jet, and hence the susceptibility to disturbances introduced through the tabs. If applied appropriately, such passive disturbances as tabs can

produce improvements in mixing, as observed in figures 4.5 and 4.6.

4.2 Discussion

The present experimental study documents the effects of simple passive control of a jet in crossflow via a small triangular tab placed about the periphery of the jet exit. Effects on jet shear layer instabilities, structure and mixing are quantified. The study extends the flow regimes and geometrical parameter space examined in previous works on tabbed jets in crossflow, taking advantage of more recent observations of a transition in the upstream shear layer in the absence of tabs (Megerian et al. (2007)), and then exploring tabs at conditions for which the USL in the absence of the tab was convectively unstable ($J = 61$) and absolutely unstable ($J = 7$). The presence of a tab was seen to weaken and delay the initiation of the USL instability in both flow regimes, in some cases rather extensively, where the significance of such alterations were generally dependent upon the original strength of the instability in the absence of a tab, and the relative location of the tab with respect to the upstream edge of the jet exit.

In many ways the effect of the single tab on the naturally absolutely unstable JICF with $J = 7$ was different, from a stability and structural perspective, from the tab's effect on the naturally convectively unstable jet with $J = 61$. The tab caused the $J = 7$ AU USL to become effectively CU for most orientations, especially closer to the upstream region (fig. 4.1), and yet the effect on the jet cross-sectional structure was relatively small, with a flattening or introduction of slight asymmetries in the CVP (fig. 4.3). The slight asymmetries were consistent with such weakening in the USL instabilities, though the dramatic changes in spectral characteristics might imply greater changes than those actually observed in the jet structure. In contrast, the tab caused the USL for the $J = 61$ JICF to weaken when placed at the upstream location, but beyond that point there was little discernible change to the spectral characteristics (fig. 4.2). Yet the effects of the tab position on the jet's

cross-sectional structure, even when there was little obvious change in the USL, were quite significant (fig. 4.4), leading to apparent flipping of the asymmetric CVP-like structure, though the specific downstream location at which the image slice was taken could influence this orientation. While there was at least at some level a logical connection between tab-generated shear layer characteristics and jet structural characteristics alteration, a more consistent connection was observed between the predicted wavemaker regions for AU and CU jets from the work of Regan and Mahesh (2019) and the tab orientations having the greatest effects. For naturally AU shear layers such as with $J = 7$, the wavemaker region in the upstream region was consistent with the effectiveness of tab placement in that region (e.g., fig. 4.3(b)), while for $J = 61$, the wavemaker's extending along the entire upstream shear layer of the jet and wrapping around the jet suggested the effectiveness of perturbation or jet placement at multiple locations around the jet periphery. While there are limited computational conditions for such comparisons, the correspondence here is intriguing, and bears more extensive exploration.

Despite these differences in specific tab influence on the JICF in these two different regimes, the overall effects of the tab on jet molecular mixing were similar in terms of the degree of reduction in unmixedness (figs. 4.5 and 4.6)), though there were some specific differences, even between left and right orientations of the tab, clearly relating to the asymmetries in jet cross-sectional structure. Hence further exploration of the influence of such tabs, not just for a wider range of flow conditions, but also for the effects on details of the alterations in the dynamical characteristics, are of great value. The latter is the subject of a separate research study from which additional insights on the flow alterations may be obtained (Harris et al. (2020a)), and is presented in a slightly modified format in the following chapter.

CHAPTER 5

Simultaneous PLIF/PIV

The results presented in this chapter are taken with slight modification from the article "Effect of tabs on transverse jet nearfield vorticity dynamics", currently submitted for publication.

5.1 Results

5.1.1 Jet Structure and Mixing: Comparisons with High Resolution PLIF

As previously noted, high-resolution PLIF-only imaging of an equidensity JICF with tabs was performed in Harris et al. (2020b), with a jet Reynolds number of $Re_j = 2300$, and an acetone mole fraction of $\psi = 0.218$. For transverse jets with a naturally absolutely unstable upstream shear layer (for $J = 6$) and a convectively unstable USL (for $J = 61$), the high-resolution PLIF imaging demonstrates that placement of a tab directly in the upstream/windward side of the jet periphery has the greatest influence in weakening the shear layer instabilities, especially for the $J = 6$ case, and acts as well to alter the jet cross-sectional shape, especially in the case for $J = 61$. Remarkably, despite weakening and even altering the symmetric CVP structure for $J = 6$, the upstream tab actually causes an improvement in molecular mixing, i.e., a reduction in the spatially evolving Unmixedness parameter U. As the tab orientation is rotated azimuthally away from the upstream toward the downstream of the jet, the resulting influence of the tab is diminished and the mixing enhancement generally lessened, but with a few exceptions. Given that the present experiments explored the influence of tabs on nearfield vorticity and shear layer dynamics via simultaneous PLIF and PIV imaging, but

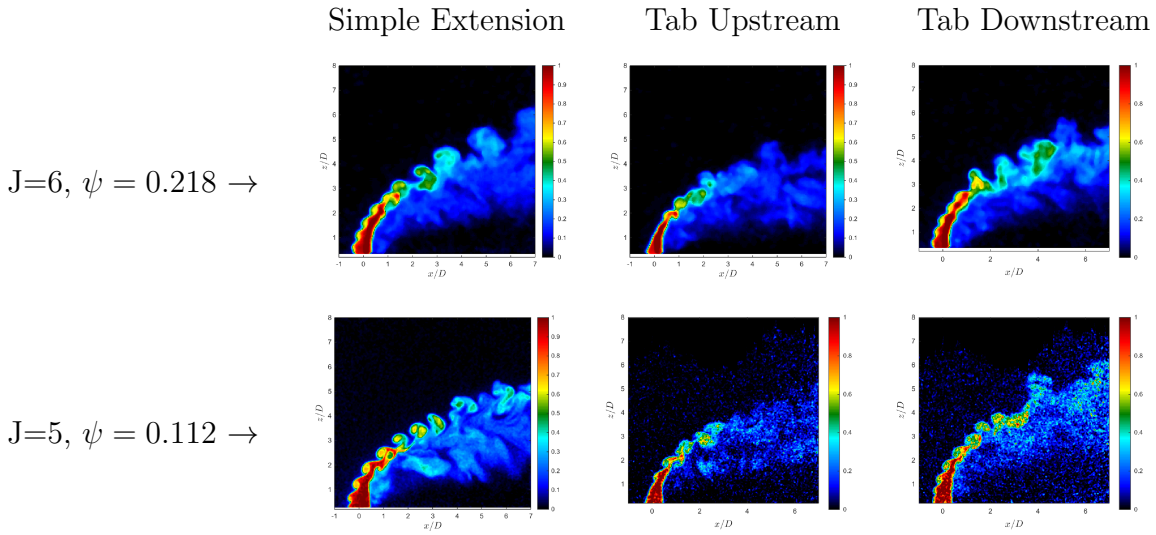

Figure 5.1: Structural Characteristics of instantaneous centerplane high-resolution PLIF imaging at a momentum flux ratio of $J = 6$ **(TOP)** and lower-resolution PLIF portion of simultaneous PLIF and PIV imaging at a momentum flux ratio of $J = 5$ **(BOTTOM)**. Represented are the jet with a simple non-tabbed nozzle extension, the tab upstream, and the tab downstream. High resolution PLIF images are from Harris (2020).

for values of $\psi = 0.112$ and $Re_j = 1900$, it was of interest to compare jet structural and mixing characteristics between the studies. This was done not only to demonstrate the similarity in tab effects for a given state of the USL, but also to verify the usefulness of even a lesser degree of PLIF resolution in extracting overall trends in mixing metrics.

Sample comparisons between the high-resolution PLIF and PLIF images extracted from the simultaneous PLIF and PIV data are shown in figure 5.1. These instantaneous centerplane images correspond to high resolution imaging at $J = 6$ (Harris (2020)) and $Re = 2300$, and the lower resolution images from the present PLIF/PIV study at $J = 5$ and $Re = 1900$, both of which in the absence of tabs produced strongly absolutely unstable upstream shear layers (Shoji et al. (2020b)). Images in figure 5.1 corresponded to the transverse jet with the tabless insert and for tabs placed in upstream and downstream locations. These conditions

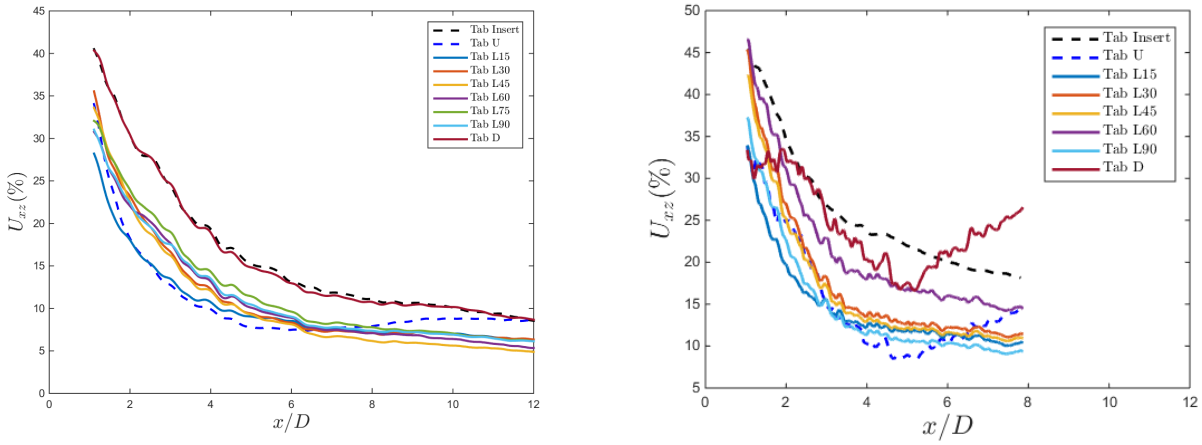

Figure 5.2: Unmixedness as a function of scaled downstream distance x/D for the simple non-tabbed nozzle insert case and various tab orientations about the jet periphery with (a) high resolution PLIF flow conditions at $J = 6$ (fome Harris et al. (2020b)), and (b) simultaneous PLIF and PIV flow conditions at $J = 5$.

represent extremes in the observed influence of the tabs. For the jets without the tab, the overall features of the jet looked quite similar to one another, with strong upstream shear layer rollup; in fact, applying a power-law fit to the maximum concentration locii from the jet mean produced similar jet trajectories between the $J = 5$ and $J = 6$ cases here (Harris (2020)). For cases with the tab positioned upstream, there was a clear smearing or delay in the upstream shear layer vorticity rollup dynamics for both cases. These observations were consistent with results in Harris et al. (2020b) for $J = 7$. Positioning the tab downstream did not appear to alter the shear layer structures at all, again consistent with $J = 7$ results. Other USL structural changes with tabs at other positions were similar between the $J = 5$ and $J = 6$ cases; these are documented in Harris (2020).

These and other PLIF images can be analyzed as described above to yield the local centerplane-based Unmixedness, per equation (1.8), applied for each local centerplane slice

and averaged over 500 realizations, and are shown in figure 5.2, for the tabless insert as well as upstream, downstream, and various locations of the tab in the "left" orientation; similar trends were observed for tab placement in the "right" side, per Harris et al. (2020b). For the unmixedness values produced from the simultaneous PLIF/PIV data, it should be noted that in some cases due to the lower acetone mole fraction (and thus the lower fraction of PLIF tracer), the light contamination from the green laser, and the additional oil/smoke particles within the flowfield, caused the PLIF imaging to have poorer signal-to-noise ratios and thus yielded noisier calculations of the molecular mixing. While the noiser images appeared for the cases with tabs upstream and downstream (figure 5.2(b)), there was nevertheless good correspondence in terms of trends, for these and other tab positions, to the high resolution trends shown in figure 5.2(a). As noted earlier, the significant weakening of the USL by the upstream tab, which had a small influence on the CVP for these cases, appeared to improve mixing, i.e., to reduce local Unmixedness, while the downstream tab appeared to have little influence on USL dynamics and, correspondingly, on Unmixedness as compared with the tabless jet condition. And as the positioning of the tab was azimuthally rotated about the jet periphery, it was seen in general to reduce the improvement in mixing. Such trends in mixing and structural characteristics were also seen for a transitional jet and convectively unstable jet at higher J values (Harris (2020)). Thus, we ascertain that the present explorations of vortical structures and dynamics extracted from PIV data may be utilized to interpret the mixing results from Harris et al. (2020b), as well as to understand the role of tabs in transverse jet behavior and optimization more completely.

5.1.2 Centerplane and Cross-sectional Vorticity

One area of great interest in the present PIV-based experiments involves quantification of the vorticity field in both the centerplane ($x-z$) and cross-sectional plane ($y-z$). The early work of Zaman and Foss (1997) and Zaman (1998) suggests that upstream and downstream tab placements are ineffective due to the generation of vorticity opposite to the CVP in the

case of the former, and the pressure gradient in the wake of the jet in the case of the latter. It is noted that these experiments are performed at fairly large momentum flux ratios, however, exceeding $J = 21$. Our recent high resolution PLIF imaging of the tabbed JICF (Harris et al. (2020b)) demonstrates that both upstream- and downstream- positioned tabs can influence jet cross-sectional structure and mixing, depending on the flow regime and the nature of the USL in the absence of tabs. Understanding the vorticity evolution in this flowfield can thus assist in interpreting other flow features, especially those related to the dynamics of the USL and its roll in CVP structure.

Figure 5.3 shows instantaneous snapshots of vorticity along the centerplane of the JICF at a momentum flux ratio of $J = 5$, for the non-tabbed jet (with the thin round template extension), the tab upstream, and the tab downstream. Corresponding mean cross-sectional vorticity images for the same flow and jet geometrical configurations as in figure 5.3 are shown in figure 5.4, with images provided at three different downstream locations (x/D = -0.5, 0.0, and 0.5). For the instantaneous centerplane vorticity without a tab (figure 5.3(a)), the vortex rollup initiated very close to the jet exit along the upstream shear layer, at about 0.5 diameters, while the downstream vorticity did not begin to pinch off until almost 1 diameter after that in the USL. This vorticity evolution was consistent with that for an AU/GU USL for the nozzle-generated jet in the absence of the thin extension indicated in earlier studies by Gevorkyan et al. (2018), including vorticity magnitude and shear layer instability differences between the windward and leeside of the jet (Davitian et al. (2010a); Regan and Mahesh (2017); Gevorkyan et al. (2018)). To further examine the vorticity generation at the jet exit, the mean cross-sectional vorticity evolution of the jet at the three different locations at or near the jet exit in figure 5.4(a) showed that in general the vorticity initiation was relatively symmetric at the upstream edge (x/D = -0.5) and at the center of the jet ($x/D = 0.0$) for the jet without a physical tab. The vorticity at the downstream edge of the jet exit, at x/D = +0.5, was slightly asymmetric for the tabless jet, interestingly. This overall behavior in fig. 5.4(a) was not unexpected given that the upstream shear layer is naturally absolutely

(a) Simple Non-tabbed Extension

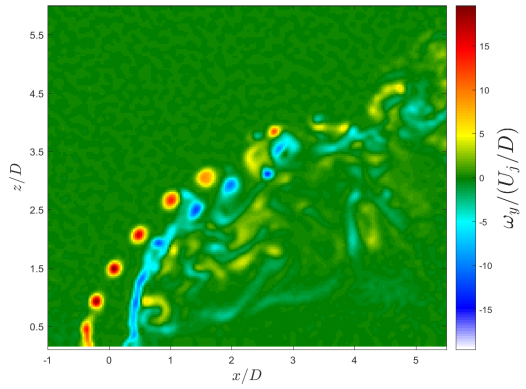

(b) Tab Upstream

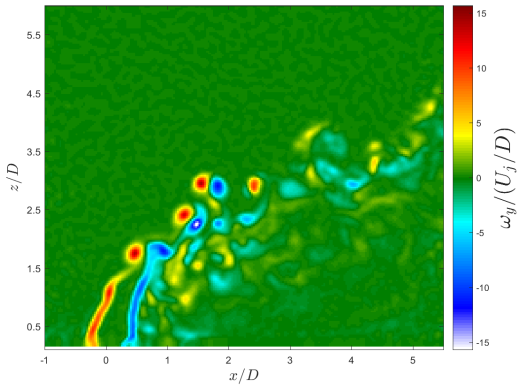

(c) Tab Downstream

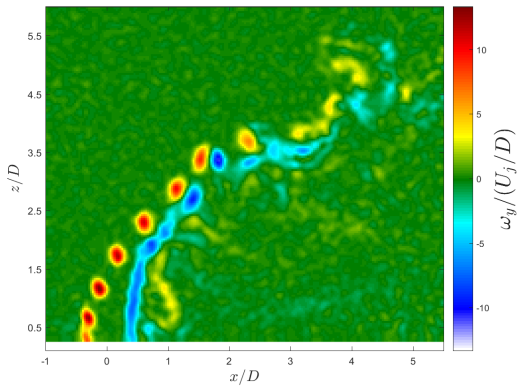

Figure 5.3: Centerplane images of the instantaneous vorticty field extracted from stereo-PIV for the absolutely unstable jet at $J = 5$ and $Re_j = 1900$, and with (a) the non-tabbed jet, (b) the tab upstream, and (c) the tab downstream. The colorbars are scaled to the maximum and minimum vorticity values contained within all images shown.

unstable for $J = 5$ for this jet mixture (Shoji et al. (2020b)),and growth of asymmetries are proven to be suppressed by the larger dominant axisymmetric USL instability mode (Alves et al. (2007); Regan and Mahesh (2017)), resulting in symmetric CVP structures (Getsinger et al. (2014); Harris et al. (2020b)).

When a tab was placed in the upstream edge of the jet at $J = 5$, the centerplane

instantaneous vorticity image (figure 5.3(b)) showed the upstream vorticity initiation to be delayed by $0.50 - 0.75$ diameters, and the overall magnitude of the vorticity in this plane to be significantly weakened as compared with the characteristics shown for the non-tabbed jet (fig. 5.3(a)). These observations were consistent with the observed delay and significant weakening of upstream shear layer instabilities for the naturally absolutely unstable jet at $J = 7$ in our separate JICF results with an upstream tab (Harris et al. (2020b)). Interestingly, in figure 5.4(b) the upstream tab caused the downstream vorticity dynamics to have nearly the same vortex pinch off location as for the non-tabbed jet, as well as a slight increase in the maximum downstream vorticity. This may be interpreted by examining the cross-sectional vorticity evolution (figure 5.4(b)), where the tab upstream significantly weakened the vorticity generation along the windward side of the jet, shown (as expected) by the vorticity magnitudes at $x/D = -0.5$. But as the jet evolved to the two later cross-sectional locations, $x/D = 0.0$ and $+0.5$, the vorticity actually became slightly stronger than for the non-tabbed jet. The apparent net result of the tab upstream was a dampening of the vorticity generation directly in the upstream region, yet a small but notable increase in vorticity production along the sides and downstream edge of the jet. Though in principle the net vorticity generation from a tab upstream should reorient and act to cancel or at least weaken the CVP, the strengthening of vorticity generation in the downstream region actually created a greater symmetry in the downstream vorticity field and hence produced contributions to a symmetric CVP. These observations on the upstream tab were consistent with earlier findings by Zaman (1998), who found that while the overall circulation from the vorticity isocontours may be lower with the tab upstream, the counter-rotating vortex pair still produces almost identical magnitudes of vorticity at the vortex cores to those for non-tabbed jets. These observations in figure 5.4(b) were also consistent with and help to explain PLIF-based cross-sectional jet structures in Harris et al. (2020b) for the case with an upstream tab at $J = 7$. In this case the CVP becomes only slightly flattened in comparison to the usual CVP for the non-tabbed transverse jet.

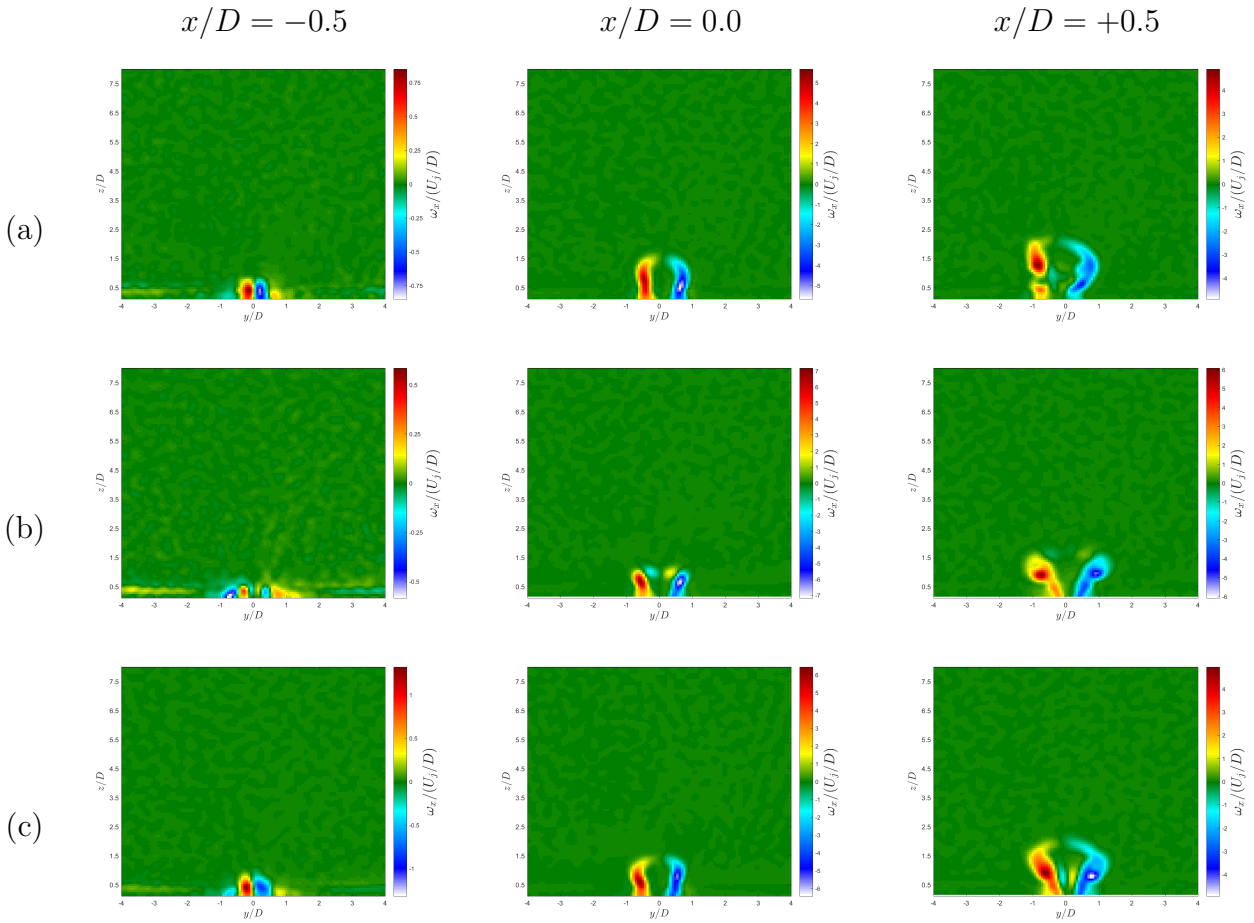

Figure 5.4: Mean cross-sectional vorticity images averaged over 500 instantaneous realizations, at cross-sectional locations of the upstream leading edge of the jet exit ($x/D = -0.5$), center of the jet exit ($x/D = 0.0$), and the downstream trailing edge of the jet exit ($x/D = +0.5$). Images correspond to the (a) non-tabbed jet, (b) tab upstream jet, and (c) tab downstream jet, with $J = 5$ and $Re_j = 1900$. The colorbars are scaled to the maximum and minimum vorticity values contained within all images shown.

For a transverse jet with a tab placed at the downstream edge of the orifice, both Liscinsky et al. (1995) and Zaman and Foss (1997) find no difference in the overall vorticity and mixing dynamics compared with the non-tabbed jet, although as noted earlier, their experiments are performed at fairly large momentum flux ratios, exceeding $J = 21$. For a lower momentum

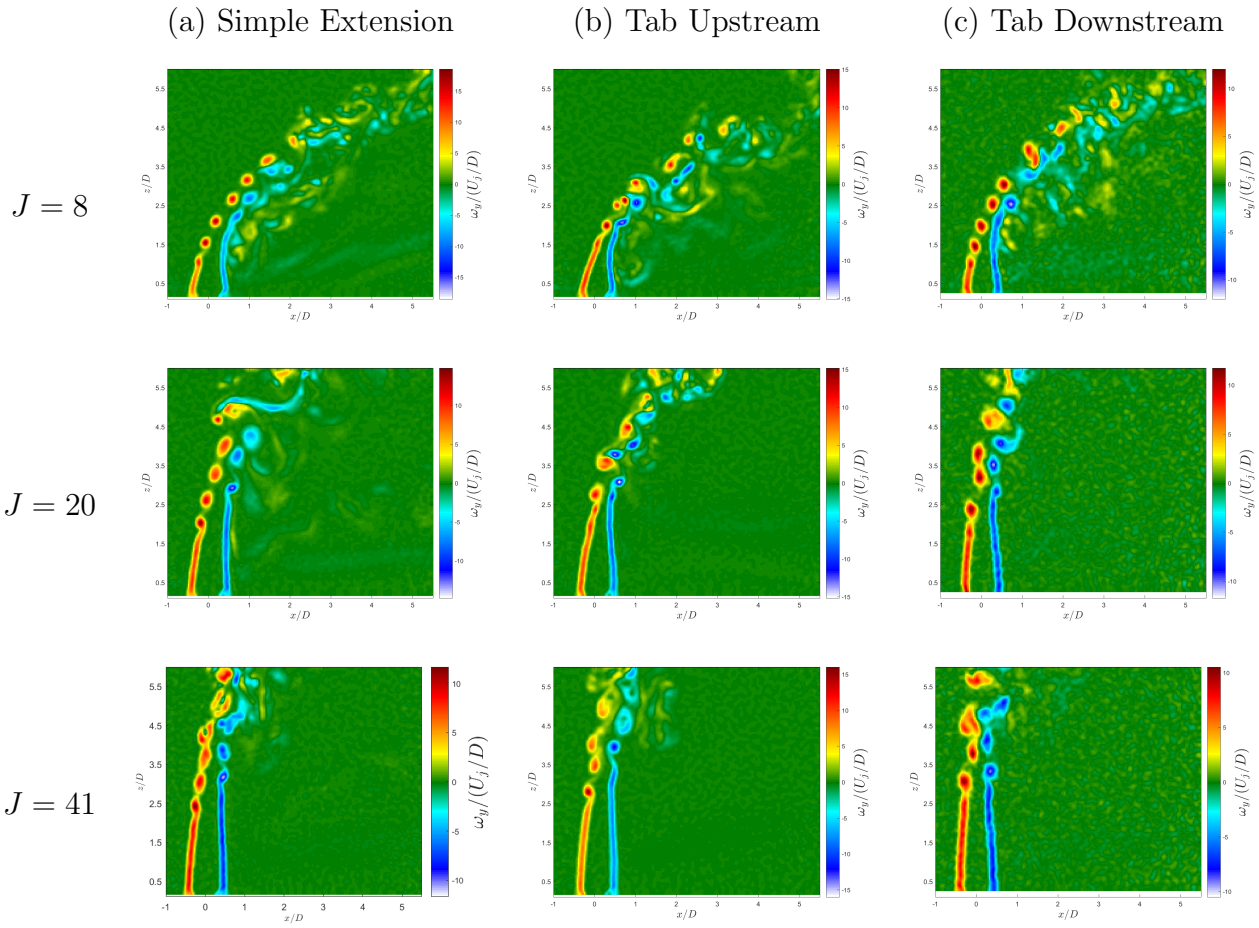

Figure 5.5: Centerplane images of the instantaneous vorticty field extracted from stereo-PIV for the absolutely unstable jet at $J = 5$, absolutely unstable jet near the critical transition at $J = 8$, and convectively unstable jets at $J = 20$ and $J = 41$, all with a jet Reynolds number of $Re_j = 1900$ for (a) the non-tabbed jet, (b) the tab upstream, and (c) the tab downstream. The colorbars are scaled to the maximum and minimum vorticity values contained within all images shown.

flux ratio, $J = 7$, studied in Harris et al. (2020b), the downstream tab causes the USL to become significantly weaker, transitioning from an absolute instability to a convective instability, although the degree of weakening in the USL is not as significant as that produced by an upstream tab. In the present study, figure 5.3(c) indicates that, while the vortex rollup along both the upstream and downstream sides of the jet initiated at nearly the same

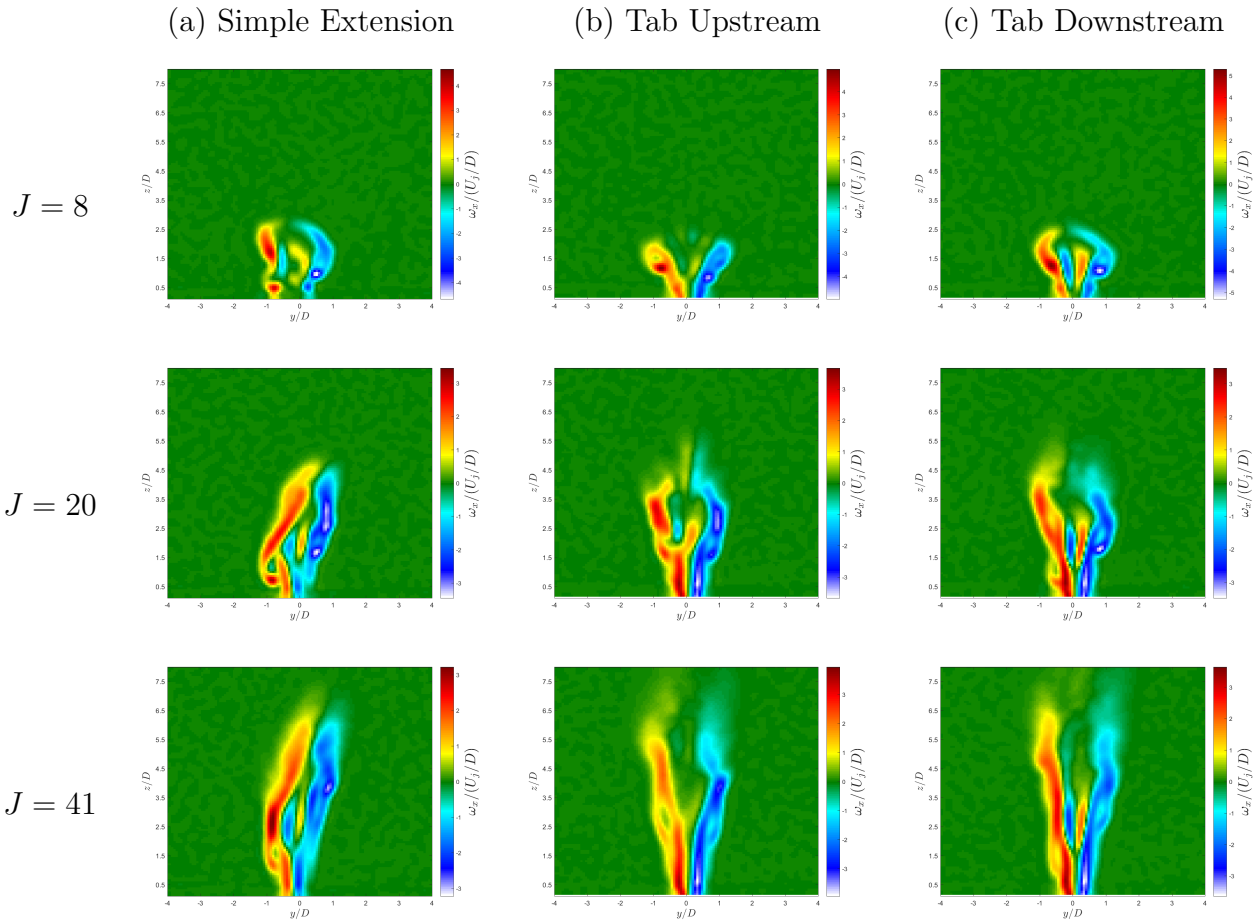

Figure 5.6: Mean cross-sectional vorticity images averaged over 500 instantaneous realizations, at the cross-sectional location of the downstream trailing edge of the jet exit ($x/D = +0.5$). Images correspond to the (a) non-tabbed jet, (b) tab upstream jet, and (c) tab downstream jet, for the absolutely unstable jet at $J = 5$, absolutely unstable jet near the critical transition at $J = 8$, and convectively unstable jets at $J = 20$ and $J = 41$, all with a jet Reynolds number of $Re_j = 1900$. The colorbars are scaled to the maximum and minimum vorticity values contained within all images shown.

locations as the non-tabbed jet, the magnitudes of vorticity from both sides of the jet were significantly weakened, consistent with the weakening of the instability characteristics for the jet at $J = 7$ in Harris et al. (2020b). The cross-sectional vorticity magnitudes at various

downstream locations in figure 5.4(c) show that a downstream tab produced nearly the same overall magnitude of vorticity as that is generated for the non-tabbed jet, and in fact for the most evolved view of the jet at $x/D = +0.5$, the vorticity production was more symmetric than for the non-tabbed jet, though not quite as symmetric as for the upstream tab (fig. 5.4(b) at $x/D = +0.5$). Thus, while vorticity directly in the upstream and downstream shear layers was weakened by the presence of the tab downstream, the overall vorticity produced in the sides of the jet remained relatively unchanged, leading to the relatively symmetric CVP structure observed far downstream for the case of $J = 7$ in Harris et al. (2020b). Hence there was consistency in the nearfield vorticity generation (for both centerplane and cross-sectional planes) with jet cross-sectional shape in the low J regime.

At larger values of J, as noted previously, the non-tabbed flush nozzle-injected JICF has an increasingly asymmetric jet cross-sectional shape as J increases (Getsinger et al. (2014)). Harris et al. (2020b) observe that at a large momentum flux ratio ($J = 61$), while upstream or downstream tabs have a relatively minor influence on hotwire-based USL instabilities, the tabs can have a significant impact on cross-sectional shape, even acting to flip the asymmetric cross-section's orientation. While this influence is consistent with the identification of wavemaker regions for the convectively unstable JICF in the simulations of Regan and Mahesh (2019), it is of interest to explore here the differences in vorticity evolution at higher J values. Figure 5.5 shows representative instantaneous vorticity fields in the centerplane, for larger values of J (8, 20, and 41) for the non-tabbed JICF with a thin extension, as well as cases with the tab placed upstream and downstream. Figure 5.6 contains corresponding cross-sectional mean vorticity images at a downstream location $x/D = +0.5$, for these same flow and jet geometrical conditions. This location for the downstream cross-sectional vorticity field tended to produce the greatest differences among the different jet configurations. Instantaneous centerplane vorticity images in figure 5.5 suggested that for each jet configuration, as the crossflow velocity was reduced (in order to increase J), upstream and downstream shear layer rollup was delayed further along the

layer. For the non-tabbed jet, this trend was consistent with earlier findings in Getsinger et al. (2014) and Gevorkyan et al. (2018). In comparing the different jet configurations, the upstream tab caused a further delay in the USL vorticity rollup as compared with the non-tabbed case, but for the tab placed downstream at higher J values there was relatively little change, similar to the case where $J = 5$ in figure 5.3. The magnitudes in figure 5.5 showed that both upstream and downstream shear layers had a stronger degree of vorticity generation for the non-tabbed case than for either case with tabs in figure 5.5.

Cross-sectional mean vorticity fields for the three different configurations, shown for $J = 8$, 20, and 41 in Figure 5.6, indicate that the degree of asymmetry for the non-tabbed jet increased for larger J values, as seen further downstream in cross-sectional PLIF imaging (Getsinger et al. (2014)). The presence of a tab, either at the upstream or the downstream location, tended to make the vorticity field more symmetric, though the results were not exactly the same for these two different tabbed configurations. This somewhat improved cross-sectional symmetry was also seen for the upstream tab and, to a lesser degree, for the downstream tab in acetone PLIF imaging experiments in Harris et al. (2020b).

Lastly, symmetry breaking tab orientations were explored to determine the implications of positioning an asymmetrically oriented tab at the exit plane and thus creating an azimuthal vorticity distribution for the development of the CVP, recalling that Peterson and Plesniak (2004) suggest such an asymmetric distribution could give rise to asymmetries in the jet further downstream. The high resolution PLIF imaging of a tabbed jet in Harris et al. (2020b) show that as the tab orientation is azimuthally rotated away from the upstream edge of the jet, the cross-sectional structure shows a bulk deflection of the jet away from the location (right vs. left) of the tab, and as the momentum flux ratio increases, the tab is able to produce more pronounced alterations to the naturally asymmetric jet cross-sectional structure. In the present experiments, figure 5.7 shows instantaneous centerplane vorticity images and mean cross-sectional vorticity images at $x/D = +0.5$ for symmetry breaking tab orientations at $J = 5$, the flow condition for which tabs had a more dramatic effect on

Simple Extension

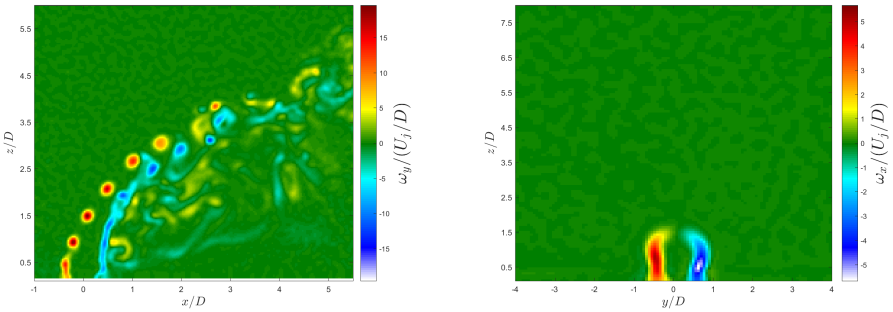

Tab L15

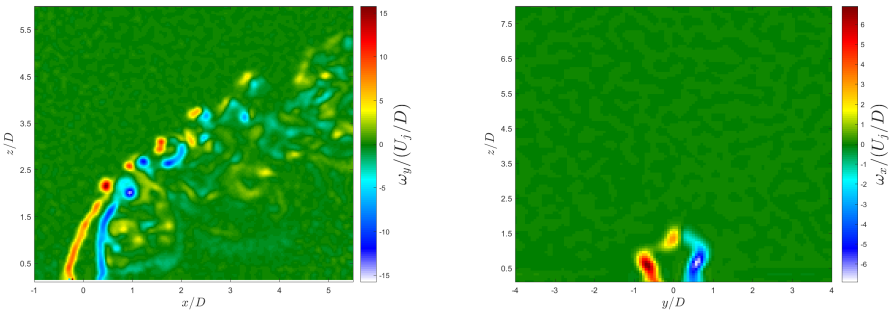

Tab L30

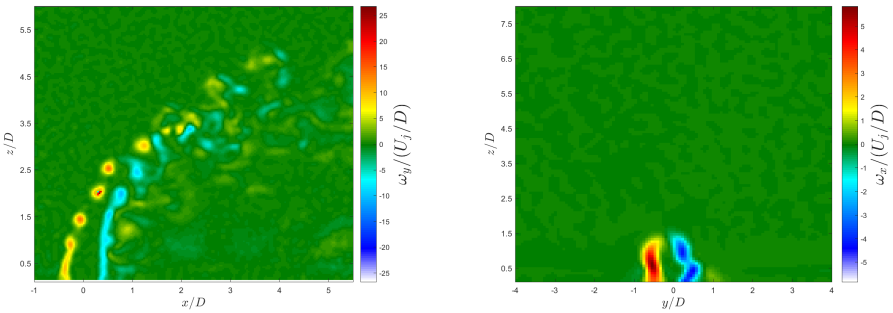

Tab L45

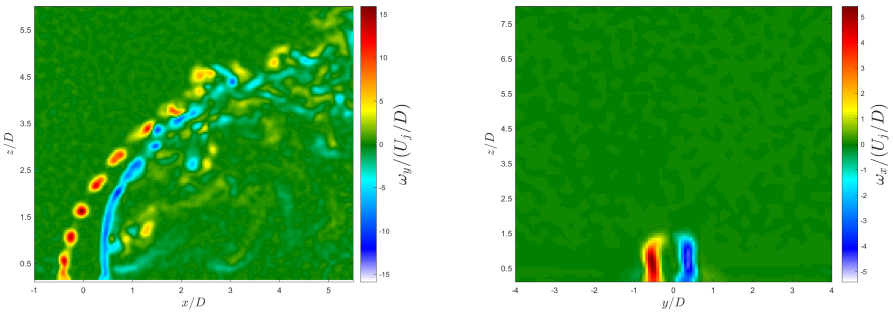

Figure 5.7: continues to following page

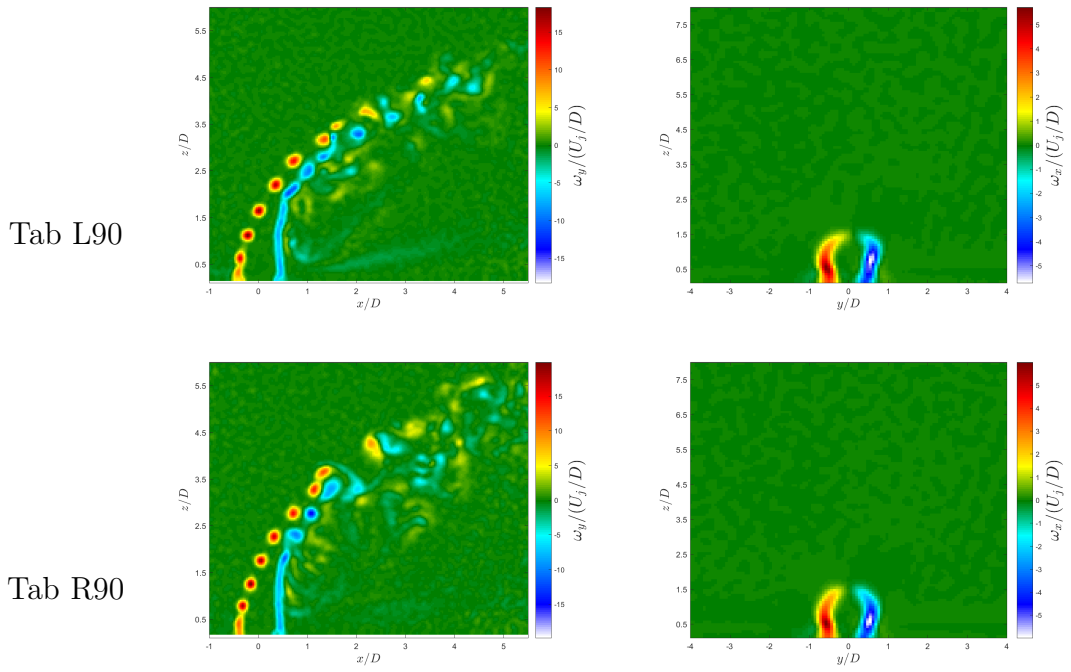

Figure 5.7: Centerplane images of the instantaneous vorticty field, and mean cross-sectional vorticity images averaged over 500 instantaneous realizations at the center of the jet exit ($x/D = 0.0$). Flow conditions are for $J = 5$ and $Re_j = 1900$, for symmetry breaking tab orientations. The colorbars are scaled to the maximum and minimum vorticity values contained within all images shown.

upstream shear layer dynamics. The centerplane vorticity field showed a rather significant delay in the strength of the upstream shear layer instabilities and vortex rollup for a tab placed closer to the upstream region (e.g., L15). As the tab was moved azimuthally about the jet periphery, the delay in USL vortex rollup was lessened, to the point where, by position L30 or L45, and definitely by L90 (or R90), there was very little discernible difference with respect to the jet with the non-tabbed simple extension in figure 5.7. In terms of the mean cross-sectional vorticity in the figure, the azimuthally placed tabs at L15 and L30 tended to introduce asymmetry at the jet exit, generally consistent with asymmetric cross-sectional PLIF images of the JICF under similar conditions in Harris et al. (2020b).

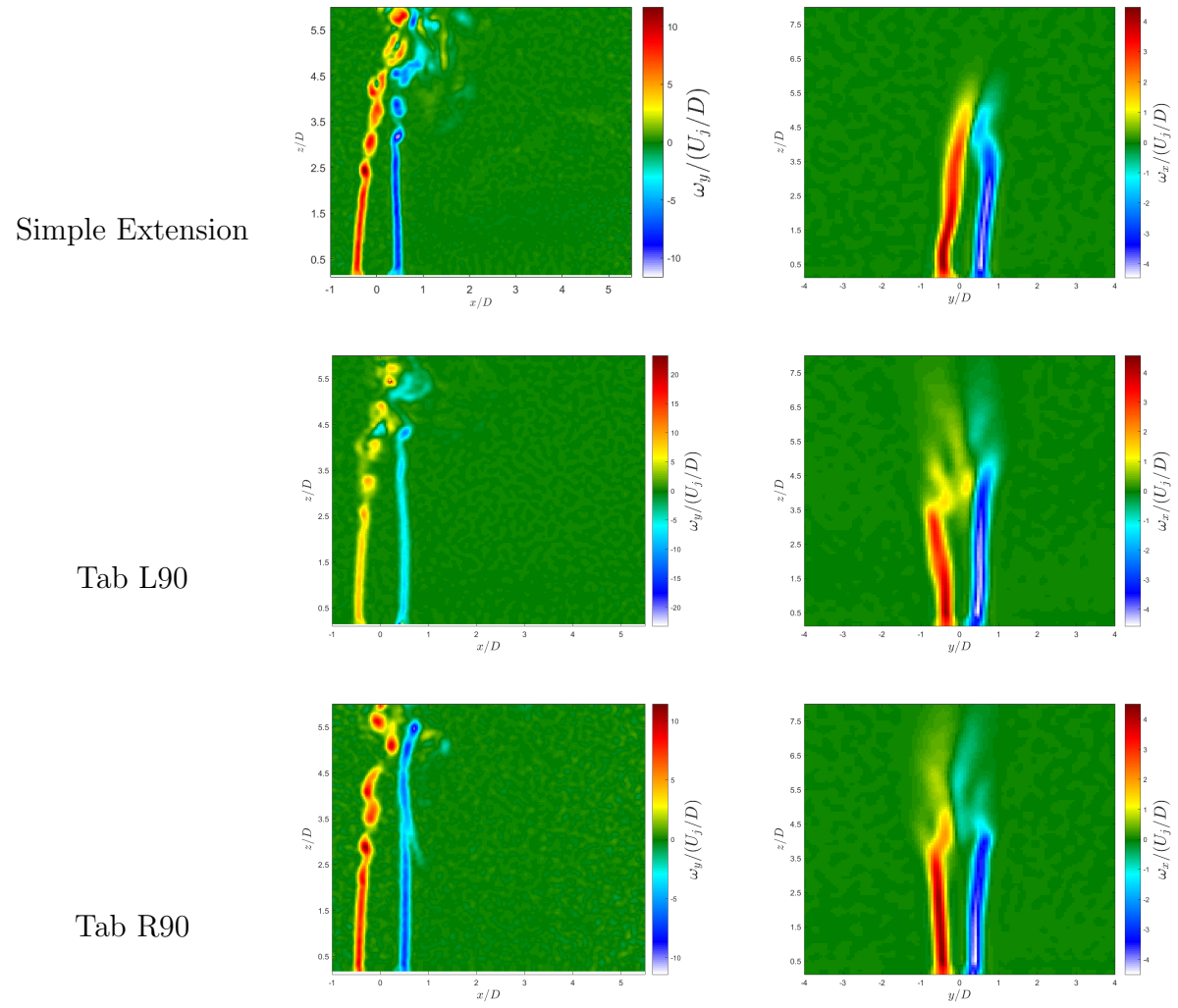

Figure 5.8: Centerplane images of the instantaneous vorticty field, and mean cross-sectional vorticity images averaged over 500 instantaneous realizations at the center of the jet exit ($x/D = 0.0$). Flow conditions are for $J = 41$ and $Re_j = 1900$, for symmetry breaking tab orientations. The colorbars are scaled to the maximum and minimum vorticity values contained within all images shown.

For the JICF at a higher momentum flux ratio, the naturally asymmetric cross-section was more significantly influenced by specific tab locations, per the studies in Harris et al. (2020b). Instantaneous centerplane and mean cross-sectional vorticity fields at a large value

of $J = 41$, are shown in figure 5.8. Close inspection indicates that the left and right oriented tabs at the "extreme" conditions L90 and R90 actually produced different delays in the USL vorticity rollup, and the cross-sectional vorticity fields were also different from one another (and were asymmetric with respect to the jet centerplane). These differences were manifested further downstream in high resolution PLIF images (Harris et al. (2020b)), with a perceptible deflection of the jet and vorticity field away from the location of the tab. The slight difference in the asymmetric vorticity production between the tab 90° to the left or right of the upstream may be a result of the inherent asymmetry already present in the transverse jet at $J = 41$.

5.1.3 POD Analysis and Counter Current Shear Layer Analogy

Beyond the effects on the vorticity generation and evolution near the jet exit, the tab's influence on other dynamics within the transverse jet flowfield may be explored via snapshot proper orthogonal decomposition (POD)(Sirovich (1987)) applied to the velocity vector fields from the centerplane stereo-PIV imaging. This approach has been explored in other studies of the JICF (Meyer et al. (2007); Schlatter et al. (2011); Gevorkyan et al. (2018)) as a means of extracting mode structures from instantaneous snapshots of the flow and identifying dominant instabilities in the flowfield. In the present studies, snapshot POD analysis was applied to all 500 instantaneous realizations of the flowfield for each test case considered, well above the 300 snapshots required for statistical convergence (Shoji (2017)). The resolved mode structures were ordered in terms of their respective magnitudes of total kinetic energy fluctuation, helping to reveal characteristic flow features and dynamics which might otherwise be hidden or masked by the chaotic flowfield. Figures 5.9-5.11 depict the four most energetic mode structures, along with their respective contributions to the total kinetic energy fluctuation, for the transverse jet without a tab, with the tab upstream, and with the tab downstream at momentum flux ratios of $J = 5$, $J = 8$, and $J = 41$, respectively. Only $J = 41$ had an USL which was clearly convectively unstable in the absence

(a) (b) (c)

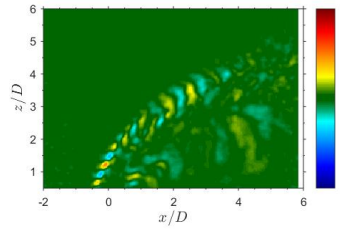

Mode 1 (7.02% of TKE)

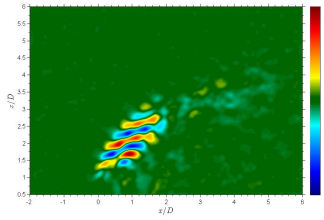

Mode 1 (4.67% of TKE)

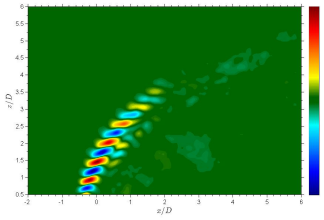

Mode 1 (5.52% of TKE)

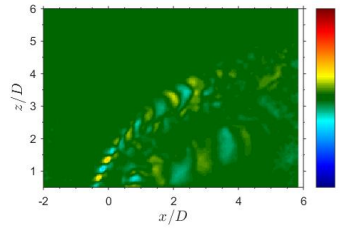

Mode 2 (6.66% of TKE)

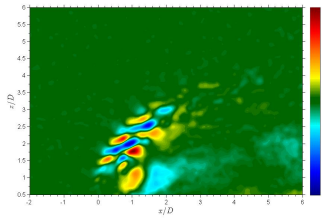

Mode 2 (3.91% of TKE)

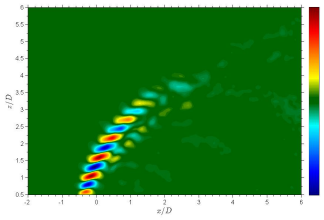

Mode 2 (5.23% of TKE)

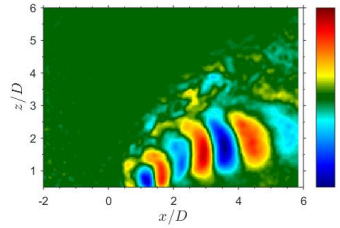

Mode 3 (2.90% of TKE)

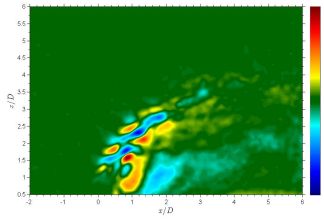

Mode 3 (3.37% of TKE)

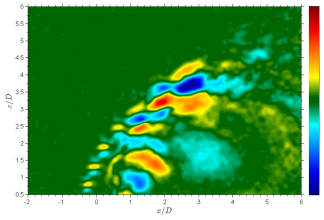

Mode 3 (2.38% of TKE)

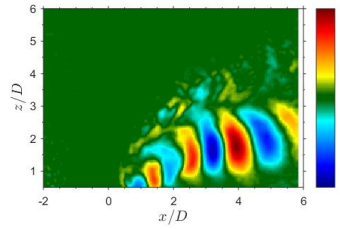

Mode 4 (2.64% of TKE)

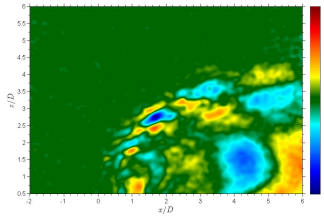

Mode 4 (2.50% of TKE)

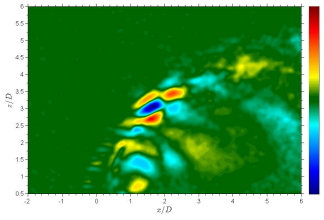

Mode 4 (2.34% of TKE)

Figure 5.9: PIV based POD mode structures extracted from 500 instantaneous snaphots of the centerplane velocity field at $J = 5$, for (a) the non-tabbed jet, (b) the tab upstream, and (c) the tab downstream. The modes are sorted according to their respective percentages of total kinetic energy fluctuation content. The colorbar in each image represents the mode scaled by its own norm and the mean jet velocity at the jet exit U_j.

(a) (b) (c)

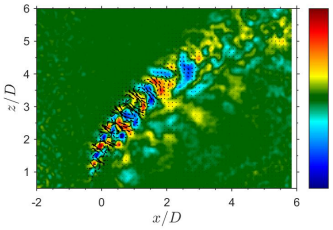

Mode 1 (6.24% of TKE)

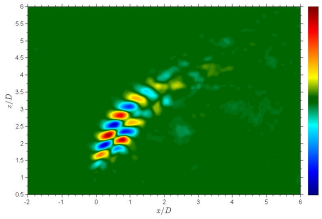

Mode 1 (4.78% of TKE)

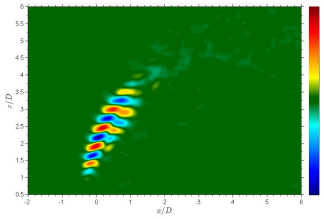

Mode 1 (4.19% of TKE)

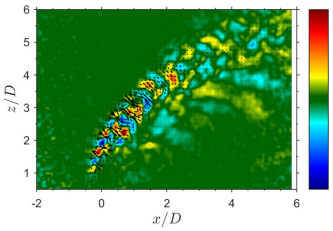

Mode 2 (5.47% of TKE)

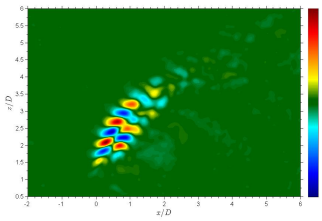

Mode 2 (4.36% of TKE)

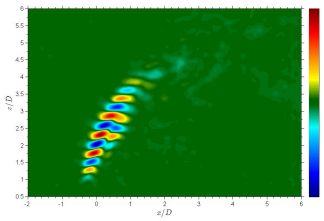

Mode 2 (3.97% of TKE)

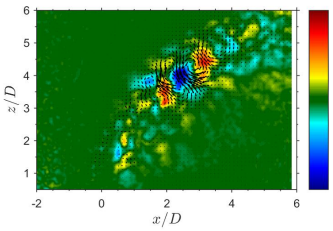

Mode 3 (4.04% of TKE)

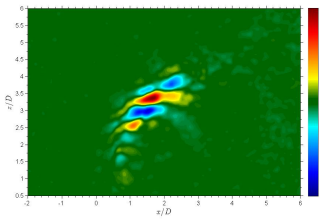

Mode 3 (3.05% of TKE)

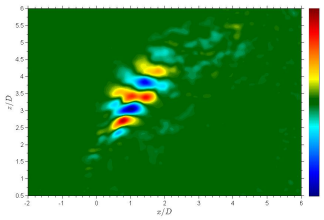

Mode 3 (3.47% of TKE)

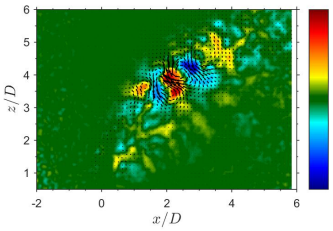

Mode 4 (3.58% of TKE)

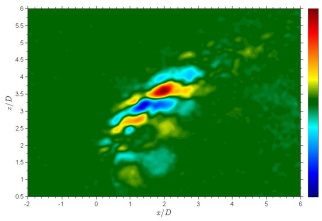

Mode 4 (2.71% of TKE)

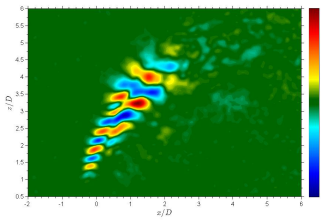

Mode 4 (3.14% of TKE)

Figure 5.10: PIV based POD mode structures extracted from 500 instantaneous snaphots of the centerplane velocity field at $J = 8$, for (a) the non-tabbed jet, (b) the tab upstream, and (c) the tab downstream. The modes are sorted according to their respective percentages of total kinetic energy fluctuation content. The colorbar in each image represents the mode scaled by its own norm and the mean jet velocity at the jet exit U_j.

of a tab (Shoji et al. (2020b)). The non-tabbed mode structures over the momentum flux ratio range in question (Figures 5.9-5.11((a)(1)-(a)(4))) agreed quite well with the dynamics seen in the snapshot POD for the flush nozzle injected JICF for the same momentum flux ratio range by Gevorkyan et al. (2018), even when the latter did not include a thin circular extension as in the present experiments. In the non-tabbed jet mode structures, for all three J values, the first two most dominant modes displayed isolated structures within the shear layer of the jet, and as the momentum flux ratio decreased, these modes were initiated closer to the jet exit, much like the vortex rollup and shear layer instability characteristics. As noted in Gevorkyan et al. (2018), such isolation of the mode structures in the shear layer agrees with dynamic mode decomposition (DMD) analysis of DNS JICF studies by Iyer and Mahesh (2016). For low momentum flux ratios, especially at $J = 5$ but also at $J = 8$, the structures were contained entirely within the upstream shear layer of the jet, while at higher momentum flux ratios, as shown by the first two modes at $J = 41$ (figure 5.11((a)(1)-(a)(2))), the the dominant mode structures spanned the upstream and downstream shear layers, and appeared to be merged, analogous to the expansion of the wavemaker region to the downstream shear layer documented in the DNS in Regan and Mahesh (2019), and the origination of the dominant eignenmode on the downstream side of the jet as shown in Regan and Mahesh (2017), both for a convectively unstable jet at $J = 16$ and $Re_j = 2000$. It is also noted that the wake structures were more pronounced as the momentum flux ratio was decreased and as the the jet became more bent over. The increasing contribution of the wake structures resulted in a decreasing energy content contained within the jet shear layer modes, reducing the energy content within the first mode from 11% to 7% in going from $J = 41$ to $J = 5$. These wake features were most dominant in the non-tabbed jet at $J = 5$ (figure 5.9((a)(3)-(a)(4))), where large scale structures denoting in and out of plane velocity form in the jet wake. Gevorkyan et al. (2018) and Fric and Roshko (1994) note such structures are largely associated with the wake vortices which act to entrain crossflow boundary layer fluid up into the jet.

(a) (b) (c)

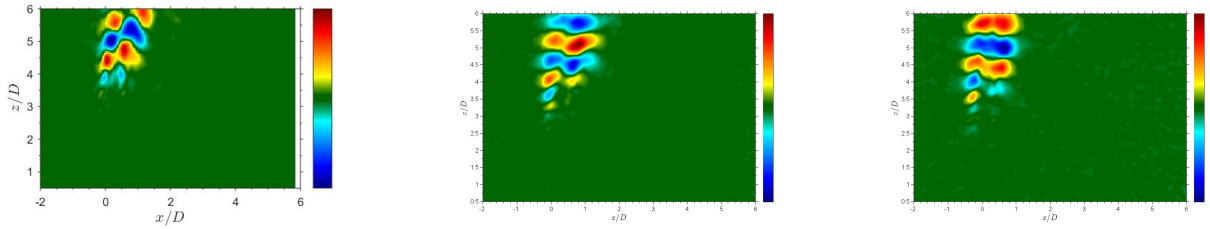

Mode 1 (11.72% of TKE) Mode 1 (9.87% of TKE) Mode 1 (9.77% of TKE)

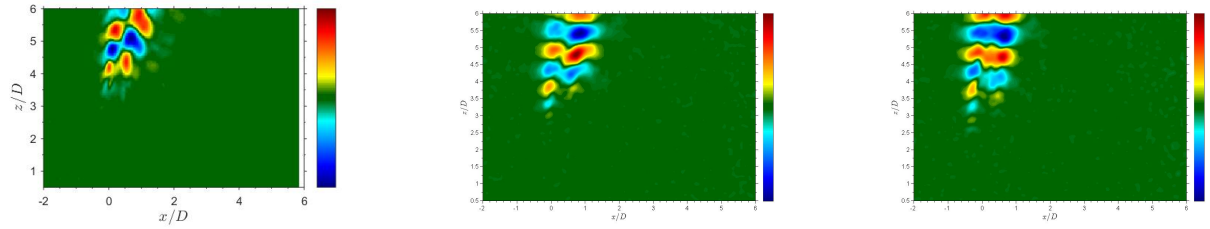

Mode 2 (11.00% of TKE) Mode 2 (9.19% of TKE) Mode 2 (8.91% of TKE)

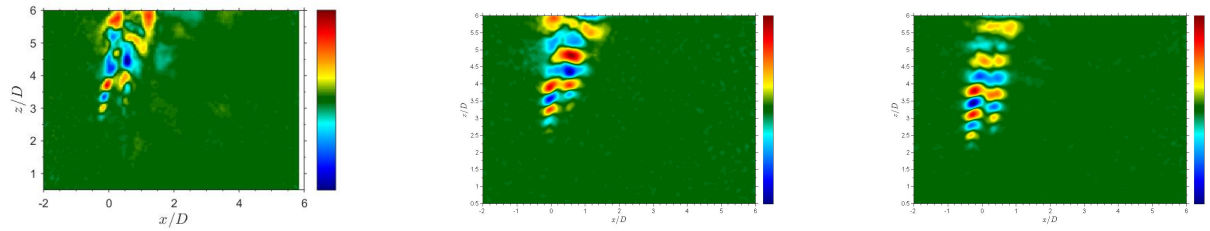

Mode 3 (3.87% of TKE) Mode 3 (4.85% of TKE) Mode 3 (4.06% of TKE)

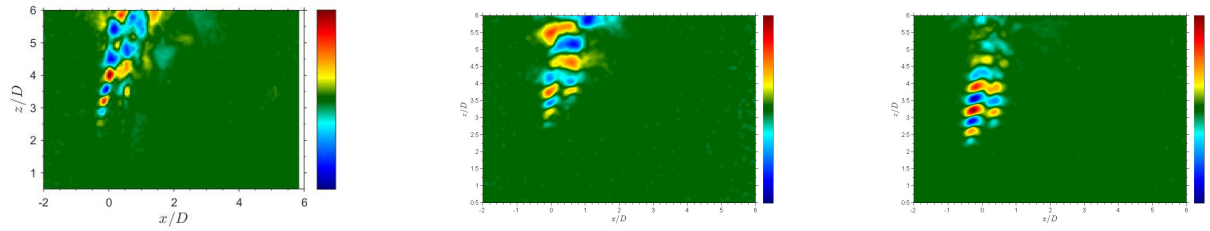

Mode 4 (3.33% of TKE) Mode 4 (4.41% of TKE) Mode 4 (3.64% of TKE)

Figure 5.11: PIV based POD mode structures extracted from 500 instantaneous snaphots of the centerplane velocity field at $J = 41$, for (a) the non-tabbed jet, (b) the tab upstream, and (c) the tab downstream. The modes are sorted according to their respective percentages of total kinetic energy fluctuation content. The colorbar in each image represents the mode scaled by its own norm and the mean jet velocity at the jet exit U_j.

Placement of the tab in the upstream region of the jet exit, as seen from the vorticity field in section 5.1.2, and in the USL stability and mixing analyses from Harris et al. (2020b), results in the most significant alterations to the JICF flowfield. The POD modes for each of the momentum flux ratios (figures 5.9-5.11((b)(1)-(b)(4))) reaffirmed these observations, in that the energy content contained within the first 2 (nominally shear layer) modes was decreased as compared with the non-tabbed JICF at the same flow conditions, hence with a weakening of the upstream shear layer vorticity dynamics. As momentum flux ratio was decreased, the differences in energy content between the non-tabbed and upstream tabbed jets became smaller in magnitude, though the mode structures became much more different from one another, e.g., for the first two modes at $J = 5$ in figure 5.9. These observations were likely related to the increasing significance of the wake structures as the jet became more bent over, with a transfer of kinetic energy from the USL to the wake structures; this trend was not explicitly associated with the presence of the tab. The difference in the most energetic mode shapes for $J = 5$, however, with a broadened region over which oscillations occurred with the upstream tab, was clearly the result of the tab placement. Similar mode shape alterations as well as a transfer of energy from shear layer to wake structures was observed for the upstream tab with $J = 8$ in figure 5.10((b)(1)-(b)(4)), though to a lesser degree than for $J = 5$. Given that $J = 41$ produced a JICF that was largely upright, the presence of wake structures was not detected, and thus even in the presence of the tab upstream, did not demonstrate a dramatic decrease in the energy content of the modes. When the tab was placed in the downstream edge of the jet, alterations in the mode structure and energy transfer from the shear layer to the wake were similar to effects observed for the upstream tabs at $J = 8$ and especially at $J = 41$, but there were greater differences for $J = 5$. There were clear upstream and downstream mode structures in the first and second POD modes for the case of the downstream tab with $J = 5$ (fig. 5.9(c)) as compared with the non-tabbed insert in figure 5.9(a), which only displayed clear USL structures. This observation was consistent with hotwire-based alterations in spectral characteristics of the

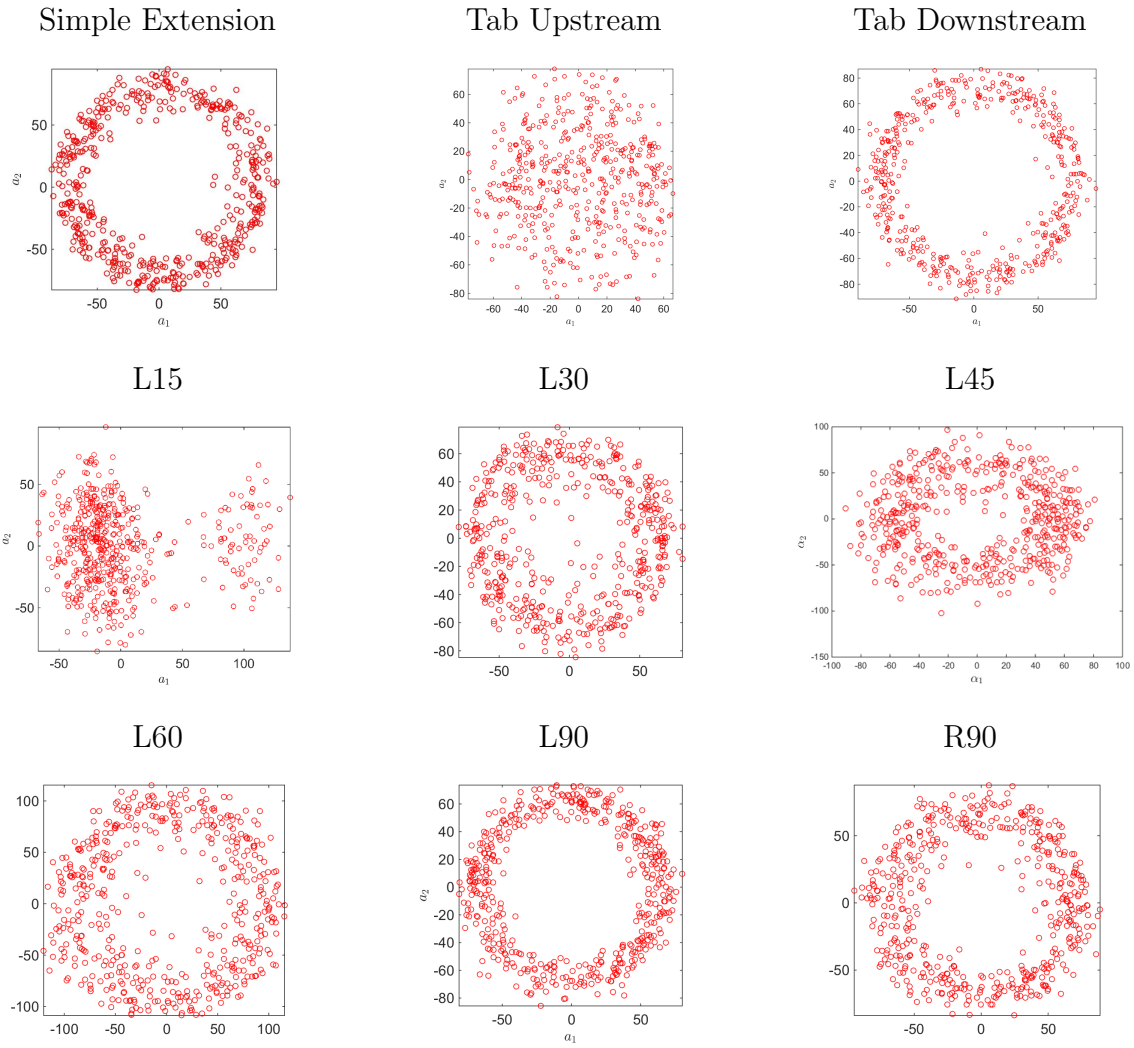

Figure 5.12: PIV based POD coefficients of the first 2 modes plotted against each other. Data are extracted from 500 instantaneous snapshots of the centerplane velocity field at $J = 5$, for a variety of tab configurations.

naturally absolutely unstable JICF when the tab was placed downstream; the downstream tab as well as the upstream tab weakened the USL's instabilities (Harris et al. (2020b)).

POD analysis also enables one to analyze the fluctuations in magnitude of the respective mode coefficients across the series of original snapshots, as has been done by Meyer

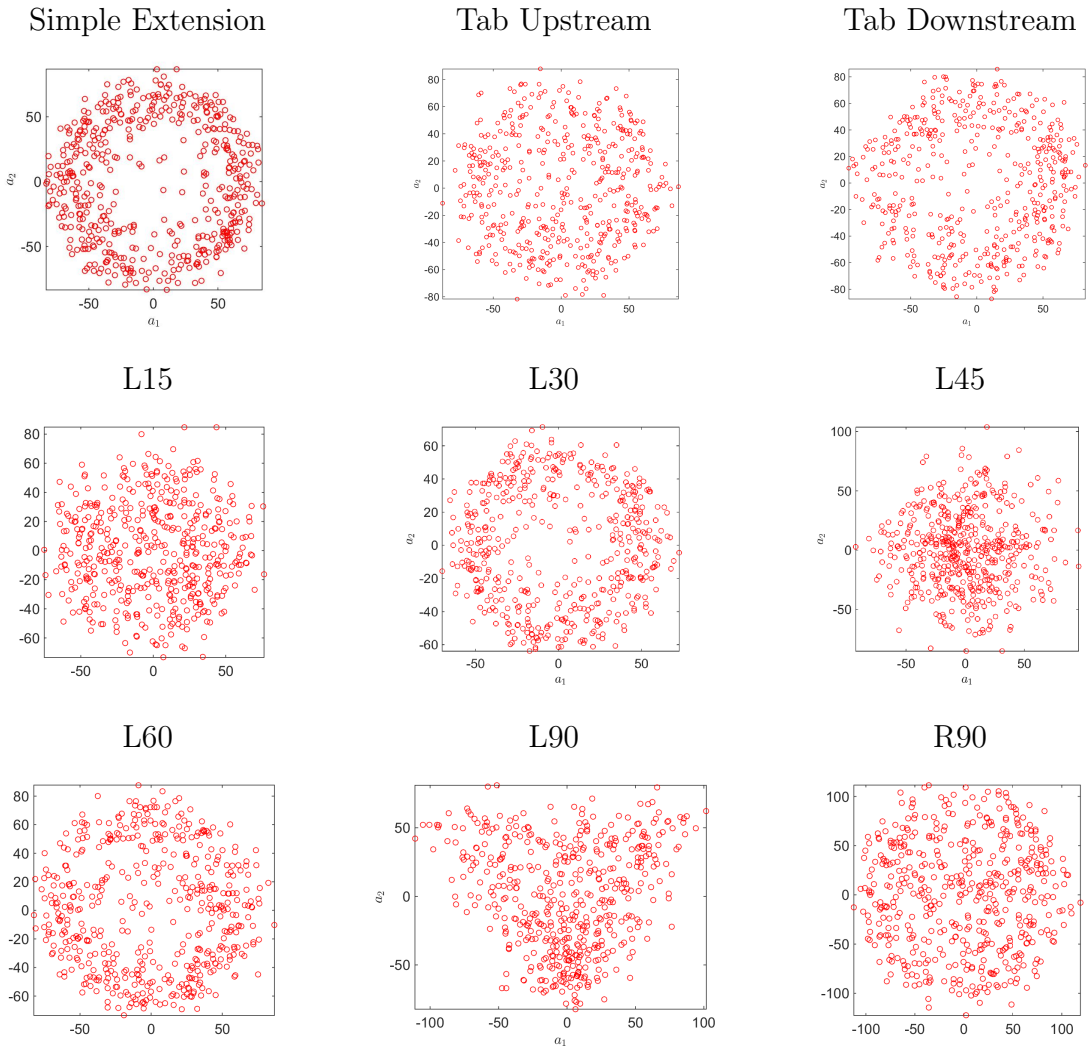

Figure 5.13: PIV based POD coefficients of the first 2 modes plotted against each other. Data are extracted from 500 instantaneous snapshots of the centerplane velocity field at $J = 8$, for a variety of tab configurations.

et al. (2007) and Gevorkyan et al. (2018), and thus to study correlations in the evolution of the dynamics in the flow. When treating a specific snapshot image, the magnitude of each respective coefficient represents the contribution of that particular mode in forming a summation from all of the modes to reconstruct the snapshot. If the mode coefficients from select mode pairs are then plotted against one another, it is possible to determine if

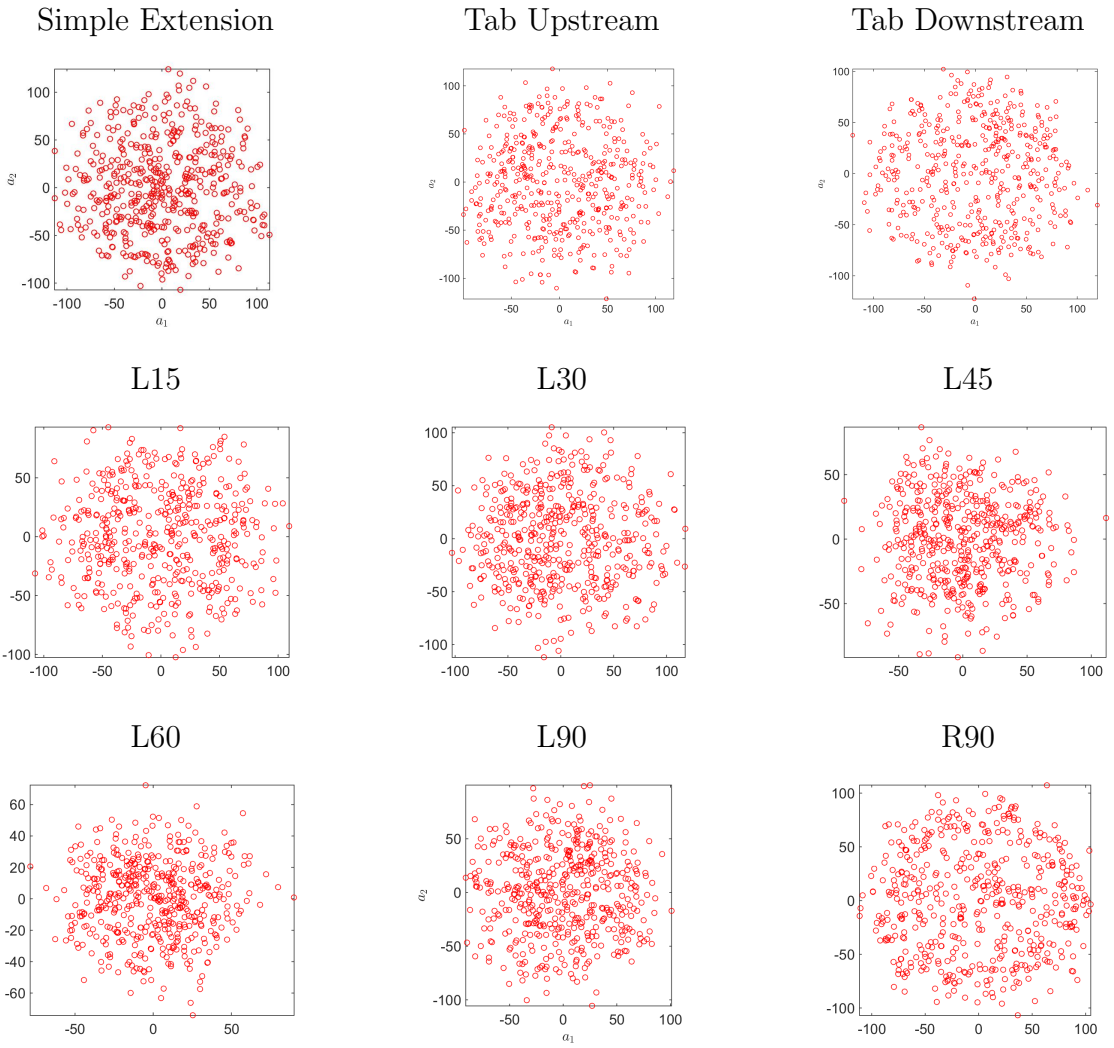

Figure 5.14: PIV based POD coefficients of the first 2 modes plotted against each other. Data are extracted from 500 instantaneous snapshots of the centerplane velocity field at $J = 41$, for a variety of tab configurations.

the respective modes are at all correlated in their evolution over time. Gevorkyan et al. (2018) demonstrates for the absolutely unstable jet at $J = 5$ that when the first two mode coefficients are plotted against one another for all 500 snapshots, the plot resembles that of a ring, representative of a periodic traveling wave, and that the dominant jet dynamical behavior may be characterized by linear combinations of the first two modes. From a phase

space perspective, the appearance of a ring is illustrative of a simple limit cycle attractor between the first two mode coefficients, indicating a periodic behavior dominated by a singular frequency, though the exact frequency content in the present study was not recoverable since the snapshot POD was not time resolved. For the JICF with a convectively unstable USL, however, Gevorkyan et al. (2018) show that the ring-like plot of the first two mode coefficients deteriorates to a diffuse blob, where no limit cycle behavior is detectable. Instead the coefficient plots rightly illustrate the broadband frequency content of shear layer instabilities in a convectively unstable flow, consistent with corresponding hotwire measurements of the USL. An understanding of the effects of tabs on JICF dynamical characteristics can benefit from this approach as well.

Figure 5.12 shows plots comparing the coefficients of the first two most energetic proper orthogonal modes for the flowfield at $J = 5$ for the non-tabbed jet with a simple thin extension,, and for tab placements in the upstream, downstream, and symmetry breaking tab orientations about the jet exit periphery. Clearly, as was seen by Gevorkyan et al. (2018) for the flush nozzle-injected jet at $J = 5$, the resulting coefficient plot for the non-tabbed jet created a ring, indicative of a limit cycle behavior associated with the upstream shear layer structures, as expected for an absolutely unstable flow. When the tab was then placed in the upstream of the jet, the ring like representation was not recovered, and instead a diffuse blob was formed, much like typical phase portraits for a convectively unstable flow. Such a finding was not unexpected in that Harris et al. (2020b) document a transition in the USL instabilities from absolute to convective instability with the tab upstream for $J = 7$ and $Re_j = 2300$ based on spectral contour plots. That study also notes a similar, though much less severe, transition in the shear layer instabilities when the tab is positioned downstream, while the current coefficient plots actually retained the ring shape, suggesting here that the flow remained absolutely unstable at $J = 5$ for such tab placement. We note that the prior investigation examines a momentum flux ratio closer to the critical transition between absolute and convective instability ($J = 7$), and hence is more likely to be affected by small

alterations in the flow. In contrast, the momentum flux ratio of $J = 5$ in the current study was more strongly absolutely unstable and further from the critical transition for these flow conditions. Hence while the tab upstream was able to transition the flow from absolute to convective instability, even for the strong absolutely unstable flow at $J = 5$, the weaker influence of the tab downstream resulted in the flow's remaining absolutely unstable. This observation was also seen in the USL vorticity generation for the downstream tab at $J = 5$ in figure 5.3; its instantaneous structure was remarkably similar to that of the non-tabbed jet, but was quite different from that of the tab positioned at the upstream. The coefficient plots in figure 5.13 for $J = 8$ reinforced this idea of the impact of the tab being dependent on the closeness of the USL instability state to absolute instability. The non-tabbed jet here was still absolutely unstable, though more weakly so as it was closer to the critical transition around $J \approx 9 - 10$, and when the tab was placed in either the upstream or downstream, the resulting coefficient plot showed more diffuse blobs rather than a circle, as would be expected for a flowfield that was convectively unstable. Further extension of this evaluation to tab configurations at $J = 41$ in figure 5.14 showed the expected diffuse blobs in the coefficient plots for all tab orientations, as the flow is known to be naturally convectively unstable, and the tab acted to further weaken the flowfield instabilities. Interestingly, the resulting coefficient plots for symmetry breaking tab orientations for all three momentum flux ratios were generally consistent with the trends in USL spectra in Harris et al. (2020b), as well as the vorticity analysis in section 5.1.2 of this study, demonstrating that the influence of the tab was most significant when the USL was naturally strongly absolutely unstable. For the flow at $J = 5$, in figure 5.9, besides the upstream tab, there were additional alterations in the coefficient plots, though not as severe, when the tab was situated at L15 and L45 positions. Separate studies (Harris (2020); Harris et al. (2020b)) show downstream cross-sectional asymmetries for such cases, with a more significant bulk deflection of the CVP. The altered (non blob-like) structures for these two cases in figure 5.9 suggested additional complexity in the dynamics that could warrant further exploration. As for the other cases, for

Template Configuration	θ/D	Experiment USL
Simple Extension	0.0304	AU
Tab Upstream	0.0405	CU
Tab L90	0.0322	AU
Tab R90	0.0315	AU
Tab Downstream	0.0363	AU

Table 5.1: For $J = 5$ and $Re_j = 1900$, the upstream jet momentum thickness at the jet exit (scaled by D) and the hotwire-based state of the upstream shear layer.

$J = 8$ in figure 5.10, only the downstream and L90 tab configuration showed some evidence of periodicity in the flow, while other cases indicated weakening of the disturbances to become like a convectively unstable flowfield. For $J = 41$ in figure 5.11, the coefficient plots showed no significant alterations with the presence of tabs at any position, generally consistent with spectral characteristics and centerplane imaging for the CU JICF documented in Harris et al. (2020b).

In addition to the vorticity field and POD analysis of the velocity field extracted from the present experiments, the local velocity field in the vicinity of the upstream region of the jet exit for different tab (and tabless) configurations was also examined. Such measurements enabled exploration of the influence of the tabs on the local upstream shear layer flowfield in the context changes in the jet's upstream momentum thickness. As noted previously, the flush nozzle-based experiments of Shoji et al. (2020b) demonstrate that as the upstream momentum thickness of the exiting jet becomes larger, the degree or strength of counter-current flow required to cause transition from CU to AU increases. Hence for the same crossflow and jet bulk velocity conditions, a thicker upstream momentum thickness θ could create a weaker instability in the USL; this is also consistent with a diminished growth rate of the axisymmetric instability mode for the high momentum flux ratio JICF (Alves et al. (2008)).

Template Configuration	θ/D	Experiment USL
Simple Extension	0.0293	AU
Tab Upstream	0.0376	CU
Tab L90	0.0323	CU
Tab R90	0.0314	CU
Tab Downstream	0.0349	CU

Table 5.2: For $J = 8$ and $Re_j = 1900$, the upstream jet momentum thickness at the jet exit (scaled by D) and the hotwire-based state of the upstream shear layer.

To explore the effect of a tab placed at various locations on the upstream jet momentum thickness θ, the velocity field in the $x - z$ plane at the upstream region of the jet near the jet exit, extracted from PIV measurements, was used, with details on the method of extraction described in Shoji et al. (2020b). This method was applied to all jet configurations here, including a range of tab positions. The results for $J = 5$ for various tab orientations are given in table 5.1, where the scaled upstream momentum thickness θ/D, and state of the USL as determined via hotwire anemometry (AU or CU) are given. The data in Table 1, and the corresponding data for $J = 8$ in Table 2, showed an interesting correspondence between the larger values of θ and the observed state of the USL per hotwire measurements, which, interestingly, were also consistent with the POD coefficient plots. Even when the tab was placed azimuthally at a position well away from the jet's upstream shear layer, the small and moderate increases in upstream momentum thickness θ were consistent with the state of the jet's dynamics as observed in the hotwire measurements and in POD coefficient plots. We also note, as suggested in Harris et al. (2020b), that the momentum thickness of the jet was significantly increased over the non-tabbed jet when the tab was upstream, and moderately so when the tab was downstream. Thickening of the momentum thickness was typically reduced as the tab orientation was rotated away from the upstream, having the least impact when placed directly in the sides of the jet. As stated when discussing

the POD coefficient plots, some unusual behavior in the shear layer dynamics (e.g., L45 for $J = 8$) may be due to the large asymmetric deflection of the jet structure, whereby the shear layer dynamics were not entirely captured in the centerplane view of the evolving jet. Also possible is that asymmetric instabilities may be initiated and growing to compete with the axisymmetric mode, such that analysis of the periodicity of the upstream shear layer from the coefficient plots may not be accurately recovered due to coupling of the instability modes contaminating the simple limit cycle behavior.

5.2 Discussion

Simultaneous stereo PIV and acetone PLIF experiments enabled extensive examination of the vorticity dynamics associated with a gaseous jet in crossflow and its alteration by triangular tabs situated at various locations within the jet periphery. The ability to vary jet-to-crossflow momentum flux ratio J as well as tab position provided a large parameter space to be explored, including conditions for which the USL was naturally absolutely unstable ($J = 5$ and 8) and naturally convectively unstable ($J = 20$ and 41). Consistent with corresponding experiments involving high resolution PLIF imaging (Harris et al. (2020b)), placement of the tab at or near the upstream region of the jet exit had the most significant influence on improving mixing, i.e., in reducing local Unmixedness (e.g., as in fig. 5.2), but understanding the influence of the tabs on vorticity generation and evolution, as well as correspondence between USL dynamics and overall jet dynamics, required the stereo PIV-based findings in the present study.

In terms of centerplane-based vorticity evolution, placement of a tab in the upstream or near-upstream location caused a delay in upstream shear layer rollup and, as quantified here, a reduction in USL vorticity associated with a thickening of the upstream jet momentum thickness. This delay was seen irrespective of J range, that is, whether the USL was naturally AU or CU in the absence of a tab (figs. 5.3, 5.5, 5.7). The influence of downstream tab

placement or tab placement much further from the upstream, e.g., at or beyond 45 degrees from the upstream location, was observed to have a rather minimal effect on the USL instability delay, though in most cases such placement had a significant symmetrizing influence on nearfield cross-sectional vorticity dynamics. This influence on cross-sectional vorticity generation and evolution very close to the jet exit could be used to explain rather significant alterations in farfield cross-sectional shape and symmetry observed in corresponding PLIF-only experiments, which in turn did contribute to an improvement in molecular mixing. But specific positioning of the tab for a given set of flow conditions, especially at higher J values where there was a naturally asymmetric cross-sectional orientation, could have different effects on the vorticity. Hence the current studies and methods could contribute to a database for determining optimal jet/tab configurations for given flow conditions.

Proper orthogonal decomposition (POD) modes extracted from centerplane velocity field measurements showed significant influence of tab placement on jet upstream and downstream vorticity as well as wake structures, again, depending on J. Phase portraits extracted from POD mode coefficient plots produced periodic (circular) shapes for tab placement corresponding to conditions for which the USL was determined in separate hotwire measurements Harris et al. (2020b) and instantaneous vorticity fields to be absolutely unstable. This suggests that dynamical characteristics revealed through POD mode shapes and coefficient plots could be used to develop characteristic signatures for transverse jet behavior that relate directly to their structure and scalar mixing characteristics. The present study, and its high resolution PLIF-only counterpart in Harris et al. (2020b), involved a rather wide parameter space to generate such signatures for various J values, tab positions, and visualization orientations. But there are additional parameters which could be varied to study the flow for optimization purposes. Contemporary modeling tools, e.g., methods for evolving Reduced Order Models for the flowfield, could be very useful for predicting the most effective configurations for given applications and flow conditions. This is a subject of ongoing investigation.

Part II

Axisymmetric Excitation of the Jet in Crossflow

CHAPTER 6

Motivation and Features of the Forced JICF

6.1 Motivation

Recent work by Shoji et al. (2019) distinguish that for square wave excitation of a weak CU flow, the stroke ratio producing the best molecular mixing is very near the established value of $L/D \approx 4$ suggested by Gharib et al. (1998) for a starting jet. They also note as the crossflow is strengthened and the jet eventually transitions to an AU flow, the optimal stroke ratio for best molecular mixing is reduced, analogous to the trends in optimal vortex ring formation with reducing r_{ring} set forth by Sau and Mahesh (2008). Interestingly, Sau and Mahesh (2008) demonstrate that for an isolated vortical structure, stroke ratios greater than the optimal values for vortex ring formation, which produce a trailing column of jet fluid behind the fully filled vortex ring, should enhance the mixing process more than just the fully filled ring, owing to an enhanced downstream entrainment from the trailing column. Quite importantly, Shoji et al. (2019) illuminates that stroke ratios corresponding to the best spread and penetration, long thought of as indicators of improved mixing of the jet, do not necessarily correspond with the stroke ratio for best molecular mixing. Likewise, Sau and Mahesh (2010) determines the stoke ratios for best spread and penetration do not coincide with the optimal stroke ratio for the formation of a fully filled vortex ring, that is, until the ring velocity ratio is quite large (very weak crossflow). Johari (2006) notes that differences in the jet penetration are attributable to the relative interaction between successive vortex structures, where fully filled vortex rings, having a smaller celerity than partially filled rings, interact sooner in the jet nearfield. They further postulate that selective determination of the

pulsing parameters can achieve both initially deeply penetrating vortical structures in the nearfield, followed by interactions between these vortical structures for improved mixing by a prescribed downstream location. However, to date, little insight has been gained with respect to inducing interactions between successive vortical structures in tandem with prescribing the nature of these issuing vortex rings, especially when considering vortex rings with trailing columns.

Additionally, investigations by Shoji (2017) demonstrate that the precise waveform shape of a square wave excitation, specifically the introduction of ringing or overshoot and undershoot of the ideal/prescribed waveform, may be important in the developing structural dynamics of the flowfield. Interestingly though, the numerical work of Sau and Mahesh (2010) demonstrate that for square wave excitation of the JICF, that the exact coherence or shape of the waveform is not necessarily important, and instead suggests the net stroke ratio, ring velocity ratio, and imparted circulation to the generated vortex ring are the important parameters. In the extrema of a comparison between square wave and sine wave excitation though, the square wave excitation waveforms are much more effective than sinusoidal excitation in affecting an AU jet, when matching the excitation $u_{j,rms}$ amongst the various forcing waveforms (M'Closkey et al. (2002); Davitian et al. (2010b); Shoji et al. (2019)). Even more, when the $u_{j,rms}$ of sine wave excitation is increased over that of the square wave excitation, thereby imparting greater energy to the jet, the square wave is still able to produce more pronounced alterations to the jet structure (Shoji (2017)). The general ineffectiveness of sinusoidal forcing when applied to an AU JICF is understood through the lock-in characteristics of the jet, where the strength of the natural instabilities along the USL of the jet are quite difficult to overcome unless the sinusoidal forcing amplitude is quite large (Shoji et al. (2020c)). However, very little is understood about why the square wave forcing, when applied at the same forcing frequency as the sine wave forcing is so effective, and interestingly, lock-in characteristics remain unquantified for the square wave forcing.

The experimental study in chapter 7 sought to further improve upon the molecular mix-

ing enhancements demonstrated from square wave forcing through control of the vortex rings formed, as well as the subsequent interactions between such structures in the evolving flow-field. The investigation of the JICF was explored through the forced excitation of the jet flow by an acoustic double-pulse waveform, wherein during a single forcing period, $T = 1/f_f$, two distinct and independently controlled square wave pulses were generated. Henceforth referred to as double-pulse forcing, the excitation method surmised that the independent pulses would generate vortex rings of differing strengths and celerity so as to induce a fast propagating vortex ring catching up to a slower ring, yielding vortex interactions/collisions to promote vortex merger/breakdown, and thereby potentially enhance the overall mixing process. Quantitative measurements were made through application of mixing evaluations to scalar concentration images in the jet centerplane and cross-section from acetone PLIF imaging. The main flow conditions investigated were for a transitionally CU/AU and an AU jet flows. The experiments of chapter 8 then further examine the synchronization characteristics specifically of an AU JICF for sine wave, square wave, and double-pulse forcing. The resulting implications on downstream dynamics, structure, and mixing were treated via simultaneous PLIF/PIV imaging, POD analysis, and phase space analysis of the jet from vertical velocity measurements along the upstream shear layer.

6.2 Supplemental Setup and Experiment Modifications

The general experimental setup and configurations are given in chapter 2, which details the wind tunnel, flow plumbing, optical setup, and diagnostic tools and methods. Here details are given which were specific to the studies conducted in chapters 7 and 8. For this experimental investigation of the JICF, the jet injector was given by a flush nozzle with a lager exit diameter of $D = 7.59mm$, as compared to the flush nozzle jet injector implemented in part 2.3.2 and detailed in section 2.1.1. The nozzle was still given by a 5^{th} order polynomial contraction which produced a top-hat velocity profile and relatively

thin momentum thickness at the nozzle exit. This nozzle corresponded to the one which is implemented by M'Closkey et al. (2002) and Shapiro et al. (2006) for square wave excitation of the jet. Maintaining the flush nature of injection to the wind tunnel was accomplished through affixing the jet injection system to the removable floor shown in figure 2.2(a). To limit the amount of distortion of the applied actuation, the long pipe was removed, and the acoustic forcing plenum was attached directly to the nozzle.

Two distinct flow conditions were treated within these studies, corresponding to flow for the high-resolution PLIF imaging, and the simultaneous PLIF/PIV imaging with complimenting hotwire based analyses, respectively. The jet in chapter 7 consisted of an equidensity flow with constituent species mole fractions of 0.218, 0.234, and 0.548 for the acetone, He, and N_2 respectively. The jet had a Reynolds number of $Re_j = 1800$, with a resulting bulk jet velocity of $U_j = 3.31m/s$, and specifically looked at momentum flux ratios of $J = 10$ and $J = 7$, which corresponded to a transitionally CU/AU jet and an AU jet, respectively. In chapter 8, the equidensity jet instead had constituent species mole fractions of 0.112, 0.100, and 0.788 for the acetone, He, and N_2 respectively. The flow had a Reynolds number of $Re_j = 1800$, with a bulk jet velocity of $U_j = 3.42m/s$ and examined a singular AU jet at a momentum flux ratio of $J = 6$. The flow conditions treated for this chapter were slightly different from those of chapter 7 owing to the slight changes in the jet constituent species.

6.2.1 Hotwire Anemometry

A single-component boundary-layer-type hotwire anemometry probe (Dantec 55P15) was utilized to evaluate the spectral characteristics along the USL of the jet. The probe was inserted from the side of the test chamber through a port access, and was oriented such that the wire was parallel with the free-stream crossflow. Translation of the probe in the x, y, and z directions, with an accuracy of 1 μm ($1.32 * 10^-4$ jet diameters), was possible via Newport high-performance low-profile ball-bearing linear stages constructed in a triple axis traversing platform system. The shear layer spectral characteristics were based on the vertical velocity

fluctuations as the hotwire was traversed downstream along the jet USL (s/D). The output signal from the probe was sent to a 90C10 constant temperature anemometry (CTA) module in a Dantec StreamLine 90N10 frame, after which the AC and DC components of the signal were separated and conditioned via a signal conditioning system created by Hendrickson (2012). Finally, the AC component of the conditioned signal was sent to a dynamic signal analyzer (HP-35665A), whereupon the power spectral density was generated over a span of 6.4 kHz with 8 Hz resolution. Details regarding the determination of the shear layer trajectory, calibration of the hotwire probe, and other aspects of the hotwire may be found in Shoji (2017).

Resulting temporal data from the hotwire probe, placed at various downstream locations along the USL of the jet (s/D), was also utilized in nonlinear time-series analysis (NTA) of the forced jet conditions to examine synchronization or lock-in characteristics of the flow in response to the applied forcing. The NTA was implemented given its usefulness in studying the dynamics of inherently nonlinear physical processes (Kantz and Schreiber (2003)). Though the dynamics of the JICF were not directly measured, as it is inherently difficult to measure all of the state variables in order to recreate the phase space, an interpretation of their behavior was instead garnered through investigating topological features of phase space reconstructions from time delay embedding (Takens (1981)) of a single variable, since most state variables are intrinsically coupled to one another (Li and Juniper (2013a)) and are generally preserving of the original dynamical properties (Kantz and Schreiber (2003)). In this study, the state variable of interest was the USL vertical velocity, recorded in the format of hotwire voltage, and the process for recreating the shear layer dynamics in the phase space followed after the methodologies outlined by Shoji et al. (2020c) for the JICF, Li and Juniper (2013a) for a hyrdodynamically self-excited low density free jet, and Guan et al. (2018) for an externally forced self-excited thermoacoustic oscillator. In general, the hotwire based velocity readings were cast into a d-dimensional Euclidean vector of time delayed elements, where for visual representation of the phase space reconstruction the first

three dimension vectors were plotted against one another. For proper reconstruction and one-to-one projection of the original attractor in the phase space, the embedding dimension was set to be larger than a minimum value, which was determined using Cao's method (Cao (1997)), and the time delay was carefully selected as the first local minimum of the average mutual information function (Fraser and Swinney (1986)).

6.2.2 Waveform Generation and Adaptive Feed-forward Control

Generation of the acoustic excitation was made by a loudspeaker (RadioShack 40-1022B, 4 in. woofer) housed in a plenum chamber just upstream of the jet nozzle, and was driven by an amplifier (Adcom GFA-7300) with a constant signal gain of 30. To produce the waveform, a data acquisition (DAQ) board (dSPACE 1104) was used in partnership with ControlDesk software within Matlab's Simulink to send the signal from the computer to the speaker. Measurements of the resultant acoustic forcing at the jet exit were made by the hotwire anemometry system detailed in the prior section. To record the excitation waveform characteristics before significant attenuation of the signal, the hotwire was centered over the jet exit 0.1 diameters above the exit plane. The signal was again passed through the same CTA module and signal conditioning system as utilized for the spectral measurements, before both the AC and DC components were fed to the DAQ and analyzed in the computer. Digital sampling of the analog signal was made at 20 kHz with with the largest uncertainties in the velocity fluctuations on the order of 1% for a velocity of 1 m/s, as documented in prior studies (Getsinger et al. (2014)).

The double-pulse forcing consisted of two independently controllable square wave pulses generated during a single forcing period. The fundamental forcing frequency, or fundamental forcing period via $T = 1/f_f$, was $f_f = 55Hz$, and was selected to match the square wave forcing conditions explored in prior work (M'Closkey et al. (2002)) for similar flowfield parameters as those treated here (Re_j, J, S). Due to the complex nature of the waveform, the signal was composed as a Fourier series of sinusoids at the fundamental forcing frequency

and its 14 subsequent higher harmonics. Details regarding the determination of the number of harmonics and the selection of which harmonics to utilize in the Fourier series composition of the waveform are the subject of another ongoing project. For easier control, each of the 15 sinusoidal inputs was decomposed into respective $\sin(kf_f t)$ and $\cos(kf_f t)$ functions, with $f_f = 55Hz$ and $k = 1, 2, \ldots, 15$, so that respective adjustments in the amplitudes of these functions translated to alterations in the amplitude and phase of the original signal components. For all forcing cases considered the RMS of the perturbation, defined in equation 1.10, was matched so that the effective level of forcing applied, or more aptly the total impulse imparted to the jet fluid, was the same for all waveforms. The perturbation RMS applied to the jet was chosen as $u_{j,rms} = 2.0\ m/s$ for the forcing cases in chapter 7, corresponding to a relative excitation of $u'_{j,rms}/U_j = 0.60$, while the forcing amplitudes in chapter 8 were varied from $u_{j,rms} = 0.07\ m/s$ to $u_{j,rms} = 1.7\ m/s$, corresponding to a relative excitation of $u'_{j,rms}/U_j = 0.02 - 0.50$. Additionally, the mean velocity of the excitation was set to $0\ m/s$ so that the net flow of the forced jets were comparable with the unforced cases. With both the perturbation RMS and mean of the excitation fixed, the only other independent parameters needed to characterize the double-pulse forcing waveform were the temporal pulse widths, τ_1 and τ_2, as well as the temporal spacing between the two pulses, $\Delta\tau$; the pulse amplitudes were defined as a function of the other parameters.

Further complicating the waveform formation were the inherent nonlinearities of the experimental setup, the imperfect non-flat frequency response of the actuation system, and the nonlinear behavior of the JICF itself (M'Closkey et al. (2002); Shapiro et al. (2006); Davitian et al. (2010b); Shoji et al. (2019)). Earlier studies answer this through the utilization of a feedforward controller based on a mathematical inversion of a linear representation of the frequency response of the actuation system (M'Closkey et al. (2002); Shapiro et al. (2006)). Later, a more simplistic approach uses a truncated Fourier series to define the waveform, where each of the inputs' amplitude and phase were adjusted based on a linear best fit to the empirical frequency response of the actual jet waveform at the selected Fourier series

(a) Square

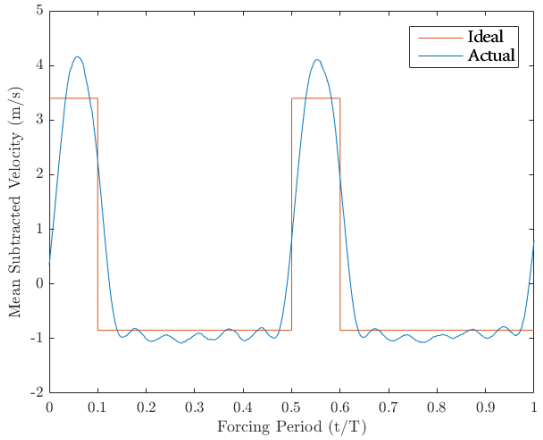

(b) Double-Pulse

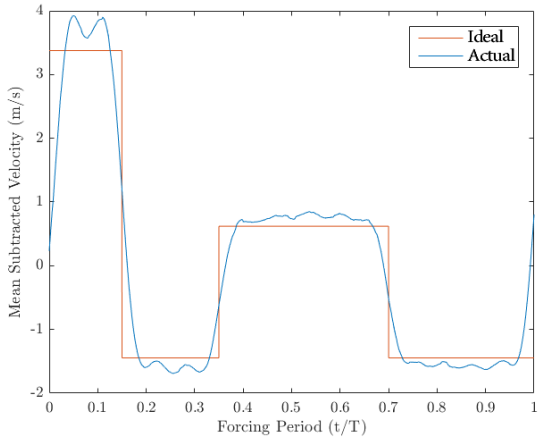

Figure 6.1: Representative depictions of actual forcing waveforms compared with their repsective ideal waveforms for (a) a $\alpha = 20\%$ duty cycle square wave, and (b) a double-pulse forcing waveform, both with a mean subtracted perturbation amplitude of $u'_{j,rms} = 1.70\ m/s$.

frequencies of interest (Davitian et al. (2010b)). This latter method eliminated the feedback element present in the prior approach, and thus could not account for other disturbances which arose in the jet flow, but still generally approximated the idealized square wave well. Most recently, Shoji et al. (2019) extends this truncated Fourier series approach to an adaptive feedforward control method and is able to converge to very well refined waveforms, and it is this methodology which is implemented in the current study to generate the double pulse forcing waveforms.

After the double-pulse waveform was mathematically prescribed, initial inputs for the 30 $\sin(kf_f t)$ and $\cos(kf_f t)$ functions, constituting the decomposed 15 term Fourier series, were established based on the desired jet velocity components and the estimated frequency response of the actuator system at the selected fundamental forcing frequency and higher harmonics. The estimation of the frequency response was determined from correlating the hotwire based jet velocity measurements with sinusoidal excitation of the jet at the fre-

quencies of interest. Additionally, a low-pass filter (1st-order Butterworth filter) at a corner frequency of 600 Hz, $\approx 11 f_f$, was applied to the desired waveform to reduce the effects of the higher order harmonics in order to lessen the production of high-frequency noise. With the initial inputs therefore defined, the actuator system was modeled as a continuously differentiable function, and the waveform inputs were individually perturbed while monitoring the jet velocity output, such that a perturbation matrix, the Jacobian of the modeled actuator system, could be experimentally determined. The perturbation magnitudes of all 30 signal components were each set relative to the magnitude of the actual input so as to prevent overly large perturbations being applied to the more sensitive harmonics. The updated waveforms were then compared with the desired waveform output to determine if it was sufficiently converged or if further iterations were necessary. Convergence was achieved when the output amplitudes of the 30 sine and cosine functions, as determined from an fast Fourier transform (FFT) of the actual waveform, deviated less than 10^{-3} from the prescribed amplitudes for the ideal waveform. This typically took less than 5 iterations. Figure 6.1 representatively depicts ideal square wave and double-pulse forcing waveforms, along with their respective final converged waveforms as measured by the hotwire anemometer just above the jet exit. The converged waveforms typically had very clean and sharp temporal upsweeps and downsweeps, though some slight ringing could be noted in the peaks. This small ringing was not easily eliminated given the complexity of the waveforms and the waveform being generated by a truncated Fourier series of only 15 terms. However, it was deemed to be of little affect given that the predominant significance lies with the coherence of the upsweep and downsweep, and the resulting net stroke ratio, ring velocity ratio, and imparted circulation to the generated vortex ring (Sau and Mahesh (2010); Shoji et al. (2019)). Greater details about the development of this feedforward adaptive control method are given in Shoji (2017) and Shoji et al. (2019).

CHAPTER 7

Axisymmetric Excitation of AU and CU Jets

7.1 Results

Forcing Case	$\tau_{input,1}/T$	$\tau_{input,2}/T$	$\Delta\tau_{1\to2}/T$	$\Delta\tau_{2\to1}/T$
0.45.70.85	0.45	0.15	0.25	0.15
0.45.60.75	0.45	0.15	0.15	0.25
0.45.55.70	0.45	0.15	0.10	0.30
0.35.60.75	0.35	0.15	0.25	0.25
0.35.50.65	0.35	0.15	0.15	0.35
0.35.45.60	0.35	0.15	0.10	0.40
0.25.50.65	0.25	0.15	0.25	0.35
0.25.40.55	0.25	0.15	0.15	0.45
0.25.35.50	0.25	0.15	0.10	0.50
0.15.40.55	0.15	0.15	0.25	0.45
0.15.30.45	0.15	0.15	0.15	0.55
0.15.25.40	0.15	0.15	0.10	0.60

Table 7.1: Test matrix of the various double-pulse forcing waveforms generated from a Fourier series of $f_f = 55\ Hz + 14$ higher harmonics, while matching the RMS of the jet velocity perturbation both temporal pulses at $u'_{j,rms} = 2.0\ m/s$. The temporal pulse widths of the first and second square wave pulses are defined by their duration normalized over a single forcing period. Respective temporal spacing between the two pulses is also normalized by the forcing period.

Table 7.1 lists the various double-pulse forcing waveforms generated in chapter 7, defining the temporal pulse widths of each pulse, and the temporal spacing between the two pulses. The naming convention derived for the double-pulse forcing was based on the initiation and termination of the two square wave pulses during a single forcing period. For example, the first case, 0.45.70.85, states the first pulse initiates at $t/T = 0.0$ and terminates at $t/T = 0.45$, having a duration of $\tau_{input,1}/T = 0.45$, and then the second pulse initiates and terminates at $t/T = 0.70$ and $t/T = 0.85$ respectively, representing a pulse duration of $\tau_{input,2}/T = 0.15$ with a temporal delay after the first pulse of $\Delta\tau_{1\rightarrow 2}/T = 0.25$. Given the double pulse wanted to explore a fast moving vortex (high celerity) catching up to and interacting with a slower moving vortex (low celerity), the naming convention was also ordered such that the slower pulse, characterized by the longer of the pulse durations, was first and the faster/shorter pulse was second. Figure 6.1 representatively depicts a single forcing period waveform of the converged double-pulse forcing for case , where the actual waveform, as measured by the hotwire located $0.1D$ above the jet exit, is in red, and the theoretical waveform is in black.

7.1.1 Spectral Measurements

As detailed earlier, the stability characteristics along the USL of the JICF have been extensively studied for a variety of Re_j, J, S, and jet injector geometry configurations (Megerian et al. (2007); Davitian et al. (2010a); Getsinger et al. (2012), 2014; Shoji et al. (2020b), 2020c; Harris et al. (2020b)). The USL instabilities are known to undergo a transition from convective instability to absolute/global instability for the acetone-seeded equidensity small flush nozzle-injected jet ($D = 4.04\ mm$) with $Re_j = 1900$ at a critical momentum flux ratio of $J_{cr} \approx 9$ (Shoji et al. (2020b)). Interestingly though, for the same flow conditions and nozzle injector, but without the acetone tracers, the transition is instead seen to occur at $J_{cr} \approx 10$ (Megerian et al. (2007)). Shoji et al. (2020b) note that this small change in critical transition due to acetone tracers is also accompanied with a change in the dominant instability frequency as well, and link the shifts to small alterations in the bulk viscosity of

the jet due to changes in the constituent species. Separate linear stability analysis (LSA) investigations by Souza et al. (2020) demonstrate the instability characteristics of the JICF, and the critical transition from a CU USL to an AU USL, are dependent upon the momentum thickness of the issuing jet, and to a small degree, jet viscous effects. However, the instability characteristics for the larger flush nozzle ($D = 7.59mm$) utilized throughout this study have not been investigated.

Figure 7.1 depicts contour plots of the shear layer spectra based on the vertical velocity fluctuations measured while traversing along the upstream shear layer trajectory of the large ($D = 7.59\ mm$) flush nozzle-injected JICF, with acetone mole fraction of $\psi = 0.218$, for a range of momentum flux ratios. At $J = 15$ and $J = 10$, in figures 7.1(a) and 7.1(b) respectively, the spectral content, which is nondimensionalized to Strouhal numbers by $St = fU_j/D$, was represented by relatively broadband instability peaks initiating at around $s/D \approx 0.7 - 1.0$. Traversing further downstream to $s/D \approx 1.5$ saw the emergence of a dominant subharmonic peak, while in general relatively weak or non-existent spectral peaks characterized the higher harmonics regardless of s/D location. These characteristics of relatively weak and broadband dominant instabilities, a lack of content at higher harmonics, and the emergence of a subharmonic peak are well established identifiers of a CU JICF (Megerian et al. (2007); Getsinger et al. (2012); Getsinger et al. (2014)). Interestingly, while these flows were CU in nature, the broadband instabilities did not exhibit the same degree of clear frequency shifting, due to a tonal interference between the hotwire and the jet (Hussain and Zaman (1978)), as is noted in the smaller flush nozzle injected JICF despite remarkably similar flow conditions (Shoji et al. (2020b)). This was suggestive of a weakening of the tonal interference, which may in part be explained by the changes in the characteristic length scales in the flowfield. In going from the small flush nozzle, with a diameter of 4.04 mm, to that of the large flush nozzle, with a diameter of 7.59 mm, the length scale was nearly doubled, while the length of the hotwire probe remained constant at 1.25 mm. Thus, the probe's relative size was cut almost in half, resulting in the weakening of the tonal inter-

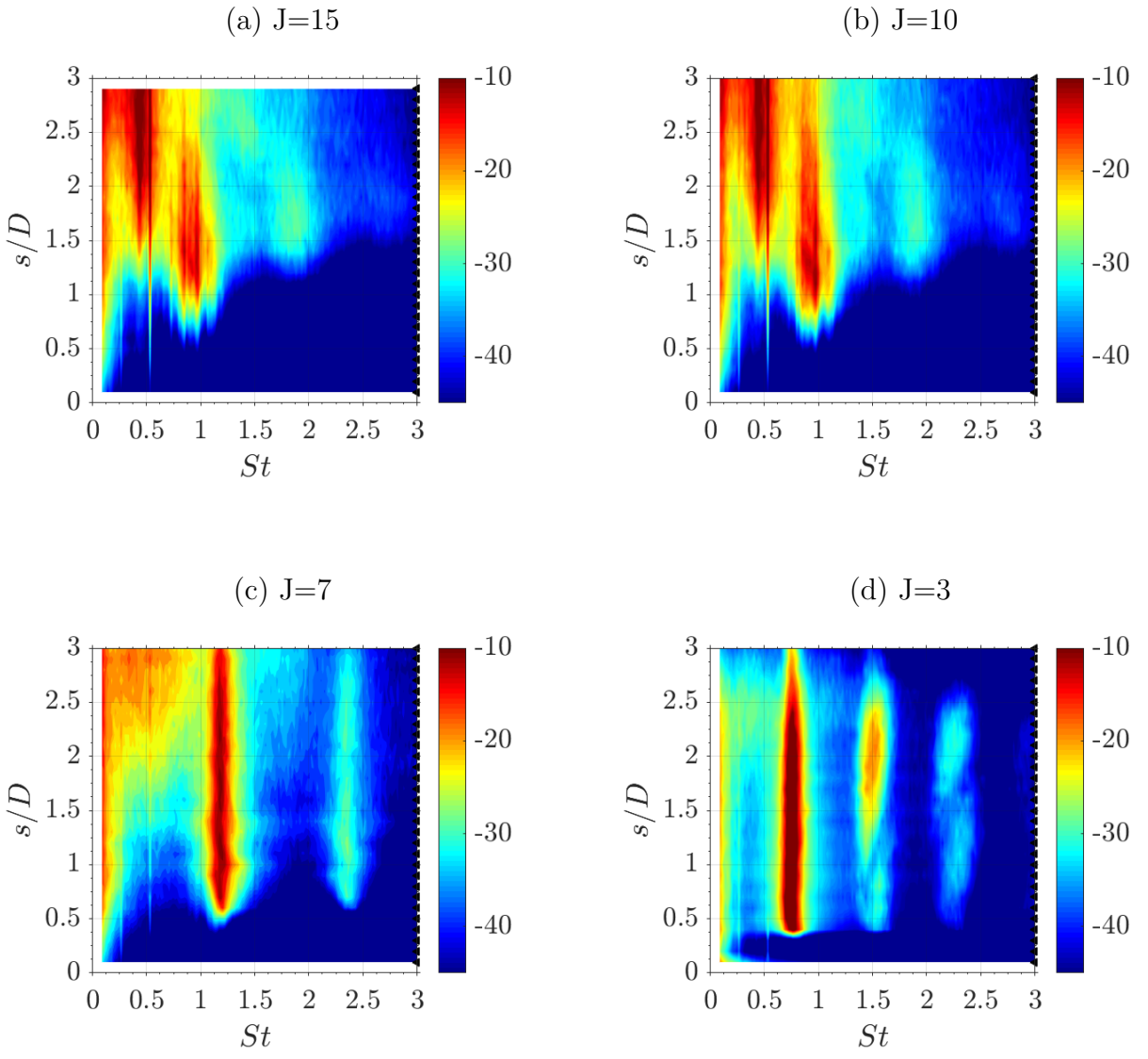

Figure 7.1: Power spectra of the upstream shear layer instabilities for the equidensity large ($D = 7.59\ mm$) flush nozzle-injected JICF with acetone mole fraction of $\psi = 0.218$, jet Reynolds number of $Re_j = 1800$, and jet velocity of $U_j = 3.31\ m/s$ at momentum flux ratios of (a) $J = 15$ with a fundamental frequency of $f_0 \approx 410\ Hz$, (b) $J = 10$ with $f_0 \approx 420\ Hz$, (c) $J = 7$ with $f_0 \approx 540\ Hz$, and (d) $J = 3$ with $f_0 \approx 340\ Hz$.

ference, which is also supported from the probe size investigations by Hussain and Zaman (1978). Looking then to figure 7.1(c) for $J = 7$, it was seen that the dominant instability initiated closer to the jet exit at $s/D \approx 0.5$, was stronger, and was more pure-toned than the instabilities for the jet in 7.1(a-b). Additionally, there was an emergence of peaks at higher harmonics and correspondingly an elimination of the sub-harmonic peak. These traits in the shear layer spectra were indicative of the JICF having transitioned from convective instability to absolute/global instability (Megerian et al. (2007); Getsinger et al. (2014); Shoji et al. (2020b)). As the momentum flux ratio was further reduced to $J = 3$, shown in figure 7.1(d), the instability characteristics depicted even stronger qualitative indicators of an AU flow initiating even closer to the jet exit.

Examination of the dominant instabilities of all J values considered in figure 7.1 demonstrated a systematic increase in the Strouhal number from $St = 0.94$ to $St = 1.24$ as J was decreased from $J = 15$ to $J = 7$, and the jet transitioned from convective to absolute instabilities in the USL. After the transition, further decreasing J decreased the dominant Strouhal number from the peak value obtained at $J = 7$, to $St = 0.78$ at $J = 3$. Shoji et al. (2020b) notes a similar peaking of the dominant instability frequency at the transition point between a CU and AU JICF for a variety of jet flow conditions. With supporting motivation from the LSA of Souza et al. (2020), the variability in these dominant instabilities may be traced to competing dynamics of a thickening of the jet momentum thickness and a strengthening of a counter-current like behavior, which originates from the small negative velocity component induced by the recirculation zone in the leading edge of the jet, as the crossflow velocity increases (decreasing J). These findings regarding the changes in the dominant instability frequency were quite important when determining which CU and AU JICF conditions to explore with the acoustic forcing, due to the resulting implications on the different flowfields locking-in to the forcing. We recall that Shoji et al. (2020c) notes forcing frequencies further away from the fundamental natural instability (f_0) are more difficult to lock-in, as are frequencies which are below the fundamental $f_f < f_0$, both of which

contribute to distinctly asymmetric "v-shaped" lock-in diagrams for the JICF. Given the double-pulse forcing has a base forcing frequency of $f_f = 55\ Hz$, having dramatic changes in the fundamental frequency of the jet would significantly impact the degree to which the jet is locked-in to the forcing. Thus, for the rest of this study only the cases of $J = 10$ and $J = 7$ are treated for the $\psi = 0.218$ jet, as their respective dominant fundamental instability frequencies were most similar while yet also retaining distinctly CU and AU upstream shear layer characteristics. Further, the forcing amplitude was maintained at $U_{j,rms} = 2.0\ m/s$, representing an excitation of just over 60% of the unforced jet velocity, which is well above the thresholds for lock-in seen by Shoji et al. (2020c). An exploration of the lock-in characteristics and their dependence on the waveform generation methodology for the double-pulse forcing are briefly discussed in the following chapter.

7.1.2 Structural Characteristics

To visualize the structural characteristics of the unforced and double-pulse forced JICF, images were recorded along the centerplane axis of the jet and at select discrete vertical slices of the jet cross-section via non-intrusive PLIF imaging. Due to the phase progressing nature of the forced data sets, wherein successive images were separated by a phase difference of $\theta \approx 3.6°$ but were acquired just over 11 forcing periods apart, the pseudo time-resolved data was able to illustrate the nearfield evolution of vortical structures which were produced. Such illustrative evolutions were not possible further downstream where there was more turbulence and the flow behavior was more chaotic. In the case of the unforced jet, the natural instability frequency was not singular enough to allow for phase locking or phase progressing imaging of the jet, and as such the recorded images were simply representative snapshots at random phases over the natural jet evolution. For the cross-sectional slices, only cases at $x/D = 0.0$ and $x/D = 0.5$ are herein depicted given the distinct focus on the generation, evolution, and eventual interaction of vortical structures in the jet nearfield.

Forcing Case	$\tau_{actual,1}/T$	$\tau_{actual,2}/T$	L_1/D	L_2/D	$r_{ring,1}$	$r_{ring,2}$
0.45.70.85	0.50 ± 0.0001	0.19 ± 0.0001	4.07 ± 0.08	2.86 ± 0.02	2.78 ± 0.02	5.11 ± 0.05
0.45.60.75	0.50 ± 0.0003	0.19 ± 0.0001	4.09 ± 0.06	2.85 ± 0.02	2.80 ± 0.02	5.11 ± 0.03
0.45.55.70	0.49 ± 0.0010	0.19 ± 0.0001	4.03 ± 0.05	2.87 ± 0.03	2.83 ± 0.01	5.13 ± 0.06
0.35.60.75	0.39 ± 0.0005	0.19 ± 0.0001	3.69 ± 0.06	2.79 ± 0.02	3.18 ± 0.02	4.96 ± 0.04
0.35.50.65	0.40 ± 0.0005	0.19 ± 0.0001	3.73 ± 0.06	2.79 ± 0.02	3.17 ± 0.02	4.97 ± 0.02
0.35.45.60	0.39 ± 0.0006	0.19 ± 0.0001	3.67 ± 0.05	2.81 ± 0.04	3.20 ± 0.02	4.98 ± 0.07
0.25.50.65	0.30 ± 0.0002	0.19 ± 0.0001	3.24 ± 0.04	2.70 ± 0.03	3.72 ± 0.03	4.76 ± 0.04
0.25.40.55	0.30 ± 0.0003	0.20 ± 0.0001	3.22 ± 0.03	2.69 ± 0.01	3.70 ± 0.01	4.72 ± 0.01
0.25.35.50	0.29 ± 0.0002	0.19 ± 0.0002	3.18 ± 0.02	2.69 ± 0.01	3.75 ± 0.01	4.79 ± 0.08
0.15.40.55	0.20 ± 0.0002	0.20 ± 0.0001	2.60 ± 0.04	2.56 ± 0.01	4.50 ± 0.03	4.48 ± 0.02
0.15.30.45	0.20 ± 0.0001	0.20 ± 0.0001	2.59 ± 0.01	2.55 ± 0.02	4.47 ± 0.03	4.46 ± 0.03
0.15.25.40	0.20 ± 0.0001	0.19 ± 0.0001	2.56 ± 0.02	2.54 ± 0.02	4.50 ± 0.03	4.50 ± 0.02

Table 7.2: Double-pulse forcing temporal pulse widths, stroke ratios, and ring velocity ratios for $J = 7$ with $U_j = 3.31\ m/s$, $U_\infty = 1.22\ m/s$, and excitation at $u'_{j,rms} = 2.0\ m/s$. The temporal pulse widths are experimentally established from hotwire measurements at $z/D = 0.1$, and the stroke ratio and ring velocity ratios are determined from equations 1.11 and 1.12.

The main forcing cases investigated dealt with a "quick pulse" that was fixed at a prescribed temporal pulse width of $\tau_2/T = 0.15$, while the temporal pulse width of the "slow pulse" (τ_1) and the temporal spacing between the two pulses ($\Delta\tau_{1\to2}/T$) were both varied. Table 7.2 lists the actual temporal pulse widths as measured by the hotwire anemometer placed just above the nozzle exit at $z/D = 0.1$. The pulse widths were slightly larger than their prescribed values given in table 7.1 by about $\Delta\tau/T = 0.05$. This was due to the imperfect nature of the jet responsiveness to the impulsive upsweeps and downsweeps of the forced waveform. Shoji (2017) demonstrates that these artifacts are able to be mitigated through adjustments to the way in which the waveform is generated, though it often is at the expense of introducing overshoot and/or ringing to the waveform, or in the form of greater complexity in building the waveform. The stroke ratios were based on integration of the temporal jet velocity over the duration of the temporal pulse width, as defined in equation 1.11, and the ring velocity ratios were established from equation 1.12. This formulation of the stroke ratio is utilized by others for flows which are also not fully modulated (Davitian et al. (2010b); Hendrickson (2012)), and was selected because there was specific interest in the formation of the vortical structures as they related to the different regimes of vortex ring formation for a JICF (Sau and Mahesh (2008); Sau and Mahesh (2010)).

Figure 7.2 illustrates where the generated quick and slow pulses resided within the different vortex ring regimes established by Sau and Mahesh (2008). The lower regime, below $r_{ring} = 2.0$, is characterized by connected hairpin vortices, while the upper left and right regimes delineate vortex rings without and with jet trailing columns respectively. The largest temporal pulse width treated had an actual duration of $\tau_1/T = 0.5$, yielding a stroke ratio of $L/D = 4.56$ and ring velocity ratio of $r_{ring} = 2.80$ with $U_\infty = 1.22\ m/s$ for $J = 7$ (blue markers), which distinctly placed the pulse in the regime of a vortex ring with a trailing column. Then, since the $u'_{j,rms}$ was constant for every pulsing condition, as the temporal pulse width was systematically decreased, the stroke ratio also decreased while the ring velocity ratio increased for a fixed jet momentum flux ratio. For the smallest temporal pulse widths

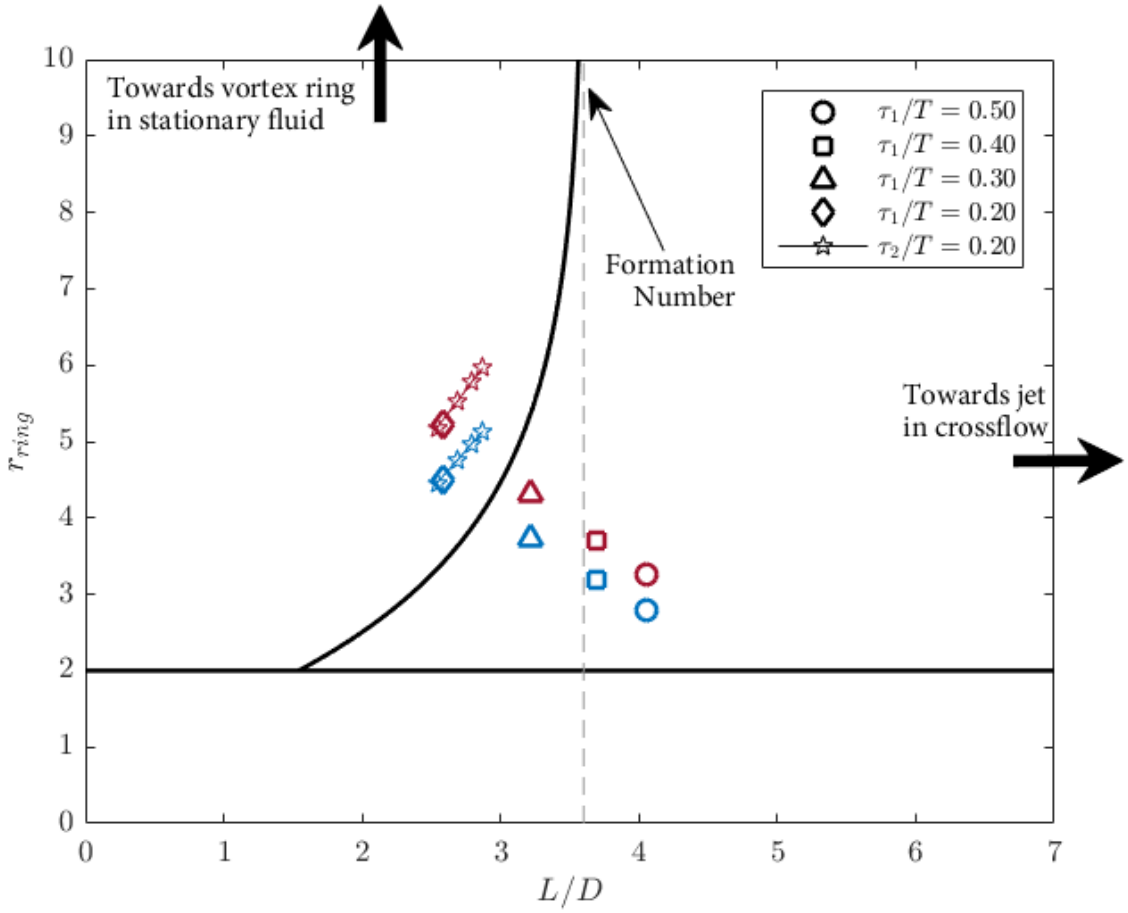

Figure 7.2: Regime map of types of vortex rings formed based on the stroke ratio and ring velocity of the single vortex in crossflow, with comparison to the present axisymmetrically forced JICF. The delineating boundaries are established from DNS investigations of isolated vortex rings in crossflow by Sau and Mahesh (2008), with the dashed line representing the formation number as $r_{ring} \to \infty$, where the vortex ring characteristics asymptotically approach a starting jet behavior. The relative L/D and r_{ring} for the different temporal pulse widths are plotted for both the $J = 7$ (blue) and $J = 10$ (red) flows at $Re_j = 1800$ and $\psi = 0.218$.

treated, corresponding to the narrowest of the slow pulses and all of the fast pulses, for the jet at $J = 7$, the stroke ratios of $L/D = 2.86 - 2.56$ and ring velocity ratios of $r_{ring} = 5.13 - 4.46$, placed the pulses in the regime of a vortex ring without a trailing column. From inspection,

it appeared an actual temporal pulse width of $\tau/T \approx 0.25$ at $J = 7$ would have produced a fully filled vortex ring, carrying the maximum amount of jet fluid possible without the generation of a trailing column. As the momentum flux ratio was increased to $J = 10$ (red markers), through the weakening of the crossflow to $U_\infty = 1.05\ m/s$, the stroke ratios remained unchanged while the ring velocity ratios were systematically shifted up by $\approx 16\%$. Due to this, each of the vortex rings formed had smaller trailing columns, or less fully filled vortex rings in the case of the $\tau/T = 0.20$ pulses, relative to the vortex rings from the same temporal pulses for the $J = 7$ flow. The respective decrease in the fullness of the vortex rings as the momentum flux ratio was lowered was quite impactful since the amount of jet fluid carried by a ring or ring with a trailing column is known to significantly impact the mixing and entrainment processes for isolated vortex rings in crossflow (Sau and Mahesh (2008)). The exact influence of the fullness of the vortex rings, and the different effects of the double-pulse forcing when applied to the AU and CU jets are treated by the mixing calculations in section 7.1.3. In addition to exploring a range of temporal pulse widths, the temporal spacing between the respective slow and quick pulse was also investigated in hopes of promoting nearfield vortical interactions between the two pulses. Three types of behaviors were noted: vortex collisions, where the quick pulse crashed into the slow pulse, vortex interactions, where the quick pulse grazed or passed in near proximity to the slow pulse, and no significant interaction, where the two pulses did not appear to interact or influence one another.

Shown in figure 7.3 are representative instantaneous centerplane representations of the unforced jet at $J = 7$ and $J = 10$, along with mean cross-sectional images at downstream locations of $x/D = 0.0$ and $x/D = 0.5$. The jets were seen to have clear and distinct representations in the scalar concentration images of the vortex rollup along the USL of the jet, with the onset of the rollup appearing at $z/D = 0.5$ for $J = 7$ and $z/D = 0.7$ for $J = 10$, which agreed quite well with the respective onsets of the dominant USL instabilities as measured by the hotwire anemometer in figure (7.1). In the cross-section, even by 0.5 diameters

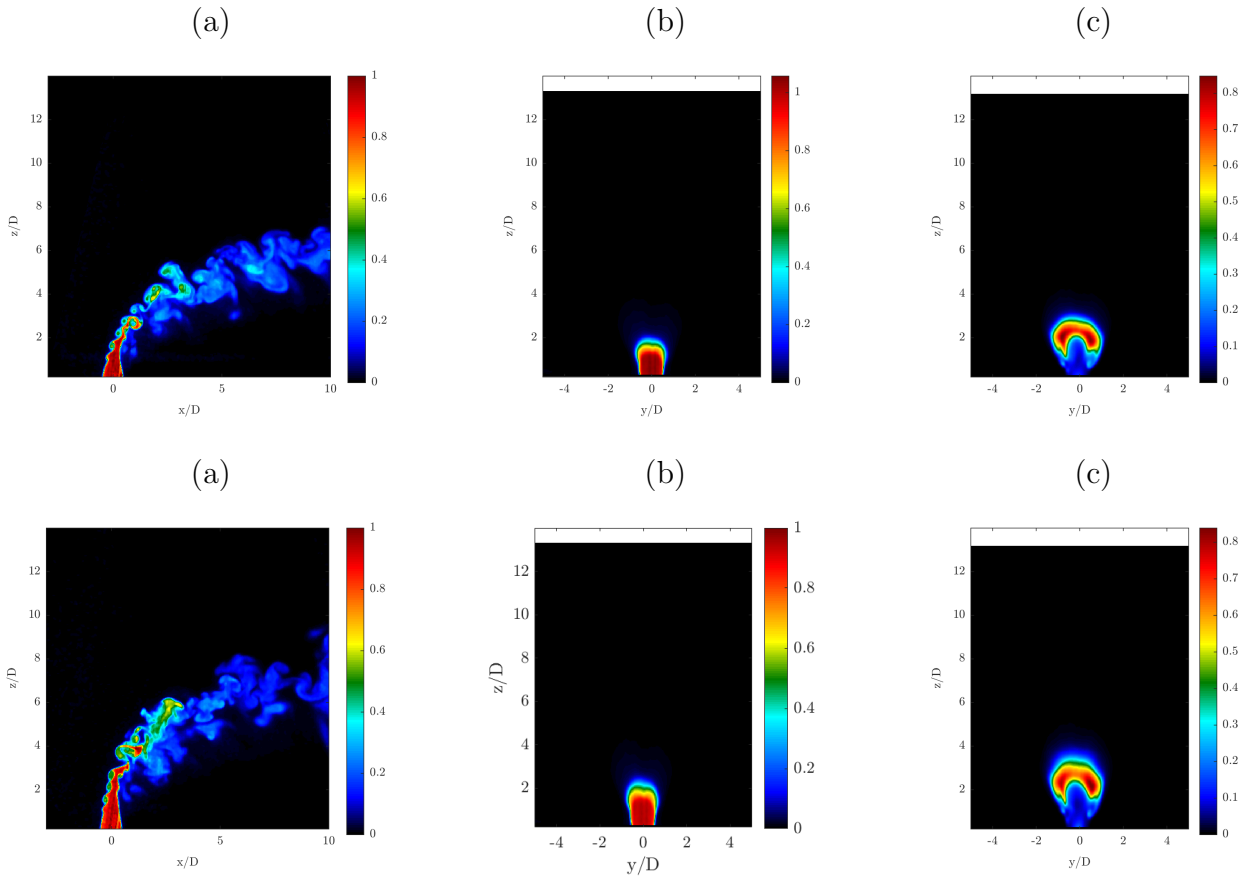

Figure 7.3: Representative structural PLIF images of the unforced AU jet at $J = 7$ and CU jet at $J = 10$, where (a) depicts the instantaneous centerplane of the jet, and (b-c) are mean cross-sectional slices of the jet at $x/D = 0.0$ and $x/D = 0.5$ respectively. The colorbar maximum for the cross-sectional images was individually scaled so as to allow quantitative comparisons with the scalar intensities noted in the jet centerplane.

downstream the jet in both cases had already developed the characteristic CVP, which for these relatively low momentum flux ratios was quite symmetric. These representative depictions of the jet served as reference for the changes to the structural features discussed for the various forcing conditions.

Figure 7.4 representatively depicts the jet evolution over a single forcing period for the

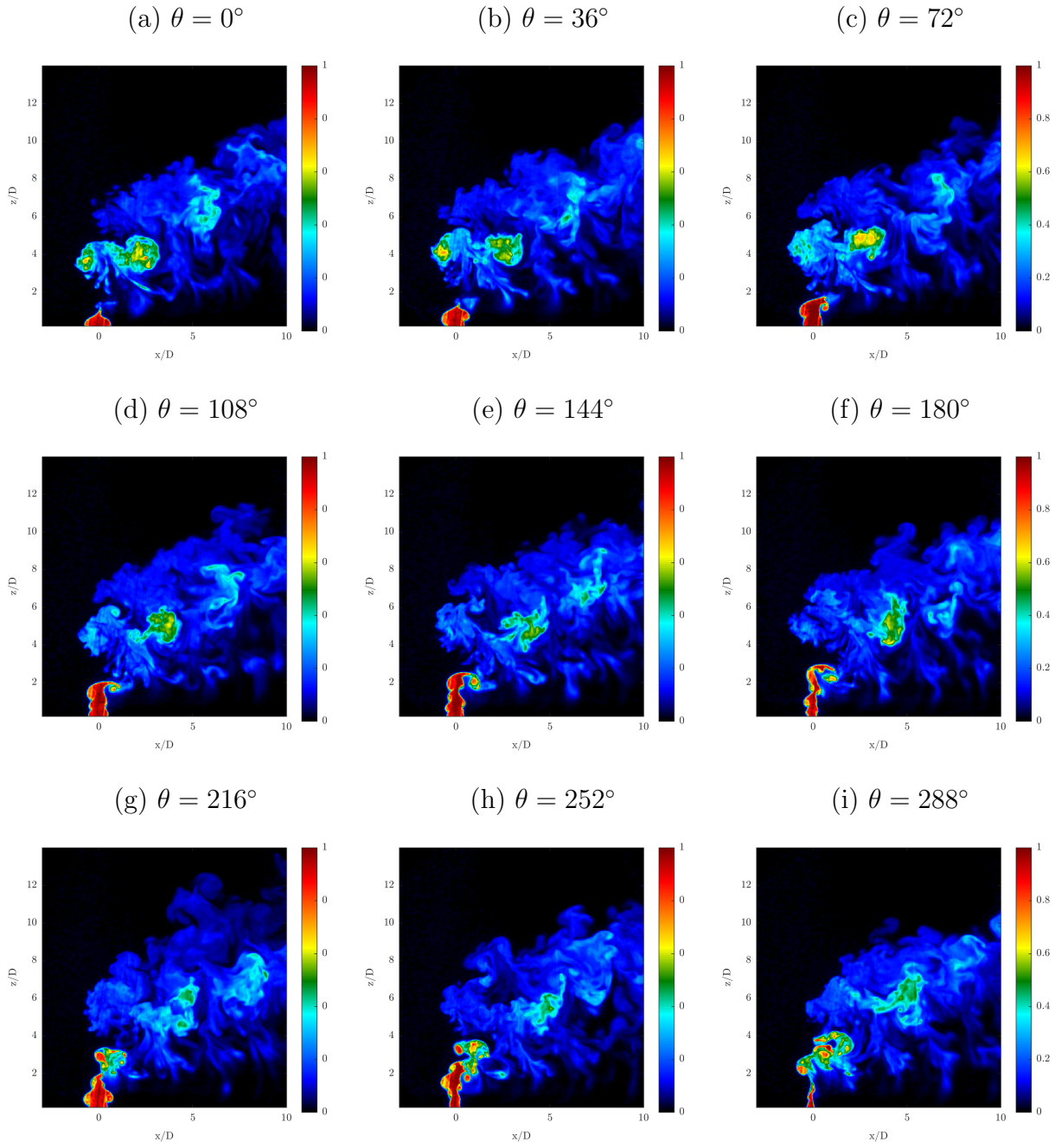

Figure 7.4: continues to following page

(j) $\theta = 324°$ (k) $x/D = 0.0$ (l) $x/D = 0.5$

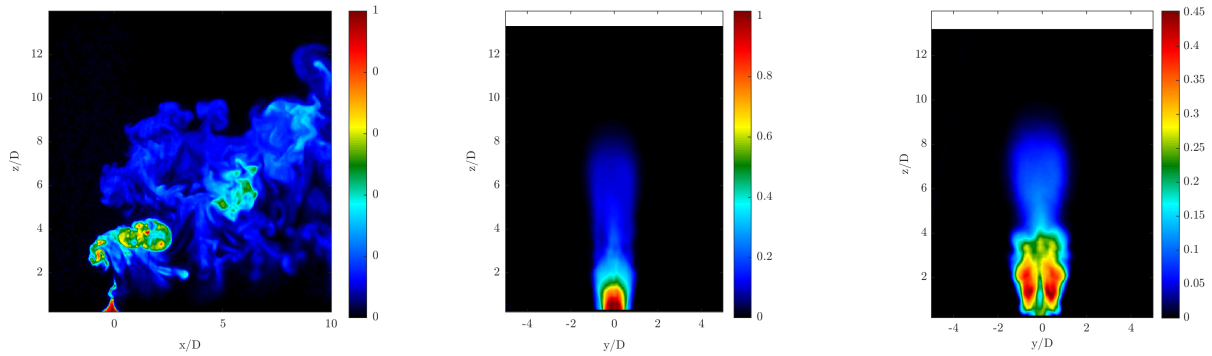

Figure 7.4: Representative structural PLIF images of the double-pulse forced AU jet at $J = 7$, for forcing case 0.45.55.70 where (a-j) depict the instantaneous centerplane phase progression for 1 forcing period at every $1/10T$, and (k-l) are mean cross-sectional slices of the jet at $x/D = 0.0$ and $x/D = 0.5$ respectively. The colorbar maximum for the cross-sectional images was scaled so as to allow quantitative comparisons with the scalar intensities noted in the jet centerplane.

double pulse forcing case of 0.45.55.70 applied to the AU case ($J = 7$), where the first image (figure 7.4(a)) was approximately at the initiation of the slow pulse, $\theta = 0°$. From figures 7.4(a-f) the slow pulse was seen to generate a vortex ring with a trailing column, which was most readily seen in figures 7.4(e-f), and was tilted downstream. The quick pulse, examined in figures 7.4(g-j), revealed the formation of a vortex ring without a distinct trailing column, which was instead tilted upstream. The qualitative characteristics of formation and tilting of the slow pulse and quick pulse vortex rings were consistent with the known behavior of isolated vortex rings in crossflow, and fully modulated JICFs, for their corresponding vortex ring regimes according to their calculated L/D and r_{ring} shown in figure 7.2 (Sau and Mahesh (2008); Sau and Mahesh (2010)). Additionally, while the slow pulse was mainly convected downstream, the quick pulse constituted the jet fluid which penetrated deeper into the flow-field. Regarding the penetration, Shusser and Gharib (2000) note that for an isolated vortex ring, as one increases the stroke ratio the vortex ring propagation velocity increases following

after a $U \sim \mathcal{O}(\Gamma^{3/2})$ order magnitude relation. However, for vortex rings in crossflow, Sau and Mahesh (2010) delineate that a vortex ring near the formation number would produce the best penetration as it maximizes the momentum of the vortex ring, and larger stroke ratios, which produce vortex rings with trailing columns, do not penetrate as deeply owing to nearfield interactions of the trailing column with the crossflow and subsequent vortical structures. Interestingly, Sau and Mahesh (2010) also comprehensively compile a number of experimental forced JICF studies, and in conjunction with DNS results, demonstrate that while the stroke ratio near the formation number should produce the best penetration, as the ring velocity ratio decreases and successive vortex rings are closer together, the forcing conditions producing the greatest overall penetration all collapse onto a single curve for stroke ratios below the ideal formation stroke ratio. Indeed it can be seen in figures 7.4(f-i) that as the quick pulse was formed, it propagated into the trailing column of the vortex ring for the slow pulse, and as compared with quick pulses for other forcing conditions wherein there was no significant interactions in the nearfield (see figure 7.6), did not penetrate as deeply. In addition to colliding with the trailing column of the slow pulse, the actual vortex rings also appeared to have a distinct collision in figures 7.4(h-j,a), where the downstream portion of the quick vortex ring, from convention having positive vorticity, collided with the upstream portion of the slow ring, which was of opposite sign. This effectively led to the breakdown of both vortex rings, and as such, this forcing case was referred to as one with clear vortex collisions. From the mean representations of the jet at $x/D = 0.0$ and $x/D = 0.5$ (figures 7.4(k-l)) it was seen that jet quite appropriately penetrated much deeper than the unforced jet, even in spite of the vortex collisions, where even at $x/D = 0.0$ the jet was already penetrating to almost $z/D = 8.0$. Interestingly, the jet still appeared to have some semblance of a CVP structure at $x/D = 0.5$, however the concentration distribution was distinctly different from that of the unforced jet (figure 7.3), where the resulting concentration appeared almost as two separate columns rather than one connected structure. Instead it was thought the mean image represented the side lobes of the vortex rings as they were produced and propa-

gated into the flowfield, and in support of this, it was noted the concentration dramatically decreased at about $z/D = 4.0$, where it was seen from the centerplane that the two vortex rings collided.

An additional forcing case for the jet at $J = 7$ is depicted in figure 7.5, representatively corresponding to conditions in which there were slight interactions between the vortex rings for the 0.35.60.75 double-pulse waveform. As with the depiction of the vortex collision case, the series of figures commenced approximately at the initiation of the slow pulse, $\theta = 0°$, where subsequent snapshots were at every 36° over a single forcing period. The temporal pulse width of the slow pulse was approximately $\tau_1/T = 0.40$, which corresponded to a vortex ring with a trailing column, as can be seen in figures 7.5(d-f). As with the slow pulse considered in the case of vortex collisions, the resulting vortex ring was tilted downstream, and relatively did not penetrate very deeply into the flowfield. Unlike in the case of the vortex collisions, when the quick pulse was formed, instead of colliding with upstream lobe of the main vortex ring, it cut directly through the trailing column and simply passed adjacent to the slow vortex ring (figures 7.5(g-j,a-c)). In interacting with the trailing column of the slow vortex ring, the downstream portions of the quick vortex ring significantly weakened, as evidenced from the scalar concentration in both the upstream and downstream portions of the vortex ring in figure 7.5(b). In accompaniment, the downstream wake of the jet was seen to have a greater presence of jet fluid near the wall boundary layer, possibly owing to the interaction of the vortex ring with the trailing column. However, due to the overall weakened interaction between the two vortex rings as compared with the vortex collisions, both rings were seen to have longer lifetimes and persisted further into the downstream, where in figure 7.5(j) the slow ring from the previous forcing period was visualized at $x/D \approx 5$ and $z/D \approx 7$, and the corresponding quick ring was at $x/D \approx 1$ and $z/D \approx 9$, though the quick ring was seen to completely propagate out of the FOV after enough time. In the cross-section (figures 7.5(k-l)), the mean jet structure depicted a region of high concentration close to the tunnel floor along with lower concentration which was deeply penetrated. Unlike the representative

(a) $\theta = 0°$ (b) $\theta = 36°$ (c) $\theta = 72°$

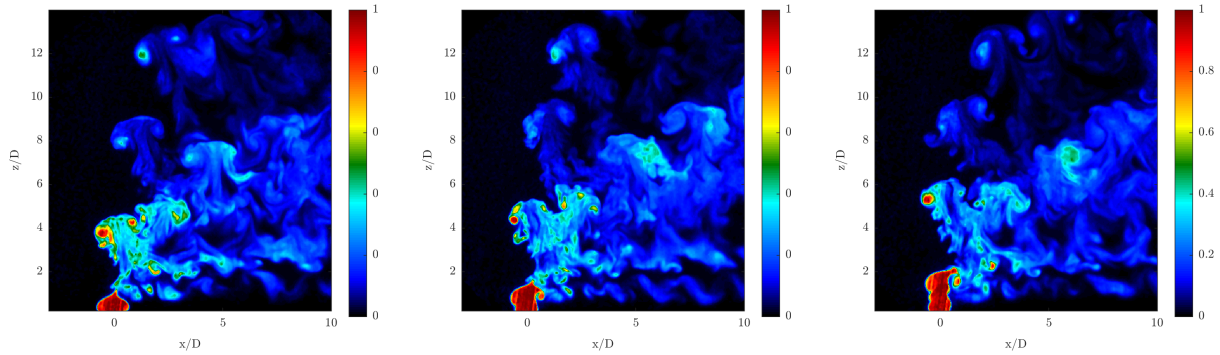

(d) $\theta = 108°$ (e) $\theta = 144°$ (f) $\theta = 180°$

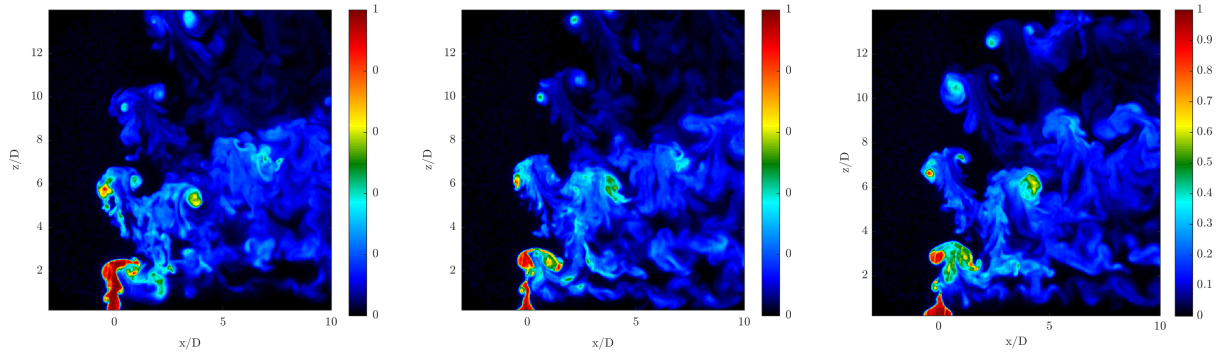

(g) $\theta = 216°$ (h) $\theta = 252°$ (i) $\theta = 288°$

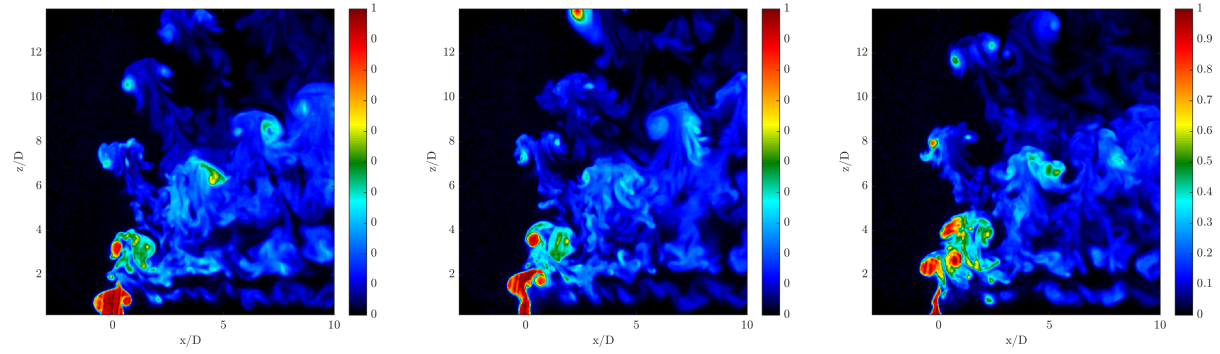

Figure 7.5: continues to following page

(j) $\theta = 324°$ (k) $x/D = 0.0$ (l) $x/D = 0.5$

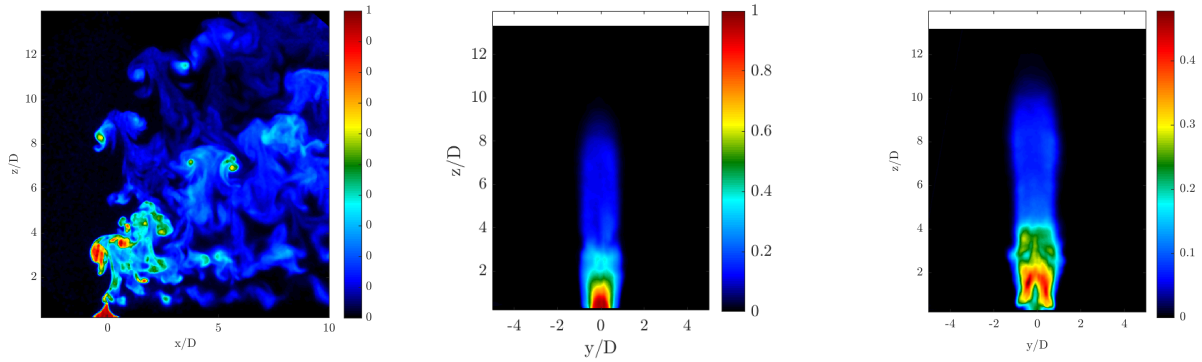

Figure 7.5: Representative structural PLIF images of the double-pulse forced AU jet at $J = 7$, for forcing case 0.35.60.75 where (a-j) depict the instantaneous centerplane phase progression for 1 forcing period at every $1/10T$, and (k-l) are mean cross-sectional slices of the jet at $x/D = 0.0$ and $x/D = 0.5$ respectively. The colorbar maximum for the cross-sectional images was scaled so as to allow quantitative comparisons with the scalar intensities noted in the jet centerplane.

vortex collisions case, the jet column was more slender at $x/D = 0.5$ and was penetrated almost two jet diameters deeper into the flowfield. These features were thought to arise from the weakened interaction between the vortex rings as compared to the vortex collision case, with knowledge that colliding vortex rings stretch and reorient in the lead up to collision (Chatelain et al. (2003); Kambe et al. (1993)), while also noting that Sau and Mahesh (2010) see distinct differences in the vortex ring stretching for ring-ring interactions vs ring-trailing column interactions.

The last representative case considered was one wherein the forcing conditions produced no significant interactions between successive vortex rings, shown in figure 7.6 for the 0.25.50.65 double-pulse waveform for the $J = 7$ jet. For this forcing condition, the temporal pulse widths of both the slow and quick pulses were matched at $\tau/T = 0.2$, where the resulting vortex rings, according to the regime map in figure 7.2, corresponded to vortex rings without a trailing column. In matching the temporal pulse width between the two

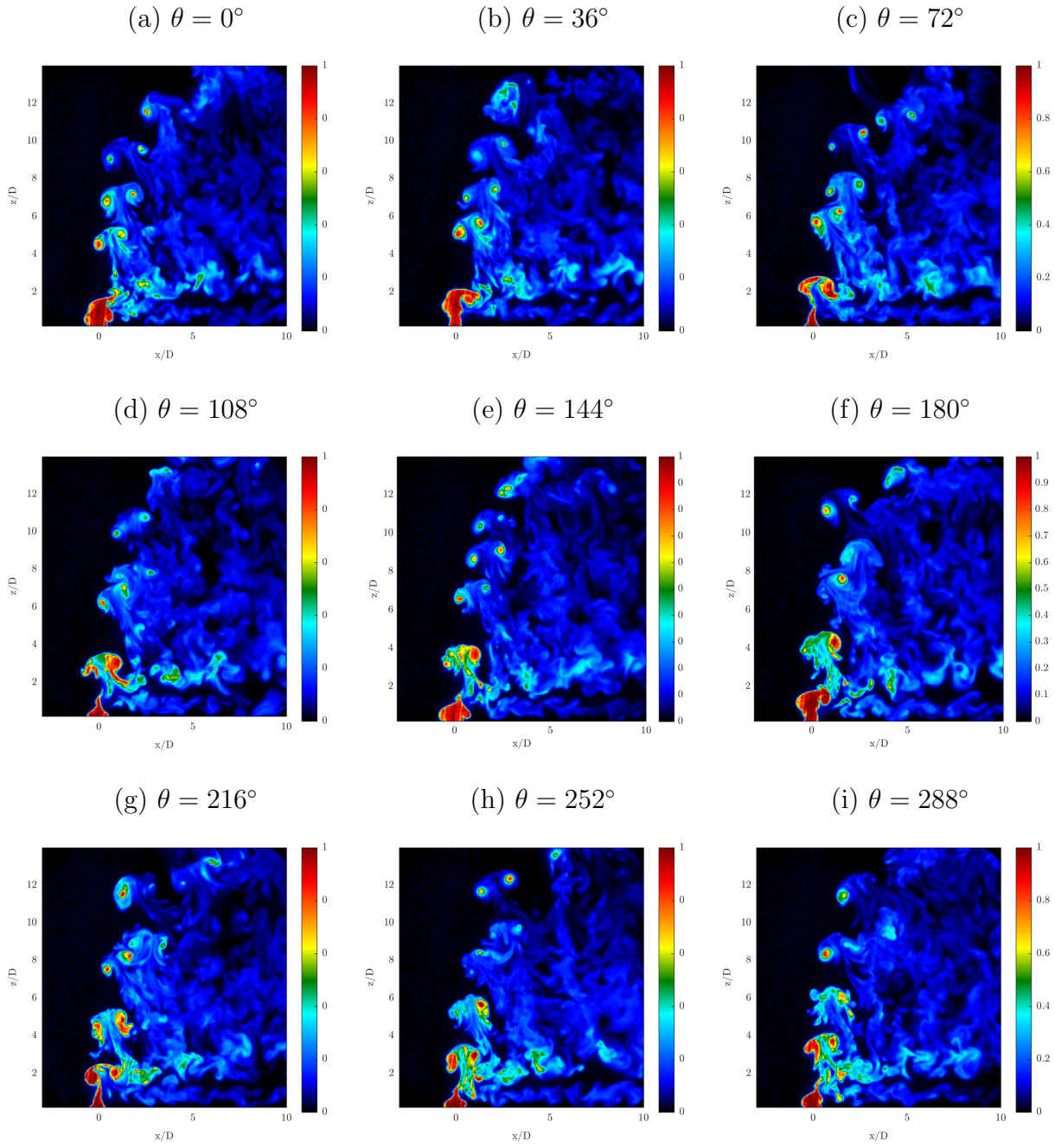

Figure 7.6: continues to following page

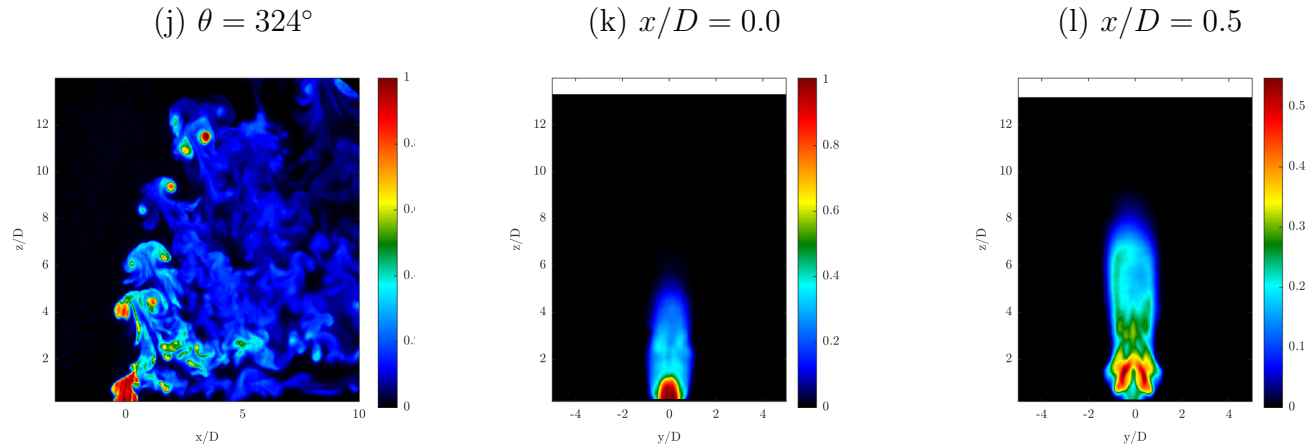

Figure 7.6: Representative structural PLIF images of the double-pulse forced AU jet at $J = 7$, for forcing case 0.15.40.55 where (a-j) depict the instantaneous centerplane phase progression for 1 forcing period at every $1/10T$, and (k-l) are mean cross-sectional slices of the jet at $x/D = 0.0$ and $x/D = 0.5$ respectively. The colorbar maximum for the cross-sectional images was scaled so as to allow quantitative comparisons with the scalar intensities noted in the jet centerplane.

pulses, the waveform was effectively square wave forcing at 110 Hz with a duty cycle of $\alpha = 30\%$, however the temporal spacing was such that they were not evenly distributed over a single forcing period, again in the hopes of promoting vortex interaction. The resulting quick and slow pulses formations are seen in figures 7.6(a-c) and 7.6(e-g) respectively, where in both cases the rings formed without a distinct trailing column and were tilted upstream. Given the lack of a trailing column, and sufficient spacing between the pulses, the vortex rings did not interact, and as a result propagated quite deeply into the flowfield. The jet fluid which appeared to follow after the slow vortex ring (figures 7.6(d-f)), visually similar to the noted trailing columns, was associated with the vortex ring passing through and entraining jet fluid which had been issued while the jet was not being pulsed, after the quick pulse from the preceding forcing period, noting a long "off" duration of $\Delta\tau_{2\to1}/T = 0.45$ of the forcing period and recalling that the jet was not quite fully modulated. The remaining jet fluid not constituting the 2 vortex rings appeared to stay quite close to the floor of the test

section even up to $x/D = 10$ downstream. Correspondingly, Sau and Mahesh (2010) notes from DNS that for the partially modulated JICF, the jet fluid which issues when the forcing waveform is not actively being pulsed lacks momentum, especially when contrasted with the high momentum carrying vortex rings, resulting in a highly bifurcated jet. For the mean cross-sectional representations of the jet (figures 7.6(k-l)) it was seen that again characteristics of a deeply penetrating jet were noted, as also seen for the vortex collisions and vortex interactions cases. Interestingly though, the concentration distribution at $x/D = 0.5$ (figure 7.6(l)) was distinctly higher in the penetrating portion of the jet structure, as compared with the preceding cases (figures 7.4(l) and 7.5(l)), which was associated with the vortex rings retaining their strength and carrying more jet fluid deeper into the flowfield. Additionally, the jet appeared to maintain a small CVP-like structure, though the penetration of this feature was less than the noted CVP in the unforced jet (figure 7.3(c)). It was thought that the jet fluid which issued when the jet was not pulsing may have been at a low enough momentum to possibly result in hairpin like structures near the jet wall, thus producing a CVP-like structure with low penetration in the jet cross-section. Further investigation is needed to explore these flow features.

Table 7.3 lists the various types of vortex ring collisions, interactions, or lack thereof which were visually distinguished for the different double-pulse forcing conditions, while the stroke ratio of the slow pulse and the temporal spacing between the pulses were systematically varied, for both the AU and CU unforced jets at $J = 7$ and $J = 10$, respectively. Quite importantly, as the momentum flux ratio was decreased, corresponding to an increase in the crossflow velocity, the interactions for a given waveform appeared to be strengthened, in some cases going from interactions between the rings or the ring and trailing column, to actual collisions of the rings. This shifting in the interactions between the rings was attributable to the noted change in the ring velocity ratio, recalling from figure 7.2 that going from $J = 10$ to $J = 7$ corresponded to a change in r_{ring} of approximately 16%, which in turn resulted in the vortex rings being more fully filled or with larger trailing columns depending upon

Forcing Case	$J = 7$	$J = 10$
0.45.70.85	Collision	Interaction
0.45.60.75	Collision	Interaction/Collision
0.45.55.70	Collision	Collision
0.35.60.75	Interaction	Interaction
0.35.50.65	Interaction	Interaction
0.35.45.60	Interaction	Interaction
0.25.50.65	Interaction/Collision	Interaction/Collision
0.25.40.55	Collision	Interaction/Collision
0.25.35.50	Collision	Interaction/Collision
0.15.40.55	No Interaction	No Interaction
0.15.30.45	Interaction/Collision	Interaction
0.15.25.40	Collision	Collision

Table 7.3: Test matrix of the various double-pulse forcing waveforms generated from a Fourier series of $f_f = 55\ Hz + 14$ higher harmonics, while matching the RMS of the jet velocity perturbation both temporal pulses at $u'_{j,rms} = 2.0\ m/s$. The temporal pulse widths of the first and second square wave pulses are defined by their duration normalized over a single forcing period. Respective temporal spacing between the two pulses is also normalized by the forcing period.

their originating vortex ring regime. Adding to the jet trailing column is noted to produce a slower moving vortex ring which does not penetrate as deeply, while an underfilled vortex ring which is made fuller, approaching a fully filled vortex ring, in the absence of another vortex ring preceding it, will actually propagate faster and penetrate deeper owing to the ring having more momentum (Sau and Mahesh (2010)). Thus, in decreasing the momentum flux ratio, the slow vortex rings were made slower, with exception for the $\tau_1/T = 0.20$ cases which did not have trailing columns, and the fast pulses were made faster, thereby enhancing the vortex ring interactions and/or collisions. For a fixed momentum flux ratio,

as the temporal pulse width of the slow pulse was systematically decreased, it was found that the vortex ring interactions became weaker. Again, this was attributable to the effect of the trailing column, whereby decreasing the pulse width produced smaller trailing columns, which promoted faster and deeper propagation of the vortex ring, that effectively helped separate the slow pulse from the ensuing quick pulse. Additionally, it was seen for all of the slow pulse temporal pulse widths considered, that as the temporal spacing between the slow pulse and the quick pulse was enlarged, the effective vortex ring interactions were weakened as the larger temporal spacing yielded greater physical separation of the pulses.

7.1.3 Mixing Quantifications

The effective mixing between the jet and crossflow was evaluated from the perspective of two historically utilized mean metrics of jet vertical spread and penetration, along with a molecular mixing quantification based on the instantaneous unmixedness parameter, all of which were determined from the scalar PLIF images in the jet centerplane. Given that the enhancement of spread and penetration have recently been shown for the JICF to not necessarily be correlated with enhanced mixing of the jet (Shoji et al. (2019); Shoji et al. (2020a)), they were still treated here for further validation of this finding, as well as serving as quantitative measurements of the structural features of the jet. Determination of the spread and penetration was based on the bounding region of the jet as defined by the 3% threshold of the jet concentration normalized by the concentration in the jet core. Calculating the unmixedness, which as noted earlier represents the second moment of the scalar concentration field, was performed with equation 1.8. Recall that lower unmixedness corresponds to better molecular mixing. For each of these evaluations of the flow the validity became unreliable after approximately $x/D = 5.0$ because certain jet forcing cases were found to propagate out of the FOV captured in the PLIF images. However, the main interest of the double-pulse forcing was actually with regard to the nearfield evolution of the jet, and in fact very informative trends were still found over this nearfield region of the developing flow.

(a) Spread

(b) Penetration

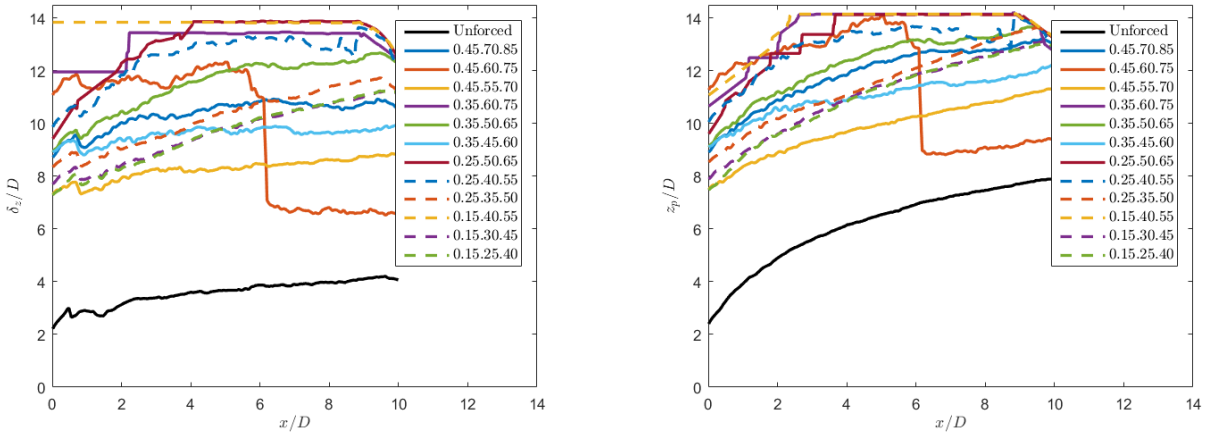

(c) Unmixedness

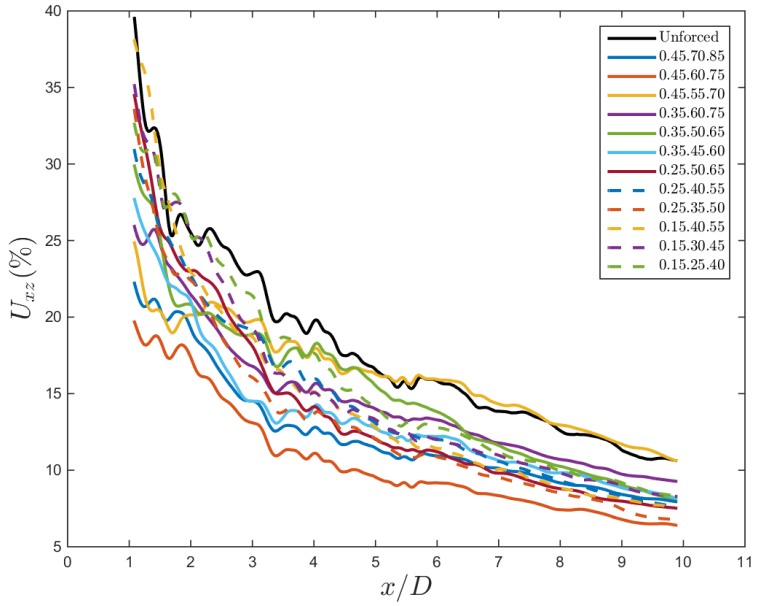

Figure 7.7: Mean and instantaneous quantifications of mixing of the JICF at $J = 7$ for a variety of double-pulse forcing cases. In the mean the (a) jet vertical spread, δ_z/D, and (b) jet penetration, z_p/D, were established based on a 3% threshold of the jet concentration normalized by the concentration of the jet core. Instantaneous mixing (c) was quantified for the downstream evolution of centerplane unmixedness U_{xz}.

Shown in figure 7.7 are the spread, penetration, and unmixedness for the AU jet at $J = 7$. For figures 7.7(a-b), it was seen that forcing cases wherein there interactions between the vortex rings were minimal, or did not exist as for the isolated case of 0.15.40.55, resulted in the best spread and penetration of the jet. Likewise, cases wherein strong vortex collisions were noted generally resulted in lower overall spread and penetration of the jet. Enlarging the temporal spacing between the slow and quick pulse for all slow pulse temporal pulse widths, with one noted exception, acted to systematically increase the penetration of the jet, quantitatively in agreement with the structural trends discussed in section 7.1.2. The lone exception was for the slow temporal pulse width of $\tau_1/T = 0.50$, where increasing the temporal spacing of the quick pulse following after the slow pulse, $\Delta\tau_{2\to1}/T$, cut the spacing between the quick pulse and the slow pulse of the following temporal forcing period, $\Delta\tau_{2\to1}/T$. This effectively still resulted in inducing vortex interactions for case 0.45.75.85, and thus did not enhance the penetration as much as the more balanced temporal spacing given in case 0.45.60.75. The noted drop in penetration for this latter case at $x/D \approx 6.0$ was due to the concentration intensity in the quick pulse dropping below the 3% threshold as a result of the mixing and entrainment processes of the ring. Though clear trends were distinguishable for the jet penetration, the jet spread was far less intuitive. Given that the jet spread was quantified from the lowest point to the highest point within the flowfield where jet fluid was present, this metric did not account for possible bifurcations of the jet, which could have led to regions which did not contain any jet fluid. Indeed, nearly all of the forcing conditions considered wherein there was not a distinct vortex collision were found to bifurcate the jet. Thus quantifications of jet spread were influenced by competing factors of jet bifurcation as well as enhancment of the overall jet penetration. In all cases the jet spread and penetration was significantly enhanced over that of the unforced jet.

For the quantifications of molecular mixing, shown in figure 7.7(c), it was found that all forcing cases enhanced the overall mixing as compared with the unforced jet, with the greatest effect being noted in the nearfield, while further downstream the unforced jet began

to converge upon the forced conditions. This trend further downstream is seen for other forced JICF experiments as well (Shoji et al. (2019); Shoji et al. (2020a); Besnard (2019)), and is simply a result of all jet conditions becoming well mixed. As expected, and quite importantly, forcing conditions which resulted in the best spread and penetration did not necessarily correspond to the best molecular mixing. Interestingly, the best molecular mixing was noted for the 0.45.60.75 forcing case, which had the largest slow pulse temporal pulse width investigated, $\tau_1 = 0.50$, producing a dominant jet trailing column. Additionally, as the temporal pulse width of the slow pulse was systematically decreased, the enhancement in mixing generally was decreased as well, where the overall worst mixing was seen for the forcing cases where both pulses were at $\tau/T = 0.2$, corresponding to vortex rings without trailing columns. This agreed with Sau and Mahesh (2008), who note that vortex rings with trailing columns actually mix more than a fully filled or underfilled vortex ring owing to the enhanced downstream entrainment of the trailing column. However, when examining all of the forcing cases wherein the slow temporal pulse width was $\tau_1 = 0.50$, dramatically different enhancements to the molecular mixing were seen, where the 0.45.55.70 case was actually the worst mixed, and even eventually converged with the unforced jet unmixedness. This illustrated a dramatic feature, that in addition to the type of vortex ring which was generated, careful care needed to be made with regard to the nearfield vortex ring interactions generated.

Figure 7.8 gives the spread, penetration, and molecular mixing for the same forcing conditions explored with the AU jet at $J = 7$, except now applied to the CU jet at $J = 10$. Looking at the spread and penetration (figures 7.8(a-b)) again resulted in similar trends as seen for the $J = 7$ jet, where as the temporal pulse width of the slow pulse was decreased and the temporal spacing enlarged, thus mitigating the nearfield vortex interactions, the jet penetration and spread were significantly enhanced over that of the unforced jet. Contrasting with the $J = 7$ cases (figures 7.7(a-b)), the forced jets generally appeared to penetrate deeper for the $J = 10$ jet at a fixed downstream location, which was expected given that the unforced

(a) Spread

(b) Penetration

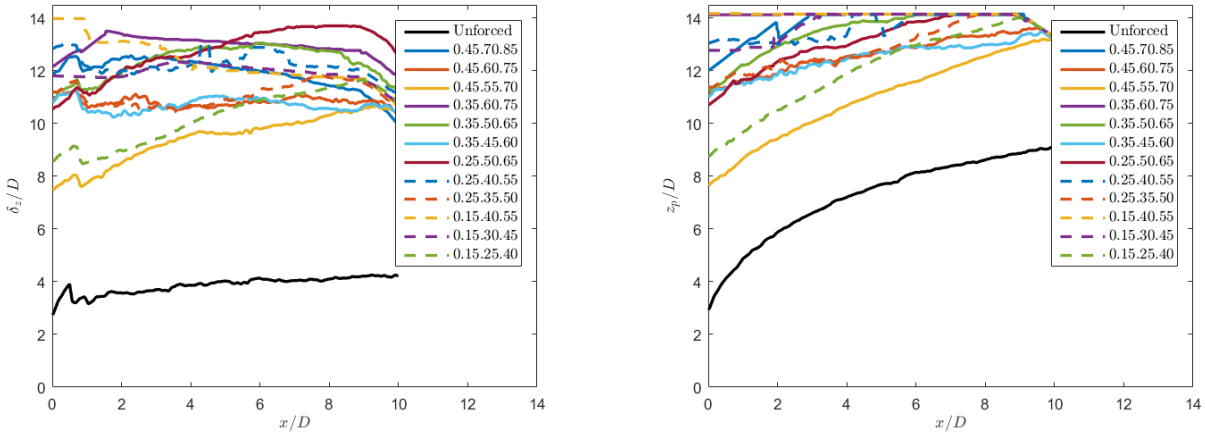

(c) Unmixedness

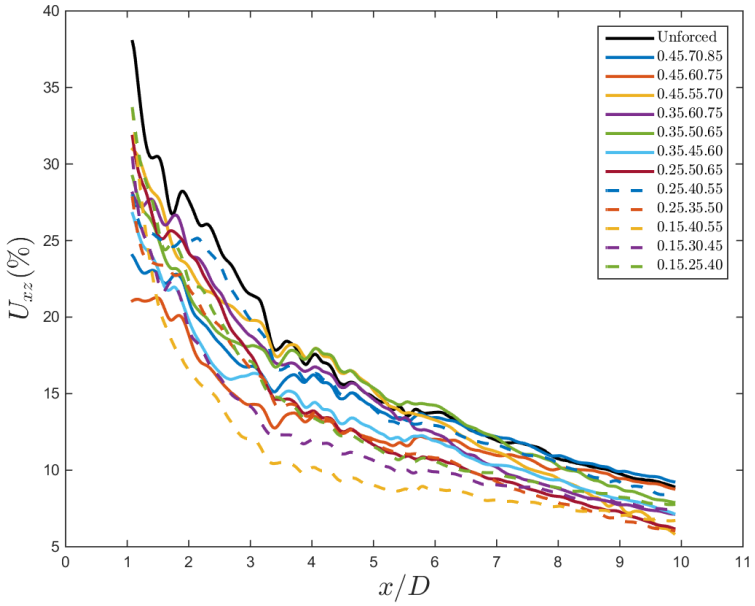

Figure 7.8: Mean and instantaneous quantifications of mixing of the JICF at $J = 10$ for a variety of double-pulse forcing cases. In the mean the (a) jet vertical spread, δ_z/D, and (b) jet penetration, z_p/D, were established based on a 3% threshold of the jet concentration normalized by the concentration of the jet core. Instantaneous mixing (c) was quantified for the downstream evolution of centerplane unmixedness U_{xz}.

jet was less bent over, and the ring velocity ratios were stronger for the issuing vortex rings as a result of the weakened crossflow velocity. In examining the molecular mixing of the jet in figure 7.8(c), the enhancement of the mixing over the unforced jet was not as dramatic as was noted for forcing of the $J = 7$ jet, noting that the unmixedness convergence downstream was even more prominent at $J = 10$. The best molecular mixers were given as the 0.15.40.55 and 0.15.30.45 forcing cases, however both of these conditions had jet fluid which penetrated out of the FOV very early on in the jet evolution, and thus are not reliable quantifications of their mixing. Remarkably, even in accounting for these cases, the forcing conditions which resulted in the best molecular mixing of the jet were not the same as those which were determined for the $J = 7$ jet. Instead, forcing cases with a slow pulse temporal pulse width of $\tau_1/T = 0.30$, distinguished by a vortex ring with a very small trailing column, produced the best molecular mixing. From the jet structural characteristics in table 7.3, these cases corresponded to where the jet had relatively strong interactions between the slow and quick vortex rings, again suggesting the importance of the vortex ring interactions as a parameter of consideration. Again however, more clear cut trends between the type of vortex ring, the degree of nearfield vortical interaction between vortex rings, and the resulting implication on mixing were difficult to quantify as direct measurements of the vorticity field were not made. The following chapter investigates this in greater detail through simultaneous PLIF/PIV measurements of the flowfield, wherein only a couple temporal pulse widths are considered, and the temporal spacing is varied significantly so as to more directly compare the influence of the vortical interactions.

7.2 Discussion

The present experimental study documented the effects of active passive control of a jet in crossflow via a novel double-pulse forcing waveform, wherein two distinct temporal pulses were generated during a single forcing period. Effects on jet structure and mixing were

quantified. The study extended the flow regime and geometrical parameter space examined in previous works on forced jets in crossflow, taking advantage of more recent observations regarding the dynamics of single vortex rings in crossflow, and vortex interactions between multiple vortex rings in crossflow for optimization of a forced jet in crossflow (Sau and Mahesh (2008); Sau and Mahesh (2010)). These dynamics were explored for both a transitionally convectively/absolutely unstable jet ($J = 10$), and a jet which was clearly absolutely unstable ($J = 7$). The application of a double-pulse waveform excitation was seen to dramatically improve mixing and alter the resulting jet structure regardless of the flow regime.

Despite the different instability characteristics of the unforced flows, overall resulting instantaneous and mean jet structures, along with mixing quantifications were quite similar for the convectively and absolutely unstable flowfields. However, relative differences were noted between the regimes for a particular forcing waveform, as a result of the relative changes in the oncoming crossflow, which was seen to alter the ring velocity ratio and formation number for a fully filled vortex ring (Sau and Mahesh (2008)). The slow pulses generated a fully filled vortex ring with a trailing column of jet fluid, while the quick pulse formed a vortex ring which was nearly fully filled. The resulting rings had different celerities, where the ring without a trailing column propagated faster than the trailing column ring, and allowed for the nearly filled ring to catch up to and interact with the trailing column ring. Selective temporal spacing of the quick pulse after the slow pulse produced cases in the nearfield of vortex collision and breakdown, slight interaction, or no significant interaction at all. Mixing quantifications suggested cases where there was nearfield collision produced the greatest enhancement in molecular mixing for the transitionally convectively/absolutely unstable jet. However, for the absolutely unstable jet, cases which produced two nearly fully filled vortex rings which did not interact, somewhat similar to simple square wave excitation, actually produced the greatest enhancement in mixing, followed by the case in which there was nearfield vortex collision between the nearly fully filled ring and the trailing column ring. These unique differences for the absolutely unstable jet are explored further in the following

chapter.

CHAPTER 8

Forcing Dynamics

8.1 Results

8.1.1 Waveform Generation and Synchronization

The flow conditions generated in the synchronization experiments were changed from those which were treated in the prior chapter (7), which dealt similarly with axisymmetric excitation of an AU and CU jet flow, to allow for simultaneous PLIF and particle image velocimetry (PIV) measurements of the excited JICF. The resulting flow was investigated at $\psi = 0.112$, $S = 1$, $Re_j = 1800$, and $J = 6$, with $U_j = 3.42\ m/s$, where the acetone mole fraction was lowered due to constraints in the flow setup with the imaging techniques utilized in the PLIF/PIV work. Accompanying the change in the flow conditions were alterations in the USL instability characteristics, a known effect for the JICF which arises as the constituent species and flow properties are varied (Shoji et al. (2020b)). Figure 8.1 depicts the spectral contour plot of the USL instabilities for this lower acetone mole fraction flow condition. The dominant instability of the jet was located at $St \approx 0.83$, $f_0 = 375$, with characteristics which were quite representative of an AU flow, having a pure-toned peak without any tonal interference, corresponding peaks at higher harmonics, and lacking a spectral peak in the subharmonic regime. Interestingly, when comparing these instabilities with the spectral content for the $J = 7$ AU jet with $\psi = 0.218$ (figure 7.1(c)), despite lowering the momentum flux ratio slightly, the lower acetone mole fraction case overall yielded a less sharp dominant instability and weaker content at the higher harmonics. In addition, the dominant instabil-

ity frequency decreased from $f_0 = 540\ Hz$, with $J = 7$ and $\psi = 0.218$, to $f_0 = 375\ Hz$, with $J = 6$ and $\psi = 0.112$. The decrease in the dominant instability frequency was due to the slightly lowered momentum flux ratio and the decrease in acetone mole fraction while maintaining all other flow conditions, and is similarly seen for the smaller flush nozzle JICF as well (Shoji et al. (2020b)).

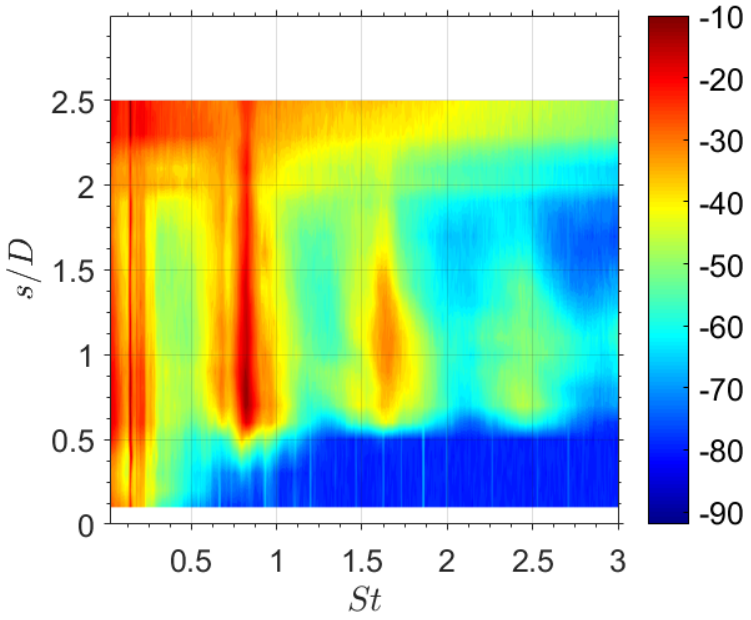

Figure 8.1: Power spectra of the upstream shear layer instabilities for the equidensity large ($D = 7.59\ mm$) flush nozzle-injected JICF with acetone mole fraction of $\psi = 0.112$, jet Reynolds number of $Re_j = 1800$, and jet velocity of $U_j = 3.42\ m/s$ at a momentum flux ratios of $J = 6$.

8.1.1.1 Experimental Lock-In

The lock-in characteristics of the AU jet were first investigated for simple square wave excitation at the forcing frequency of 55 Hz and a duty cycle of $\alpha = 30\%$. Generation of the waveforms consisted of the same procedural development as outlined for the double-pulse forcing in section 6.2.2. To investigate the impact of the number of harmonic terms utilized

in the Fourier series, the original 15 term waveform along with truncated 2, 5, and 10 term waveforms were generated and compared against simple sinusoidal excitation at $f_f = 55\ Hz$ and $f_f = 110\ Hz$. These two frequencies were considered due to the methodology by which the square wave and double-pulse forcing were generated, where the forcing period was based on $f_f = 55\ Hz$, but within a single forcing period two distinct square wave pulses were generated. So, if the two pulses were matched and evenly spaced temporally, the waveform would have been identical to square wave forcing at $f_f = 110\ Hz$, and thus the additional sinusoidal forcing at 110 Hz was also considered. To determine whether the flow was locked-in (LI), quasiperiodic (QP), or possibly not significantly responding (NR) to the forcing at all, the power spectral density (PSD) plots were analyzed and phase portraits were visually interpreted, both of which were extracted from the time series of vertical velocity fluctuations in the shear layer of the jet as measured by the hotwire anemometer. In the phase space, a dynamical feature at a single instant in time is represented by a single point, whereas as time $t \to \infty$ and multiple physical states are recast into the phase space, a trajectory is created representing the time evolution of the dynamics. Thus, the topology of the phase portrait was indicative of the type of attractor the shear layer dynamics represented. The lowest applied excitation was at a normalized perturbation magnitude of $u'_{j,rms}/U_j = 2\%$, where any smaller input excitation became contaminated with the noise floor of the hotwire and made waveform convergence difficult. The excitation amplitude was systematically increased at increments of $\Delta u'_{j,rms}/U_j = 5\%$ to a maximum input of $u'_{j,rms}/U_j = 16\%$, whereupon the jet was able to lock-in to nearly all waveforms considered, including sinusoidal excitation. While convergence of the waveforms and determination of the excitation amplitude were measured by the hotwire placed at $z/D = 0.1$ centered above the jet exit, the hotwire was placed further downstream of the jet exit plane along the jet's shear layer based trajectory at $s/D = 1.5$ for the subsequent measurements regarding the synchronization characteristics.

Figure 8.2 depicts PSD plots and phase portraits for representative cases of NR, QP, and transitional QP/LI behavior for sinusoidal forcing of the jet at 55 Hz, and LI behavior

(a) (b)

NR: No Response

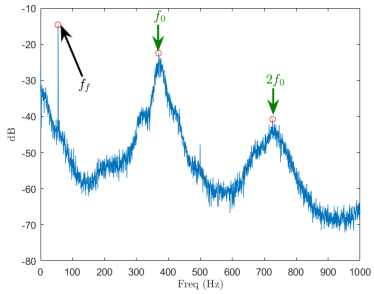

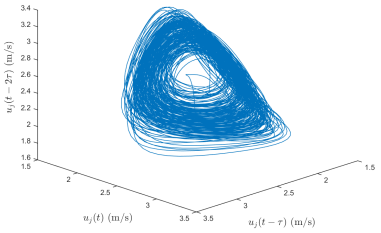

(c) (d)

QP: Quasiperiodic

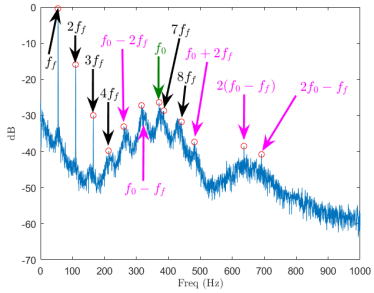

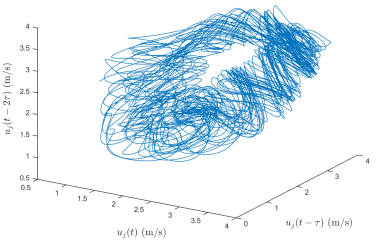

(e) (f)

Transitional

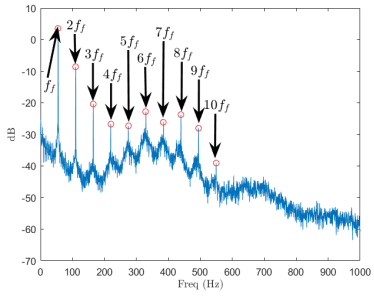

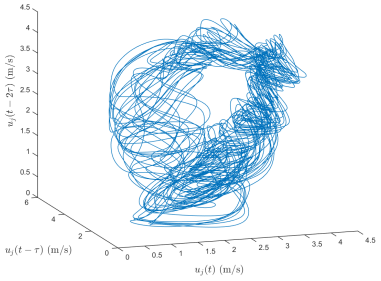

Figure 8.2: continues to following page

(g) (h)

LI: Locked-In

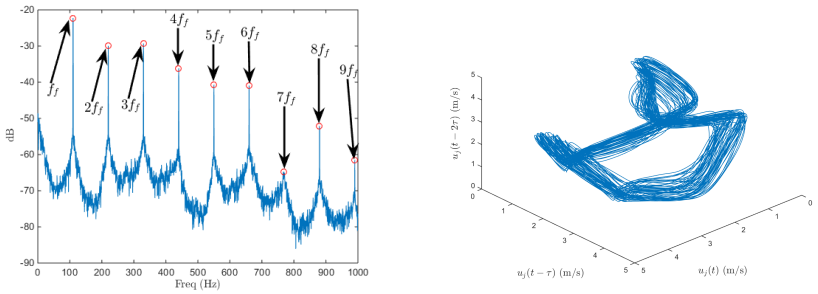

Figure 8.2: Representative PSD plots and phase portraits of the upstream shear layer vertical velocity at $s/D = 1.5$ when the jet exhibits (a-b) no response to the forcing, NR, (c-d) quasiperiodicity, QP, (e-f) transitional behavior between QP and LI, and (g-h) locking-in to the forcing, LI. PSD plots have the spectral peaks labeled in black for the forcing frequency and higher harmonics, green for the fundamental instability frequency and higher harmonics, and pink for linear combinations of the two frequencies.

of the jet for sinusoidal forcing at 110 Hz. As a baseline reference, in the absence of any forcing, the spectral characteristics were exactly those which were depicted in the spectral contour plot (figure 8.1) at $s/D = 1.5$. For sine wave forcing at 55 Hz with an excitation amplitude of $u'_{j,rms}/U_j = 2\%$, wherein there was NR of the jet to the applied forcing, the PSD plot (figure 8.2(a)) depicts characteristics nearly identical to the USL spectra without any forcing, though there was an additional less dominant isolated pure-toned spectral peak at the forcing frequency of 55 Hz. The corresponding phase portrait (figure 8.2(b)) depicted a typical closed loop trajectory in the phase space which was indicative of a simple limit cycle attractor, as was to be expected for an AU flow with a strong singular instability frequency along the USL of the jet. As the forcing was increased slightly, cases of QP behavior arose, which in the PSD (figure 8.2(c)) were characterized by spectral peaks of competing strengths at both the fundamental instability frequency and the forcing frequency. In addition, the spectra contained peaks at different linear combinations of the two dominant frequencies. In

the phase portrait (figure 8.2(d)), QP took the appropriate form of a torus-like loop, where the phase trajectory was a non-repeating non-intersecting closed path representative of the coupling between the two dominant frequencies. Interestingly, with a slight increase in the forcing amplitude to $u'_{j,rms}/U_j = 16\%$, according to the PSD (figure 8.2(e)), the jet appeared to be LI to the forcing, where no trace of the fundamental instability frequency was present. However, in the phase portrait (figure 8.2(f)), there was a portion of the trajectory which still depicted torus-like behavior. In contrast, sinusoidal forcing at 110 Hz at the same forcing amplitude of $u'_{j,rms}/U_j = 16\%$, was found to LI the jet to the forcing. In the PSD (figure 8.2(g)) the jet shear layer completely forewent the natural instabilities and was solely characterized by the forcing frequency and its higher harmonics. In the phase portrait (figure 8.2(h)), the trajectory again had a closed loop path, characteristic of a limit cycle attractor, which indicated a singular dominant frequency along the shear layer. These general traits illustrated in these representative PSD plots and phase portraits served as indicative markers of whether the jet USL was LI, QP, or displayed NR to the other waveforms and forcing amplitudes investigated.

Forcing Amplitude	0.02	0.029	0.044	0.058	0.073	0.088	0.102	0.117	0.132	0.146	0.161
Sine											
55 Hz	NSR	NSR	QP	QP	QP	QP	QP	QP	QP	QP	QP
110 Hz	QP	QP	QP	QP	QP	QP	LI	LI	LI	LI	LI
Fourier Input											
$\alpha = 30\%$, 2 terms	NSR	NSR	QP	QP	QP	QP	QP	QP	QP	LI	LI
$\alpha = 30\%$, 5 terms	QP	QP	QP	QP	QP	LI	LI	LI	LI	LI	LI
$\alpha = 30\%$, 10 terms	QP	QP	LI	LI	LI	LI	LI	LI	LI	LI	LI
$\alpha = 30\%$, 15 terms	QP	QP	LI	LI	LI	LI	LI	LI	LI	LI	LI
$\alpha = 50\%$, 15 terms	LI	LI	LI	LI	LI	LI	LI	LI	LI	LI	LI
0.35.65.80, 15 terms	LI	LI	LI	LI	LI	LI	LI	LI	LI	LI	LI

Table 8.1: Tabulation of synchronization characteristics for the JICF with $J = 7$ at $Re_j = 1800$ and $\psi = 0.112$ as forcing amplitude is systematically increased for forcing cases of: sine wave at 55 Hz and 110 Hz, uncompensated square waves from a function generator at 110 Hz with duty cycles of $\alpha = 30\%$ and $\alpha = 50\%$, Fourier generated square waves at at 110 Hz and $\alpha = 30\%$ for various number of terms, Fourier generated square wave at at 110 Hz and $\alpha = 50\%$ with 15 terms, and a double pulse forcing case with a base frequency of $f_f = 55$ Hz generated by a 15 term Fourier series. The forcing amplitude, $u'_{j,rms}$, is normalized by the mean jet velocity of $U_j = 3.42$ m/s.

Table 8.1 lists the type of synchronization characterized in the USL of the jet, as determined from analysis of PSD plots and inspection of phase portraits, for a variety of forcing waveforms and sweeping over forcing amplitudes from $u'_{j,rms}/U_j = 2\%$ to $u'_{j,rms}/U_j = 16\%$. Immediately noticeable is that sinusoidal forcing applied at $f_f = 110\ Hz$ locked-in the jet shear layer much earlier than the sinusoidal forcing at $f_f = 55\ Hz$, which agreed with the trends found by Shoji et al. (2020c) for the JICF under different flow conditions, whereby forcing closer to the fundamental instability of the jet was easier to lock-in than frequencies further away. In treating the square wave excitation of the jet, it became clear that systematically increasing the number of Fourier series harmonic terms in the waveform formation acted to enhance the progression to lock-in, significantly reducing the forcing amplitude required to achieve lock-in for the square wave with a duty cycle of $\alpha = 30\%$. Comparison between the 5 term and 10 term square waves, wherein the former was composed of harmonics all below the fundamental frequency of the jet, and the latter had terms both above and below, demonstrated that the 10 term square wave only required half as much input energy as the 5 term signal in order to lock-in the jet. This was suggestive that the enhanced ability to lock-in the jet was particularly due to the lock-in characteristics of the harmonics which were close to the fundamental instability of the jet, which as Shoji et al. (2020c) demonstrates lock-in more easily. Interestingly, for the two term Fourier composition of the $\alpha = 30\%$ duty cycle square wave excitation which was composed of sinusoids at 55 Hz and 110 Hz, the waveform was actually harder to lock-in than the sine wave forcing at 110 Hz, though easier than the sine wave forcing at 55 Hz. This would suggest that while the two term square wave was composed of these two sinusoid signals, their influence on the lock-in of the approximated square wave was not simply a linear combination of their individual behaviors, though greater investigation regarding this is needed. The number of terms was then increased to that which was utilized to compose the double-pulse forcing waveforms, and with the inclusion of 15 waveforms for the $\alpha = 30\%$ square wave, almost immediate lock-in to the forcing frequency was noted at an amplitude of $u_{j,rms}/U_j \approx\ 0.044$, which was

about 25% of the amplitude that was required for the sinusoidal waveform at $f_f = 55\ Hz$, or about 43% of that for sinusoidal forcing at 110 Hz. Even more interesting, was the noted differences in lock-in as the 15 Fourier series waveform was changed from a 30% duty cycle square wave to a 50% ducty cycle or a double-pulse forcing case of 0.35.65.80. These other waveforms were locked-in at the lowest forcing amplitude able to be applied, which was relatively much lower than the lock-in for the 30% duty cycle case, and again suggested that while each of these waveforms was composed of the same Fourier terms, their respective individual component amplitudes and the nonlinear interactions between them was significant to the jet synchronization behavior. These findings helped to inform upon and explain the noted differences of an absolutely unstable JICF in response to sine wave and square wave excitation of the jet, where significant alteration of the jet structure is seen even for low level square wave excitation, but large amplitude forcing is required for sine wave forcing to impart similar changes to the jet (Davitian et al. (2010b); Shoji et al. (2019)).

8.1.1.2 Van der Pol Oscillator Modeling

Shoji et al. (2020c) demonstrates that synchronization dynamics for the self-excited absolutely unstable JICF can be representatively depicted through a simple forced Van der Pol (VDP) oscillator model. While the investigation only considers a VDP oscillator forced by a sinusoidal waveform, there is literature which has treated alternative forcing scenarios such as square waves or even random excitation, given that the right hand side of the equation is nondiscriminatory to the type of input (Caughy (1959); Simo and Woafo (2011)). Therefore attempts were made to extend the forced VDP modeling to a JICF under square wave excitation in hopes of providing greater clarity to the underlying mechanisms of the experimental synchronization findings presented.

$$\ddot{z} - \epsilon(1 - z)^2\dot{z} + \omega_0^2 z = Bf(t) \tag{8.1}$$

The forced VDP oscillator is given mathematically by equation 8.1, where z is the dynamic variable of interest, ω_0 is the natural frequency of the self-excited system, and ϵ is the feedback parameter, controlling the degree of linear self-excitation and nonlinear self-limitation. The right-hand side of the equation is the arbitrary forcing function, which will take the form of a sine wave and Fourier series compositions of a square wave similar to the cases explored in the experiments, and B may be thought of as the relative applied forcing amplitude. For simplicity, in this investigation the epsilon parameter was chosen to be the same value of $\epsilon = 0.41$ as is experimentally determined by Shoji et al. (2020c). The flow conditions in that study are different from those which were treated here, looking instead at the JICF with a jet Reynolds number of $Re_j = 2300$, a nozzle diameter of $D = 4.04\ mm$, and a jet-to-crossflow momentum flux ratio of $J = 7$, where the acetone mole fraction was $\psi = 0.218$. However, Shoji et al. (2020b) demonstrates for a variety of jet Reynolds numbers and acetone mole fractions that the instability characteristics of the JICF are quite similar both qualitatively, and when non-dimensionally scaled, quantitatively as well. As such, for qualitative comparisons of the VDP oscillator model with the experimental synchronization characteristics, the feedback parameter was assumed to be reasonably accurate in depicting the degree of linear and non-linear behavior in the jet.

For comparative analysis with the experimentally derived lock-in characteristics, the VDP oscillator model treated simple square wave excitation at forcing frequencies of $f_f = 55\ Hz$ and $f_f = 110\ Hz$ for an ideal square wave, and approximated square wave inputs composed of 5, 10, and 15 Fourier terms. The VDP oscillator also examined a range of duty cycles (α =0.1, 0.2, 0.3, 0.4, and 0.5), and the impact of skipping over select terms in the Fourier series to further examine the significance of the individual Fourier terms and their nonlinear interactions on the synchronization characteristics, as was alluded to from the preceding lock-in experiments. The forcing was nondimensionalized by the critical forcing amplitude required to achieve LI by sinusoidal excitation at the same forcing frequency. The determination of NSR, QP, and LI was made in the same manner as was done for the

$f_f = 55\ Hz$	$\alpha = 10\%$	$\alpha = 20\%$	$\alpha = 30\%$	$\alpha = 40\%$	$\alpha = 50\%$
Fourier, 5 terms	0.370	0.496	0.597	0.749	0.739
Fourier, 10 terms	0.336	0.437	0.496	0.613	0.613
Fourier, 15 terms	0.336	0.437	0.504	0.613	0.622
Ideal Waveform	0.109	0.193	0.235	0.303	0.319

$f_f = 110\ Hz$	$\alpha = 10\%$	$\alpha = 20\%$	$\alpha = 30\%$	$\alpha = 40\%$	$\alpha = 50\%$
Fourier, 5 terms	0.333	0.365	0.542	0.677	0.522
Fourier, 10 terms	0.354	0.385	0.552	0.688	0.563
Fourier, 15 terms	0.354	0.385	0.563	0.698	0.573
Ideal Waveform	0.115	0.177	0.250	0.323	0.260

Table 8.2: Tabulation of the critical forcing amplitude (B_{cr}) for synchronization of the VDP oscillator model to square wave forcing with the ideal waveform, and approximated waveforms with 5, 10, and 15 Fourier terms. Waveforms were generated at forcing frequencies of 55 Hz and 110 Hz, for duty cycles of 0.1, 0.2, 0.3, 0.4, and 0.5. The forcing amplitude was normalized by the critical forcing amplitude required for a sinusoidal waveform with the same forcing frequency, $B_{cr}/B_{cr,sine}$.

experiments, through the inspection of phase portraits and PSD plots, though for simplicity only the critical forcing amplitude required to achieve lock-in has been presented.

From table 8.2 it can be seen that in all of the forcing cases considered, whether ideal or approximated, the VDP oscillator was able to synchronize to the square wave excitation with less energy input than needed by the sinusoidal waveform ($B_{cr}/B_{cr,sine} < 1$). Of the waveforms treated at a forcing frequency of 55 Hz,the easiest to LI was the ideal square wave forcing, which at worst only required 32% of the energy for LI as needed by the sinusoidal waveform. Somewhat less effective in achieving LI, though still at worst only 62% of the requisite energy for the sinusoidal waveform, were the Fourier series with 15 and 10 terms. The least effective was the Fourier series with 5 terms, which in all cases was 2-3 times

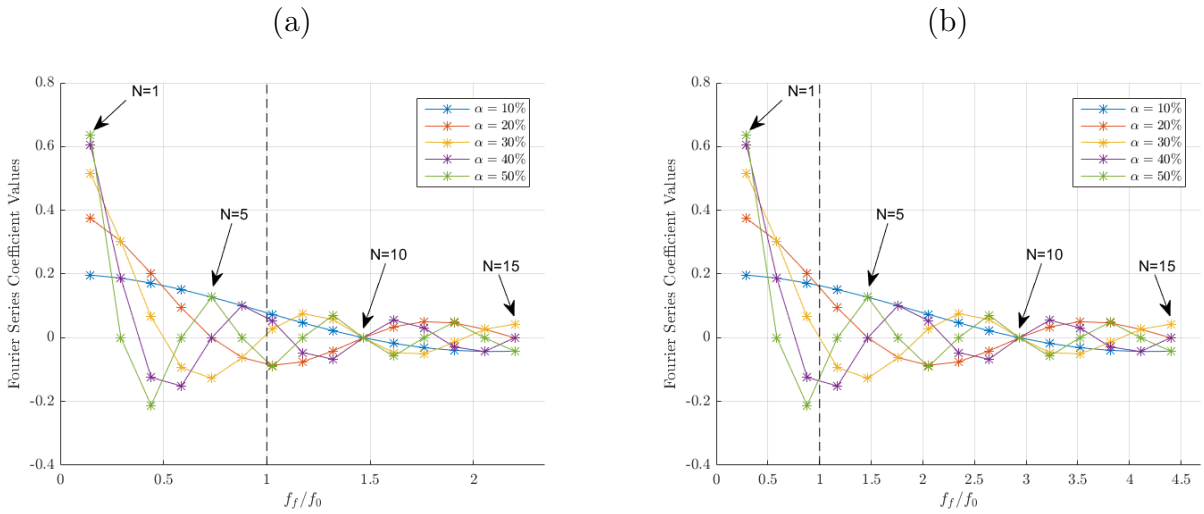

Figure 8.3: Value of coefficients for the first 15 terms of a Fourier series approximating a square wave at duty cycles of α =10%, 20%, 30%, 40%, and 50% for a fundamental excitation frequency of (a) $f_f = 55\ Hz$, and (b) $f_f = 110\ Hz$. The abscissa in both plots was normalized by the prescribed instability frequency of the VPD oscillator ($\omega_0 = 375\ Hz$), which was selected to match the fundamental instability frequency of the JICF experiments.

less effective than the ideal square wave input, and at worst required 75% of the energy of the sinusoidal waveform. These trends of increased forcing to achieve LI as the number of Fourier terms decreased agreed very well with the noted trends in the experimentally derived LI behavior for different square wave excitation waveforms. Interestingly, as was seen in the experiments, though increasing the number of Fourier terms reduced the critical amplitude for LI, it appeared the added benefit was negligible beyond 10 terms, noting nearly identical critical forcing amplitudes as seen with the 15 term series. As noted by Li and Juniper (2013a) in their investigation of a thermodynamically self-excited jet, the VDP oscillator model produces a generally symmetric v-shaped LI diagram about the natural frequency of the system, and therefore forcing frequencies which are further from the natural frequency are harder to LI than those which are closer. Despite the nonlinearity of the VDP model, it seems the individual contributions from the higher Fourier terms were not significant unless

they were relatively close to the natural frequency of the system or had input magnitudes which were quite large, which is aided visually in figure 8.3(a). Further in support of this analysis was the general LI trends distinguished when the excitation frequency was then given as $f_f = 110\ Hz$, which are also given in table 8.2 and figure 8.3(b). While Fourier terms 4-10 were contained within $\pm\frac{1}{2}f_f/f_0$ of natural frequency when $f_f = 55\ Hz$, only terms 2-5 were contained within that same range when $f_f = 110\ Hz$, and additionally those terms occurred earlier in the Fourier series as well, in general meaning the coefficient magnitudes were also larger than those which were in close proximity with $f_f = 55\ Hz$. The net result of this was critical amplitudes for LI which were nearly matched for the 5, 10 and 15 term Fourier series, with the 5 term series actually requiring the least energy to achieve LI. Each of the Fourier series contained the same terms in close proximity to the natural frequency of the system, which allowed for the similar LI characteristics. The slight, though quantifiable, differences in the critical forcing amplitude between the 5, 10, and 15 term Fourier series arose due to a redistribution of the applied energy to the higher harmonic terms which were less impactful than the terms closer to the natural frequency of the system. And yet, this general similarity between all of the Fourier series waveform approximations was not distinguished in the experimental LI results which maintained a distinct difference between the 5 and 10 term series. This was attributed to the VDP oscillator having a symmetric v-shaped LI diagram, while the JICF is shown to have an asymmetric LI diagram where forcing frequencies above the natural frequency remain relatively easy to LI, and thus maintained the importance of larger terms in the experimental Fourier series waveforms (Shoji et al. (2020c)). Intriguingly, for the VDP forcing at $f_f = 55\ Hz$ it was found quite consistently that as duty cycle increased towards 50%, the required forcing amplitude for LI also increased. However, for $f_f = 110\ Hz$, even for the ideal square wave input, the $\alpha = 40\%$ waveform was harder to LI than $\alpha = 50\%$. This again was also suggestive of the significance that both magnitude and relative proximity to the natural frequency each of the individual Fourier terms had on the overall synchronization characteristics despite the nonlinearity of

5 Term Fourier Series	$\alpha = 10\%$	$\alpha = 20\%$	$\alpha = 30\%$	$\alpha = 40\%$	$\alpha = 50\%$
Terms 1, 2, 8, 9, 10	0.655	0.588	0.664	0.706	0.807
Terms 1, 3, 8, 9, 10	0.613	0.664	0.697	0.790	0.790
Terms 1, 4, 8, 9, 10	0.597	0.597	0.681	0.756	0.806
Terms 1, 5, 8, 9, 10	0.546	0.697	0.689	0.798	0.681

Table 8.3: Tabulation of the critical forcing amplitude (B_{cr}) for synchronization of the VDP oscillator model to square wave excitation waveforms at $f_f = 55\ Hz$ with 5 selected terms from the Fourier series. Waveforms were generated for duty cycles of 0.1, 0.2, 0.3, 0.4, and 0.5, and the forcing amplitude was normalized by the critical forcing amplitude required for a sinusoidal waveform with the same forcing frequency, $B_{cr}/B_{cr,sine}$.

the system.

To further explore the possible significance that select terms in the Fourier series may have on achieving LI, the square wave excitation at $f_f = 55\ Hz$ was additionally treated given a Fourier series with different terms purposefully omitted. Table 8.3 lists the critical LI amplitudes for the different 5 term waveforms which were considered, and figure 8.4 depicts the resulting square wave approximations relative to the ideal input for a square wave, representatively shown for the waveforms with a duty cycle of $\alpha = 30\%$. Quite uniformly across the different Fourier approximations and duty cycles treated, the cases which were most difficult to LI were ones in which the second included term had a zero value and thus did not contribute at all to the excitation (i.e. term 5 for $\alpha = 20\%$ and 40%, or terms 2 and 4 for $\alpha = 50\%$, as given in figure 8.4(a)). Of greater interest was the resulting trends for the waveforms with $alpha = 10\%$ and $alpha = 30\%$, wherein each of the terms had a finite contribution to the excitation of the system. The waveforms with $\alpha = 10\%$ demonstrated that as the second term in the approximation was systematically shifted closer to the natural frequency of the system, and in spite of a corresponding decrease in magnitude of the term, the resulting waveform actually became easier to LI. Extension of this analysis to

(a) $R^2 = 86\%$

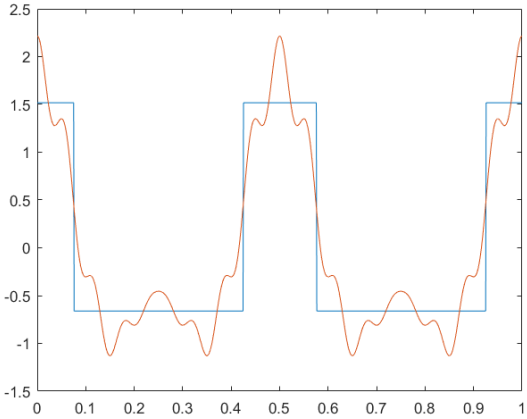

(b) $R^2 = 63\%$

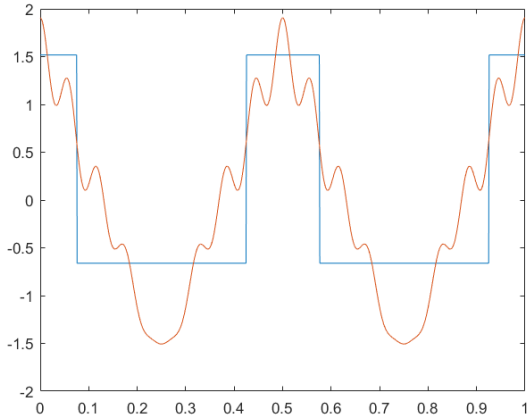

(c) $R^2 = 65\%$

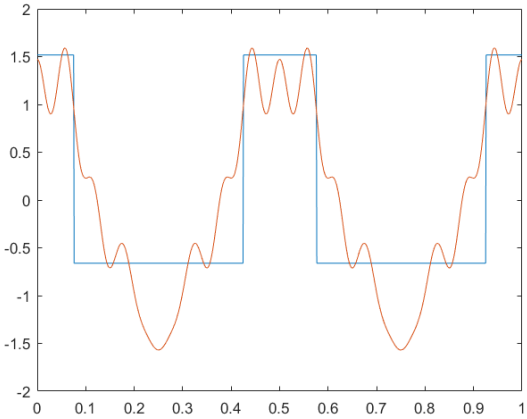

(d) $R^2 = 67\%$

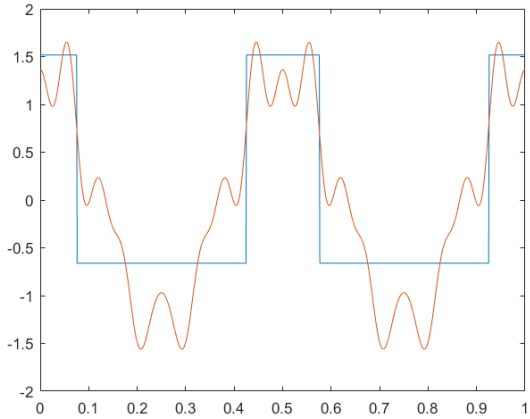

Figure 8.4: Representations of approximated $\alpha = 30\%$ square wave excitation waveforms at $f_f = 55\ Hz$ with 5 selected terms from the Fourier series plotted against the ideal square wave input: (a) terms 1, 2, 8, 9, and 10 with an r-squared of 86%, (b) terms 1, 3, 8, 9, and 10 with an r-squared of 63%, (c) terms 1, 4, 8, 9, and 10 with an r-squared of 65%, and (d) terms 1, 5, 8, 9, and 10 with an r-squared of 67%. The approximated waveforms are given in red, while the ideal waveform is given in blue. For accurate comparison the mean and RMS of the waveforms were matched.

the $\alpha = 30\%$ duty cycle only further supported this complex interplay between the magnitude of the included term and the relative proximity of the term to the natural frequency of the self-excited system. Looking at figure 8.4, for all of the $\alpha = 30\%$ cases there was significant ringing and/or overshoot of the approximated waveform, though this was more minimal in the case of the waveform with Fourier terms 1, 2, 8, 9, and 10 (figure 8.4(a)). This was not unexpected given that waveform included the second term of the Fourier series, which from figure 8.3(a) is seen to be of greater magnitude than terms 3, 4, or 5. Interestingly, though the waveform which included the second Fourier term better approximated the square wave, with an r-squared of 86% compared to $63\% - 67\%$, and indeed was the easiest to LI, the other waveforms actually had very similar critical forcing amplitudes required for LI of the excited system, indicative of the more pronounced impact of the terms which were nearer to the natural frequency of the system. These findings quite importantly further substantiate the importance of the methodology by which an excitation waveform is applied to a self-excited system, and help to illuminate upon some of the dynamical differences between sine wave and square wave or double-pulse excitation of the JICF.

8.1.2 Vortex Rings and Jet Dynamics

8.1.2.1 Vorticity and Structure

Multiple experimental (Getsinger et al. (2014); Shoji et al. (2019); Shoji et al. (2020a); Harris et al. (2020b); Harris et al. (2020a)), numerical (Cortelezzi and Karagozian (2001); Marzouk and Ghoniem (2007); Regan and Mahesh (2019)), and theoretical (Alves et al. (2007); Alves et al. (2008); Souza et al. (2020)) studies quite definitively show that alterations to the instability characteristics and vortex dynamics near the jet exit significantly impact the resulting flow characteristics further downstream in the flowfield. Specifically, Shoji et al. (2019) demonstrate enhancement in mixing efficacy when the jet is excited with a square wave rather than a sinusoidal waveform. Likewise, chapter 7 demonstrated similar findings for a

double-pulse forcing waveform, and additionally pointed out distinct differences in vortex ring formation and jet mixing if the jet was naturally AU or CU. Thus, one aspect of great interest to explore for the different forcing waveforms was how differing states of synchronization to the applied forcing augmented dynamics in the nearfield of the jet, such as those associated with the vortex rollup along the jet USL, and ultimately the resulting implications for the formation, strength, and symmetry of the CVP further downstream. Specific focus was given to the $f_f = 110\ Hz$ sinusoidal waveform and the 0.35.65.80 double-pulse waveform which were examined in the experimental synchronization analysis in section 8.1.1.1. To visualize the flow, stereo-PIV imaging was applied in the jet centerplane, and at cross-sectional slices of the jet at downstream locations of $x/D = 0.0$ and $x/D = 1.0$, from which vorticity calculations were extracted. Additionally, further downstream at cross-sectional locations of $x/D = 1.5$, $x/D = 2.5$, and $x/D = 5.5$, acetone PLIF imaging was applied to examine the structural evolution of the jet from scalar concentration measurements. The flow conditions for the jet were kept consistent with the earlier experimental synchronization analysis in section 8.1.1.1, while the applied forcing consisted of excitation at non-dimensional forcing amplitudes of $u'_{j,rms}/U_j = 0.0$ (unforced jet), 0.02, 0.16, 0.41, and 0.50, to investigate how jet synchronization states of NSR, QP, LI, and well above LI influenced the vortex ring formation, interactions, and downstream jet structure. Figures 8.5 and 8.6 present the mean quantifications of the vorticity in the centerplane and $x/D = 0.0$ and $x/D = 1.0$ cross-sectional locations, along with the mean cross-sectional structure at $x/D = 5.5$ for the 0.35.65.80 double-pulse waveform and the $f_f = 110\ Hz$ sinusoidal waveform, respectively.

Figure 8.5 depicts the vorticity and structural characteristics of the jet subject to the 0.35.65.80 double-pulse axisymmetric forcing. The unforced jet, given in figure 8.5(a), produced a flow which was quite symmetric in the cross-sectional vorticity and structure. From the cross-section at $x/D = 1.0$, the distinct folding and tilting of the vorticity associated with the upstream and downstream shear layers was visually noted. The relatively strong vortex rollup along the shear layers and the symmetric CVP formation were extremely con-

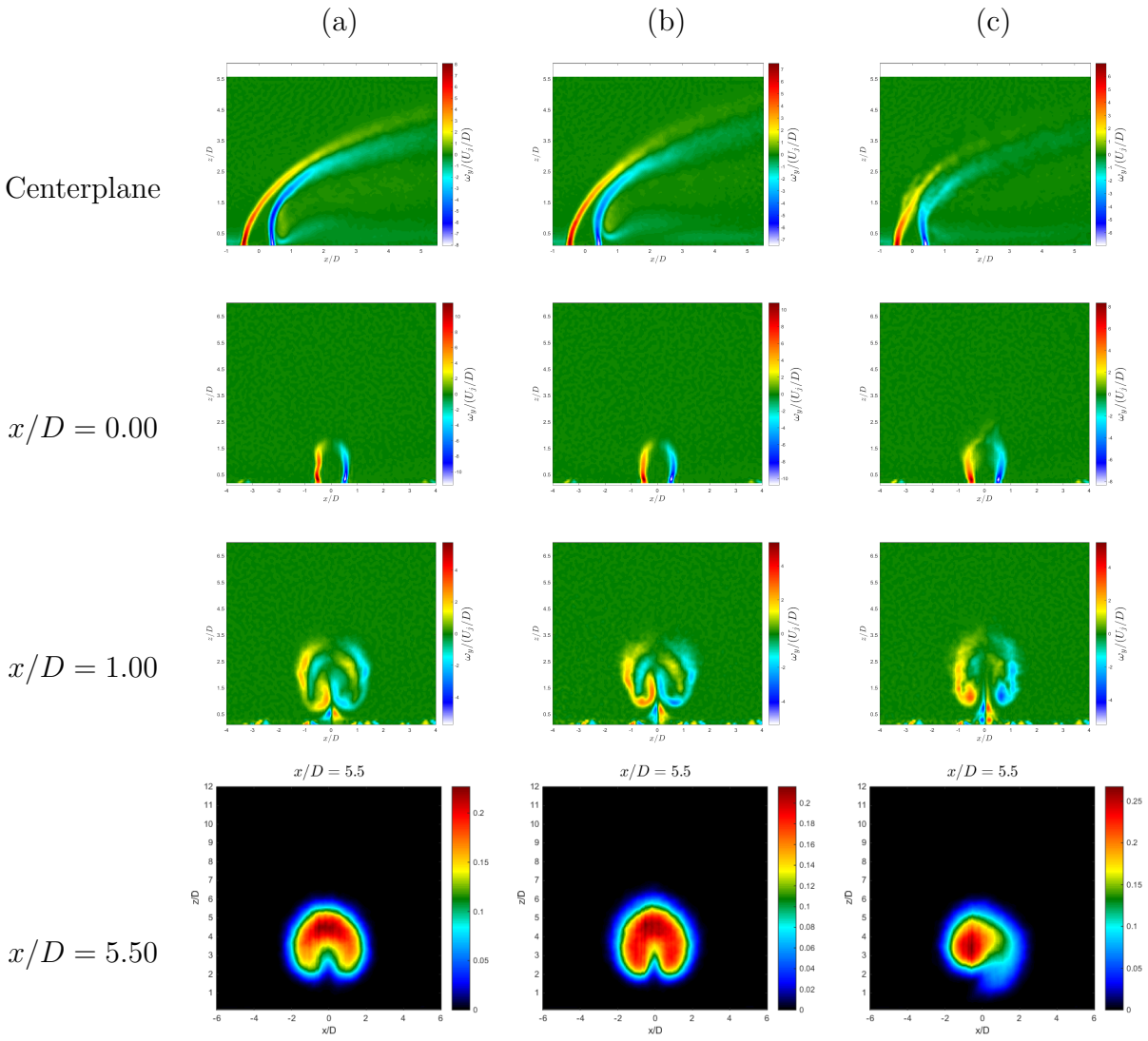

Figure 8.5: continues to following page

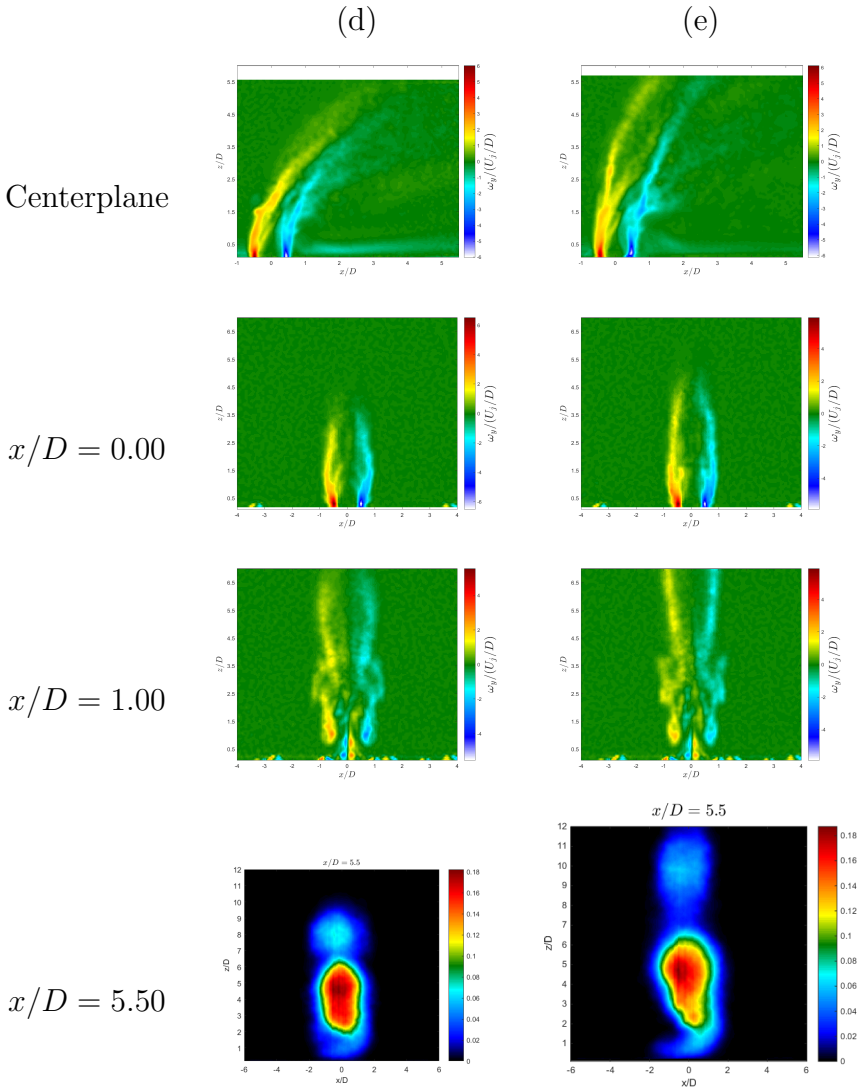

Figure 8.5: Depictions of the mean vorticity along the jet centerplane, mean vorticity at jet cross-sectional locations of $x/D = 0.0$ and $x/D = 1.0$, and the mean cross-sectional jet structure at $x/D = 5.5$ for the 0.35.65.80 double-pulse waveform axisymmetric excitation of the jet, with excitation amplitudes of (a) $u'_{j,rms}/U_j = 0.00$, (b) $u'_{j,rms}/U_j = 0.02$, (c) $u'_{j,rms}/U_j = 0.16$, (d) $u'_{j,rms}/U_j = 0.41$, and (e) $u'_{j,rms}/U_j = 0.50$. The images are averaged over 600 instantaneous realizations, and the colorbars are individually scaled to the maximum and minimum values contained within each mean image. The vorticity and structural data were extracted from stereo-PIV and scalar PLIF imaging, respectively.

sistent with characteristics seen by others for a naturally AU JICF (Getsinger et al. (2014); Shoji et al. (2019); Regan and Mahesh (2019); Harris et al. (2020a)). For an applied forcing of $u'_{j,rms}/U_j = 0.02$, the jet was found to LI to the 0.35.65.80 double-pulse waveform according to table 8.1, though as shown in figure 8.5(b), the overall vorticity distribution remained relatively unchanged from that of the unforced jet. Interestingly though, the shape and overall concentration in the CVP structure at $x/D = 5.5$ were slightly improved, which likely owed to the more pure-toned instabilities along the USL for the LI jet as compared to the relatively more broad peak of the natural jet instabilities. From figure 8.5(c), further increasing the forcing beyond that which was needed for LI, to $u'_{j,rms}/U_j = 0.16$, resulted in the apparent elimination of the CVP according to the jet structure at $x/D = 5.5$. From the mean vorticity along the upstream and downstream shear layers in the centerplane, it appeared the leading and trailing edges of the vortex rings interacted sooner and broke down in the more nearfield of the flow. Such features of vortex breakdown were similarly noted by the weaker vorticity concentrations in the upper portion of the tilted and folded vortex rings at $x/D = 1.00$. Continued increasing of the forcing amplitude well above that needed for LI of the jet, at $u'_{j,rms}/U_j = 0.41$ and $u'_{j,rms}/U_j = 0.50$, produced dramatic alterations to the flowfield, as shown in figures 8.5(d-e). From both the cross-sectional structure of the jet at $x/D = 5.5$, and the trajectories of the vortex rings from the mean centerplane vorticity, the jet appeared to be bifurcated. Such bifurcations were also visually denoted in chapter 7 for an analogous AU jet excited by double-pulse forcing, and is seen by others for a JICF excited by simple square wave forcing (Eroglu and Breidenthal (2001); M'Closkey et al. (2002); Shapiro et al. (2006); Sau and Mahesh (2010); Shoji et al. (2019)). Examination of the cross-sectional structure revealed that the largest portion of the jet was concentrated near to the wall boundary, and a relatively weak structure penetrated much deeper into the flowfield, representing the vortex rings produced by the slow and fast pulses respectively. Some of the concentration very near the wall boundary for these cases was associated with a trailing column of jet fluid aft of the fully filled vortex ring produced by the slow pulse, as

was distinguished in chapter 7 for a characteristically similar AU JICF with a double-pulse excitation at $u'_{j,rms}/U_j = 0.60$.

Figure 8.6 depicts the vorticity and structural characteristics of the jet subject to the sinusoidal axisymmetric forcing. The characteristics of the unforced jet were given again in figure 8.6(a) for simplicity of comparisons with the other excited flows. Much like the double-pulse excitation, the vorticity distribution for the sinusoidal waveform at an excitation amplitude of $u'_{j,rms}/U_j = 0.02$, in figure 8.6(b), was nearly identical to the unforced jet. However, unlike the double-pulse waveform, the cross-sectional structure also remained the same as the unforced jet, which was not unexpected given the flow had not LI to the sinusoidal forcing for this amplitude of excitation. Interestingly, the sinusoidal excitation at $u'_{j,rms}/U_j = 0.16$, shown in figure 8.6(c), produced vorticity and structural characteristics which were very similar to those for the double pulse waveform with the same forcing amplitude, noting the apparent elimination of the CVP, and more pronounced vortical interactions in the jet nearfield. This was somewhat unexpected given the numerous studies which note square wave excitation of an AU jet produces more distinctive alterations to the flow compared to sine wave excitation (M'Closkey et al. (2002); Davitian et al. (2010b); Shoji et al. (2019)), and even more surprising given the jet had just achieved LI for the sinusoidal forcing while the applied double-pulse waveform was well beyond the threshold for LI. While the vorticity and structure were generally quite similar between the sinusoidal and 0.35.65.80 double-pulse waveforms at the lower forcing amplitudes, increases in forcing amplitude above the LI threshold for the sinusoidal waveform, to $u'_{j,rms}/U_j = 0.41$ and $u'_{j,rms}/U_j = 0.50$ in figures 8.6(d-e), did not not continue to produce the same characteristic changes to the flow as were noted for the double-pulse waveform (figures 8.5(d-e)). Most noticeably, while the jet penetration continued to increase with the increasing excitation, the jet never became bifurcated as was seen for the double-pulse waveform, and consequentially the wall boundary region was lacking of any jet structures. In the centerplane, the vorticity from the windward and leeward sides of the jet continued to interact and breakdown in the jet nearfield, however

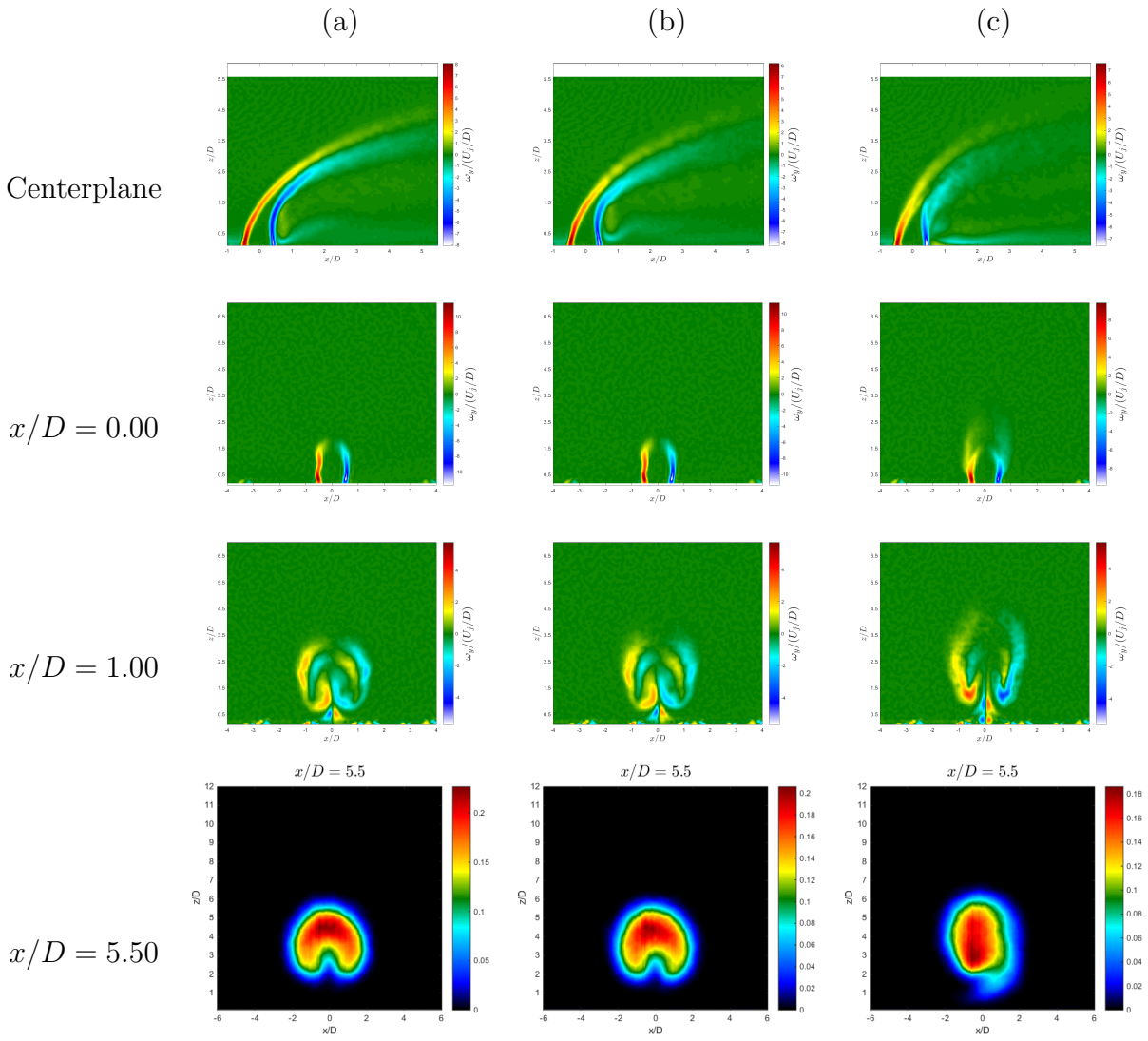

Figure 8.6: continues to following page

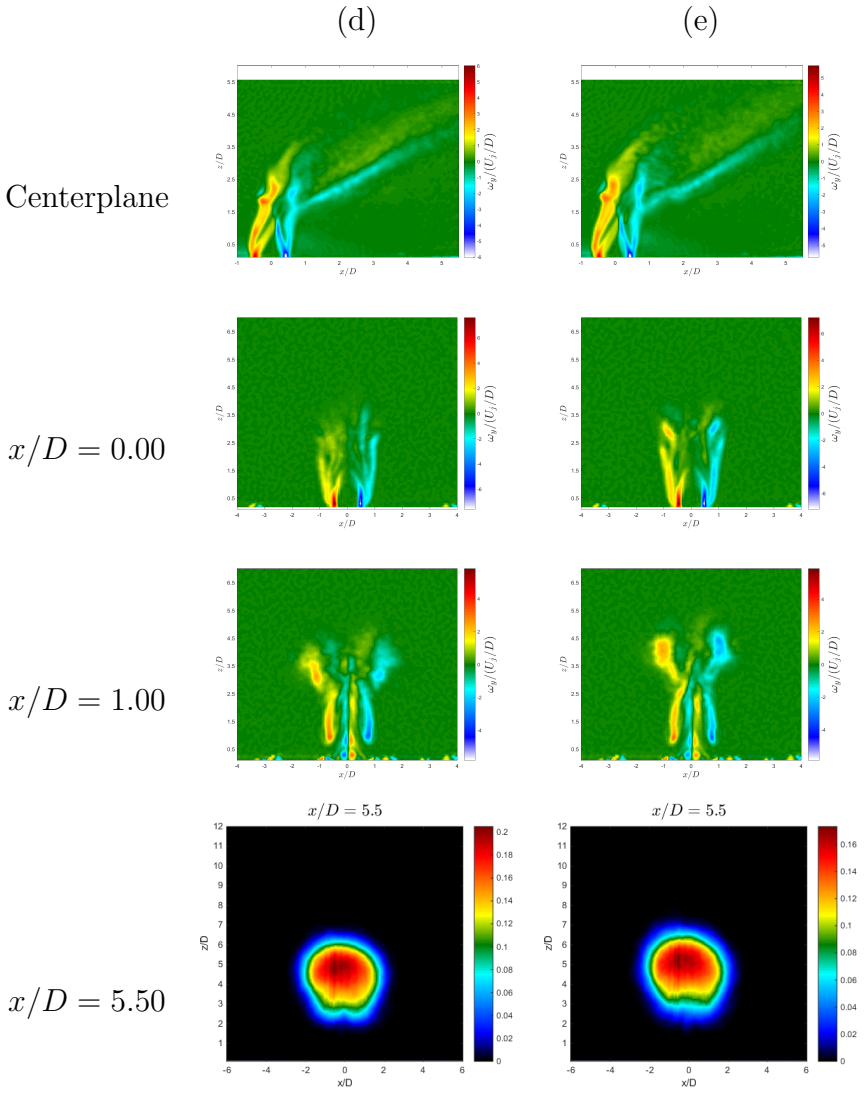

Figure 8.6: Depictions of the mean vorticity along the jet centerplane, mean vorticity at jet cross-sectional locations of $x/D = 0.0$ and $x/D = 1.0$, and the mean cross-sectional jet structure at $x/D = 5.5$ for the sinusoidal waveform axisymmetric excitation of the jet, with excitation amplitudes of (a) $u'_{j,rms}/U_j = 0.00$, (b) $u'_{j,rms}/U_j = 0.02$, (c) $u'_{j,rms}/U_j = 0.16$, (d) $u'_{j,rms}/U_j = 0.41$, and (e) $u'_{j,rms}/U_j = 0.50$. The images are averaged over 600 instantaneous realizations, and the colorbars are individually scaled to the maximum and minimum values contained within each mean image. The vorticity and structural data were extracted from stereo-PIV and scalar PLIF imaging, respectively.

there was a distinct, though much weaker, persistence of the vorticity along the lee side of the jet continuing beyond $x/D = 4.0$ in the downstream. Given that the flow was not fully modulated by the forcing, this persisting lee side vorticity may have been associated with vortex rollup which was formed while the jet was not actively pulsing to form a vortex ring, where the windward portion of the vorticity is not evident because it was subsequently enveloped by the propagating vortex ring induced by the forcing which followed after it.

8.1.2.2 POD Analysis

To explore the underlying structures, dynamics, and dominant instabilities of the flowfield from instantaneous snapshots of the flow, snapshot proper orthogonal decomposition (POD)(Sirovich (1987)) was applied to the velocity vector fields from the centerplane stereo-PIV imaging; this technique has been utilized in other studies of the JICF (Meyer et al. (2007); Schlatter et al. (2011); Gevorkyan et al. (2018); Shoji (2017);nBesnard (2019); Harris et al. (2020a)). In the present study, snapshot POD analysis was applied to 600 instantaneous realizations of the flowfield for each test case considered, well above the 300 snapshots required for statistical convergence (Shoji (2017)). Further still, in cases where the flow was synchronized to the applied forcing, the imaging rate was such that pseudo time resolved data was acquired with approximately 135 images per single forcing period, providing refined examination of the flow. The resolved mode structures were ordered in terms of their respective magnitudes of total kinetic energy fluctuation, helping to reveal characteristic flow features and dynamics which might otherwise be hidden or masked by the chaotic flowfield. Figures 8.8 and 8.7 depict the four most energetic mode structures, along with their respective contributions to the total kinetic energy fluctuation, for the transverse jet with the sinusoidal and double-pulse axisymmetric excitation cases discussed above in section 8.1.2.1. The POD analysis was further extended to examine potential correlations in the evolution of these mode dynamics across the series of original snapshots. For a specific snapshot image, the value of each respective coefficient represented the contribution of that particular

mode in the reconstruction of the original snapshot from all of the modes. By plotting the mode coefficients of the first three most dominant modes against one another for each of the individual snapshots, a phase portrait was generated depicting the coupling, or lack thereof, of the mode dynamics in the phase space. These phase portraits for both the sinusoidal and double-pulse forcing are shown in figure 8.10 for each of the forcing amplitudes considered.

Figure 8.7(a) and 8.8(a) depict the mode dynamics of the unforced jet, where modes 1 and 2, which together account for approximately 12% of the total kinetic energy of the jet, depict structures are quite concentrated in the upstream shear layer of the jet, representative of the shear layer vortex rollup, while modes 3 and 4 feature more of the wake structures, which may be representative of the upright wake vortices. Recalling the spectral contour plot of the USL instabilities in figure 8.1, it is shown that the unforced jet was naturally AU, possessing a singular dominant instability frequency which persisted multiple diameters downstream along the shear layer (s/D). For the POD coefficient mapping in figure 8.9(a), the plotting of mode 1 against mode 2 indeed produced a ring-like trajectory of points, which in the phase space is representative of a limit cycle attractor. Other studies of the JICF likewise see a ringlike coefficient plot of the first two modes for an AU flow, stating it is representative of a periodic traveling wave along the shear layer, and that the dominant shear layer jet dynamical behavior may be characterized by linear combinations of the first two modes (Meyer et al. (2007); Gevorkyan et al. (2018); Shoji (2017); Besnard (2019); Harris et al. (2020a)). Looking then to the less energetic modes 3 and 4 in figures 8.7(a) and 8.8(a) instead featured coherent structures in the wake region of the jet, which may be representative of the upright wake vortices and the interaction between the near wall dynamics and those of the jet wake. Also, as the shear layer structures spatially ended in modes 1 and 2 at approximately $z/D = 2.5 - 3.0$, there was an emergence of larger more diffuse structures along the shear layer seen in modes 3 and 4, which may be indicative of the merger and breakdown of the shear layer vortices. Interestingly, from global linear stability analysis (GLSA) of DNS of an AU JICF at $J = 4$ and $Re_j = 2000$, Regan and Mahesh (2017)

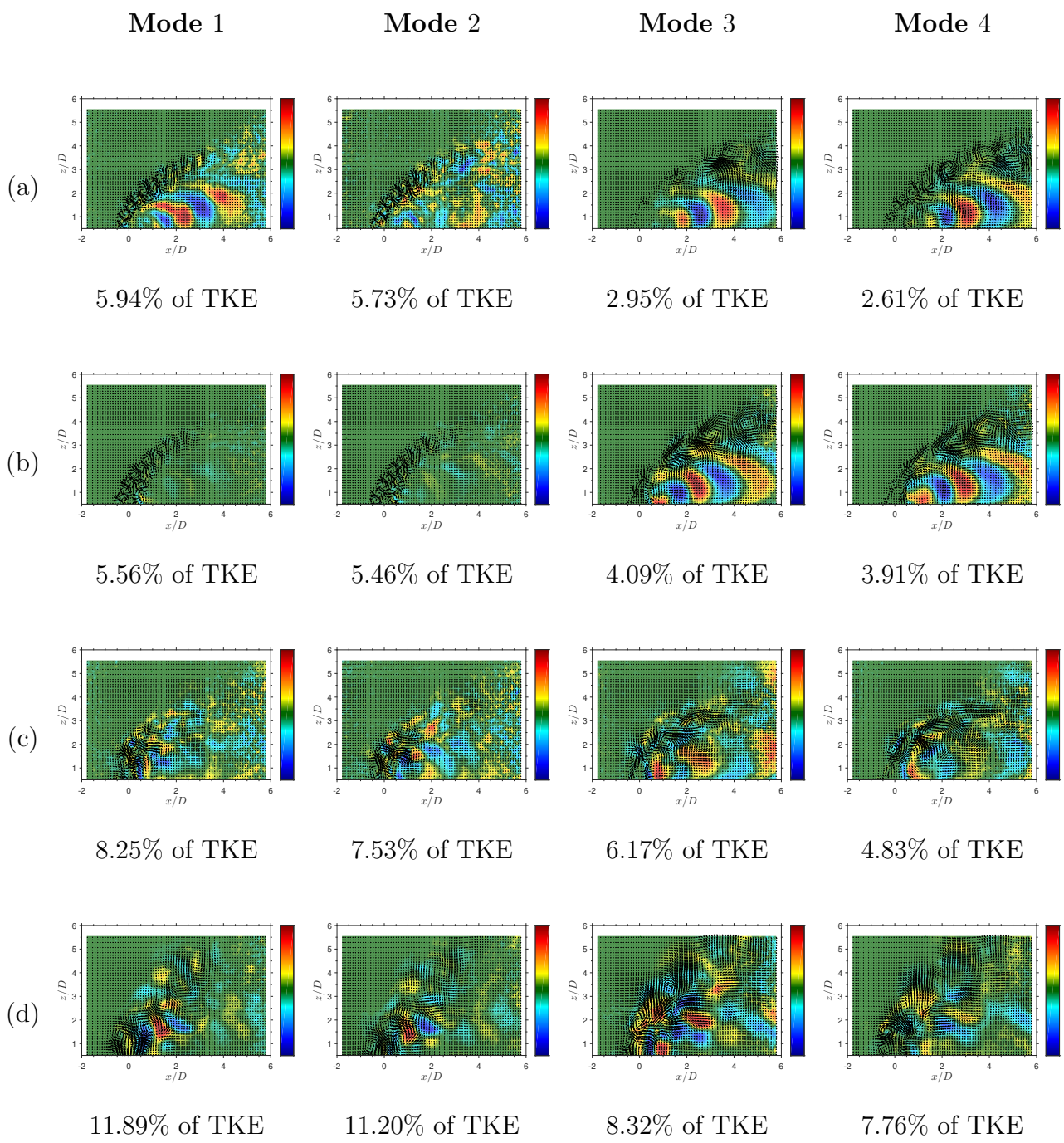

Figure 8.7: continues to following page

(e)

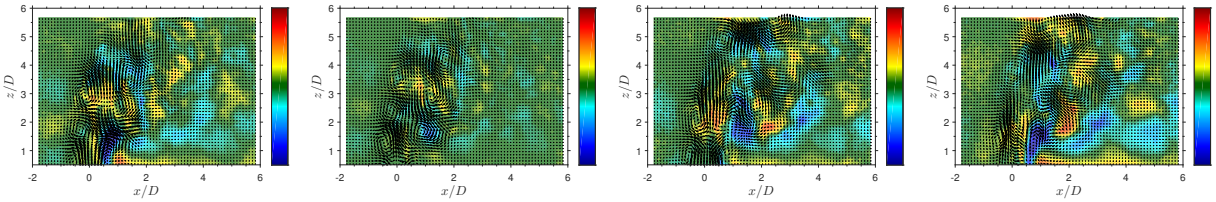

16.21% of TKE 13.15% of TKE 11.23% of TKE 10.51% of TKE

Figure 8.7: PIV based POD mode structures extracted from 600 instantaneous snapshots of the centerplane velocity field for the 0.35.65.80 double-pulse waveform axisymmetric excitation of the jet, with (a) $u'_{j,rms}/U_j = 0.00$, (b) $u'_{j,rms}/U_j = 0.02$, (c) $u'_{j,rms}/U_j = 0.16$, (d) $u'_{j,rms}/U_j = 0.41$, and (e) $u'_{j,rms}/U_j = 0.50$. The modes are sorted according to their respective percentages of total kinetic energy fluctuation content. The colorbar in each image represents the mode scaled by its own norm and the mean jet velocity at the jet exit U_j.

likewise note multiple wake modes after the more dominant shear layer modes. They indicate the modes are qualitatively quite similar to one another, though all have quantitatively differing spectral content in the relatively low frequency regime. They attribute the distinct differences in wake frequencies, as compared with those of the shear layer, to the modes being associated with the jet diameter and shear layer respectively. As such, readdressing the POD coefficient mapping in figure 8.9(b) finds that mode 3 did not possess a coherent or distinguishable relationship with modes 1 and 2, which was not unexpected given the distinct spectral differences in shear layer and wake modes as noted by Regan and Mahesh (2017), and that the vortex merger and breakdown had relatively diffuse spectral content as shown from the subharmonic regime of the spectral contour plot in figure 8.1 for locations further downstream along the shear layer.

At the relatively low energy forcing of $u'_{j,rms}/U_j = 0.02$ it was shown from synchronization analysis that the jet had already LI to the double-pulse forcing, whereas the sinusoidal forcing at $f_f = 110\ Hz$ presented with QP behavior. The POD modes in figures 8.8(b) and 8.7(b) similarly presented distinctly different alterations in both the mode structures and energy

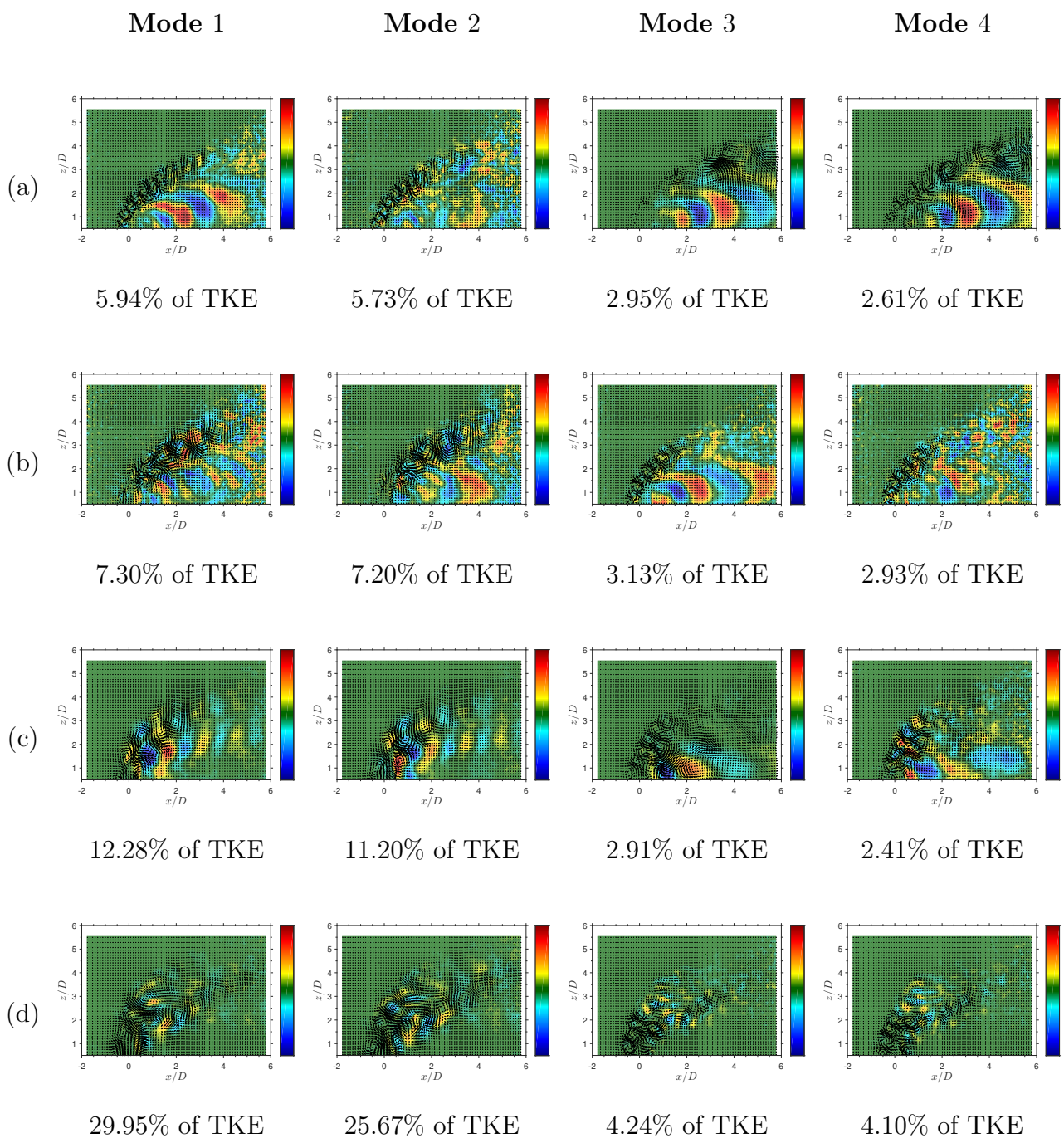

Figure 8.8: continues to following page

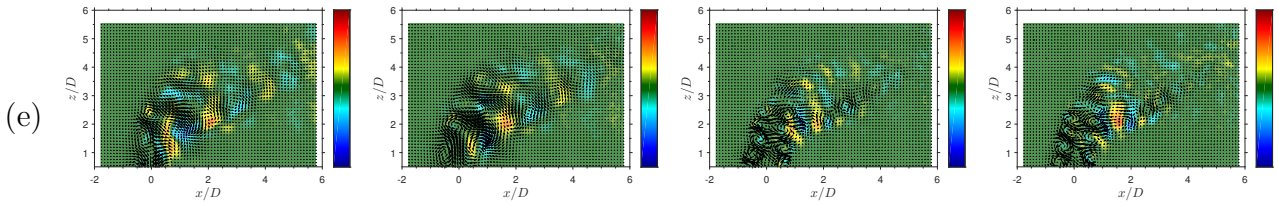

Figure 8.8: PIV based POD mode structures extracted from 600 instantaneous snapshots of the centerplane velocity field for the sinusoidal waveform axisymmetric excitation of the jet, with (a) $u'_{j,rms}/U_j = 0.00$, (b) $u'_{j,rms}/U_j = 0.02$, (c) $u'_{j,rms}/U_j = 0.16$, (d) $u'_{j,rms}/U_j = 0.41$, and (e) $u'_{j,rms}/U_j = 0.50$. The modes are sorted according to their respective percentages of total kinetic energy fluctuation content. The colorbar in each image represents the mode scaled by its own norm and the mean jet velocity at the jet exit U_j.

distribution as compared both with one another and the unforced jet dynamics. For the double-pulse excitation in figure 8.7(b), modes 1 and 2 were similar to the unforced jet modes (figure 8.7(a)) in structurally representing the USL dynamics, though the dynamics in the wake region were less pronounced. In modes 3 and 4, the wake structures were very similar to those of the unforced jet, however the shear layer structures did not initiate in the same downstream location, and in fact appeared more elongated or stretched along the shear layer compared with those in modes 3 and 4 of the unforced jet. This is not surprising since the USL was LI to the forcing rather than the natural frequency of the jet, and as Johari (2006) notes for a modulated JICF, alterations to the strength of successive vortical structures impacts the downstream location of vortical interactions. Quite interestingly, while the energy content for modes 1 and 2 remained quite similar to the first two unforced jet modes, modes 3 and 4 in the double-pulse forcing were actually strengthened by a couple percent over those of the unforced jet modes. Recalling that Regan and Mahesh (2017) note the wake modes originate along the downstream side of the jet alluded that while the excitation achieved LI for USL dynamics, it may have also augmented the downstream

shear layer and thus strengthened the wake dynamics as well. Interestingly, while the mode coefficient phase portrait for the double-pulse waveform in figure 8.10(a) produced a ringlike shape between modes 1 and 2, despite the strengthening influence of the forcing on modes 3 and 4, mode 3 still did not present with any periodic coupling to modes 1 and 2. For the sinusoidal excitation in figure 8.8(b) the POD modes were dramatically different from those of the unforced and double-pulse forced jets. Most importantly, the modes which depicted the dynamics along the USL of the jet were given by modes 3 and 4 rather than modes 1 and 2. The mode structures looked remarkably similar to those of mode 1 and 2 for the unforced jet (figure 8.8(a)), though their relative total energy content was significantly reduced. Instead, modes 1 and 2 for the sinusoidal forcing were given by dynamics which initiated a few diameters downstream along the shear layer of the jet, and also had features in the wake region, though these were not as coherent as the wake dynamics noted for the unforced and double-pulse forced jets. In terms of energy content, modes 1 and 2 had higher percentages of total kinetic energy compared with the unforced jet, however given that each of the POD mode sets were individually scaled by their own norm, it is likely that the quasiperiodicity weakened the dynamics along the shear layer, and thus relatively the downstream shear layer dynamics and wake structures were strengthened. Interestingly, looking at mode coefficient phase portrait for the sinusoidal waveform in figure 8.10(a), while the USL dynamics were not LI to the forcing, modes 1 and 2 did indeed reproduce a ring-like phase trajectory which was decoupled from mode 3 which represented the USL dynamics.

Stronger axisymmetric excitation of the jet at $u'_{j,rms}/U_j = 0.16$ corresponded to a jet which was beyond LI for the double-pulse forcing and just having achieved LI for the sinusoidal forcing, with the corresponding POD modes for these forcing cases given in figures 8.7(c) and 8.8(c), respectively. For the double-pulse forcing, modes 1 and 2 depicted dynamics which spanned across both the USL and downstream shear layer (DSL) of the jet, from very near the jet exit to approximately $z/D = 2.0$. Generally the natural/unforced instabilities along the USL and DSL yield vortex rollup which is delayed along the DSL relative

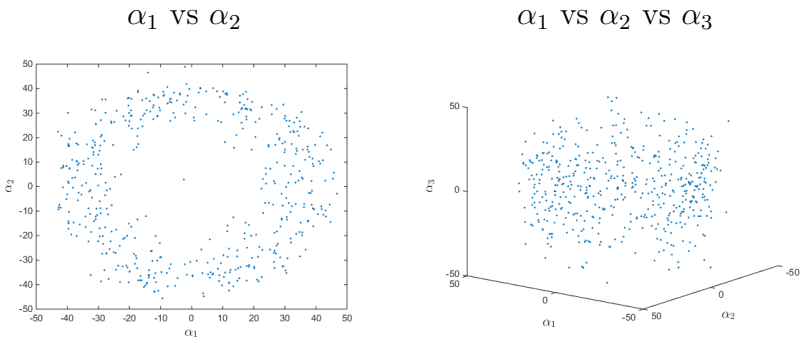

Figure 8.9: PIV based POD coefficients of (a) the first 2 modes plotted against each other, and (b) the first 3 modes plotted against each other. Data are extracted from 600 instantaneous snapshots of the centerplane velocity field for the unforced jet.

to that along the USL owing to an induced upward velocity from the leeside portion of the vortex ring (Marzouk and Ghoniem (2007)). However, due to the double-pulse forcing, the DSL portion of the vortex ring was initiated much earlier and was dynamically coupled with the USL. POD modes 3 and 4 for the double-pulse waveform were still representative of vortex interactions along the shear layer and dynamics in the wake region of the jet. The total energy kinetic energy composed by the four modes was about 27%, which was significantly increased over 19% and 17% for the $u'_{j,rms}/U_j = 0.02$ forced and unforced cases respectively. This was representative of the greater coherence and strength of the resultant dynamical features due to the increased energy applied from the forcing. In the mode coefficient phase portrait in figure 8.10(b), all three modes were periodically coupled, and the modes produced a double loop trajectory which was indicative of the two distinct and unique vortex rings which were generated during the single forcing period. For the sinusoidal waveform, even though the jet was LI at $u'_{j,rms}/U_j = 0.16$ and the mean jet vorticity and structural characteristics were quite similar to those for the double-pulse forcing (figures 8.5(c) and 8.6(c)), the POD mode structures (figure 8.8(c)) remained ordered like those with the excitation at $u'_{j,rms}/U_j = 0.02$ (figure 8.8(b)), with modes 1 and 2 depicting apparent vortex

merger and interaction dynamics after the jet had evolved passed $z/D = 2.0$, while the less energetic modes 3 and 4 represented the USL vortex rollup. Like the double-pulse forcing, the increased forcing amplitude resulted in more of the kinetic energy being represented by the first four POD modes as compared to the lower amplitude forcing case and the unforced jet, with combined kinetic energy percentages of 29%, 21%, and 17%, respectively. From the mode coefficient phase portrait in figure 8.10(b), the sinusoidal forcing again yielded a ring-like trajectory, demonstrating the periodic coupling between modes 1 and 2 for the vortex merger and interaction dynamics. Somewhat surprisingly, despite the USL having been LI to the forcing, the USL dynamics in mode 3 and 4 were not distinguishably coupled with the dynamics from modes 1 and 2.

Figures 8.7(d-e) and 8.8(d-e) depict the POD modes for subsequent further increases to the applied double-pulse and sinusoidal forcing to amplitudes of $u'_{j,rms}/U_j = 0.41$ and $u'_{j,rms}/U_j = 0.50$. The increasing strength of the forcing well above that which was required to LI the jet to either of the waveforms continued to accentuate and strengthen the characteristic dynamics noted for the forcing waveforms at $u'_{j,rms}/U_j = 0.16$ (figures 8.7(c) and 8.8(c)). However, delineating clear and distinct dynamical structures from the modes for the stronger double-pulse forcing (figures 8.7(d-e)) was difficult. The was attributable to the complexity associated with the production of two vortex rings of differing celerities, trajectories, and propagating speeds, as was visually shown in section 5.1.2 when examining the mean jet vorticity in the centerplane and multiple cross-sectional locations. The mode coefficient phase portraits for the double-pulse forcing in figures 8.10(c-d) continued to produce a double-loop phase trajectory which increased in strength and coherence along with the strength of the forcing. The sinusoidal forcing in figures 8.8(d-e), with the more simplistic waveform composition, had modes structures which clearly still represented the vortex merger/interaction dynamics in modes 1 and 2 and the USL vortex rollup in modes 3 and 4. Interestingly, with the larger amplitude forcing, the sinusoidal waveform was actually able to produce distinct vortex rings where the vortex rollup along the DSL was initiated earlier

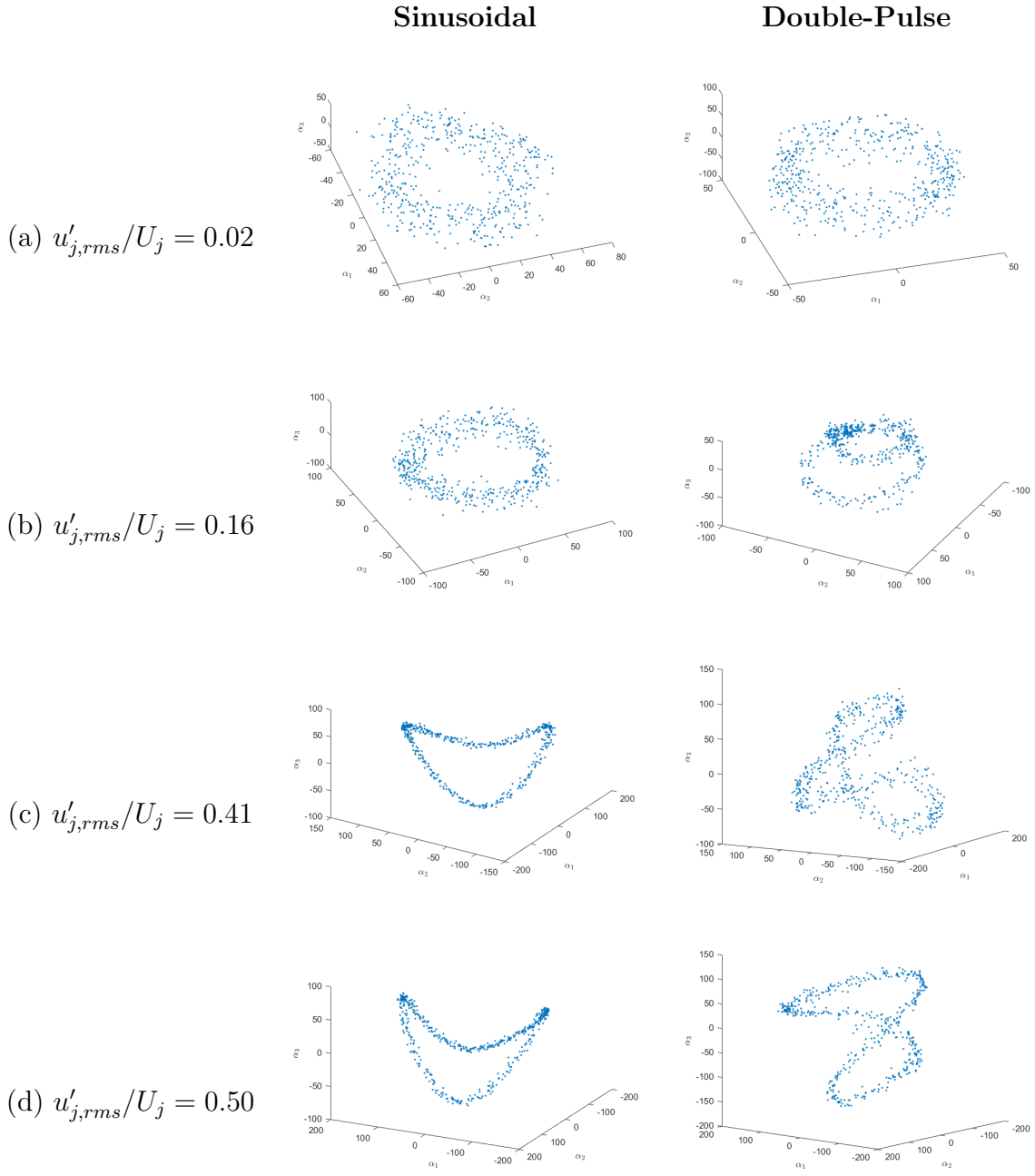

Figure 8.10: PIV based POD coefficients of the first 3 modes plotted against each other. Data are extracted from 600 instantaneous snapshots of the centerplane velocity field for the 0.35.65.80 double-pulse waveform and the sinusoidal $f_f = 110\ Hz$ waveform axisymmetric excitation of the jet, with (a) $u'_{j,rms}/U_j = 0.02$, (b) $u'_{j,rms}/U_j = 0.16$, (c) $u'_{j,rms}/U_j = 0.41$, and (d) $u'_{j,rms}/U_j = 0.50$.

and was more obviously coupled to the rollup along the USL, which was achieved more easily at lower forcing amplitudes for the double-pulse waveform (figure 8.7(c)). Also, for these larger amplitude sinusoidal forcing cases the jet dynamics were noted at larger z/D locations, indicative of a more deeply penetrating jet which unlike the double-pulse forcing was not bifurcated, as shown from the mean centerplane and cross-sectional vorticity in section 8.1.2.1. Accompanying the lack of jet bifurcation for the sinusoidal excitation was the additional elimination of dynamics in the wake region of the jet, in part due to the more deeply penetrating nature of the jet. With the increasing forcing amplitude of both waveforms, the total kinetic energy percentages also significantly increased until the first four modes were accounting for over 50% of the total kinetic energy of the flow, though the energy continued to remain relatively more distributed across the modes for the double-pulse forcing owing to the complexity of the waveform and vortex generation, merger and breakdown. In the mode coefficient phase portraits in figures 8.10(c-d), the double-pulse waveform continued to produce a double-loop phase trajectory, while the sinusoidal waveform continued to produce a simple single-loop trajectory, both of which increased in strength and coherence with the increasing forcing amplitude. Importantly, with the stronger sinusoidal forcing, mode 3 became distinguishably linked to modes 1 and 2 and was found to have twice the frequency of the first two modes, which indeed supports that modes 1 and 2 may represent the vortex merger of the shear layer dynamics found in modes 3 and 4.

8.1.2.3 Phase Space

While the dynamics of the sinusoidal forcing were relatively straight forward, and more well understood given prior investigations of a JICF excited axisymmetrically by a sinuous waveform (Narayanan et al. (2003); Davitian et al. (2010b); Shoji et al. (2020a); Shoji et al. (2020c)), the double-pulse forcing left questions remaining about implications to the dynamics when the temporal spacing between the two pulses was altered, or likewise if the strength and temporal pulse-width of the pulses was changed. Indeed, distinct changes

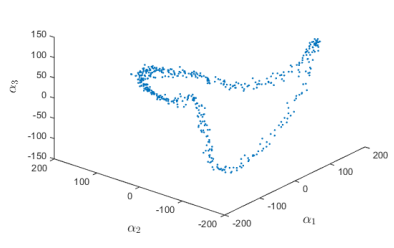

(a) 0.35.40.55

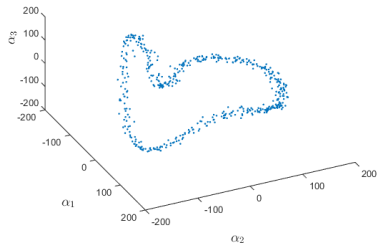

(b) 0.35.45.60

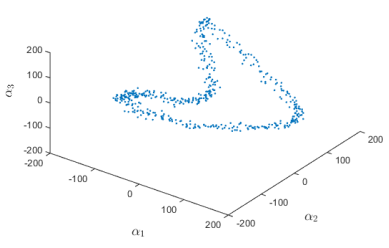

(c) 0.35.50.65

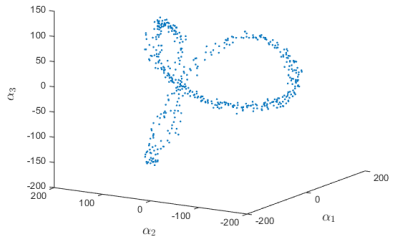

(d) 0.35.55.70

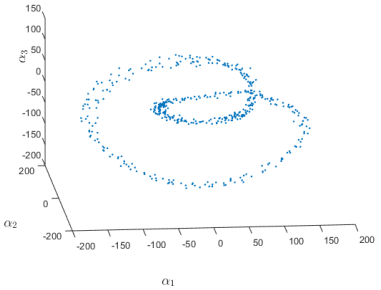

(e) 0.35.60.75

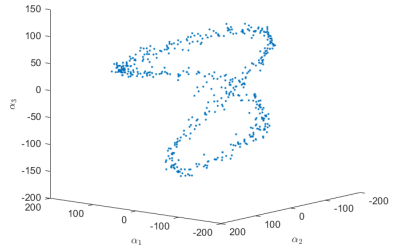

(f) 0.35.65.80

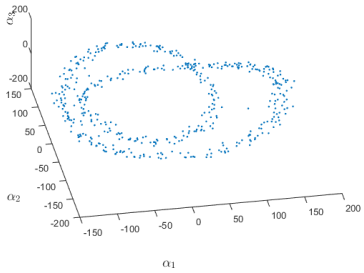

(h) 0.35.70.85

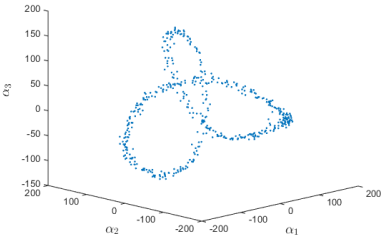

(i) 0.35.75.90

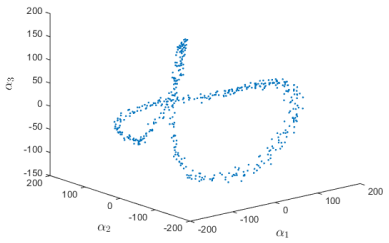

(j) 0.35.80.55

Figure 8.11: PIV based POD coefficients of the first 3 modes plotted against each other. Data are extracted from 600 instantaneous snaphots of the centerplane velocity field for double-pulse waveforms with a forcing amplitude of $u'_{j,rms}/U_j = 0.50$. The temporal pulse-width of the slow and quick pulses were fixed at $\tau_1/T = 0.35$ and $\tau_2/T = 0.15$ respectively, while the temporal spacing was varied.

in the mixing and apparent structural interactions were detailed for various double-pulse forcing waveforms applied to CU and AU jets in chapter 7, however the dynamics were not not extensively and deterministically explored. Thus, to further expand upon the noted characteristics seen in chapter 7, double-pulse forcing was applied with the same temporal pulse-widths as the 0.35.65.80 waveform investigated above, with the temporal pulse-widths of the slow and fast pulses given by $\tau_1/T = 0.35$ and $\tau_2/T = 0.15$ respectively, though the temporal spacing between the two pulses was systematically increased from $\Delta\tau_{1\rightarrow2}/T = 0.05$, by increments of $t/T = 0.05$, until $\Delta\tau_{2\rightarrow1}/T = 0.05$. The forcing was applied at an amplitude of $u'_{j,rms}/U_j = 0.50$, which was seen from figures 8.5, 8.7, and 8.10 for the 0.35.65.80 waveform to result in the most pronounced and identifiable alterations to the jet structure and dynamics of the flowfield. For simplicity, figures 8.11(a-i) only depict the mode coefficient phase portraits which were composed from the first 3 most dominant POD modes for each respective forcing waveform. Figure 8.11(a) corresponded to waveform 0.35.40.55, where temporally the fast pulse was issued from the jet exit $\Delta\tau_{1\rightarrow2}/T = 0.05$ temporally after the slow pulse, and dynamically the phase portrait actually looked remarkably similar to that which was seen earlier in figure 8.10(e) for the sinusoidal forcing, interestingly lacking the distinct double-loop trajectory which had been noted in figure 8.10(e) for the 0.35.65.80 double-pulse forcing. Continued increasing of the temporal spacing between the slow and fast pulse did not note the emergence of the double-loop phase trajectory from the first three mode dynamics until waveform 0.35.55.70 in figure 8.11(d), where the quick pulse followed $\Delta\tau_{1\rightarrow2}/T = 0.20$ temporally after the slow pulse. The double-loop phase space trajectory then remained readily identifiable through figures 8.11(e-h), until waveform 0.35.80.95 in figure 8.11(i). The 0.35.80.95 waveform was the extrema of the cases treated, where the quick pulse was issued $\Delta\tau_{1\rightarrow2}/T = 0.45$ temporally after the slow pulse, and as a result the subsequent slow pulse from the following forcing period issued only $\Delta\tau_{2\rightarrow1}/T = 0.05$ temporally after the quick pulse. From the trends in the trajectory shape across all of the portraits in figure 8.11 it became apparent that the temporal spacing between the termination of the slow pulse

and the emergence of the quick pulse, $\Delta\tau_{1\to2}/T$, was much more significant in controlling the onset of the double-loop trajectory as compared with the temporal spacing between the termination of the quick pulse and the emergence of the slow pulse, $\Delta\tau_{2\to1}/T$.

The phase space reconstructions from the POD mode coefficients in figures 8.10 and 8.11 represent the dynamics contained within the entire FOV that was analyzed in the snapshot images, which spanned nearly six diameters into the downstream wake region of the jet. However, a great deal of the dynamics and eventual impacts on the evolution of the jet were concerned with the nearfield characteristics of the flow. As such, phase portraits generated from hotwire measurements, based on time-delay embedding of the vertical velocity fluctuations along the USL of the jet, were generated for a range of select shear layer trajectory locations to compare with the phase space constructions from the POD analysis with the large FOV. Shown in figures 8.12-8.15 are these hotwire based phase portraits at shear layer locations from $s/D = 0.5$ to 2.6, for the 0.35.45.60, 0.35.55.70, 0.35.65.80, and 0.35.75.90 double-pulse waveforms. As intuitively expected, the vertical velocity fluctuations of the forced jet at the exit plane were represented by a clear double-loop phase space trajectory for each of the double-pulse waveforms considered (figures 8.12(a), 8.13(a), 8.14(a), and 8.15(a)), given the production of two differing vortex rings during a single forcing period. As was likewise alluded to from the POD-based phase portraits, the persistence of this double-loop phase trajectory along the jet shear layer was found to be quite dependent upon the temporal spacing between the slow and quick pulses of the waveform. The 0.35.45.60 waveform noted almost immediate deterioration of the secondary loop, as seen in figures 8.12(b-e), and was associated with the quick pulse interacting with the slow pulse in the jet nearfield, promoting vortex merger and breakdown. For the 0.35.55.70, 0.35.65.80, and 0.35.75.90 waveforms, the temporal spacing between the quick and slow pulses was much larger, and thus the secondary loop remained quite prominent even as far downstream as $s/D = 1.6$, shown in figures 8.13(f), 8.14(f), and 8.15(f), respectively. Beyond $s/D = 1.6$, the secondary loop was less distinguishable, and in some cases was merely represented by a

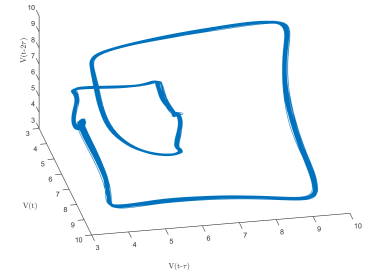

(a) Center of jet exit

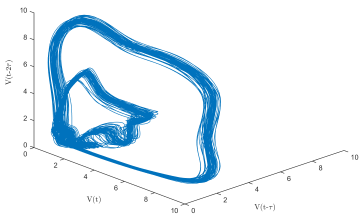

(b) $s/D = 0.5$

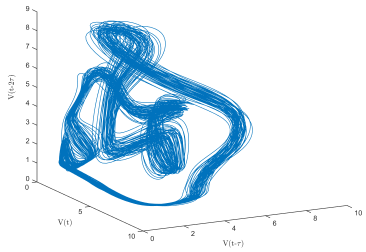

(c) $s/D = 1.0$

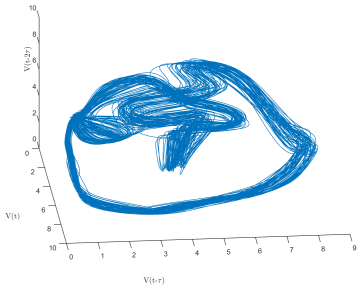

(d) $s/D = 1.2$

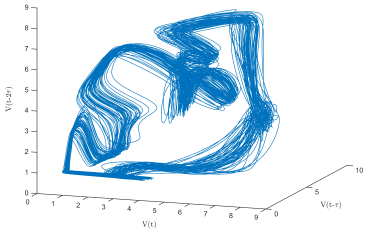

(e) $s/D = 1.4$

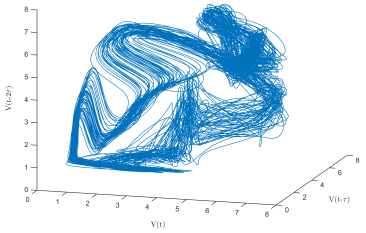

(f) $s/D = 1.6$

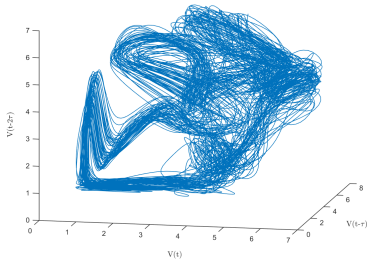

(g) $s/D = 1.8$

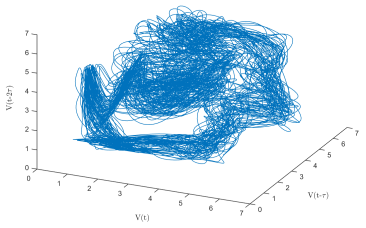

(h) $s/D = 2.0$

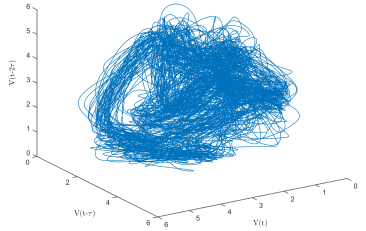

(i) $s/D = 2.2$

Figure 8.12: continues to following page

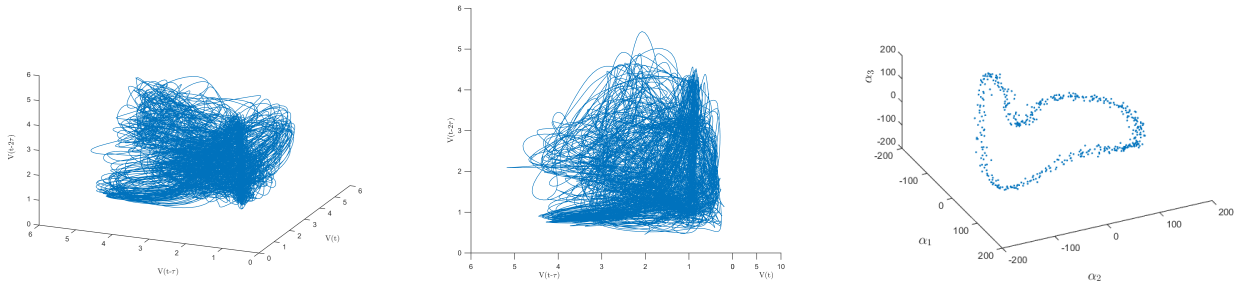

(j) $s/D = 2.4$ (k) $s/D = 2.6$ (l)POD α_1 vs α_2 vs α_3

Figure 8.12: Phase portraits from time delay embedding of the hotwire based measurements of vertical velocity fluctuations along the USL of the jet for the 0.35.45.60 double-pulse waveform with a $u'_{j,rms}/U_j = 0.50$ amplitude of excitation. For reference, figure (a) measures the jet flow centered just above the nozzle exit plane to represent the input waveform dynamics before significant distortion and evolution of the flow. For comparison, figure (l) gives the POD based phase space reconstruction from the coefficients for the 3 dominant modes plotted for 600 instantaneous snapshots of the jet.

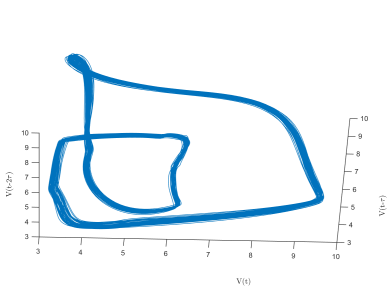

(a) Center of jet exit

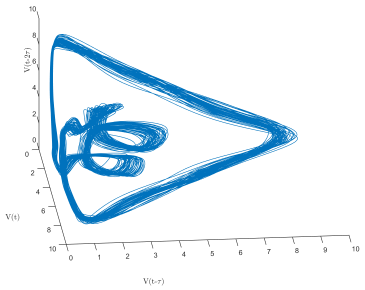

(b) $s/D = 0.5$

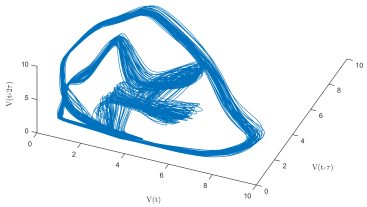

(c) $s/D = 1.0$

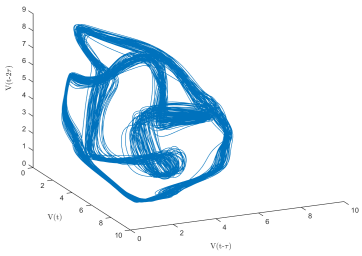

(d) $s/D = 1.2$

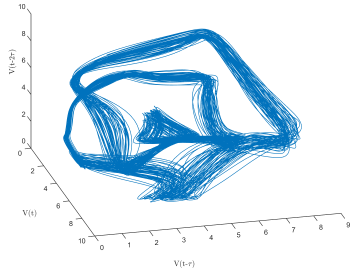

(e) $s/D = 1.4$

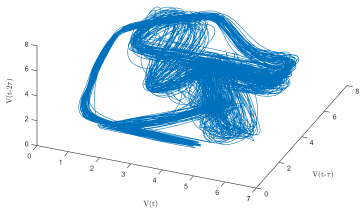

(f) $s/D = 1.6$

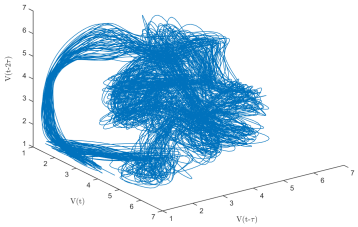

(g) $s/D = 1.8$

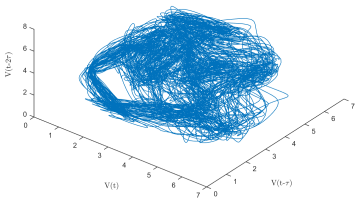

(h) $s/D = 2.0$

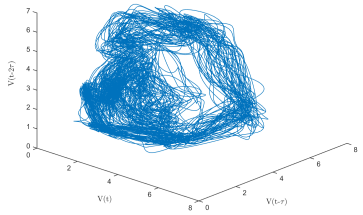

(i) $s/D = 2.2$

Figure 8.13: continues to following page

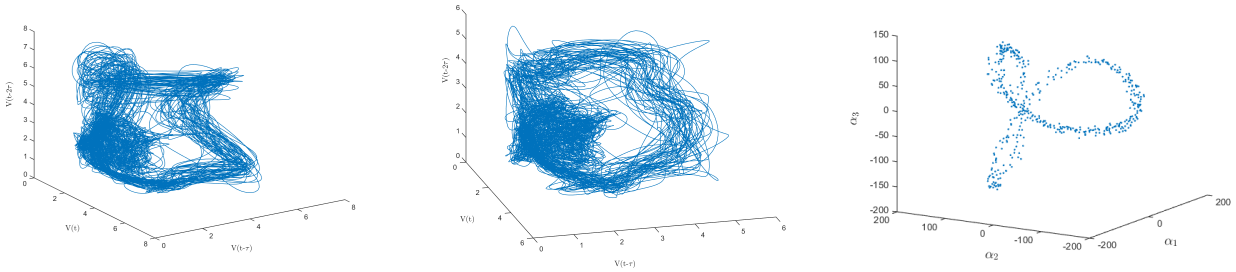

(j) $s/D = 2.4$ (k) $s/D = 2.6$ (l)POD α_1 vs α_2 vs α_3

Figure 8.13: Phase portraits from time delay embedding of the hotwire based measurements of vertical velocity fluctuations along the USL of the jet for the 0.35.55.70 double-pulse waveform with a $u'_{j,rms}/U_j = 0.50$ amplitude of excitation. For reference, figure (a) measures the jet flow centered just above the nozzle exit plane to represent the the input waveform dynamics before significant distortion and evolution of the flow. For comparison, figure (l) gives the POD based phase space reconstruction from the coefficients for the 3 dominant modes plotted for 600 instantaneous snapshots of the jet.

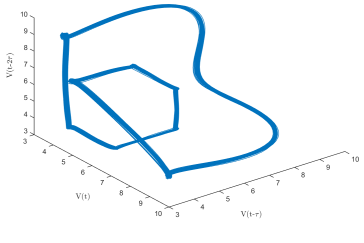

(a) Center of jet exit

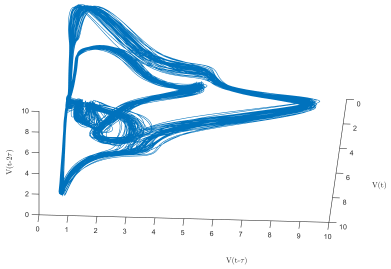

(b) $s/D = 0.5$

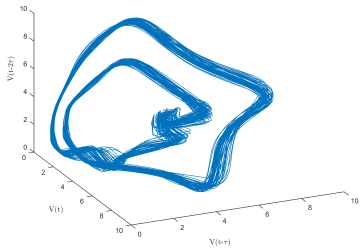

(c) $s/D = 1.0$

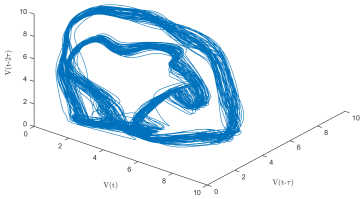

(d) $s/D = 1.2$

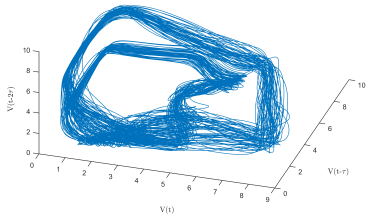

(e) $s/D = 1.4$

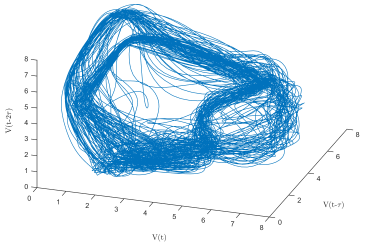

(f) $s/D = 1.6$

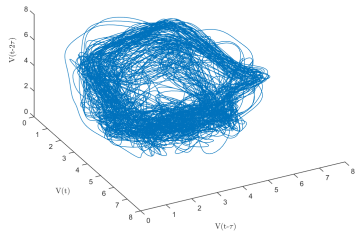

(g) $s/D = 1.8$

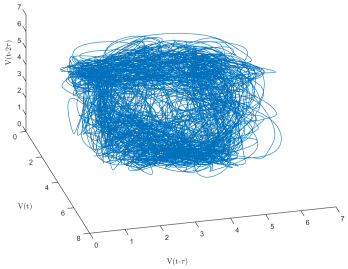

(h) $s/D = 2.0$

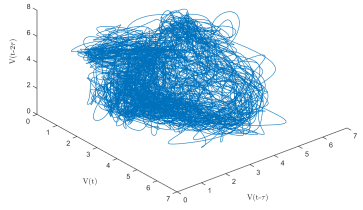

(i) $s/D = 2.2$

Figure 8.14: continues to following page

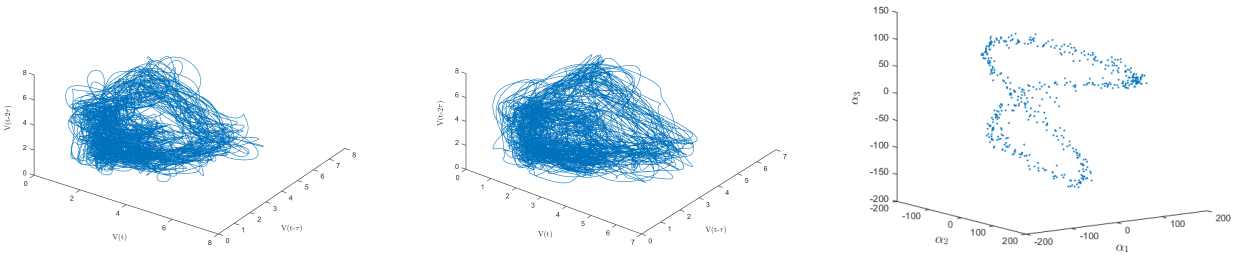

(j) $s/D = 2.4$ (k) $s/D = 2.6$ (l)POD α_1 vs α_2 vs α_3

Figure 8.14: Phase portraits from time delay embedding of the hotwire based measurements of vertical velocity fluctuations along the USL of the jet for the 0.35.65.80 double-pulse waveform with a $u'_{j,rms}/U_j = 0.50$ amplitude of excitation. For reference, figure (a) measures the jet flow centered just above the nozzle exit plane to represent the the input waveform dynamics before significant distortion and evolution of the flow. For comparison, figure (l) gives the POD based phase space reconstruction from the coefficients for the 3 dominant modes plotted for 600 instantaneous snapshots of the jet.

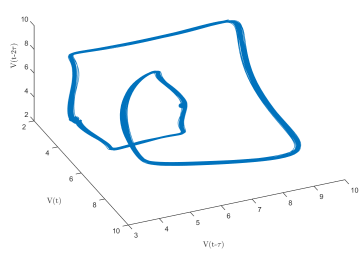

(a) Center of jet exit

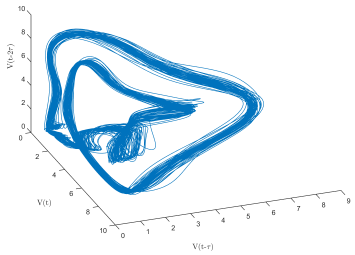

(b) $s/D = 0.5$

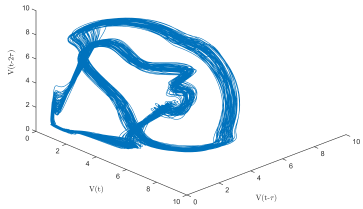

(c) $s/D = 1.0$

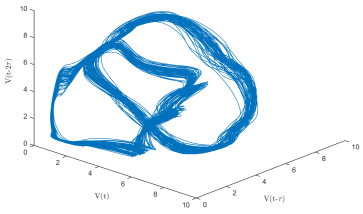

(d) $s/D = 1.2$

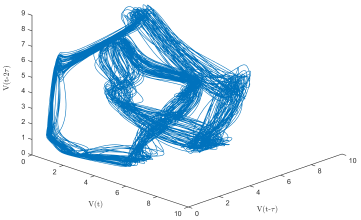

(e) $s/D = 1.4$

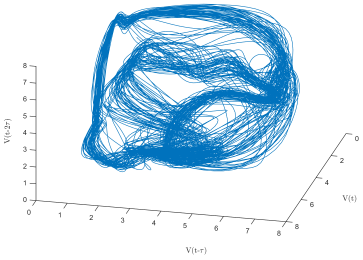

(f) $s/D = 1.6$

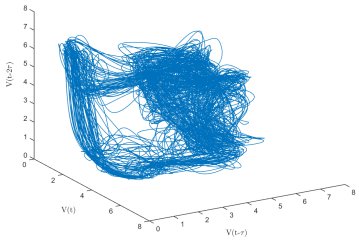

(g) $s/D = 1.8$

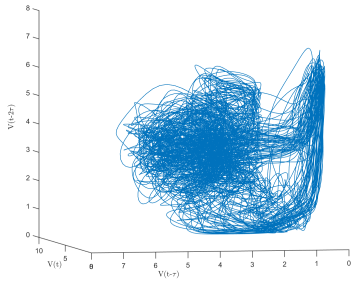

(h) $s/D = 2.0$

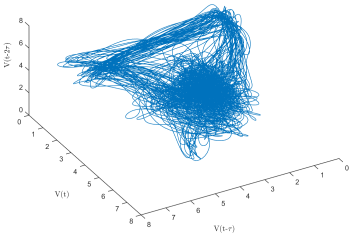

(i) $s/D = 2.2$

Figure 8.15: continues to following page

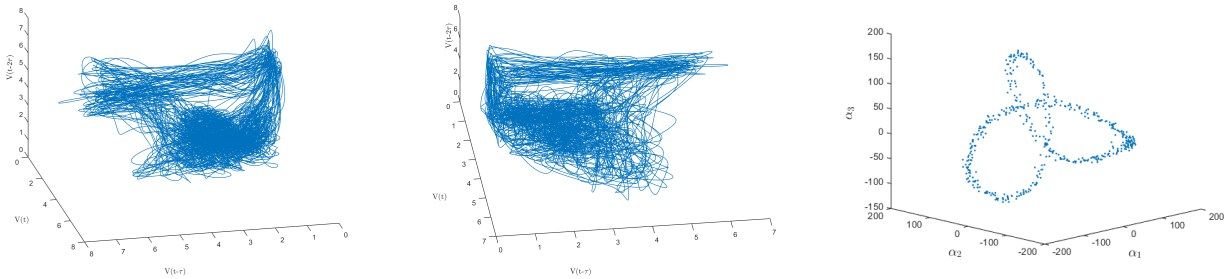

(j) $s/D = 2.4$ (k) $s/D = 2.6$ (l)POD α_1 vs α_2 vs α_3

Figure 8.15: Phase portraits from time delay embedding of the hotwire based measurements of vertical velocity fluctuations along the USL of the jet for the 0.35.75.90 double-pulse waveform with a $u'_{j,rms}/U_j = 0.50$ amplitude of excitation. For reference, figure (a) measures the jet flow centered just above the nozzle exit plane to represent the the input waveform dynamics before significant distortion and evolution of the flow. For comparison, figure (l) gives the POD based phase space reconstruction from the coefficients for the 3 dominant modes plotted for 600 instantaneous snapshots of the jet.

chaotic blob with no coherent trajectory at all, e.g. figures 8.13(g) and 8.15(g), and was attributed to a combination of the hotwire being situated along the dominant upstream shear layer trajectory, and the bifurcated nature of the jet. As the vortex rings propagated into the flowfield, their respective trajectories deviated owing to the distinct differences in celerity and strength of the rings, as representatively shown from the centerplane mean vorticity image of the 0.35.65.80 waveform in figure 8.5(e), and quite aptly visually depicted in chapter 7 for an analogously double-pulse forced jet. However, when acquiring measurements of the vertical velocity fluctuations, it was the upstream edge of the vortex ring associated with the quick pulse which was quantitatively established as the shear layer trajectory of the jet, and thus further downstream along the shear layer the hotwire did not detect any fluctuations associated with the vortex ring from the slow pulse. In all cases, progressing downstream along the shear layer resulted in trajectories in the phase portraits which were more diffuse and chaotic, which was representative of the onset of chaos in the flow and the breakdown of the vortex rings, the extent of which, as mentioned, was found to be very closely linked with the temporal spacing between the quick and slow pulses of the waveform.

Quite interestingly, an additional dynamic in the double-pulse excited jet flow was characterized by the hotwire based phase portraits which was not seen from the vorticity and structural images, the POD modes, or the POD coefficient based phase space reconstructions. It was found, representatively in the 0.35.65.80 waveform at $s/D = 0.5$ (figure 8.14(b)), that a phase space trajectory with an additional spiraling aspect over a portion of the smaller of the two loops could be produced, though it is not as clearly seen from the given projection of the 3D plot. The smaller of the two loops was representative of the vortex ring produced by the slow pulse, and the spiraling was found to be the emergence of quasiperiodicity due to instabilities which formed on the shear layer of the jet trailing column aft of the vortex ring. Though not shown here, these trailing column vortices were tracked in the pseudo time-resolved imaging, whereby determination of the instability frequency for the trailing column was made via calculations of the wavelength between successive trailing column vor-

tices (Kyle and Sreenivasan (1993)), resulting in an an estimated instability frequency of around $350 - 400\ Hz$. Zhao et al. (2000) note, from vorticity analysis of a starting jet, that these trailing column vortices are associated with a Kelvin-Helmholtz instability along the shear layer, and also point out their presence accelerates the pinch-off process and affects the overall circulation of the leading vortex ring. Other starting jet studies additionally point out the trailing column can continue to affect the main vortex ring even after pinch-off, with one particular example being the merger of the trailing vortices into the main vortex ring (Gharib et al. (1998); O'farrell and Dabiri (2010); Gao and Yu (2012)). Numerical simulations of a vortex ring in crossflow by Sau and Mahesh (2010) distinguish that the presence of a trailing column following a fully filled vortex ring acts to enhance the downstream entrainment in the crossflow, and even more, for a particular vortex ring velocity ratio, given by equation 1.12, there exists an optimal length to the trailing column.

8.1.3 Mixing

Shoji et al. (2019) demonstrates that when the JICF is CU, application of square or sinusoidal excitation to the jet improves the molecular mixing quantifications, but when the flow is AU, square wave excitation is more effective than sine wave forcing in enhancing the molecular mixing. Additionally, chapter 7 revealed significant enhancement to the mixing efficacy of an AU and CU JICF when the jet was axisymmetrically excited by a double-pulse forcing waveform. However the dependence of these results on the underlying dynamics, such as the state of synchronization of the jet to the forcing or the nearfield vortical interactions between successive vortex rings, and the relative enhancement in mixing of the double-pulse forcing compared with sine or square wave excitation was not investigated. Thus, the forcing conditions extensively examined in the preceding synchronization and dynamics sections (sections 8.1.1.1 and 8.1.2.1) were extended to analysis of the efficacy of molecular mixing between the jet and crossflow. The molecular mixing was quantified based on the instantaneous unmixedness parameter, which was determined from scalar PLIF images in

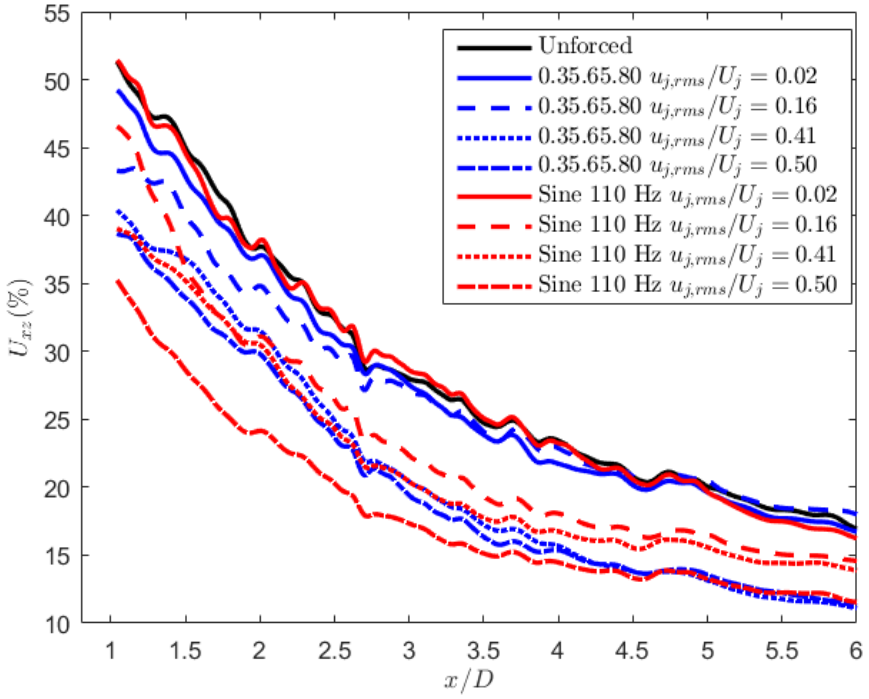

Figure 8.16: Evolution of centerplane unmixedness, U_{xz}, for the AU jet at $J = 6$, $Re_j = 1800$, and $\psi = 0.112$ with $f_f = 110\ Hz$ sinusoidal waveform (red) and 0.35.65.80 double-pulse waveform (blue) axisymmetric excitation of the jet for forcing amplitudes from $u'_{j,rms}/U_j = 0.00$ to $u'_{j,rms}/U_j = 0.50$. Lower unmixedness corresponds to better molecular mixing.

the jet centerplane. Calculating the unmixedness, which represents the second moment of the scalar concentration field, was performed with equation 1.8, where lower values of unmixedness correspond to better molecular mixing. For each of these evaluations of the flow the validity became unreliable after approximately $x/D = 5.5$ because certain jet forcing cases were found to propagate out of the FOV captured in the PLIF images.

Figure 8.16 presents the centerplane based instantaneous molecular mixing quantifications of the JICF when axisymmetrically excited by the $f_f = 110\ Hz$ sinusoidal and 0.35.65.80 double pulse waveforms investigated in sections 8.1.1.1 and 8.1.2.1, for forcing amplitudes corresponding to synchronization states of NSR, QP, LI and well beyond LI. As

was similarly noted earlier with the vorticity, jet structure, POD modes, and POD-based phase portraits, the sinusoidal and double-pulse forcing at $u'_{j,rms}/U_j = 0.02$ resulted in mixing characteristics which were qualitatively and quantitatively the same as the unforced jet, further indicative of the lack of improvements to the flowfield for such low level excitation. At an excitation amplitude of $u'_{j,rms}/U_j = 0.16$, the jet was just able to LI to the sinusoidal forcing, while the double-pulse forcing was firmly LI, and yet it was actually the sinusoidal forcing which demonstrated significant enhancement of the molecular mixing. This forcing amplitude condition interestingly also noted slightly different vorticity distributions between the two waveforms in the jet cross-sections at $x/D = 1.0$, significantly stronger dynamics for the sinusoidal forcing in the POD modes, and the emergence of the double-loop trajectory in the POD mode coefficient phase space of the double-pulse waveform. This suggested that while being able to achieve LI of the jet to the forcing was important in altering the vortex rollup along the jet shear layer, the effective fullness, celerity, and circulation of the vortex rings, and the resulting degree of induced vortical interactions was more important. Further increasing the forcing to $u'_{j,rms}/U_j = 0.41$ marked a flip in the effectiveness of the two waveforms, were the double-pulse forcing produced the better molecular mixing. Both waveforms were characterized by more distinct nearfield interactions and breakdown of the shear layer vortices, however, the double-pulse waveform was slightly more pronounced in vertical elongation of the vorticity and jet structure, noting the onset of jet bifurcation. As the forcing amplitude was increased to $u'_{j,rms}/U_j = 0.50$, the more efficient forcing waveform again transitioned, in this case with the sinusoidal waveform as the most efficient mixer. The caveat to this was that the differences in mixing efficacy were only noted in the nearfield of the jet, where by $x/D = 4.0$ the double-pulse forcing waveform had converged and actually slightly overtook the sinusoidal forcing in their respective quantitative mixing calculations. For these cases, the sinusoidal forcing generated a flow structure with accompanying dynamics which were extremely similar to the forcing at $u'_{j,rms}/U_j = 0.41$, however the increased strength of the double-pulse forcing acted to more substantially bifurcate the jet, and as

a result presumably detracted slightly from the nearfield interaction and breakdown of the vortical structures. Also, by continuing to increase the forcing amplitude of either waveform, while maintaining the forcing frequency and waveform shape, had the effect of systematically increasing the effective stroke ratios attributable to the vortex rings produced, and thus was altering the fullness, strength, and celerity of the vortex rings. These interesting trends in the improvements to the molecular mixing, and the potential effectiveness of the double-pulse forcing, further substantiated the need for selective optimization of the temporal spacing and temporal pulse-widths for a given forcing waveform rather than the degree to which the jet was LI to the forcing.

To systematically determine which type of forcing waveform was optimal for altering the dynamics and mixing characteristics of the unforced flow, sinusoidal forcing was compared with square wave and double-pulse forcing waveforms, all at the same forcing frequency of $f_f = 110\ Hz$ and forcing amplitude of $u'_{j,rms}/U_j = 0.50$; the forcing frequency for the double-pulse was given as 55 Hz, but it was effectively 110 Hz because a single forcing period consisted of two distinct pulses. Figure 8.17(a) presents the unmixedness quantifications along the jet centerplane for the square wave forcing cases. All of the waveforms improved the molecular mixing of the jet, where the best mixer was the square wave with a 40% duty cycle. From separate analysis not herein presented, the stroke ratio and ring velocity ratio associated with the $\alpha = 40\%$ square wave suggested the vortex rings produced were fully filled rings without the presence of a trailing column of jet fluid, according to the work by Sau and Mahesh (2010). The waveforms with duty cycles which were smaller than $\alpha = 40\%$ produced mixing enhancements which were more moderate as a result of relatively weak vortex rings which quickly penetrated and mixed but did not carry significant amounts of jet fluid into the flowfield. Duty cycles which were larger than $\alpha = 40\%$ yielded vortex rings with trailing columns, which Sau and Mahesh (2008) note act to entrain crossflow fluid, however the largest duty cycle case of $\alpha = 60\%$ actually appeared to worsen the molecular mixing of the jet. These trends in the molecular mixing of square wave excitation of an

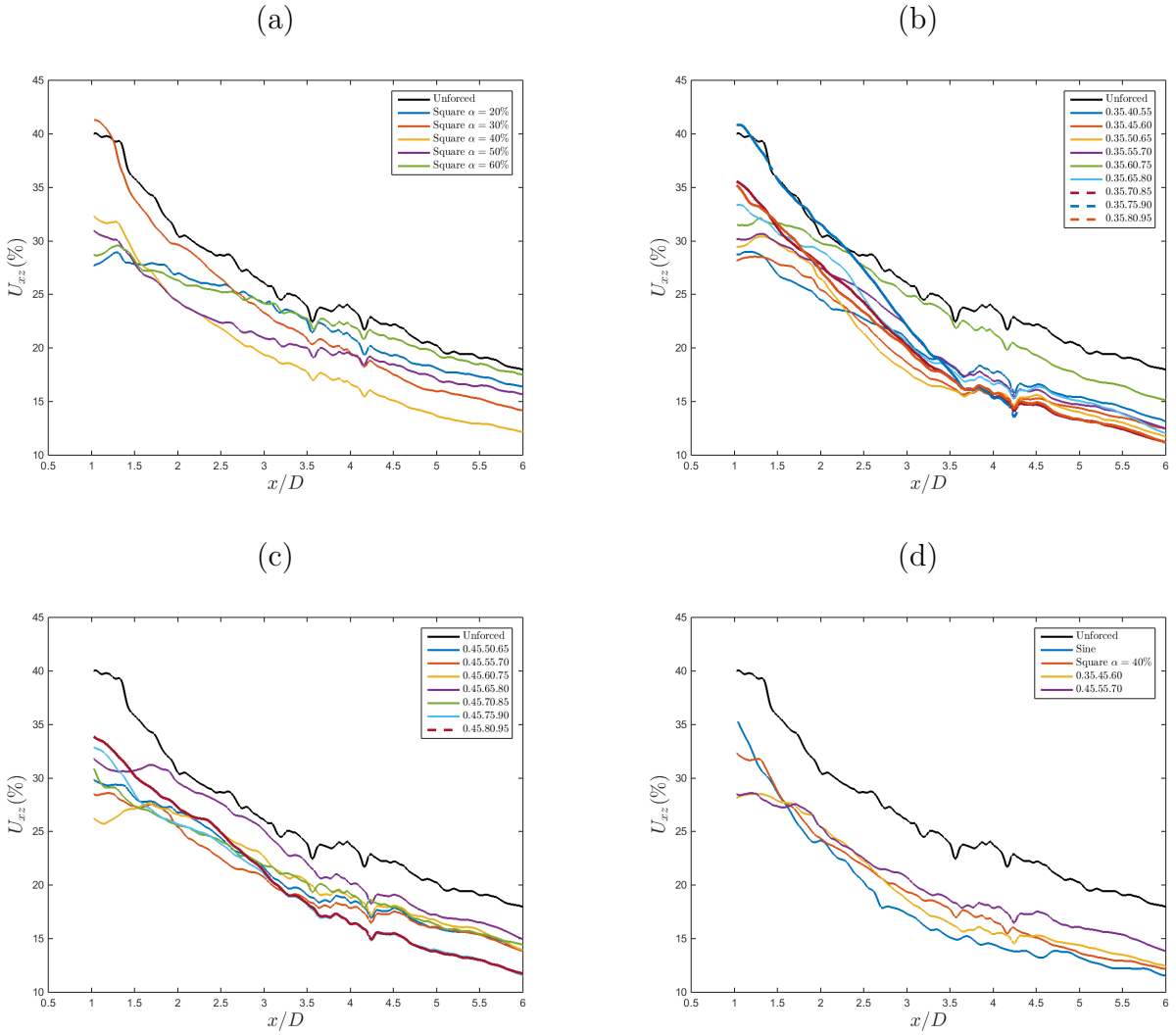

Figure 8.17: Evolution of the instantaneous centerplane unmixedness averaged over 600 images, U_{xz}, for the AU jet at $J = 6$, $Re_j = 1800$, and $\psi = 0.112$ with $u'_{j,rms}/U_j = 0.50$ amplitude axisymmetric excitation of the jet for: (a) $f_f = 110\ Hz$ square waves with various duty cycles, (b) double-pulse waveforms with the temporal pulse-widths fixed at $\tau_1/T = 0.35$ and $\tau_2/T = 0.15$, while the temporal spacing between pulses was varied, and (c) double-pulse waveforms with the temporal pulse-widths fixed at $\tau_1/T = 0.45$ and $\tau_2/T = 0.15$, while the temporal spacing between pulses was varied. (d) Singular figure comparing the mixing for sinusoidal, square, and double-pulse excitation waveforms. Lower unmixedness corresponds to better molecular mixing.

AU jet were similarly noted by Shoji et al. (2019). Figures 8.17(b-c) consider a variety of double pulse excitation waveforms where the temporal spacing between the quick and slow pulses was varied while maintaining the temporal pulse-widths of the two distinct pulses, to investigate the implications of the strength and location of induced nearfield vortical interactions on the mixing. Figure 8.17(b) treated the double-pulse waveforms with slow and quick temporal pulse-widths of $\tau_1/T = 0.35$ and $\tau_2/T = 0.15$ respectively, where the best molecular mixer was found to be waveform 0.35.45.60. Dynamically, this case was the waveform that eliminated the double-loop trajectory in the phase space most rapidly (figure 8.12), which was representative of the significant nearfield interaction and breakdown of the vortex rings. Interestingly, as the double-loop phase trajectory became more pronounced, highlighting the accentuated bifurcated nature of the jet and reduction in vortical interactions, the enhancements to the molecular mixing became more minimal. Synonymously, the improvements in molecular mixing were more significant when the quick pulse followed closely after the slow pulse, as logically the quick pulse more easily able to catch up to the slower pulse and interact with a portion of the vortex ring or trailing column, rather than the reverse of attempting to have the slow pulse catch the quick pulse. Figure 8.17(c) also depicted molecular mixing for double-pulse excitation of the jet, but with a broadened temporal pulse-width of $\tau_1/T = 0.45$. The resultant mixing enhancement looked nearly the same for all of the waveforms considered as all of the temporal spacings between the quick and slow pulses were able to produce nearfield vortex interactions and breakdown. This resulted from a combination of a reduction in the maximum possible temporal spacing between successive pulses, and that the generated slow pulse had an even larger trailing column and smaller celerity. Despite the similar mixing for each of the waves, the 0.45.50.65 or 0.45.55.70 waveforms were considered the best molecular mixers, which again supported the quick pulse issuing closely after the slow pulse rather than the reverse. Figure 8.17(d) plotted the mixing characteristics for the most effective double-pulse and square wave waveforms along with the sinusoidal waveform at the same forcing frequency. Quite appropriately all of the waveforms

demonstrated remarkable improvement in the overall mixing of the jet as compared to an unforced flow, and in general the most efficient mixers were all relatively similar in terms of optimal enhancement throughout the flow. This again lends support to the suggested importance of the generated vortex ring dynamics, such as celerity and stroke ratio, are in fact the important parameters of consideration, rather than the shape or coherence of the waveform (Sau and Mahesh (2010)). However, in delineating between the different forcing waveforms considered, it appears that double pulse forcing can be more effective than simple square wave forcing, though the full extent of this effectiveness would be further validated through investigations of additional waveform shapes, with different temporal pulse-widths for the slow and fast pulses. Beyond this, it appeared the sinusoidal waveform was the most effective at this applied forcing amplitude, which may be in part due to the propensity for the square and double pulse waveforms to generated a bifurcated flow, which herein has been seen as a less effective flowfield for mixing. This is a matter of continued interest and exploration.

8.1.4 Alternative Forcing Waveforms

Throughout the investigation of the dynamics and synchronization characteristics of the axisymmetrically forced jet, it became clear that at relatively large forcing amplitudes the dynamics of the jet were fundamentally altered, and in the phase space, synchronization states other than a simple limit cycle attractor were generated. It was optimistically thought that a forcing condition may give rise to a strange non-chaotic attractor (SNA) phase state projection of the flowfield dynamics, given some of the complex Lissajous-like phase space constructions from POD coefficient mapping of a helically excited JICF noted by Besnard (2019), and onset of a SNA given strong external periodic acoustic excitation of a self-excited thermoacoustic oscillator seen by Guan et al. (2018). However, no such SNA in the phase space was generated from the simple periodic excitation of the jet, which Prasad et al. (2001) note as an extremely difficult method of producing a SNA. It was thus of interest

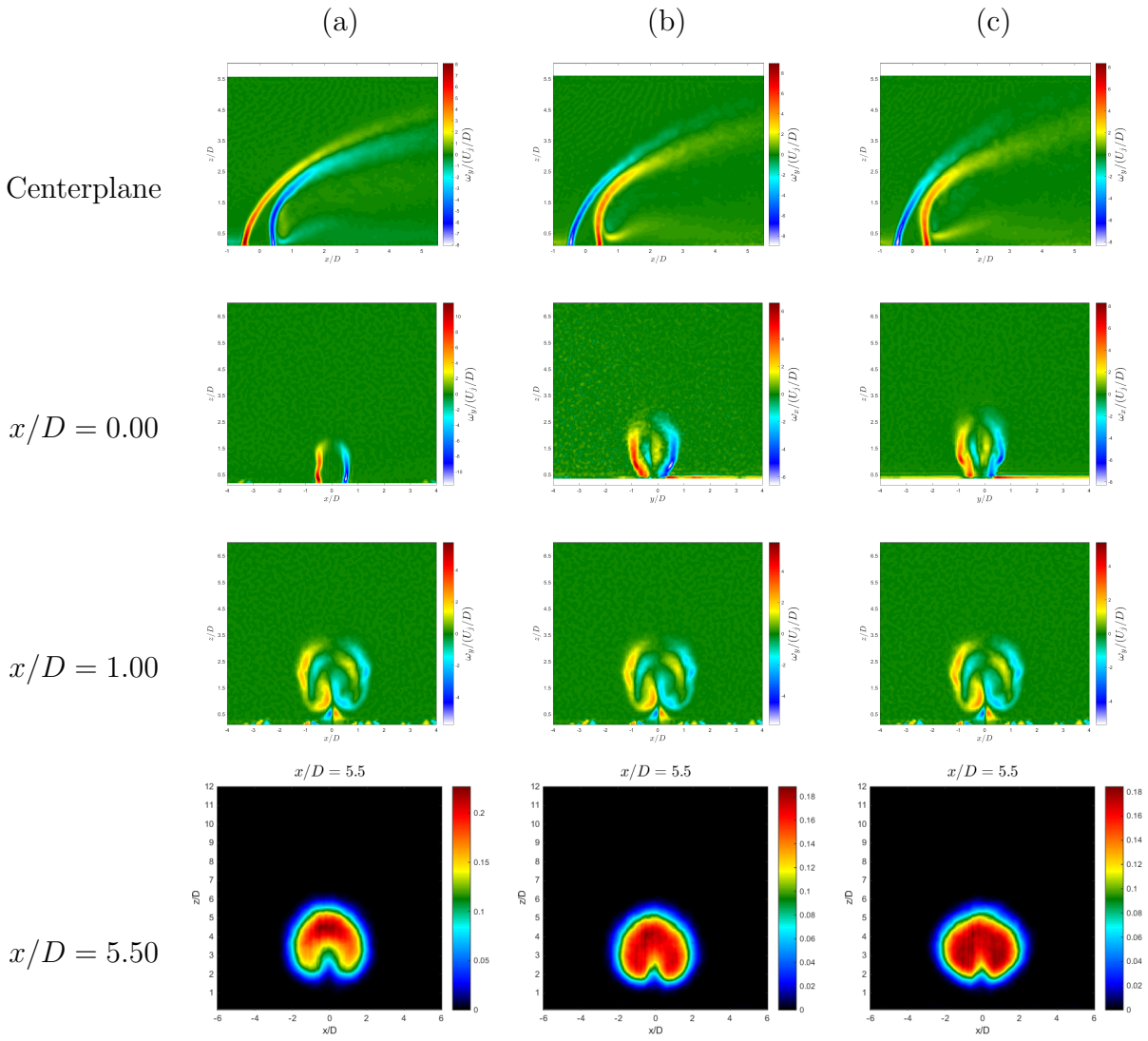

Figure 8.18: continues to following page

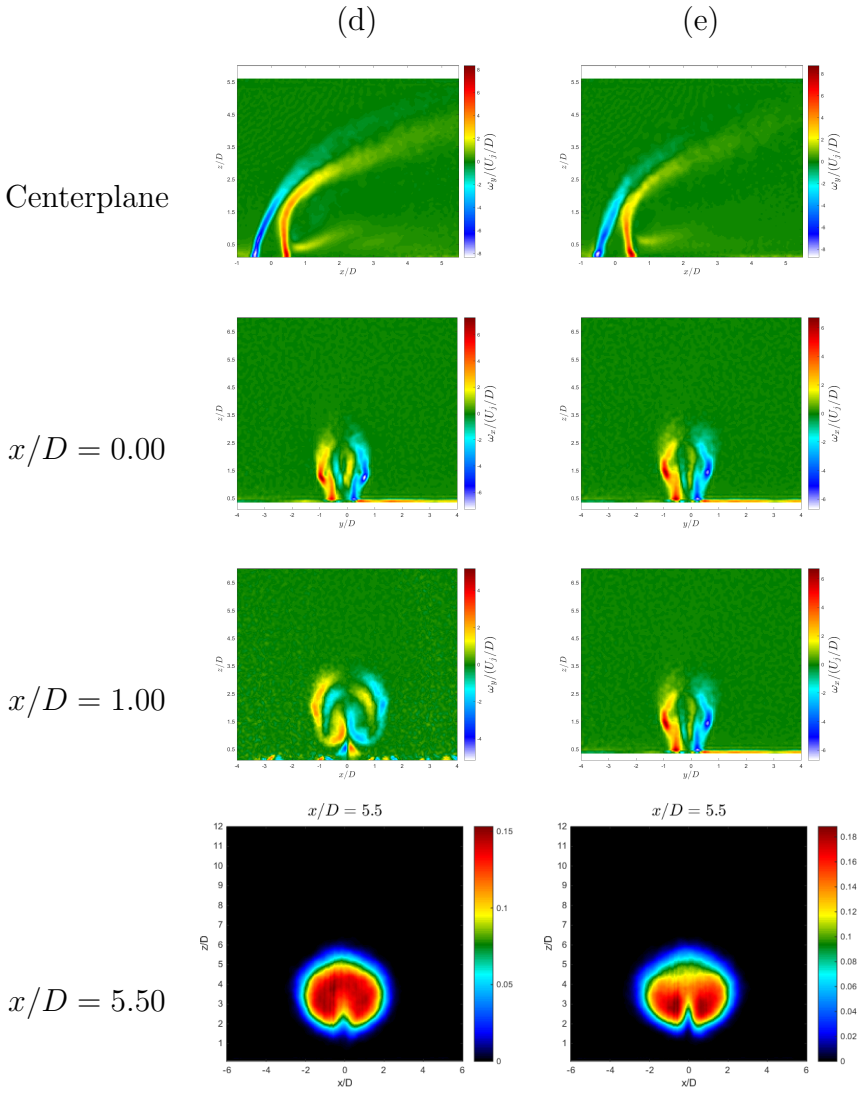

Figure 8.18: Depictions of the mean vorticity along the jet centerplane, mean vorticity at jet cross-sectional locations of $x/D = 0.4$ and $x/D = 1.0$, and the mean cross-sectional jet structure at $x/D = 5.5$ for the incommensurate waveform axisymmetric excitation of the jet, with excitation amplitudes of (a) $u'_{j,rms}/U_j = 0.00$, (b) $u'_{j,rms}/U_j = 0.06$, (c) $u'_{j,rms}/U_j = 0.16$, (d) $u'_{j,rms}/U_j = 0.20$, and (e) $u'_{j,rms}/U_j = 0.29$. The images are averaged over 600 instantaneous realizations, and the colorbars are individually scaled to the maximum and minimum values contained within each mean image. The vorticity and structural data were extracted from stereo-PIV and scalar PLIF imaging, respectively.

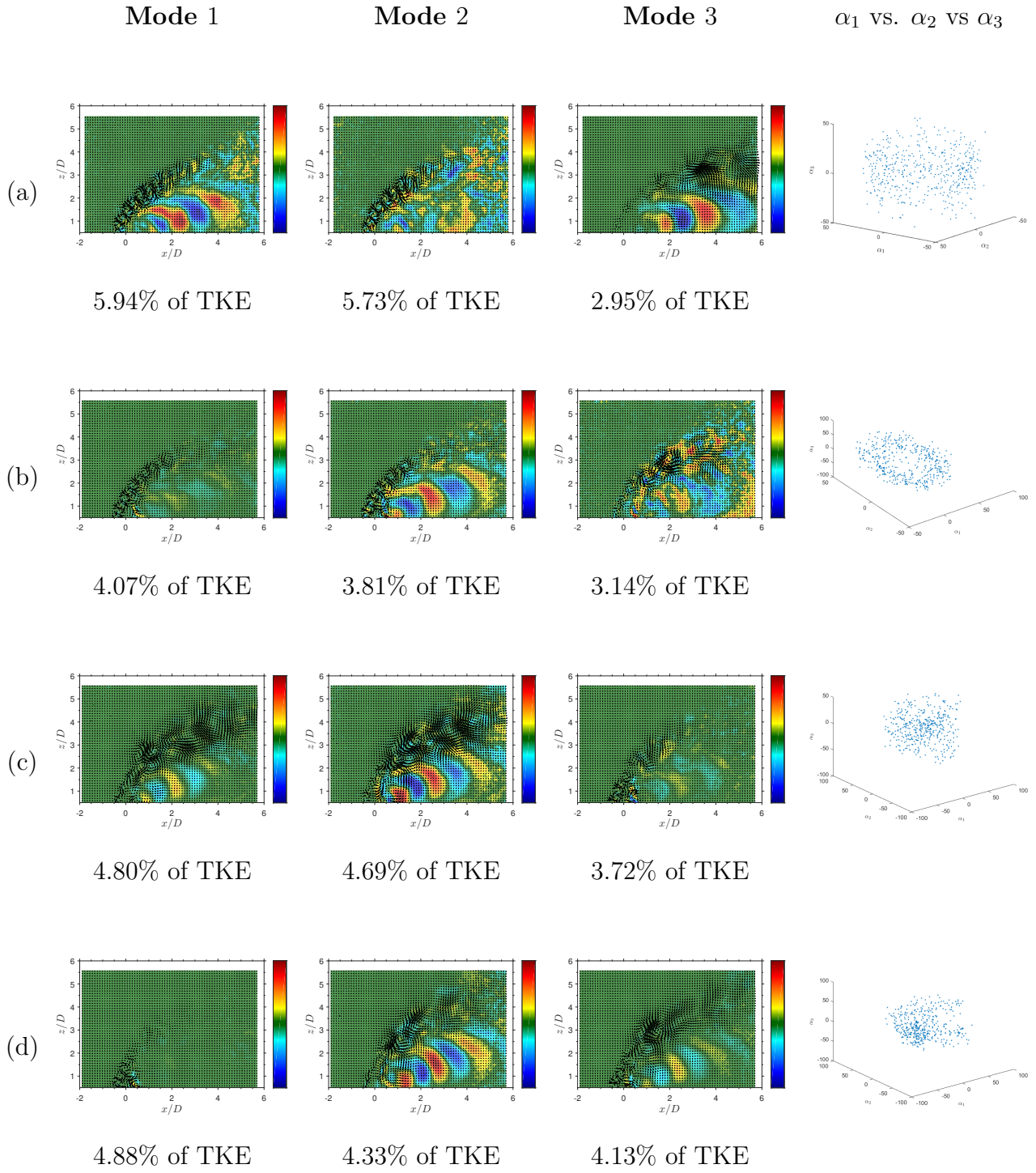

Figure 8.19: continues to following page

(e)

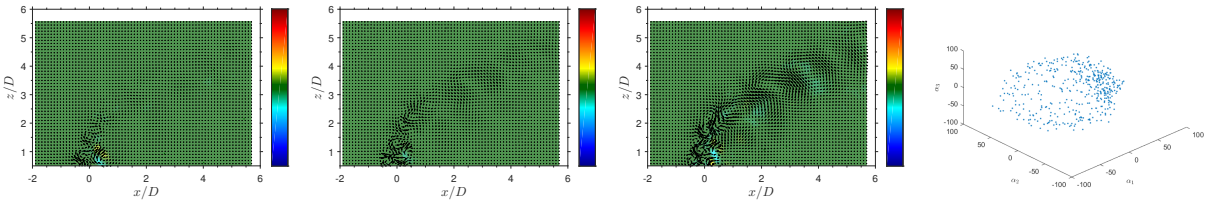

10.19% of TKE 7.20% of TKE 6.15% of TKE

Figure 8.19: PIV based POD mode structures for the first 3 modes, and phase space reconstructions of mode dynamics from mode coefficient plots of α_1 vs. α_2 vs α_3, extracted from 600 instantaneous snapshots of the centerplane velocity field for the incommensurate waveform axisymmetric excitation of the jet, with excitation amplitudes of (a) $u'_{j,rms}/U_j = 0.00$, (b) $u'_{j,rms}/U_j = 0.06$, (c) $u'_{j,rms}/U_j = 0.16$, (d) $u'_{j,rms}/U_j = 0.20$, and (e) $u'_{j,rms}/U_j = 0.29$. The modes are sorted according to their respective percentages of total kinetic energy fluctuation content. The colorbar in each image represents the mode scaled by its own norm and the mean jet velocity at the jet exit U_j.

to see if a SNA could be forcibly induced from the careful selection of a different excitation waveform, in hopes of studying how such a dynamical state would impact the mixing of the jet flow. The inducement of a SNA is generally most readily formed experimentally from the application of quasiperiodic forcing applied to a nonlinear dynamical system (Ditto et al. (1990); Zhou et al. (1992); Liu and Zhu (1996); Zhu and Liu (1997); Yang and Bilimgut (1997)). Thus, the applied forcing waveform was selected as a linear combination of two simple sinusoidal excitation waveforms with equal forcing amplitudes, which had frequencies that were incommensurate with each other, as well as the natural instability of the jet. The natural jet instability for the AU flow was approximately $f_0 = 375\ Hz$, and the selected forcing frequencies were $f_{f,1} = 421\ Hz$ and $f_{f,2} = 500\ Hz$. Forcing was applied at amplitudes ranging from $u'_{j,rms}/U_j = 0.06$ to $u'_{j,rms}/U_j = 0.29$.

Shown in figure 8.18 are the centerplane and $x/D = 0.4$ and $x/D = 1.0$ cross-sectional mean vorticity distributions, along with structural characteristics further downstream at $x/D = 5.5$ for the quasiperiodic or incommensurate-frequency forcing waveforms. Impres-

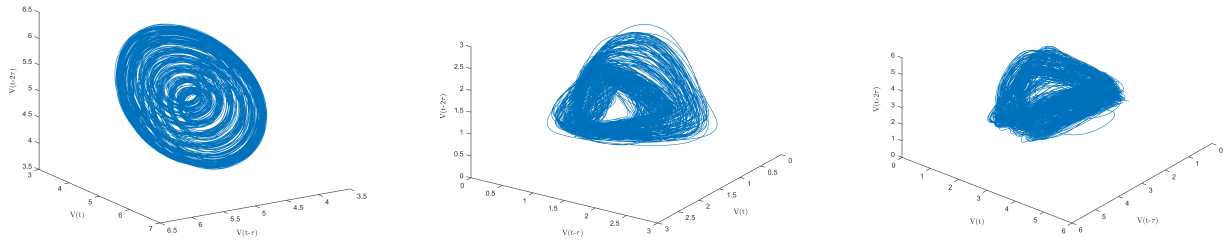

(a) Center of jet exit (b) $s/D = 0.5$ (c) $s/D = 1.0$

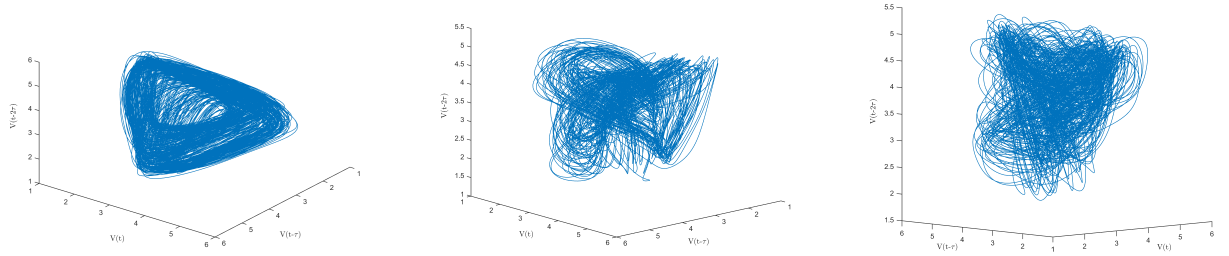

(d) $s/D = 1.2$ (e) $s/D = 1.4$ (f) $s/D = 1.6$

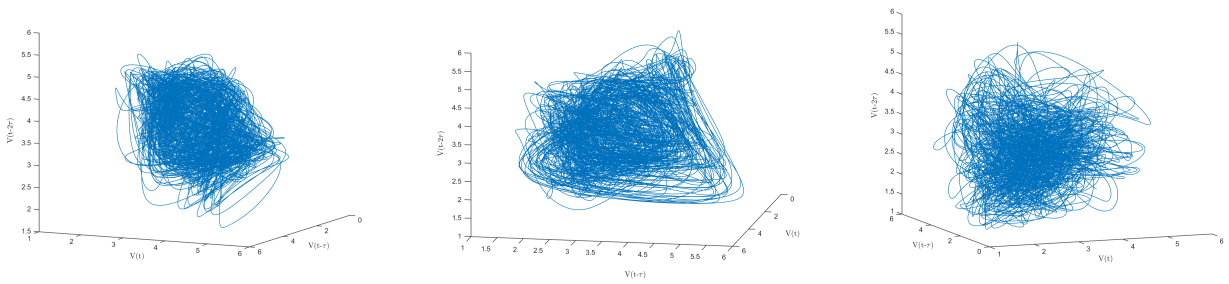

(g) $s/D = 1.8$ (h) $s/D = 2.0$ (i) $s/D = 2.2$

Figure 8.20: continues to following page

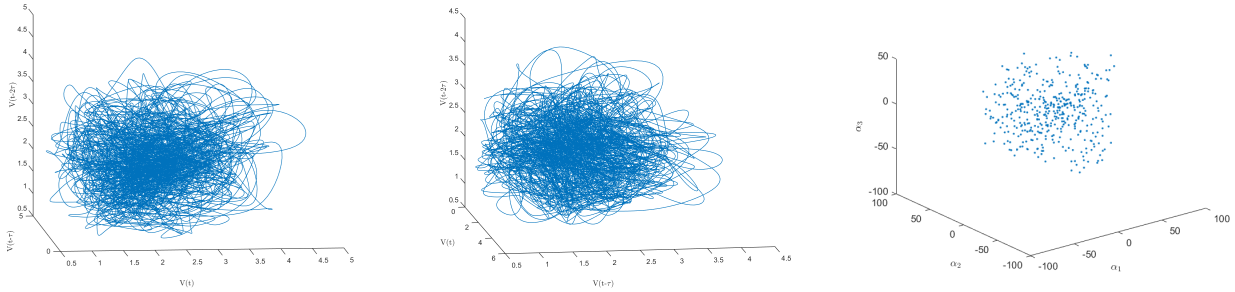

(j) $s/D = 2.4$ (k) $s/D = 2.5$ (l)POD α_1 vs α_2 vs α_3

Figure 8.20: Phase portraits from time delay embedding of the hotwire based measurements of vertical velocity fluctuations along the USL of the jet for the incommensurate waveform axisymmetric excitation of the jet, with a $u'_{j,rms}/U_j = 0.16$ amplitude of excitation. For reference, figure (a) measures the jet flow centered just above the nozzle exit plane to represent the the input waveform dynamics before significant distortion and evolution of the flow. For comparison, figure (l) gives the POD based phase space reconstruction from the coefficients for the 3 dominant modes plotted for 600 instantaneous snapshots of the jet.

sively, all of the the structures and vorticity distributions were remarkably similar to the unforced jet. Even for a maximum applied forcing amplitude of $u'_{j,rms}/U_j = 0.29$ (figure 8.18(e)), nearly 30% of the jet mean flow, the resulting jet did not penetrate more deeply into the flowfield or produce a bifurcation, characteristics which were seen with the sinusoidal and double-pulse waveforms. However it was noted that while the overall trajectory and strength of vortical structures remained consistent, as the forcing increased there was a slight deterioration of the shear layer vorticity earlier in the evolution of the jet flow. Additionally the cross-sectional CVP structure, as depicted from the PLIF-based scalar concentration of the jet at $x/D = 5.5$, evolved into more distinct lobes with less jet fluid concentrated in the top portion of the CVP, where the top portion of the CVP is generally given by the upstream and downstream shear layers which have folded together. This was suggestive that the shear layers were indeed responsive to the applied forcing, and the nearfield vortex evolution and

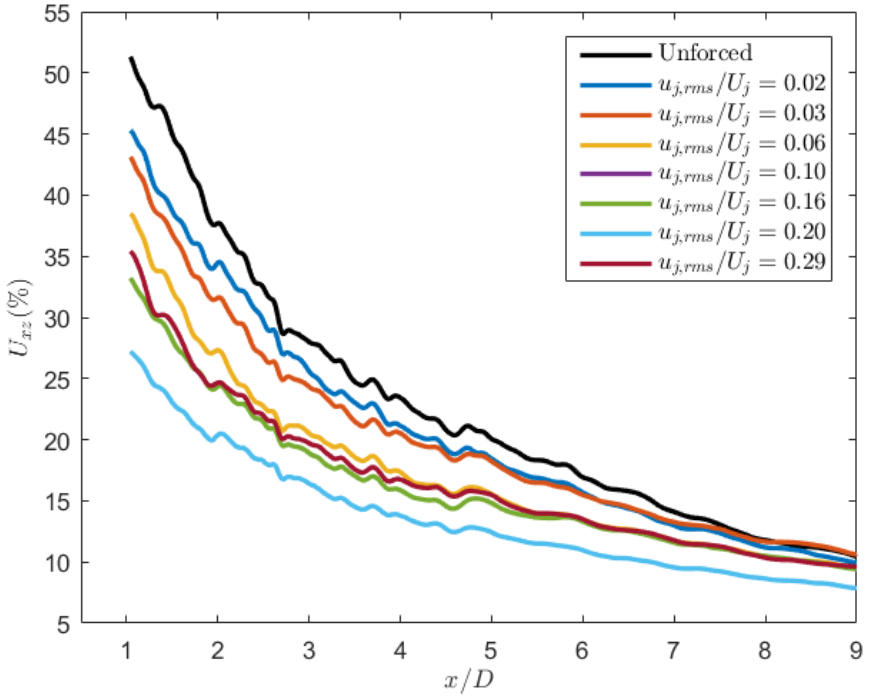

Figure 8.21: Evolution of centerplane unmixedness, U_{xz}, for the AU jet at $J = 6$, $Re_j = 1800$, and $\psi = 0.112$ with incommensurate ($f_{f,1} = 421\ Hz$ and $f_{f,2} = 500\ Hz$) axisymmetric excitation of the jet for forcing amplitudes from $u'_{j,rms}/U_j = 0.00$ to $u'_{j,rms}/U_j = 0.29$. Lower unmixedness corresponds to better molecular mixing.

breakdown were impacted.

To investigate the impact of the forcing on the underlying jet dynamics, particularly those along the upstream shear layer, snapshot POD was applied to the centerplane PIV images. Figure 8.19 depicts the first 3 most dominant POD modes along with the representative phase space reconstruction of these dynamics from plotting of the mode coefficients. The dynamics of the unforced jet, which have been discussed extensively in the prior sections, are given in figure 8.19(a) for reference. Interestingly, unlike the modes associated with the sinusoidal or double-pulse forcing, as the incommensurate forcing was applied, the kinetic energy percentages in the first three modes actually decreased, and it was not until the

maximum forcing amplitude treated ($u'_{j,rms}/U_j = 0.29$) that the kinetic energy percentages overcame those for the unforced jet. With the exception of this higher forcing amplitude case, all of the dynamic structures in the modes featured the USL vortices, the upright wake structures connected between the downstream of the jet and the wall boundary region, and some element of vortex interaction or merger along the jet shear layer, though the relative ordering of these dynamics in the modes was inconsistent. Given the similar energy percentages across the 3 modes for the forced cases, the changes in the ordering of the modes was not considered of extreme significance. For the mode dynamics of the most excited jet in figure 8.19(e), the first three modes were represented by dynamics isolated solely along the upstream shear layer of the jet. Aside from the unforced jet, the phase space constructions from the POD mode coefficient plots depicted no coherent phase trajectory, and further actually eliminated the periodic coupling between the USL dynamics in modes 1 and 2 which was noted in the unforced jet. The application of the forcing signal, in combination with the natural instability frequency of the jet, resulted in three incommensurate frequencies competing along the shear layer of the jet, and as such produced dynamics which were more difficult to represent from a singular mode. This accounted for the more distributed energy content of the dominant modes, and the lack of coherent periodicity in the shear layer dynamics. For additional investigation of the shear layer dynamics, the jet was explored via hotwire-based phase portraits of the vertical velocity fluctuations along the USL of the jet at multiple locations along the shear layer. Figure 8.20 gives a representative depiction of these dynamics for the incommensurate forcing with a $u'_{j,rms}/U_j = 0.16$ amplitude of excitation. As was likewise noted from the POD modes and coefficient mapping, the dynamics along the shear layer very quickly deteriorated in coherence, where in the phase space the ring like limit-cycle attractor was eliminated by $s/D = 1.3$ for this forcing amplitude. Interestingly, for the phase portraits in the range of $s/D = 1.3-1.6$, the trajectories revealed shapes which appeared quite chaotic, there were some distinctly identifiable features or repeated paths. These types of phase portraits were quite possibly representative of a strange attractor,

however no additional calculations or experiments have been conducted to verify such as classification of the state space.

Despite the necessitation of additional studies to further validate the generation of a strange attractor dynamical system for the axisymmetrically excited JICF, the preliminary investigation of incommensurate forcing of the jet was extended to analyze the resulting efficacy of mixing. Figure 8.21 shows the resulting molecular mixing for the various forcing conditions, as quantified by the instantaneous unmixedness parameter applied along the centerplane of the jet. Quite impressively, every forcing condition was able to improve the molecular mixing of the flowfield, even for a forcing amplitude of $u'_{j,rms}/U_j = 0.02$, which had previously not demonstrated alterations to the mixing with application of a sinusoidal or double-pulse waveform. The improvements in mixing were also seen to systematically enhance as the forcing amplitude was systematically increased, with the forcing amplitude of $u'_{j,rms}/U_j = 0.29$ as the lone exception. Instead, the second largest forcing amplitude of $u'_{j,rms}/U_j = 0.20$ was found to produce the best enhancements in molecular mixing, and quite remarkably was able to still generate enhancements to the mixing even further downstream at $x/D = 9.0$, whereby generally all of the mixing trends are seen to have coalesced. The regression in mixing enhancement as the forcing amplitude was increased from $u'_{j,rms}/U_j = 0.20$ to $u'_{j,rms}/U_j = 0.29$ coincided with similarly distinct changes in the jet vorticity, cross-sectional structure, and POD mode dynamics. It is thought that perhaps increasing the forcing to $u'_{j,rms}/U_j = 0.29$ resulted in the quasiperiodicity of the incommensurate forcing completely overpowering the jet natural instabilities such that the desired interactions between the three frequencies for the promotion of a SNA gave way to a simple QP flowfield. It may also be that the increased strength of the forcing killed off the wake dynamics as no such structures were seen in the first 3 dominant POD modes from figure 8.19(e), noting that the wake structures act to entrain wall boundary fluid into the jet, and thus enhance the mixing processes. Still, the incommensurate frequency forcing is seen to significantly improve the efficacy of mixing compared with the unforced jet, and even

that of the sinusoidal, square, or double-pulse waveforms in figure 8.17(d), and as such it is of extreme interest to continue to explore the underlying dynamics of such quasiperiodic forcing waveforms and the possibility of SNA flowfields.

8.2 Discussion

Hotwire based synchronization analyses provided for significant insights to the documented (M'Closkey et al. (2002); Davitian et al. (2010b); Shoji et al. (2019)) distinct differences in jet spread penetration and mixing between sinusoidal and square wave excitation of an absolutely unstable JICF. Experimentation demonstrated over 80% energy reduction in the required amplitude to achieve lock-in when implementing a square wave excitation rather than a sinusoidal one. Variation in the duty cycle of the applied square wave also proved to influence the ability of the jet to synchronize with the forcing. Generation of the square wave was accomplished with a 15-term Fourier series, where the reduction in the number of terms corresponded to a reduction in the ability to lock-in the forcing. Similar findings regarding the required forcing amplitude to achieve lock-in when changing the duty cycle or number of terms in the Fourier series were also noted by an analogous Van der Pol oscillator model.

Proper orthogonal decomposition (POD) modes extracted from centerplane velocity field measurements showed significant influence of both sinusoidal and double-pulse forcing of the jet, where the resulting dynamics were characteristically different owing to the different shapes of the waveforms. Sinusoidal forcing generated a slightly deeper penetrating jet, while double-pulse forcing, at higher forcing amplitudes, generated a bifurcated jet structure. At larger forcing amplitude the sinusoidal forcing was represented by stronger and more coherent mode structures, while the double-pulse forcing produced a more complex and structurally chaotic set of mode structures owing to the induced nearfield vortex interactions and breakdown. Phase portraits extracted from POD mode coefficient plots produced periodic

(circular) shapes for sinusoidal excitation, while double-pulse forcing produced a double loop trajectory indicative of the two distinct pulses during a single forcing period. Both sets of phase portraits were were complimented by separate phase space reconstructions from time delay-embedding analysis of hotwire based measurements of the vertical velocity along the USL of the jet.

Mixing quantifications when comparing sinusoidal and double-pulse waveforms, as the relative forcing amplitude was increased, did not demonstrate consistent trends in mixing improvement. The mixing enhancements appeared linked to the synchronization of the forcing, the fullness of the vortex rings, and the relative nearfield interaction of the produced vortical structures. These dependencies were further demonstrated in examination of double-pulse waveforms with differing duty pulse-widths and temporal spacing between pulses, at a fixed forcing amplitude. Cases wherein the jet had nearfield vortical interactions and breakdown, resulting in a more singular loop shape in the POD coefficient plots, produced the greatest enhancement in the molecular mixing. The best molecular mixers for double-pulse forcing, square wave forcing, and sinusoidal forcing all generated similar mixing enhancements, suggestive that the shape of the forcing waveform generating the vortical structures may not be as important as the resulting dynamics of the vortex ring produced, as promoted by Sau and Mahesh (2010).

Preliminary investigations into application of a quasiperiodic forcing waveform demonstrates significant enhancements to the flowfield. POD modes, centerplane vorticity, and cross-sectional jet structure reveal nearly identical characteristics with the unforced jet, regardless of forcing amplitude. Mixing quantifications demonstrate significant enhancements with the forcing, complimenting a slight enhanced coherence of the cross-sectional CVP. Meanwhile POD mode coefficient plotting and hotwire based vertical velocity phase portraits illustrate the possible generation of a strange attractor, though additional investigation is needed for validation.

Part III

Coaxial Jet in Crossflow

CHAPTER 9

Motivation and Features of the Coaxial JICF

9.1 Motivation

In consideration of the significant dependence of the CVP development on the nearfield jet dynamics, numerous studies have focused distinctly on the shear layer vortices and the USL instabilities in the nearfield of the jet exit. Among the more important findings in the experiments, with confirmation in theory and computations, is that as the momentum flux ratio J and/or the density ratio S are decreased, there is a critical transition along the jet's upstream shear layer from a weak convective instability to that of a strong, pure-tone absolute or global instability (Megerian et al. (2007); Getsinger et al. (2012); Alves et al. (2007), (2008); Iyer and Mahesh (2016); Regan and Mahesh (2017); Shoji et al. (2020b)). In further understanding the underlying mechanisms of the transition of the USL instabilities, recent experimental (Shoji et al. (2020b)) and numerical (Iyer and Mahesh (2016)) works find that the leading edge of the jet just after the injection plane can be modeled after a counter-current shear layer (CCSL) analogy, arising from the relative degree of counter-flow induced by the recirculation zone and hovering vortex on the leading edge of the jet, and that the determination of the transition in the USL instabilities qualitatively agrees with the LSA of a hyperbolic-tangent CCSL by Huerre and Monkewitz (1985). Specifically this determination is based on the shear layer velocity ratio, given as R_1 in equation 1.6, is large enough, the counterflow between the streams can create transition from convective to absolute instability in the shear layer. Even more recently, Souza et al. (2020) demonstrate excellent quantitative and qualitative agreement in the transition of the jet instabilities when

accounting for curvature and viscous effects, and matching the momentum thickness of the experimental jet flow in the LSA. Relating the instabilities to the CVP, both experimental (Getsinger et al. (2014)) and numerical (Regan and Mahesh (2017)) studies importantly demonstrate that while an absolutely unstable (AU) shear layer produces a CVP which is quite symmetric, as the instabilities become weakly convectively unstable (CU) there is a susceptibility for the CVP to develop asymmetrically, with Gevorkyan et al. (2016) noting that generally more symmetric CVP generation is associated with better molecular mixing of the jet. As such it is desirable to induce absolute instability in the flow so as to create stronger vortex rollup along the USL leading to a strong symmetric CVP and thereby improve the molecular mixing throughout the flowfield.

Given the analogous relationship between the instability characteristics of the JICF and a CCSL, and studies which demonstrate the significance of coflow or counterflow on the instability characteristics of free coaxial jets (Jendoubi and Strykowski (1994); Sevilla et al. (2002); Talamelli and Gavarini (2006)), it was of interest to introduce small amounts of suction to a naturally CU JICF to investigate the alterations brought about in the nearfield shear layer instabilities, jet dynamics further downstream, CVP formation, and mixing characteristics of the jet. The flow particularly treated a CU JICF with flow properties of $S = 1.00$, $J = 41$, $Re_j = 1900$, and acetone mole fraction of $\Psi = 0.112$, where the resulting structure in the mean cross-section of the jet is shown quite consistently to produce an asymmetric CVP (Harris et al. (2020a)). Coaxial jet flow was introduced from suction applied along a narrow $\theta = 36^\circ$ azimuthal span of the outer nozzle, and was investigated for symmetry preserving orientations about the jet periphery, i.e. directly in the upstream and downstream edges of the jet respectively. The suction flow rate was systematically increased from 0 to 60 $scfh$. Diagnostic measurements consisted of hotwire-based shear layer spectral contour plots of the instabilities along the USL of the jet, PIV imaging of the jet centerplane for investigation of the vorticity generation and flow dynamics, and PLIF imaging of the jet centerplane and cross-sectional locations for evaluation of the jet structure and molecular mixing.

9.2 Supplemental Setup and Experiment Modifications

The general experimental setup and configurations are given in chapter 2, which details the wind tunnel, flow plumbing, optical setup, and diagnostic tools and methods. Here details are given which were specific to the studies conducted in chapter 10. For this experimental investigation of the JICF, the jet injector was given by a coaxial flush nozzle, a depiction of which is given in figure 9.1. The inner nozzle was machined with the same 5^{th} order polynomial contraction, which produced a top-hat velocity profile and relatively thin momentum thickness at the nozzle exit, as the flush nozzle detailed in section 2.1.1; the nozzle diameter was $D = 3.81\ mm$. The wall thickness between the inner and outer nozzles was designed to the limiting constraints of machinability so as to minimize the influence of a wall thickness effect between the two flows. The resulting annular wall thickness was a mere 0.12 diameters, and the diameter of the outer annulus was $D = 5.94\ mm$. Suction into the outer annulus entered into an internal chamber which then fed into four equally spaced plumbing connections in the sides of the nozzle; the inclusion of four equidistant ports was implemented so as to promote uniform suction about the azimuth of the outer annulus. The plumbing lines then merged and were connected to a flow meter which registered flow rates ranging from 0 to 60 $scfh$. Following the flow meter was a vacuum pump (Welch Duoseal 1402B-01) which provided the pressure drop to generate the suction at the nozzle. Maintaining the flush nature of injection to the wind tunnel was accomplished through affixing the jet injection system to the removable floor shown in figure 2.2(a). In order to selectively apply suction only in the upstream or downstream edges of the jet, industrial ducting tape was applied over the wind tunnel floor and nozzle exit to seal portions of the outer annulus.

A singular flow condition was treated within this study, consisting of an equidensity flow with constituent species mole fractions of 0.112, 0.100, and 0.788 for the acetone, He, and N_2 respectively. The flow had a Reynolds number of $Re_j = 1900$, with a bulk jet velocity of $U_j = 7.19\ m/s$ and examined a singular CU jet at a momentum flux ratio of $J = 41$, given the

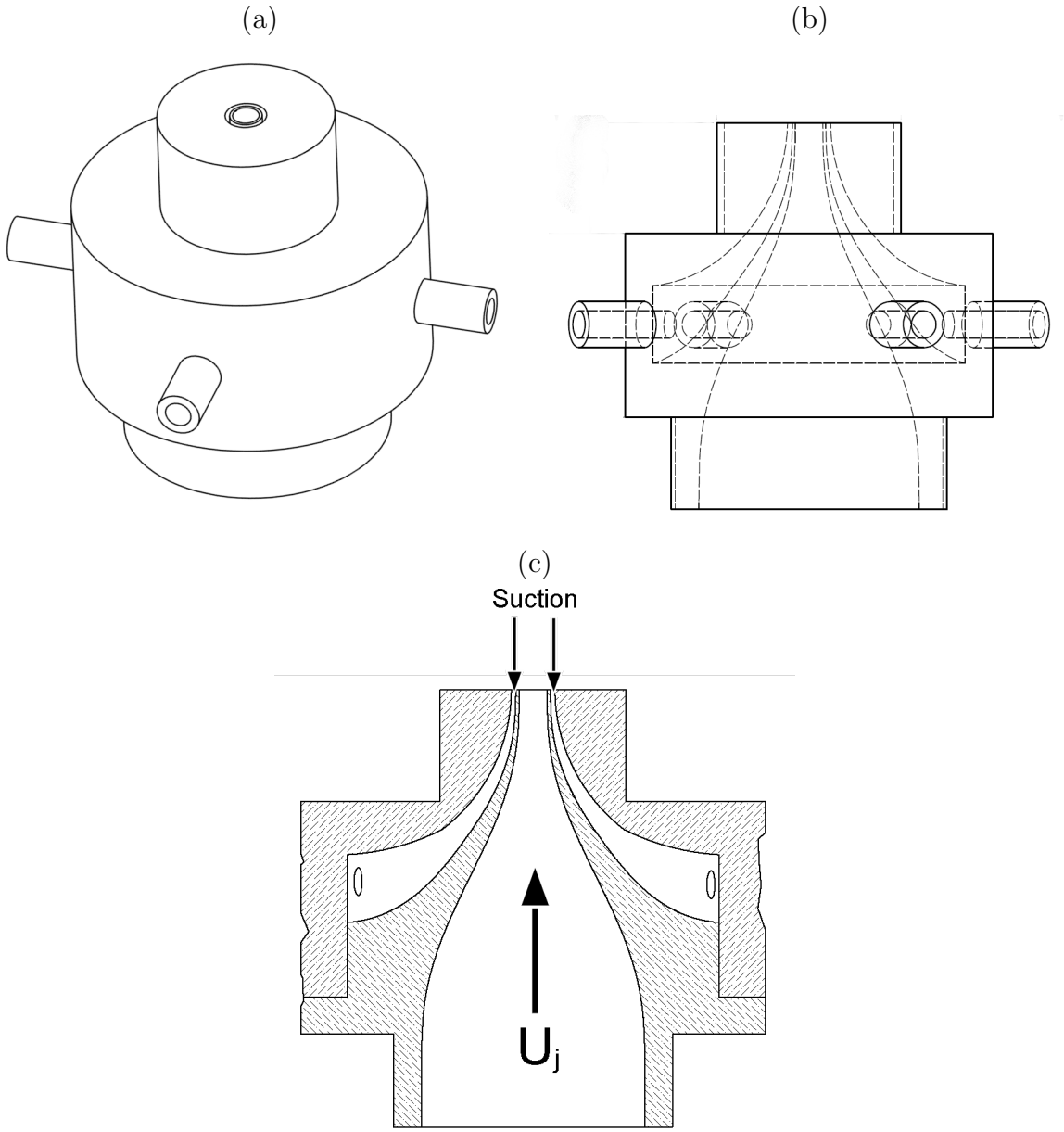

Figure 9.1: (a) Shaded and (b) line renderings of the coaxial nozzle configuration. (c) Depiction of inner and outer annulus nozzle profiles with flow directions representatively indicated.

historical evidence of a significant asymmetry in the jet cross-section for this flow condition (Getsinger et al. (2014); Gevorkyan et al. (2016); Besnard (2019)), and suction flow rates ranging from 0 to 60 $scfh$. The methodology by which the suction flow rate was controlled

Case	Flowmeter Reading	Vertical Velocity
1	05 scfh	$-0.12\ m/s$
2	10 scfh	$-0.22\ m/s$
3	15 scfh	$-0.46\ m/s$
4	20 scfh	$-0.53\ m/s$
5	25 scfh	$-0.88\ m/s$
6	30 scfh	$-1.13\ m/s$
7	35 scfh	$-1.38\ m/s$
8	40 scfh	$-1.53\ m/s$
9	45 scfh	$-1.80\ m/s$
10	50 scfh	$-2.08\ m/s$
11	60 scfh	$-4.30\ m/s$

Table 9.1: Quantification of the induced vertical velocity component in from the applied suction as quantified from stereo-PIV imaging. Velocities are listed relative to the flowmeter volumetric flowrate reading.

involved the use of a manual flow meter, connected at a distance of multiple meters from the suction opening in the tunnel floor. In light of the extensive length of plumbing and number of connections, along with the relatively small flow rates, the resulting induced flow rates at the suction opening were experimentally quantified to overcome any calculations related to head loss, which more than likely would have simply introduced even greater errors to the experiment. The determination of the suction strength involved stereo-PIV imaging with a small FOV just above the suction opening. The jet was left off, and the crossflow was initiated at the lowest possible velocity so as to allow for the seeding of tracer particles in the flowfield for the PIV, without augmenting the natural flow induced by the suction. The resulting induced flows are given by their vertical velocity component as extracted from averaging the recorded jet velocity spanning the suction orifice opening as close to the tunnel

floor as the imaging would allow. The resulting velocities are listed in table 9.1 for the various suction settings considered.

CHAPTER 10

CU Jet with Upstream and Downstream Suction

10.1 Results

10.1.1 Spectral Characteristics

Experimentally, one of the evaluation methods for exploring instabilities within the jet in crossflow is through observations of characteristics and features in hotwire-based spectral contour plots of vertical velocity power spectra along the evolving shear layer trajectory. When the flow is convectively unstable, the contour plots depict relatively weak broadband instability peaks, frequency shifting along the trajectory due to a tonal interference with the hotwire probe (Hussain and Zaman (1978); Getsinger et al. (2012)), and the formation of a subharmonic instability peak. When the flow becomes absolutely unstable, the contour plots show a stronger and more pure-toned instability with higher harmonics which do not vary significantly along the shear layer, in addition to elimination of the subharmonic presence. For an equidensity flush nozzle-injected jet with a jet Reynolds number of $Re_j = 1900$ and an acetone mole fraction of $\psi = 0.112$, the critical transition from convective to absolute instability takes place at $J_{cr} \approx 9$ (Shoji et al. (2020b)). For the present studies, a naturally CU jet at $J = 41$ was utilized as the baseline flow condition, where the jet consisted of a top-hat velocity profile generated from a 5^{th} order polynomial contracting nozzle shape. Figures 10.1(a) and 10.2(a) show the representative spectral contour plot for this jet in the absence of any external annular suction, henceforth referred to as the unaltered jet. Along the abscissa, frequency content was non-dimensionalized to show a Strouhal number based on jet diameter,

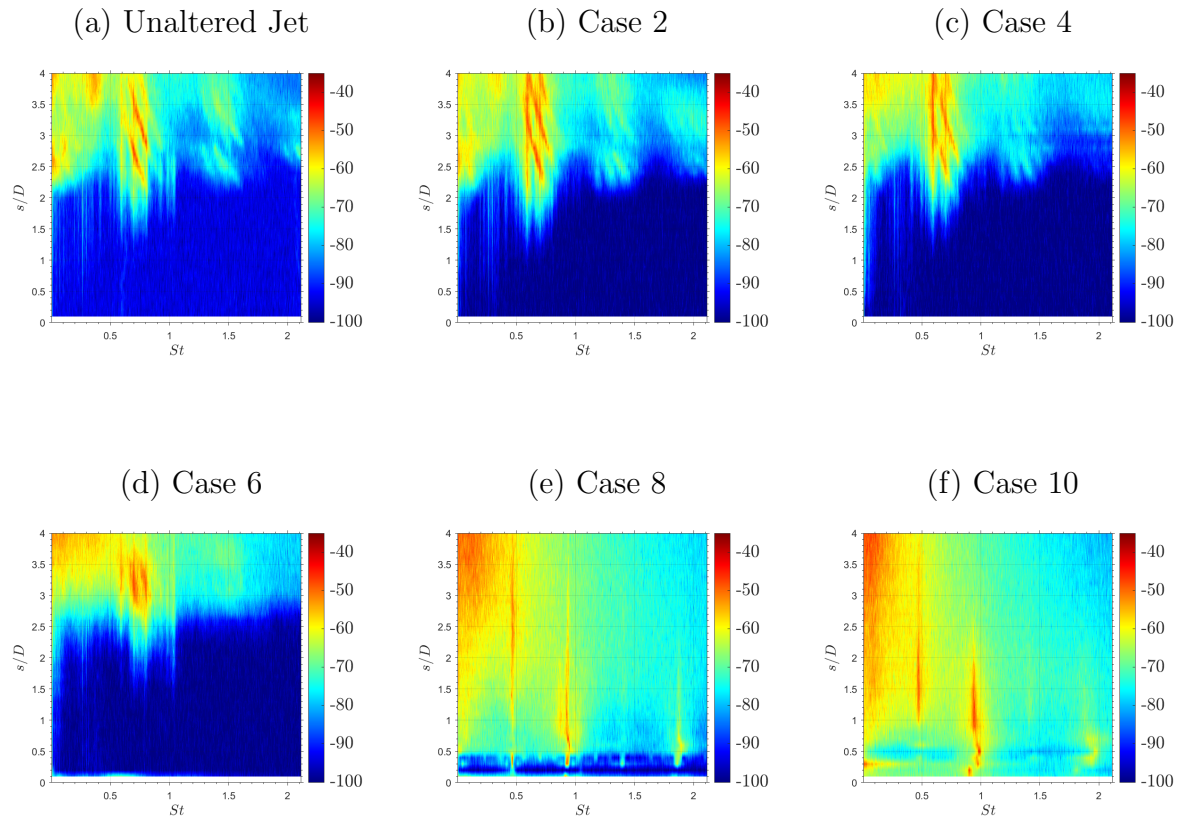

Figure 10.1: Upstream shear layer spectral contour maps of the shear layer instabilities evolving along the shear layer for an acetone seeded, equidensity, $Re_j = 1900$ jet at $J = 41$, with (a) the unaltered jet, absent any suction, and (b-f) suction applied locally in the upstream edge of the jet for suction cases 2, 4, 6, 8, and 10.

$St \equiv fD/U_j$, while in the ordinate the shear layer trajectory location s was normalized by the jet exit diameter D. As expected, and quite consistent with prior documentation for the same flow condition in Shoji et al. (2020b) and Harris et al. (2020a), the shear layer spectra was characterized by weak instabilities which originated around $s/D = 2.0$, exhibited notable frequency shifting over a dominant instability band of $St_0 \approx 0.6 - 0.85$, and presented with the growth of a subharmonic instability beyond $s/D = 3.5$.

Figure 10.1 gives depictions of spectral contour plots of the USL instabilities as suction

was applied locally at the injection plane in the leading edge of the jet, and the strength of the suction was systematically increased according to the values given in table 9.1. For suction cases 2 and 4 in figures 10.1(b-c), corresponding to induced vertical counterflow velocities of $V_2 = -0.22\ m/s$ and $V_2 = -0.53\ m/s$, the shear layer spectral characteristics were very similar to those of the unaltered jet in figure 10.1(a). Suction case 6, which yielded an induced vertical velocity $V_2 = -1.13\ m/s$, also was unable to produce a transition in the instabilities from CU to AU along the USL of the jet. Instead, as shown in figure 10.1(d), the instability characteristics appeared actually to be further weakened instead of enhanced, noting the significantly less dominant spectral peaks and the delayed onset of the instabilities until $s/D \approx 2.7$ downstream. Then quite abruptly, as the suction was increased for case 8, resulting in an induced velocity of $V_2 = -1.53\ m/s$, the shear layer spectra in figure 10.1(f) was found to transition to that of an AU flow. The instabilities were extremely pure-toned at a fundamental Strouhal number of $St_0 = 0.47$ along with higher harmonics, they were initiated close to the jet exit plane at $s/D = 0.2$, and the presence of a subharmonic in the downstream was eliminated. Further increasing of the suction, to an induced velocity of $V_2 = -2.08\ m/s$ for case 10, resulted in spectral characteristics shown in figure 10.1(g), which remained AU and quite similar to those for case 8. While the jet was able to be induced into transitioning from a CU shear layer to an AU USL going from case 6 to case 8, the way in which the flow progressed and then transitioned was somewhat unexpected. Previous work with the JICF note as the momentum flux ratio or the density ratio are decreased, the instabilities are progressively enhanced towards an AU flow, where the frequency shifting due to the tonal interference becomes more minimal, the onset of the instabilities slowly shift closer to the nearfield of the jet exit, and the subharmonic peak slowly diminishes (Getsinger et al. (2012); Shoji et al. (2020b)). Yet, in the coaxial JICF as the suction was increased, thereby producing a stronger counterflow at the leading edge of the jet, the instabilities were instead weakened before then abruptly transitioning to an AU flow. Additionally, based on the linear stability work by Souza et al. (2020), the unaltered $J = 41$ jet flow, having an

upstream momentum thickness of $\theta/D = 0.0262$ and a peak jet velocity of $V_1 = 7.12\ m/s$, is suggested to transition from convective to absolute instability when the shear layer velocity ratio (1.6) achieves at minimum a value of $R_{1,cr} = 1.216$, or a counterflow velocity of only $V_2 = -0.66\ m/s$. However, the jet did not become AU until an induced counterflow velocity of $V_2 = -1.53\ m/s$. This apparent inconsistency, in conjunction with the noted unusual trends in the transition of the instabilities, was thought to be a result of alterations to the jet momentum thickness, as it is known a thickening of the shear layer momentum thickness has a stabilizing effect on the flow (Michalke (1984); Souza et al. (2020)). Another aspect of consideration is the possible generation of a secondary shear layer instability from the induced counterflow and surrounding crossflow. Other studies of coflowing coaxial jets note that multiple instability modes can exist due to the presence of both an outer and inner shear layer, and that the dynamics and determination of convective or absolute instability for the inner shear layer is heavily dependent on the outer shear layer (Sevilla et al. (2002); Talamelli and Gavarini (2006)).

Suction was also selectively applied in the downstream edge of the jet nozzle periphery of the exit plane, where the suction, or the degree of locally induced counterflow, was methodically increased in accordance with the flow cases in table 9.1. The resulting spectral contour plots of instabilities along the shear layer, on the upstream side of the jet, are shown in figure 10.2. The relative interest in exploring augmentations of the downstream shear layer (DSL) arises from the significance of the DSL vortex rollup in the development of the CVP (Kelso et al. (1996); Cortelezzi and Karagozian (2001); Marzouk and Ghoniem (2007)). Also, Regan and Mahesh (2019) note the persistence of dominant instabilities along the DSL of a CU jet at $J = 16$ and $Re_j = 2000$, and additionally establish the existence of a wavemaker region on the downstream side of the jet demarcating where the jet is most sensitive to perturbations. Figure 10.2(a) corresponds to the shear layer instability characteristics for the unaltered jet flow without any applied suction, while figures 10.2(b-f) represent suction cases 4-10 where the induced counterflow velocity ranged from $V_2 = -0.53$ to $-2.08\ m/s$

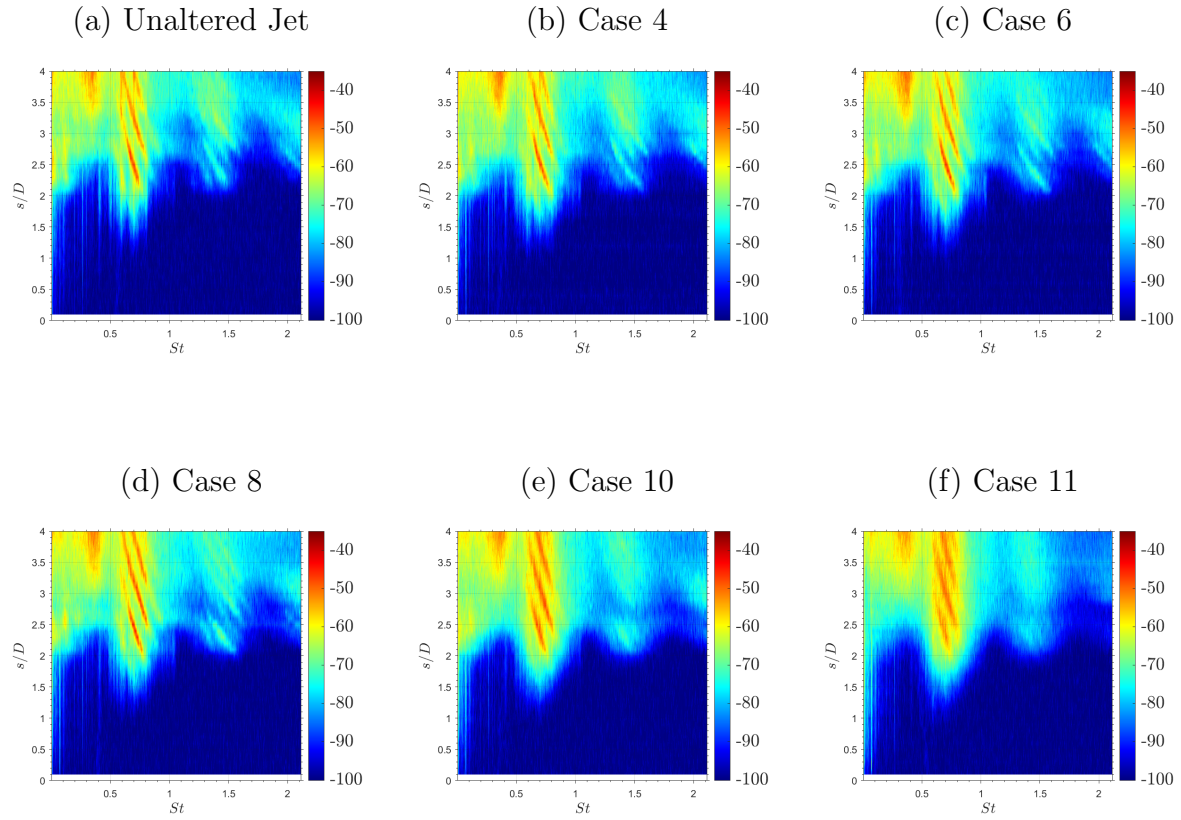

Figure 10.2: Upstream shear layer spectral contour maps of the shear layer instabilities evolving along the shear layer for an acetone seeded, equidensity, $Re_j = 1900$ jet at $J = 41$, with (a) the unaltered jet, absent any suction, and (b-f) suction applied locally in the downstream edge of the jet for suction cases 4, 6, 8, 10, and 11.

respectively. Interestingly, almost no perceptible alterations in the USL instability characteristics of the flow were noted. To this end, and additional suction case was explored wherein the induced velocity was $V_2 = -4.30\ m/s$ (case 11), for which the spectral contour plot is shown in figure 10.2(g). Even with an induced counterflow velocity of roughly 60% of the jet bulk velocity, the instabilities remained clearly CU and characteristically still looked quite nearly identical to the unaltered jet, though with some slight weakening or broadening of the dominant spectral peaks. The inability of the USL instabilities to be transitioned

by the suction on the downstream of the jet was not entirely surprising given that Regan and Mahesh (2019) note for a jet at $J = 16$ and $Re_j = 2000$ that based on the instability characteristics and localization of the wavemaker region, the DSL could be classified as AU, despite the USL of the jet having CU instability characteristics. Additionally, Regan and Mahesh (2017) point out that these DSL instabilities do not interact with the USL until the termination of the potential core, and suggest this as the reason for the lack of visualization of the DSL instabilities along the USL of the jet. Thus, while the applied suction cases may be enacting changes to the flowfield and the overall dynamics, they were not able to be represented in the spectral characteristics along the USL of the jet.

10.1.2 Jet Structure

The structural characteristics of the coaxial jet-in-crossflow were explored through instantaneous centerplane and mean cross-section PLIF images. Representative PLIF images are shown in figure 10.3 for suction locally applied in the upstream edge of the jet and in figure 10.4 for suction locally applied in the downstream edge of the jet. The color bars for the images represent the relative concentration of jet fluid scaled from 0 for pure crossflow to 1 for pure jet fluid, as was found in the potential core visible in the centerplane images. Cross-sectional concentration values were calibrated by a comparison of the spatially averaged cross-sectional concentration with that in a thin slice of a mean centerplane image, as described in Gevorkyan et al. (2016). Hence the upper limit of the concentration scales corresponded to the maximum value within each individual image. Cross-sectional images represent an average of 500 instantaneous snapshots of the flowfield, and in the experiments were taken at x/D locations of 2.5, 5.5, and 10.5 downstream of the jet injection. In figures 10.3 and 10.4, only cross-sectional images corresponding to $x/D = 10.5$ are shown since they depict the more developed and visually obvious implications of the induced counterflow on the jet structure. The overall study investigated multiple suction cases as detailed in table 9.1, but herein only a few of the more significant results are discussed, which deal primarily

with the conditions examined in the preceding section, 10.1.1. The jet flow in the absence of any suction was given in figures 10.3(a) and 10.4(a) where in the cross-section at $x/D = 10.5$ the jet was represented by a highly asymmetric structure, forming a sort of reverse question mark shape with a small tertiary vortical structure, as observed in earlier studies for the nozzle-generated JICF at a high momentum flux ratio (Getsinger et al. (2014); Shoji et al. (2020a); Besnard (2019); Harris et al. (2020b)). As explored in the preceding section, the jet has a relatively weak CU USL, and as a result it is susceptible to perturbations or imperfections in the incoming flow (Getsinger et al. (2014)). Such natural asymmetries are consistent with earlier linear stability analyses suggesting that growth rates for natural helical instability modes for the JICF at larger momentum flux ratios J have different positive and negative signs (Alves et al. (2007)), and thus could be associated with asymmetry in the flow. Regan and Mahesh (2019) note that the helical modes for a CU jet at $J = 16$ and $Re_j = 2000$, as derived from adjoint analysis of the DNS, originate from the leading edge of the jet at the exit plane and slightly inside the jet nozzle. However, Regan and Mahesh (2019) additionally note that the wavemaker regions for these helical instability modes are located along the sides of the jet and elevated slightly from the exit plane, which is further suggestive that the jet asymmetry in part may arise from a disturbance or asymmetry in the issuing crossflow, which then interacts with the wavemaker region of the jet helical modes. From the centerplane, the jet was represented by a relatively upright structure with vortex rollup along the USL which initiated about $z/D = 2.0$ downstream, and also had a lower penetrating bifurcated flow, though not visible due to its off-centerline trajectory, which evolved into the tertiary structure noted in the cross-section.

The instantaneous centerplane and mean cross-sectional images for suction in the upstream edge of the jet in figure 10.3(a-c) show that the jets with suction less than that applied for case 6, producing an induced counterflow velocities less than $V_2 = -1.13\ m/s$, were similar to the unaltered jet in terms of overall spread and penetration in the centerplane and relative cross-sectional symmetry, though there were some subtle differences along

(a) Unaltered Jet

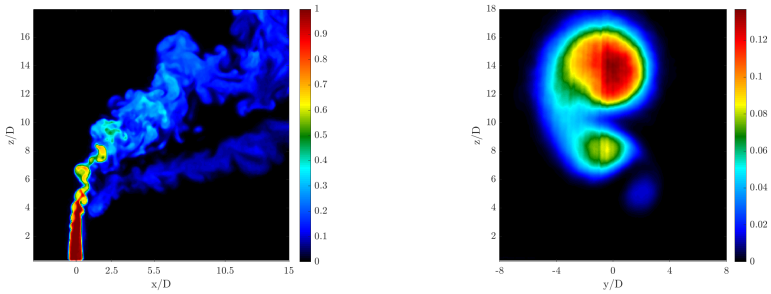

(b) Case 2

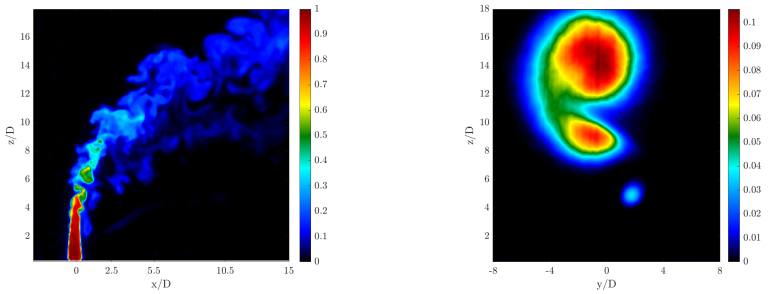

(c) Case 4

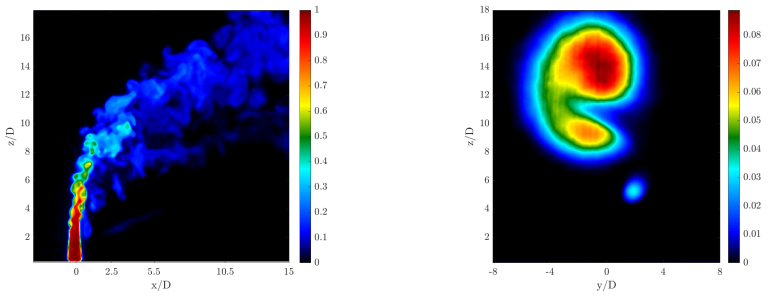

(d) Case 6

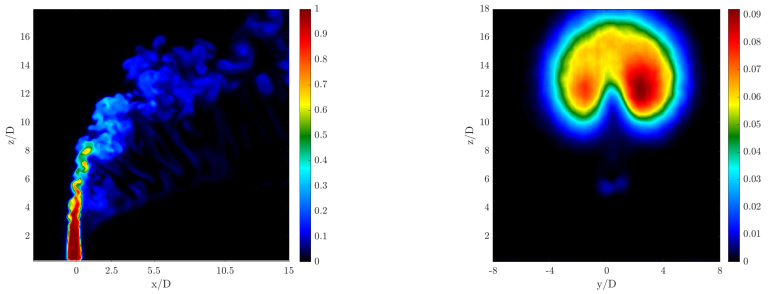

(e) Case 8

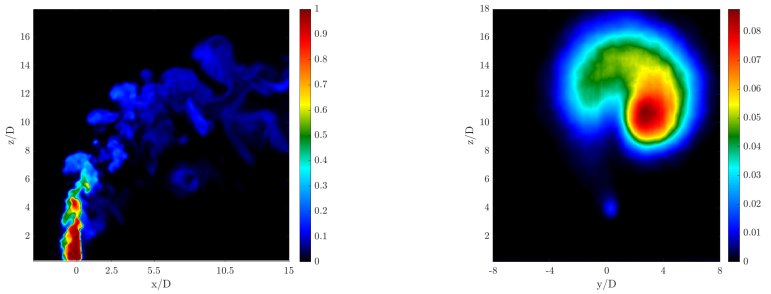

Figure 10.3: continues to following page

(f) Case 10

(g) Case 11

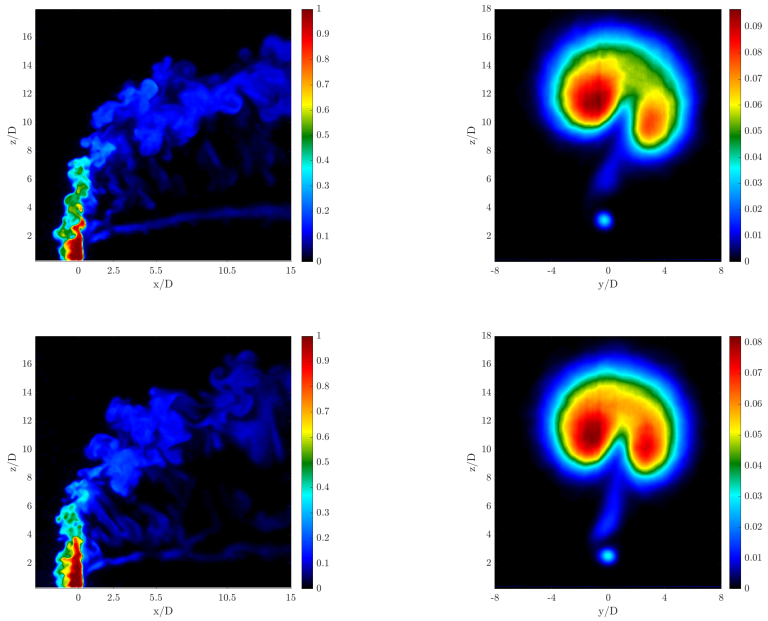

Figure 10.3: Structural Characteristics for momentum flux ratio of $J = 7$ for an acetone seeded, equidensity, $Re_j = 1900$ jet at $J = 41$, with (a) the unaltered jet, absent any suction, and (b-f) suction applied locally in the upstream edge of the jet for suction cases 2, 4, 6, 8, 10, and 11. Shown for each condition is an instantaneous centerplane image and mean cross-sectional PLIF image at $x/D = 10.5$. The colorbar maximum for the cross-sectional images was scaled so as to allow quantitative comparisons with the scalar intensities noted in the jet centerplane.

the USL of the jets. In the instantaneous centerplane images, one initially sees clear USL vortex rollup for the unaltered jet, but then as the suction was applied and systematically increased, the weakening in the USL preceding the transition to an AU USL as indicated in figure 10.1 was manifested in a weakening and smoothed imaging of the upstream shear layer. This weakening was also observed in the centerplane for suction case 6 (fig. 10.3(d)) which depicted the most significant weakening of the USL instabilities (10.1(d)), however in the cross-section the resulting CVP structure was significantly changed from the characteristic asymmetric reverse question mark shape to a symmetric looking CVP without the presence of a tertiary structure. Thus, while the flow was not able bring about an AU USL

and thereby overwhelm the growth of the helical modes with that of the axisymmetric mode, it is thought it was able to apply enough of an influence in the symmetry plane of the jet to overcome and damp out the growth of the helical modes. According to the spectral characteristics along the USL, applied suction in the upstream for case 8 and beyond resulted in a transition of the jet to that of an AU flow. Interestingly, this corresponded with distinct alterations in the structural characteristics along the leading edge of the jet as well, as shown from the centerplane in figures 10.3(e-g) for suction cases 8, 10, and 11. In these cases the USL of the jet was significantly perturbed, having a dramatically shortened potential core and a region of lower concentration jet fluid which evolved in front of the main jet shear layer in the nearfield, and in the farfield having a jet which penetrated less and also had re-emergence of a very low penetrating bifurcated flow. The presence of jet fluid upstream of the leading edge of the jet is thought to come about from the relative strength of the suction presenting a significant pressure drop ahead of the jet which resulted in the jet being expanded outwards, and possibly for the strongest suction cases even drawn out of the flowfield into the suction plumbing. Cross-sectionally the jet CVP remained mostly symmetric, though there was a slight tilting of the structure towards the right half-plane which was thought to be due to possible imprecise alignment of the suction directly in the centerplane of the jet, again noting the sensitivity of the jet to slight imperfections or asymmetries in the flowfield. As mentioned from the centerplane, in the cross-section the jet was also characterized by the renewed presence of a tertiary flow structure, although with the applied suction it was found to remain quite centered beneath the CVP, and was additionally connected to the CVP structure by a thin band of jet fluid. The symmetrization of the tertiary structure and linking of the structure to the CVP is similarly seen by Getsinger et al. (2014) for a $S = 1$, $J = 61$, $Re_j = 2300$ JICF as the J or Re_J are systematically increased or decreased, respectively, while holding the other parameter fixed. Either change is characterized by a weakening of the USL, and in the case of decreasing Re_j with fixed J, also is accompanied by a thickening of the upstream shear layer momentum thickness. Such similar changes in

the cross-sectional structure, along with the significant presence of jet fluid ahead of the potential core of the jet, is further supportive of a thickened momentum thickness of the shear layer in the leading edge of the jet.

Interestingly, in spite of the lack of changes to the USL instabilities from the application of suction in the downstream edge of the jet exit, there were significant alterations noted in the centerplane and cross-sectional structures of the jet, as depicted in figure 10.4. Much like with the suction applied upstream, for the suction cases preceding case 6 in figures 10.4(a-c), the jet was not significantly affected in either the centerplane or cross-section. For suction case 6 (fig. 10.4(d)), the CVP was again found to become quite symmetric and absent the presence of a tertiary structure, which was supportive of the significance of the DSL in the jet dynamics as is likewise recently demonstrated by a tabbed JICF (Harris et al. (2020b)). In the centerplane, the vortex rollup along the USL remained completely unchanged with no signs of weakening or smoothing, which agreed well with the USL instabilities in figure 10.2. As the suction was further increased from case 6 to case 11, dramatic alterations to the potential core region of the jet were again distinguished in the centerplane by a broadening of the jet as jet fluid was drawn out by the pressure drop created by the suction. Even more than with the suction upstream, due to the more favorable pressure gradient in the downstream wake region of the jet, it is thought that for stronger suction cases some of the jet fluid may have been unavoidably drawn into the suction plumbing. This was supportive of the significant weakening and shrinking of the jet structure noted in both the centerplane and cross-section in figures 10.4(e-g). Interestingly, for suction which was stronger than case 6, the tertiary flow structure seen in the cross-section was not found to form again, and additionally the CVP remained quite symmetric, suggestive of a different state of dynamic stability for the CVP compared to when suction was applied along the upstream of the jet. Cases 8-11 also featured, from the cross-sectional perspective, a prominent thin column of jet fluid which stretched from the wall to the underside of the CVP. From the centerplane, this structure was seen to originate from the downstream edge of the jet column, and extended

(a) Unaltered Jet

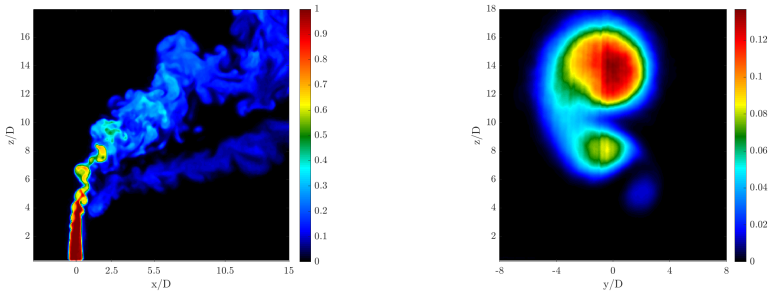

(b) Case 2

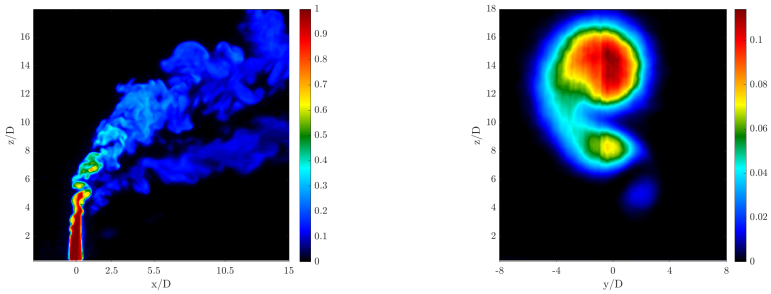

(c) Case 4

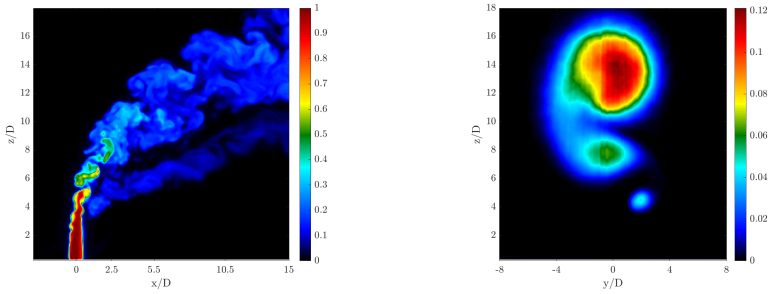

(d) Case 6

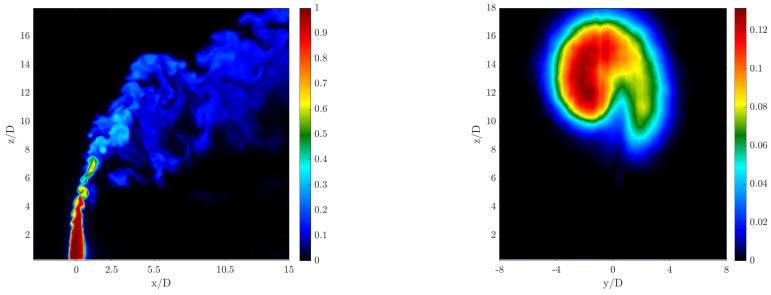

(e) Case 8

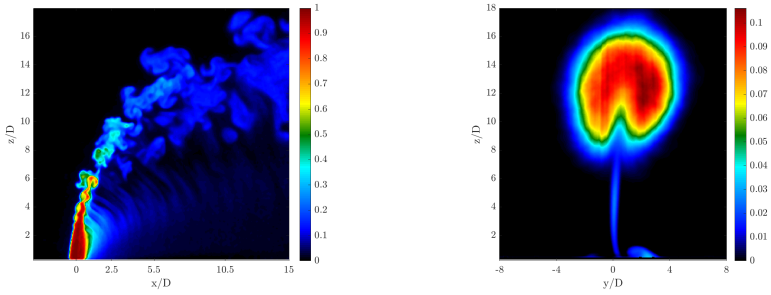

Figure 10.4: continues to following page

(f) Case 10

(g) Case 11

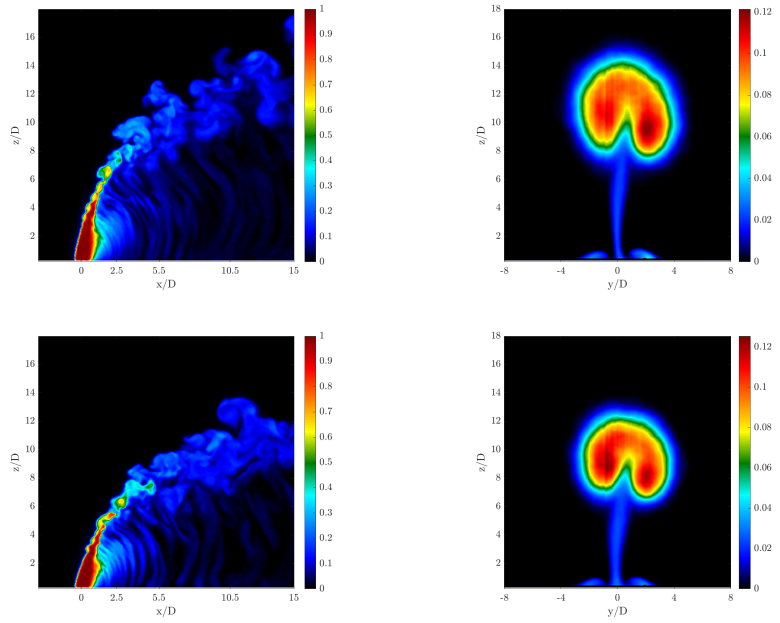

Figure 10.4: Structural Characteristics for momentum flux ratio of $J = 7$ for an acetone seeded, equidensity, $Re_j = 1900$ jet at $J = 41$, with (a) the unaltered jet, absent any suction, and (b-f) suction applied locally in the downstream edge of the jet for suction cases 2, 4, 6, 8, 10, and 11. Shown for each condition is an instantaneous centerplane image and mean cross-sectional PLIF image at $x/D = 10.5$. The colorbar maximum for the cross-sectional images was scaled so as to allow quantitative comparisons with the scalar intensities noted in the jet centerplane.

downstream into the jet wake, the extent of which increased with increasing suction strength. It is thought that these flow structures were visualizations of wake vortices, which were visible due to jet fluid being drawn into the near wall region of the jet wake by the applied suction, which then allowed the fluid to be entrained by the wake vortices, knowing such vortical structures originate on the downstream side of the jet where the jet efflux and wall boundary layers intersect, and that they draw wall boundary fluid into the jet (Kelso et al. (1996); Milanovic et al. (2012)). Interestingly, while wake vortices are generally sporadically or periodically shed behind the jet column at off centerline locations, the upright column herein depicted appeared quite centered behind the jet. It is thought the suction may thus

additionally act as a stabilizer of the wake vortex shedding not unlike that of suction applied behind a circular cylinder in stabilization or suppression of wake vortices (Rashidi et al. (2016)). Additionally, though quite subtle, the cross-section also depicted two small lobes of jet fluid near the wall boundary on either side of the jet which spatially would be consistent with the characteristic horseshoe vortex system, with the uncharacteristic persistence of such a structure into the far downstream due to the stabilizing influence of the suction.

10.1.3 Vorticity and POD Dynamics

Recent work of tabbed JICF demonstrates that upstream and downstream tab placements significantly impact the generation of vorticity along the jet shear layer, which consequentially augmented the development of the jet cross-sectional structure further downstream, and when placed in the upstream edge of the jet, significantly weakened the USL instabilities (Harris et al. (2020a)). Additionally, the analogy of a CCSL for investigation of the instabilities of the JICF is based off of the velocity profile of the issuing jet, specifically in the upstream edge of the jet (Iyer and Mahesh (2016); Shoji et al. (2020b)). As such, one area of great interest in the present experiment involved quantification of the velocity and vorticity field in the centerplane ($x - z$) of the jet, where understanding of the exiting jet velocity profile is able to be compared with the CCSL analogy, and the vorticity evolution in this flowfield can assist in interpreting other flow features, especially those related to the dynamics of the USL and its roll in CVP development.

Figure 10.5 presents the mean and representative instantaneous centerplane vorticity images of the jet for in an unaltered state, and for cases of increasing suction applied in the upstream edge of the jet which corresponded with the cases shown for the structural characteristics in figure 10.3. The unaltered jet in figure 10.5(a) had vortex rollup characteristics which were consistent with those typical of a JICF with a larger J value, where rollup along the USL was generated earlier than the DSL owing to the induced upward velocity along the DSL from the leeside portion of the vortex ring (Marzouk and Ghoniem (2007)). Much

(a) Unaltered Jet

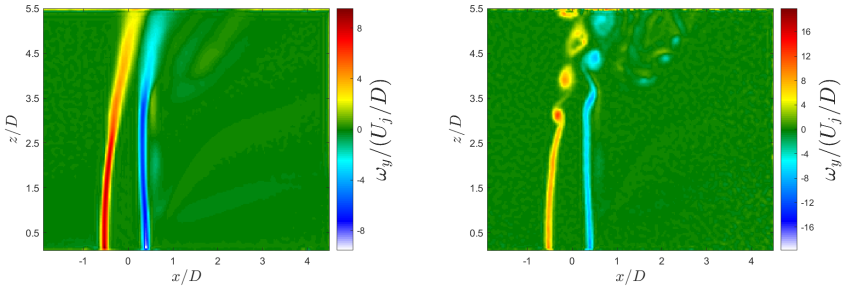

(b) Case 2

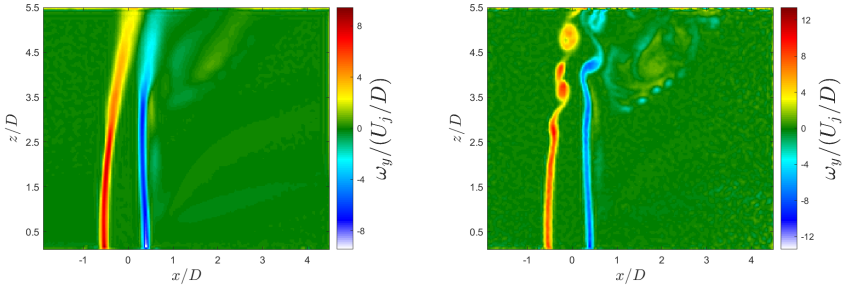

(c) Case 4

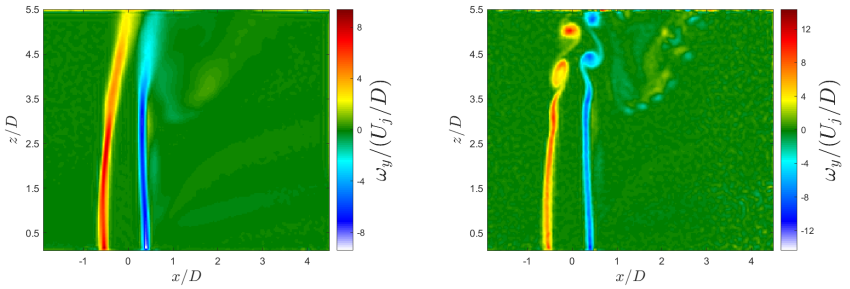

(d) Case 6

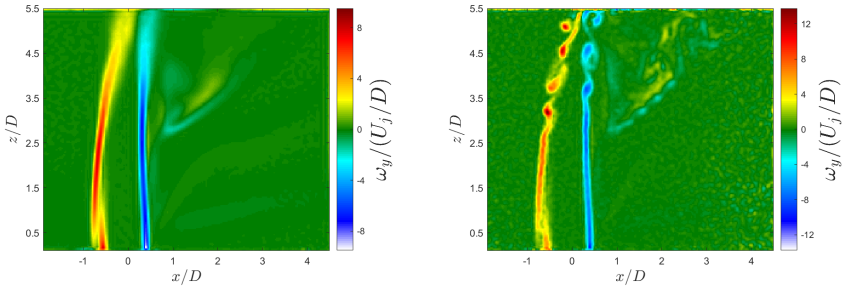

(e) Case 8

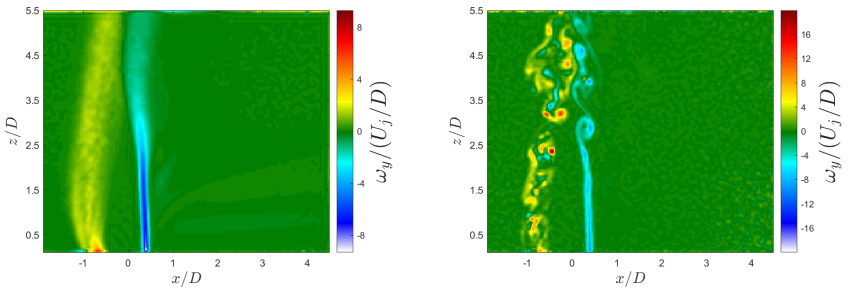

Figure 10.5: continues to following page

(f) Case 10

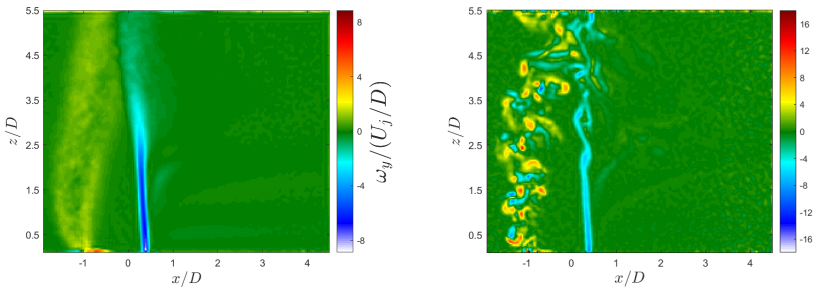

(g) Case 11

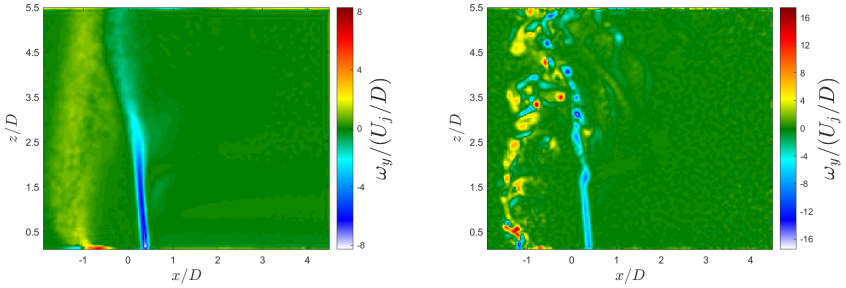

Figure 10.5: Mean and instantaneous vorticity images for an acetone seeded, equidensity, $Re_j = 1900$ jet at $J = 41$, with (a) the unaltered jet, absent any suction, and (b-f) suction applied locally in the upstream edge of the jet for suction cases 2, 4, 6, 8, 10, and 11. The colorbars are individually scaled to the maximum and minimum values contained within each mean image, and nondimensionalized by the jet nozzle diameter, D, and bulk velocity, U_j.

like the with the spectral and structural characteristics, little was seen in the mean or instantaneous vorticity in way of alterations to the flowfield for suction cases below case 6. For suction case 6 in figure 10.3(d) there was a slight break in the shear layer vorticity at $s/D = 0.5$, which was well below $s/D \approx 2.5$, where the instantaneous vorticity and the shear layer spectral characteristics each depicted the onset of vortex rollup and instabilities, respectively. As the suction was further increased for suction cases 8, 10, and 11 (figs. 10.5(e-g)) the slight break gave way to seemingly random vortex generation which initiated just after the jet exit plane and nearly one diameter upwind of the upstream edge of the jet exit ($x/D = -1.5$). In the mean images, the upstream vorticity became progressively more diffuse, and the length of the vorticity along the DSL also appeared to shorten, with the

increasing suction strength. This break and subsequent onset of chaotic appearing vorticity formation along the shear layer was suggestive of a widening of the jet shear layer due to the suction, where the dominant shear layer eventually appeared to transition outside of the jet column entirely to the region of the shear layer interface between the induced suction velocity and the oncoming crossflow. This apparent shift in origination of the shear layer vortices was again supportive of the concept of competing shear layer instability modes from the existence of shear layers, as seen for coflowing jets (Sevilla et al. (2002); Talamelli and Gavarini (2006)), though this is a topic in need of further investigation.

Also examined were mean and instantaneous centerplane vorticity images of the jet with suction applied in the downstream edge of the jet, where the suction cases were consistent with those in figure 10.4. Once again the vortex rollup for cases 2 and 4 (figs. 10.6(b-c)) depicted no noticeable changes in the shear layer dynamics along either the upstream or downstream of the jet. In fact, quite consistent with the shear layer instability characteristics in figure 10.2, the vortex rollup along the USL remained essentially unchanged, aside from the shear layer trajectory, for all of the suction cases considered. Much like for the USL with suction in the upstream edge of the jet, suction downstream for cases 8, 10, and 11 in figures 10.6(e-g) depicted a dramatic breaking of the vorticity along the DSL of the jet. From the mean images, as the strength of the suction increased, the location of breaking of the vorticity grew progressively higher along the jet, and like with the upstream suction was suggestive of the translation of the shear layer outward due to an expansion of the jet column induced by the suction. Interestingly, in all of the cases the DSL vorticity remained more coherent, likely due to the more favorable pressure gradient in the wake region of the jet column, and additionally had a relatively consistent sort of reattachment of the DSL to the main jet at a downstream location of $z/D \approx 2.5$. This coincided quite well with the initiation instabilities and vortex rollup along the USL of the jet. It is thought therefore that the apparent breaking of the DSL vorticity may be possibly described by a severe stretching to the downstream portion of the vortex ring, where the upright legs of the rings

(a) Unaltered Jet

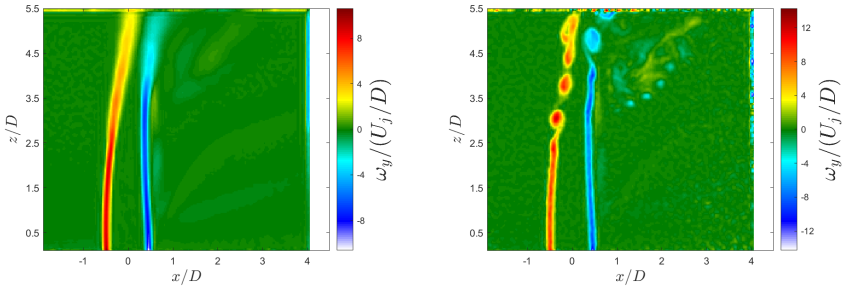

(b) Case 2

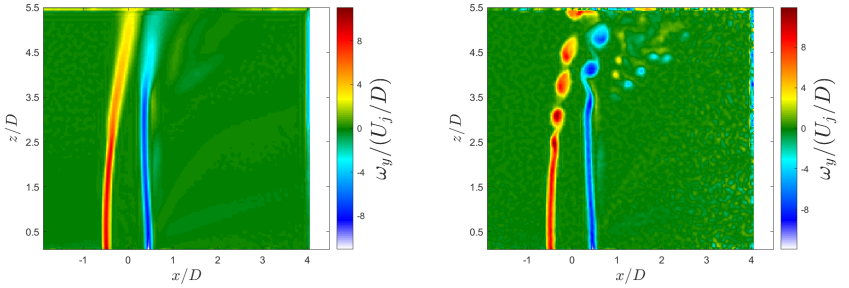

(c) Case 4

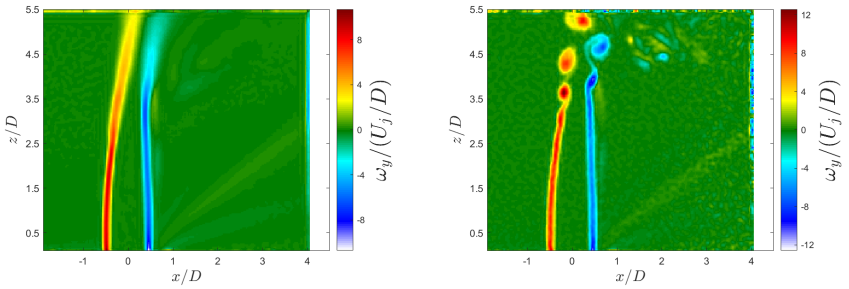

(d) Case 6

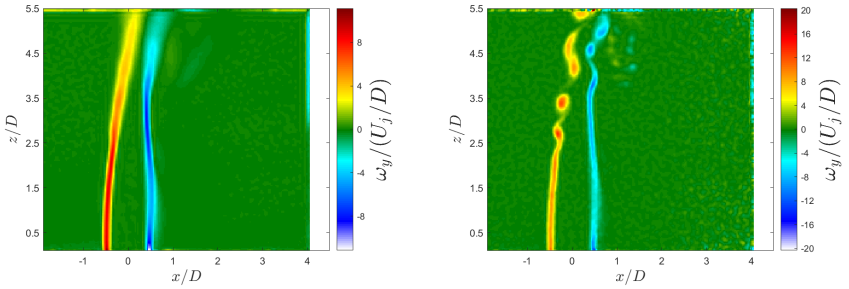

(e) Case 8

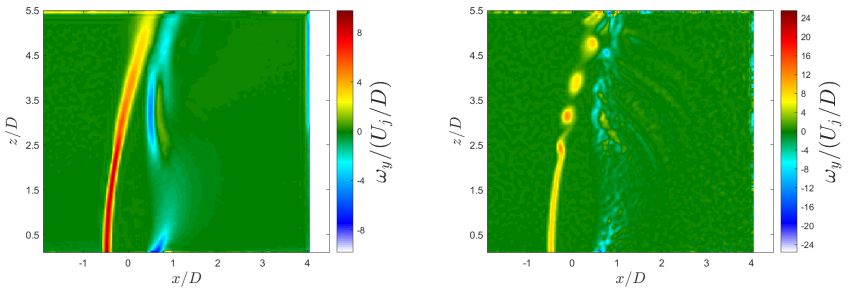

Figure 10.6: continues to following page

(f) Case 10

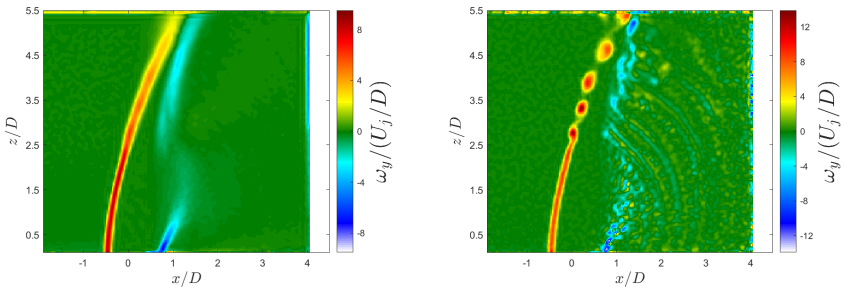

(g) Case 11

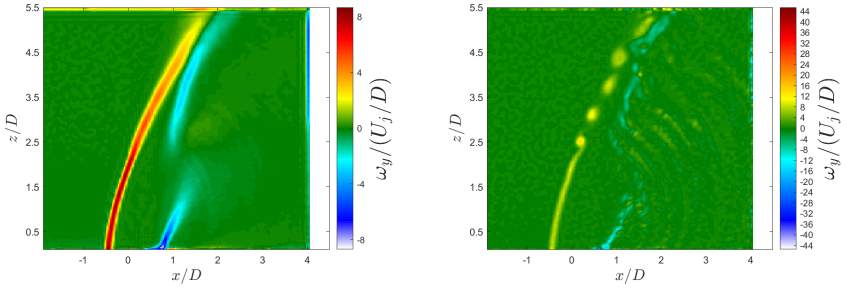

Figure 10.6: Mean and instantaneous vorticity images for an acetone seeded, equidensity, $Re_j = 1900$ jet at $J = 41$, with (a) the unaltered jet, absent any suction, and (b-f) suction applied locally in the downstream edge of the jet for suction cases 2, 4, 6, 8, 10, and 11. The colorbars are individually scaled to the maximum and minimum values contained within each mean image, and nondimensionalized by the jet nozzle diameter, D, and bulk velocity, U_j.

described by Marzouk and Ghoniem (2007) became anchored to the wall boundary due to the suction, and thus resembled upright wake vortices further downstream, as seen from the instantaneous vorticity images. However, the persistence of these structures and their point of origin is a matter requiring further study, especially given the origin of the wake vortices for an unperturbed JICF is still a matter of debate (Milanovic et al. (2012)).

10.1.3.1 POD Dynamics

Beyond the effects on the vorticity generation and evolution near the jet exit, the influence of the suction on other dynamics within the transverse jet flowfield may be explored via

snapshot proper orthogonal decomposition (POD)(Sirovich (1987)) applied to the velocity vector fields from the centerplane stereo-PIV imaging. This approach has been explored in other studies of the JICF (Meyer et al. (2007); Schlatter et al. (2011); Gevorkyan et al. (2018); Harris et al. (2020a)) as a means of extracting mode structures from instantaneous snapshots of the flow and identifying dominant instabilities in the flowfield. In the present studies, snapshot POD analysis was applied to all 500 instantaneous realizations of the flowfield for each test case considered, well above the 300 snapshots required for statistical convergence (Shoji (2017)). The resolved mode structures were ordered in terms of their respective magnitudes of total kinetic energy fluctuation, helping to reveal characteristic flow features and dynamics which might otherwise be hidden or masked by the chaotic flowfield. Figures 10.7 and 10.8 depict the four most energetic mode structures, along with their respective contributions to the total kinetic energy fluctuation, for the unaltered transverse jet, and for cases with suction locally applied in the upstream and downstream edges of thet jet, respectively. Given the extensive preceding evidence of a lack of alterations to the flowfield when the suction was below case 6, only suction cases 6, 8, and 10 are depicted as they represented the suction conditions with the most significant alterations in the shear layer instabilities, jet structure, and vorticity characteristics for both the suction upstream and downstream configurations. The unaltered jet at $J = 41$ in figures 10.7(a) and 10.8(a) agreed quite well with the dynamics seen in the snapshot POD for the flush nozzle injected JICF for the same momentum flux ratio range by Gevorkyan et al. (2018) and Harris et al. (2020a). In the mode structures, the first two most dominant modes displayed isolated structures within the shear layer of the jet, much like the vortex rollup and shear layer instability characteristics, where the the dominant mode structures spanned the upstream and downstream shear layers, and appeared to be merged. This was analogous to the the wavemaker region documented in the DNS in Regan and Mahesh (2019), which spanned the upstream and wrapped around to the downstream of the jet, and also the noted origination of the dominant eignenmode on the downstream side of the jet as shown in Regan and Mahesh

(2017), both for a convectively unstable jet at $J = 16$ and $Re_j = 2000$. In the bottom row of figure 10.7(a) the coefficients for the first two most energetic modes were plotted against one another for each of the 500 snapshots of the flowfield. Other studies of the JICF state that when the modes structures are similarly along the USL of the jet, and the coefficient mapping produces a ringlike trajectory, it is representative of a periodic traveling wave along the shear layer, and that the dominant shear layer jet dynamical behavior may be characterized by linear combinations of the first two modes (Meyer et al. (2007); Gevorkyan et al. (2018); Shoji (2017); Besnard (2019); Harris et al. (2020a)). In this flow, since the USL of the unaltered jet was naturally CU, there was no coherent phase trajectory or shape to the coefficient plots, instead depicted by a diffuse incoherent blob of points.

Alterations to the dynamics of the flowfield when suction was applied in the upstream edge of the jet are depicted in figure 10.7 for suction cases 6, 8, and 10 along with the unaltered jet. In all of the modes presented, the dominant structures were isolated along the shear layer. As the forcing became quite strong, in cases 8 and 10 (figs. 10.7(c-d)), the modes were actually found to attach to the leading edge of the suction opening, with structures which were slightly curved from the location of the main jet towards the suction. This was suggestive of the proposed translation of the shear layer to the outer edge of the suction, and additionally that some of the jet flow may have been drawn into the jet plumbing. These mode structures along the USL of the jet were also quite wide compared with those of the unaltered jet, representative of a thickening of the shear layer momentum thicknesses. Quite distinctly, as the suction increased in strength, the total kinetic energy content contained in the first four POD modes was systematically decreased. The unaltered jet contained 42.8% of the jet energy whereas cases 6, 8, and 10 contained 21.2%, 16.1%, and 11.1% respectively. This was reflective of the increasing complexity of representing the dynamics of the jet, as an increasing number of modes was required to reproduce the jet with a consistent percentage of the total energy content. While this was quite appropriate for suction case 6, which had significantly weakened instability characteristics along the USL of the jet as shown in figure

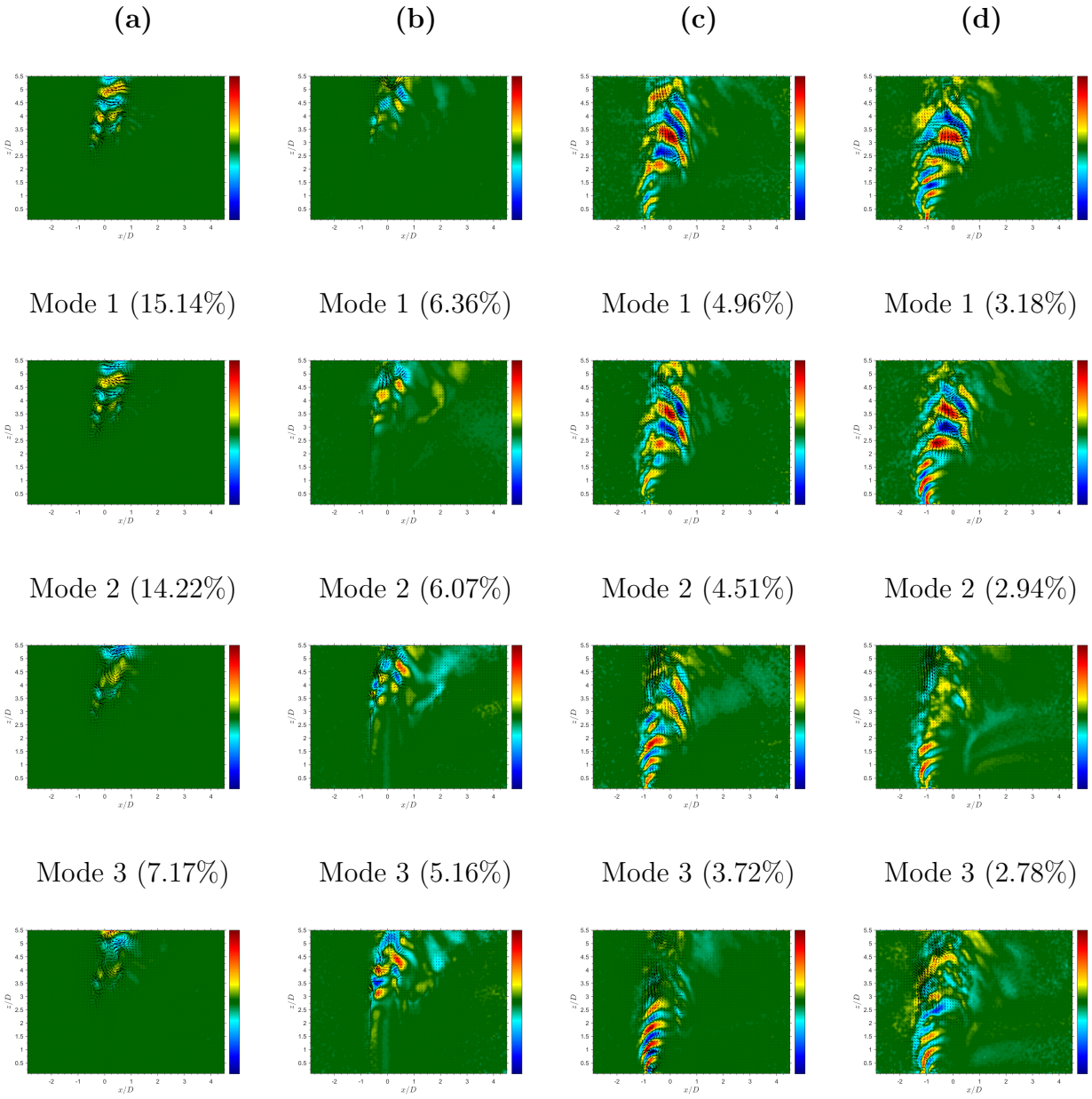

Figure 10.7: continues to following page

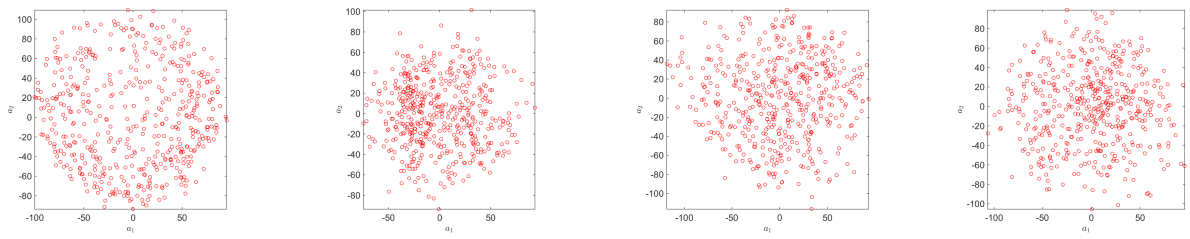

Figure 10.7: PIV based POD mode structures extracted from 500 instantaneous snaphots of the centerplane velocity field at $J = 41$, for (a) the unaltered jet, and upstream suction for (b) case 6, (c) case 8, and (d) case 10. The modes are sorted according to their respective percentages of total kinetic energy fluctuation content. The colorbar in each image represents the mode scaled by its own norm and the mean jet velocity at the jet exit U_j. The bottom row depicts PIV based POD coefficients of the first 2 modes plotted against each other.

10.1(d), these findings were somewhat surprising for suction cases 8 and 10 where the USL instabilities were found to be strengthened from a convective to absolute instability (figs. 10.1(e-f)). To this end, the coefficient plotting of α_1 vs α_2 was also unable to reproduce a ring-like trajectory, which historically has been consistently present for an AU JICF (Meyer et al. (2007); Schlatter et al. (2011); Gevorkyan et al. (2018); Shoji (2017); Besnard (2019); Harris et al. (2020a)). The reasoning behind this is thought to reside within the FOV over which the POD analysis was utilized. The mode coefficients represent the multiplier applied to the given modes, and thus periodicity between coefficients 1 and 2 would indicate that the structures depicted within the entire FOV were representable with a certain degree of periodicity. Recalling the USL spectra, it was seen that once the flow had transitioned to an absolute instability, the dominant instability only persisted until $s/D = 2.0$ along the jet shear layer, after which the subharmnonic became dominant, indicative of the emergence of pairing of the USL vortices. Visual inspection of the modes for cases 8 and 10 indeed demonstrate coherent and seemingly repeated structures up until $s/D \approx 2.0$, whereby larger dynamic structures are formed further downstream. It is therefore thought that if the FOV

of the POD was altered so as to investigate the USL of the jet in a more isolated manner, the dynamics would as a result be more reflective of the instabilities in the spectral contour plots.

Figure 10.8 represents the dynamics of the jet with suction cases 6, 8, and 10 applied in the downstream edge of the jet exit, and the unaltered jet dynamics for comparative purposes. As was likewise demonstrated by the upstream suction, systematic increases in the strength of the suction resulted in the flowfield becoming dynamically more complex, as quantified by the lower total kinetic energy content contained within the first 4 modes. However, unlike with the seemingly counterintuitive behavior of the upstream suction, an increasingly complex flow system was supported by the consistent weakening of the USL instabilities in figure 10.2 for all suction cases treated. Also consistent with the further weakening of the CU USL instabilities was the diffuse blob-like mode coefficient plots. All of the resulting mode structures featured the upstream and downstream shear layers, representative of the vortex rollup, and again in a consistent manner with the onset of the shear layer instabilities in the contour plots, the rollup location remained relatively constant regardless of the suction strength in the downstream. As was similarly seen from the jet structural characteristics, the mode structures for suction cases 8 and 10 in figures 10.8(c-d) additionally featured upright structures in the wake region of the jet, the prominence of which increased as the suction was strengthened. Interestingly, these wake structures directly connected to structures which represented dynamics along the DSL of the jet. This was supportive of these apparent wake vortices being associated with the legs of the folded and tilted vortex ring (Marzouk and Ghoniem (2007)). Gevorkyan et al. (2018) and Fric and Roshko (1994) note such wake structures are largely associated with the wake vortices which act to entrain crossflow boundary layer fluid up into the jet.

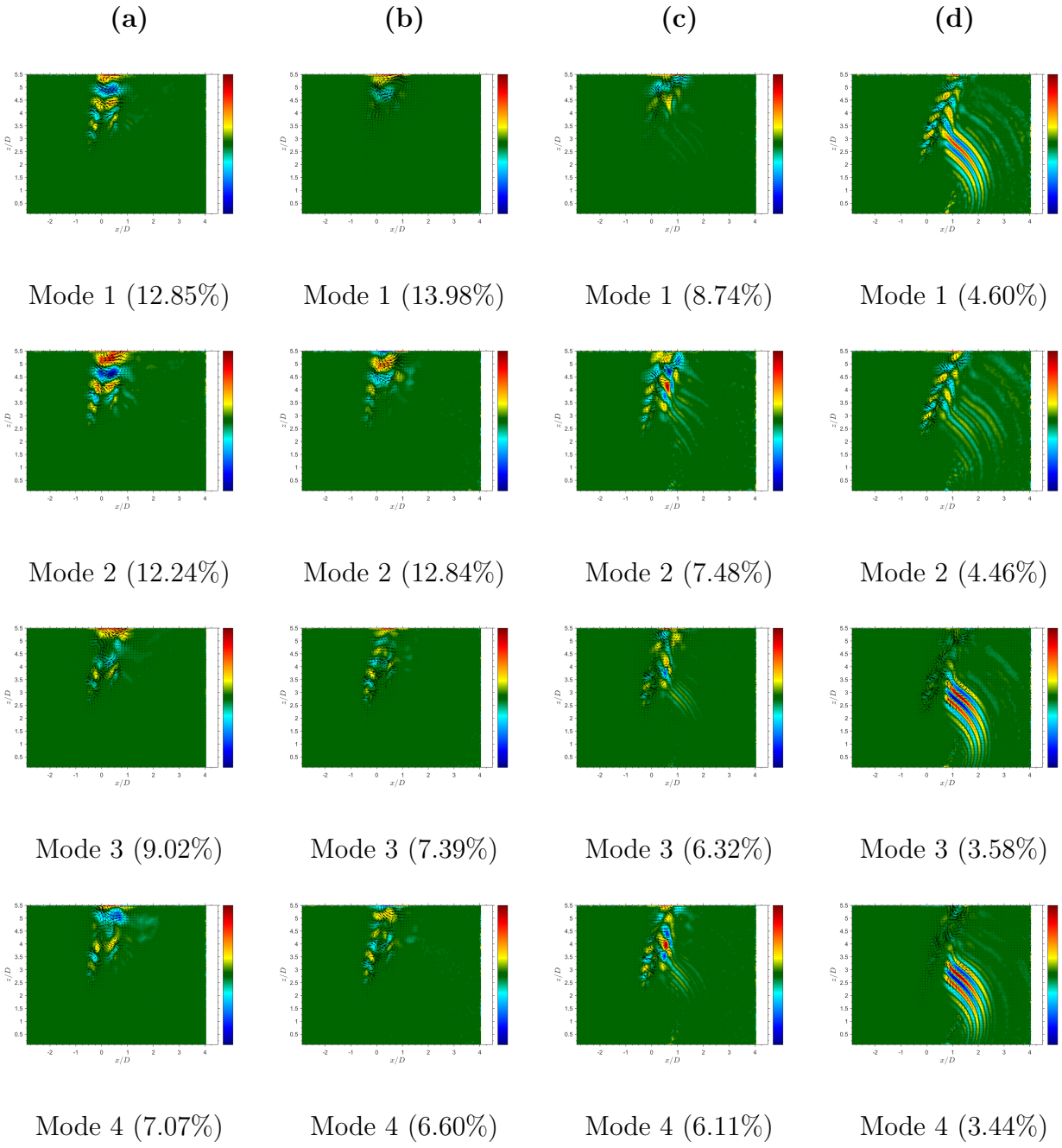

Figure 10.8: continues to following page

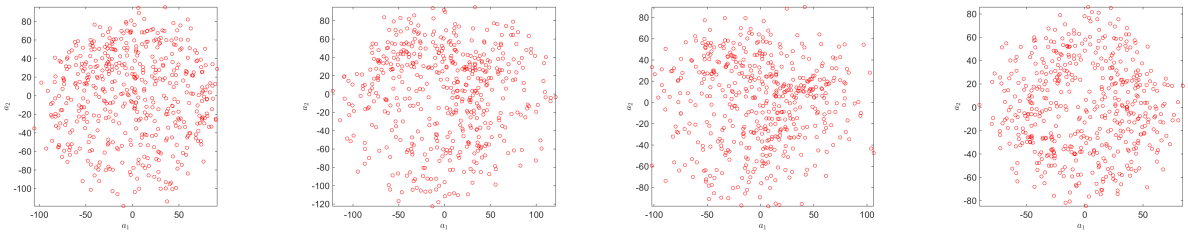

Figure 10.8: PIV based POD mode structures extracted from 500 instantaneous snapshots of the centerplane velocity field at $J = 41$, for (a) the unaltered jet, and upstream suction for (b) case 6, (c) case 8, and (d) case 10. The modes are sorted according to their respective percentages of total kinetic energy fluctuation content. The colorbar in each image represents the mode scaled by its own norm and the mean jet velocity at the jet exit U_j. The bottom row depicts PIV based POD coefficients of the first 2 modes plotted against each other.

10.1.3.2 CCSL

In addition to the vorticity field and POD analysis of the velocity field extracted from the present experiments, the local velocity field in the vicinity of the upstream region of the jet exit various strengths of suction applied in the upstream edge of the jet was also examined. Such measurements enabled exploration of the influence of the upstream suction on the local USL flowfield in the context changes in the jet's upstream momentum thickness. As noted previously, the flush nozzle-based experiments of Shoji et al. (2020b) demonstrate that as the upstream momentum thickness of the exiting jet becomes larger, the degree or strength of counter-current flow required to cause transition from CU to AU increases. Hence for the same crossflow and jet bulk velocity conditions, a thicker upstream momentum thickness θ could create a weaker instability in the USL as documented by Harris et al. (2020a) for a tabbed JICF; this is also consistent with a diminished growth rate of the axisymmetric instability mode for the high momentum flux ratio JICF (Alves et al. (2008)).

To explore the effect of upstream suction on the upstream jet momentum thickness θ, the velocity field in the $x - z$ plane at the upstream region of the jet near the jet exit,

	R_1	θ/D	Experiment USL
No Suction	1.164	0.0262	CU
Case 1	1.206	0.0282	CU
Case 2	1.211	0.0287	CU
Case 3	1.212	0.0293	CU
Case 4	1.213	0.0305	CU
Case 5	1.323	0.0387	CU
Case 6	1.360	0.0410	CU
Case 7	1.418	0.0492	CU/AU
Case 8	1.451	0.0543	AU
Case 9	1.483	0.0728	AU
Case 10	1.518	0.0866	AU

Table 10.1: For $J = 41$ and $Re_j = 1900$ with suction applied locally along the upstream edge of the jet, the shear layer velocity ratio, upstream jet momentum thickness at the jet exit (scaled by D) and the hotwire-based state of the upstream shear layer.

extracted from PIV measurements, was used, with details on the method of extraction described in Shoji et al. (2020b). This method was applied to all jet suction cases here. The results are given in table 10.1, where the approximated shear layer velocity ratio R_1, scaled upstream momentum thickness θ/D, and state of the USL as determined via hotwire anemometry (AU or CU) are given. The data showed an interesting competing dominance between the calculated R_1 value, and the momentum thickness θ/D. Recalling from the CCSL analogy, for a fixed momentum thickness as the shear layer velocity ratio is increased, the jet will transition from convective to absolute instability, and likewise as the shear layer velocity ratio is fixed and the momentum thickness is thinned, the jet will transition to absolute instabilities, assuming the R_1 value is sufficiently large (Souza et al. (2020)). As such, while the applied suction was successful at introducing a stronger counter-current flow

thereby increasing the R_1 value, it also came at the expense of thickening the momentum thickness of the shear layer. According to the hotwire based evaluations of the shear layer instabilities, the enhanced strength of the shear layer velocity ratio was able to overtake the momentum thickness dominance by around suction case 7, after which the shear layer spectral characteristics were clearly AU. However, the exact delineation of absolute or convective instability as based on the CCSL analogy is as of yet unsubstantiated, so it is unclear if the modifications to the flow, through the addition of suction over a finite region and spanning only the local upstream region of the jet, will still be able to be accurately represented by the CCSL analogy. With regard to the suction applied in the downstream edge of the jet, the upstream momentum thicknesses and shear layer velocity ratios were not investigated given the shear layer spectral characteristics did not indicate a transition in the flow from convective to absolute instability. Additionally, Harris et al. (2020a) notes for similar analyses of a tabbed JICF, that placement of the tab in the downstream did not significantly alter the upstream velocity profile.

10.1.4 Mixing

Lastly it was of interest to investigate the resulting implications of the significant alterations to shear layer instabilities, vortex dynamics, and CVP formation and symmetry on the efficacy of molecular mixing of the jet, recalling the general correlation between the shear layer dynamics, CVP symmetry, and enhancement of molecular mixing (Getsinger et al. (2014); Gevorkyan et al. (2016)). Quantification of the molecular mixing between the jet and crossflow was explored via the unmixedness parameter, which as detailed in other portions of this dissertation represents the second moment of the scalar concentration field, and can be derived from the PLIF images. The equation defining unmixedness in the jet cross-section is shown in equation (1.8), where the lower the local unmixedness, U, the better the molecular mixing. The unmixedness was calculated from centerplane and cross-sectional views of the jet, where the former provided a continuous downstream evolution of the jet mixing, and

the latter provided a more complete picture of the local mixing for a particular downstream location. In either approach, the general mixing trends as the jet evolves are shown to be generally in agreement with one another (Gevorkyan et al. (2016)). For each of these evaluations of the flow the validity became more unreliable with the increasing strength of the suction as it currently remains undetermined to what extent jet fluid is removed from the flowfield by the suction apparatus. As such these mixing trends are considered quite preliminary and in need of further validation.

Figure 10.9 gives the centerplane and cross-sectional based quantifications of the molecular mixing of the jet flow with the application of suction in the upstream edge of the jet (figs. 10.9(a-b)) and downstream edge of the jet (figs. 10.9(c-d)). Importantly, the general mixing trends noted by the centerplane and cross-section perspectives of the jet were quite consistent. They demonstrated that as the suction was applied, regardless of placement in the upstream or downstream shear layer, the overall mixing was enhanced. Not surprisingly, as the strength of the suction was increased, the degree of mixing enhancement was also found to increase. Interestingly, qualitatively between the upstream and downstream suction cases, the suction upstream generated more significant mixing enhancement in the nearfield of the flow (i.e. $x/D \approx 1.0 - 3.0$). This is thought to arise from the suction generating more dynamically complex flow structures along the leading edge of the jet, and in the case of strong enough suction (case 8 and beyond) actually producing an USL which was AU, promoting stronger vortex rollup and CVP formation. The enhanced mixing with suction upstream or downstream was ultimately thought to be well associated with the symmetrization of the CVP structure, noting that in general a more symmetric CVP is associated with better molecular mixing (Gevorkyan et al. (2016)). Unfortunately, these mixing trends are quite circumspect due to the possible loss of jet fluid from the system, and further the degree to which this was present would depend on the strength of the suction, thereby prohibiting direct quantitative comparisons between differing strengths of suction. It is a matter of ongoing interest to rectify this, or possibly quantify the volumetric flow rate of jet fluid being

(a) Centerplane Upstream

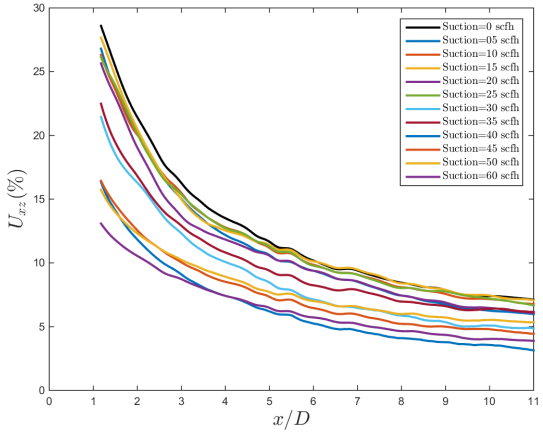

(b) Cross-sectional Upstream

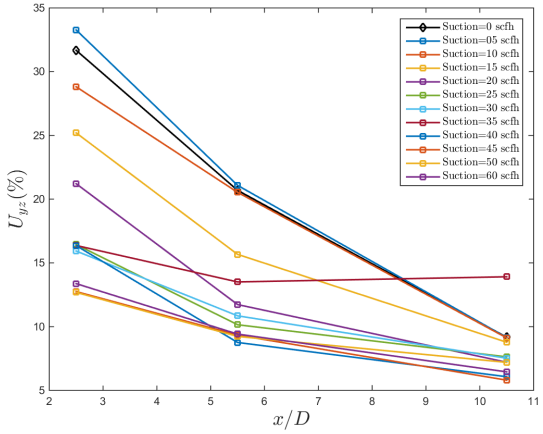

(a) Centerplane Downstream

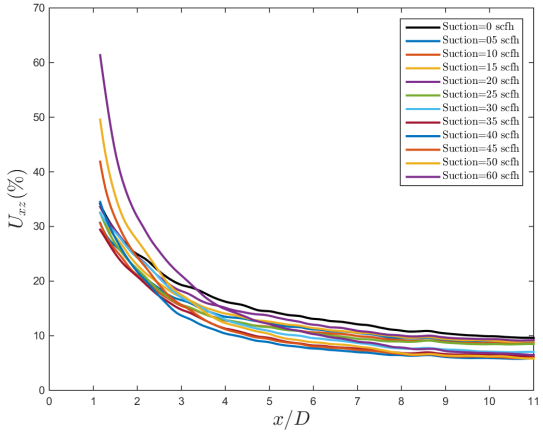

(b) Cross-sectional Downstream

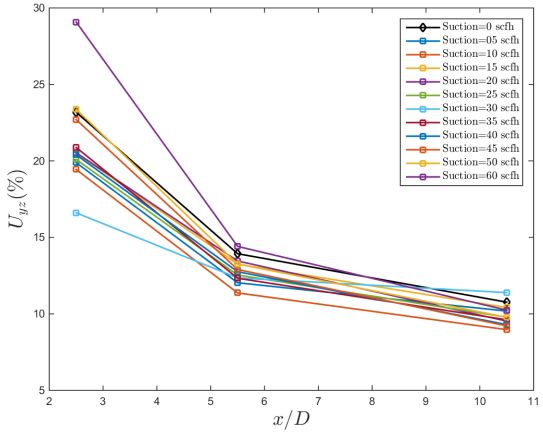

Figure 10.9: Downstream evolution of centerplane unmixedness U_{xz} and cross-section-based unmixedness U_{yz} with $J = 41$ and $Re_j = 1900$, for the unaltered jet with suction applied locally in the (a-b) upstream edge, and (c-d) downstream edge of the jet exit.

removed such that an appropriate scaling could be implemented for more direct comparisons.

10.2 Discussion

The present experimental study documented the effects of augmentation of a convectively unstable jet in crossflow ($J = 41$) via a small section of induced counterflow about the periphery of the jet exit. Effects on jet shear layer instabilities, structure, vorticity, dynamics, and mixing are quantified. The study builds upon the analogies of a counter current shear layer approximation by Iyer and Mahesh (2016) and Shoji et al. (2020b) as applied in the leading edge of the jet exit, and the ideas of a wavemaker region proposed by Regan and Mahesh (2019) and experimentally supported by Harris et al. (2020b) and Harris et al. (2020a). The presence of suction was seen to weaken the instability characteristics along the USL when applied in both the upstream and downstream edges of the jet. However, for the suction upstream, the jet was seen to suddenly transition from a convectively unstable flow to an absolutely unstable flow for a moderate amount of suction. The transition of the shear layer instabilities was seen to be dependent upon competing effects of increasing strength of the shear layer velocity ratio and thickening of the momentum thickness.

Instantaneous and mean centerplane vorticity images, along with PIV based POD modes demonstrated alterations of the upstream shear layer dynamics with the suction upstream and downstream that were similar to those noted by the instability characteristics. Increasing strength of suction upstream, progressively promoted the translation of the shear layer by over 1/2 diameter upstream of the jet, just ahead of the suction, and initiated the dynamics systematically closer to the jet exit. Suction downstream was unable to alter the upstream dynamics at all, though downstream there was the promotion of upright wake-like structures which were more dominant and better connected to the tunnel wall as the suction was strengthened. POD coefficient plots did not depict explicit agreement with the instability characteristics, though this was thought to possibly arise from the FOV applied in the

POD analysis, and is being investigated further. From cross-sectional PLIF imaging the inherent asymmetric jet structure was progressively made more symmetric as the suction was increased for either the upstream or downstream.

Quantifications of mixing demonstrated significant enhancement in the molecular mixing as compared with the unaltered jet. This was thought to arise from the promotion of a more symmetric CVP structure, known to be generally associated with better molecular mixing. However, the mixing enhancement is also thought to partially arise from possible extraction of jet fluid from the tunnel due to the suction, and thus some of the mixing trends are considered not entirely well substantiated given the lack of a normalization factor to accurately compare the different jets. This is a matter of ongoing consideration and investigation.

CHAPTER 11

Future Endeavors

While the present investigations have proven to be quite illuminating pursuant to multiple avenues within the exploration of the JICF, there are still many questions remaining and possible new directions of interest to explore. They are given as follows:

- Further exploration of the passive control of the JICF. The critical alterations to instability characteristics, vorticity production, and cross-sectional symmetry of the CVP would be of interest to explore with lower density jets wherein the fundamental dynamics along the upstream shear layer and the transition between convective and absolute instability has been shown to be quite different. Additionally exploring possible coupling of the passive control with active control measures of helical or axisymmetric excitation of the jet could be of interest.

- Exploration of helical excitation applied to the JICF, expanding upon the work of Besnard (2019). Besnard (2019) investigated four speakers placed about the periphery of the jet to excite the first helical modes (± 1). A greater number of speakers, with better frequency response in the most unstable regime of the helical modes could allow for easier excitation of the helical modes and possible excitation of more helical modes ($> \pm 1$).

- Further investigation of the synchronization analysis of the JICF. Investigation for various waveforms as applied to the smaller flush nozzle where the natural absolutely unstable jet has stronger and more pure tone instabilities could provide cleaner and

more readily understood synchronization states, and further the experimental understanding of the different harmonic terms within the Fourier series approximation of a square wave.

- Further investigation of the double-pulse forcing of the JICF. The findings demonstrate a remarkable ability to induce vortex ring interactions and breakdown, yet it is still somewhat unclear how certain parameters should be optimized, as for example the temporal pulse width of the slow pulse within applied to an absolutely unstable jet. Greater exploration of the ring velocity ratio versus stroke ratio, designated by Sau and Mahesh (2008)) for vortex rings in crossflow, could be quite significant in understanding limitations of double-pulse forcing and other forcing waveforms.

- Continued exploration of quasiperiodic/incommensurate frequency forcing is of significant interest given the extremely promising results. It would be prudent to explore alternative incommensurate frequency combinations to investigate the influence of their respective proximities to the natural jet instability. Also it is still uncertain if the applied forcing in fact produces a strange attractor in the phase space, and if so how such a dynamical state can be effectively harnessed.

- Continued exploration of the coaxial jet with suction is needed given the current limitations with possible flow loss. Correcting or calibrating for this constraint is important for proper evaluation of various metrics, such as mixing of the jet and crossflow. Additionally it could be quite interesting to explore placement of the suction at a variety of off-centerline locations about the jet periphery, analogous to the tabbed JICF studies, to investigate possible effects of enhancing vortex rollup along the side of the jet or possible suppression of the folding of the jet column.

- Utilizing the coaxial nozzle configuration could also allow for exploration of a coflowing JICF. This could have relevance for multiple engine applications where coflowing jet fluid are introduced.

- Application of machine learning techniques could be of use to help identify flow structures and features which usually require computationally intensive calculations to compute. Simultaneous PLIF and PIV imaging has been shown to have a correlation between the scalar dissipation rate and the strain rate. The possible ability for machine learning to be applied to easily attainable PLIF images to establish the location and strength of vortices, and even more the strain rate along the shear layer of the jet could be of immense help.

- The CCSL has significant relevance to the JICF as a tool in helping to determine the state of the instabilities along the USL of the jet. It would be significant to explore the bounds of the applicability of this analogy such as within jets with thicker momentum thicknesses, exploring different jet exit velocity profiles, examining variation in the jet density ratio, and the significance of suction and coflow (coaxial nozzle and elevated nozzle) in the the leading edge of the jet.

APPENDIX A

Jet Flow Calculations

Characterization of the JICF was given by the jet-to-crossflow density ratio S, the jet-to-crossflow velocity ratio R, the jet-to-crossflow momentum flux ratio J, and the jet Reynolds number Re_j. For the experiments performed, these parameters were selected, and then the flow rates of the jet and crossflow necessary to produce the desired flowfield were then mathematically determined utilizing a process which is herein detailed. Initially, the density of the crossflow fluid was determined from measurements of the ambient temperature and pressure in the room, which along with the desired density ratio, fixed the density of the jet fluid. The density of the jet fluid was utilized to determine the molecular weight of the jet from the ideal gas law, and from the molecular weight of the jet, each of the mole fractions of the jet fluid constituent species could be established.

Depending on the type of experimental diagnostics implemented, different constituent species were utilized to form the jet flow. Prior experiments consisted of a pure N_2 jet (Megerian et al. (2007); Davitian et al. (2010b); Getsinger et al. (2012)), and more recent investigations wherein PLIF was employed utilized a mixture of N_2, He, and acetone ($CH_3-CO-CH_3$) (Getsinger et al. (2014); Gevorkyan et al. (2016); Shoji et al. (2020a); Shoji et al. (2019); Besnard (2019); Harris et al. (2020b)). In the case of pure N_2, the calculations were relatively straight forward given a singular species composing the jet flow, while in the case of the PLIF imaging experiments, the determination of the mole fractions for the respective constituent species necessitated a system of equations for the three unknowns. The first two equations were given by the summation of the species mole fractions equaling one, and the

summation of the respective molecular weights of the species, multiplied by their respective mole fractions, equaling the average molecular weight of the jet fluid, which was already fixed as discussed. To close the problem, information was garnered from the acetone seeding chamber. Extensive work on the use of acetone as a tracer particle for LIF was performed by Lozano (1992), and in fact they establish a relationship, given in the following equation

$$log_{10}P_{ace} = 7.125267 - \frac{1214.208}{230.002 + T_{seeder}} \tag{A.1}$$

where the vapor pressure of acetone, given here in units of Torr, is calculated based off of the temperature, in units of Celsius, within the chamber. This pressure was then corrected by the gauge pressure reading of the seeding chamber, and utilized with Dalton's law to determine the partial pressures of each of the constituent species. Thus quite evident from this calculation, was the fact that altering the flow rates into the acetone seeding chamber, and the temperature at which the seeding chamber was maintained, affected the gauge pressure within the chamber, and thus impacted the acetone seeding density. As such, an iterative approach was utilized, whereby the flow was allowed to converge and the acetone seeding chamber temperature and pressure to stabilize, and then the flow conditions were recalculated based on the stabilized pressure and temperature readings, until the readings were matched with the input within $\approx 1\%$.

After determining the respective mole fractions of the jet flow, the viscosity of the resulting fluid mixture was established. Given a mixture of gases, the Reichenberg method for computing the viscosity of the fluid was implemented as is detailed extensively in equations (9-5.1) through (9-5.12) in Poling et al. (2001). Thus with an established viscosity for the gas mixture, the known parameter of the jet diameter, and the prescribed jet Reynolds number were utilized to determine a jet velocity, and consequentially total volumetric flow rate. Again utilizing Dalton's law, and the known mole fractions of the constituent species, it was possible to prescribe the flow rates of the N_2 and He respectively. The resulting flow was then validated through the use of a bubble meter in the same manner as which the flow controllers are calibrated.

The determination of the flow parameters was made slightly more complex when treating low density flows, or implementing simultaneous PLIF and PIV imaging, as it was necessary to partition the flow. In the case of the low density jets this was done so as to not seed too much acetone into the flow given that the acetone is much more dense than air, and the control of the acetone mole fraction was limited by how low of a temperature the regenerative cooler could chill the acetone. In the case of the simultaneous imaging, the flow was split so that both the PLIF tracer (acetone), and the PIV tracer (DEHS oil), could be seeded into the flow. The seeding was done in parallel rather than in series due to clogging constraints within either seeding chamber posed by the introduction of the other respective tracer. For both the low denstiy jets and the simultaneous imaging, these issues were circumvented by splitting off a portion of the flow from the main jet before entering the acetone seeding chamber, and then reintroducing it to the main flow downstream of the acetone chamber. Quite obviously this impacted the system of equations utilized to determine the respective mole fractions of the constituent species. Given the experiment only implemented three flow controllers, the flow through the acetone chamber, deemed the PLIF line, in these cases was limited to either pure N_2 or pure He, while the bypassed fluid, deemed the PIV line for simplicity, was able to be composed of either pure N_2, pure He, or a mixture of the two. As such, the determination of the mole fractions was a sort of compounding calculation, whereby first the relative mole fractions of the constituent species within the PLIF and PIV lines were respectively determined, and then the mole fractions of the PLIF flow and the PIV flows were established based on the desired output properties of the jet. These mole fractions were then simply multiplied with the respective relative mole fractions, and like species combined, to yield the overall mole fractions of the constituent species for the jet flow. Following this, the remaining calculations were the same as above, utilizing the Reichenberg method and Dalton's law. The flow rate issuing from the jet nozzle was again validated with a bubble meter.

APPENDIX B

Transverse Jet Instabiltities and Counter-Current Shear Layer Analogy

The results presented in this section are taken with slight modification from the article "On the origins of transverse jet shear layer instability transition", published in the Journal of Fluid Mechanics (Shoji et al. (2020b)).

B.1 Shear layer instabilities for different jet mixtures

Prior experimental studies provide extensive evidence that the USL for the equidensity flush nozzle-injected JICF, consisting of pure N_2 injected into air, becomes globally unstable when J is brought to or below $J_{cr} \approx 10$ (Megerian et al. (2007); Davitian et al. (2010a)), or that the low density JICF consisting of He-N_2 mixtures becomes absolutely/globally unstable when $J \lesssim 10$ and/or $S \lesssim 0.40$ (Getsinger et al. (2012)). Among the most compelling pieces of evidence for this transition is the significant alteration in hotwire-based USL spectral characteristics with changes in flow conditions, although there are many additional documented features associated with this transition (Davitian et al. (2010a)). The hotwire is traversed along the USL trajectory coordinate s/D (see figure 1.3), determined based on a power-law fit to the maximum gradient in the local vertical velocity field. For the low density JICF ($S < 1$) and hence for continuously varying density fields, which present difficulties in hotwire velocity calibration, the USL trajectory as well as spectral characteristics may be determined based on uncalibrated hotwire voltage (Getsinger et al. (2012)) since the

Jet constituents	S	ψ	J_{cr}	U_j **(m/s)**	μ_j **(10^{-5} (kg/m/s)**
N_2	1.0	0.0	≈ 10	7.07	1.745
N_2, He, and acetone (PLIF/PIV)	1.0	0.112	≈ 8	6.80	1.729
N_2, He, and acetone (PLIF)	1.0	0.218	$\lesssim 7$	6.49	1.653
N_2 and He	0.35	0.0	> 52	22.34	1.995
He and acetone (PLIF/PIV)	0.35	0.113	≈ 41	22.14	1.964

Table B.1: For various jet gas constituents with increasing acetone mole fraction, ψ, shown are mean jet velocity and absolute viscosity required for matching $Re_j = 1900$ for two different density ratios, $S = 1.0$ and 0.35. Values of the estimated critical momentum flux ratio J_{cr} based on hotwire measurements are also given.

uncalibrated hotwire signal still yields the same frequency content at various locations as a calibrated hotwire.

In the present experiments, spectral characteristics of the JICF were acquired via hotwire anemometry for the same overall flow conditions (Re_j, J, S) but with different mixtures of species in the jet fluid. These mixtures corresponded to experiments employing different optical diagnostics. Relevant parameters are quantified in table B.1 for both equidensity and low density ($S = 0.35$) flush nozzle-injected jets for the case $Re_j = 1900$. Gas constituents included pure nitrogen associated with earlier equidensity experiments (Megerian et al. (2007); Getsinger et al. (2012)) and mixtures of nitrogen and helium with acetone for simultaneous PLIF/PIV ($\psi = 0.112$) and for higher resolution PLIF-only experiments ($\psi = 0.218$) typically used to quantify molecular mixing (Gevorkyan et al. (2016)). Gas constituents corresponding to the simultaneous PLIF/PIV experiments did not include DEHS oil so as to enable hotwire usage for spectral measurements.

Figure B.1 shows fine resolution spectral magnitude contour plots for the equidensity JICF, representing the hotwire response to vertical velocity fluctuations measured along the upstream shear layer trajectory s/D, for a fixed jet Reynolds number ($Re_j = 1900$) with different momentum flux ratios J. Data are shown for different mixtures of species

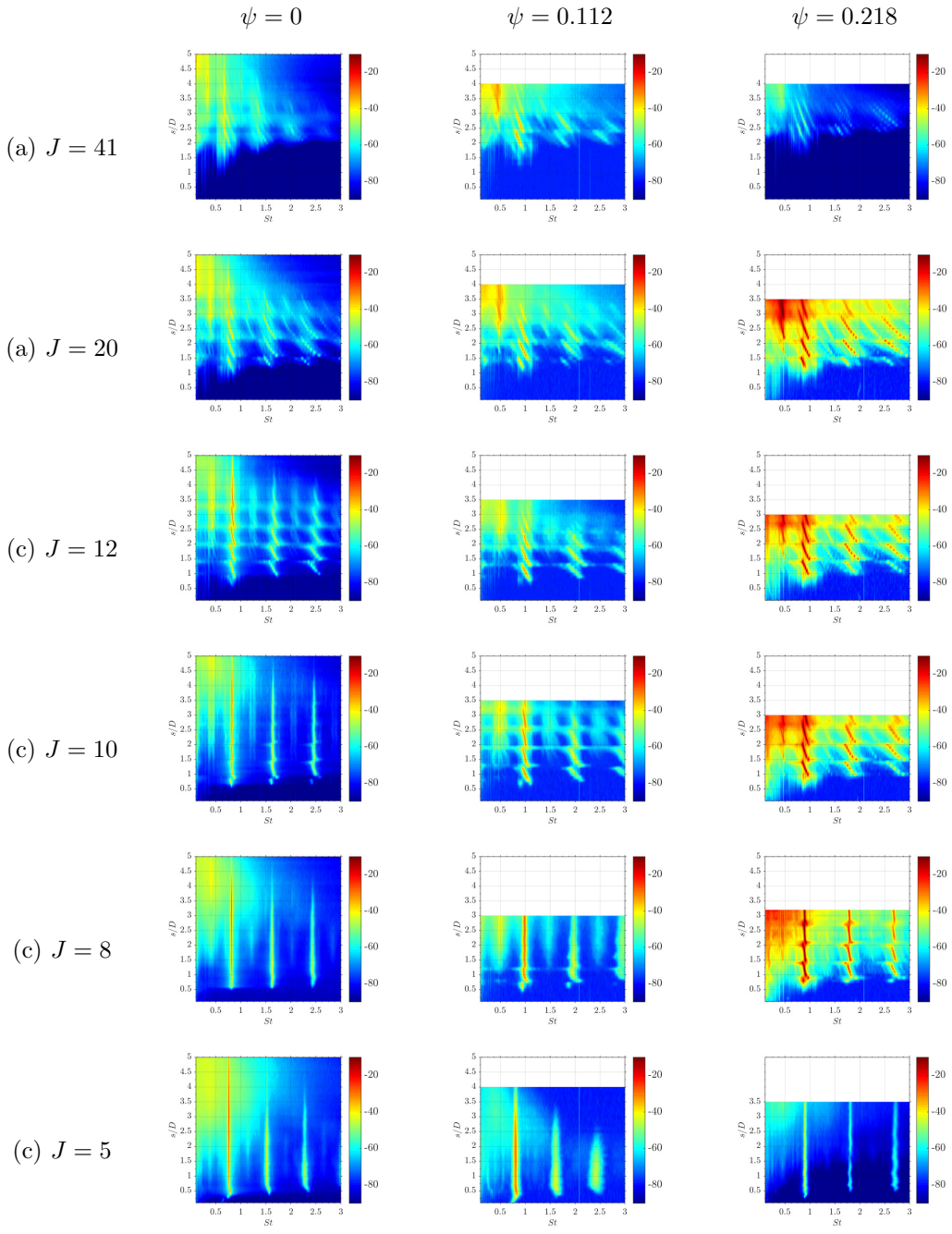

Figure B.1: Spectral contour maps of the hotwire-based velocity disturbances along the USL trajectory coordinate s/D for the JICF at $Re_j = 1900$ and $S = 1.0$ with varying J and acetone mole fraction ψ, corresponding to jets with N_2 only ($\psi = 0$, reproduced from original data in Getsinger et al. (2012)), the jet mixture for simultaneous PLIF and PIV ($\psi = 0.112$), and the PLIF-only experiments ($\psi = 0.218$). The colorbar represents disturbance amplitude in dB.

in the jet fluid, corresponding to different mole fractions of acetone: $\psi = 0$ for the pure N_2 jet (approximately the same as for PIV-only experiments), $\psi = 0.0112$ for typical simultaneous PLIF/PIV experimental conditions, and $\psi = 0.218$ for the typical PLIF-only experiments. Interestingly, while the overall change in USL spectral characteristics from convectively unstable behavior at $J = 41$ to absolutely or globally unstable behavior at $J = 5$ was similar, there were subtle differences as transition from CU to AU took place, based on ψ. Interestingly, despite the careful matching of Re_j, S, and J values here, the mixture of constituent gases in the jet affected the evolution of upstream shear layer, both qualitatively and quantitatively. This observation will be discussed and explored further below. At $J = 41$, 20, and 12, multiple spatially-evolving instabilities in the USL were observed, with frequency-shifting along the trajectory s/D resulting from tonal interference between the successively strengthening shear layer instability and the hotwire probe (Hussain and Zaman (1978); Getsinger et al. (2012)). The average of the shifting frequencies was considered to correspond to a fundamental frequency f_o, as done in prior studies (Megerian et al. (2007); Davitian et al. (2010a); Getsinger et al. (2012)). Subharmonic development, representing vortex merger, was more prominent at these higher J values, while higher harmonics appeared to be strengthened with a reduction in J as crossflow velocity U_∞ increased. These spectral characteristics corresponded to the behavior of a convectively unstable USL, as discussed in prior JICF stability studies (Megerian et al. (2007); Davitian et al. (2010a); Getsinger et al. (2012)). But with the addition of increasing concentrations of acetone, and with the presence of helium and nitrogen designed to create $S = 1$, the location of initiation of the instability (s/D) was delayed, especially as J was reduced, suggesting a slight weakening of the shear layer instability with increasing acetone concentration. There were also increases in the estimated average fundamental frequency f_o and hence Strouhal number St_o associated with the initiation of the instability as ψ was increased.

As the momentum flux ratio was reduced to the range close to initiation of an absolutely unstable USL for the pure nitrogen jet, near $J = 10$ (Megerian et al. (2007); Davitian et al.

(2010a); Getsinger et al. (2012))., figure B.1d indicates that the effect of acetone in the jet mixture was not only to delay the onset of the instability, but to cause its characteristics to be associated with convective instability rather than the pure-tone, spatially invariant absolute instability observed for $\psi = 0$ at this flow condition. Even at $J = 8$ (figure B.1e), there was evidence of a weakening of the shear layer, with a very low level of tonal interference, especially at $\psi = 0.218$, which typically would not be classified as characteristic of globally unstable (GU) flow. At a much lower value of $J = 5$, shown in figure B.1f, all jet mixtures produced the typical AU/GU behavior, with a strong pure-tone instability initiated close to the jet exit, a clear fundamental frequency f_o, and the absence of subharmonic disturbances. For these lower J values there were nevertheless small increases in St_o with increasing ψ.

To verify that the phenomena observed in figure B.1 reflected actual USL behavior and that acetone itself was not affecting hotwire performance, spectral measurements were also made outside of the USL, where there was little or no acetone present. For these spectral measurements the hotwire probe was initially situated at a fixed USL trajectory location then traversed upstream, in the negative x direction, fixing y and z locations. There were no substantive alterations in spectral character (other than strength of the instabilities) as the hotwire was moved outside of the USL into the air crossflow, and in addition, St_o did not vary. Thus it was determined that alterations in the USL transition and J_{cr} for the acetone-seeded JICF reflected actual physical phenomena and were not affected by the measurement method.

Similar alterations in fundamental St_o values and J_{cr} were observed in other acetone-seeded JICF experiments for a range of operating conditions, where deviations from established values of J_{cr} occurred when acetone was present in the jet fluid. Yet overall trends associated with the variation in St_o with J were consistent with prior equidensity flush nozzle-injected JICF results in the absence of acetone (Megerian et al. (2007)). This is shown in figure B.2 for various equidensity flow conditions, with different Re_j values, gas constituents, and with two different nozzle diameters. For a fixed Re_j and acetone concentration, as J

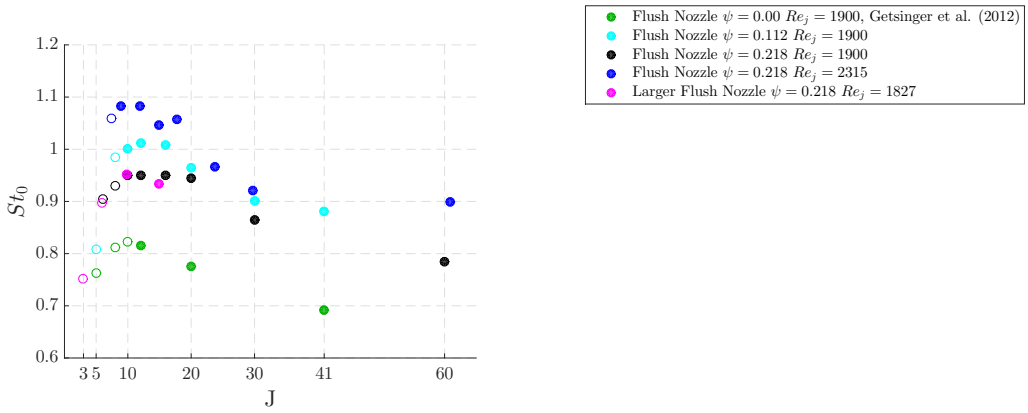

Figure B.2: Variation in Strouhal number St_o for the fundamental USL mode based on jet diameter and mean jet velocity U_j as a function of J for the equidensity flush nozzle- and larger flush nozzle-injected JICF. Data are shown for Re_j and acetone mole fractions ψ. Filled and open symbols represent the hotwire-determined convectively and globally unstable USL, respectively.

was reduced from a large value by increasing the crossflow velocity, frequency f_o and hence St_o values from hotwire-based spectra corresponding to convectively unstable flow always increased before reaching a peak at $J \approx J_{cr}$, and then decreased after the transition to global instability for $J < J_{cr}$. Figure B.2 demonstrates a minimal influence of jet diameter for the same Reynolds number (e.g., comparing black and purple symbols), but a somewhat larger influence of Re_j and ψ on J_{cr} (e.g., comparing green and dark blue symbols). Increasing the mole fraction of acetone appeared to reduce the value of J_{cr}, seen as the J value at which the closed or filled symbols became open ones for a given set of conditions in figure B.2. For a given S and Re_j, a smaller J_{cr} corresponded to an increase in the crossflow velocity U_∞ required to create transition to absolute instability. Increasing acetone concentrations also caused an increase in f_o and hence in St_o, consistent with spectral contour plots (figure B.1).

The reduction in hotwire-estimated J_{cr} with increasing concentrations of acetone in the jet fluid is recorded in table B.1 for both equidensity and low density flush nozzle-injected jets for experiments with a fixed $Re_j = 1900$. Because jet density and Reynolds number were

matched in these experiments for each J value studied, and because the absolute viscosity of the mixture did vary among the cases for different concentrations of acetone, as determined via the Wilke formula (Bird et al. (1960)) and the Reichenberg method (Poling et al. (2001)), the actual mean jet velocity U_j at the exit plane necessarily differed slightly for the different acetone concentrations with otherwise constant bulk flow properties. The changes in J_{cr} observed in figure B.2 and in table B.1 with acetone addition may be interpreted in the context of flow in the vicinity of the USL near the injection location, as will be shown.

B.2 Analogy to counter-current shear layer

Iyer and Mahesh (2016) computationally demonstrate the phenomenological similarity in the USL instability transition for the flush nozzle-injected transverse jet to that for the counter-current shear layer based on the CCSL velocity ratio R_1 in the centerplane, defined in equation (1.6). The present study explored this similarity based on numerous experimental datasets, using velocities extracted from PIV-only data for density ratios $S = 1.00$, 0.70, 0.55, and 0.35 (without the presence of acetone in the jet), taken from Getsinger et al. (2012), and also using the PIV portion of simultaneous PLIF and PIV experiments at $S = 1.00$ and 0.35, many of which were taken from Shoji (2017) and Gevorkyan et al. (2018). Hence the acetone mole fractions in this comparison were relatively small, $\psi = 0.112$.

To extract the mixing layer (CCSL) velocity ratio R_1 from PIV-based data, the same method as that used computationally in Iyer and Mahesh (2016) was applied. First, the USL was defined by the magnitude of mean vorticity in the out-of-plane direction, $|\omega_y|$, as shown, for example, in figure B.3a for the equidensity JICF with $J = 20$. The normal direction to the USL, n/D, may be defined from the $|\omega_y|$ field, displayed using multiple lines close to the jet exit in figure B.3a. As done in the numerical studies Iyer and Mahesh (2016), mean vertical velocity distributions then can be extracted at different locations s/D just downstream of the jet exit, along the layer-normal direction n/D, as shown in figure

B.3b. These velocity distributions were observed to have regions of both negative vertical velocity upstream of the USL center and positive vertical velocity within the jet but outside of the USL, including a fairly uniform velocity profile near the jet center, consistent with a nozzle-generated top hat-like exit profile (examples of which, for a range of conditions, may be found in Gevorkyan et al. (2018)). The nearfield velocity profiles in figure B.3b appeared quite analogous to those for a counter-current shear layer, and hence V_1 and V_2 could be extracted from such PIV-based data to evaluate the CCSL velocity ratio R_1 via equation (1.6). More details on the method of estimation of R_1 for the JICF may be found in Iyer and Mahesh (2016). In the present experiments, the region upstream of the layer for which negative (vertically downward) flow occurred extended to distances in the negative layer-normal direction that depended on J. This negative flow region extended to approximately $n/D \approxeq -0.5$ for higher J values such as $J = 41$, but for lower J values such as 5, this region extended further, to $n/D \approxeq -2.0$.

Resultant R_1 values for a range of experimental conditions with the flush nozzle are shown in figure B.4a for the equidensity JICF and in figures B.4b, B.4c, and B.4d for the low density JICF at density ratios S equal to 0.70, 0.55, and 0.35, respectively. Filled and open symbols represent convectively and absolutely/globally unstable transverse jet upstream shear layer conditions, respectively, determined experimentally via hotwire-measured spectral characteristics such as those shown in fig. B.1. In addition, for most of the cases in figures B.4a-d, separate PIV-based proper orthogonal decomposition (POD) mode coefficient plots were examined to verify consistency with AU shear layer identification. As described in detail in Meyer et al. (2007) and Gevorkyan et al. (2018), using snapshot POD analysis of the PIV-based jet centerplane data, plots of the POD coefficents of the first and second modes become circular when there is a periodic traveling wave flow structure consistent with an absolutely unstable upstream shear layer. Such behavior in the PIV-based experiments was used to verify consistency with the stability condition for the USL identified via hotwire anemometry and indicated by the open circles in figure B.4. The dashed lines in each plot

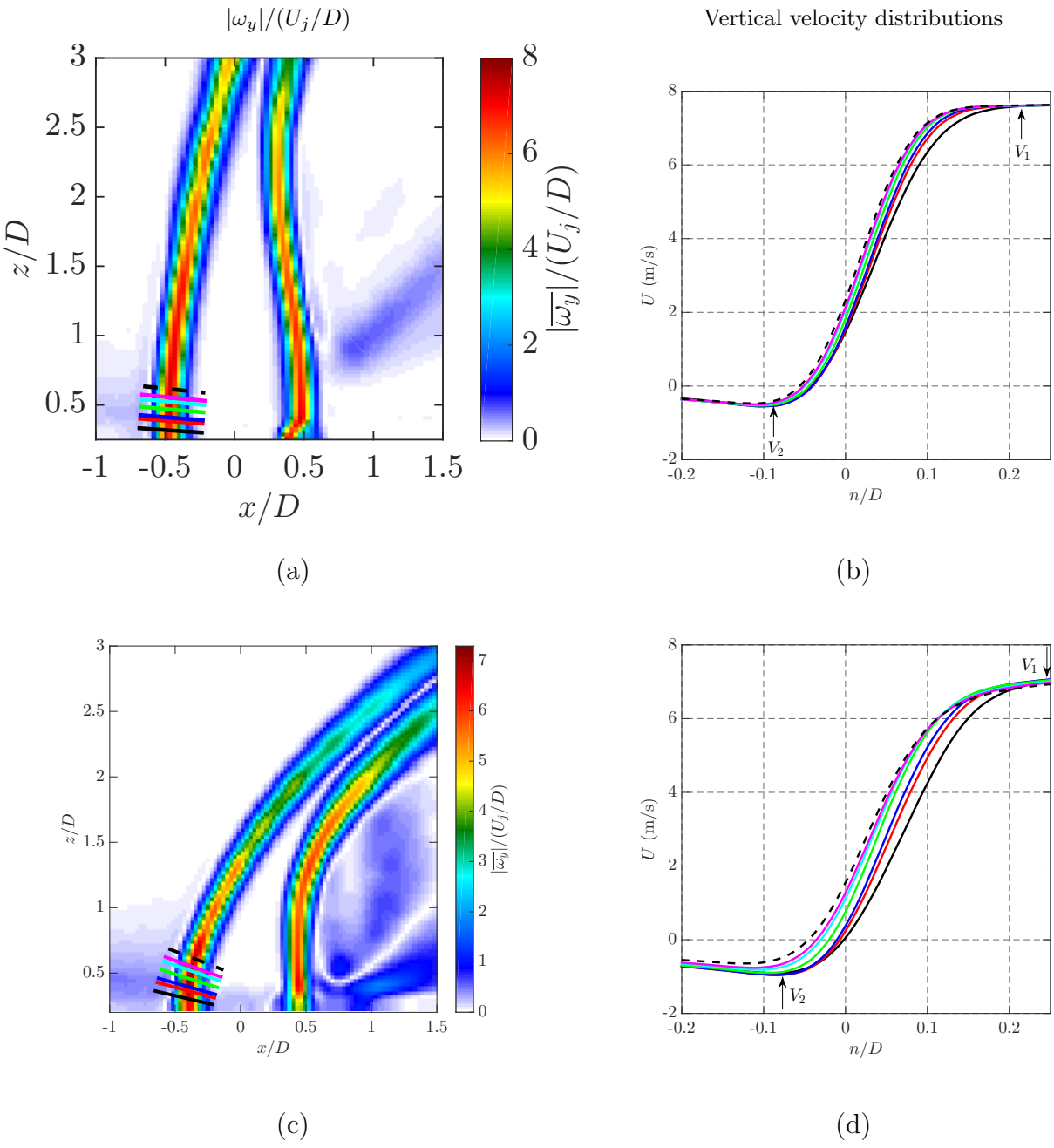

Figure B.3: (a) and (c) Normalized magnitude of vorticity in the out-of-plane direction, $|\omega_y|$, for $J = 20$ and $J = 5$, respectively. (b) and (d) Vertical mean jet velocity distributions in the USL trajectory-normal direction, n/D, at variable trajectory locations, s/D, corresponding to $J = 20$ and $J = 5$, respectively, with the same line colors as in parts (a) and (c). Flow conditions correspond to the equidensity, nozzle-injected JICF with $Re_j = 1900$ and $\psi = 0.112$.

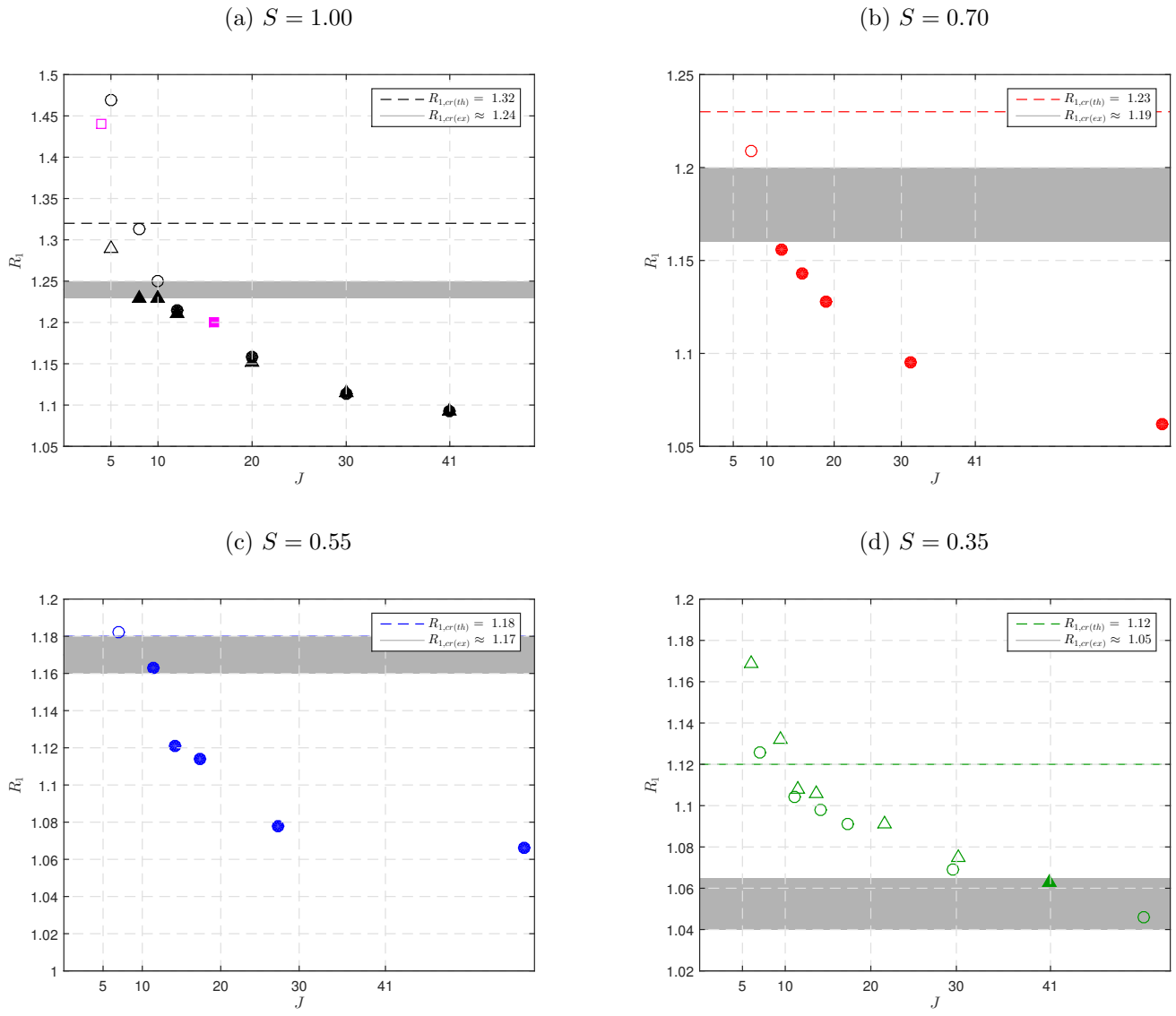

Figure B.4: Data points show R_1 vs. J for the JICF at different density ratios S for a fixed $Re_j = 1900$. Dashed lines corresponding to the color of datapoints represent the theoretical velocity ratio, $R_{1,cr(th)}$, for the 2D CCSL, while the gray region represents the range of experimentally observed values, $R_{1,cr(ex)}$. Circles represent R_1 values extracted from PIV-only experiments, while triangle symbols are based on data from simultaneous PLIF/PIV experiments with acetone at $\psi \approx 0.112$. Filled and open symbols represent convectively and absolutely/globally unstable conditions, respectively, determined via hotwire anemometry. In (a), the purple squares represent R_1 determined from equidensity DNS by Iyer and Mahesh (2016) at $Re_j = 2000$.

indicate the established (theoretical) 2D CCSL velocity ratio, $R_{1,cr(th)}$, for transition from a CU to AU shear layer for the given density ratio. These values are predicted by inviscid linear stability theory for the planar CCSL with $S = 1$ from Huerre and Monkewitz (1985). For $S < 1$, theoretical values of $R_{1,cr(th)}$ were extracted from the study by Pavithran and Redekopp (1989) for the counter-current shear layer, although it is noted that use of the Crocco-Busemann relation to compute density profiles can be inaccurate in representing the nearfield and thus prediction of stability characteristics for light and hot jets (Coenen and Sevilla (2012)). For all cases in figure B.4, dashed lines theoretically distinguish convectively unstable conditions ($R_1 < R_{1,cr}$) from absolutely unstable conditions ($R_1 > R_{1,cr}$) for the CCSL. The transition from filled to open symbols in the figures enables estimation of the experimentally determined value or range of values for the critical velocity ratio, $R_{1,cr(ex)}$, indicated by the shaded regions in the figures.

For the equidensity JICF without acetone in figure B.4a (circles), corresponding to PIV-only experiments from which V_1 and V_2 were extracted, AU conditions occurred when $J \lesssim 10$ according to hotwire measurements. The corresponding value of R_1 at this AU transition was approximately 1.24, below the theoretical critical value, $R_{1,cr(th)} = 1.32$. While there was a quantitative difference in the critical value of R_1, as one might expect for comparisons of a round, deflected shear layer with an idealized planar shear layer separated by infinite flow regions, the trends in the figure were consistent with the concept of the counter-current shear layer. That is, lower J values producing absolute instability in the transverse jet corresponded to larger R_1 values, exceeding a critical value and thus being consistent with a self-excited CCSL. Hotwire-determined convectively unstable conditions, with filled symbols in figure B.4a, similarly corresponded to $R_1 < R_{1,cr(ex)} \approx 1.24$. These trends were also consistent with the DNS results for two different velocity ratios computed by Iyer and Mahesh (2016), shown for reference in figure B.4a. These two computed datapoints for R_1 not only straddled the experimentally-estimated value $R_{1,cr(ex)} \approx 1.24$, but also were consistent with the trends in the range of values shown by the experimental datapoints (circles, in the absence

of acetone).

For the equidensity experiments with acetone present, V_1 and V_2 extracted from the PIV portion of simultaneous PLIF and PIV measurements showed small yet systematic reductions in V_1 and less-negative values of V_2 as compared with extracted values in PIV-only experiments at the same J and Re_j. These changes are reflected in the altered values of R_1 shown by the triangle symbols in figure B.4a, where the critical condition changed to $J_{cr} \lesssim 8$, with $R_{1,cr(ex)} \approx 1.23$. The differing J_{cr} values associated with USL transition with and without acetone in figure B.4a appeared to be associated with the slightly altered USL counter-current shear layer-like velocity distributions and the resulting small differences in the values of V_1 and V_2 close to the jet's exit, thus producing a slightly different R_1. These differences in the velocity distributions resulted from small differences in the mean exit velocity U_j that were required to match both Re_j and S for a given J when the jet mixture contained acetone, with a different overall absolute viscosity μ_j, as noted in Section B.1. Hence, while in both equidensity cases in figure B.4a there was consistency in trends in the USL instability transition (from CU to AU, corresponding to increases in R_1), there was a small quantitative difference in $R_{1,cr}$ as well as in J_{cr}.

For the low density JICF, trends in increasing R_1 with a reduction in J at matched Re_j and S were also consistent with the CCSL model, shown in figures B.4b, B.4c, and B.4d. The theoretical value of $R_{1,cr(th)}$ determined from Pavithran and Redekopp (1989) was somewhat larger than the PIV-based value of $R_{1,cr(ex)}$ for density ratio $S = 0.70$ (figure B.4b), though the band in which the transition from CU to AU took place (at $J_{cr} \lesssim 10$) was relatively wide in terms of estimating the critical R_1 range. For $S = 0.55$ (figure B.4c), the theoretical value of $R_{1,cr(th)}$ was slightly higher than the band at which PIV-only experiments indicated a transition from convective to absolute instability. Consistent with findings in Getsinger et al. (2012), the very low density conditions for $S = 0.35$ in figure B.4d generally showed absolutely unstable USL conditions for virtually all J values explored. An exception for the case with acetone present occurred at $J = 41$, where the

spectra were not quite the same as those associated with absolute instability, with a small degree of tonal interference. This condition for $J = 41$ and $S = 0.35$, which may have been marginally convectively unstable, produced CCSL velocity profiles corresponding to $R_1 \approx 1.065$, well below that of the theoretical critical value of $R_{1,cr(th)} = 1.12$ for this density ratio. We note that in Getsinger et al. (2012), hotwire measurements indicated that either $J < 10$ or $S < 0.40$ produced an absolutely/globally unstable USL, but data in figure B.4d suggested that a J value greater than 41 at $S = 0.35$ in the presence of acetone, or potentially greater than $J = 52$ without acetone, could produce a convectively unstable upstream shear layer, although such conditions were not attainable in the present experiments. Overall, then, there was general consistency between JICF shear layer transition and transition in a counter-current shear layer model from convective to absolute instability, even though the critical values of R_1 were typically smaller in the experiments than from the inviscid 2D CCSL analysis. These findings suggest that the mechanism by which the JICF upstream shear layer transition takes place, at least for the flush nozzle, could relate to the strengthening local counterflow occurring at the jet exit.

It should be noted that the CCSL model here also provided some evidence for a mechanism for the development of the self-sustained global instability in the jet's upstream shear layer. Huerre and Monkewitz (1990) note that, as a flow transitions from convective to absolute instability, a "zone of local absolute instability" forms. As the zone grows beyond a critical size, the system can become globally unstable, with a Hopf bifurcation to a self-sustained global mode. Huerre and Monkewitz note that the existence of this region of local absolute instability is a necessary though not sufficient condition for the existence of an amplified global mode. Evidence of global instability in the flush nozzle-injected transverse jet for a small enough J value, including evidence of a Hopf bifurcation (Davitian et al. (2010a); Regan and Mahesh (2017)) has already been documented both experimentally and computationally. The region of negative flow upstream of injection for the transverse jet, found here to grow in the negative n/D direction as crossflow velocity was increased (e.g., as

in figure B.3), could indeed represent this growing "zone of absolute instability", providing additional evidence for transition to a global mode. This phenomenon appeared to occur even for the somewhat thick counter-current shear layers created by this nozzle, as will be discussed below.

Additional features of the CCSL for which experimental data from the round JICF may be compared with 2D theory include the Strouhal number associated with the fundamental shear layer instability but where the length scale of interest is the momentum thickness of the local nearfield counter-current shear layer shown in figure B.3. The linear stability theory of Huerre and Monkewitz (1985) for the equidensity 2D CCSL suggests the critical velocity ratio $R_{1,cr} = 1.315$ corresponds to a non-dimensional frequency of 0.192, which may be written in terms of a momentum thickness-based Strouhal number $St_\theta \equiv f_o\theta_o/2\bar{V} = 0.0153$, where the average velocity in the counter-current shear layer takes the form $\bar{V} \equiv \frac{1}{2}(V_1 + V_2)$. For the two dimensional CCSL in figure B.3b, the momentum thickness in the nearfield region of the layer may be approximated as

$$\theta_{CCSL} = \int_{n_{V_2}}^{n_{V_1}} \frac{u(n) - V_2}{V_1 - V_2}\left(1 - \frac{u(n) - V_2}{V_1 - V_2}\right) dn \tag{B.1}$$

where the limits of integration represent locations in the layer-normal direction at which the velocities reach the values of V_1 and V_2. Strykowski and Niccum (1991) compare an experimentally determined Strouhal number with the theoretical value of Huerre and Monkewitz (1985), but alter the limits of integration for eqn. (B.1) so that the lower limit is chosen to minimize uncertainties caused by very low velocities in the vicinity of the negative counter-flow. That lower limit n_L corresponds to the location at which $\left(u - \bar{V}\right)/(V_1 - V_2) = -0.4$. This produces a momentum thickness designated here as θ_{n_L}. On this basis, the Strouhal number extracted from the Strykowski and Niccum (1991) experiments at $R_1 = 1.4$ (above the critical limit) is $St_{\theta_{n_L}} = 0.0185$. At a velocity ratio below the critical limit for the transition to absolute instability for the CCSL, at $R_1 = 1$, Strykowski and Niccum (1991)

observe that $St_{\theta_{n_L}} = 0.012$, in agreement with the Strouhal number associated with the free jet shear layer by Hussain and Zaman (1978). Hussain and Zaman (1978) note the prevalence of a "shear layer mode" at which vortex pairing has occurred, hence is associated with the subharmonic mode for the free jet, downstream of the spatial locations at which the authors observe tonal interference by a hotwire probe producing frequency shifting of the fundamental mode; such subharmonic modes were seen for the transverse jet at higher momentum flux ratios, e.g., in figures B.1a-B.1c.

In the present experiments for the JICF, one can make quantitative comparisons with the theoretical 2D CCSL-based Strouhal numbers by evaluating relevant CCSL momentum thicknesses, either based on the definition in eqn. (B.1) for θ_{CCSL} or based on θ_{n_L}. Figure B.5 shows the variations in momentum thickness θ_{CCSL} with J for the equidensity JICF at $Re_j = 1900$. The aforementioned differences in velocity magnitudes V_1 and V_2 with and without acetone, resulting from the effects of acetone on absolute viscosity and thus on the mean jet velocity U_j and crossflow velocity U_∞ required to match Re_j and S for a given J, affected the CCSL velocity profiles and hence the momentum thicknesses. With the addition of acetone at the mole fraction shown for simultaneous PLIF and PIV, $\psi \approx 0.112$, figure B.5 showed a reduction in non-dimensional momentum thickness θ_{CCSL}/D of approximately 17% for the range of J values shown. Corresponding values of θ_{nL}/D showed a similar reduction.

These differences in non-dimensional momentum thickness with and without acetone provided additional insights into the possible reasons for observed differences in the values of the critical CCSL velocity ratio R_1 for the equidensity cases with and without acetone shown in figure B.4a. One would expect that the quantitative nature of the instabilities should be the same, based on the flowfield's dependence on non-dimensional parameters J, Re, and S for a given transverse jet condition. The differences in the upstream shear layer and the instabilities with and without acetone for the same values of these non-dimensional parameters suggested that an additional non-dimensional parameter could be relevant to the nature of the instabilities, per non-dimensional analysis. This non-dimensional parameter

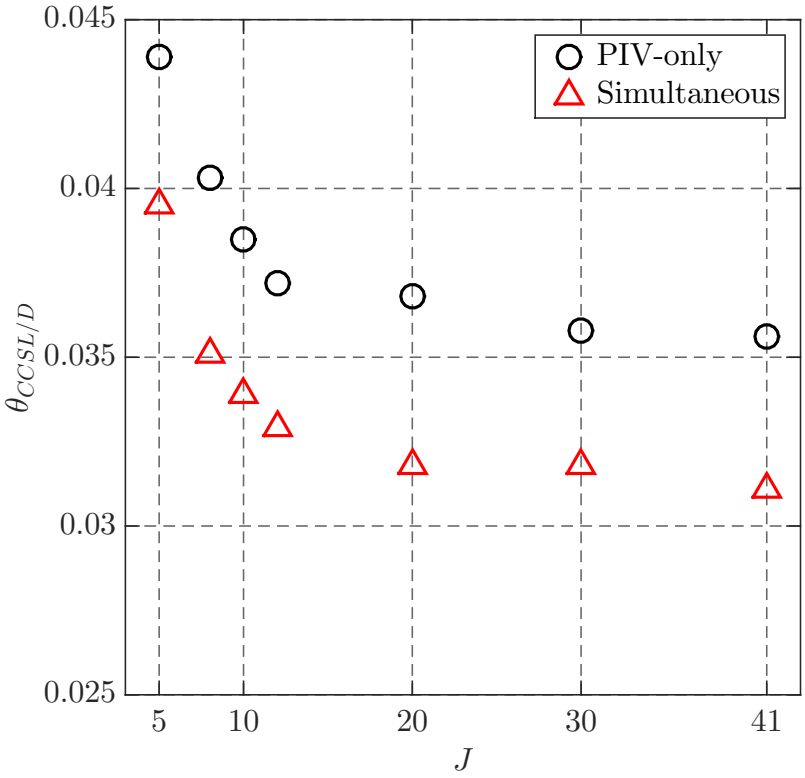

Figure B.5: Variation in momentum thickness θ_{CCSL} (scaled by D) for the local counter-current shear layer as a function of J for the equidensity JICF at $Re_j = 1900$. Results for data extracted from PIV-only experiments, without acetone, and simultaneous PLIF/PIV experiments, with acetone present at $\psi \approx 0.112$, are shown.

appeared to be the ratio of the jet-to-crossflow absolute viscosities, μ_j/μ_∞, causing the scaled CCSL momentum thickness θ/D to be dependent on the presence of acetone, as shown in figure B.5. This issue will be discussed further below.

It is noted that the relatively large momentum thicknesses in figure B.5, for example, producing D/θ_{CCSL} values as large as 32 for $J = 41$ with acetone and as small as 23 for $J = 5$ without acetone, were thicker than those typically considered to be thin enough so that shear layer curvature effects may be considered negligible (D/θ of the order 50, per Huerre

and Monkewitz (1985), and larger, on the order 230, by Strykowski and Niccum (1991)). The momentum thickness can impact application of planar CCSL inviscid instability theory in predicting fundamental instability frequencies, as noted by Strykowski and Niccum (1991)). For example, linear stability analysis for the planar CCSL (Jendoubi and Strykowski (1994)) suggests that the critical value of $R_{1,cr}$ can change with more significant reductions in D/θ, which in the case of the JICF would correspond to lower J conditions, e.g., $J = 5$. Yet the actual experimental values of R_1 for this range of momentum thicknesses and J values shown in figure B.4a were very close to DNS-based results (Iyer and Mahesh (2016)) for similar flow conditions. For the strongly deflected jet in crossflow, one would expect curvature effects in the round jet as well as the increasingly non-parallel flow along the curved upstream shear layer to be inconsistent with an idealized 2D counter-current shear layer, as also noted by Iyer and Mahesh (2016). Nevertheless, it is remarkable that the quantitative prediction of transition to JICF global instability was generally close to values of $R_{1,cr(th)}$ predicted by inviscid 2D LSA, both with and without the presence of acetone, indicated in figure B.4. Hence it was of interest to utilize momentum thickness in comparing the present instability frequencies with established ranges of Strouhal number for the planar CCSL.

Figure B.6 shows the variation in Strouhal number based on θ_{CCSL} derived from PIV-only and simultaneous PLIF/PIV experimental datasets for the equidensity JICF at $Re_j = 1900$. Remarkably, for a Strouhal number based on CCSL-based momentum thickness scaling rather than diameter D, and based on twice the average velocity in the counter-current shear layer, $2\bar{V}$ rather than average jet velocity U_j (which does not capture the effect of the local negative flow upstream of the jet), there was a generally good collapse of the data for cases with and without acetone in the jet fluid. An exception was seen in the case of the very low momentum flux ratio jet, with $J = 5$, which as noted previously had the thickest and most deflected upstream shear layer. It is remarkable that St_θ values with and without acetone at a given J value collapsed onto one another for most cases in figure B.6, in contrast to the differing Strouhal numbers based on diameter and mean jet velocity in figure B.2, shown

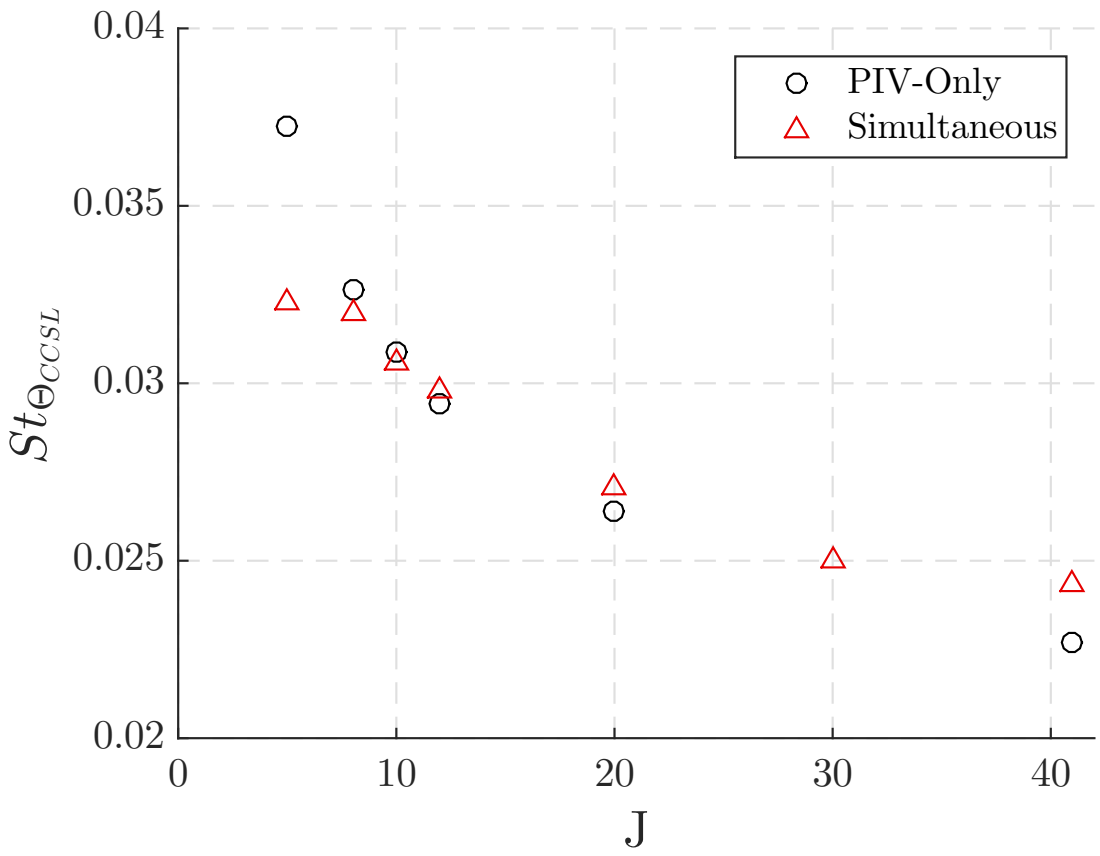

Figure B.6: Variation in Strouhal number based on momentum thickness, $St_{\theta_{CCSL}} \equiv f_o\theta_{CCSL}/2\bar{V}$, as a function of J for the equidensity JICF case at $Re_j = 1900$. Results for data extracted from PIV-only experiments, without acetone, and simultaneous PLIF/PIV experiments, with acetone present at $\psi \approx 0.112$, are shown.

by datapoints indicated in green and cyan. The results in figure B.6 thus provided further evidence for the importance of the non-dimensional parameter θ/D, related to differences in jet fluid viscosity, and the relevance of the CCSL model in interpreting JICF shear layer instability transition. For the clearly convectively unstable flows at $J = 41$, for example, St_θ was of the order 0.023 to 0.024, corresponding to St_o values of approximately 0.7 without acetone and approximately 0.9 with an acetone mole fraction $\psi = 0.112$ (figure B.2). These frequencies corresponded to the fundamental mode for the convectively unstable JICF with

spectral characteristics as in figures B.1a; the observed subharmonics thus had St_θ values of the order 0.011-0.012. The $J = 41$ condition here produced $R_1 \approx 1.09$, below the experimentally observed critical condition for the CCSL, $R_{1,cr} \approx 1.24$. These measured Strouhal numbers associated with $R_1 \approx 1.09$ were approximately twice as large as those observed for the free jet by Hussain and Zaman (1978) and Strykowski and Niccum (1991) at $R_1 = 1.0$. As J was reduced and the critical condition for transition to global instability approached in figure B.6, the values of St_θ increased to the range of 0.03 ($J = 10$) to 0.037 ($J = 5$ with acetone), also approximately twice as large as established theory and experiments for the planar CCSL (Huerre and Monkewitz (1985); Strykowski and Niccum (1991)). The well-established trend for the CCSL, whereby Strouhal number increases rather abruptly as one approaches the critical condition (Strykowski and Niccum (1991)) is consistent with observations in figure B.6.

These differences in fundamental Strouhal number St_θ between the present experiments and the established 2D CCSL values were likely not so much the result of slightly different counter-current shear layer velocity ratios R_1 at transition as the relatively large CCSL momentum thickness at and beyond critical conditions, as noted previously. More importantly, Huerre and Monkewitz (1990) note that the frequency selection criterion for global instability depends on how the absolutely unstable frequency evolves spatially, which in turn depends on the development of the base flow for the flowfield. The spatial development in a counter-current, planar mixing layer is typically much slower than the spatial development observed in a transverse jet, as indicated in earlier transverse jet stability studies (Alves et al. (2007); Alves et al. (2008)), and the global frequency determination here is not a local feature of the flow, in contrast to the determination of the critical parameter ($R_{1,cr}$) for the onset of absolute instability. Hence in many respects one would not expect the JICF Strouhal numbers St_θ to correspond very closely to the established values for the planar CCSL.

APPENDIX C

Additional Tabbed JICF Results

C.1 Structural Characteristics

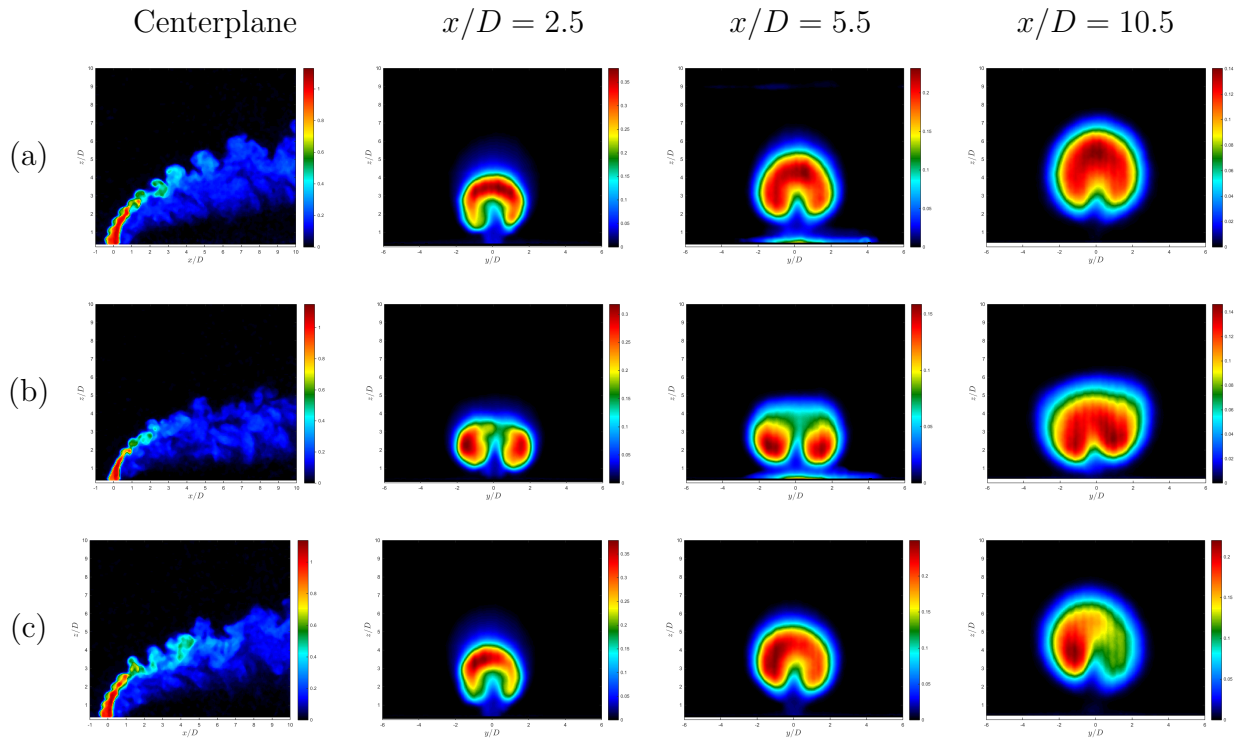

Figure C.1: Structural Characteristics for momentum flux ratio of $J = 6$ for: (a) the non-tabbed case, (b) the tab upstream, and (c) the tab downstream, as realized from PLIF images of the instantaneous centerplane and mean cross-section at $x/D = 2.5$, 5.5, and 10.5.

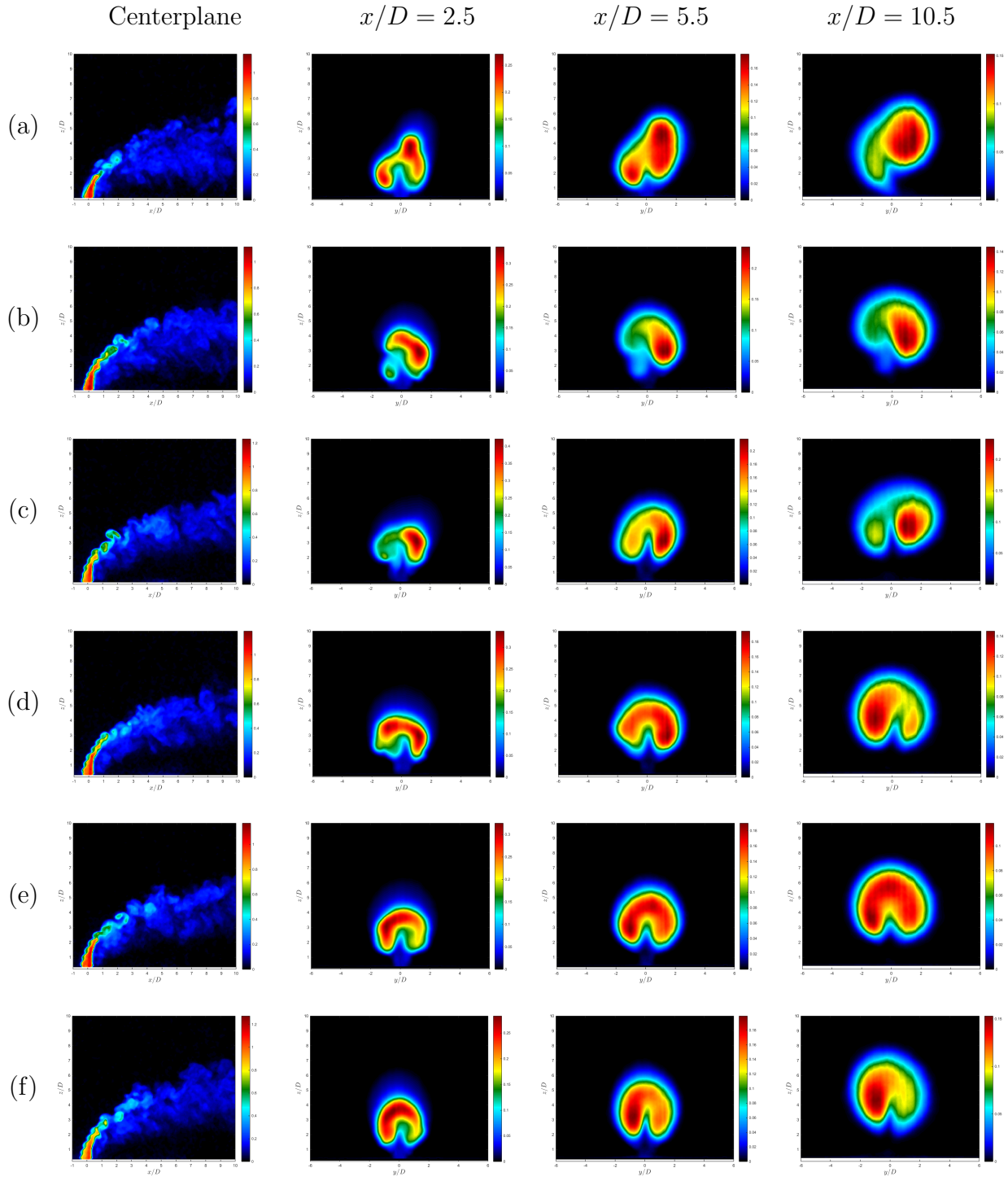

Figure C.2: Structural Characteristics for momentum flux ratio of $J = 6$ for left oriented tab locations of: (a) L15, (b) L30, (c) L45, (d) L60, (e) L75, and (f) L90, as realized from PLIF images of the instantaneous centerplane and mean cross-section at $x/D = 2.5$, 5.5, and 10.5.

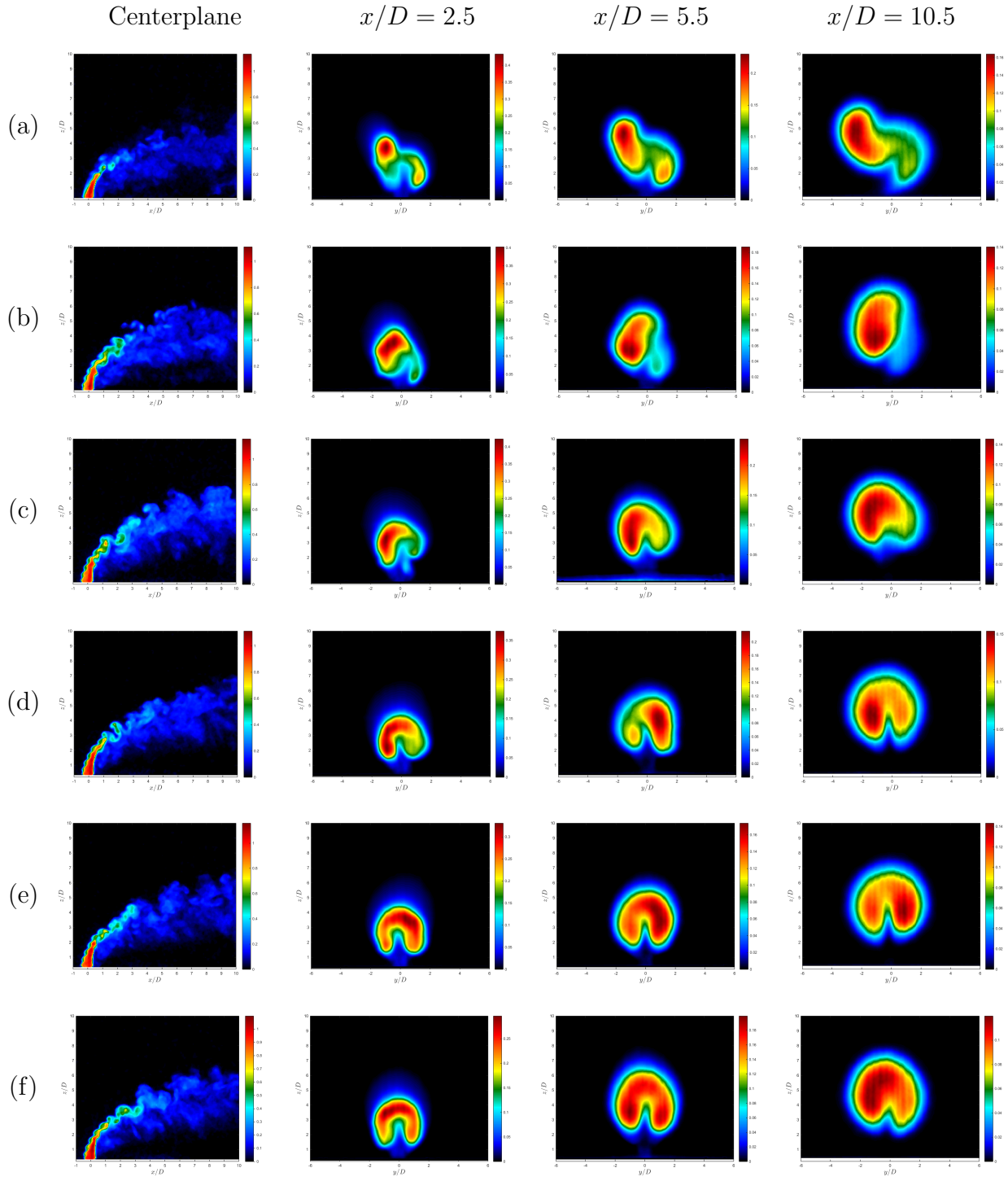

Figure C.3: Structural Characteristics for momentum flux ratio of $J = 6$ for right oriented tab locations of: (a) R15, (b) R30, (c) R45, (d) R60, (e) R75, and (f) R90, as realized from PLIF images of the instantaneous centerplane and mean cross-section at $x/D = 2.5$, 5.5, and 10.5.

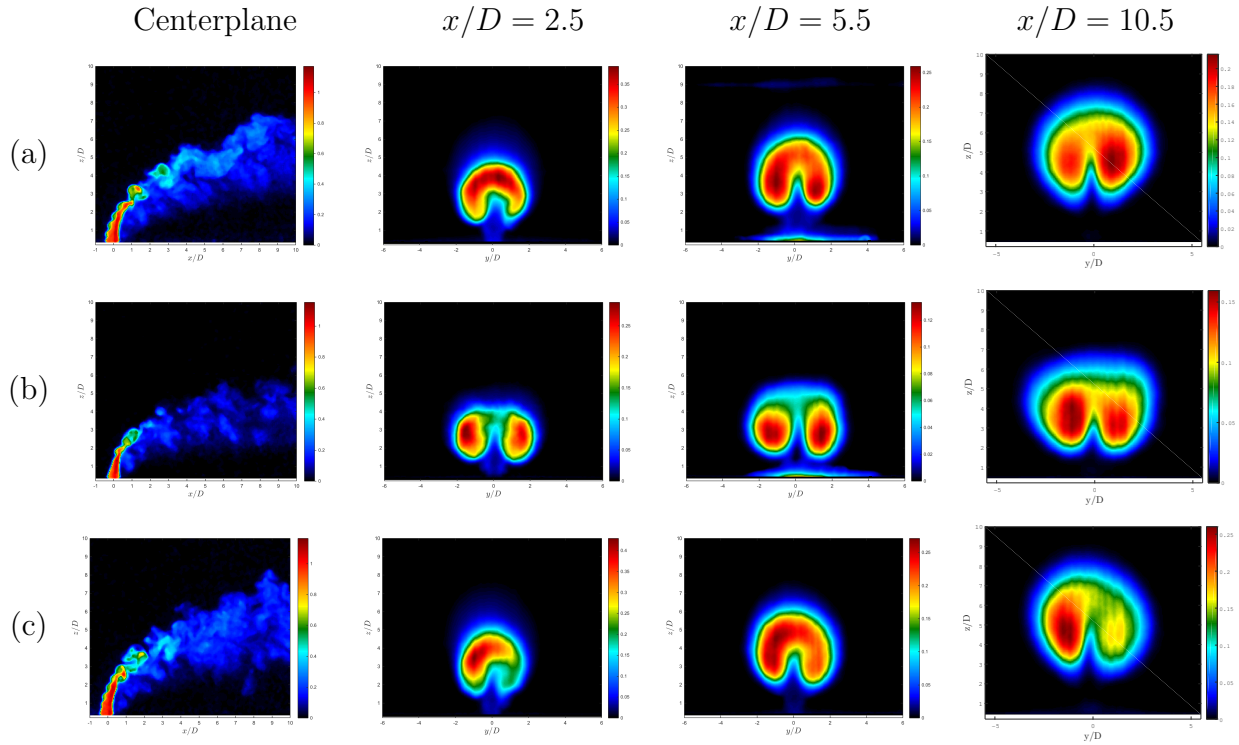

Figure C.4: Structural Characteristics for momentum flux ratio of $J = 7$ for: (a) the non-tabbed case, (b) the tab upstream, and (c) the tab downstream, as realized from PLIF images of the instantaneous centerplane and mean cross-section at $x/D = 2.5$, 5.5, and 10.5.

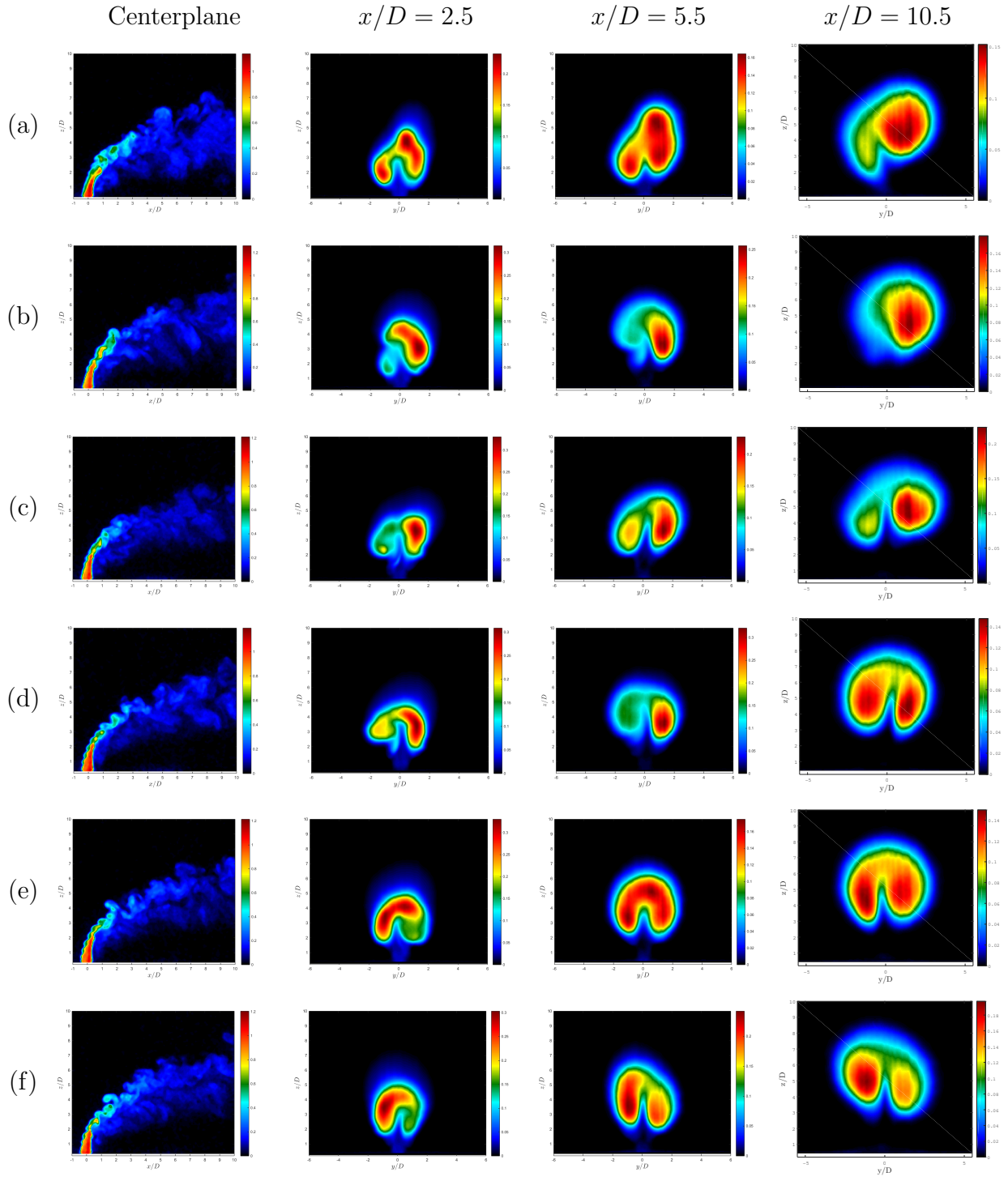

Figure C.5: Structural Characteristics for momentum flux ratio of $J = 7$ for left oriented tab locations of: (a) L15, (b) L30, (c) L45, (d) L60, (e) L75, and (f) L90, as realized from PLIF images of the instantaneous centerplane and mean cross-section at $x/D = 2.5$, 5.5, and 10.5.

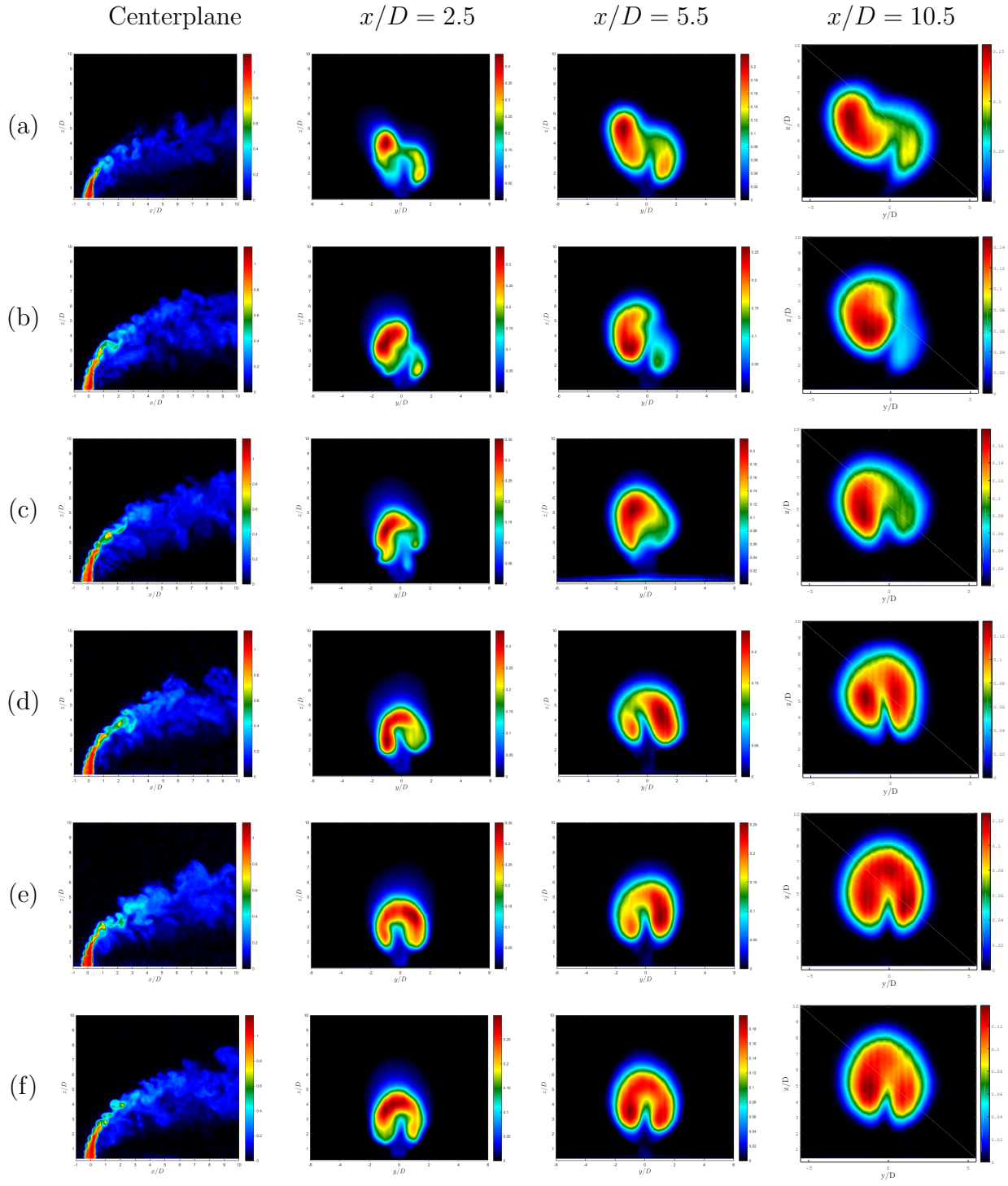

Figure C.6: Structural Characteristics for momentum flux ratio of $J = 7$ for right oriented tab locations of: (a) R15, (b) R30, (c) R45, (d) R60, (e) R75, and (f) R90, as realized from PLIF images of the instantaneous centerplane and mean cross-section at $x/D = 2.5$, 5.5, and 10.5.

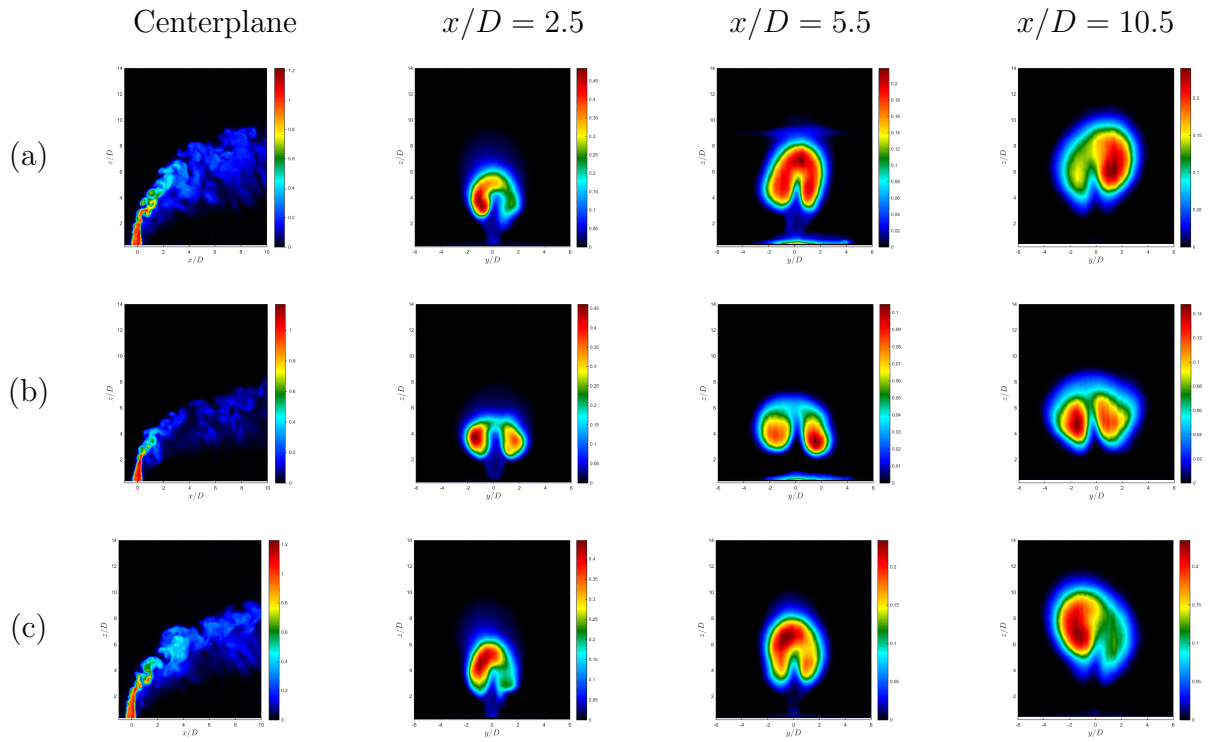

Figure C.7: Structural Characteristics for momentum flux ratio of $J = 12$ for: (a) the non-tabbed case, (b) the tab upstream, and (c) the tab downstream, as realized from PLIF images of the instantaneous centerplane and mean cross-section at $x/D = 2.5$, 5.5, and 10.5.

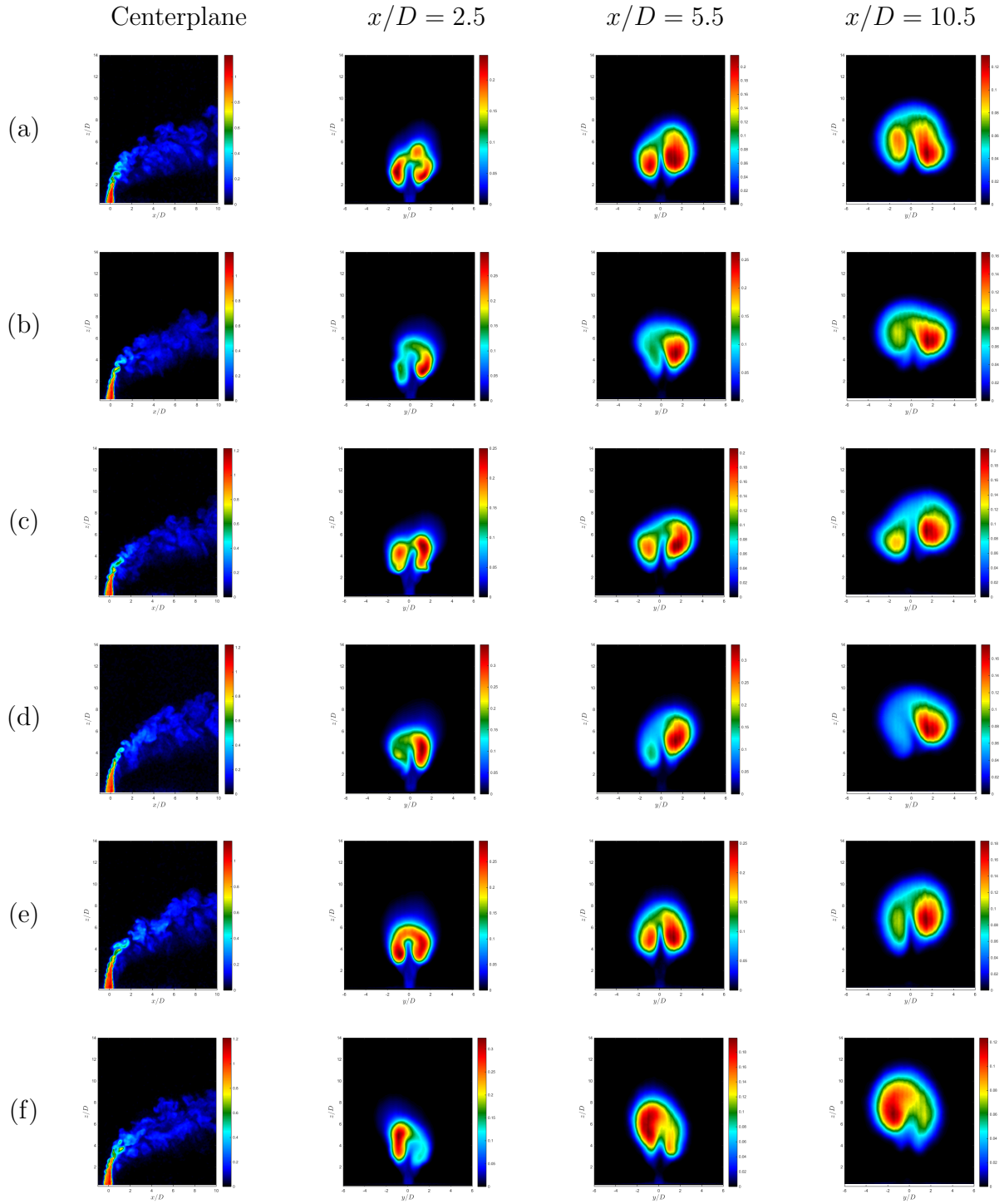

Figure C.8: Structural Characteristics for momentum flux ratio of $J = 12$ for left oriented tab locations of: (a) L15, (b) L30, (c) L45, (d) L60, (e) L75, and (f) L90, as realized from PLIF images of the instantaneous centerplane and mean cross-section at $x/D = 2.5$, 5.5, and 10.5.

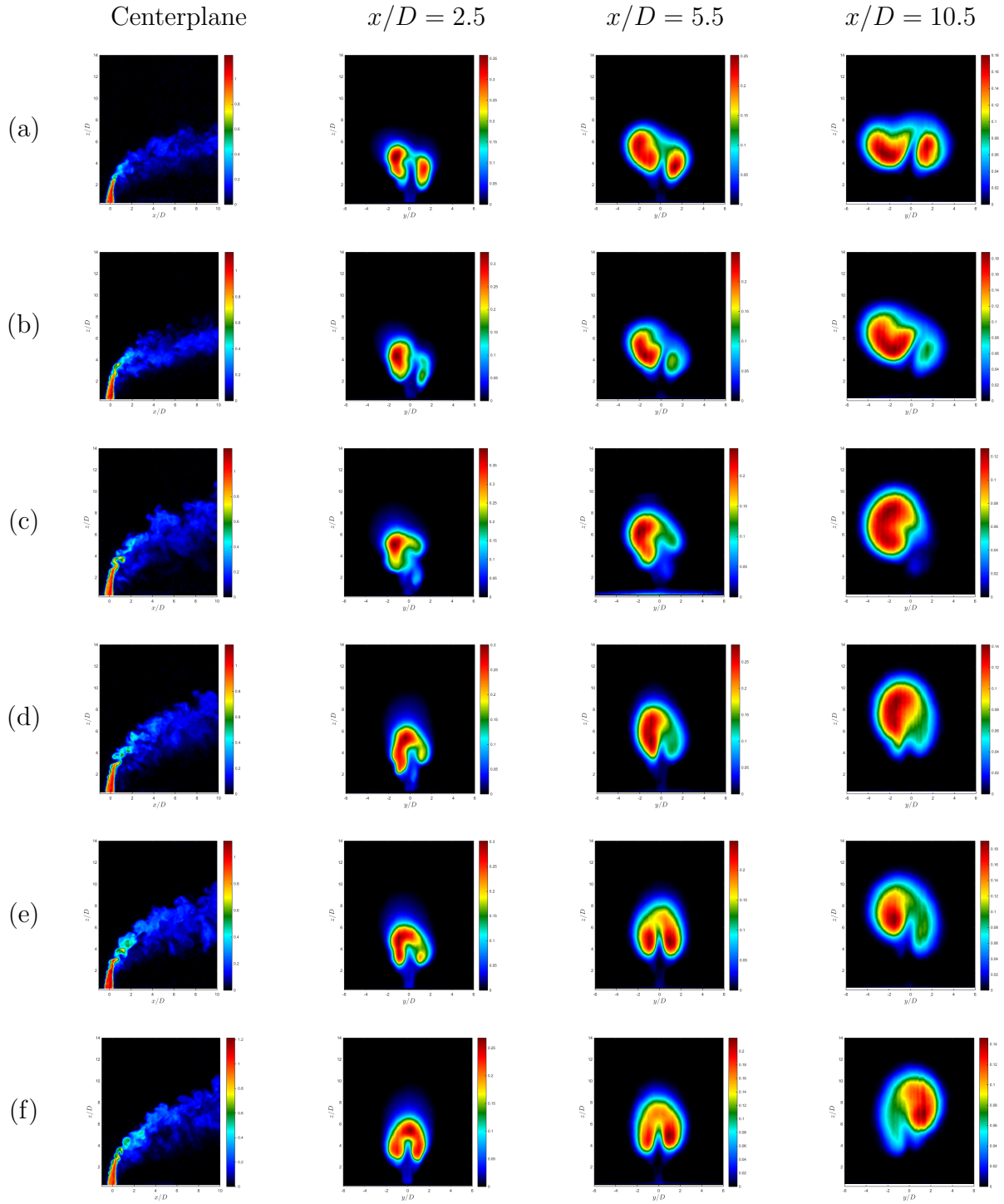

Figure C.9: Structural Characteristics for momentum flux ratio of $J = 12$ for right oriented tab locations of: (a) R15, (b) R30, (c) R45, (d) R60, (e) R75, and (f) R90, as realized from PLIF images of the instantaneous centerplane and mean cross-section at $x/D = 2.5$, 5.5, and 10.5.

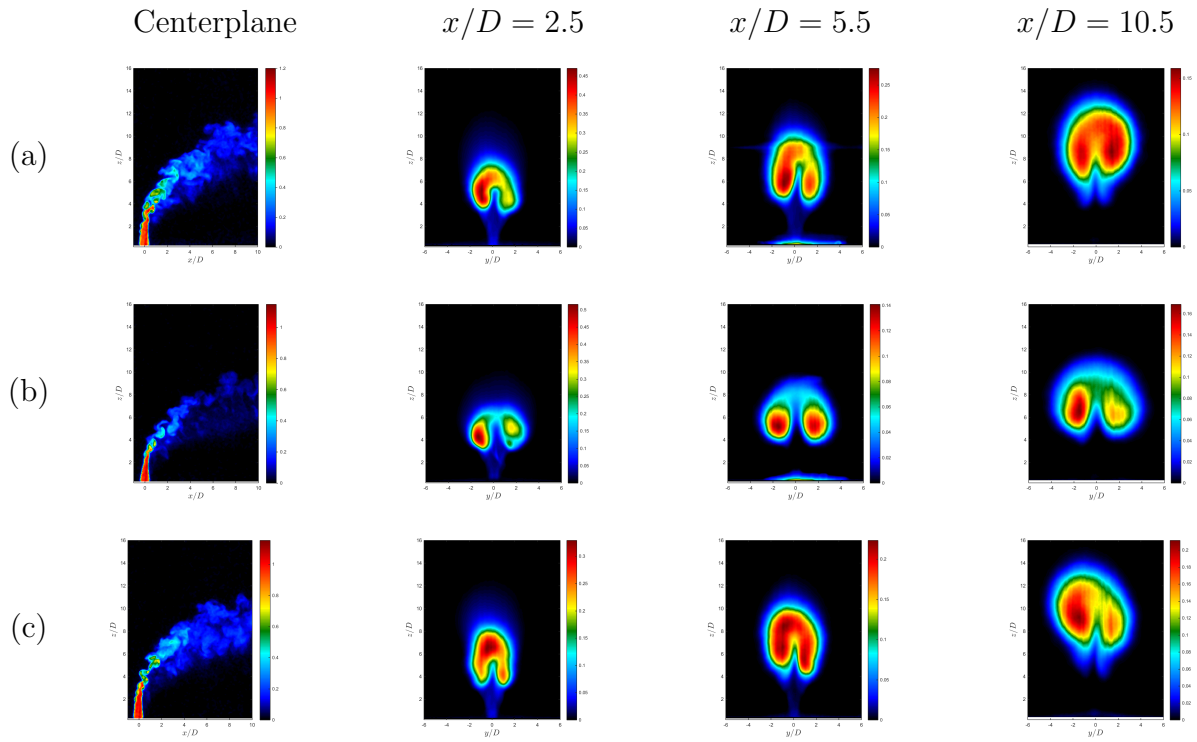

Figure C.10: Structural Characteristics for momentum flux ratio of $J = 18$ for: (a) the non-tabbed case, (b) the tab upstream, and (c) the tab downstream, as realized from PLIF images of the instantaneous centerplane and mean cross-section at $x/D = 2.5$, 5.5, and 10.5.

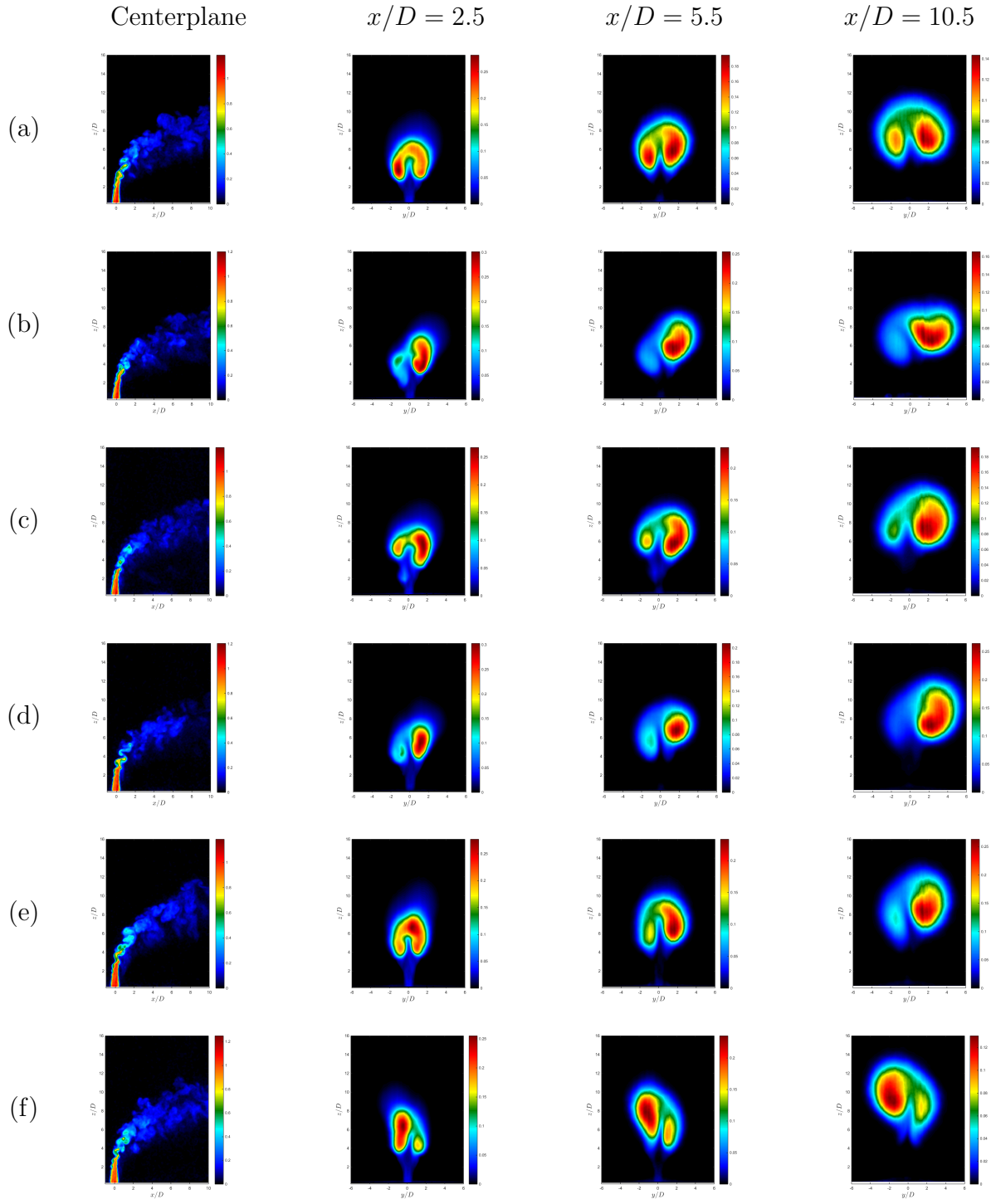

Figure C.11: Structural Characteristics for momentum flux ratio of $J = 18$ for left oriented tab locations of: (a) L15, (b) L30, (c) L45, (d) L60, (e) L75, and (f) L90, as realized from PLIF images of the instantaneous centerplane and mean cross-section at $x/D = 2.5$, 5.5, and 10.5.

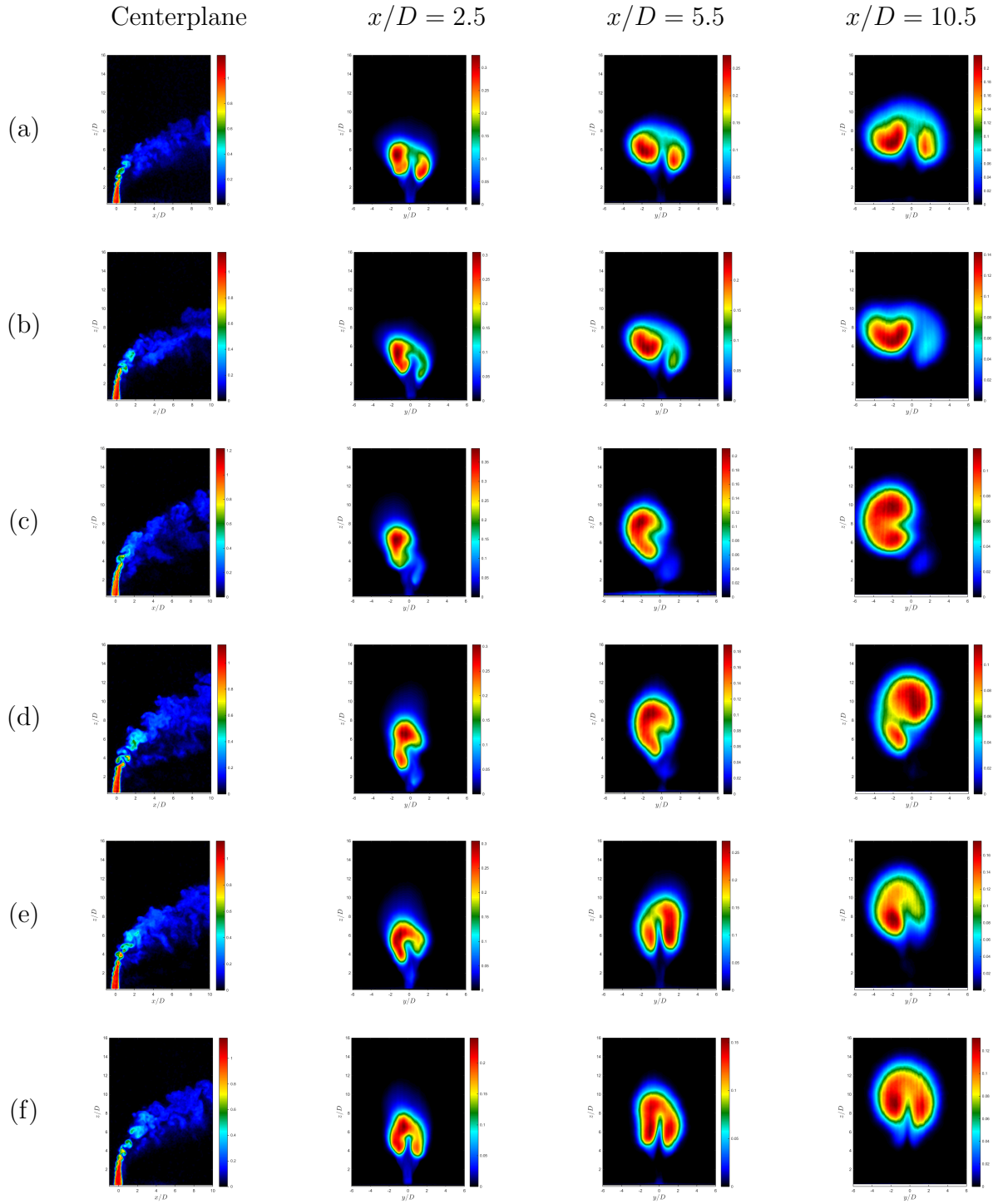

Figure C.12: Structural Characteristics for momentum flux ratio of $J = 18$ for right oriented tab locations of: (a) R15, (b) R30, (c) R45, (d) R60, (e) R75, and (f) R90, as realized from PLIF images of the instantaneous centerplane and mean cross-section at $x/D = 2.5$, 5.5, and 10.5.

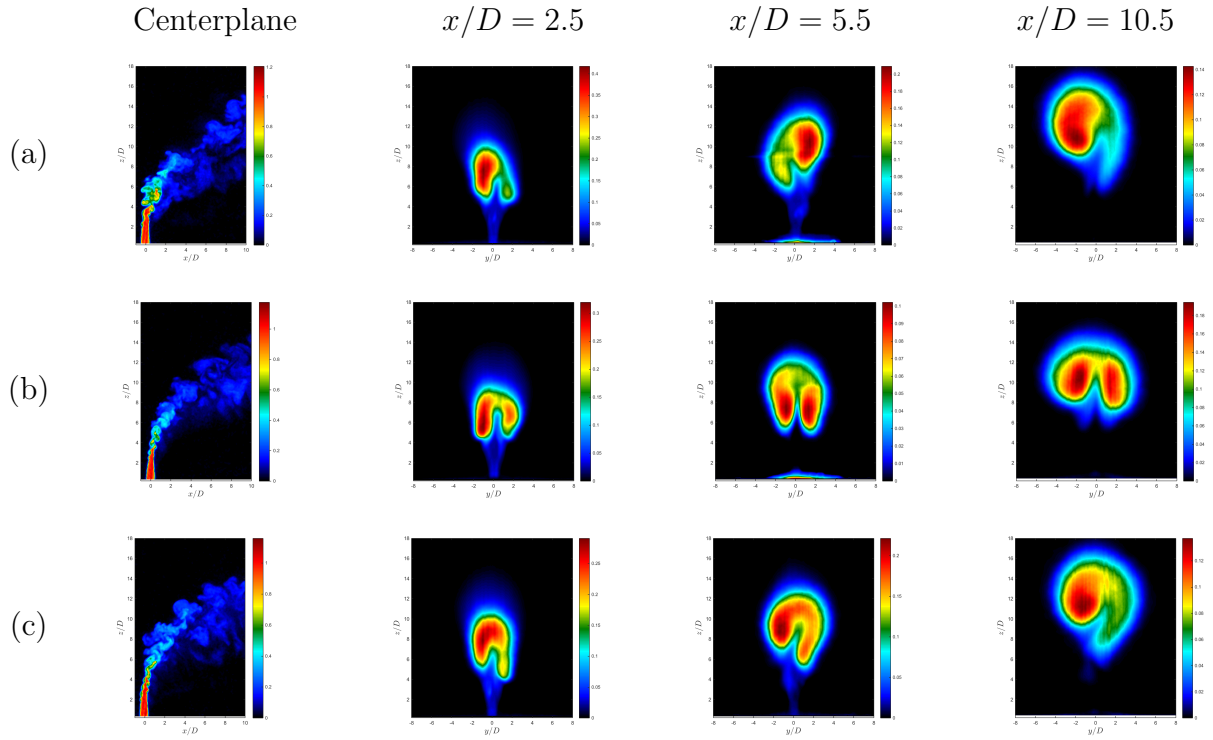

Figure C.13: Structural Characteristics for momentum flux ratio of $J = 30$ for: (a) the non-tabbed case, (b) the tab upstream, and (c) the tab downstream, as realized from PLIF images of the instantaneous centerplane and mean cross-section at $x/D = 2.5$, 5.5, and 10.5.

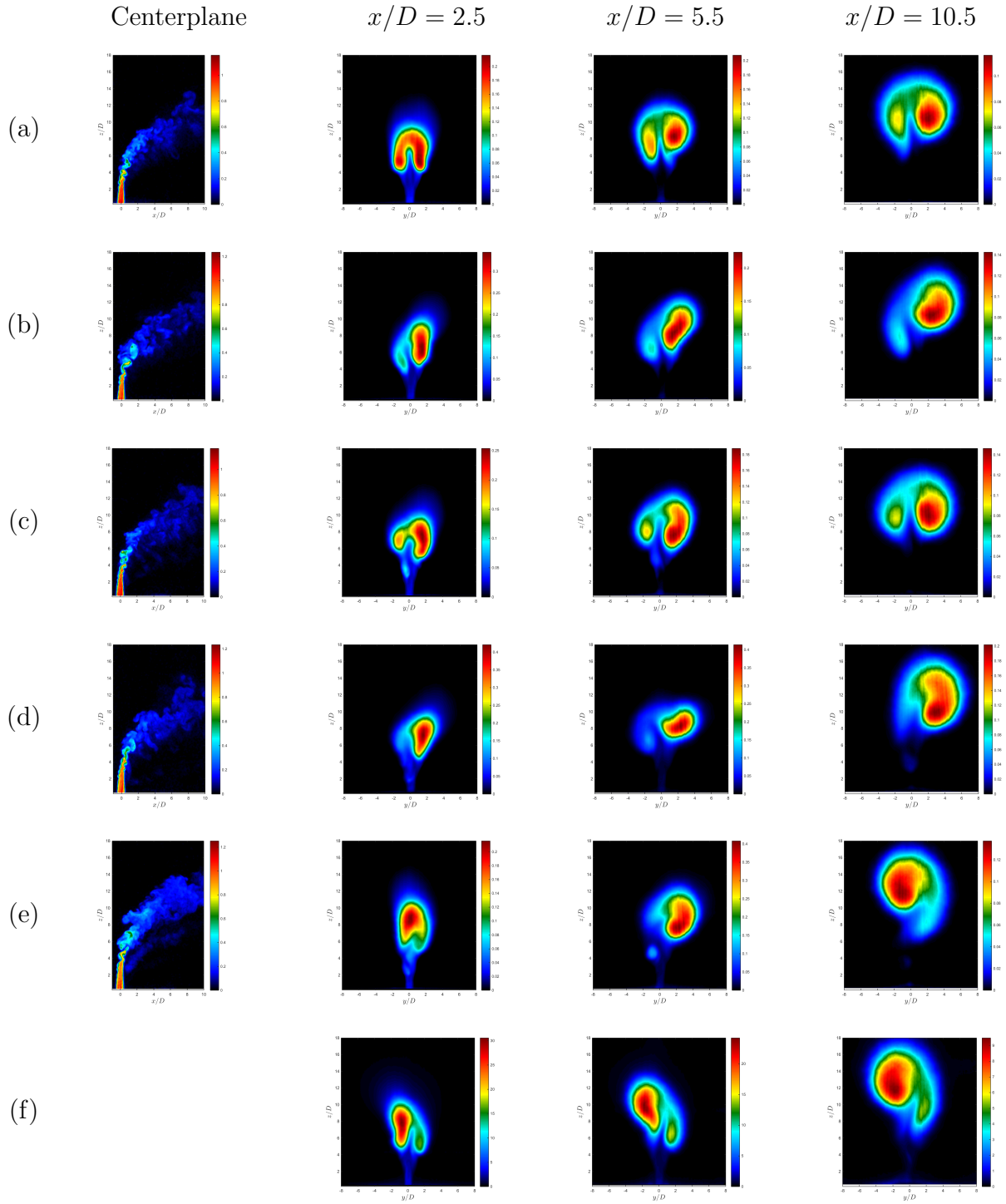

Figure C.14: Structural Characteristics for momentum flux ratio of $J = 30$ for left oriented tab locations of: (a) L15, (b) L30, (c) L45, (d) L60, (e) L75, and (f) L90, as realized from PLIF images of the instantaneous centerplane and mean cross-section at $x/D = 2.5$, 5.5, and 10.5.

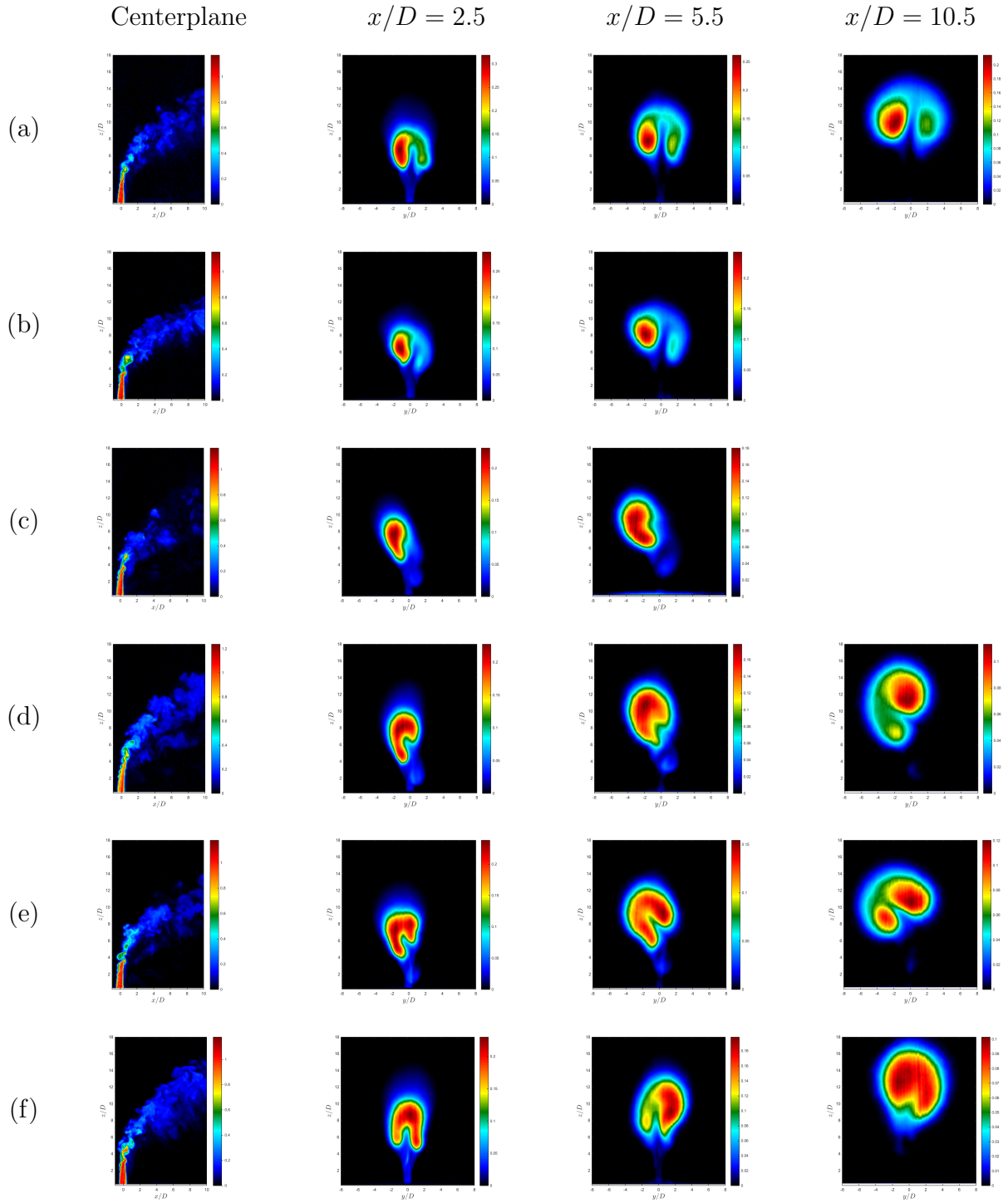

Figure C.15: Structural Characteristics for momentum flux ratio of $J = 30$ for right oriented tab locations of: (a) R15, (b) R30, (c) R45, (d) R60, (e) R75, and (f) R90, as realized from PLIF images of the instantaneous centerplane and mean cross-section at $x/D = 2.5$, 5.5, and 10.5.

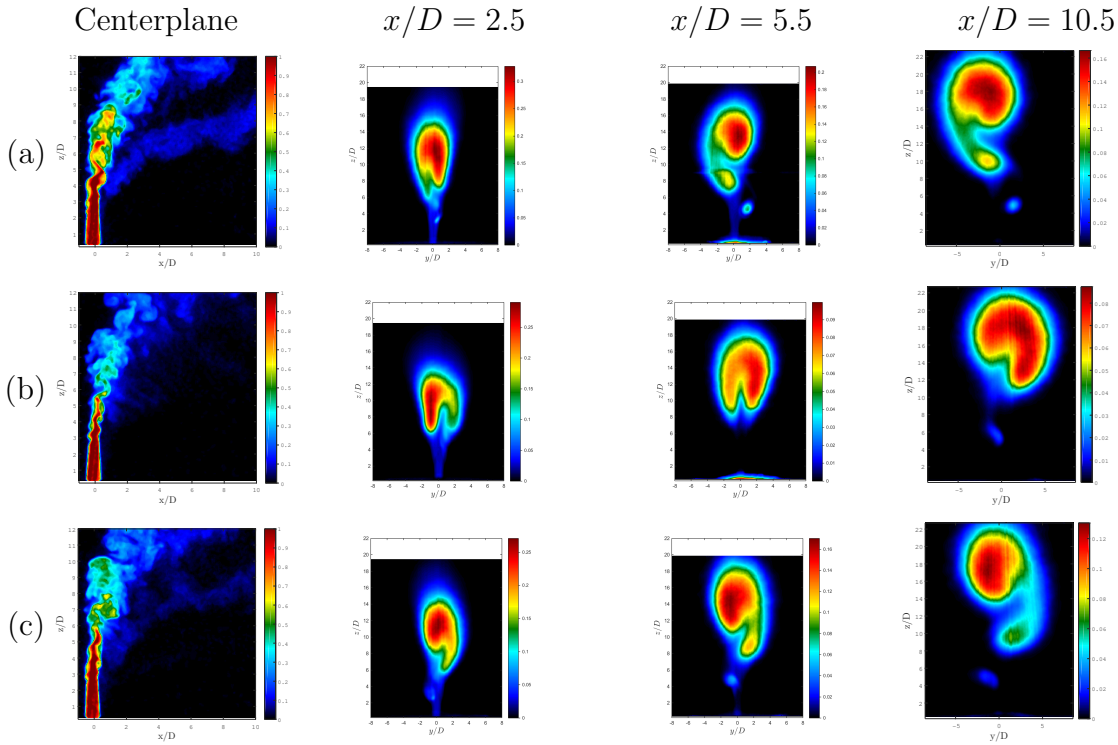

Figure C.16: Structural Characteristics for momentum flux ratio of $J = 61$ for: (a) the non-tabbed case, (b) the tab upstream, and (c) the tab downstream, as realized from PLIF images of the instantaneous centerplane and mean cross-section at $x/D = 2.5$, 5.5, and 10.5.

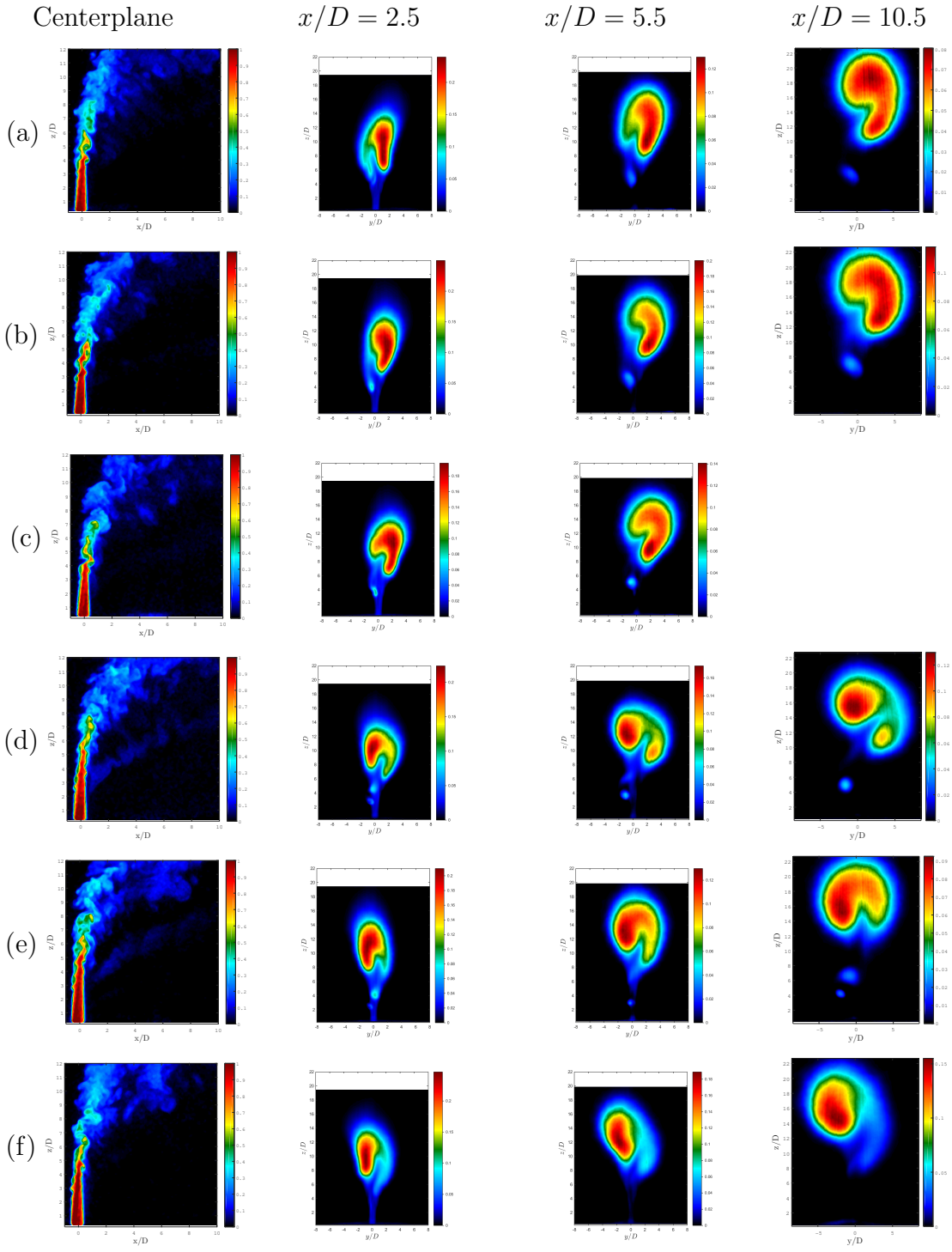

Figure C.17: Structural Characteristics for momentum flux ratio of $J = 61$ for left oriented tab locations of: (a) L15, (b) L30, (c) L45, (d) L60, (e) L75, and (f) L90, as realized from PLIF images of the instantaneous centerplane and mean cross-section at $x/D = 2.5$, 5.5, and 10.5.

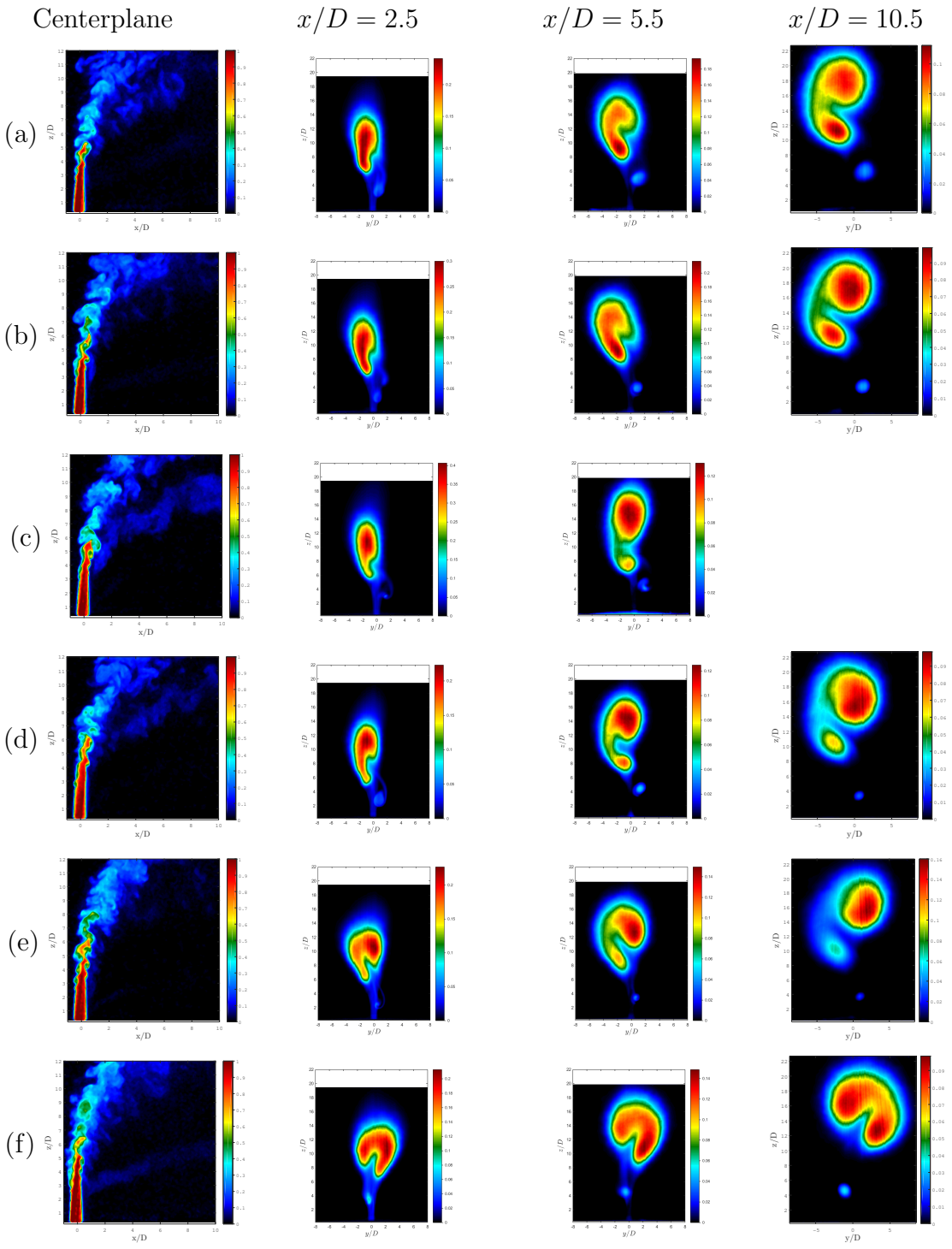

Figure C.18: Structural Characteristics for momentum flux ratio of $J = 61$ for right oriented tab locations of: (a) R15, (b) R30, (c) R45, (d) R60, (e) R75, and (f) R90, as realized from PLIF images of the instantaneous centerplane and mean cross-section at $x/D = 2.5$, 5.5, and 10.5.

C.2 Mixing Characteristics

Left Oriented Tab Positions

(a) Centerplane unmixedness (left)

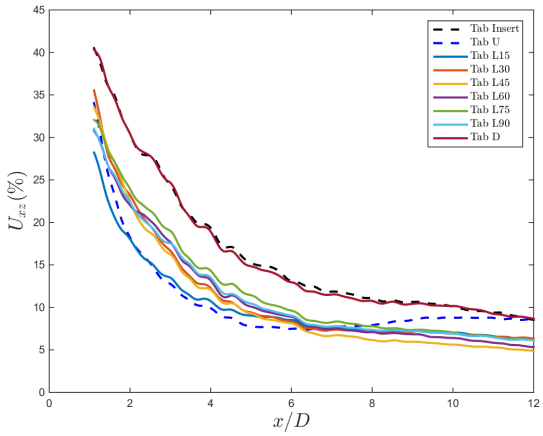

(b) Cross-sectional unmixedness (left)

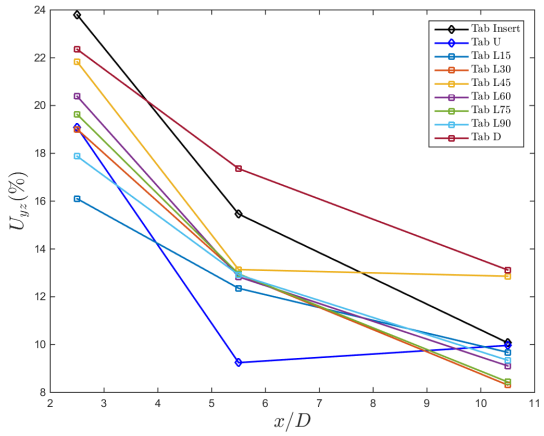

Right Oriented Tab Positions

(c) Centerplane unmixedness (right)

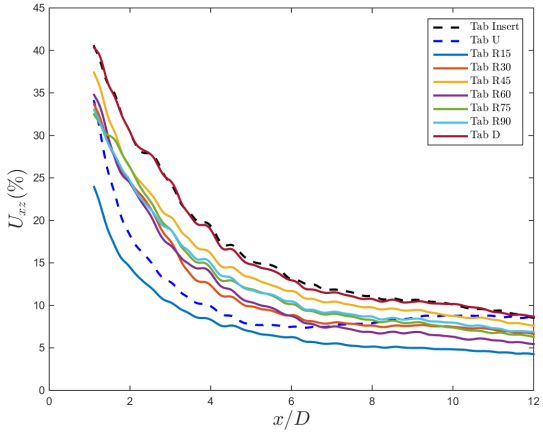

(d) Cross-sectional unmixedness (right)

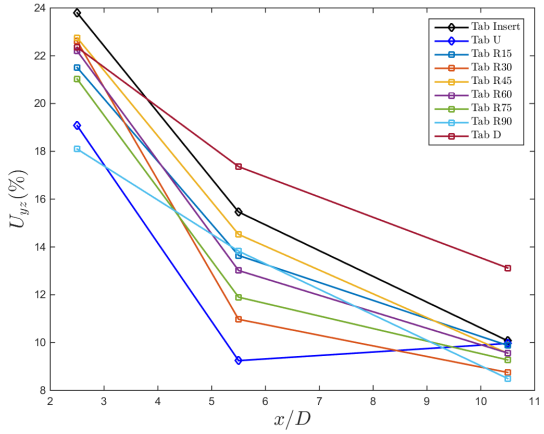

Figure C.19: Downstream evolution of centerplane unmixedness U_{xz} and cross-section-based unmixedness U_{yz} for $J = 6$, for the non-tabbed case and various tab orientations about the jet periphery.

Left Oriented Tab Positions

(a) Centerplane unmixedness (left)

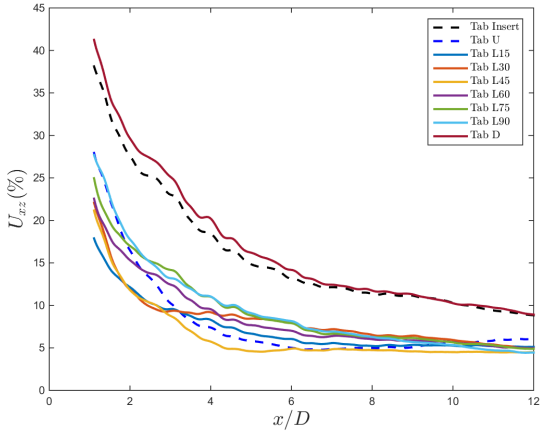

(b) Cross-sectional unmixedness (left)

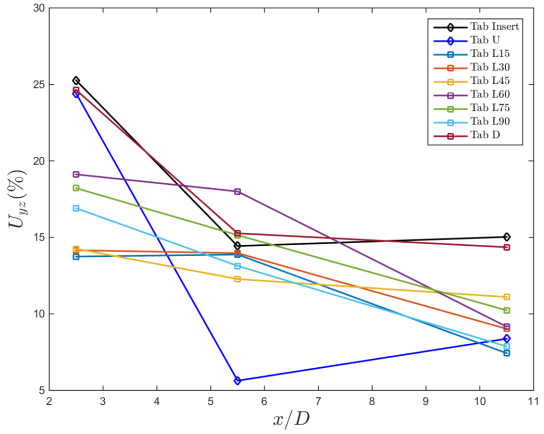

Right Oriented Tab Positions

(c) Centerplane unmixedness (right)

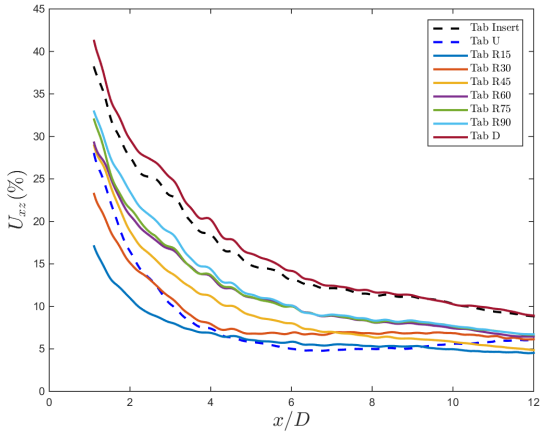

(d) Cross-sectional unmixedness (right)

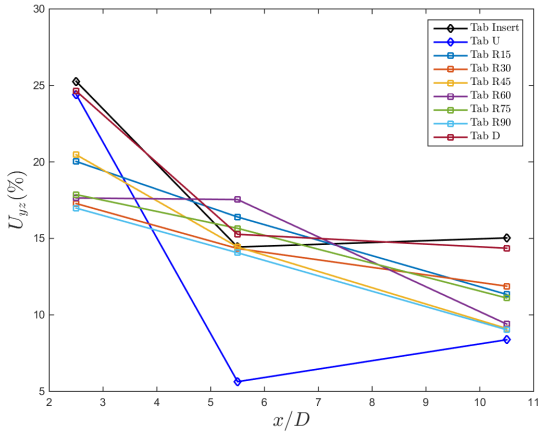

Figure C.20: Downstream evolution of centerplane unmixedness U_{xz} and cross-section-based unmixedness U_{yz} for $J = 12$, for the non-tabbed case and various tab orientations about the jet periphery.

Left Oriented Tab Positions

(a) Centerplane unmixedness (left)

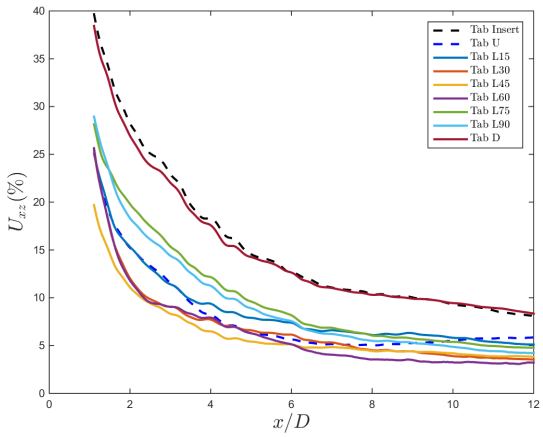

(b) Cross-sectional unmixedness (left)

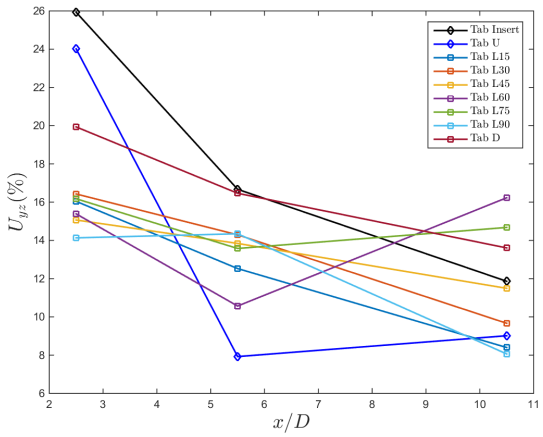

Right Oriented Tab Positions

(c) Centerplane unmixedness (right)

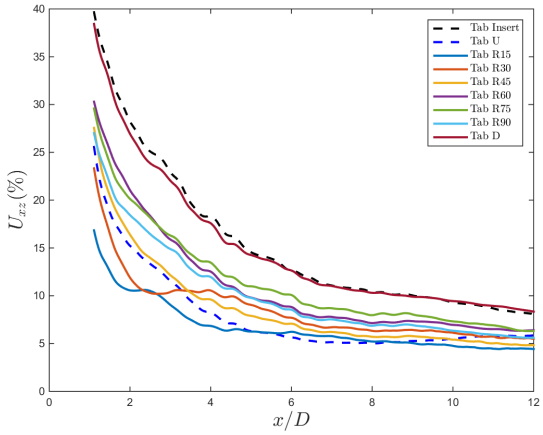

(d) Cross-sectional unmixedness (right)

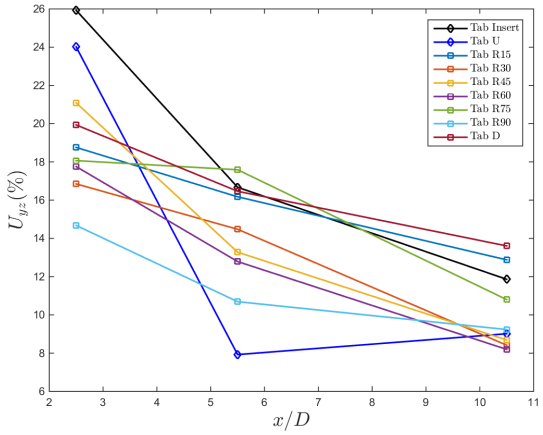

Figure C.21: Downstream evolution of centerplane unmixedness U_{xz} and cross-section-based unmixedness U_{yz} for $J = 18$, for the non-tabbed case and various tab orientations about the jet periphery.

Left Oriented Tab Positions

(a) Centerplane unmixedness (left)

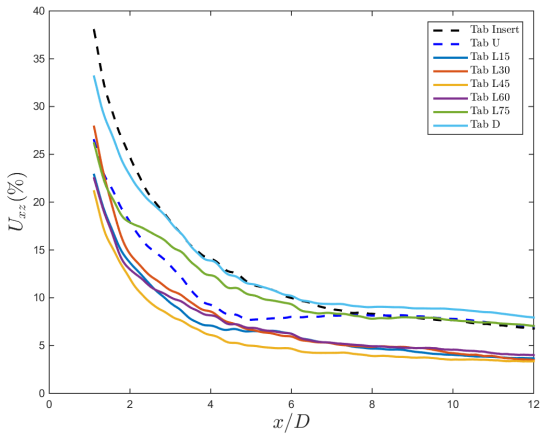

(b) Cross-sectional unmixedness (left)

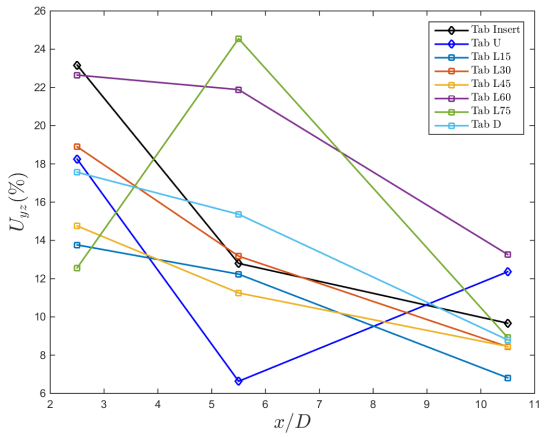

Right Oriented Tab Positions

(c) Centerplane unmixedness (right)

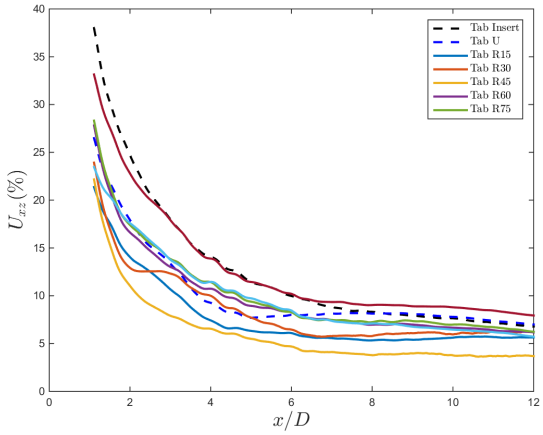

(d) Cross-sectional unmixedness (right)

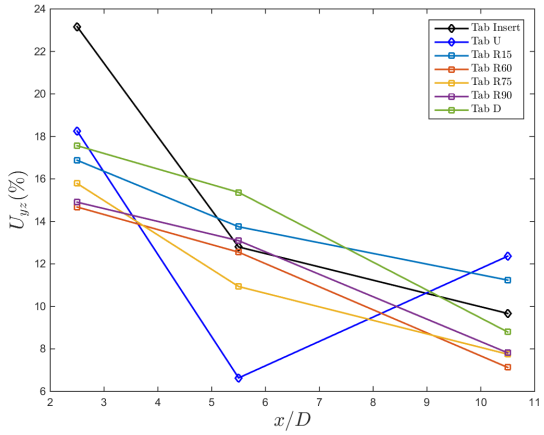

Figure C.22: Downstream evolution of centerplane unmixedness U_{xz} and cross-section-based unmixedness U_{yz} for $J = 30$, for the non-tabbed case and various tab orientations about the jet periphery.

C.3 Centerplane and Cross-sectional Vorticity

Simple Extension

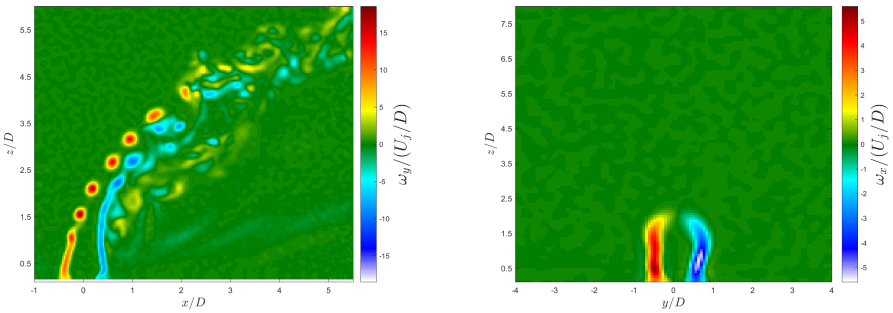

Tab L15

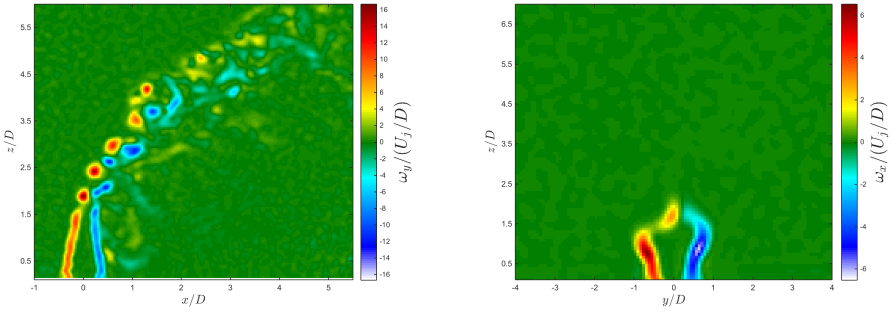

Tab L30

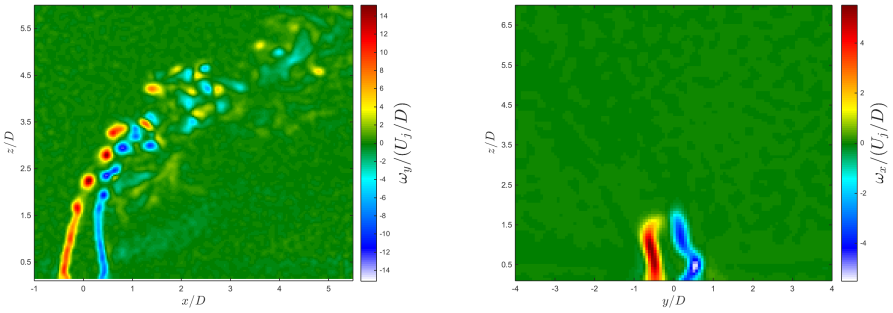

Tab L45

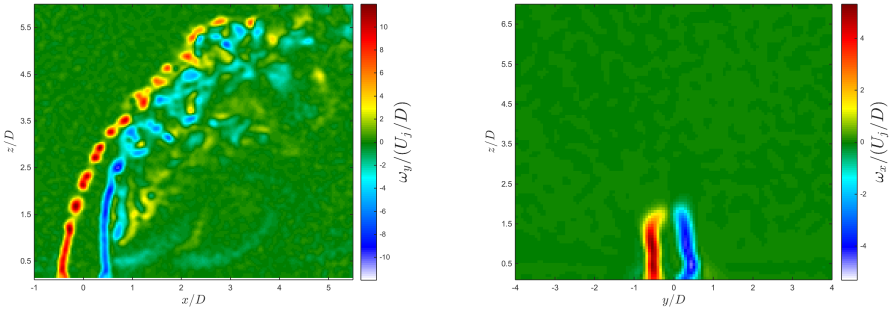

Figure C.23: continues to following page

Tab L90

Tab R90

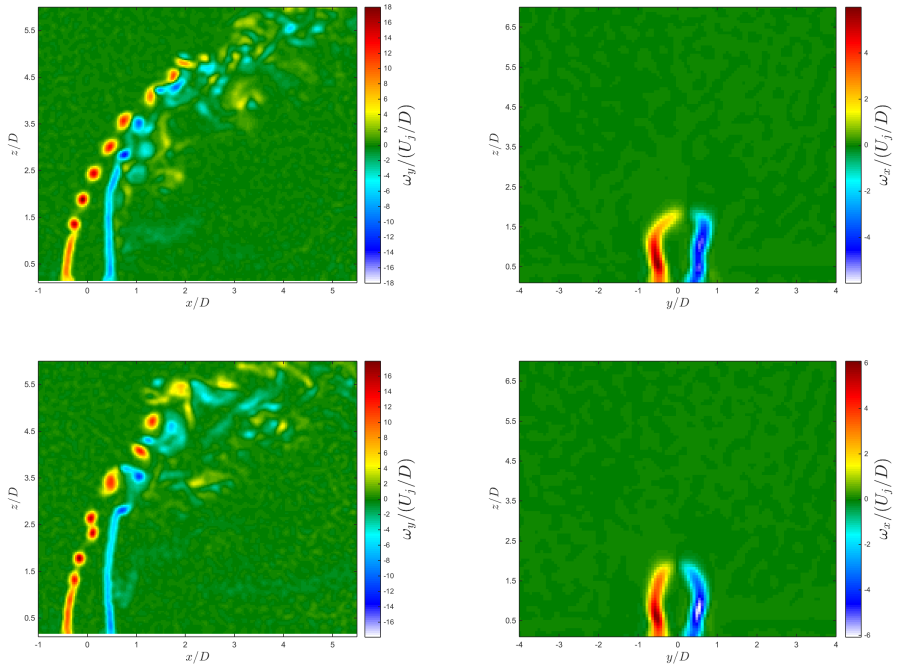

Figure C.23: Centerplane images of the instantaneous vorticty field, and mean cross-sectional vorticity images averaged over 500 instantaneous realizations at the center of the jet exit ($x/D = 0.0$). Flow conditions are for $J = 8$ and $Re_j = 1900$, for symmetry breaking tab orientations. The colorbars are scaled to the maximum and minimum vorticity values contained within all images shown.

Simple Extension

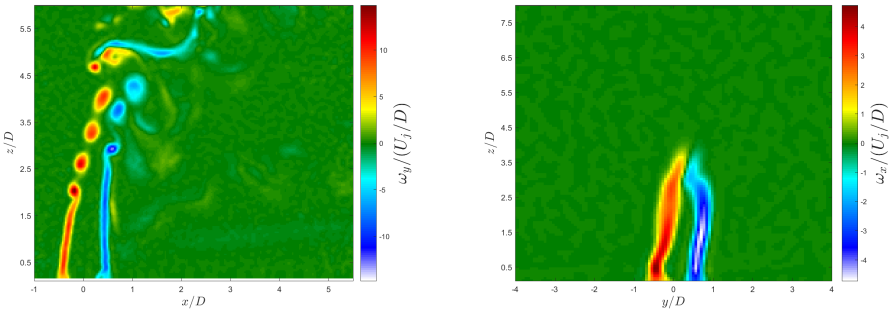

Tab L15

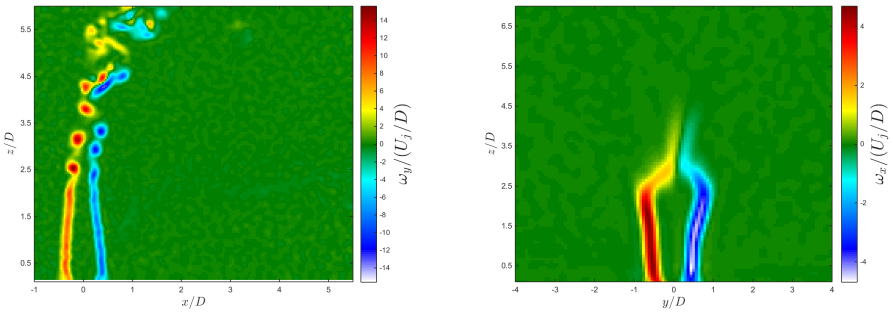

Tab L30

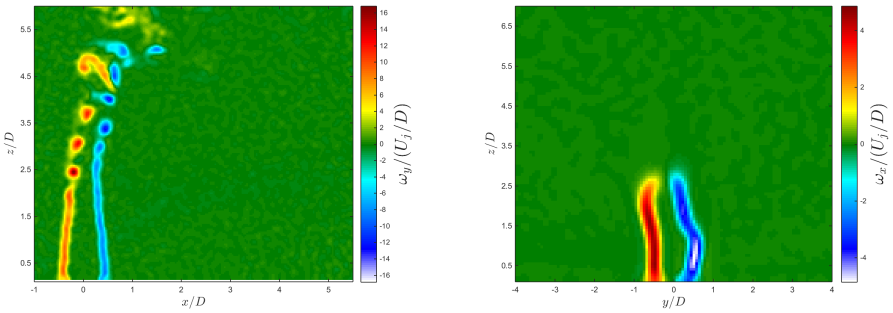

Tab L45

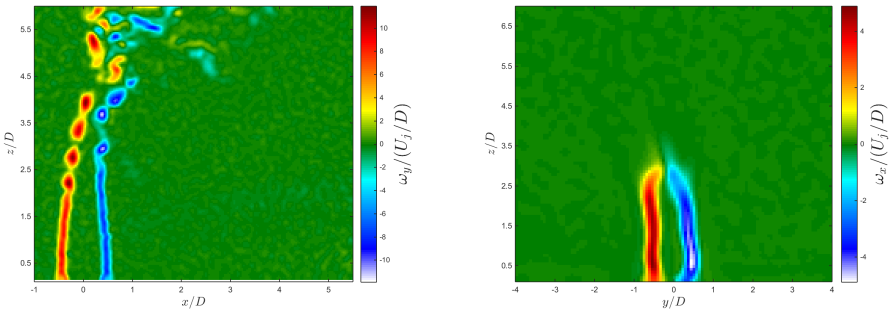

Figure C.24: continues to following page

Tab L90

Tab R90

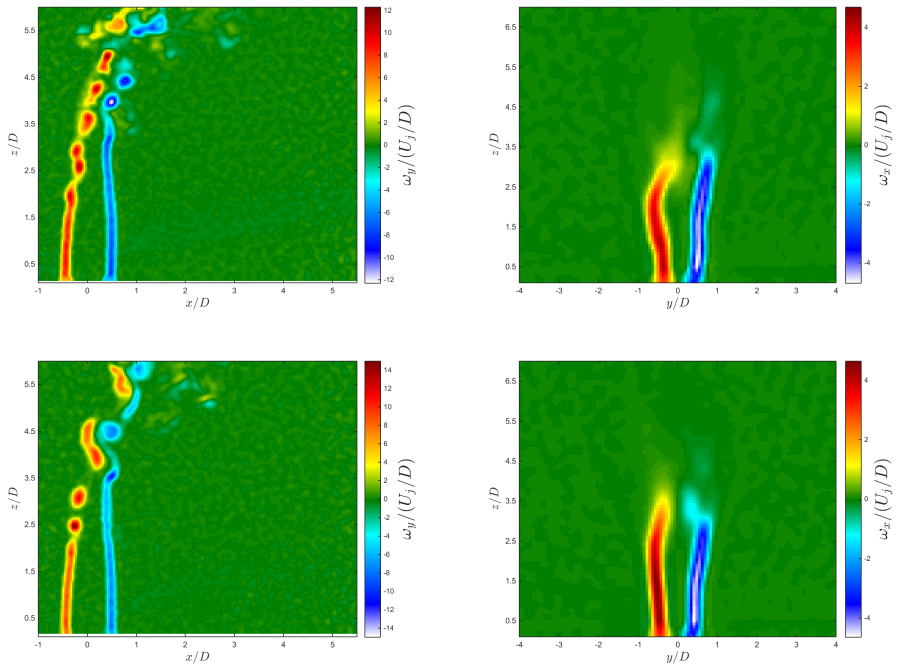

Figure C.24: Centerplane images of the instantaneous vorticty field, and mean cross-sectional vorticity images averaged over 500 instantaneous realizations at the center of the jet exit ($x/D = 0.0$). Flow conditions are for $J = 20$ and $Re_j = 1900$, for symmetry breaking tab orientations. The colorbars are scaled to the maximum and minimum vorticity values contained within all images shown.

Simple Extension

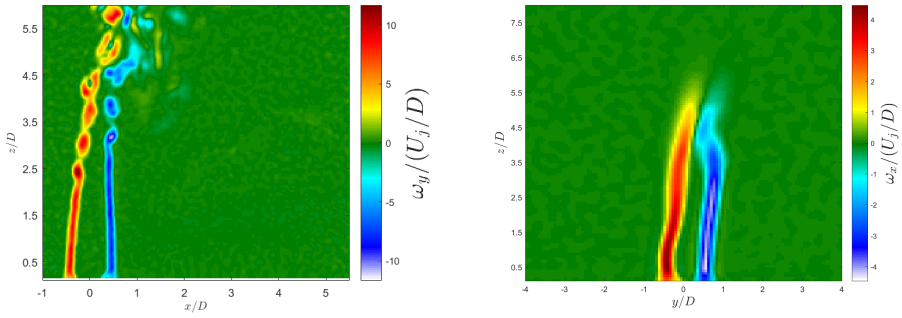

Tab L15

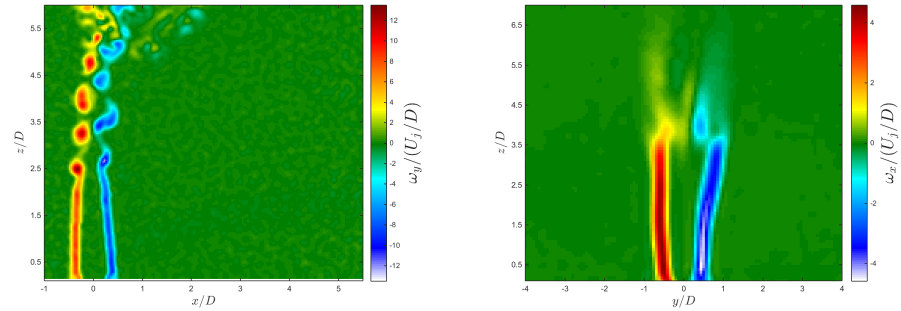

Tab L30

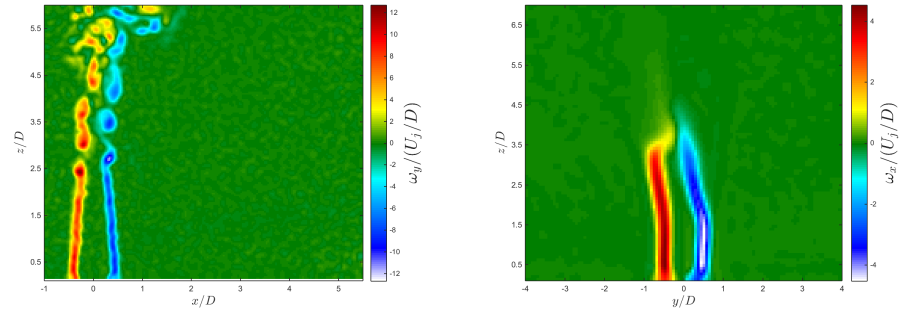

Tab L45

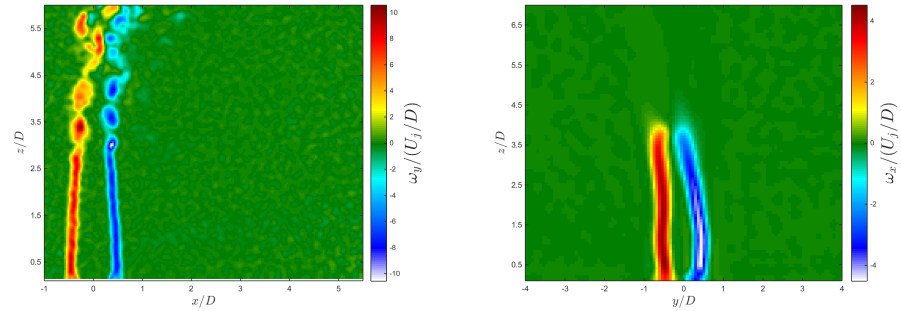

Figure C.25: Centerplane images of the instantaneous vorticty field, and mean cross-sectional vorticity images averaged over 500 instantaneous realizations at the center of the jet exit ($x/D = 0.0$). Flow conditions are for $J = 41$ and $Re_j = 1900$, for symmetry breaking tab orientations. The colorbars are scaled to the maximum and minimum vorticity values contained within all images shown.

C.4 POD Analysis

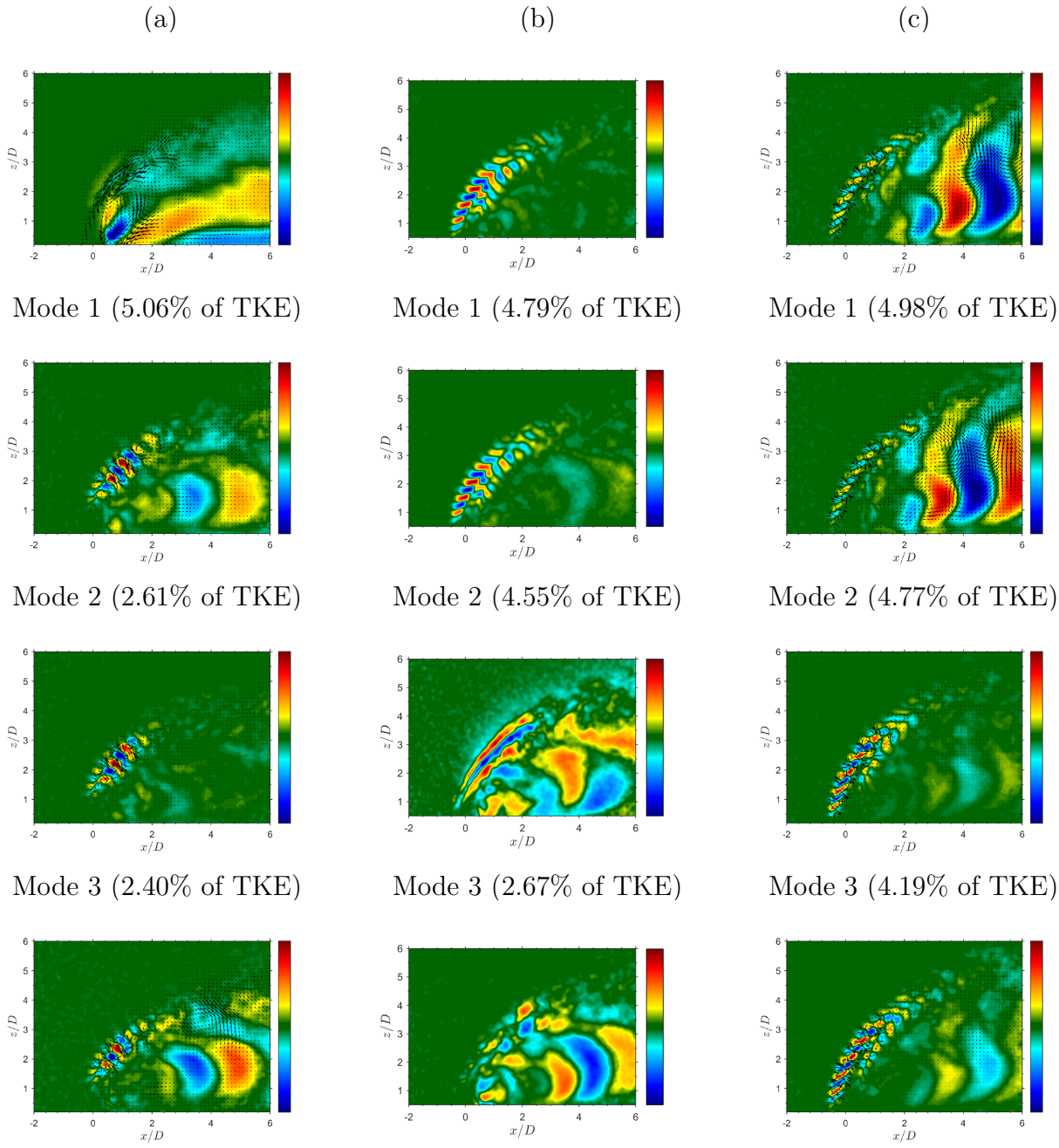

Figure C.26: PIV based POD mode structures extracted from 500 instantaneous snaphots of the centerplane velocity field at $J = 5$, for (a) the tab at L15, (b) the tab at L30, and (c) the tab at L45. The modes are sorted according to their respective percentages of total kinetic energy fluctuation content. The colorbar in each image represents the mode scaled by its own norm and the mean jet velocity at the jet exit U_j.

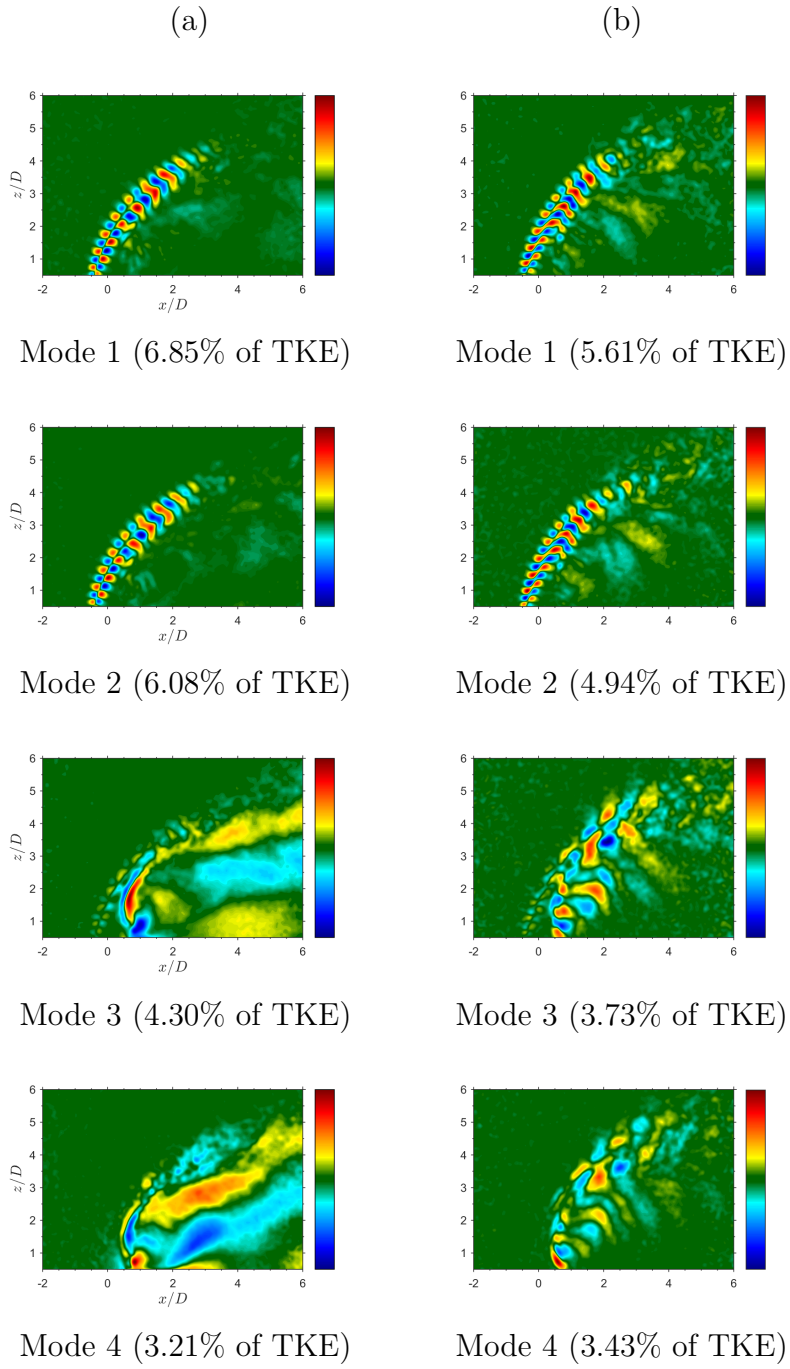

Figure C.27: PIV based POD mode structures extracted from 500 instantaneous snaphots of the centerplane velocity field at $J = 5$, for (a) the tab at L90, and (b) the tab at R90. The modes are sorted according to their respective percentages of total kinetic energy fluctuation content. The colorbar in each image represents the mode scaled by its own norm and the mean jet velocity at the jet exit U_j.

(a) (b) (c)

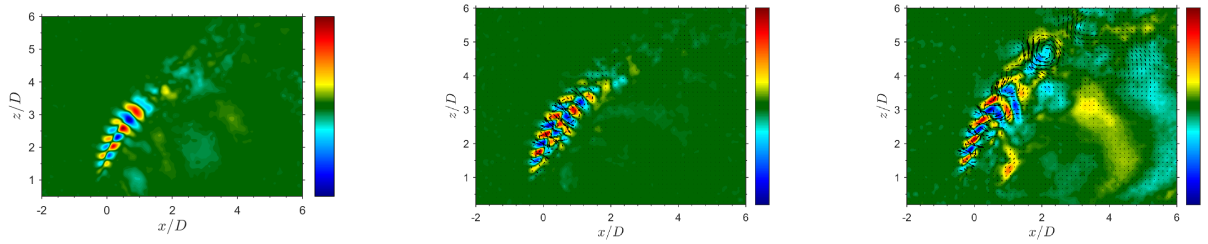

Mode 1 (3.58% of TKE) Mode 1 (4.69% of TKE) Mode 1 (2.57% of TKE)

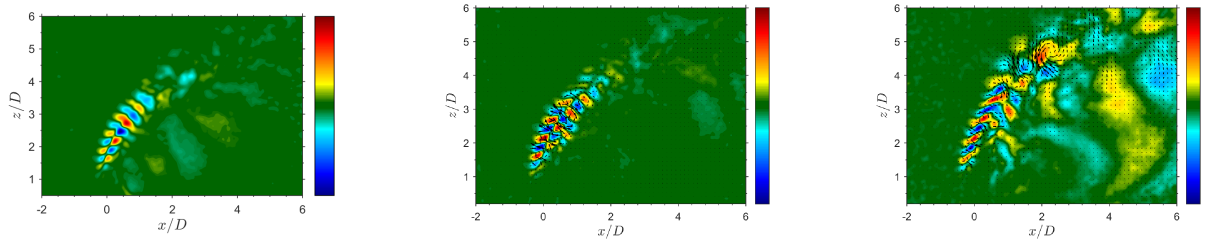

Mode 2 (2.96% of TKE) Mode 2 (4.26% of TKE) Mode 2 (2.47% of TKE)

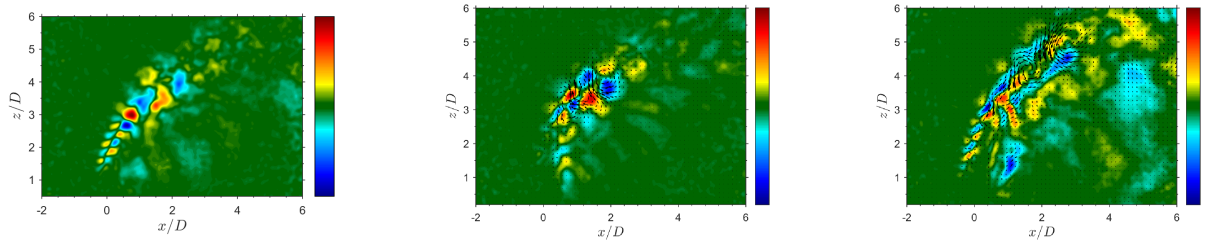

Mode 3 (2.62% of TKE) Mode 3 (2.82% of TKE) Mode 3 (2.38% of TKE)

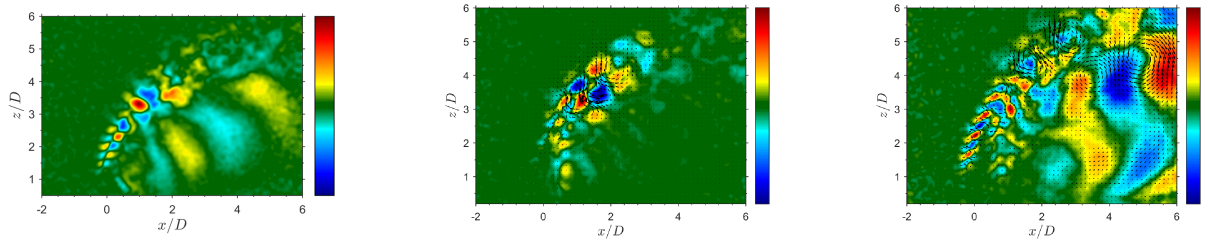

Mode 4 (2.54% of TKE) Mode 4 (2.73% of TKE) Mode 4 (2.26% of TKE)

Figure C.28: PIV based POD mode structures extracted from 500 instantaneous snaphots of the centerplane velocity field at $J = 8$, for (a) the tab at L15, (b) the tab at L30, and (c) the tab at L45. The modes are sorted according to their respective percentages of total kinetic energy fluctuation content. The colorbar in each image represents the mode scaled by its own norm and the mean jet velocity at the jet exit U_j.

(a) (b)

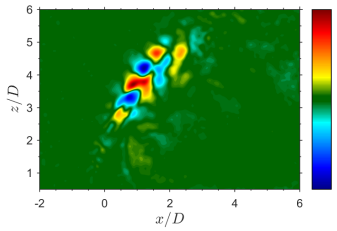

Mode 1 (4.48% of TKE)

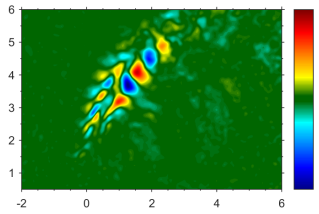

Mode 1 (6.61% of TKE)

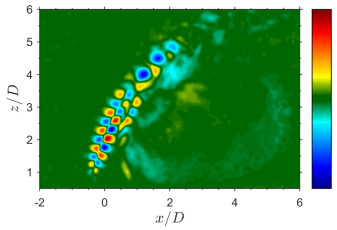

Mode 2 (4.16% of TKE)

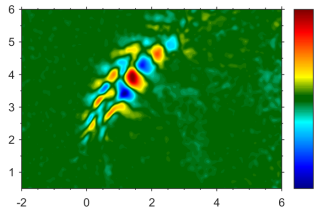

Mode 2 (6.34% of TKE)

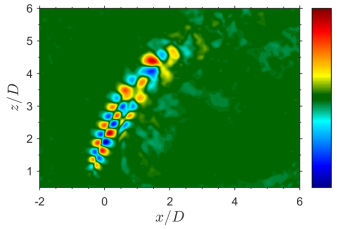

Mode 3 (3.86% of TKE)

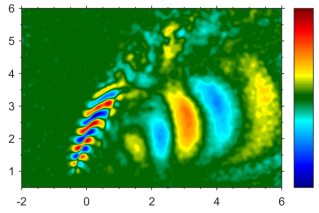

Mode 3 (2.37% of TKE)

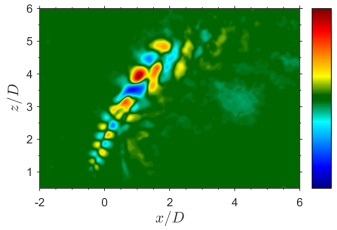

Mode 4 (3.76% of TKE)

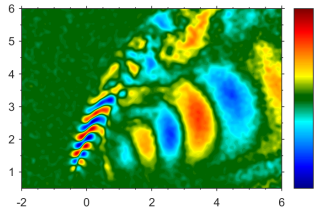

Mode 4 (2.09% of TKE)

Figure C.29: PIV based POD mode structures extracted from 500 instantaneous snaphots of the centerplane velocity field at $J = 8$, for (a) the tab at L90, and (b) the tab at R90. The modes are sorted according to their respective percentages of total kinetic energy fluctuation content. The colorbar in each image represents the mode scaled by its own norm and the mean jet velocity at the jet exit U_j.

(a) (b) (c)

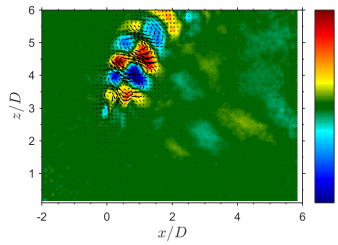

Mode 1 (10.98% of TKE)

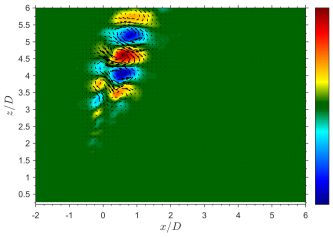

Mode 1 (9.01% of TKE)

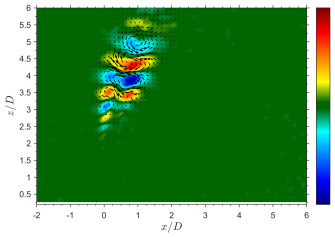

Mode 1 (6.86% of TKE)

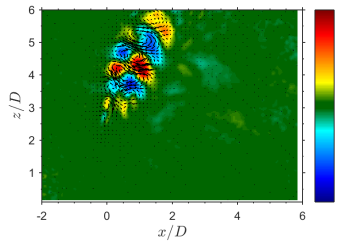

Mode 2 (10.38% of TKE)

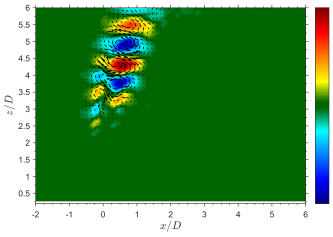

Mode 2 (8.83% of TKE)

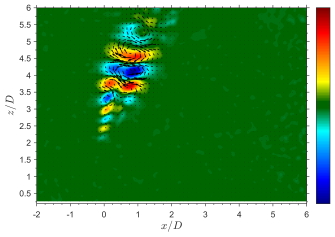

Mode 2 (5.48% of TKE)

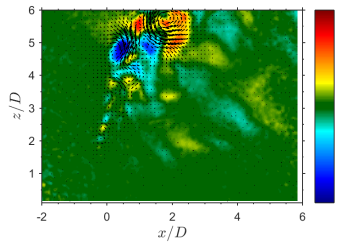

Mode 3 (4.72% of TKE)

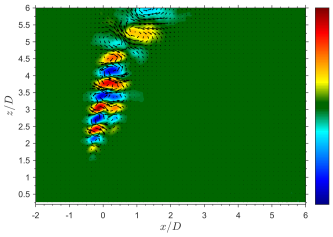

Mode 3 (4.62% of TKE)

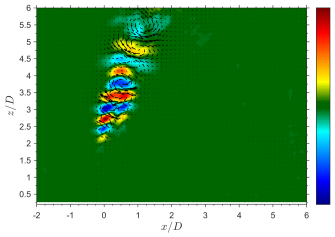

Mode 3 (3.75% of TKE)

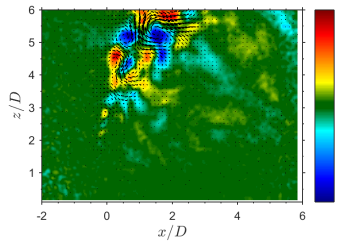

Mode 4 (4.25% of TKE)

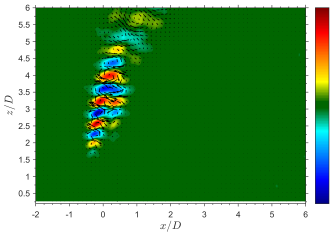

Mode 4 (4.39% of TKE)

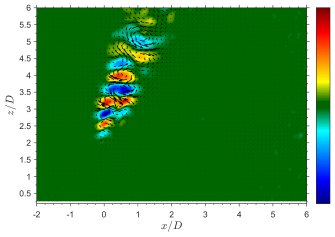

Mode 4 (3.71% of TKE)

Figure C.30: PIV based POD mode structures extracted from 500 instantaneous snaphots of the centerplane velocity field at $J = 20$, (a) the non-tabbed jet, (b) the tab upstream, and (c) the tab downstream. The modes are sorted according to their respective percentages of total kinetic energy fluctuation content. The colorbar in each image represents the mode scaled by its own norm and the mean jet velocity at the jet exit U_j.

(a) (b) (c)

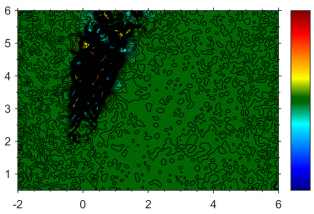

Mode 1 (7.66% of TKE)

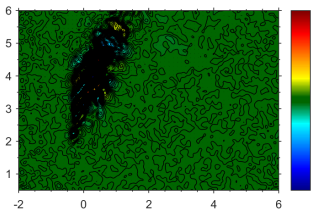

Mode 1 (6.07% of TKE)

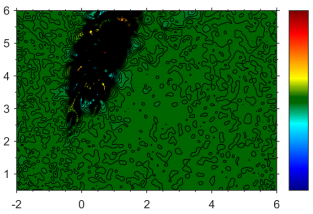

Mode 1 (8.93% of TKE)

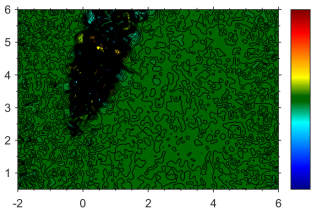

Mode 2 (6.57% of TKE)

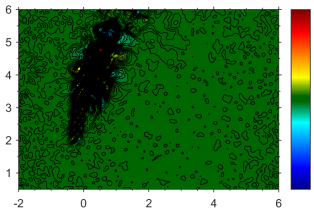

Mode 2 (5.70% of TKE)

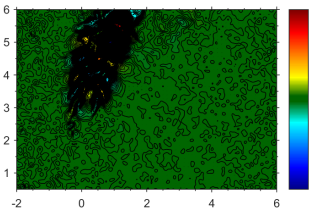

Mode 2 (7.69% of TKE)

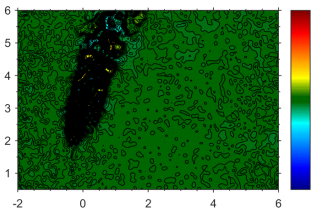

Mode 3 (4.16% of TKE)

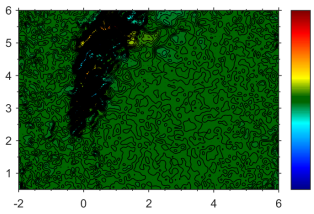

Mode 3 (3.57% of TKE)

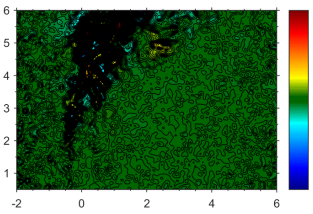

Mode 3 (4.24% of TKE)

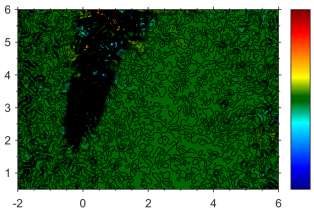

Mode 4 (3.99% of TKE)

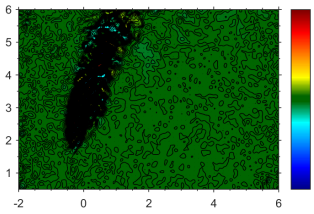

Mode 4 (3.33% of TKE)

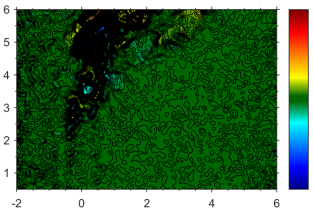

Mode 4 (3.86% of TKE)

Figure C.31: PIV based POD mode structures extracted from 500 instantaneous snaphots of the centerplane velocity field at $J = 20$, for (a) the tab at L15, (b) the tab at L30, and (c) the tab at L45. The modes are sorted according to their respective percentages of total kinetic energy fluctuation content. The colorbar in each image represents the mode scaled by its own norm and the mean jet velocity at the jet exit U_j.

(a) (b)

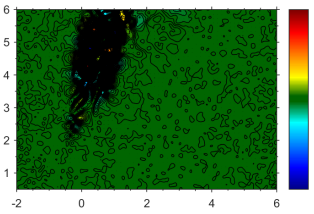

Mode 1 (9.19% of TKE)

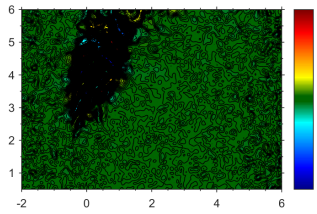

Mode 1 (13.14% of TKE)

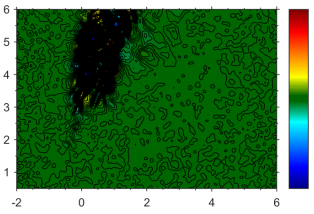

Mode 2 (8.12% of TKE)

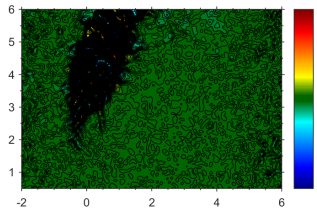

Mode 2 (12.83% of TKE)

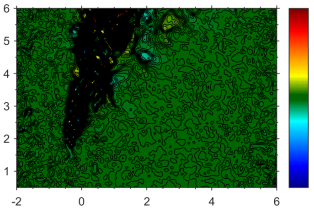

Mode 3 (3.78% of TKE)

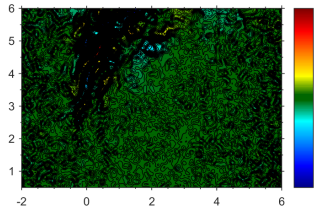

Mode 3 (4.30% of TKE)

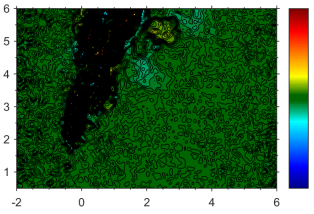

Mode 4 (3.33% of TKE)

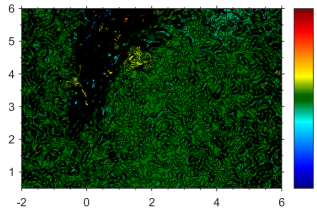

Mode 4 (3.82% of TKE)

Figure C.32: PIV based POD mode structures extracted from 500 instantaneous snaphots of the centerplane velocity field at $J = 20$, for (a) the tab at L90, and (b) the tab at R90. The modes are sorted according to their respective percentages of total kinetic energy fluctuation content. The colorbar in each image represents the mode scaled by its own norm and the mean jet velocity at the jet exit U_j.

(a) (b) (c)

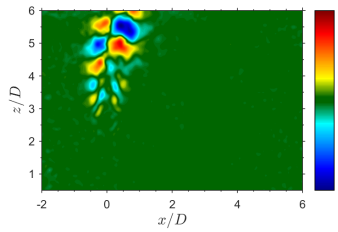

Mode 1 (9.31% of TKE)

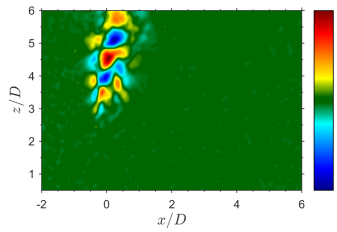

Mode 1 (9.09% of TKE)

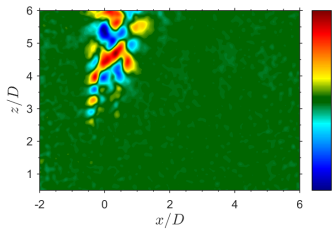

Mode 1 (6.46% of TKE)

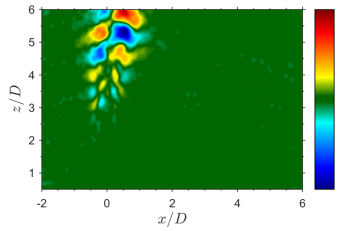

Mode 2 (7.37% of TKE)

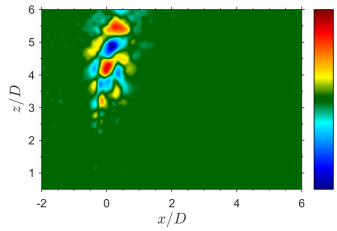

Mode 2 (7.59% of TKE)

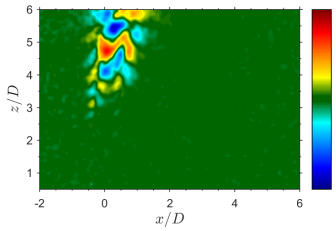

Mode 2 (5.98% of TKE)

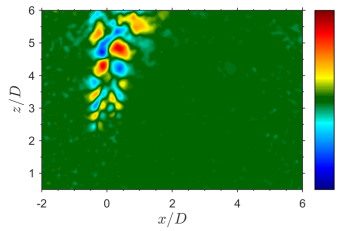

Mode 3 (4.13% of TKE)

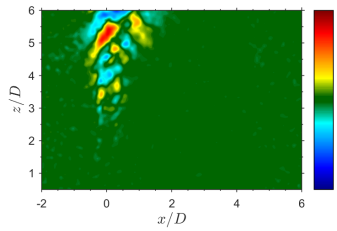

Mode 3 (4.90% of TKE)

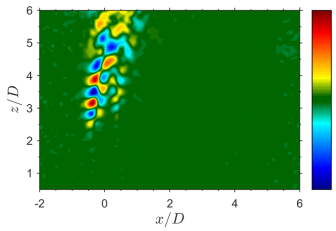

Mode 3 (3.75% of TKE)

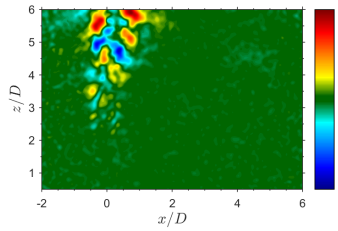

Mode 4 (3.80% of TKE)

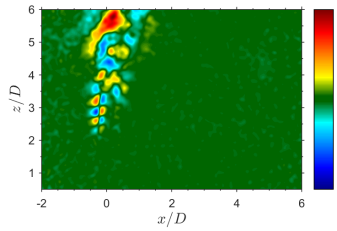

Mode 4 (4.52% of TKE)

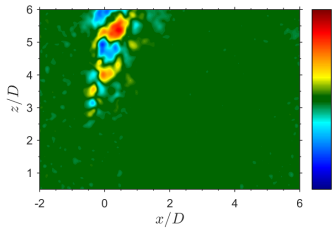

Mode 4 (3.50% of TKE)

Figure C.33: PIV based POD mode structures extracted from 500 instantaneous snaphots of the centerplane velocity field at $J = 41$, for (a) the tab at L15, (b) the tab at L30, and (c) the tab at L45. The modes are sorted according to their respective percentages of total kinetic energy fluctuation content. The colorbar in each image represents the mode scaled by its own norm and the mean jet velocity at the jet exit U_j.

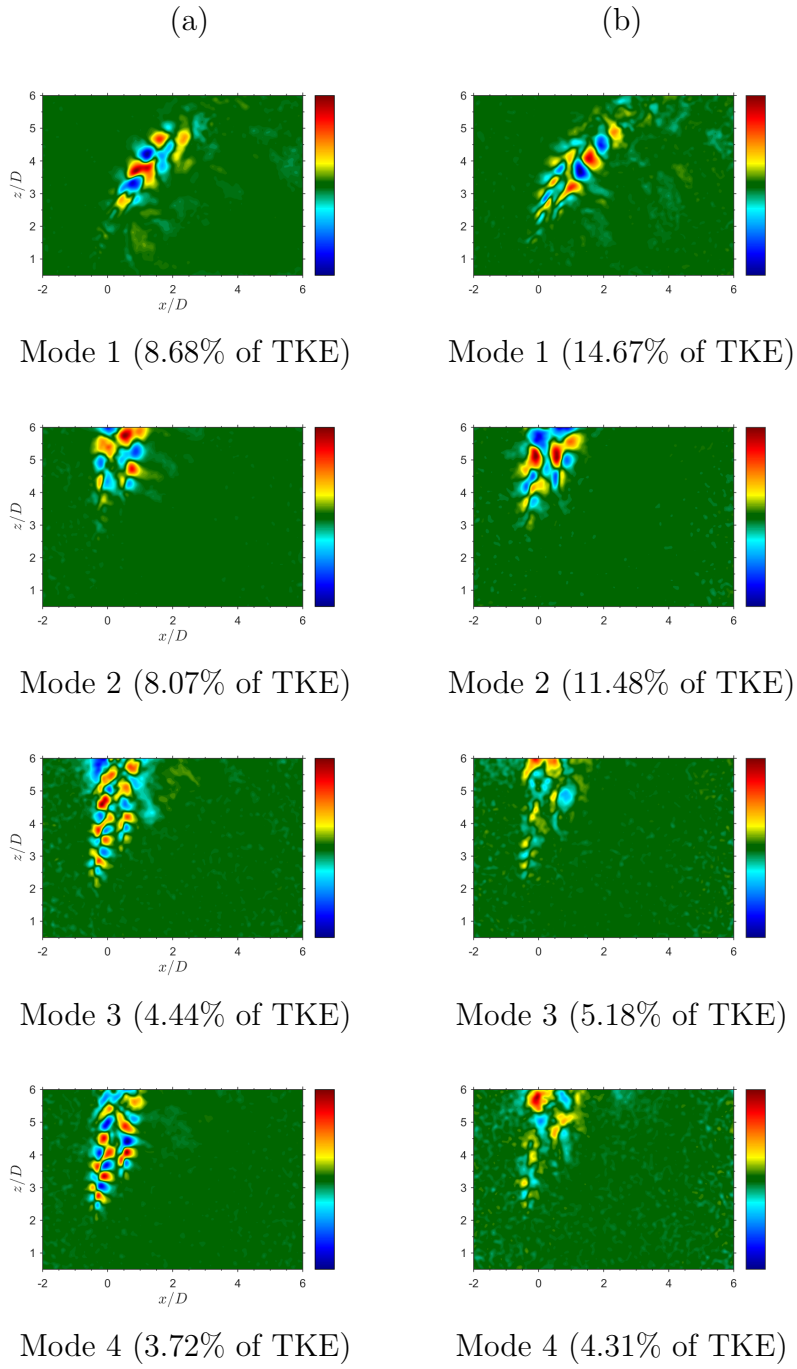

Figure C.34: PIV based POD mode structures extracted from 500 instantaneous snaphots of the centerplane velocity field at $J = 41$, for (a) the tab at L90, and (b) the tab at R90. The modes are sorted according to their respective percentages of total kinetic energy fluctuation content. The colorbar in each image represents the mode scaled by its own norm and the mean jet velocity at the jet exit U_j.

APPENDIX D

Additional Axisymmetrically Forced JICF Results

D.1 Structural Characteristics

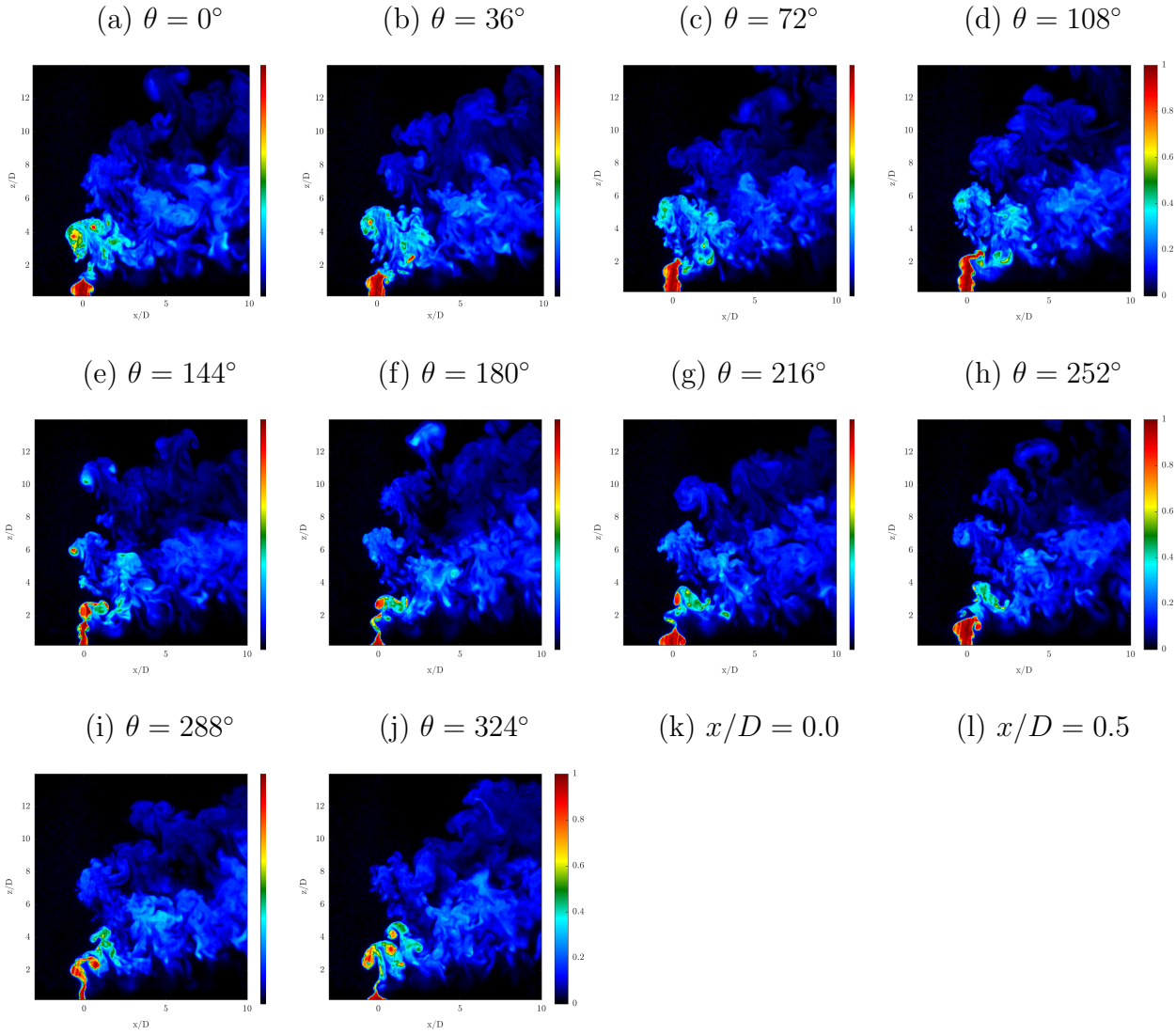

Figure D.1: Representative structural PLIF images of the double-pulse forced AU jet at $J = 7$, for forcing case 0.45.70.85 where (a-j) depict the instantaneous centerplane phase progression for 1 forcing period at every $1/10T$, and (k-l) are mean cross-sectional slices of the jet at $x/D = 0.0$ and $x/D = 0.5$ respectively. The colorbar maximum for the cross-sectional images was scaled so as to allow quantitative comparisons with the scalar intensities noted in the jet centerplane.

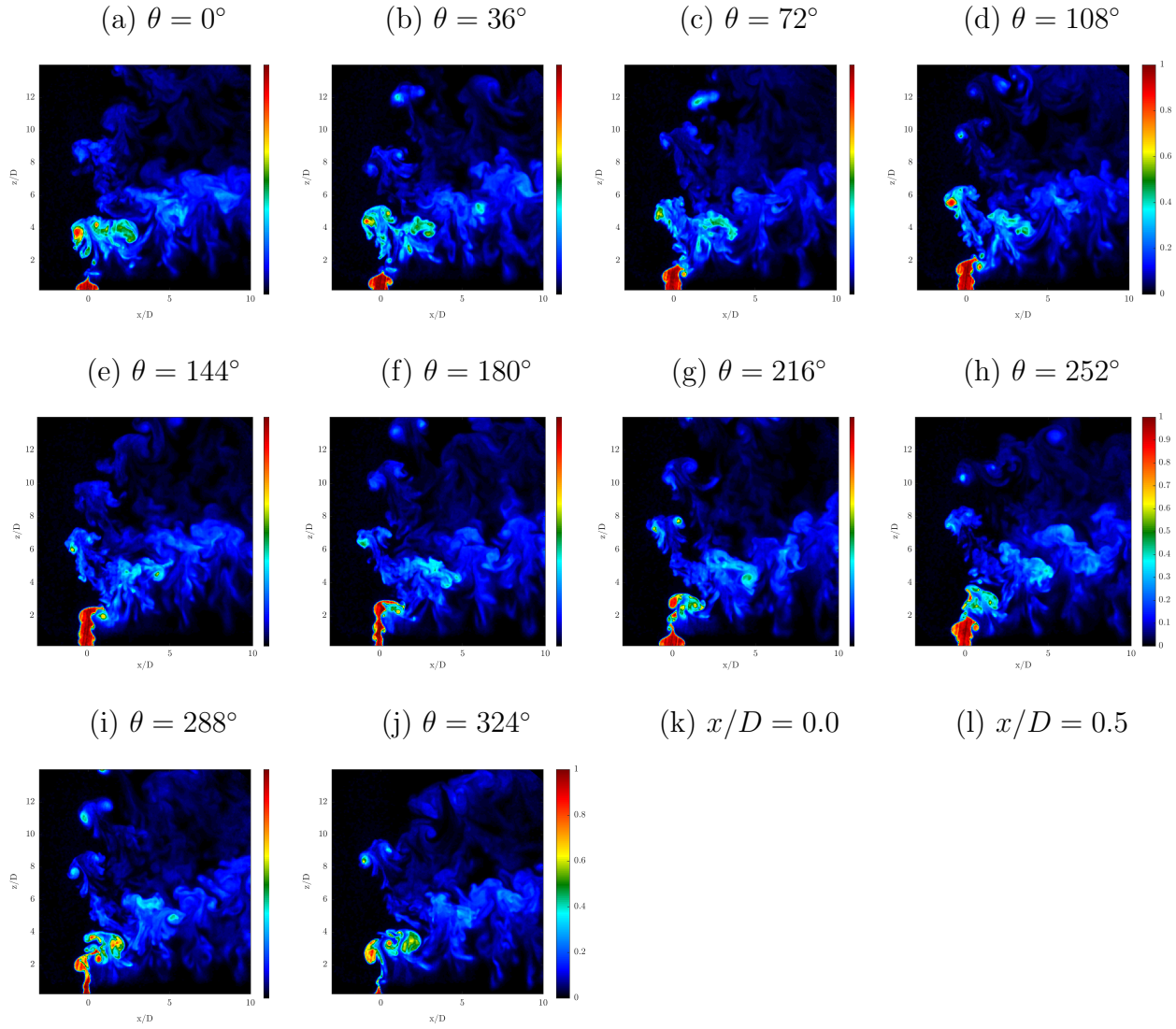

Figure D.2: Representative structural PLIF images of the double-pulse forced AU jet at $J = 7$, for forcing case 0.45.60.75 where (a-j) depict the instantaneous centerplane phase progression for 1 forcing period at every $1/10T$, and (k-l) are mean cross-sectional slices of the jet at $x/D = 0.0$ and $x/D = 0.5$ respectively. The colorbar maximum for the cross-sectional images was scaled so as to allow quantitative comparisons with the scalar intensities noted in the jet centerplane.

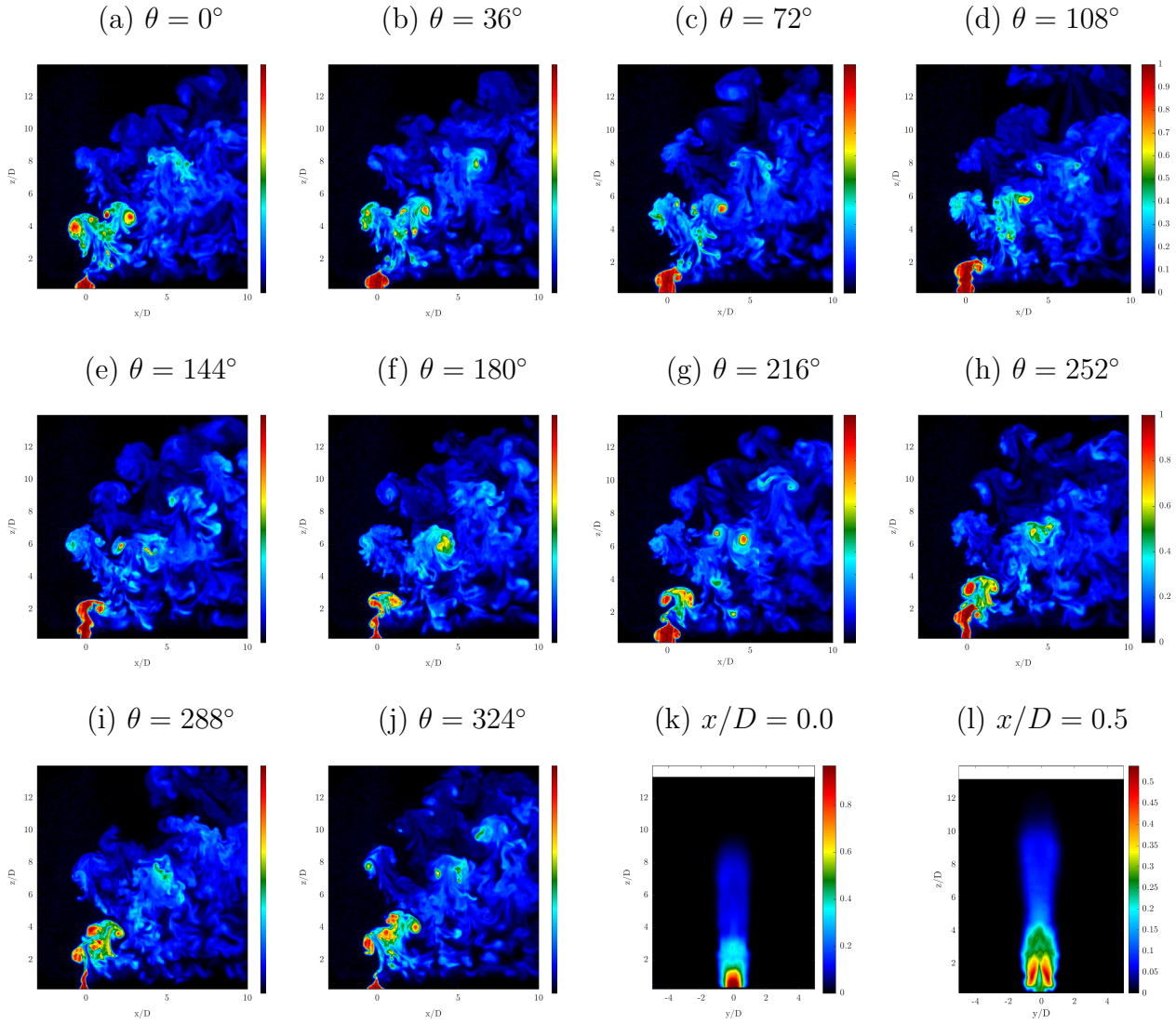

Figure D.3: Representative structural PLIF images of the double-pulse forced AU jet at $J = 7$, for forcing case 0.35.50.65 where (a-j) depict the instantaneous centerplane phase progression for 1 forcing period at every $1/10T$, and (k-l) are mean cross-sectional slices of the jet at $x/D = 0.0$ and $x/D = 0.5$ respectively. The colorbar maximum for the cross-sectional images was scaled so as to allow quantitative comparisons with the scalar intensities noted in the jet centerplane.

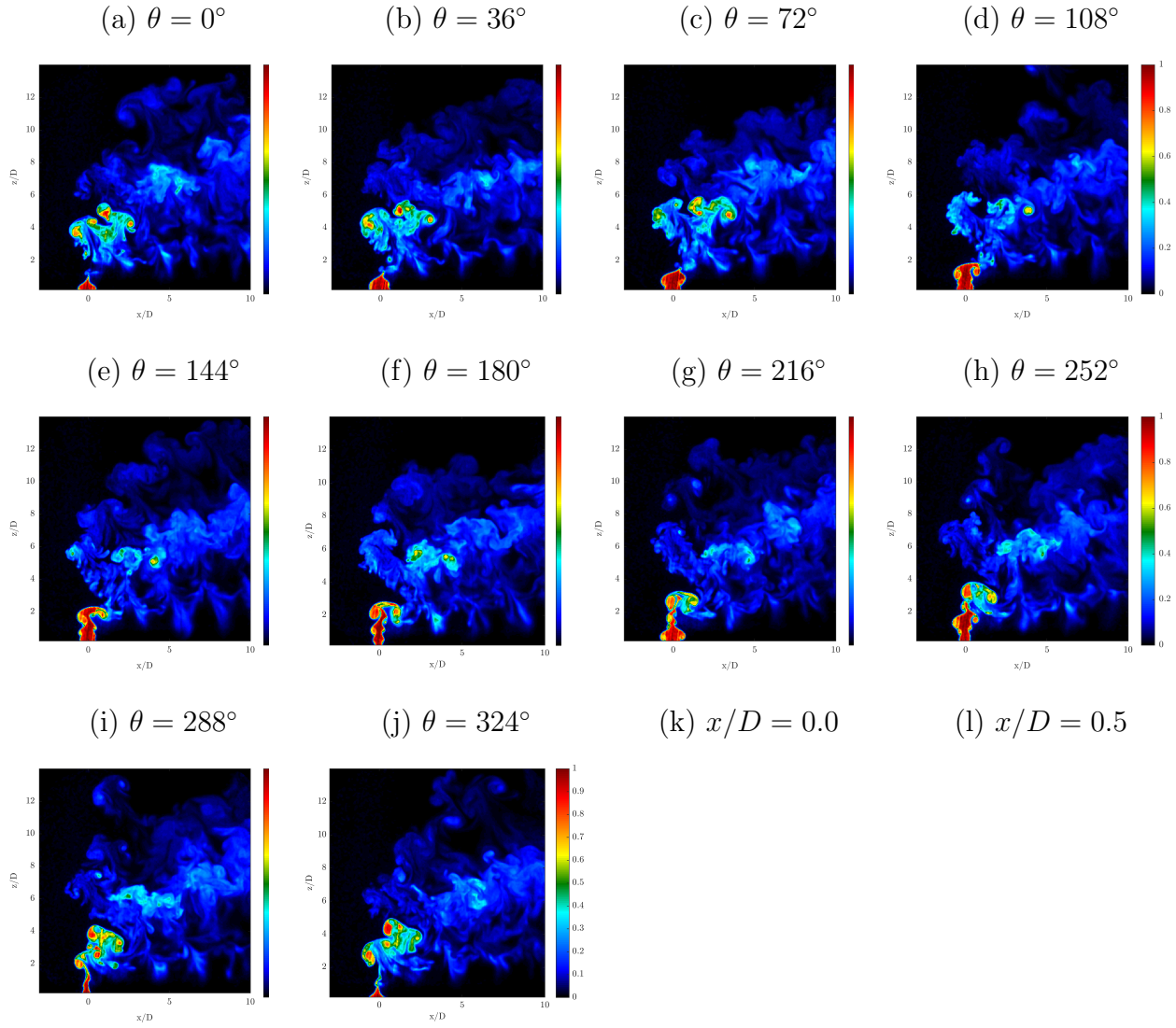

Figure D.4: Representative structural PLIF images of the double-pulse forced AU jet at $J = 7$, for forcing case 0.35.45.60 where (a-j) depict the instantaneous centerplane phase progression for 1 forcing period at every $1/10T$, and (k-l) are mean cross-sectional slices of the jet at $x/D = 0.0$ and $x/D = 0.5$ respectively. The colorbar maximum for the cross-sectional images was scaled so as to allow quantitative comparisons with the scalar intensities noted in the jet centerplane.

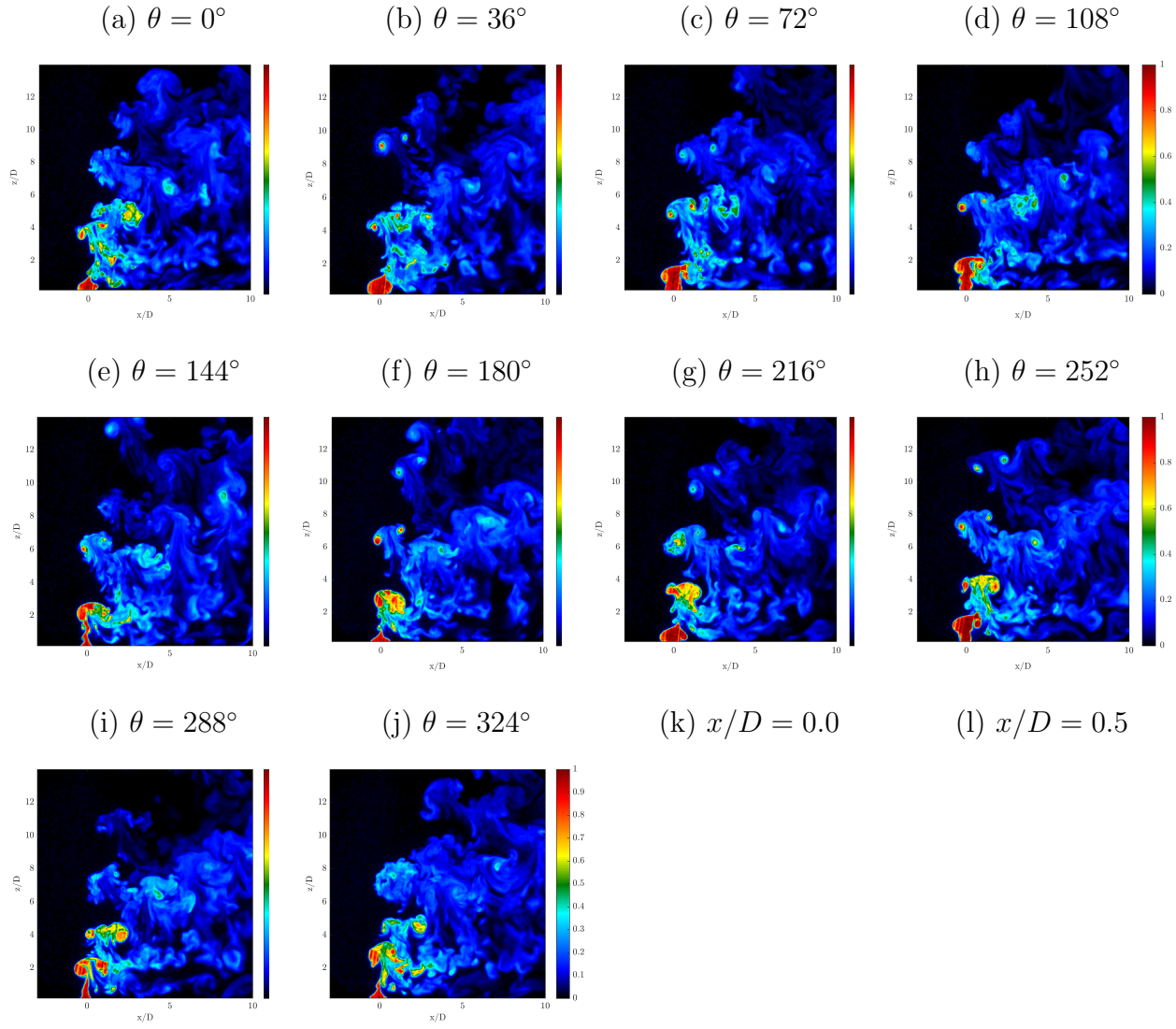

Figure D.5: Representative structural PLIF images of the double-pulse forced AU jet at $J = 7$, for forcing case 0.25.50.65 where (a-j) depict the instantaneous centerplane phase progression for 1 forcing period at every $1/10T$, and (k-l) are mean cross-sectional slices of the jet at $x/D = 0.0$ and $x/D = 0.5$ respectively. The colorbar maximum for the cross-sectional images was scaled so as to allow quantitative comparisons with the scalar intensities noted in the jet centerplane.

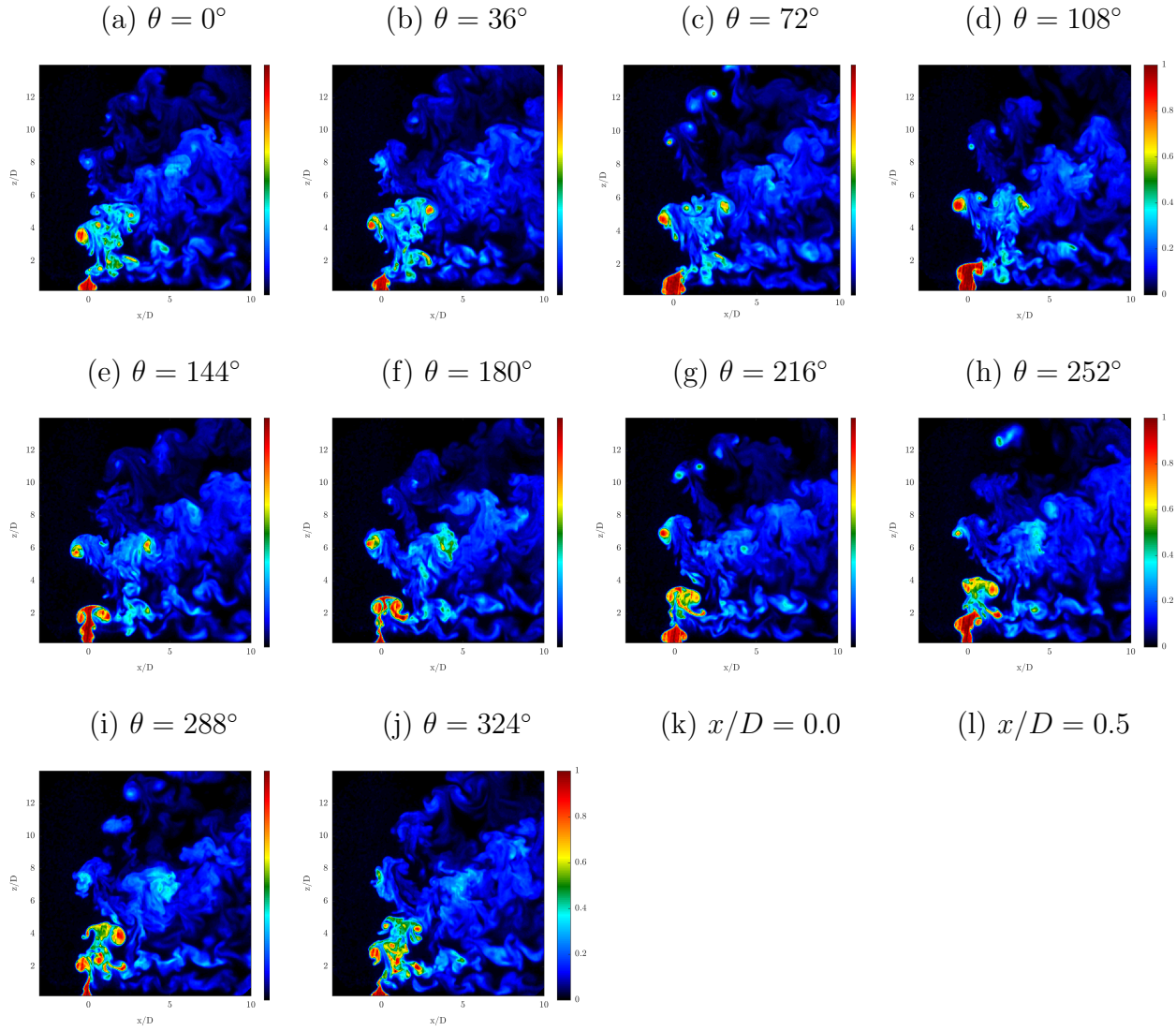

Figure D.6: Representative structural PLIF images of the double-pulse forced AU jet at $J = 7$, for forcing case 0.25.40.55 where (a-j) depict the instantaneous centerplane phase progression for 1 forcing period at every $1/10T$, and (k-l) are mean cross-sectional slices of the jet at $x/D = 0.0$ and $x/D = 0.5$ respectively. The colorbar maximum for the cross-sectional images was scaled so as to allow quantitative comparisons with the scalar intensities noted in the jet centerplane.

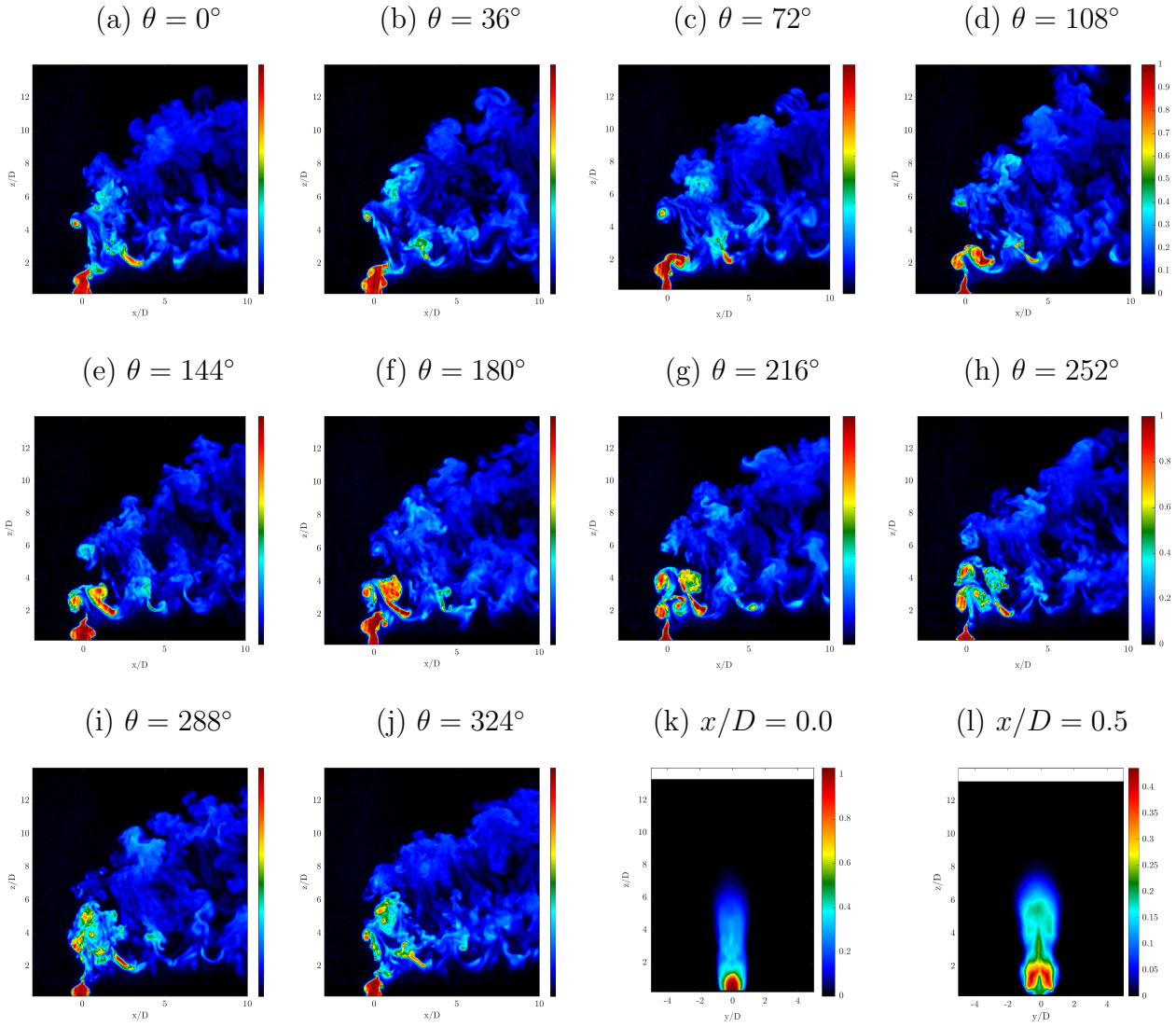

Figure D.7: Representative structural PLIF images of the double-pulse forced AU jet at $J = 7$, for forcing case 0.15.30.45 where (a-j) depict the instantaneous centerplane phase progression for 1 forcing period at every $1/10T$, and (k-l) are mean cross-sectional slices of the jet at $x/D = 0.0$ and $x/D = 0.5$ respectively. The colorbar maximum for the cross-sectional images was scaled so as to allow quantitative comparisons with the scalar intensities noted in the jet centerplane.

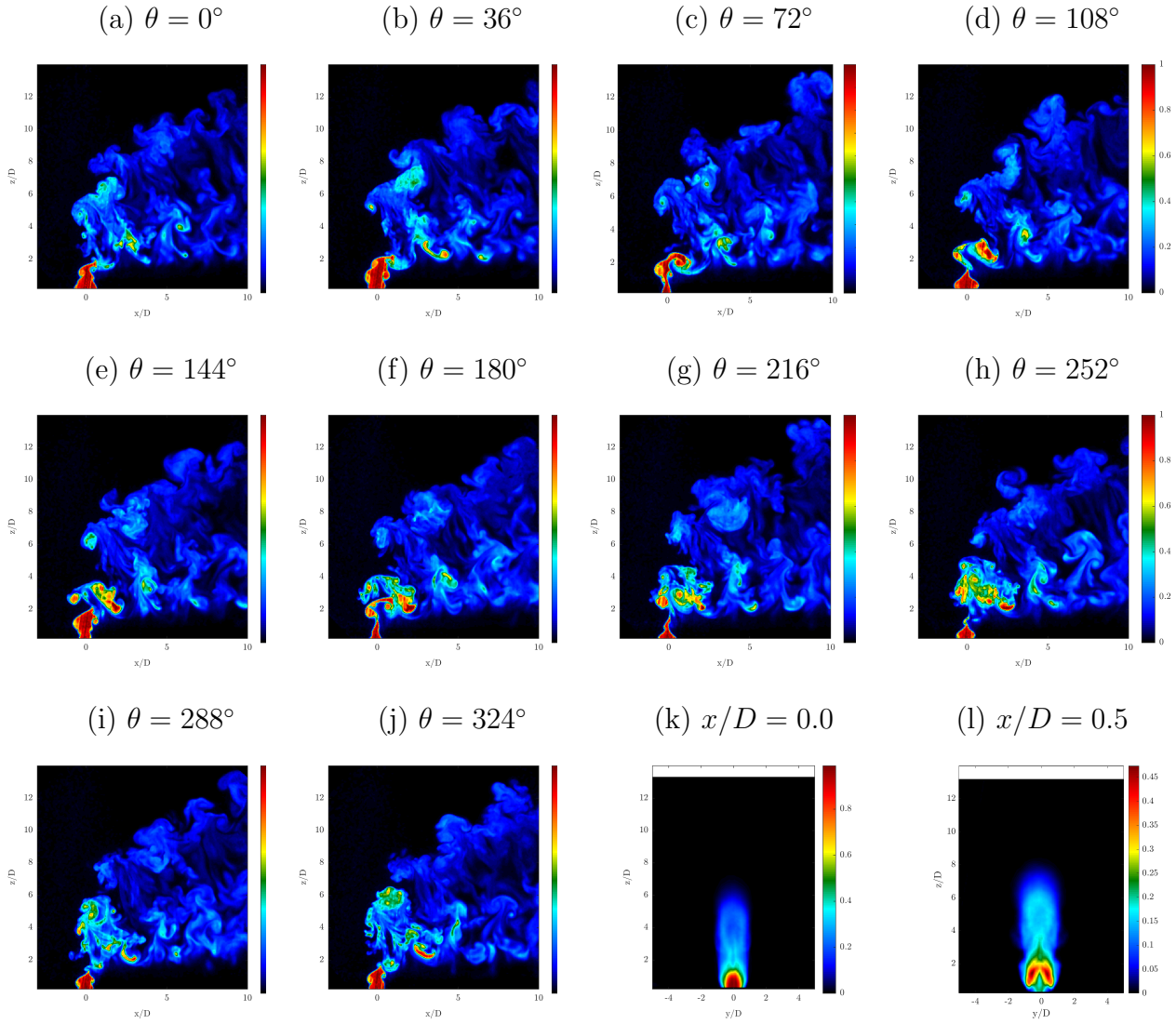

Figure D.8: Representative structural PLIF images of the double-pulse forced AU jet at $J = 7$, for forcing case 0.15.25.40 where (a-j) depict the instantaneous centerplane phase progression for 1 forcing period at every $1/10T$, and (k-l) are mean cross-sectional slices of the jet at $x/D = 0.0$ and $x/D = 0.5$ respectively. The colorbar maximum for the cross-sectional images was scaled so as to allow quantitative comparisons with the scalar intensities noted in the jet centerplane.

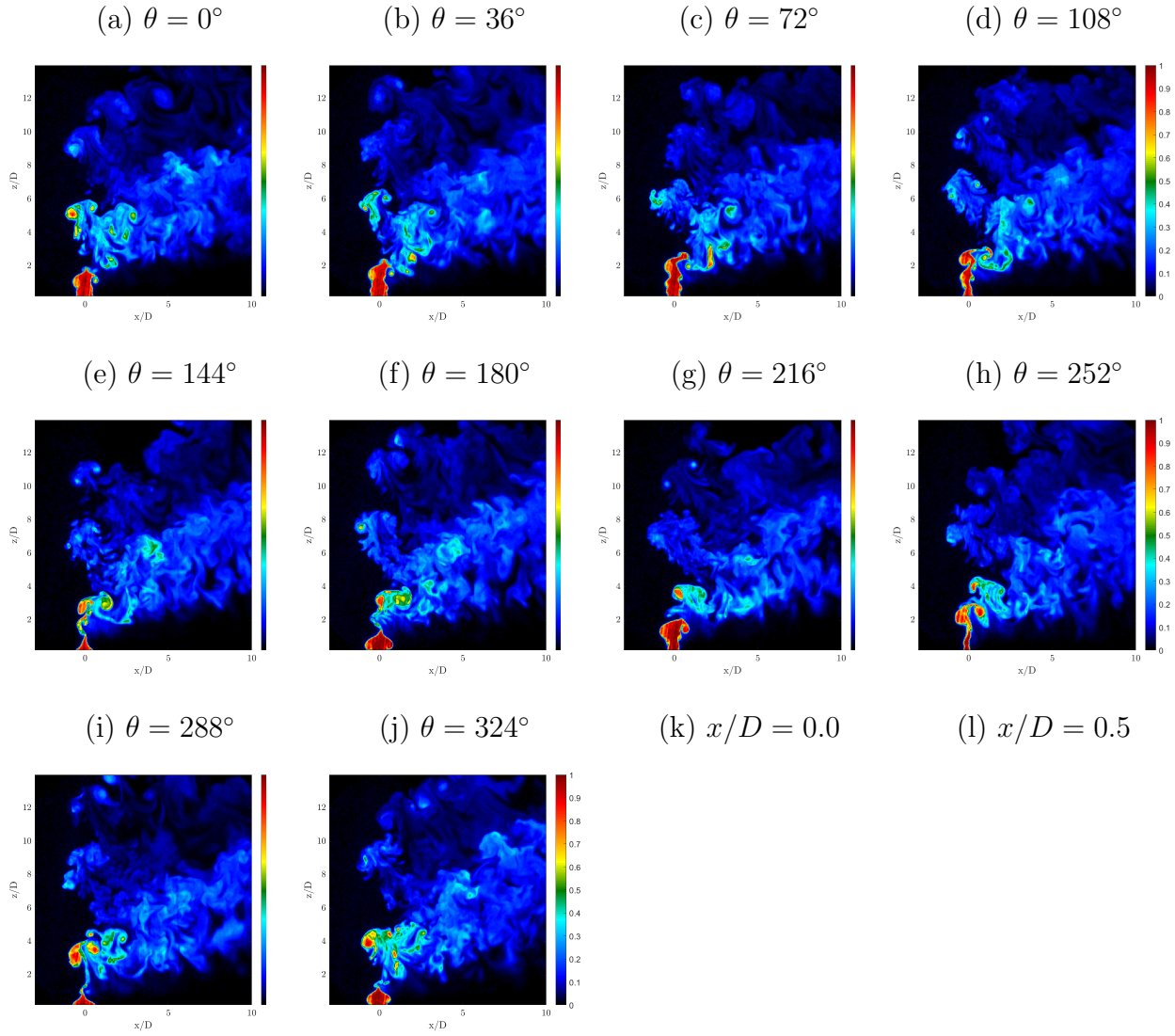

Figure D.9: Representative structural PLIF images of the double-pulse forced AU jet at $J = 10$, for forcing case 0.45.70.85 where (a-j) depict the instantaneous centerplane phase progression for 1 forcing period at every $1/10T$, and (k-l) are mean cross-sectional slices of the jet at $x/D = 0.0$ and $x/D = 0.5$ respectively. The colorbar maximum for the cross-sectional images was scaled so as to allow quantitative comparisons with the scalar intensities noted in the jet centerplane.

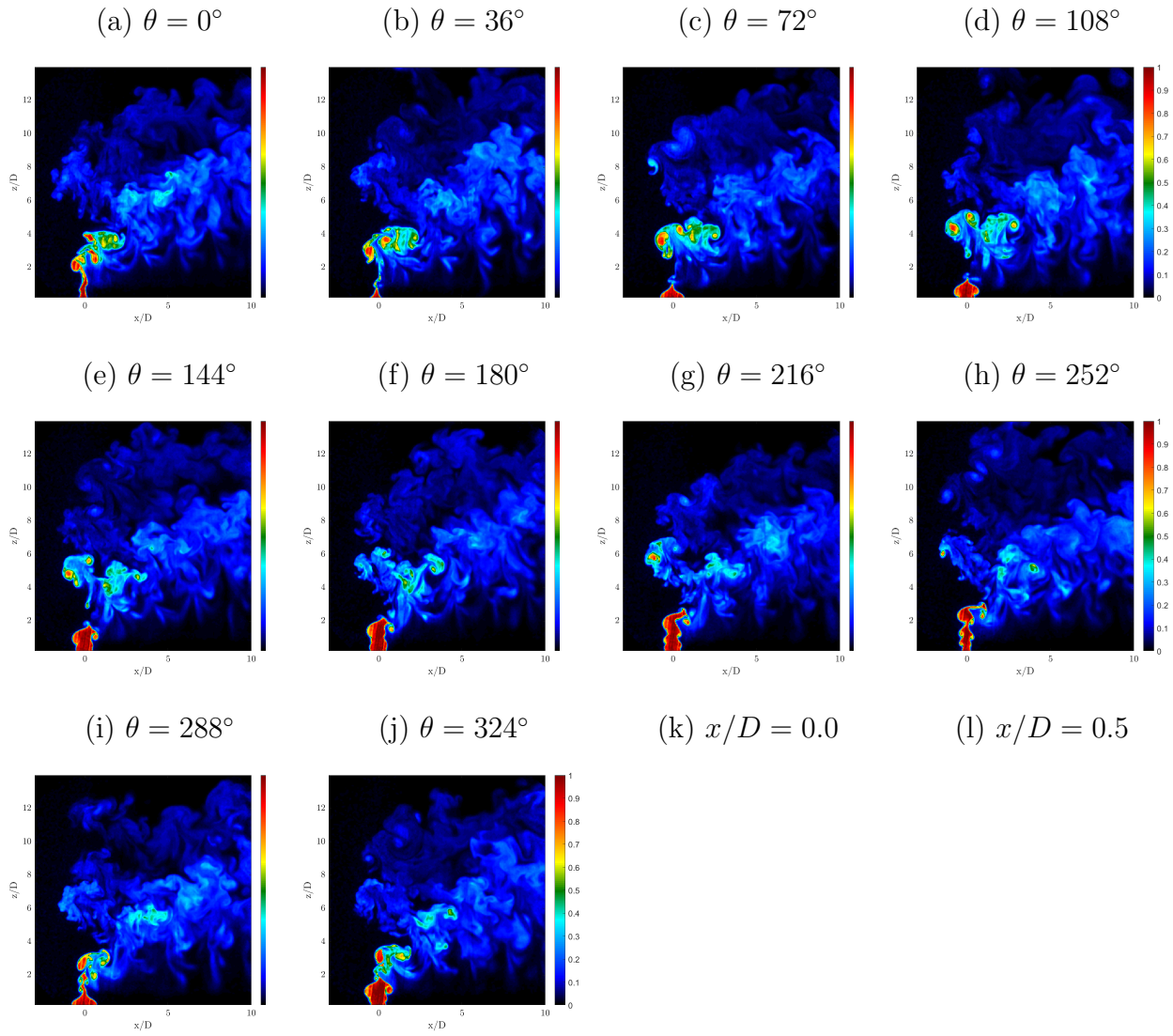

Figure D.10: Representative structural PLIF images of the double-pulse forced AU jet at $J = 10$, for forcing case 0.45.60.75 where (a-j) depict the instantaneous centerplane phase progression for 1 forcing period at every $1/10T$, and (k-l) are mean cross-sectional slices of the jet at $x/D = 0.0$ and $x/D = 0.5$ respectively. The colorbar maximum for the cross-sectional images was scaled so as to allow quantitative comparisons with the scalar intensities noted in the jet centerplane.

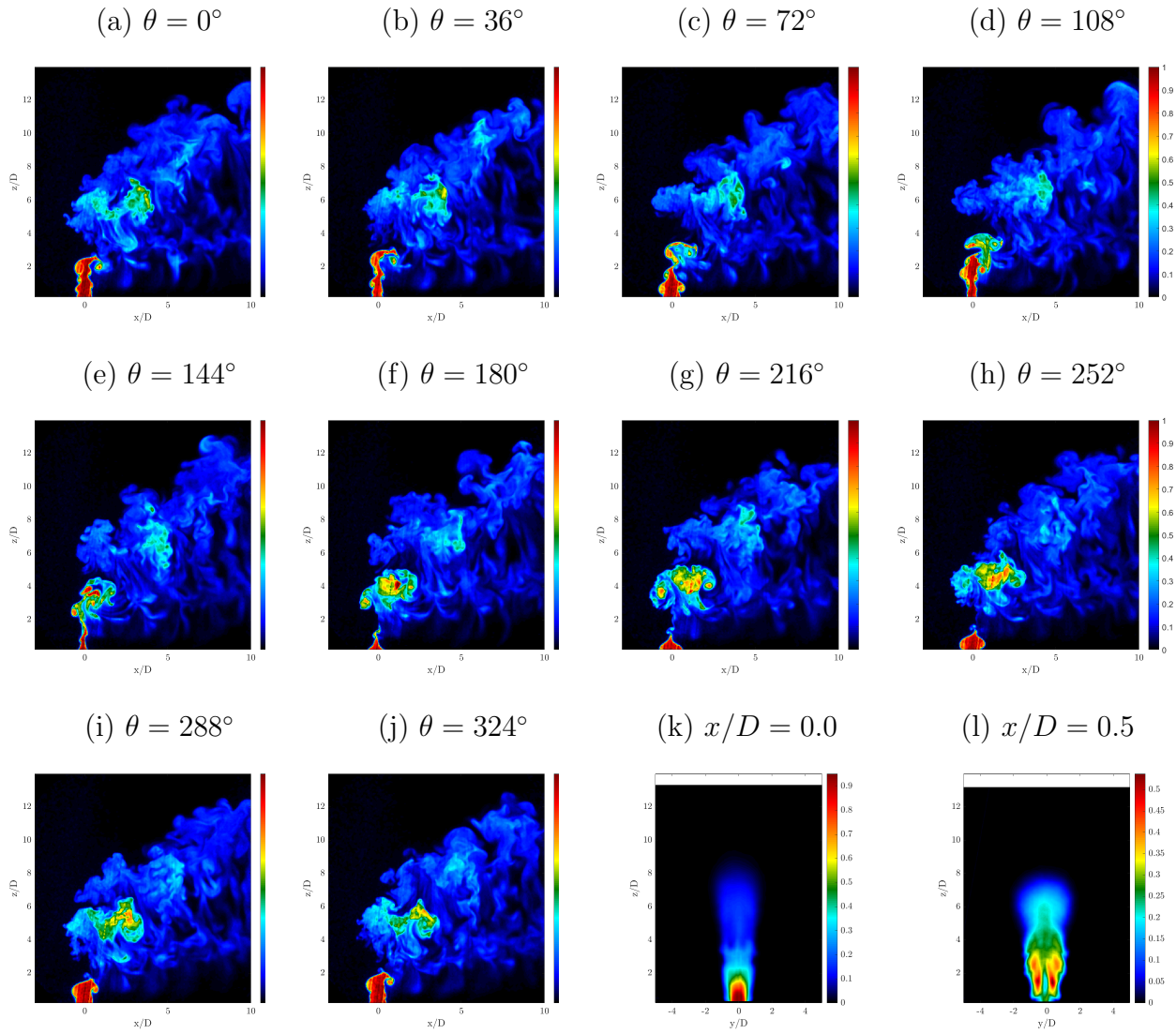

Figure D.11: Representative structural PLIF images of the double-pulse forced AU jet at $J = 10$, for forcing case 0.45.55.70 where (a-j) depict the instantaneous centerplane phase progression for 1 forcing period at every $1/10T$, and (k-l) are mean cross-sectional slices of the jet at $x/D = 0.0$ and $x/D = 0.5$ respectively. The colorbar maximum for the cross-sectional images was scaled so as to allow quantitative comparisons with the scalar intensities noted in the jet centerplane.

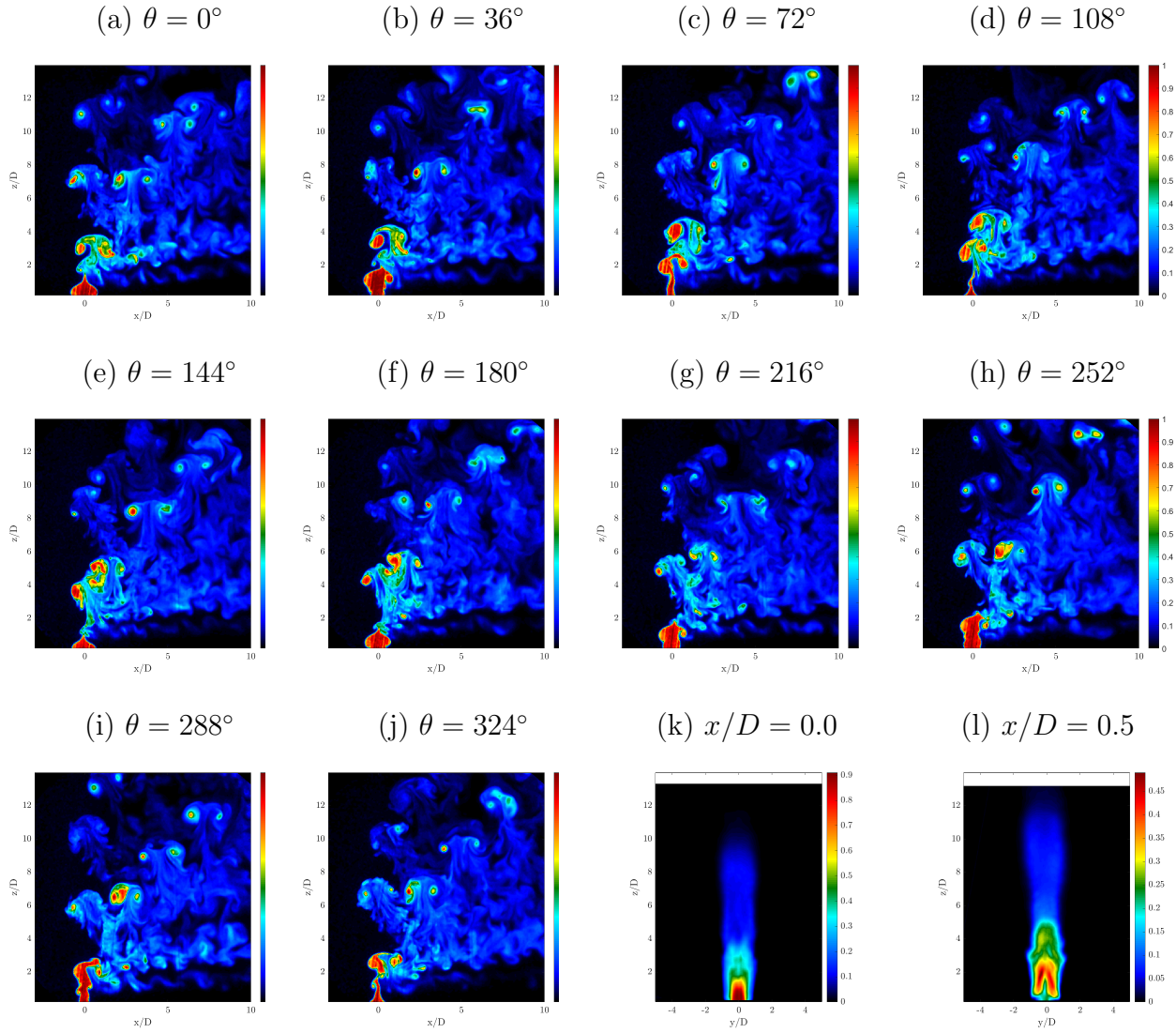

Figure D.12: Representative structural PLIF images of the double-pulse forced AU jet at $J = 10$, for forcing case 0.35.60.75 where (a-j) depict the instantaneous centerplane phase progression for 1 forcing period at every $1/10T$, and (k-l) are mean cross-sectional slices of the jet at $x/D = 0.0$ and $x/D = 0.5$ respectively. The colorbar maximum for the cross-sectional images was scaled so as to allow quantitative comparisons with the scalar intensities noted in the jet centerplane.

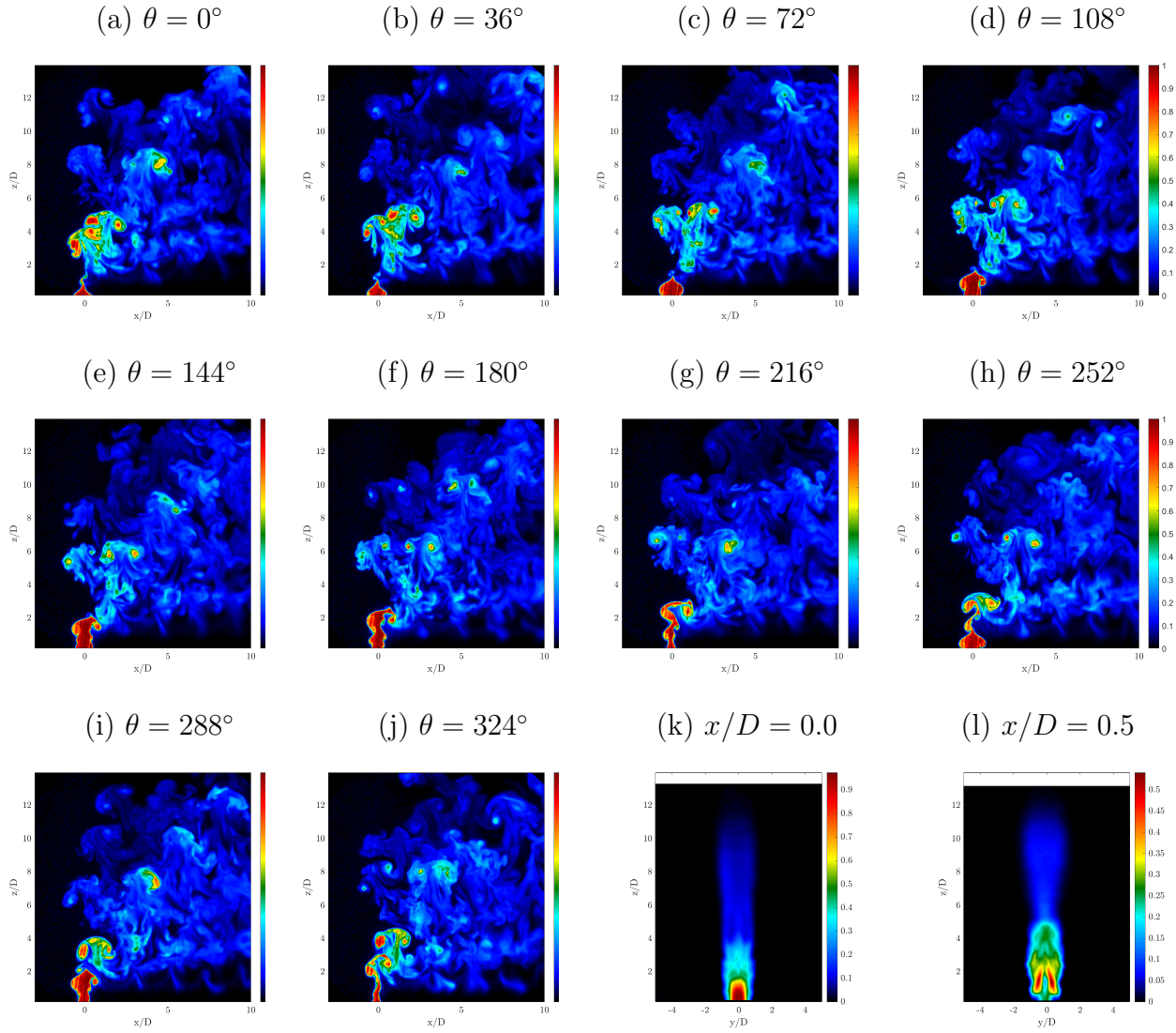

Figure D.13: Representative structural PLIF images of the double-pulse forced AU jet at $J = 10$, for forcing case 0.35.50.65 where (a-j) depict the instantaneous centerplane phase progression for 1 forcing period at every $1/10T$, and (k-l) are mean cross-sectional slices of the jet at $x/D = 0.0$ and $x/D = 0.5$ respectively. The colorbar maximum for the cross-sectional images was scaled so as to allow quantitative comparisons with the scalar intensities noted in the jet centerplane.

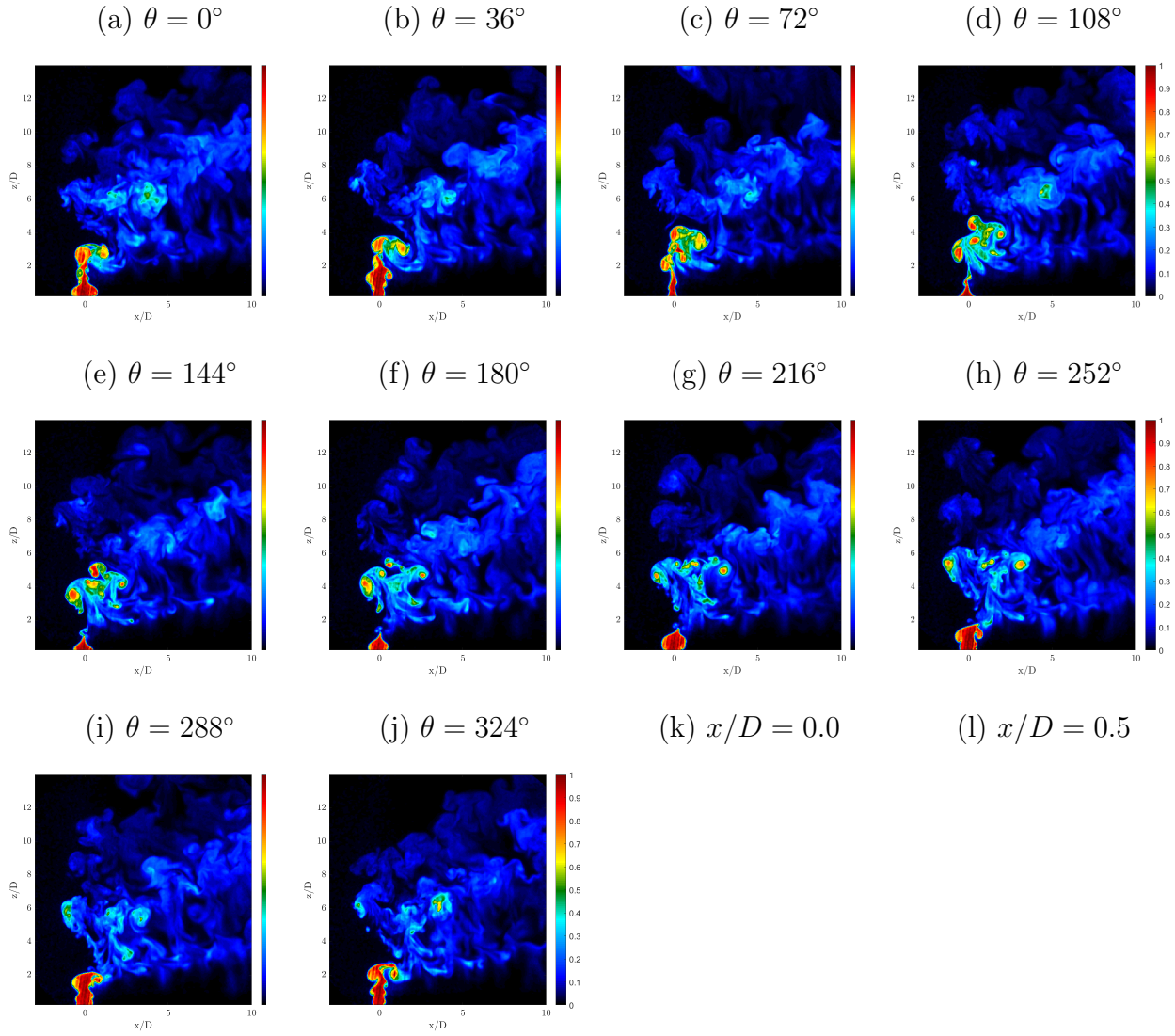

Figure D.14: Representative structural PLIF images of the double-pulse forced AU jet at $J = 10$, for forcing case 0.35.45.60 where (a-j) depict the instantaneous centerplane phase progression for 1 forcing period at every $1/10T$, and (k-l) are mean cross-sectional slices of the jet at $x/D = 0.0$ and $x/D = 0.5$ respectively. The colorbar maximum for the cross-sectional images was scaled so as to allow quantitative comparisons with the scalar intensities noted in the jet centerplane.

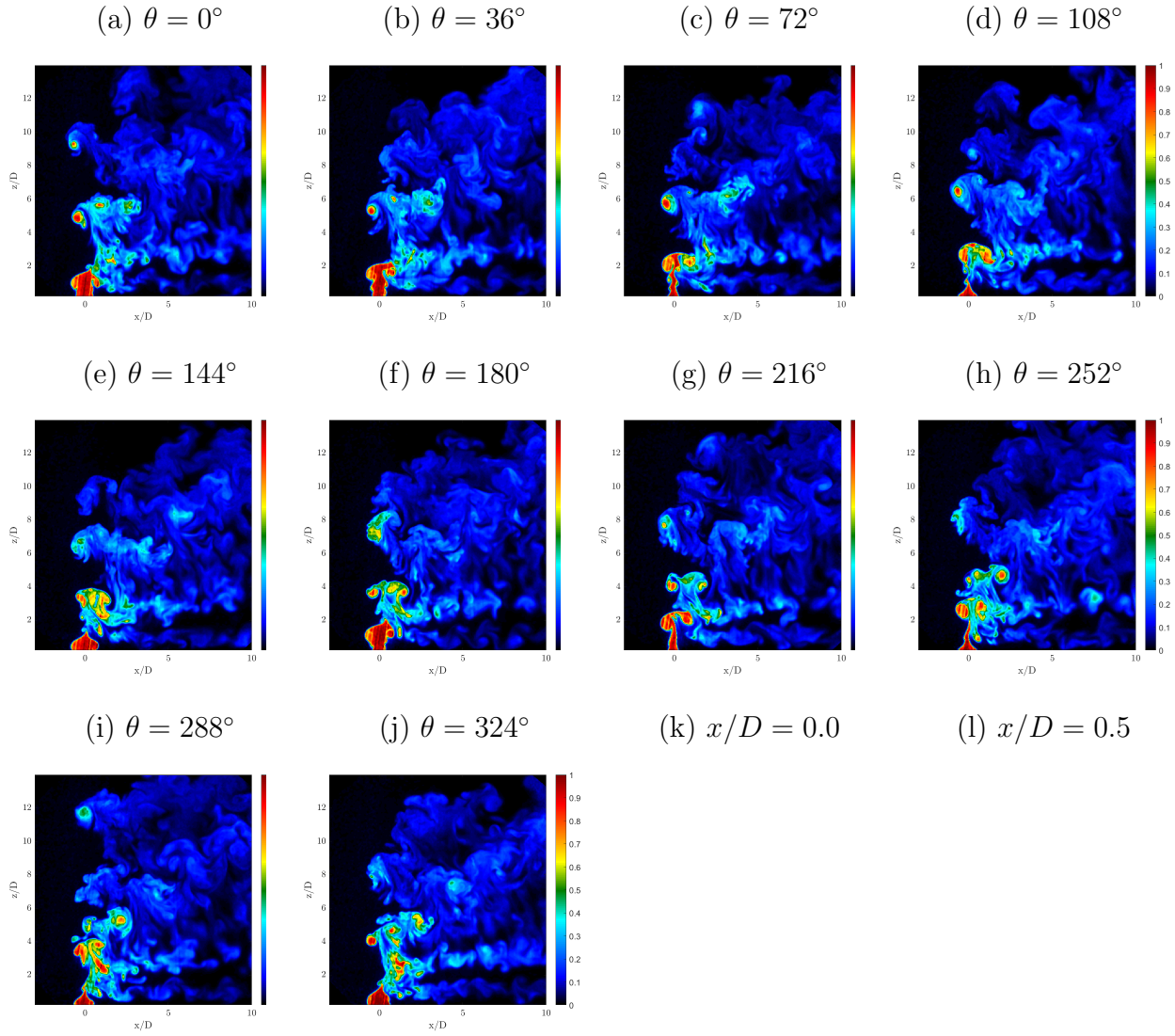

Figure D.15: Representative structural PLIF images of the double-pulse forced AU jet at $J = 10$, for forcing case 0.25.50.65 where (a-j) depict the instantaneous centerplane phase progression for 1 forcing period at every $1/10T$, and (k-l) are mean cross-sectional slices of the jet at $x/D = 0.0$ and $x/D = 0.5$ respectively. The colorbar maximum for the cross-sectional images was scaled so as to allow quantitative comparisons with the scalar intensities noted in the jet centerplane.

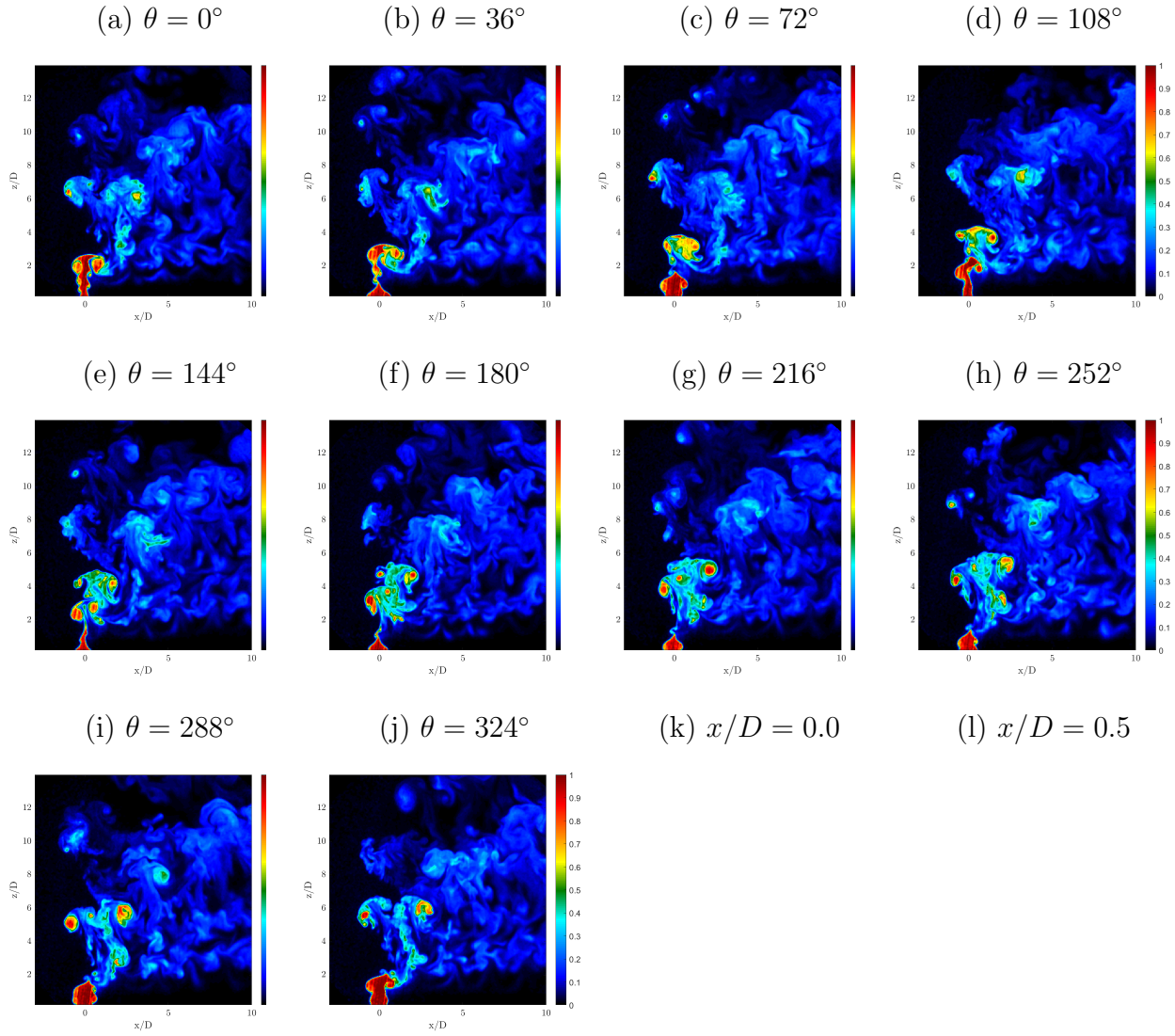

Figure D.16: Representative structural PLIF images of the double-pulse forced AU jet at $J = 10$, for forcing case 0.25.40.55 where (a-j) depict the instantaneous centerplane phase progression for 1 forcing period at every $1/10T$, and (k-l) are mean cross-sectional slices of the jet at $x/D = 0.0$ and $x/D = 0.5$ respectively. The colorbar maximum for the cross-sectional images was scaled so as to allow quantitative comparisons with the scalar intensities noted in the jet centerplane.

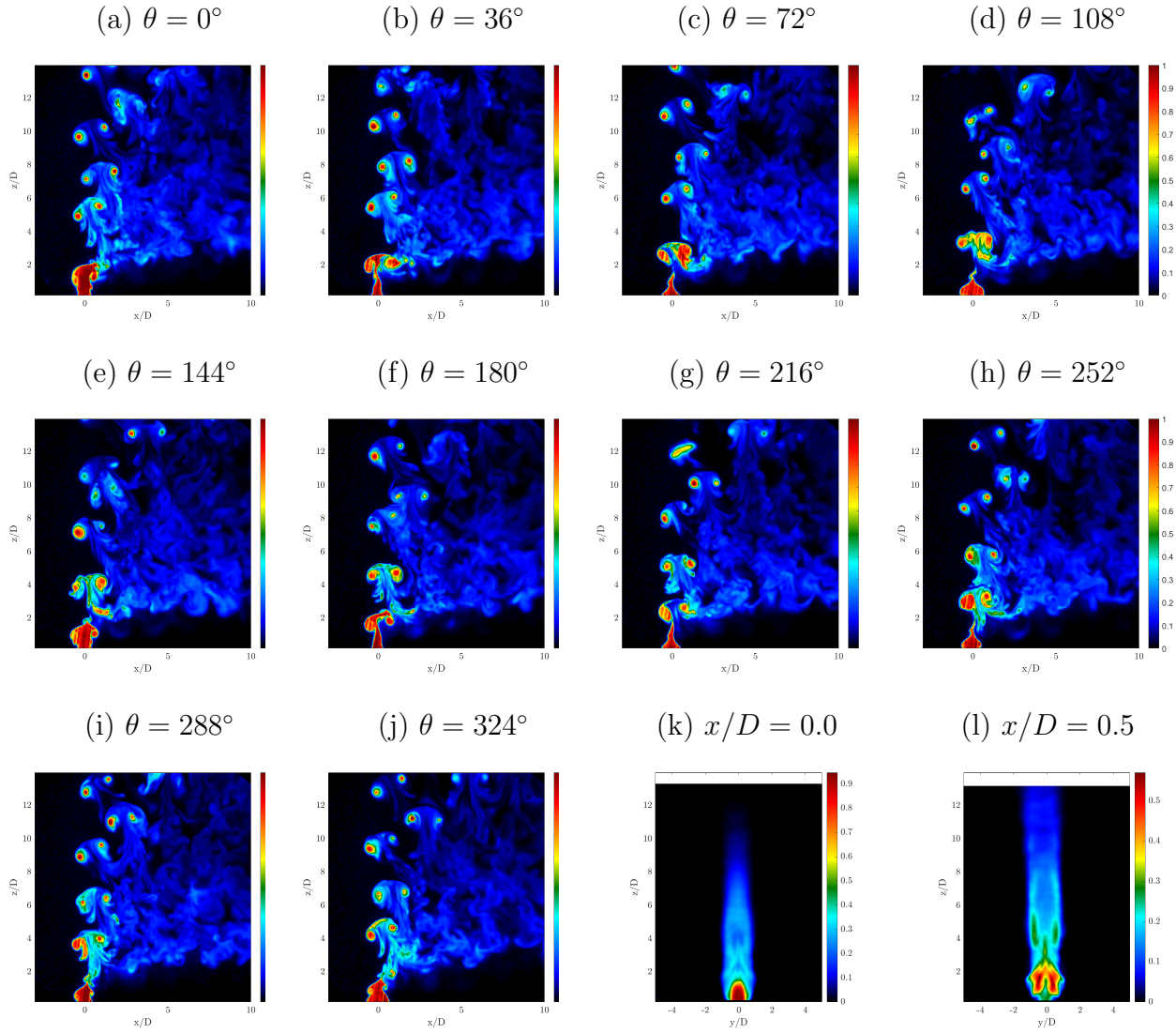

Figure D.17: Representative structural PLIF images of the double-pulse forced AU jet at $J = 10$, for forcing case 0.15.40.55 where (a-j) depict the instantaneous centerplane phase progression for 1 forcing period at every $1/10T$, and (k-l) are mean cross-sectional slices of the jet at $x/D = 0.0$ and $x/D = 0.5$ respectively. The colorbar maximum for the cross-sectional images was scaled so as to allow quantitative comparisons with the scalar intensities noted in the jet centerplane.

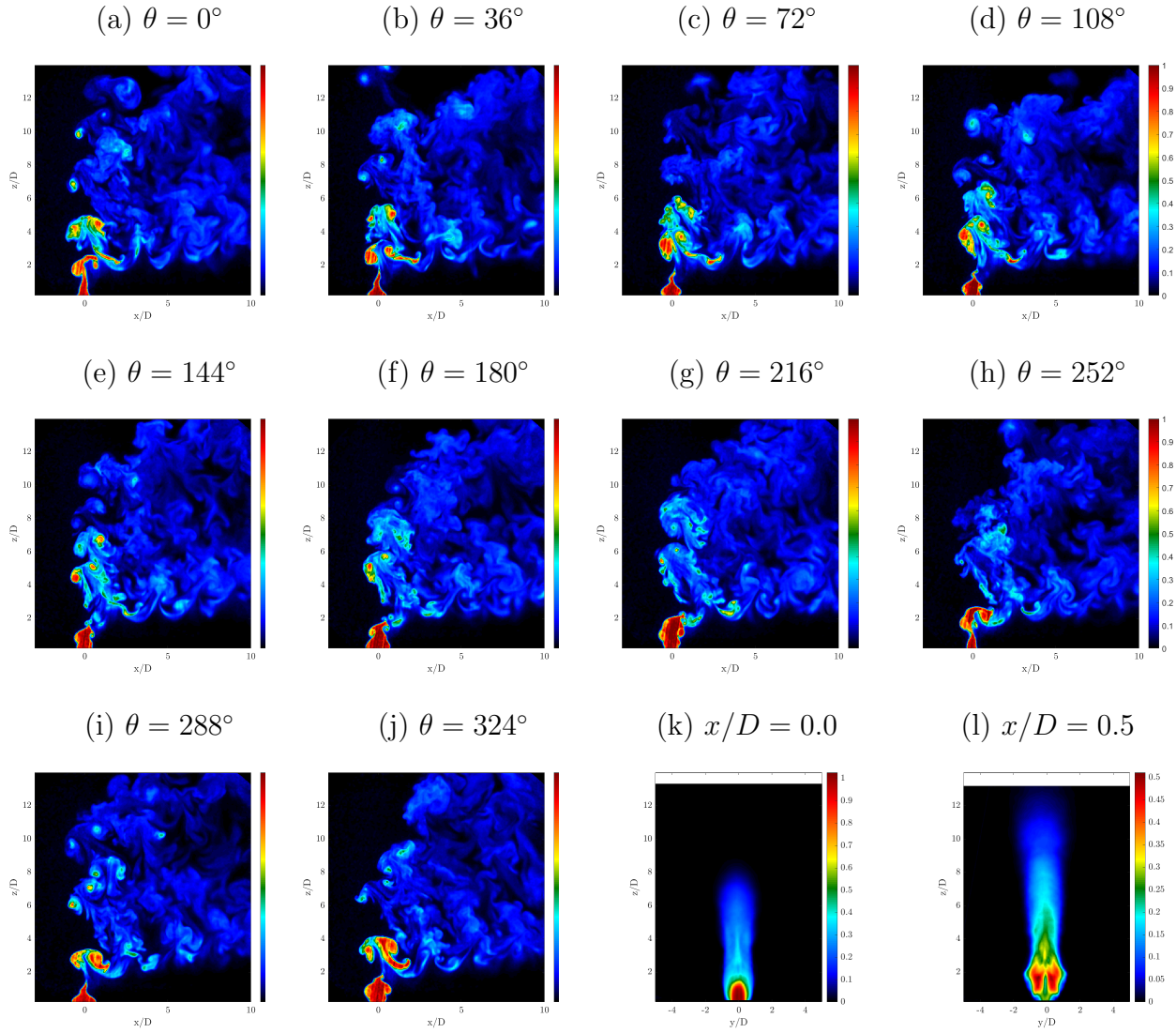

Figure D.18: Representative structural PLIF images of the double-pulse forced AU jet at $J = 10$, for forcing case 0.15.30.45 where (a-j) depict the instantaneous centerplane phase progression for 1 forcing period at every $1/10T$, and (k-l) are mean cross-sectional slices of the jet at $x/D = 0.0$ and $x/D = 0.5$ respectively. The colorbar maximum for the cross-sectional images was scaled so as to allow quantitative comparisons with the scalar intensities noted in the jet centerplane.

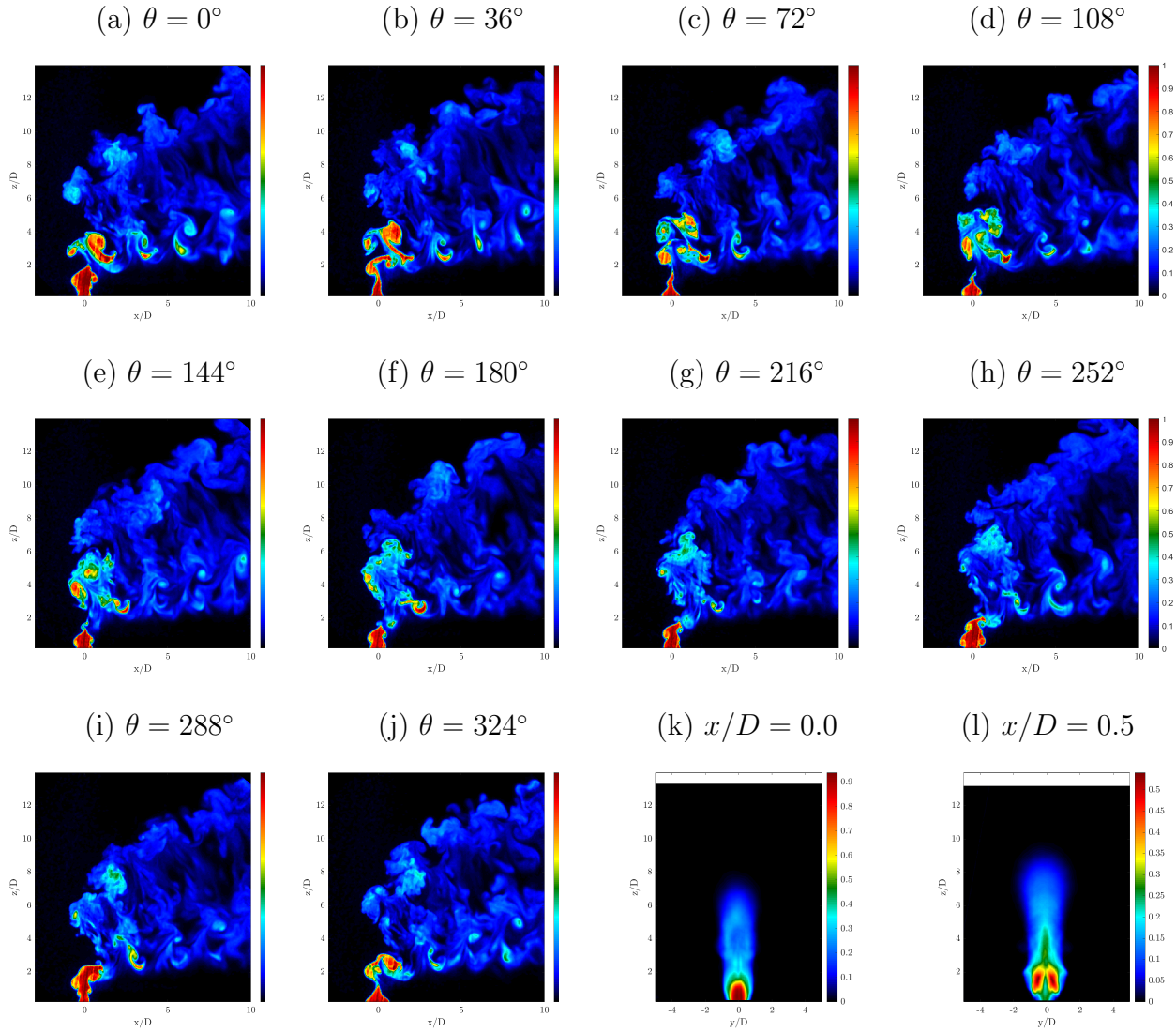

Figure D.19: Representative structural PLIF images of the double-pulse forced AU jet at $J = 10$, for forcing case 0.15.25.40 where (a-j) depict the instantaneous centerplane phase progression for 1 forcing period at every $1/10T$, and (k-l) are mean cross-sectional slices of the jet at $x/D = 0.0$ and $x/D = 0.5$ respectively. The colorbar maximum for the cross-sectional images was scaled so as to allow quantitative comparisons with the scalar intensities noted in the jet centerplane.

D.2 Vortex Rings and Jet Dynamics

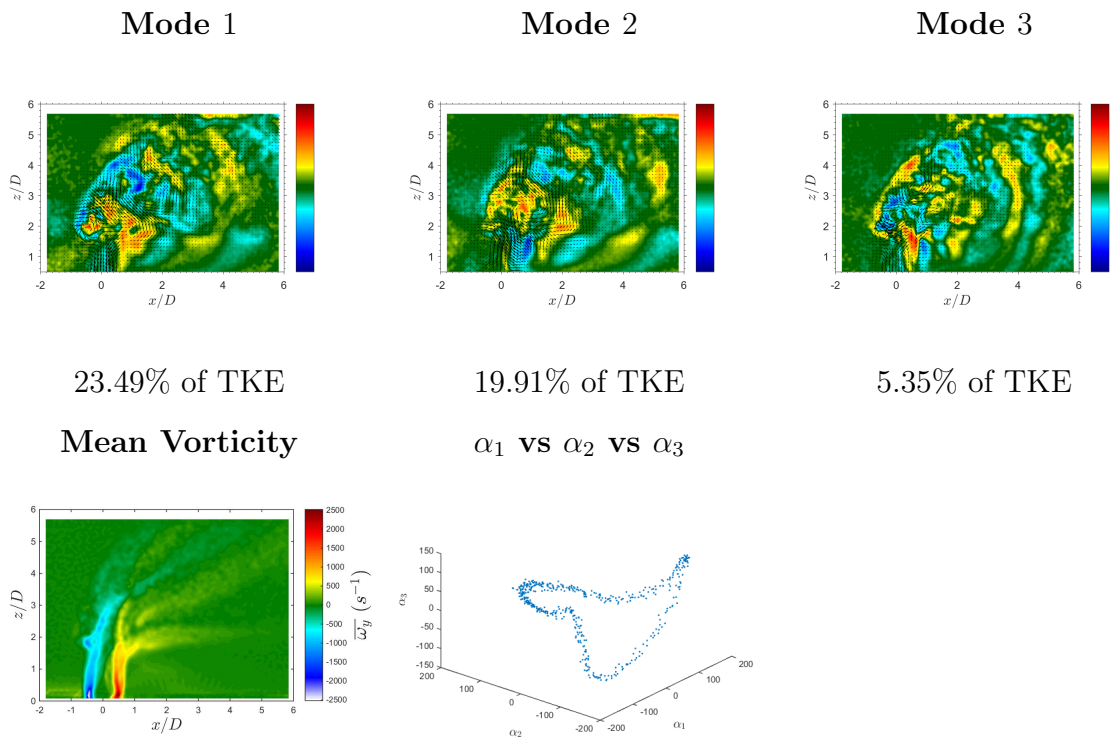

Figure D.20: PIV based POD mode structures extracted from 600 instantaneous snapshots of the centerplane velocity field for the 0.35.40.55 double-pulse waveform axisymmetric excitation of the jet at $u'_{j,rms}/U_j = 0.50$, along with the mode coefficient plot of α_1 vs α_2 vs α_3, and a representation of the mean vorticity of the jet along the centerplane. The modes are sorted according to their respective percentages of total kinetic energy fluctuation content, while the colorbar in each mode image represents the mode scaled by its own norm and the mean jet velocity at the jet exit U_j.

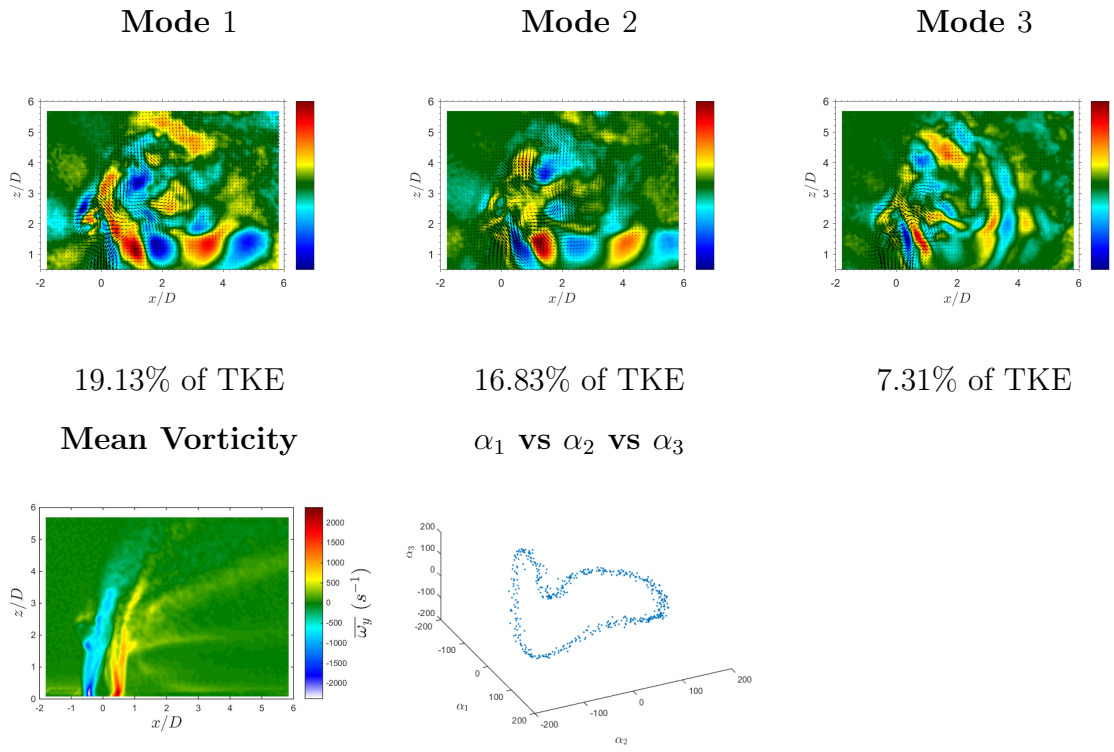

Figure D.21: PIV based POD mode structures extracted from 600 instantaneous snapshots of the centerplane velocity field for the 0.35.45.60 double-pulse waveform axisymmetric excitation of the jet at $u'_{j,rms}/U_j = 0.50$, along with the mode coefficient plot of α_1 vs α_2 vs α_3, and a representation of the mean vorticity of the jet along the centerplane. The modes are sorted according to their respective percentages of total kinetic energy fluctuation content, while the colorbar in each mode image represents the mode scaled by its own norm and the mean jet velocity at the jet exit U_j.

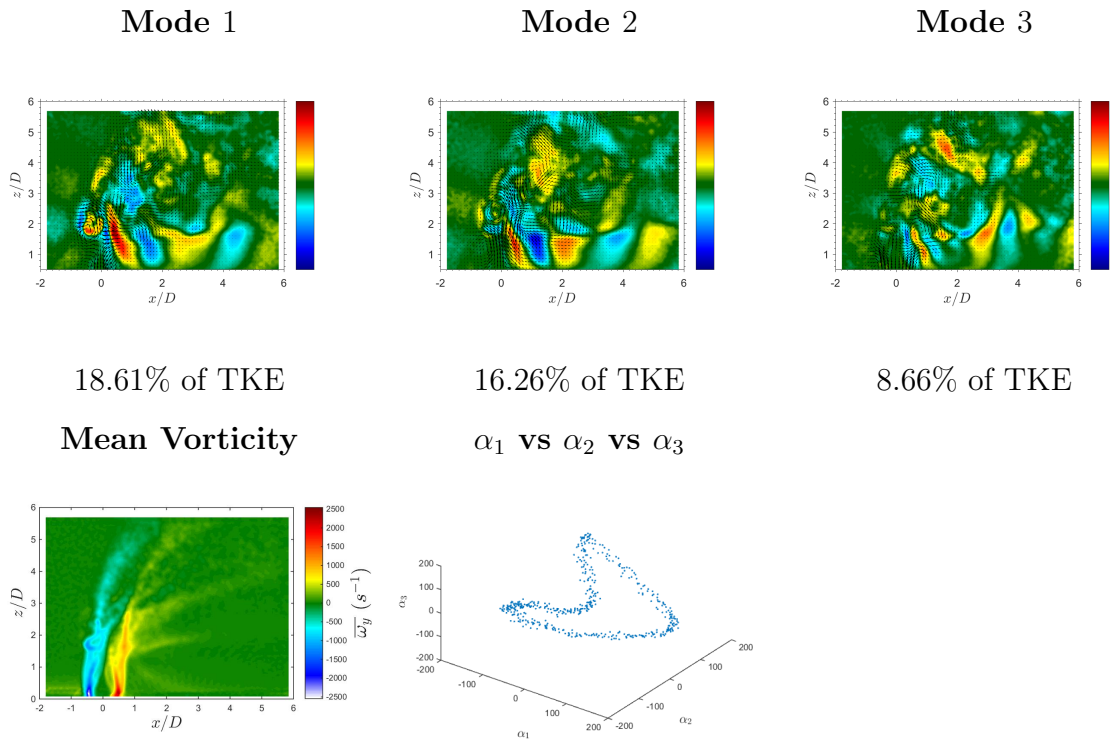

Figure D.22: PIV based POD mode structures extracted from 600 instantaneous snapshots of the centerplane velocity field for the 0.35.50.65 double-pulse waveform axisymmetric excitation of the jet at $u'_{j,rms}/U_j = 0.50$, along with the mode coefficient plot of α_1 vs α_2 vs α_3, and a representation of the mean vorticity of the jet along the centerplane. The modes are sorted according to their respective percentages of total kinetic energy fluctuation content, while the colorbar in each mode image represents the mode scaled by its own norm and the mean jet velocity at the jet exit U_j.

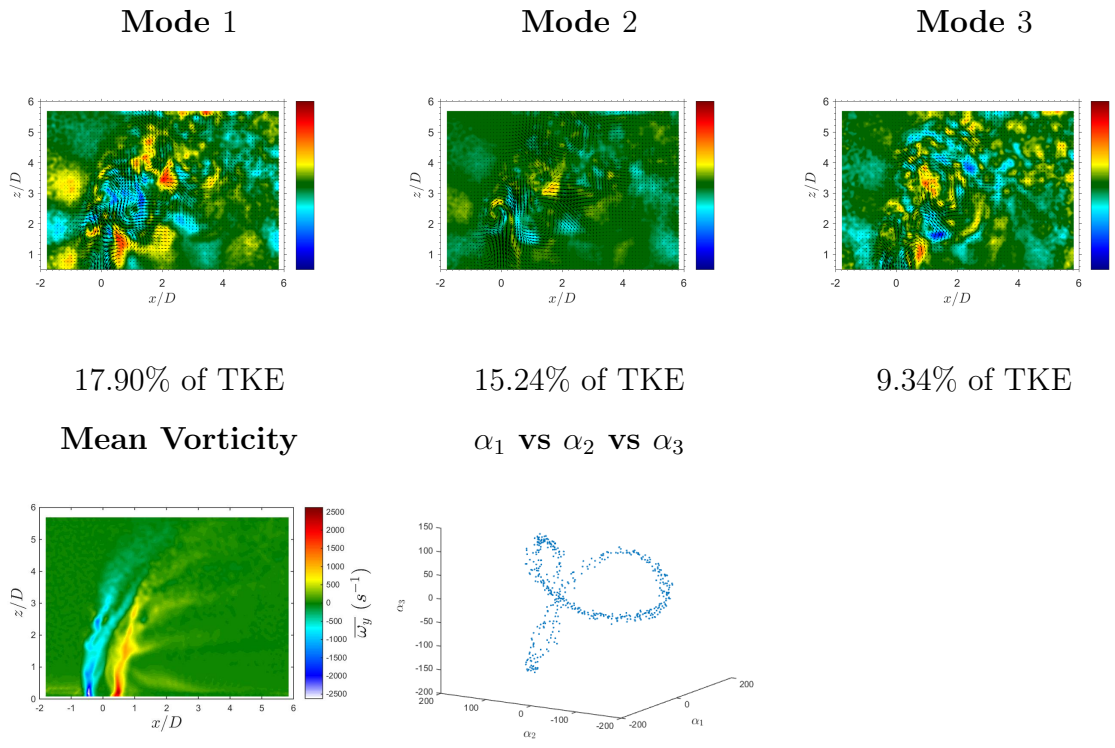

Figure D.23: PIV based POD mode structures extracted from 600 instantaneous snapshots of the centerplane velocity field for the 0.35.55.70 double-pulse waveform axisymmetric excitation of the jet at $u'_{j,rms}/U_j = 0.50$, along with the mode coefficient plot of α_1 vs α_2 vs α_3, and a representation of the mean vorticity of the jet along the centerplane. The modes are sorted according to their respective percentages of total kinetic energy fluctuation content, while the colorbar in each mode image represents the mode scaled by its own norm and the mean jet velocity at the jet exit U_j.

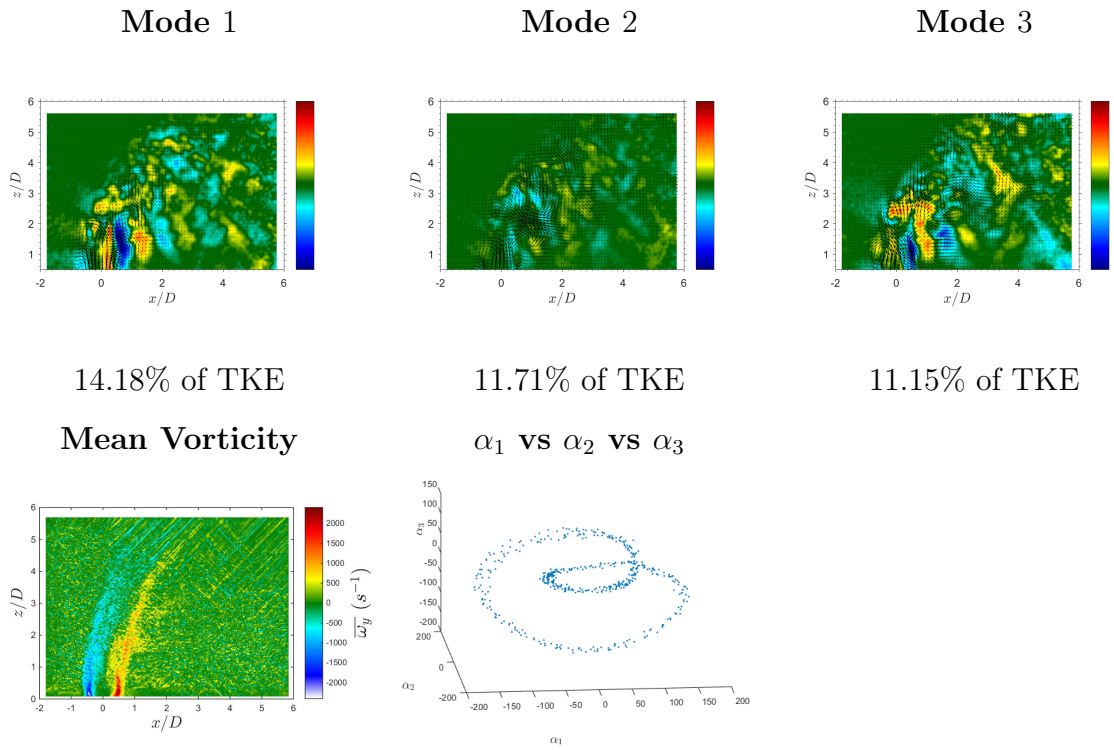

Figure D.24: PIV based POD mode structures extracted from 600 instantaneous snapshots of the centerplane velocity field for the 0.35.60.75 double-pulse waveform axisymmetric excitation of the jet at $u'_{j,rms}/U_j = 0.50$, along with the mode coefficient plot of α_1 vs α_2 vs α_3, and a representation of the mean vorticity of the jet along the centerplane. The modes are sorted according to their respective percentages of total kinetic energy fluctuation content, while the colorbar in each mode image represents the mode scaled by its own norm and the mean jet velocity at the jet exit U_j.

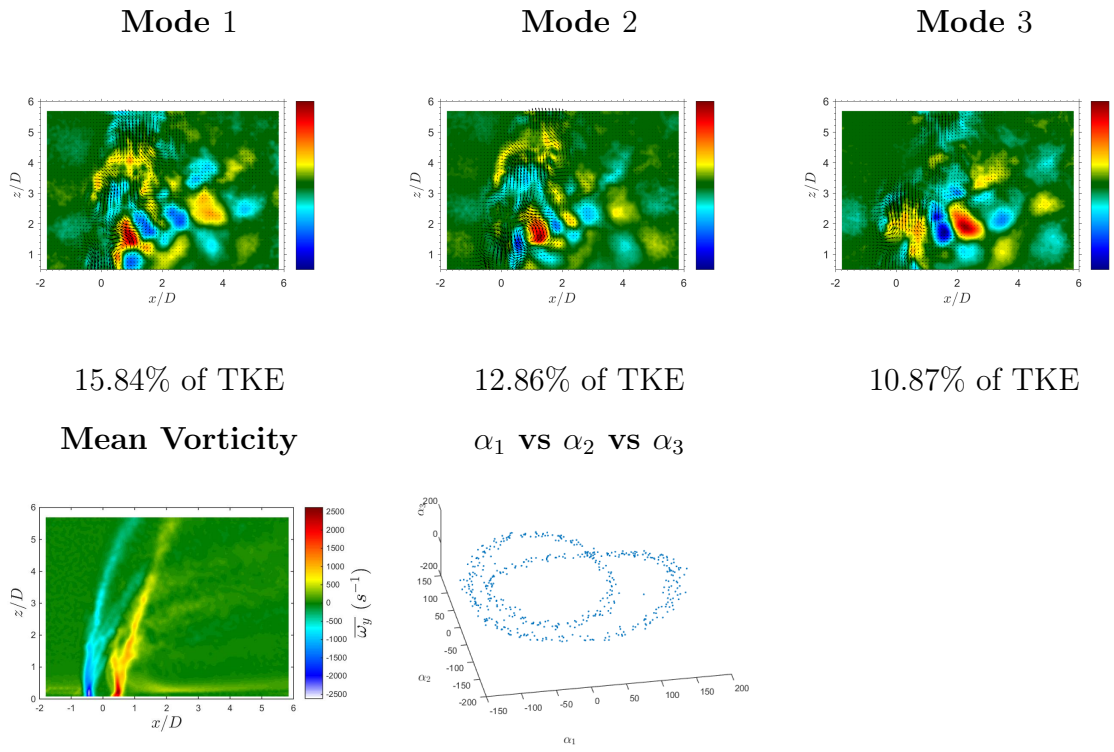

Figure D.25: PIV based POD mode structures extracted from 600 instantaneous snapshots of the centerplane velocity field for the 0.35.70.85 double-pulse waveform axisymmetric excitation of the jet at $u'_{j,rms}/U_j = 0.50$, along with the mode coefficient plot of α_1 vs α_2 vs α_3, and a representation of the mean vorticity of the jet along the centerplane. The modes are sorted according to their respective percentages of total kinetic energy fluctuation content, while the colorbar in each mode image represents the mode scaled by its own norm and the mean jet velocity at the jet exit U_j.

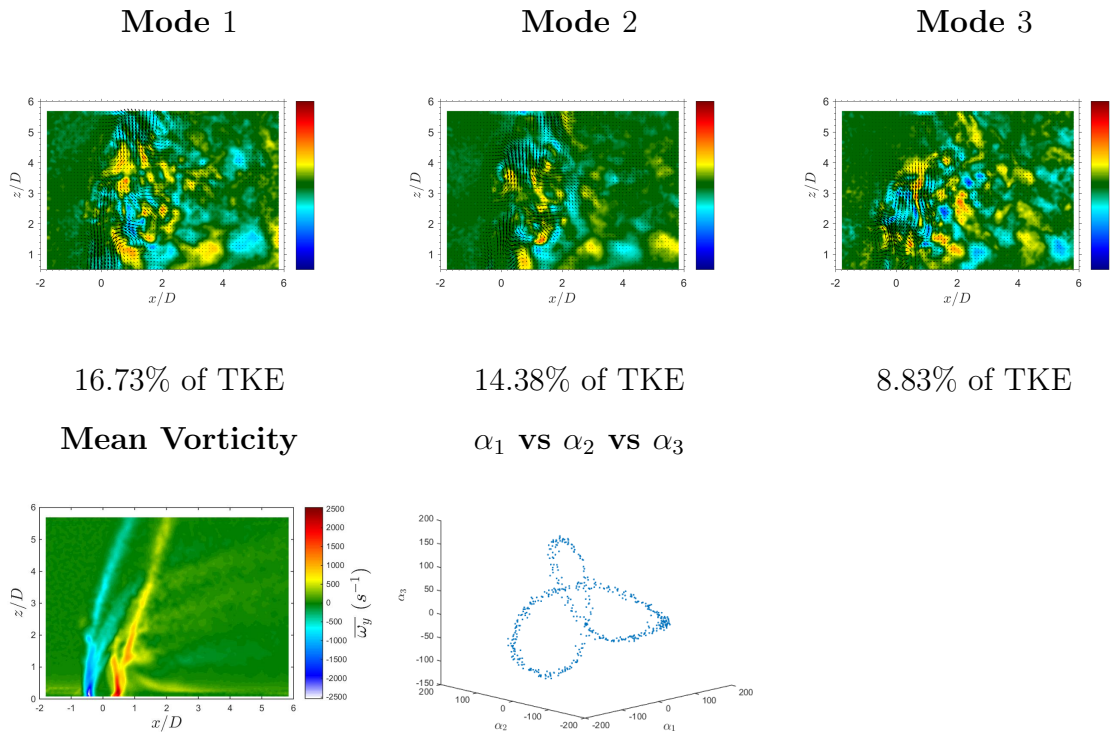

Figure D.26: PIV based POD mode structures extracted from 600 instantaneous snapshots of the centerplane velocity field for the 0.35.75.90 double-pulse waveform axisymmetric excitation of the jet at $u'_{j,rms}/U_j = 0.50$, along with the mode coefficient plot of α_1 vs α_2 vs α_3, and a representation of the mean vorticity of the jet along the centerplane. The modes are sorted according to their respective percentages of total kinetic energy fluctuation content, while the colorbar in each mode image represents the mode scaled by its own norm and the mean jet velocity at the jet exit U_j.

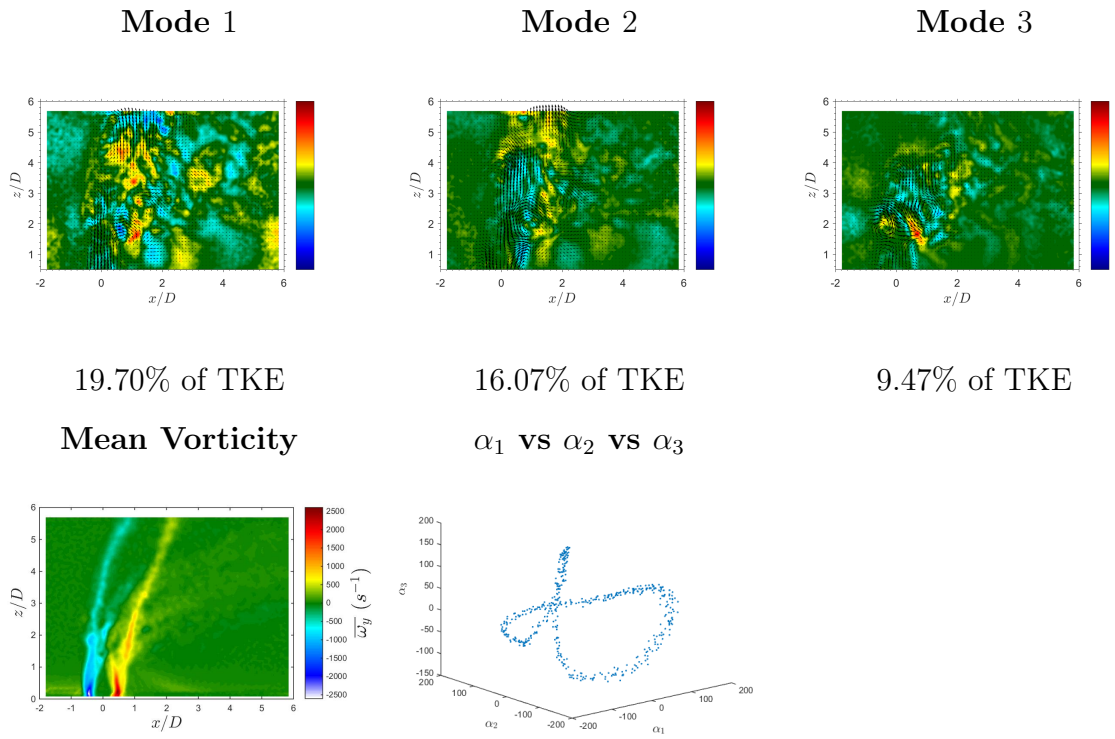

Figure D.27: PIV based POD mode structures extracted from 600 instantaneous snapshots of the centerplane velocity field for the 0.35.80.95 double-pulse waveform axisymmetric excitation of the jet at $u'_{j,rms}/U_j = 0.50$, along with the mode coefficient plot of α_1 vs α_2 vs α_3, and a representation of the mean vorticity of the jet along the centerplane. The modes are sorted according to their respective percentages of total kinetic energy fluctuation content, while the colorbar in each mode image represents the mode scaled by its own norm and the mean jet velocity at the jet exit U_j.

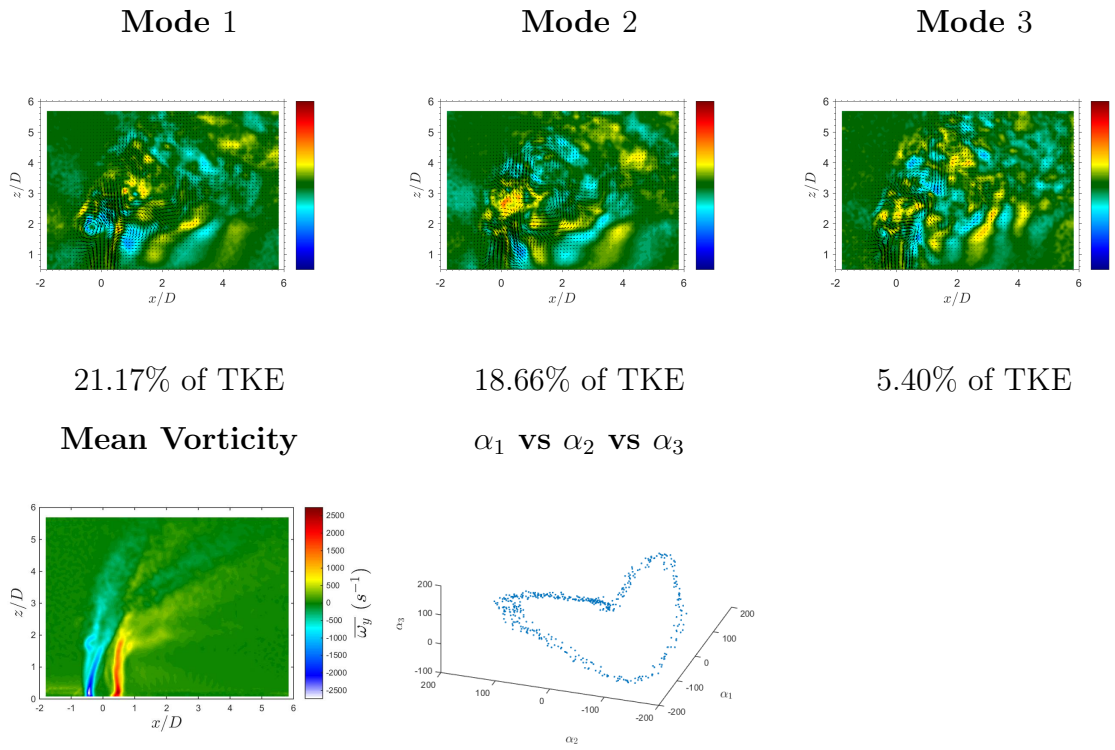

Figure D.28: PIV based POD mode structures extracted from 600 instantaneous snapshots of the centerplane velocity field for the 0.45.50.65 double-pulse waveform axisymmetric excitation of the jet at $u'_{j,rms}/U_j = 0.50$, along with the mode coefficient plot of α_1 vs α_2 vs α_3, and a representation of the mean vorticity of the jet along the centerplane. The modes are sorted according to their respective percentages of total kinetic energy fluctuation content, while the colorbar in each mode image represents the mode scaled by its own norm and the mean jet velocity at the jet exit U_j.

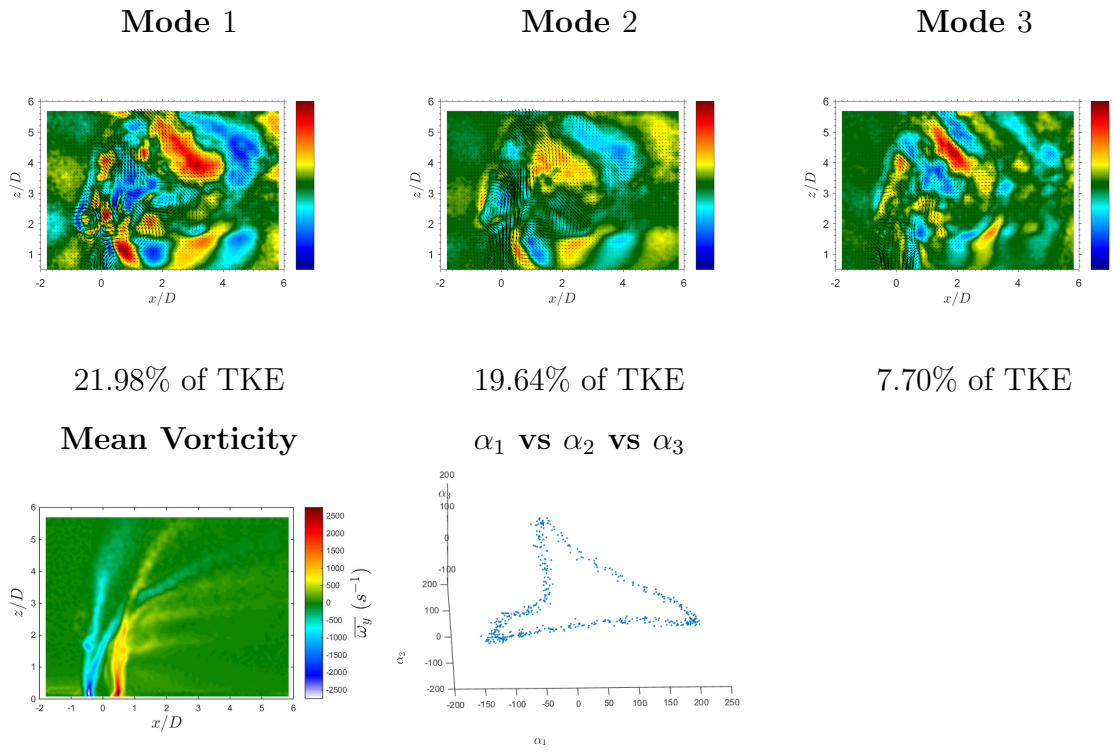

Figure D.29: PIV based POD mode structures extracted from 600 instantaneous snapshots of the centerplane velocity field for the 0.45.55.70 double-pulse waveform axisymmetric excitation of the jet at $u'_{j,rms}/U_j = 0.50$, along with the mode coefficient plot of α_1 vs α_2 vs α_3, and a representation of the mean vorticity of the jet along the centerplane. The modes are sorted according to their respective percentages of total kinetic energy fluctuation content, while the colorbar in each mode image represents the mode scaled by its own norm and the mean jet velocity at the jet exit U_j.

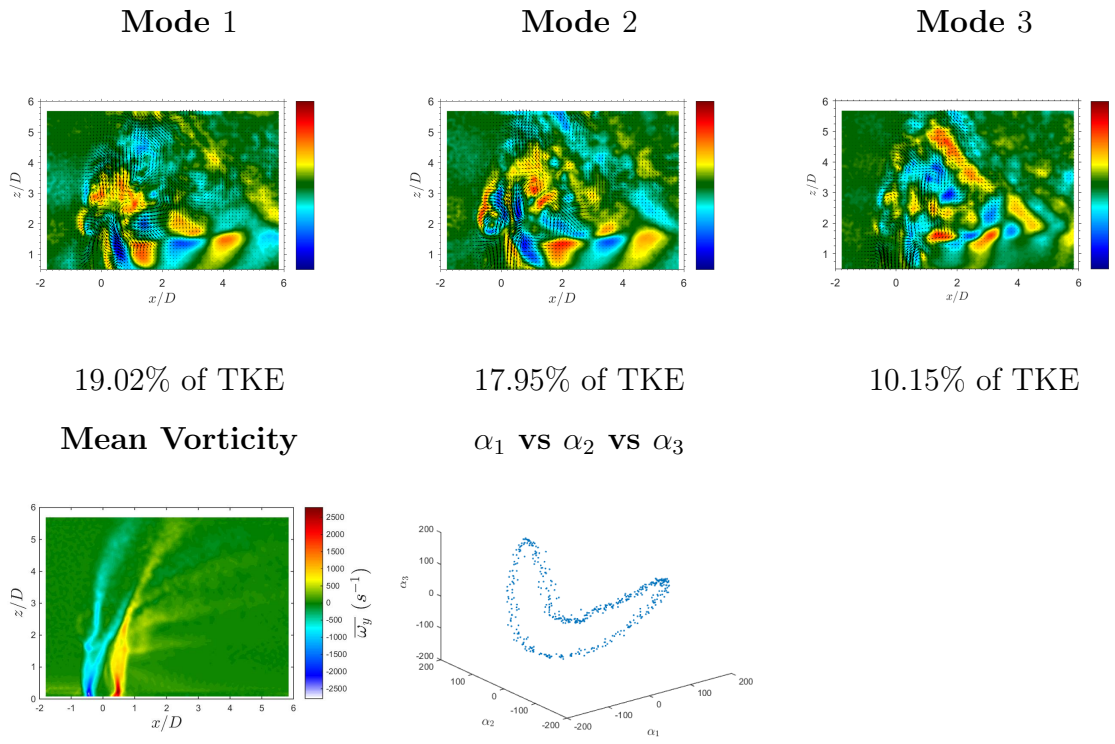

Figure D.30: PIV based POD mode structures extracted from 600 instantaneous snapshots of the centerplane velocity field for the 0.45.60.75 double-pulse waveform axisymmetric excitation of the jet at $u'_{j,rms}/U_j = 0.50$, along with the mode coefficient plot of α_1 vs α_2 vs α_3, and a representation of the mean vorticity of the jet along the centerplane. The modes are sorted according to their respective percentages of total kinetic energy fluctuation content, while the colorbar in each mode image represents the mode scaled by its own norm and the mean jet velocity at the jet exit U_j.

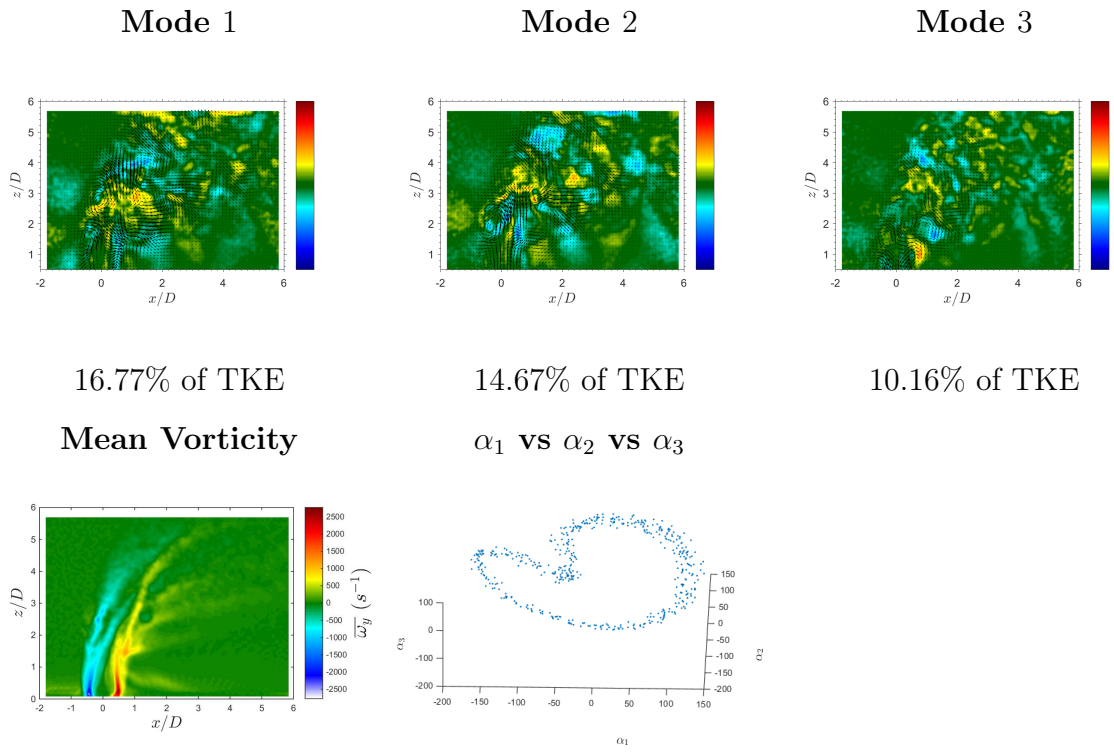

Figure D.31: PIV based POD mode structures extracted from 600 instantaneous snapshots of the centerplane velocity field for the 0.45.65.80 double-pulse waveform axisymmetric excitation of the jet at $u'_{j,rms}/U_j = 0.50$, along with the mode coefficient plot of α_1 vs α_2 vs α_3, and a representation of the mean vorticity of the jet along the centerplane. The modes are sorted according to their respective percentages of total kinetic energy fluctuation content, while the colorbar in each mode image represents the mode scaled by its own norm and the mean jet velocity at the jet exit U_j.

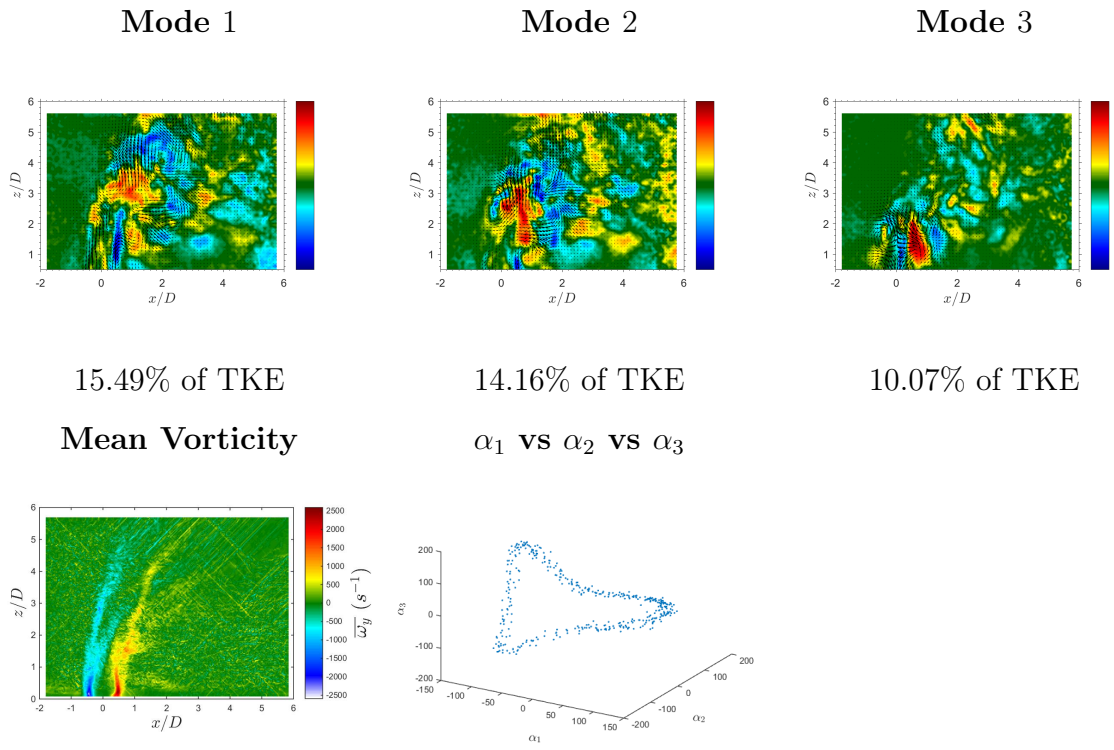

Figure D.32: PIV based POD mode structures extracted from 600 instantaneous snapshots of the centerplane velocity field for the 0.45.70.85 double-pulse waveform axisymmetric excitation of the jet at $u'_{j,rms}/U_j = 0.50$, along with the mode coefficient plot of α_1 vs α_2 vs α_3, and a representation of the mean vorticity of the jet along the centerplane. The modes are sorted according to their respective percentages of total kinetic energy fluctuation content, while the colorbar in each mode image represents the mode scaled by its own norm and the mean jet velocity at the jet exit U_j.

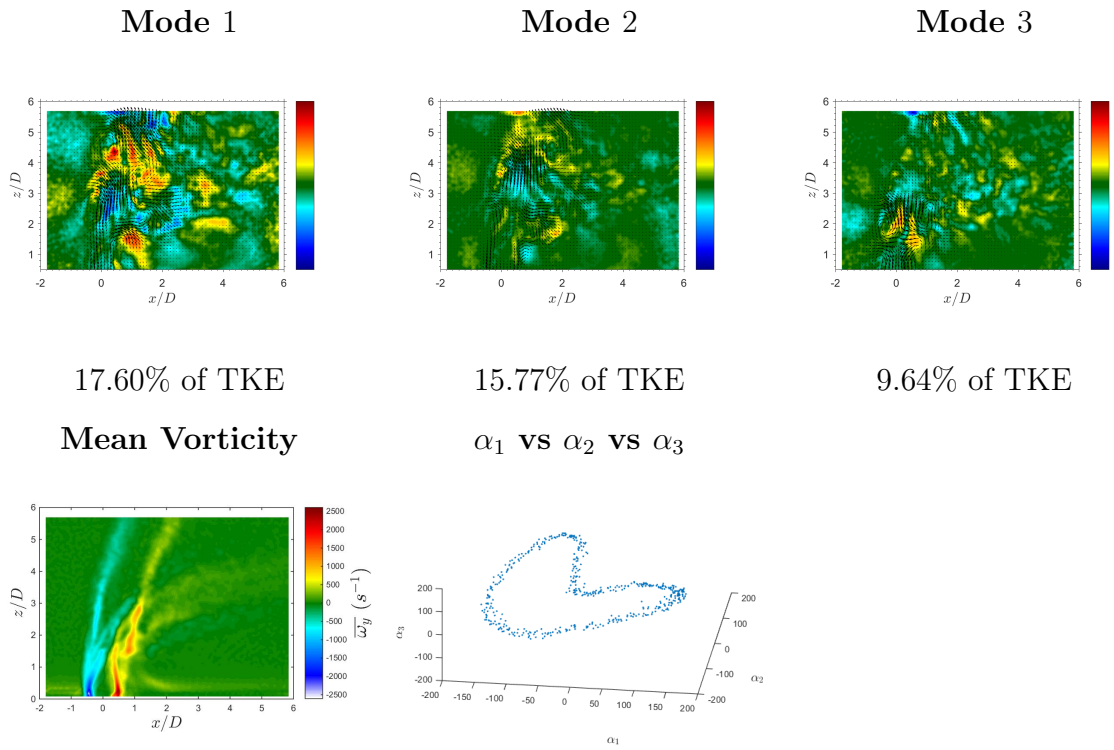

Figure D.33: PIV based POD mode structures extracted from 600 instantaneous snapshots of the centerplane velocity field for the 0.45.75.90 double-pulse waveform axisymmetric excitation of the jet at $u'_{j,rms}/U_j = 0.50$, along with the mode coefficient plot of α_1 vs α_2 vs α_3, and a representation of the mean vorticity of the jet along the centerplane. The modes are sorted according to their respective percentages of total kinetic energy fluctuation content, while the colorbar in each mode image represents the mode scaled by its own norm and the mean jet velocity at the jet exit U_j.

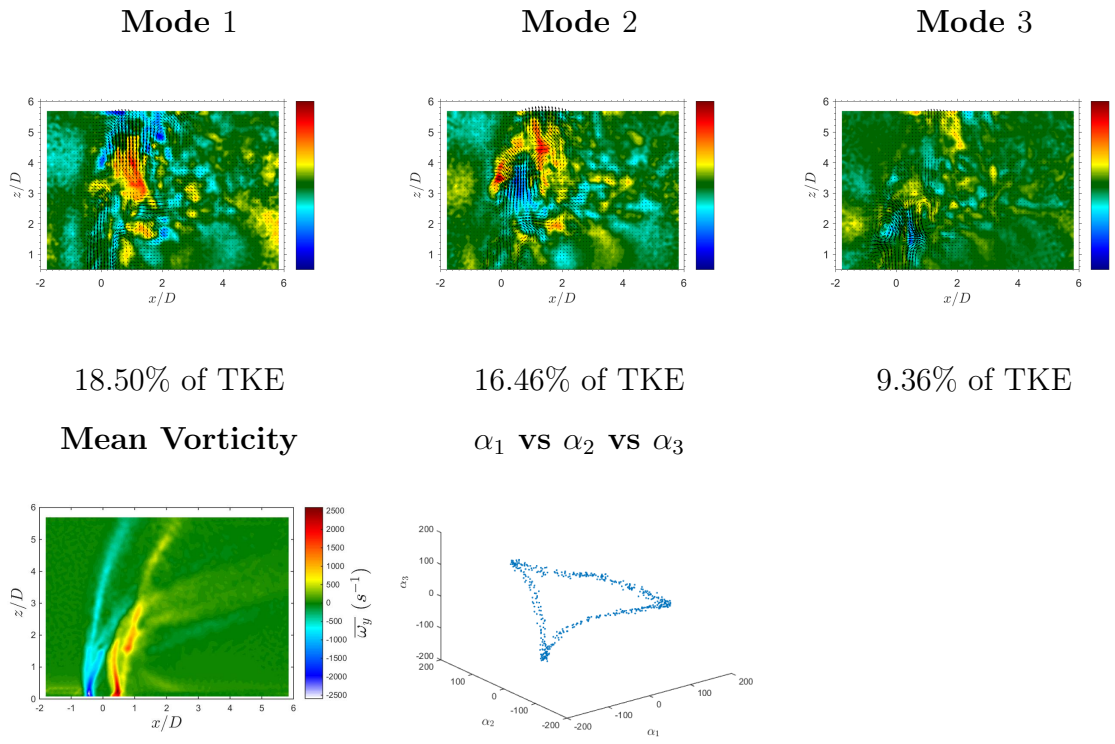

Figure D.34: PIV based POD mode structures extracted from 600 instantaneous snapshots of the centerplane velocity field for the 0.45.80.95 double-pulse waveform axisymmetric excitation of the jet at $u'_{j,rms}/U_j = 0.50$, along with the mode coefficient plot of α_1 vs α_2 vs α_3, and a representation of the mean vorticity of the jet along the centerplane. The modes are sorted according to their respective percentages of total kinetic energy fluctuation content, while the colorbar in each mode image represents the mode scaled by its own norm and the mean jet velocity at the jet exit U_j.

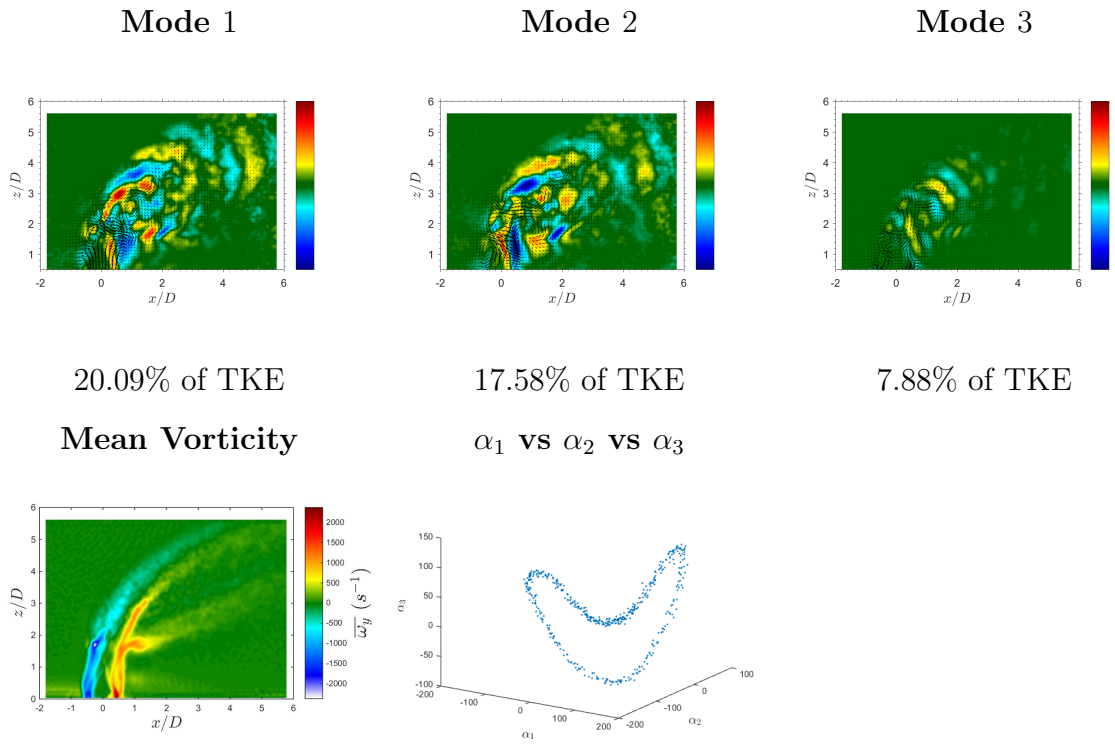

Figure D.35: PIV based POD mode structures extracted from 600 instantaneous snapshots of the centerplane velocity field for the $f_f = 110\ Hz$ square wave excitation of the jet with $\alpha = 20\%$ at $u'_{j,rms}/U_j = 0.50$, along with the mode coefficient plot of α_1 vs α_2 vs α_3, and a representation of the mean vorticity of the jet along the centerplane. The modes are sorted according to their respective percentages of total kinetic energy fluctuation content, while the colorbar in each mode image represents the mode scaled by its own norm and the mean jet velocity at the jet exit U_j.

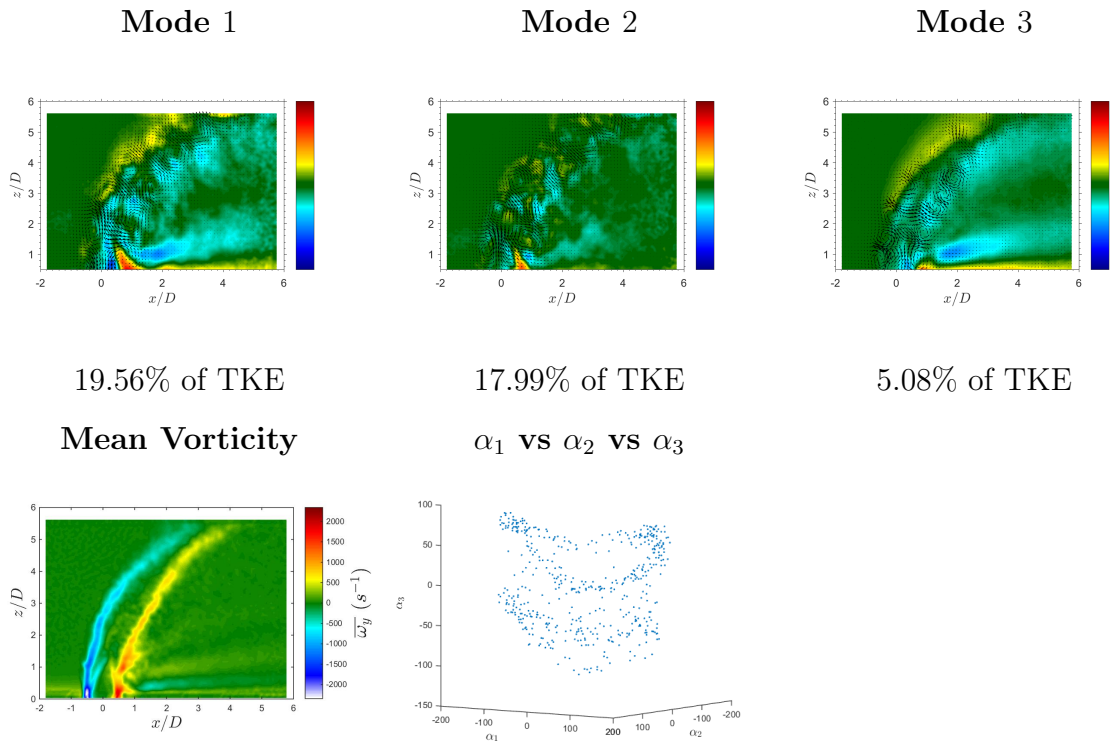

Figure D.36: PIV based POD mode structures extracted from 600 instantaneous snapshots of the centerplane velocity field for the $f_f = 110\ Hz$ square wave excitation of the jet with $\alpha = 30\%$ at $u'_{j,rms}/U_j = 0.50$, along with the mode coefficient plot of α_1 vs α_2 vs α_3, and a representation of the mean vorticity of the jet along the centerplane. The modes are sorted according to their respective percentages of total kinetic energy fluctuation content, while the colorbar in each mode image represents the mode scaled by its own norm and the mean jet velocity at the jet exit U_j.

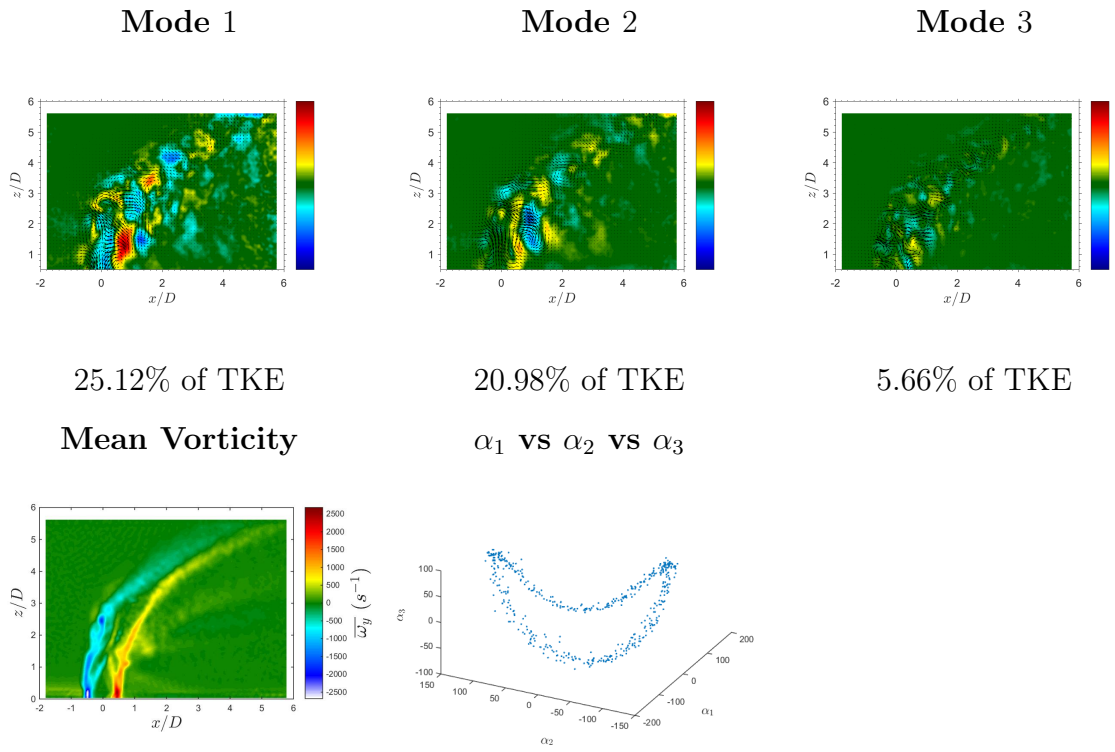

Figure D.37: PIV based POD mode structures extracted from 600 instantaneous snapshots of the centerplane velocity field for the $f_f = 110\ Hz$ square wave excitation of the jet with $\alpha = 40\%$ at $u'_{j,rms}/U_j = 0.50$, along with the mode coefficient plot of α_1 vs α_2 vs α_3, and a representation of the mean vorticity of the jet along the centerplane. The modes are sorted according to their respective percentages of total kinetic energy fluctuation content, while the colorbar in each mode image represents the mode scaled by its own norm and the mean jet velocity at the jet exit U_j.

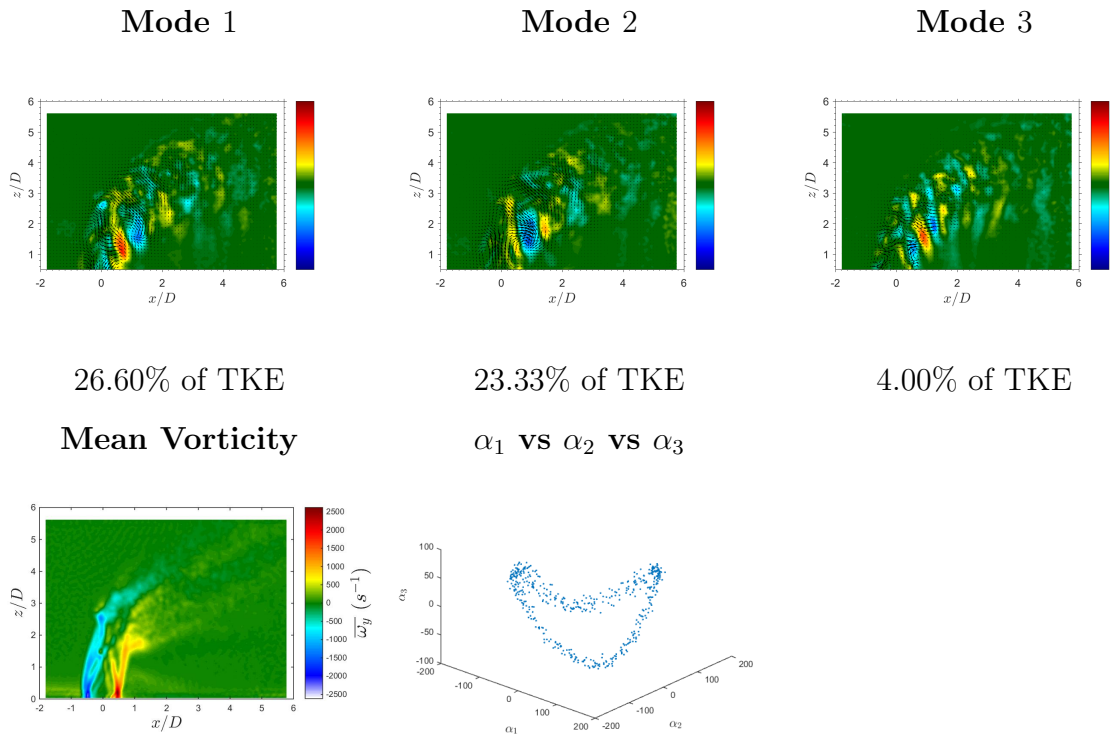

Figure D.38: PIV based POD mode structures extracted from 600 instantaneous snapshots of the centerplane velocity field for the $f_f = 110\ Hz$ square wave excitation of the jet with $\alpha = 50\%$ at $u'_{j,rms}/U_j = 0.50$, along with the mode coefficient plot of α_1 vs α_2 vs α_3, and a representation of the mean vorticity of the jet along the centerplane. The modes are sorted according to their respective percentages of total kinetic energy fluctuation content, while the colorbar in each mode image represents the mode scaled by its own norm and the mean jet velocity at the jet exit U_j.

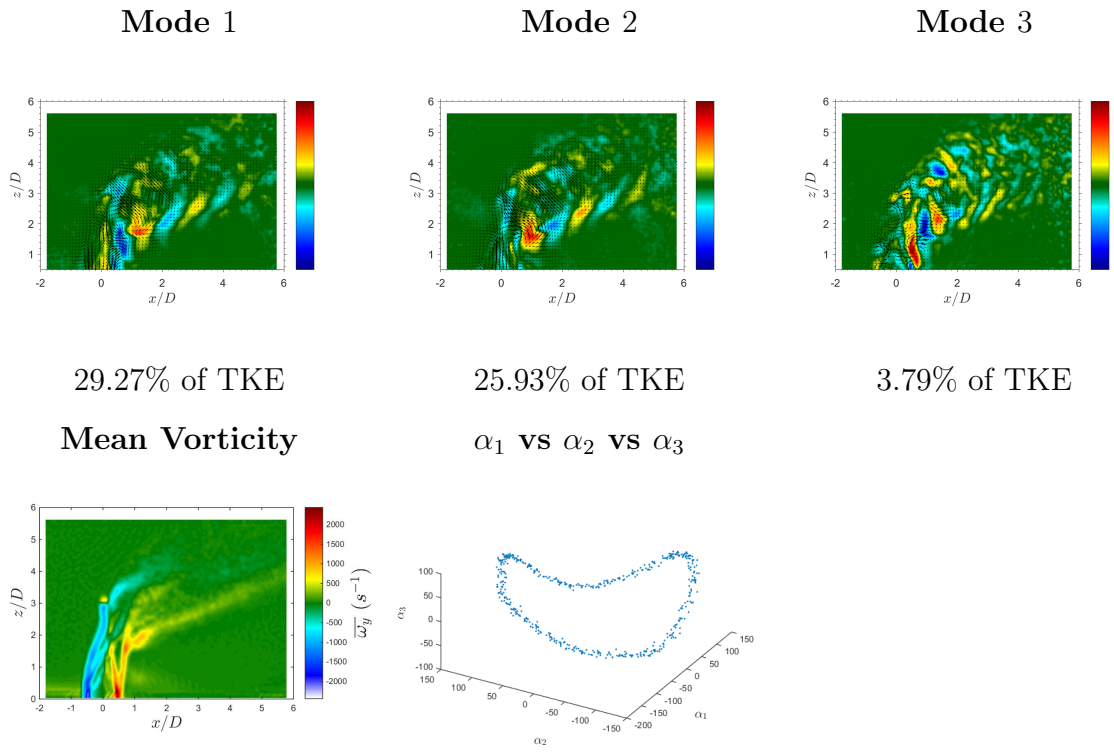

Figure D.39: PIV based POD mode structures extracted from 600 instantaneous snapshots of the centerplane velocity field for the $f_f = 110\ Hz$ square wave excitation of the jet with $\alpha = 60\%$ at $u'_{j,rms}/U_j = 0.50$, along with the mode coefficient plot of α_1 vs α_2 vs α_3, and a representation of the mean vorticity of the jet along the centerplane. The modes are sorted according to their respective percentages of total kinetic energy fluctuation content, while the colorbar in each mode image represents the mode scaled by its own norm and the mean jet velocity at the jet exit U_j.

D.3 Alternative Waveforms

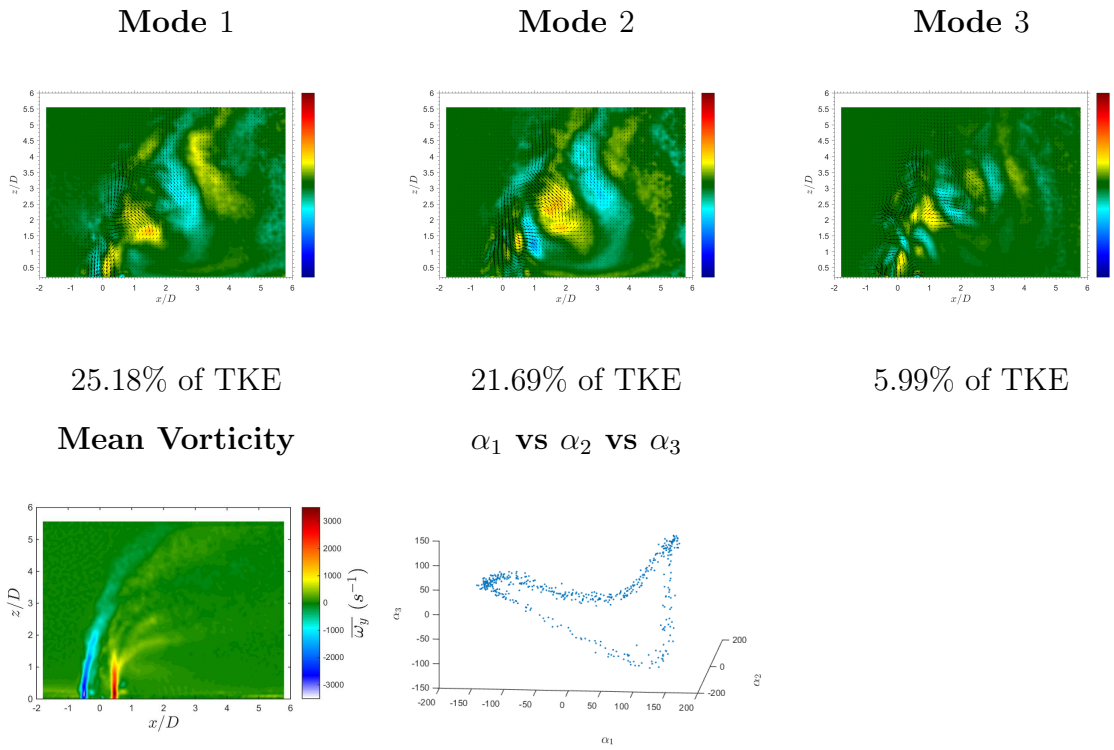

Figure D.40: PIV based POD mode structures extracted from 600 instantaneous snapshots of the centerplane velocity field for the $f_f = 110\ Hz$ sawtooth excitation of the jet with at $u'_{j,rms}/U_j = 0.50$, along with the mode coefficient plot of α_1 vs α_2 vs α_3, and a representation of the mean vorticity of the jet along the centerplane. The modes are sorted according to their respective percentages of total kinetic energy fluctuation content, while the colorbar in each mode image represents the mode scaled by its own norm and the mean jet velocity at the jet exit U_j.

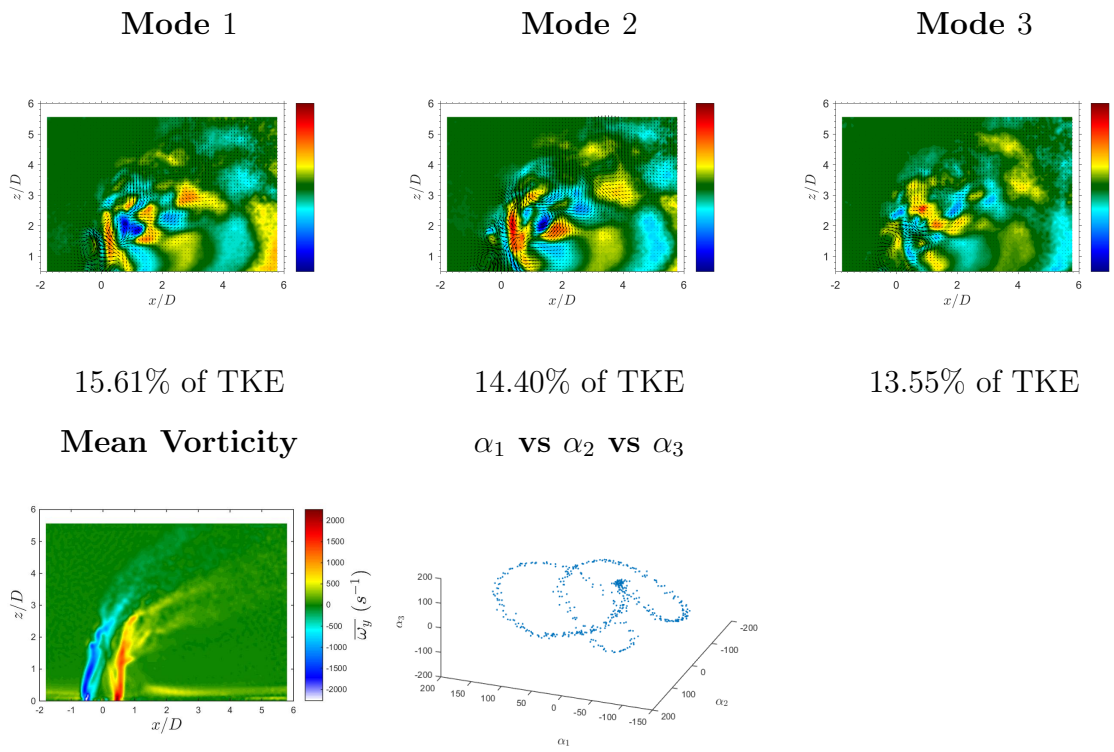

Figure D.41: PIV based POD mode structures extracted from 600 instantaneous snapshots of the centerplane velocity field for the 0.26.42.58.74.84 triple-pulse waveform axisymmetric excitation of the jet at $u'_{j,rms}/U_j = 0.50$, along with the mode coefficient plot of α_1 vs α_2 vs α_3, and a representation of the mean vorticity of the jet along the centerplane. The modes are sorted according to their respective percentages of total kinetic energy fluctuation content, while the colorbar in each mode image represents the mode scaled by its own norm and the mean jet velocity at the jet exit U_j.

Bibliography

J. S. Abbitt, C. Segal, J. C. McDaniel, R. H. Krauss, and R. B. Whitehurst. Experimental supersonic hydrogen combustion employing staged injection behind a rearward-facing step. *Journal of Propulsion and Power*, 9:472–478, 1993.

R. J. Adrian and J. Westerweel. *Particle Image Velocimetry*. Cambridge University Press, New York, 2011.

K. K. Ahuja and W. H. Brown. Shear flow control by mechanical tabs. *AIAA*, 1989. Paper 89-0994.

L. S. de B. Alves, R. E. Kelly, and A. R. Karagozian. Local stability analysis of an inviscid transverse jet. *J. Fluid Mech.*, 581:401–418, 2007.

L. S. de B. Alves, R. E. Kelly, and A. R. Karagozian. Transverse-jet shear-leyer instabilities. part 2. linear analysis for larger jet-to-crossflow velocity ratio. *J. Fluid Mech.*, 602:383–401, 2008.

T. J. Anderson, W. Proscia, and J. M. Cohen. Modulation of a liquid-fuel jet in an unstready crossflow. *Proceedings of AMSE Turbomachinery Expo*, pages 1–9, 2001. Paper 2001-GT-0048.

J. Andreopoulos. On the structure of jets in a crossflow. *J. Fluid Mech.*, 157:163–197, 1985.

S. Bagheri, P. Schlatter, P. J. Schmid, and D. S. Henningson. Global stability of a jet in crossflow. *J. Fluid Mech.*, 624:33–44, 2009.

C. J. Baker. The turbulent horseshoe vortex. *Journal of Wind Engineering and Industrial Aerodynamics*, 6:9–23, 1980.

J. M. M. Barata. Multiple jet/wall/cross-wind interaction relevant to vstol ground effects. *AIAA Aviation Forum*, 2013.

J. B. Barlow, W. H. Rae Jr., and A. Pope. *Low Speed Wind Tunnel Testing*. Wiley-Interscience, 3rd edition, 1999.

G. Batchelor and A. Gill. Analysis of the stability of axisymmetric jets. *J. Fluid Mech.*, 14 (4):529–551, 1962.

J. Beer and N. Chigier. *Combustion Aerodynamics*. Elsevier Science Ltd, 1972.

A. Ben-Yakar. *Experimental Investigation of Mixing and Ignition of Transverse Jets in Supersonic Crossflows*. PhD thesis, Stanford University, 2000.

A. Ben-Yakar, M. R. Kamel, C. I. Morris, and R. K. Hanson. Hypersonic combustion and mixing studies using simultaneous oh-plif and schlieren imaging. *36th AIAA Aerospace Science Meeting and Exhibit*, 1998. AIAA Paper 98-0940.

A. Besnard. *External Asymmetric Forcing of Convectively Unstable Transverse Jets*. Phd dissertation, University of California, Los Angeles, 2019.

G. Binder and M. Favre-Marinet. Mixing improvements in pulsating turbulent jets. *ASME Symposium on Fluid Mechanics of Mixing*, pages 167–172, 1973.

R. B. Bird, W. E. Stewart, and E. N. Lightfoot. *Transport Phenomena*. John Wiley & Sons, New York, 1960.

J. N. Blanchard, Y. Brunet, and A. Merlen. Influence of a counter rotating vortex pair on the stability of a jet in crossflow: an experimental study by flow visualizations. *Experiments in Fluids*, 26:63–74, 1999.

P. Blossey, S. Narayanan, and T. R. Bewley. Dynamics and control of a jet in a cross-flow: direct numerical simulations and experiments. *Proceedings of IUTAM Symposium on Turbulent Mixing and Combustion*, 2001.

H. Bockhorn, D. Mewes, W. Peukert, and H.-J. Warnecke, editors. *Micro and Macro Mixing*. Springer, 2010.

D. G. Bogard and K. A. Thole. Gas turbine film cooling. *Journal of Propulsion and Power*, 22(2):249–270, 2005.

D. G. Bohl and J. F. Foss. Characteristics of the velocity and streamwise vorticity fields in a developing tabbed jet. *AIAA*, 1995. Paper 95-0102.

J. P. Bons, R. Sondergaard, and R. B. River. The fluid dynamics of lpt blade separation control using pulsed jets. *Journal of Turbomachinery*, 124(1):77–85, 2002.

C. T. Bowman. Control of combustion-generated nitrogen oxide emissions: Technology driven by regulation. *Twenty-Fourth Symposium on Combustion*, 24:859–878, 1992.

L. J. S. Bradbury and A. H. Khadem. The distortion of a jet by tabs. *Journal of FLuid Mechanics*, 70(4):801–813, 1975.

J. E. Broadwell and R. E. Breidenthal. Structure and mixing of a transverse jet in incompressible flow. *Journal of Fluid Mechanics*, 148:405–412, 1984.

T. W. F. Brown. Some factors in the use of high temperatures in gas turbines. *Proceedings of the Institution of Mechanical Engineers*, 162(1):167–185, 1950.

T. A. Brzustowski, S. Gollahalli, and H. Sullivan. The turbulent hydrogen diffusion flame in a crosswind. *Combustion Science and Technology*, 58:407–430, 1977.

A. Bunyajitradulya and S. Sathapornnanon. Sensitivity to tab disturbance of the mean flow structure of nonswirling jet and swirling jet in crossflow. *Physics of Fluids*, 17(4), 2005. 045102.

R. Camussi, G. Guj, and A. Stella. Experimental study of a jet in a crossflow at very low reynolds number. *J. Fluid Mech.*, 454:113–144, 2002.

K. Canzonieri. Experimental studies of low density jets in crossflow. Master's thesis, University of California, Los Angeles, 2009.

L. Cao. Practical method for determining the minimum embedding dimension of a scalar time series. *Phys. D Nonlinear Phenom*, 110:43–50, 1997.

M. J. Carletti, C. B. Rogers, and D. E. Parekh. Parametric study of jet mixing enhancement by vortex generators, tabs, and deflector plates. *ASME-Publications-FED*, 237:303–312, 1996.

J. Cassidy and H. T. Falvey. Observations of unsteady flow arising after vortex breakdown. *J. Fluid Mech.*, 41:727–736, 1970.

T. K. Caughy. Response of van der pol's oscillator to random excitation. *Journal of Applied Mechanics*, 1959.

R. C. Chanaud. Observations of oscillatory motion in certain swirling flows. *J. Fluid Mech.*, 21:111–127, 1965.

Y. K. Chang and A. D. Vakili. Dynamics of vortex rings in crossflow. *Physics of Fluids*, 7: 1583–1597, 1995.

P. Chatelain, D. Kivotides, and A. Leonard. Reconnection of colliding vortex rings. *Physical Review Letters*, 90(5), 2003.

J. M. Cimbala, D. R. Stinebring, A. L. Treaster, and M. L. Billet annd M. M. Walters. Experimental investigation of a jet impinging on a ground plane in crossflow. *Journal of Aircraft*, 25(10):923–931, 1988.

N. T. Clemens. *Encyclopedia of Imaging Science and Technology*. Wiley and Sons, 2002.

Wilfried Coenen and Alejandro Sevilla. The structure of the absolutely unstable regions in the near field of low-density jets. *Journal of Fluid Mechanics*, 713:123â€“149, 2012. doi: 10.1017/jfm.2012.441.

J. Cohen and I. Wygnanski. The evolution of instabilities in the axisymmetric jet. part 1. the linear growth of disturbances near the nozzle. *J. Fluid Mech.*, 176:191–219, 1987a.

J. Cohen and I. Wygnanski. The evolution of instabilities in the axisymmetric jet. part 2. the flow resulting from the interaction between two waves. *J. Fluid Mech.*, 176:221–235, 1987b.

F. Colettie, C. J. Elkins, and J. K. Eaton. An inclined jet in crossflow under the effect of streamwise pressure gradients. *Experiments in Fluids*, 54:1589, 2013.

T. C. Corke, F. Shakib, and H. M. Nagib. Mode swelection and resonant phase locking in unstable axisymmetric jets. *J. Fluid Mech.*, 223:253–311, 1991.

S. M. Correa. A review of nox formation under gas-turbine combustion conditions. *Combustion Science and Technology*, 87:329–362, 1993.

S. Corrsin. Simple theory of an idealized turbulent mixer. *AIChE Journal*, 3(3):329–330, 1957.

S. Corrsin. The isotropic turbulent mixer. *AIChE Journal*, 10(6):870–877, 1964.

L. Cortelezzi and A. R. Karagozian. On the formation of the counter-rotating vortex pair in transverse jets. *J. Fluid Mech.*, 446:347–373, 2001.

A. Coussement, O. Gicquel, and G. Degrez. Large eddy simulation of a pulsed jet in crossflow. *J. Fluid Mech.*, 695:1–34, 2012.

S. C. Crow and F. H. Champagne. Orderly structure in jet turbulence. *J. Fluid Mech.*, 48 (3):547–591, 1971.

E. T. Curran. Scramjet engines: the first forty years. *Journal of Propulsion and Power*, 17 (6):1138–1148, 1996.

P. V. Danckwerts. The definition and measurement of some characteristics of mixtures. *Applied Science Research*, A3:279–296, 1952.

J. Davitian, D. Getsinger, C. Hendrickson, and A. R. Karagozian. Transition to global instability in transverse-jet shear layers. *J. Fluid Mech.*, 661:294–315, 2010a.

J. Davitian, C. Hendrickson, D. Getsinger, R. T. M'Closkey, and A. R. Karagozian. Strategic control of transverse jet shear layer instabilities. *AIAA Journal*, 48(9):2145–2156, 2010b.

J. A. Denev, J. Fr ohlich, C. J. Falconi, and H. Bockhorn. Direct numerical simulation, analysis and modelling of mixing processes in a round jet in crossflow. *"Micro and Macro Mixing"*, H.Bockhorn, D.Mewes, W.Peukert, and H.-J.Warnecke, Eds., Springer:143–164, 2010.

P. E. Dimotakis and P. L. Miller. Some consequences of the boundedness of scalar fluctuations. *Physics of Fluids A: Fluid Dynamics*, 2(11):1919–1920, 1990.

W. L. Ditto, M. L. Spano, H. T. Savage, S. N. Rauseo, J. Heagy, and E. Ott. Experimental observation of a strange nonchaotic attractor. *Phys. Rev. Lett.*, 65:533–536, 1990.

S. L. Dixon and C. Hall. *Fluid Mechanics and Thermodynamics of Turbomachinery*. Butterworth-Heinemann, 7th edition, 2013.

D. R. Dowling and P. E. Dimotakis. Similarity of the concentration field of gas-phase turbulent jets. *J. Fluid Mech.*, 218:109–141, 1990.

P. W. Duck and M. R. Foster. The inviscid stability of a trailing line vortex. *Journal of Applied Mathematics and Physics (ZAMP)*, 31:524–532, 1980.

W. A. Eckerle and H. Scheibani adn J. Awad. Experimental measurements of vortex development downstream of a lobed forced mixer. *J. Eng. Gas Turbines Power*, 114:63, 1992.

S. V. Ekkad, S. Ou, and R. B. River. Effect of jet pulsation and duty cycle on film cooling from a single jet on a leading edge model. *Journal of Turbomachinery*, 128(3):564–571, 2006.

H. F. Elattar, A. Fouda, and A. S. Bin-Mahfouz. Cfd modelling of flow and mixing characteristics for multiple rows jets injected radially into a non-reacting crossflow. *Journal of Mechanical Science and Technology*, 30(1):185–198, 2016.

R. Eldredge and J. Bons. Active control of a separating boundary layer with steady vortex generating jets- detailed flow measurements. *42nd AIAA Aerospace Sciences Meeting and Exhibit*, 2004.

A. Eroglu and R. E. Breidenthal. Structure, penetration, and mixing of pulsed jets in crossflow. *AIAA Journal*, 39(3):417–423, 2001.

R. Fearn and R. Weston. Vorticity associated with a jet in a crossflow. *AIAA*, 12:1666–1671, 1974.

D. J. Forliti, D. V. Salazar, and A. J. Bishop. Physics-based scaling laws for confined and unconfined transverse jets. *Experiments in Fluids*, 56(36):1–16, 2015.

M. J. Foust, D. Thomsen, R. Stickles, C. Cooper, and W. Dodds. Development of the ge aviation low emissions taps combustor for next generation aricraft engines. *50th AIAA Aerospace Science Meeting*, 2012.

A. M. Fraser and H. L. Swinney. Independent coordinates for strange attractors from mutual information. *Phys. Rev. A*, 33(1134), 1986.

T. F. Fric and A. Roshko. Vortical structure in the wake of a transverse jet. *J. Fluid Mech.*, 279:1–47, 1994.

F. Gallaire and J.-M. Chomaz. Mode selection in swirling jet experiments: a linear stability analysis. *J. Fluid Mech.*, 494:223–253, 2004.

L. Gao and S. C. M. Yu. Development of the trailing shear layer ing a starting jet during pinch-off. *J. Fluid Mech.*, 700:382–405, 2012.

A. K. Garg and S. Leibovich. Spectral characteristics of vortex breakdown flowfields. *Physics of Fluids*, 22:2053–2064, 1979.

D. R. Getsinger. *Shear Layer Instabilities adn Mixing in Variable Density Transverse Jet Flows*. PhD thesis, University of California, Los Angeles, 2012.

D. R. Getsinger, C. Hendrickson, and A. R. Karagozian. Shear layer instabilities in low-density transverse jets. *Experiments in Fluids*, 53:783–801, 2012.

D. R. Getsinger, L. Gevorkyan, O.I. Smith, and A. R. Karagozian. Structural and stability characteristics of jets in crossflow. *J. Fluid Mech.*, 760:342–367, 2014.

L. Gevorkyan. *Structure and Mixing Characterization of Variable Density Transverse Jet Flows*. Phd dissertation, University of California, Los Angeles, 2015.

L. Gevorkyan, D. Getsinger, O. I. Smith, and A. R. Karagozian. Structural and stability characteristics of jets in crossflow. *AIAA*, 2014. Paper 2014-0230.

L. Gevorkyan, T. Shoji, D. R. Getsinger, O. I. Smith, and A. R. Karagozian. Transverse jet mixing characteristics. *J. Fluid Mech.*, 790:237–274, 2016.

L. Gevorkyan, T. Shoji, W. Y. Peng, and A. R. Karagozian. Influence of the velocity field on scalar transport in gaseous transverse jets. *J. Fluid Mech.*, 834:173–219, 2018.

J. B. Ghandhi. Spatial resolution and noise considerations in determining scalar dissipation rate from passive scalar image data. *Experiments in Fluids*, 40:577–588, 2006.

M. Gharib, E. Rambod, and K. Shariff. A universal time scale for vortex ring formation. *J. Fluid Mech.*, 360:121–141, 1998.

M. Gruber, J. Donbar, C. Carter, and K-Y Hsu. Mixing and combustion studies using cavity-based flameholders in a supersonic flow. *Journal of Propulsion and Power*, 20(5): 769–778, 2004.

Y. Guan, M. Murugesan, and L. K. B. Li. Strange nonchaotic and chaotic attractors in a self-excited thermoacoustic oscillator subjected to external periodic forcing. *Chaos*, 28 (093109), 2018.

O. Gubanov and L. Cortelezzi. Towards the design of an optimal mixer. *J. Fluid Mech.*, 651:27–53, 2010.

I. Gursul. Unsteady flow phenomena over delta wings at high angle of attack. *AIAA Journal*, 32(2):225–231, 1994.

I. Gursul. Effects of nonaxisymmetric forcing on a swirling jet with vortex breakdown. *Journal of Fluids Engineering*, 118:316–321, 1996.

E. Gutmark and C. M. Ho. On the preferred modes of the spreading rates of jets. *Physics of Fluids*, 26:2932–2938, 1983.

E. J. Gutmark and F. F. Grinstein. Flow control with noncircular jets. *Annual Review of Fluid Mechanics*, 31:239–272, 1999.

E. J. Gutmark, K. C. Shadow, T. P. Parr, D. M. Hanson-Parr, and K. J. Wilson. Noncircular jets in combustion systems. *Experiments in Fluids*, 7:248, 1989.

M. P. Hallberg and P. J. Strykowski. On the universality of global modes in low-density axisymmetric jets. *J. Fluid Mech.*, 569:493–507, 2006.

D. Hammond and L. Redekopp. Global dynamics of symmetric and asymmetric wakes. *J. Fluid Mech.*, 331:231–260, 1997.

J-C Han, S. Dutta, and S. Ekkad. *Gas Turbine Heat Transfer and Cooling Technology*. CRC Press, 2nd edition, 2012.

R. K. Hanson, J. M. Seitzman, and P. H. Haul. Planar laser-fluorescence imaging of combustion gases. *Applied Physics*, 50(B):441–454, 1990.

E. W. Harris. *As of Yet: Untitled*. PhD thesis, University of California, Los Angeles, 2020.

E. W. Harris, A. Besnard, and A. R. Karagozian. Effect of tabs on transverse jet nearfield vorticity dynamics. *Submitted for Publication*, 2020a.

E. W. Harris, A. Besnard, and A. R. Karagozian. Effect of tabs on transverse jet instabilities, structure and mixing. *Submitted for Publication*, 2020b.

E. F. Hasselbrink and M. G. Mungal. Transverse jets and jet flames. part 1. scaling laws for strong transverse jets. *J. Fluid Mech.*, 443:1–25, 2001.

B. A. Haven and M. Kurosaka. Kidney and anti-kidney vortices in crossflow jets. *J. Fluid Mech.*, 352:27–64, 1997.

J. Heicklen. The fluorescence and phosphorescence of biacetyl vapor and acetone vapor. *Journal of the American Chemistry Society*, 81(15):3863–3866, 1958.

C. Hendrickson. *Identification and Control of the Jet in Crossflow*. PhD thesis, University of California, Los Angeles, 2012.

C. Hendrickson and R. M'Closkey. Phase compensation strategies for modulated-demodulated control with application to pulsed jet injection. *ASME Journal of Dynamic Systems, Measurement, and Control*, 134, 2012.

A. Hilgers and B. J. Boersma. Optimization of turbulent jet mixing. *Fluid Dynamics Research*, 29:345–368, 2001.

P. Hill and C. Peterson. *Mechanics and Thermodynamics of Propulsion*. Pearson, 2nd edition, 1991.

W. G. Hill and P. R. Greene. Increased turbulent jet mixing rates obtained by self-excited acoustic oscillations. *Journal of Fluid Engineering*, 99(3):520–525, 1977.

C. M. Ho and E. J. Gutmark. Vortex induction and mass entrainment in a small-aspect ratio elliptic jet. *J. Fluid Mech.*, 179:383, 1987.

J. D. Holdeman. Mixing of multiple jets in a confined subsonic crossflow. *Prog. Energy Comb. Sci.*, 19(1):31–70, 1993.

H. Hu, T. Saga, T. Kobayashi, and N. Taniguchi. Passive control on jet mixing flows by using vortex generators. *Proceedings of the Sixth Triennial International Symposioum on Fluid Control, Measurement and Visualization*, 2000.

P. Huerre. *Perspectives in Fluid Dynamics: A Collective Introduction to Current Research*. Cambridge University Press, 2000.

P. Huerre and P. A. Monkewitz. Absolute and convective instabilities in free shear flows. *J. Fluid Mech.*, 159:151–168, 1985.

P. Huerre and P. A. Monkewitz. Local and global instabilities in spatially developing flows. *Annual Review of Fluid Mechanics*, 22:473–537, 1990.

R. W. Humble, G. N. Henry, and W. J. Larson. *Space Propulsion Analysis and Design*. McGraw Hill Publishing, 2nd edition, 1995.

H. S. Husain and A. K. M. F. Hussain. Controlled excitation of elliptic jets. *Physics of Fluids*, 26:2763, 1983.

A. K. M. F. Hussain. Coherent structures and turbulence. *J. Fluid Mech.*, 173:303, 1986.

A. K. M. F. Hussain and K.B. M. Q. Zaman. The free shear layer tone phenomenon and probe interference. *J. Fluid Mech.*, 87:349–383, 1978.

M. Ilak, P. Schlatter, S. Bagheri, and D. S. Henningson. Bifurcation and stability analysis of a jet in crossflow. *J. Fluid Mech.*, 696:94–121, 2012.

P. S. Iyer and K. Mahesh. A numerical study of shear layer characteristics for low-speed transverse jets. *J. Fluid Mech.*, 790:275–307, 2016.

S. Jendoubi and P. J. Strykowski. Absolute and convective instability of axisymmetric jets with external flow. *Physics of Fluids*, 6:3000–3009, 1994.

H. Johari. Scaling of fully pulsed jets in crossflow. *AIAA Journal*, 44(11):2719–2725, 2006.

H. Johari, M. Pacheco-Tougas, and J. C. Hermanson. Penetration and mixing of fully modulated turbulent jets in crossflow. *AIAA Journal*, 37(7):842–850, 1999.

M. P. Juniper, L. K. B. Li, and J. W. Nichols. Forcing of self-excited round jet diffusion flames. *Proceedings of the Combustion Institute*, 32:1191–1198, 2009.

T. Kambe, T. Minota, and M. Takaoka. Oblique collision of two vortex rings and its acoustic emmisions. *Physical Review E*, 48(3):1866–1881, 1993.

Y. Kamotani and I. Greber. Experiments on a turbulent jet in a cross flow. *AIAA Journal*, 10(11):1425–1429, 1972.

H. Kantz and T. Schreiber. *Nonlinear Time Series Analysis*. Cambridge University Press, 2nd edition, 2003.

A. R. Karagozian. An analytical model for the vorticity associated with a transverse jet. *AIAA Journal*, 24:429–436, 1986.

A. R. Karagozian. Transverse jets and their control. *Progress in Energy and Combustion Science*, 36:531–553, 2010.

A. R. Karagozian. The jet in crossflow. *Physics of Fluids*, 26(101303):1–17, 2014.

A. R. Karagozian, K. S. C. Wang, A-T Le, and O. I. Smith. Transverse gas jet injection behind a rearward-facing step. *Journal of Propulsion and Power*, 12(6):1129–1136, 1996.

J. F. Keffer and W. D. Baines. The round turbulent jet in a cross-wind. *J. Fluid Mech.*, 15 (4):481–496, 1963.

R. M. Kelso and A. J. Smits. Horseshoe vortex systems resulting from the interaction between a laminar boundary layer and a transverse jet. *Physics of Fluids*, 7:153–158, 1995.

R. M. Kelso, T. T. Lim, and A. E. Perry. An experimental study of round jets in cross-flow. *J. Fluid Mech.*, 306:111–144, 1996.

J. L. Kerrebrock. *Aircraft Engines and Gas Turbines*. The MIT Press, 2nd edition, 1992.

W. Kollman. The pdf approach to turbulent flow. *Theoratical and Computational Fluid Dynamics*, 1(5):249–285, 1990.

P. S. Kothnur and N. T. Clemens. Effects of unsteady strain rate on scalar dissipation structures in turbulent planar jets. *Physics of Fluids*, 17, 2005.

A. Krothapalli, L. Lourenco, and J. M. Buchlin. Separated flow upstream of a jet in crossflow. *AIAA Journal*, 28(3):414–420, 1990.

A. Kukukova, J. Aubin, and S. M. Kresta. A new definition of mixing and segregation: three dimensions of a key process variable. *Chemical Engineering Research and Design*, 87:633–647, 2009.

S. M. Kusek, T. C. Corke, and P. Reisenthel. Seeding of helical modes in the initial region of an axisymmetric jet. *Experiments in Fluids*, 10:116–124, 1990.

D. M. Kuzo. *An Experimental Study of the Turbulent Transverse Jet*. PhD thesis, California Institute of Technology, 1995.

D. M. Kyle and K. R. Sreenivasan. The instability and breakdown of a round varaiable-density jet. *J. Fluid Mech.*, 249:619–664, 1993.

M. J. Landman and P. G. Saffman. The three-dimensional instability of strained vortices in a viscous fluid. *Physics of Fluids*, 30:2339–2342, 1987.

J. Lee and R. S. Brodkey. Turbulent motion and mixing in a pipe. *AIChE*, 10(2):187–193, 1964.

S. W. Lee, J. S. Lee, and S. T. Ro. Experimental study on the flow characteristics of streamwise inclined jets in crossflow on flat plate. *International Gas Turbine and Aeroengine Congress and Exposition*, 1992. Paper 92-GT-181.

T. Lee and R. Budwig. Two improved methods for low-speed hot-wire calibration. *Measurement Science and Technology*, 2:643–646, 1991.

E. LeGrives. Mixing process induced by the vorticity associated with the penetration of a jet into a cross flow. *J. Eng. Power*, 100(3):455–475, 1978.

S. Leibovich. Vortex stability and breakdown: survey and extension. *AIAA Journal*, 22(9): 1192–1206, 1983.

M. Lessen, P. Singh, and F. Paillet. The stability of a trailing line vortex. part 1. inviscid theory. *J. Fluid Mech.*, 63(4):753–763, 1974.

L. K. B. Li. *Forcing of Global Unstable Jets and Flames*. PhD thesis, University of Cambridge, 2011.

L. K. B. Li and M. P. Juniper. Lock-in and quasiperiodicity in a forced hydrodynamically self-excited jet. *J. Fluid Mech.*, 726:624–655, 2013a.

FD. Liepmann and M. Gharib. The role of streamwise worticity in the near-field entrainent of round jets. *J. Fluid Mech.*, 245:643–668, 1992.

K. M. K. Lim, T. H. New, and H. M. Tsai. Vortex dynamics in jets from v-notched nozzles. *2nd AIAA Flow Control Conference*, 2004.

T. T. Lim. On the role of kelvin-helmholtz-like instability in the formation of turbulent vortex rings. *Fluid Dynamics Research*, 27(1):47–56, 1997.

T. T. Lim, R. M. Kelso, and A. E Perry. A visual study of vortex rings fired transversely into a cross-flow. *13th Australasian Fluid Mechanics Conference*, 2:961–964, 1998.

D. S. Liscinsky, B. True, and J. D. Holdeman. Effect of initial conditions on a single jet in crossflow. *NASA technical memorandum 106477*, 1994.

D. S. Liscinsky, B. True, and J. D. Holdeman. Effects of initial conditions on a single jet in crossflow. *AIAA*, 1995. Paper 95-2998.

Z. Liu and Z. Zhu. Strange nonchaotic attractors from quasiperiodically forced ueda's circuit. *Int. J. Bifurcation and Chaos*, 6:1383–1388, 1996.

E. K. Longmire and L. H. Duong. Bifurcating jets generated with stepped and sawtoothed nozzles. *Physics of Fluids*, 8:978–992, 1996.

E. K. Longmire, J. K. Eaton, and C. J. Elkins. Control of jet structure by crown-shaped nozzles. *AIAA Journal*, 30:505, 1992.

A. Lozano. *Laser-Excited Luminescent Tracers for Planar Concentration Measurements in Gaseous Jets*. PhD thesis, Stanford, 1992.

A. Lozano, B. Yip, and R. K. Hanson. Acetone: A tracer for concentration measurements in gaseous flows by planar laser-induced fluorescence. *Experiments in Fluids*, 13:369–376, 1992.

K. Mahesh. The interaction of jets with crossflow. *Annu. Rev. Fluid Mech.*, 45:379–407, 2013.

R. J. Margason. Fifty years of jet in cross flow research. *AGARD-CP-534*, 1993.

Y. M. Marzouk and A. F. Ghoniem. Vorticity structure and evolution in a transverse jet. *J. Fluid Mech.*, 575:267–305, 2007.

G. Mathew, I. Mezić, and L. Petzold. A multiscale measure for mixing and its application. *42nd IEEE Conference on Decision and Control*, 2003.

G. Mathew, I. Mezić, and L. Petzold. A multiscale measure of mixing. *Physica D*, 211:23–46, 2005.

G. E. Mattingly and C. C. Chang. Unstable waves on an axisymmetric jet column. *J. Fluid Mech.*, 65(3):541–560, 1974.

E. W. Mayer and K. G. Powell. Viscous and inviscid instabilities of a trailing vortex. *J. Fluid Mech.*, 245:91–114, 1992.

R. G. McKinney, D. Sepulveda, W. Sowa, and A. K. Cheung. The pratt adn whitney talon x low emissions combustor: revolutionary results with evolutionary technology. *45th AIAA Aerospace Sciences Meeting and Exhibit*, 2007.

R. T. M'Closkey, J. King, L. Cortelezzi, and A. R. Karagozian. The actively controlled jet in crossflow. *J. Fluid Mech.*, 452:325–335, 2002.

B. K. McMillan, J. L. Palmer, and R. K. Hanson. Temporally resolved, two-line fluorescence imaging of no temperature in a transverse jet in a supersonic cross flow. *Applied Optics*, 32(36):7532–7542, 1993.

S. Megerian, J. Davitian, L.S. de B. Alves, and A. R. Karagozian. Transverse-jet shear-layer instabilities. part 1. experimental studies. *J. Fluid Mech.*, 593:93–129, 2007.

K. E. Meyer, J. M. Pedersen, and O. Özcan. A turbulent jet in crossflow analysed with proper orthogonal decomposition. *J. Fluid Mech.*, 583:199–227, 2007.

A. Michalke. Instabilitat eines kompressiblem ruden friestrahls unter beruck-sichtingung des einflusses der strahlgrenzschichtdicke. *Z. Fluzwiss*, 9:319–328, 1971.

A. Michalke. Survey on jet instability theory. *Prog. Aerospace Sci.*, 21:159–199, 1984.

I. Milanovic, K. B. M. Q. Zaman, and T. J. Bencic. Unstead wake vortices in jets in crossflow. *Journal of Visualization*, 15(1):45–55, 2012.

D. N. Miller, P. J. Yagle, and J. W. Hamstra. Fluidic throat skewing for thrust vectoring in fixed-geometry nozzles. *AIAA*, 1999. Paper 99-0365.

M. G. Mitchell, O. I. Smith, and A. R. Karagozian. Passive fuel-air mixing and emissions control via lobed injectors. *AIAA Journal*, 42(1):61–69, 2004.

M. F. Modest. *Radiative Heat Transfer*. Academic Press, 3rd edition, 2013.

P. A. Monkewitz, D. W Bechert adn B. Barsikow, and B. Lehmann. Self-excited oscillations and mixing in a heated round jet. *J. Fluid Mech.*, 213:611–639, 1990.

Z. M. Moussa, J. W. Trischka, and S. Eskinazi. The nearfield in the mixing of a round jet with a cross-stream. *J. Fluid Mech.*, 80:49–80, 1977.

F. Muldoon and S. Acharya. Direct numerical simulation of pulsed jets in crossflow. *Computers & Fluids*, 39:1745–1773, 2010.

S. Muppidi and K. Mahesh. Study on trajectories of jets in crossflow using direst numerical simulations. *J. Fluid Mech.*, 530:81–100, 2005.

S. Muppidi and K. Mahesh. Direct numerical simulation of round turbulent jets in crossflow. *J. Fluid Mech.*, 574:59–84, 2007.

S. Narayanan, P. Barooah, and J. M. Cohen. Dynamics and control of an isolated jet in crossflow. *AIAA Journal*, 41(15):2316–2330, 2003.

T. H. New, T. T. Lim, and S. C. Luo. On the effects of velocity profiles on the topological structures of a jet in crossflow. *TSFP-1 Proceedings*, pages 647–652, 1999.

T. H. New, T. T. Lim, and S. C. Luo. Elliptic jets in cross flow. *J. Fluid Mech.*, 494:119–140, 2003.

T. H. New, T. T. Lim, and S. C. Luo. Effects of jet velocity profiles on a round jet in cross-flow. *Experiments in Fluids*, 40:859–875, 2006.

T. T. Nguyen and A. R. Karagozian. Liquid fuel jet in subsonic crossflow. *Jornal of Propulsion and Power*, 8(1):21–29, 1992.

C. E. Niederhaus, F. H. Champagne, and J. W. Jaobs. Scalar transport in a swirling transverse jet. *AIAA Journal*, 35(11):1697–1704, 1997.

C. O'farrell and J. O. Dabiri. A lagrangian approach to identifying vortex pinch-off. *Chaos*, 20, 2010.

T. S. Oh and J. A. Schetz. Finite element simulation of complex jets in a crossflow for v/stol applications. *J. Aircraft*, 27:389–399, 1990.

M. N. O. O'Sullivan, J. K. Krasnodebski, I. A. Waitz, and E. M. Greitzer adm C. S. Tan. Computational study of viscous effects on lobed mixer flow features and performance. *Journal of Propulsion and Power*, 12(3):449–456, 1996.

J. Panda and D. K. McLaughlin. Experiments on the instabilities of a swirling jet. *Physics of Fluids*, 6:263–276, 1994.

S. Pavithran and L. G. Redekopp. The absolute-convective transition in subsonic mixing layers. *Physics of Fluids A: Fluid Dynamics*, 1:1736–1739, 1989.

R. A. Petersen and M. M. Samet. On the preferred mode of jet instability. *J. Fluid Mech.*, 194:153–173, 1988.

S. D. Peterson and M. W. Plesniak. Evolution of jets emanating from short holes into crossflow. *J. Fluid Mech.*, 503:57–91, 2004.

P. Plaschko. Helical instabilities of slowly divergent jets. *J. Fluid Mech.*, 92(2):209–215, 1979.

M. W. Plesniak and D. M. Cusano. Scalar mixing in a confined rectangular jet in crossflow. *J. Fluid Mech.*, 524:1–45, 2005.

B. E. Poling, J. M. Prausnitz, and J. P. O'Connell. *The Properties of Gases and Liquids.* McGraw-Hill, New York, 5th edition, 2001.

A. Prasad, S. S. Negi, and R. Ramaswamy. Strange nonchaotic attractors. *Int. J. of Bifurcation and Chaos*, 11(2):291–309, 2001.

B. D. Pratte and W. D. Baines. Profiles of the round turbulent jet in a cross flow. *Journal of the Hydraulics Division ASCE*, 92:53–64, 1967.

M. Provansal, C. Mathis, and L. Boyer. Bernard-von karman instability: transient and forced ragimes. *J. Fluid Mech.*, 182:1–22, 1987.

W. R. Quinn. Turbulent free jet flows issuing from sharp-edged rectangular slots: the influence of slot aspect-ratio. *Exp. Therm. Fluid Sci.*, 5:203–215, 1992.

L. J. Radziemski, R. W. Solarz, and J. A. Paisner, editors. *Laser Spectroscopy and Its Applications*, volume 11 of *Optical Engineering.* Marcel Dekker, New York and Basel, 1987.

J. W. Ramsey and R. J. Goldstein. Interaction of a heated jet with a deflecting stream. *Journal of Heat Transfer*, 93(4):365–372, 1971.

S. Rashidi, M. Hayatdavoodi, and J. A. Esfahani. Vortex shedding suppresion and wae control: a review. *Ocean Engineering*, 126:57–80, 2016.

M. A. Regan and K. Mahesh. Global linear stability analysis of jets in cross-flow. *J. Fluid Mech.*, 828:812–836, 2017.

M. A. Regan and K. Mahesh. Adjoint sensitivity and optimal perturbations of the low-speed jets in cross-flow. *J. Fluid Mech.*, 877:330–372, August 2019.

W. C. Reynolds, D. E. Parekh, P. J. D. Juvet, and M. J. D. Lee. Bifurcating and blooming jets. *Annual Review in Fluid Mechanics*, 35(1):295–315, 2003.

P. J. W. Roberts and G. Toms. Inclined dense jets in flowing current. *J. Hydraul. Eng.*, 113 (3):323–340, 1987.

F. W. Roos and J. T. Kegelman. Recent explorations of leading-edge vortex flowfields. *NASA High Angle-of-attack Technology Conference*, 1990.

M. Rudman. Simulation of the near field of a jet in cross flow. *Experimental Thermal and Fluid Science*, 12:134–141, 1996.

M. Samimy, J.-H. Kim, J. Kastner, I. Adamoich, and Y. Utkin. Active control of high-speed and high-reynolds-number jets using plasma actuators. *J. Fluid Mech.*, 578:305–330, 2007.

S. Samuelsen. Rich burn, quick-mix, lean burn (rql) combustor. *The Gas Turbine Handbook*, pages 227–233, 2016.

A. Sau, T.-W. Hsu, S.-H. Ou, and R. R. Hwang. Growth of kidney and antikidney vortices over a square. *Physics of Fluids*, 18(12), 2006. 128102-1.

R. Sau and K. Mahesh. Passive scalar mixing in vortex rings. *J. Fluid Mech.*, 582:449–461, 2007.

R. Sau and K. Mahesh. Dynamics and mixing of vortex rings in crossflow. *J. Fluid Mech.*, 604:389–409, 2008.

R. Sau and K. Mahesh. Optimization of pulsed jets in crossflow. *J. Fluid Mech.*, 653:365–390, 2010.

P. Schlatter, S. Bagheri, and D. S. Henningson. Self-sustained global oscillations in a jet in crossflow. *Theoratical and Computational Fluid Dynamics*, 25:29–146, 2011.

F. Schlegel, D. Wee, Y. Marzouk, and A. Ghoniem. Contributions of the wall boundary layer to the formation of the counter-rotating vortex pair in transverse jets. *J. Fluid Mech.*, 676:461–490, 2011.

P. J. Schmid and D. S. Henningson. *Stability and Transition in Shear Flows*. Springer, 2001.

T. Schuller, J. King, A. Majamaki, A. R. Karagozian, and L. Cortelezzi. An experimental study of acustically controlled gas jets in crossflow. *Bull. Am. Phys. Soc.*, 44(8):111, 1999.

A. Sevilla, J. M. Gordillo, and C. Martinez-Bazan. The effect of the diameter ratio on the shear absolute and convective instability of free coflowing jets. *Physics of Fluids*, 14(9): 3028–3038, 2002.

J. Shan and P. Dimotakis. Reynolds-number effects and anisotropy in transverse-jet mixing. *J. Fluid Mech.*, 566:47–96, 2006.

S. Shapiro, J. King, R. T. M'Closkey, and A. R. Karagozian. Optimization of controlled jets in crossflow. *AIAA Journal*, 44:1292–1298, 2006.

T. Shoji. *Mixing and Structural Characteristics of Unforced and Forced Jets in Crossflow*. Phd dissertation, University of California, Los Angeles, 2017.

T. Shoji, A. Besnard, E. W. Harris, R. T. M'Closkey, and A. R. Karagozian. Effects of axisymetric square-wave excitation on transverse jet structure and mixing. *AIAA Journal*, 57(5):1862–1876, 2019.

T. Shoji, E. W. Harris, A. Besnard, and A. R. Karagozian. Effects of sinusoidal excitation on transverse jet dynamics structure and mixing. *AIAA Journal*, 2020a.

T. Shoji, E. W. Harris, A. Besnard, S. G. Schein, and A. R. Karagozian. On the origins of transverse shear layer instability transition. *J. Fluid Mech.*, 890(A7), 2020b.

T. Shoji, E. W. Harris, A. Besnard, S. G. Schein, and A. R. Karagozian. Transverse jet lock-in and quasiperiodicity. *Phys. Rev. Fuids*, 5(013901), 2020c.

M. Shusser and M. Gharib. Energy and velocity of a forming vortex ring. *Physics of Fluids*, 12(3):618–621, 2000.

H. Simo and P. Woafo. Bifurcation structure of a van der pol oscillator subjected to nonsinusoidal excitation. *International Journal of Bifurcation and Chaos*, 22(1):1–8, 2011.

P. I. Singh and M. S. Uberoi. Experiments on vortex stability. *Physics of Fluids*, 19(12): 1858–1863, 1976.

L. Sirovich. Turbulence and the dynamics of coherent structures. *Q. Appl. Maths*, 45: 561–590, 1987.

L. L. Smith, A. J. Majamaki, I. T. Lam, O. Delabroy, A. R. Karagozian, F. E. Marble, and O. I. Smith. Mixing enahncement in a lobed injector. *Physics of Fluids*, 9(3):667–678, 1997.

S. H. Smith. *The Scalar Concentration Field of the Axisymmetric Jet in Crossflow*. PhD thesis, Stanford, 1996.

S. H. Smith and M. G. Mungal. Mixing, structure, and scaling of the jet in crossflow. *J. Fluid Mech.*, 357:83–122, 1998.

D. B. de Souza, R. B. Freitas, and L. S. de B. Alves. Viscous and inviscid threshold for convective and absolute stability of axisymmetric free jet flows. *Not Set*, 2020.

K. R. Sreenivasan, S. Raghu, and D. Kyle. Absolute instability in variable density round jets. *Experiments in Fluids*, 7(5):309–317, 1989.

P. J. Strange and D. G. Crighton. Spinning modes on axisymmetric jets. part 1. *J. Fluid Mech.*, 134:231–245, 1983.

P. J. Strykowski and D. L. Niccum. The stability of countercurrent mixing layers in circular jets. *J. Fluid Mech.*, 227:309–343, 1991.

P. J. Strykowski and D. L. Niccum. The influence of velocity and density ratio on the dynamics of spatially developing mixing layers. *Physics of Fluids A: Fluid Dynamics*, 4 (4):770–781, 1992.

L. K. Su and M. G. Mungal. Simultaneous measurements of scalar and velocity field evolution in turbulent crossflowing jets. *J. Fluid Mech.*, 513:1–45, 2004.

N. Syred and J. M. Beer. Combustion in swirling flows: a review. *Combustion and Flame*, 23:143–201, 1974.

F. Takens. Detecting strange attractors in turbulence. *Dynamical Systems and Turbulence*, 898:366–381, 1981.

A. Talamelli and I. Gavarini. Linear instability characteristics of incompressible coaxial jets. *Flow Turbulence Combust*, 76:221–240, 2006.

M. C. Thurber, F. Grisch, B. J. Kirby, M. Votsmeier, and R. K. Hanson. Measurements and modeling of acetone laser-induced fluorescence with implications for termoerature-imaging diagnostics. *Applied Optics*, 37:4963–4978, 1998.

K. Toyoda and A. K. M. F. Hussain. Vortical structures of noncircular jets. *4th Proc. Asian Congr. Fluid Mech.*, pages A117–127, 1989.

I. van Cruyningen. *Quantitative Imaging of Turbulent Gaseous Jes Using Planar Laser-Induced Fluorescence*. PhD thesis, Stanford, 1990.

P. J. Vermeulen and W. K. Yu. An experimental study of the mixing by an acoustically pulsed axisymmetrical air-jet. *International Journal of Turbo & Jet Engines*, 4(3-4):225–237, 1987.

P. J. Vermeulen, J. Odgers, and V. Ramesh. Acoustic control of dilution-air mixing in a gas turbine combustor. *Journal of Engineering for Gas Turbines and Power*, 104(4):844–852, 1982.

P. J. Vermeulen, V. Ramesh, and W. K. Yu. Measurements of entrainment by acoustically pulsed axisymmetric air jets. *ASME Journal of Engineering for Gas Turbines and Power*, 108(3):479–484, 1986.

P. J. Vermeulen, C.-F. Chin, and W. K. Yu. An experimental study of the mixing behavior of an acoustically pulsed air jet with a confined crossflow. *AIAA*, 1988. Paper 88-3296.

P. J. Vermeulen, P. Grabinski, and V. Ramesh. Mixing of an acoustically excited air jet with a confined hot crossflow. *Journal of Engineering for Gas Turbines and Power*, 114:46–54, 1992.

P. J. Vermeulen, V. Ramesh, G. C. Meng, D. N. Miller, and N. Domel. Air ejector pumping enhancement through pulsing primary flow. *2nd AIAA Flow Control Conference*, 2004. Paper 2004-2621.

G. H. Wang and N. T. Clemens. Effects of imaging system blur on measurements of flow scalars and scalar gradients. *Experiments in Fluids*, 37:194–205, 2004.

K. S. C. Wang, O. I. Smith, and A. R. Karagozian. In-flight imaging of gas jets injected into subsonic and supersonic crossflows. *AIAA Journal*, 33(12):2259–2263, 1995.

D. R. Webster and E. K. Longmire. Vortex dynamics in jets from inclined nozzles. *Physics of Fluids*, 9, 1997.

J. Westerweel. Fundamentals of digital particle image velocimetry. *Meas. Sci. Technol.*, 8: 1379–1392, 1997.

B. Wieneke. Stereo-piv using self-calibration on particle images. *Experiments in Fluids*, 39: 267–280, 2005.

C. R. Wilke. A viscosity equation for gas mixtures. *Journal of Chemical Physics*, 18(4): 517–519, 1950.

R. W. Wlezien and V. Kibens. Passive control of jets with indeterminate origins. *AIAA Journal*, 24(8):1263–1270, 1986.

P. Wooler. Flow of a circular jet into a cross flow. *Journal of Aircraft*, 6(3):283–284, 1969.

J. M. Wu, A. D. Vakili, and F. M. Yu. Investigation of the interacting flow of nonsymmetric jets in cross flow. *AIAA Journal*, 26(8):940–947, 1988.

G. Xu and R. A. Antonia. Effect of different initial conditions on a turbulent round free jet. *Experiments in Fluids*, 33:677–683, 2002.

P. J. Yagle, D. N. Miller, K. B. Ginn, and J. W. Hamstra. Demonstration of fluidic throat skewing for thrust vectoring in structurally fixed nozzles. *ASME Journal of Engineering for Gas Turbines and Power*, 123(3):502–507, 2001.

T. Yang and K. Bilimgut. Experimental results of strange nonchaotic phenomenon in a second order quasi-periodically forced electronic circuit. *Phys. Lett.*, A236:494–504, 1997.

L. L. Yuan and R. L. Street. Trajectory and entrainment of a round jet in crossflow. *Physics of Fluids*, 10:2323–2335, 1998.

K. B. M. Q. Zaman. Streamwise vorticity generation and mixing enhancement in free jet by "delta tabs". *AIAA*, 1993. Paper 93-3253.

K. B. M. Q. Zaman. Spreading characteristics and thrust of jets from asymmetric nozzles. *NASA Technical Memorandum*, 1996a. NASA-TM-107132.

K. B. M. Q. Zaman. Axis switching and spreading of an asymmetrical jet: the role of coherent structure dynamics. *J. Fluid Mech.*, 1996b.

K. B. M. Q. Zaman. Reduction of jet penetration in a cross-flow by using tabs. In *34th AIAA/ASME/SAE/ASEE Joint Propulsion Conference and Exhibit*, number 98, pages 3276–3284, 1998. AIAA-98-3276.

K. B. M. Q. Zaman and J. K. Foss. The effect of vortex generators on a jet in a cross-flow. *Physics of Fluids*, 9(1):106–114, 1997.

K. B. M. Q. Zaman and I. Milanovic. Control of a jet-in-crossflow by periodically oscillating tabs. *Physics of Fluids*, 24, 2012.

K. B. M. Q. Zaman, M. F. Reeder, and M. Samimy. Effect of tabs on the evaluation of an axisymmetrical jet. *NASA Technical Memorandum*, 1991. NASA-TM104472.

K. B. M. Q. Zaman, M. F. Reeder, and M. Samimy. Supersonic jet mixing enhancement by delta tabs. *AIAA*, 1992. Paper 92-3548.

K. B. M. Q. Zaman, M. F. Reeder, and M. Samimy. Control of an axisymmetric jet using vortex generators. *Physics of Fluids*, 6(2):778–793, 1994.

S. Zhang and S. P. Schneider. Molecular-mixing measurements and turbulent structure visualizations in a round jet with tabs. *AIAA*, 1994. Paper 94-3082.

W. Zhao, S. H. Frankel, and L. G. Mongeau. Effects of trailing jet instability on vortex ring formation. *Physics of Fluids*, 12:589–596, 2000.

T. Zhou, F. Moss, and A. Bulsara. Observation of strange nonchaotic attractor in a multi-stable potential. *Phys. Rev.*, A45:5394–5400, 1992.

Z. Zhu and Z. Liu. Strange nonchaotic attractors of chua's circuit with quasiperiodic excitation. *Int. J. Bifurcation and Chaos*, 7:227–238, 1997.

T. N. Zwietering. The degree of mixing in continuous flow systems. *Chemical Engineering Science*, 11(1):1–15, 1959.